Multiphysics evaluation of low CO2 and low pH cementitious matrices exposed to Mg-bearing environments

Charlotte Dewitte

Université Fédérale
Toulouse Midi-Pyrénées

THÈSE

En vue de l'obtention du
DOCTORAT DE L'UNIVERSITÉ DE TOULOUSE
Délivré par l'Institut National des Sciences Appliquées de Toulouse

Présentée et soutenue par

Charlotte DEWITTE

Le 5 janvier 2023

Multiphysics evaluation of low CO_2 and low pH cementitious matrices exposed to Mg-bearing environments

Ecole doctorale : **MEGEP - Mécanique, Energétique, Génie civil, Procédés**

Spécialité : **Génie civil**

Unité de recherche :
LMDC - Laboratoire Matériaux et Durabilité des Constructions de Toulouse

Thèse dirigée par
Laurie LACARRIERE, Alexandre DAUZERES, Mejdi NEJI et Alexandra BERTRON

Jury

Mme Josée DUCHESNE, Présidente
Mme Siham KAMALI-BERNARD, Rapporteure
M. Benoît BARY, Rapporteur
M. David BULTEEL, Examinateur
Mme Barbara LOTHENBACH, Examinatrice
Mme Laurie LACARRIERE, Directrice de thèse
Mme Alexandra BERTRON, Co-encadrante de thèse
M. Mejdi NEJI, Co-encadrant de thèse
M. Alexandre DAUZERES, Membre invité

Université Fédérale
Toulouse Midi-Pyrénées

THÈSE

En vue de l'obtention du
DOCTORAT DE L'UNIVERSITÉ DE TOULOUSE
Délivré par l'Institut National des Sciences Appliquées de Toulouse

Présentée et soutenue par

Charlotte DEWITTE

Le 5 janvier 2023

Étude multi-physique des matrices cimentaires bas carbone et bas pH exposées à des environnements contenant du magnésium

Ecole doctorale : **MEGEP - Mécanique, Energétique, Génie civil, Procédés**

Spécialité : **Génie civil**

Unité de recherche :
LMDC - Laboratoire Matériaux et Durabilité des Constructions de Toulouse

Thèse dirigée par
Laurie LACARRIERE, Alexandre DAUZERES, Mejdi NEJI et Alexandra BERTRON

Jury

Mme Josée DUCHESNE, Présidente
Mme Siham KAMALI-BERNARD, Rapporteure
M. Benoît BARY, Rapporteur
M. David BULTEEL, Examinateur
Mme Barbara LOTHENBACH, Examinatrice
Mme Laurie LACARRIERE, Directrice de thèse
Mme Alexandra BERTRON, Co-encadrante de thèse
M. Mejdi NEJI, Co-encadrant de thèse
M. Alexandre DAUZERES, Membre invité

A ceux qui sont partis trop tôt,

A Nathalie, Christiane, Maurice, Hélène,

Je n'oublierai pas la force qui vous habitait,

C'est elle qui m'a guidée jusqu'au bout.

« Le succès n'est pas final. L'échec n'est pas fatal. C'est le courage de continuer qui compte. »,
Winston Churchill

REMERCIEMENTS

Note: *the acknowledgements are mainly written in French, except when thanking non-French speakers.*

Voici venu le moment dont j'avais rêvé, qui signifierait la fin de la thèse et l'obtention du statut de docteur. Maintenant que j'y suis, la tâche s'avère moins aisée que prévue. N'oublier personne et trouver les mots justes, cela est toujours ardu. Je le dis donc d'avance : je remercie toutes les personnes que j'aurais pu oublier. Merci d'avoir été sur ma route et de m'avoir permis d'arriver ici aujourd'hui.

Je tiens à remercier dans un premier temps mon équipe encadrante : Alexandre Dauzères, Mejdi Neji, Laurie Lacarrière, Alexandra Bertron. Merci à Alexandre pour avoir toujours veillé à ce que le moral ne descende pas trop. Merci pour les belles opportunités, notamment dans le cadre d'EURAD. Merci pour m'avoir accueillie dans ton laboratoire LETIS. Merci à Mejdi. Tu étais là au quotidien et même en congé sabbatique, à l'autre bout du monde, tu as pris le temps de relire le manuscrit. Merci d'avoir été présent pour la soutenance alors que c'était en pleine nuit en Polynésie. Dès que j'avais un problème technique, je savais à qui en parler. Même si tu n'avais pas toujours la solution, on la trouvait ensemble. Merci à Laurie, qui m'a permis de faire une transition en douceur entre l'IRSN et le LMDC pour les derniers 14 mois de thèse. Merci pour les relectures pointues, pour ta disponibilité, surtout en fin de thèse où les délais étaient très serrés. Merci à Alexandra pour ton exigence qui m'a permis d'avoir des revues mineures et en faible quantité pour mon premier papier. Merci d'avoir veillé à ce que j'améliore mon vocabulaire technique, notamment en anglais.

Je tiens à remercier le jury pour s'être déplacé, même depuis un autre continent. Je remercie particulièrement Benoît Bary et Siham Kamali-Bernard pour avoir accepté de rapporter ce manuscrit et pour avoir fourni des rapports très détaillés. Merci à Josée Duchesne pour avoir présidé mon jury de thèse. Merci à David Bulteel et Barbara Lothenbach. Merci pour vos remarques et vos interrogations qui ont permis d'améliorer ce manuscrit et de soulever de nouveaux points de recherche.

Ensuite, sans financement, il n'y aurait pas eu de thèse. Je remercie donc l'IRSN d'avoir financé ces trois ans de thèse. Merci aussi au LMDC pour le support logistique et le financement de certaines expériences. Je suis aussi très reconnaissante d'avoir pu bénéficier de l'aide financière du projet européen EURAD, WP MAGIC dans laquelle ma thèse s'inscrivait. Merci aux collègues Finlandais pour leur accueil et la formation sur la technique d'autoradiographie. Thank you to Marja Siitari-Kauppi and Juuso Sammaljärvi.

Au sein de l'IRSN, je faisais partie du Service des déchets radioactifs et des transferts dans la géosphère (SEDRE). Je remercie mes collègues, membres de ce service, notamment la cheffe de service Delphine Pellegrini, pour l'accueil chaleureux et l'aide qu'ils ont pu m'apporter. Merci aussi aux collègues du LMDC. Bon courage aux doctorants qui n'ont pas encore fini. La fin est au bout du tunnel, et la lumière est éclatante !

Je tiens à remercier Ellina Bernard. Merci pour ces réunions pendant lesquelles nous avons pu échanger sur les propriétés chimiques, thermodynamiques et microstructurales des M-S-H.

Merci aux partenaires qui ont fourni des matériaux, notamment à BASF et Septodont.

Et je n'aurais pas fait cette thèse sans toutes les personnes qui m'ont guidées et aidées sur le chemin. Merci à mes professeurs de maths, physique, chimie qui ont su entretenir et développer cet amour des sciences dès mon plus jeune âge. Merci à Abdessamad Akkaoui qui m'a fait découvrir le monde de la recherche en génie civil dans le cadre de mon TIPE. Merci à mes professeurs de classes préparatoires qui m'ont encouragée. Merci à Jean-Paul Ramond de m'avoir aidée à modifier mon parcours d'étude pour qu'il soit en adéquation avec mon projet professionnel. Merci à Jean-Claude Souche et Marie Salgues qui m'ont permis d'intégrer l'option

génie civil aux Mines d'Alès pour 6 mois et qui m'ont soutenue dans ma recherche de thèse. Sans toi Marie, je n'aurais sans doute pas fait ma thèse avec l'IRSN et le LMDC.

Thank you to Iulia Mihai and Tony Jefferson. Thank you for allowing me to do this 6-month internship in your department (Architectural, Civil & Environmental Engineering) at Cardiff University. Thanks to you, I was able to experience the world of research and moreover in a foreign country. You have welcomed me wonderfully. I was able to develop language and scientific skills.

Merci à Eric Stora, Thomas Duval, Philippe Francisco et Patrick Rougeau pour m'avoir donné l'opportunité de faire mon stage de fin d'étude au sein de votre service, au CERIB. Cette expérience a conforté mon choix de continuer dans la recherche et de réaliser une thèse.

Enfin, je tiens à remercier mes amis et ma famille. Merci à ceux qui ont pu venir à ma soutenance, votre présence signifie tellement. On ne va pas se mentir, c'est long et ennuyant une soutenance, pourtant, vous étiez là. Ces trois années de thèse ne furent pas faciles, ni de tout repos. Nous avons perdu des proches, nous avons vécu la crise COVID et bien plus. J'ai pu compter sur vous.

Merci à mes amis de classes préparatoires, depuis 8 ans, vous restez présents, quoiqu'il arrive. Merci à mes colocataires, Parisiens, Toulousains. Merci surtout pour le soutien, logistique et humain lors de ces derniers mois de thèse.

Merci à ma famille. Merci à mes parents de m'avoir donné les moyens financiers d'arriver jusqu'en thèse. Merci de m'avoir soutenue, réconfortée et accueillie lors de la crise Covid. Merci à mes sœurs pour leur soutien sans faille et leur honnêteté. Merci à ma tante, Sylvie. Je sais que tu aurais vraiment voulu être là, et c'est ça qui compte.

Encore une fois, pardon à celles et ceux que j'aurais pu oublier. Merci.

Maintenant que la thèse est finie, un nouveau chemin est à tracer. Let's climb !

RÉSUMÉ

Mots clés : Matériaux cimentaires, Dégradation, Magnésium, M-S-H, Microindentation, Microstructure, Chimie

Les matériaux cimentaires utilisés dans les ouvrages de génie civil sont généralement conçus pour résister à diverses agressions ou sollicitations pendant plusieurs dizaines voire centaines d'années. Dans le cas du stockage géologique profond des déchets radioactifs (dont l'IRSN doit évaluer la sûreté), il est même demandé une durabilité de plusieurs milliers d'années pour certains composants (massifs d'appuis des dispositifs de fermeture par exemple).

En contact d'eau douce ou d'eau de mer, la lixiviation de la matrice cimentaire s'accompagne notamment d'un enrichissement en magnésium conduisant à la formation de brucite (comblant la porosité et formant une couche protectrice) et/ou de silicate de magnésium hydratés (M-S-H) dont les propriétés sont mal connues. Avec l'émergence de nouveaux liants, la composition minéralogique des bétons hydratés change et les mécanismes d'altération en milieu aqueux contenant du magnésium sont différents de ceux rencontrés dans des matrices de ciments ordinaires riches en portlandite. La formation des M-S-H est favorisée vis-à-vis de celle de la brucite. Cette thèse a donc pour objectif : (i) de comprendre les mécanismes réactionnels de l'attaque magnésienne et de la formation des M-S-H au sein des matrices cimentaires à faible teneur en calcium, (ii) d'étudier l'influence de la formation des M-S-H sur les propriétés micro-structurelles et mécaniques et (iii) de proposer des données microstructurales et mécaniques des phases issues de la dégradation (en particulier les M-S-H) intégrables dans des modèles chemo-mécaniques.

Dans un premier temps, l'influence de la composition de la pâte cimentaire sur les phases formées lors de l'attaque magnésienne a été étudiée. La présence de portlandite implique la formation de brucite. Une hydratation non complète des liants à faible rapport CaO/SiO_2 ou C/S, même en l'absence de portlandite, peut aussi provoquer la formation de brucite. Les M-S-H se forment au sein de la pâte et correspondent à un enrichissement en magnésium en profondeur.

Dans un second temps, une caractérisation des M-S-H a été réalisée sur des pâtes de M-S-H afin d'acquérir des données sur les propriétés physiques et mécaniques intrinsèques aux M-S-H et ainsi pouvoir, via une modélisation chemo-mécanique à petite échelle, comprendre les mécanismes d'altération des propriétés sous ces attaques.

Enfin, une étude multi-physique, à l'échelle mésoscopique, de l'altération de matrices à faible teneur en calcium par des eaux contenant du magnésium a été réalisée. Deux pâtes cimentaires à bas C/S (pâte modèle à base de silice colloïdale et pâte réelle à base de fumée de silice et de laitier – notée T3) ont été exposées à des solutions avec des concentrations en Mg différentes (5 et 50 mM). La caractérisation chimique et minéralogique a permis de mettre en évidence qu'une profonde décalcification a lieu en parallèle d'un fort enrichissement en magnésium de la pâte, correspondant à la formation de M-S-H. Les caractérisations micro-structurelles et mécaniques (par indentation), réalisées pour observer l'évolution le long de la dégradation, ont montré une augmentation de la porosité et une forte chute de propriétés élastiques locales malgré la formation des M-S-H. Une homogénéisation mécanique, à partir des données déterminées précédemment sur les pâtes de M-S-H, confirment que les M-S-H issus de dégradation possèdent de faibles propriétés élastiques. L'augmentation de la concentration en Mg ne modifie pas la minéralogie et la chimie de la zone dégradée mais uniquement la profondeur dégradée. Les résultats sur la pâte réelle (T3) sont similaires à ceux de la pâte modèle, validant les résultats sur cette dernière. En complément, la pâte modèle a aussi été étudiée en lixiviation pure pour comparer l'effet de la lixiviation avec celle de l'attaque magnésienne sur les liants bas C/S. Une étude via un code de transport réactif a été réalisée pour mieux comprendre les différences de cinétique et de phénoménologie. Elle confirme que la présence de magnésium accélère la dégradation.

ABSTRACT

Key-words: Cementitious materials, Degradation, Magnesium, M-S-H, Microindentation, Microstructure, Chemistry

Cementitious materials used in civil engineering structures are generally designed to withstand various stresses and strains for several decades or even hundreds of years. In the case of deep geological disposal for radioactive waste (for which the IRSN must assess safety), durability of several thousand years is even required for certain components (e.g. support blocks for closure devices).

In contact with soft or sea water, the leaching of the cement matrix is accompanied by an enrichment in magnesium leading to the formation of brucite (filling the porosity and forming a protective layer) and/or magnesium silicate hydrates (M-S-H), the properties of which are little known. With the emergence of new binders, the mineralogical composition of hydrated concrete changes and the mechanisms of alteration in aqueous media containing magnesium are different from those encountered in ordinary portlandite-rich cements. The formation of M-S-H is favoured over that of brucite. The objectives of this thesis are therefore: (i) to understand the reaction mechanisms of magnesium attack and M-S-H formation in low-calcium cementitious matrices, (ii) to study the influence of M-S-H formation on microstructural and mechanical properties and (iii) to propose microstructural and mechanical data of M-S-H that can be integrated in chemo-mechanical models.

Firstly, the influence of the composition of the cementitious paste on the phases formed during magnesium attack was studied. The presence of portlandite implies the formation of brucite. Incomplete hydration of low CaO/SiO_2 or C/S binders, even in the absence of portlandite, can also lead to the formation of brucite. M-S-H is formed within the paste and corresponds to a deep magnesium enrichment.

Secondly, a characterization of M-S-H was carried out on M-S-H pastes in order to acquire data on the intrinsic physical and mechanical properties of M-S-H and thus to be able, via small-scale chemo-mechanical modelling, to understand the mechanisms of damaged properties under these attacks.

Finally, a multi-physical study, at the mesoscopic scale, of the damaged properties of low-calcium matrices by waters containing magnesium was carried out. Two low C/S cementitious pastes (model paste based on colloidal silica and real paste based on silica fume and slag – named T3) were exposed to solutions with different Mg concentrations (5 and 50 mM). The chemical and mineralogical characterization showed that a deep decalcification takes place in parallel with a strong magnesium enrichment of the paste, corresponding to the formation of M-S-H. Micro-structural and mechanical characterizations (by indentation), carried out to observe the evolution along the degradation, showed an increase in porosity and a strong drop of local elastic properties despite the formation of M-S-H. Mechanical homogenisation, based on previously determined M-S-H paste data, confirms that degraded M-S-H have low elastic properties. Increasing the Mg concentration does not change the mineralogy and chemistry of the degraded zone but only the degraded depth. The results on the real paste (T3) are similar to those on the model paste, validating the results on the latter. In addition, the model paste was also studied in pure leaching to compare the effect of leaching with that of magnesium attack on the low C/S binders. A study using a reactive transport code was carried out to better understand the differences in kinetics and phenomenology. It confirms that the presence of magnesium accelerates the degradation.

TABLE OF CONTENTS

Table of contents

TABLE OF FIGURES AND TABLES

Figures

Table of figures and tables

Table of figures and tables

Table of figures and tables

Table of figures and tables

Table of figures and tables

Table of figures and tables

Tables

Table of figures and tables

Table of figures and tables

GENERAL INTRODUCTION

At the end of 2017, approximately 1,620,000 m^3 of nuclear waste were already in storage or intended to be taken over by the french National Agency for Radioactive Waste Management (Agence Nationale pour la gestion des Déchets Radioactifs, ANDRA) (ANDRA 2019). In response to the growing need for a long-term disposal solution, the French National Agency for Radioactive Waste Management (ANDRA) has been given the responsibility to design and implement a possible deep geological repository in France. This project is called Centre industriel de stockage géologique (Cigéo, Industrial geological disposal centre). IRSN oversees the technical assessment of the French project to evaluate its safety. It is intended for long-lived intermediate-level waste (ILW-LL) and short- or long-lived high-level waste (HLW), or even for low-level long-lived waste (LLW-LL) if no shallow repository solution is found for the latter. Nuclear wastes would be placed in packages which would then be positioned in galleries dug into the rock several hundred metres below the surface. The principle is to place the nuclear waste in an impermeable, geologically stable medium with stable hydrogeological, geochemical, mechanical and thermal behaviour.

This disposal is based on a system composed of several barriers. A distinction is made between the natural barrier (host rock) and the technological or engineering barrier, which corresponds to the use of bentonite (a swelling clay) to close the galleries by creating a plug (Alonso et al. 2017; Fernández et al. 2017) or by filling the cavity (« Basics of the Final Disposal » 2020).

The galleries would be excavated to a depth of approximately 500 m. To seal the galleries once the packages have been deposited, swelling clay (bentonite) would be placed at the entrance between two "low-pH" concrete support blocks (Figure 1) which will maintain the swelling pressure of the clay. Figure 1 illustrates the closure system planned for the Cigéo project.

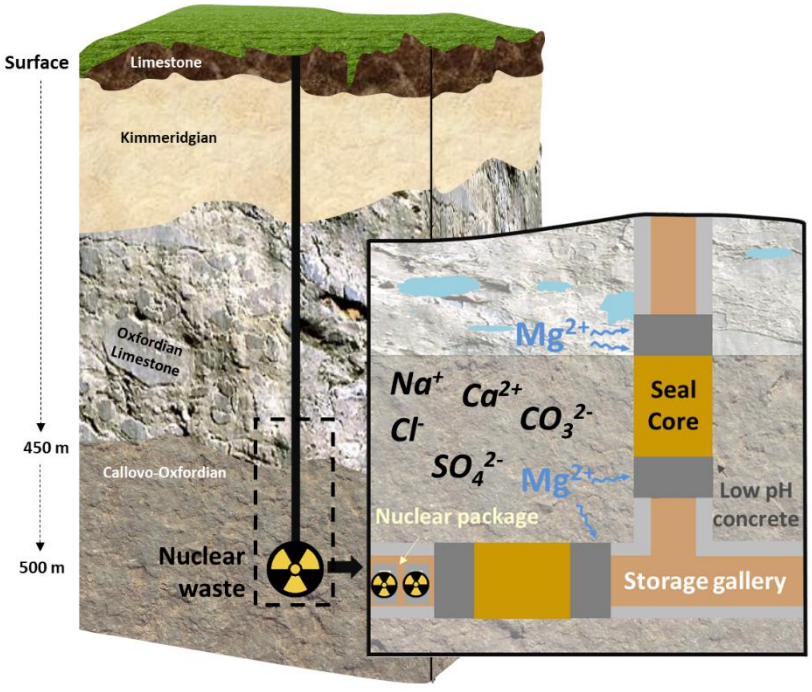

Figure 1 : Illustration of the gallery closure system

Low-pH concretes were developed to solve two problems caused by the contact of ordinary Portland cement-based concretes with clay: (i) the high alkalinity of the cementitious material could degrade the sealing properties of the clay and (ii) the temperature increase induced by the hydration of the cement in a massive structure could cause micro-cracks that are detrimental to

the durability of the material. To limit or avoid these consequences, new cementitious materials have been developed by adding silica fume, slag and/or fly ash. The pH of the interstitial solution of these hydrated materials is around 11 (hence the "low-pH" concrete designation) and the C/S molar ratio is low (<1.3) due to the high content of silica of supplementary cementitious materials.

The closure system, as presented above, requires prolonged contact between the bentonite, the host rock and the concrete bearing blocks. In addition to the mechanical stresses, especially when the bentonite swells, the bearing blocks are subject to disturbances from the aqueous environment due to the presence of chloride, magnesium, sulphate or carbonate ions. Similar durability issues are found in concrete in contact with natural waters, for example in dams or marine structures. The durability of concrete in the marine environment is a significant economic issue. France has several thousand kilometres of coastline and a large number of structures (buildings, port areas, dykes, tidal turbines, etc.) built along the sea, in the coastal strip or at sea exposed to the marine environment. Similarly, the durability of dams is a safety and economic issue in case of damage.

In all these environments (deep geological disposal, marine structures, dams, structures in contact with soft water, etc.), the chemical reactions that can occur are complex due to the diversity of ions present in the water (calcium leaching combined with the simultaneous action of chlorides, sulphates, carbonates and magnesium). The main effect of chemical degradation on unreinforced concrete is the leaching of the cementitious paste and the precipitation of secondary phases.

For Ordinary Portland Cement (OPC) based concretes or weakly substituted concretes, the effect of certain ions is often neglected because it leads to the precipitation of an external layer, and the enrichment observed is low. This is the case for magnesium, which has been little studied. With the development of new low-CO_2, low pH binders, i.e. with lower calcium contents, or in the case of structures with a very long desired lifetime, the reaction mechanisms are different. When the C/S ratio is low, little or no portlandite remains in the cementitious paste and no protective brucite layer is formed. The formation of M-S-H, with unknown physical and mechanical properties, is favoured. It is then necessary to investigate the effect of magnesium on these materials.

Consequently, the objectives of this thesis, carried out in the frame of a collaboration between IRSN and LMDC, were: (i) to understand the reaction mechanisms of magnesium attack and M-S-H formation in low-calcium cementitious matrices (especially in comparison with leaching), (ii) to study the degradation induced by Mg-bearing waters on microstructural and mechanical properties of low-CO_2 cement paste and (iii) to acquire microstructural and mechanical data of phases issued from the degradation in these new binders in Mg-bearing environments (in particular M-S-H) that can be integrated in chemo-mechanical models.

The strategy of the thesis consisted in a multi-physics study, at the mesoscopic scale, of degraded low-calcium matrices by Mg-bearing waters. Two cementitious pastes (model paste based on colloidal silica and industrial paste based on silica fume and slag – T3) were exposed to solutions with different Mg concentrations (5 and 50 mmol/L). Chemical, mineralogical, micro-structural and mechanical characterizations were performed on degraded samples along the degradation profile. In parallel, a characterization of M-S-H was carried out on cohesive, pure M-S-H pastes in order to acquire data on the intrinsic physical and mechanical properties of M-S-H and thus to be able, via small-scale chemo-mechanical modelling, to understand the mechanisms of degraded properties under these attacks.

The first chapter of this thesis is devoted to a literature review. This chapter presents the mineralogy and chemical, microstructural and mechanical properties of cement pastes, in particular those of highly substituted pastes (low-pH, low-CO_2 binders). A summary of the effects of degradation by model and real environments on these materials is proposed. The properties of the phases resulting from the magnesium attack are presented.

The second chapter focuses on the experimental strategy, the characterization methods and the material selection for the low-CO_2 cement paste degradation tests. For this purpose, a chemical

simulation was carried out to approximate the maximum C/S ratio at which brucite is no longer formed and M-S-H predominates. Then, degradation tests on several materials are carried out to confront the model with experimental data and to select two cement pastes: a low-pH model cement paste (i.e. with a simple mineralogy, a homogeneous distribution of the phases and a porosity of the order of 50%) and an industrial low-pH cement paste (with a more complex mineralogy, an inhomogeneous distribution of the phases and a lower porosity).

The third chapter presents the design of pure and cohesive M-S-H pastes and their chemical, mineralogical, microstructural and mechanical characterizations. The first part of the chapter is devoted to the choice of manufacturing protocol. Two sources of silicon (silica fume and colloidal silica) and two cure temperatures (20°C and 50°C) are tested. The phase distribution in the paste and the mineralogy of the different pastes allow to choose the most suitable protocol for the thesis. All the analyses allow to propose intrinsic microstructural and mechanical properties for M-S-H.

The fourth chapter introduces the multi-physics characterization of low-pH model cement pastes placed in 5 mmol/L (5 mM) and 50 mmol/L (50 mM) $MgCl_2$ solutions for several months. The chemical, mineralogical, microstructural and mechanical properties are studied along the degradation. The influence of the magnesium concentration on these properties and on the deterioration rates concludes the chapter.

These results are compared, in chapter 5, with the leaching of the low-pH model cement paste. It focuses on the differences in degradation rates, phenomenology, microstructure and mechanical properties. To conclude the analysis on the low-pH model paste, a mechanical homogenisation based on the electron probe microanalysis data is proposed. It allows to test the intrinsic microstructural and mechanical properties of the M-S-H determined in chapter 3.

The sixth chapter focuses on the magnesium attack of the industrial low-pH paste (T3) in 50 mM $MgCl_2$ solution. The influence of the heterogenous distribution and the more complex mineralogy of the paste, compared to the model paste, on the products and the rate of the magnesium attack is studied. The evolution of the microstructural and mechanical properties is compared to that of the model paste.

The conclusion chapter of the thesis proposes a synthesis of the contributions of this work and identifies perspectives and directions of exploration for future studies.

CHAPTER 1. LITERATURE REVIEW

Introduction

In several environments (deep geological disposal, marine structures, dams, structures in contact with soft water, etc.), the chemical reactions that can occur are complex due to the diversity of ions present in the water. For Ordinary Portland Cement (OPC) based concretes or weakly substituted concretes, the effect of certain ions is often neglected because it leads to the creation of an external layer, and the enrichment observed is low. This is the case for magnesium, which has been little studied. With the development of new low-CO_2, low pH binders, i.e. with little calcium, or in the case of structures with a very long desired lifetime, the reaction mechanisms are changing. When the C/S ratio is low, little or no portlandite remains in the cementitious paste and no protective brucite layer is formed. The formation of M-S-H, with unknown physical and mechanical properties, is favoured. It is then necessary to investigate the effect of magnesium on these materials.

The first part of this chapter reviews the mineralogical, chemical, microstructural and mechanical properties of the cement paste. It introduces small-scale mechanical characterization (indentation) and commonly used mechanical homogenisation techniques. The properties of C-S-H – the binding phases constituting the cementitious paste of concretes are detailed. The second part presents the aqueous media containing magnesium and mechanisms of the magnesium attack observed in situ and ex situ. A short literature review is proposed on model waters consisting of the different ions found in the Mg-bearing environments. Chemical, microstructural and mechanical (when available) properties of phases formed during the magnesium attack (decalcified C-S-H, amorphous silica, brucite, hydrotalcite and M-S-H) are presented.

1.1. Mineralogy and properties of low-calcium cement pastes

1.1.1. Mineralogy of the hydrated cement paste

Cement paste is formed during the hydration of cement by exothermic chemical reactions between cement and water (Nonat 2008; Taylor 1997). There are five types of common manufactured cements, noted CEM I to V (France) depending on the type and percentage of additions incorporated. The most commonly used cement is Portland cement (CEM I, also named Ordinary Portland Cement - OPC), composed of 95% of clinker. It is an anhydrous powder made up mainly of calcium silicates, aluminates and/or ferrite (Table 1-1 (Nonat 2008)). The chemistry of cement is a chemistry of oxides. In order to simplify reading and writing, the following notation is used C = CaO, S = SiO_2, A = Al_2O_3, F = Fe_2O_3, H = H_2O.

Table 1-1 : Proportion of oxides in clinker (Taylor 1997; Nonat 2008)

Constituent	Cementitious notation	Chemical formula	mass % of the different oxides in clinker
Tricalcium silicate (alite)	C_3S	Ca_3SiO_5	60 – 65
Dicalcium silicate (belite)	C_2S	Ca_2SiO_4	10 – 20
Tricalcium aluminate	C_3A	$Ca_3Al_2O_6$	8 – 12
Tetracalcium aluminoferrite	C_4AF	$Ca_4Al_2O_{10}Fe_2$	8 – 10

The hydration of cement consists of the transformation of anhydrous phases into hydrated phases, building the microstructure of the cement paste over time and endowing it with mechanical properties (Nonat 2008). When cement is in contact with water, the anhydrous phases dissolve

and hydrates precipitate. To slow down the hydration reactions responsible for the setting of cements, calcium sulphate in the form of gypsum (2 to 4% by mass) can be added. The hydration of C_3S ($(CaO)_3SiO_2$) forms portlandite (CH i.e. $Ca(OH)_2$) and calcium silicate hydrates (C-S-H). C-S-H have no fixed stoichiometry ($(CaO)_x(SiO_2)_y(H_2O)_z$). They are usually defined in terms of the Ca/Si (or C/S) molar ratio, i.e. x/y. The hydration of C_2S also leads to the formation of C-S-H and portlandite (in smaller quantities, (Nonat 2008)). The hydration of C_3A and C_4AF results in the formation of aluminate hydrated phases such as ettringite (AFt, $C_6A\bar{S}_3H_{32}$) or monosulfoaluminate (AFm, $C_4A\bar{S}H_{12}$).

New binders (cement with additions) have been developed with the following aims: (i) to reduce heat release (by spreading hydration over a longer period of time) to limit cracking risks in early age for massive structures (Sánchez de Rojas et al. 1993; Langan, Weng, et Ward 2002; Buffo-Lacarrière et al. 2011); (ii) to improve long-term mechanical performance, durability and sustainability of concrete (e.g. to resist chloride ion penetration) by optimising the granular skeleton of concrete (Juenger et al. 2012; Thomas et al. 2012); and (iii) to reduce environmental impact by using waste by-products of other industries (e.g. steel slag from the metallurgical industry) (Lauch, Dieryck, et Pollet 2016). Additions in Type II to V cements can be of different types: limestone fillers, pozzolanic additions (e.g. silica fume or fly ash) or latent hydraulic additions (e.g. slag).

In early-age hydrated Portland cement, the pH of the solution in the pores of the paste, can be as high as 13.5 due to the concentration of alkaline ions (Lothenbach et Winnefeld 2006; Vollpracht et al. 2016). The mineralogy and the pH of the hydrated paste vary depending on the type and amount of addition.

Silica fume-based cements

Silica fume is obtained during the manufacture of silicon from quartz and coal and is used in a densified form (agglomerates of individual particles) because it is difficult to handle (Taylor 1997). Silica fume is mainly composed of amorphous silica (94-98%). If well dispersed, silica fume has a high reactivity and the small particle size accelerates the pozzolanic reaction with portlandite (Mitchell, Hinczak, et Day 1998; Sánchez de Rojas, Rivera Lozano, et Frías 1999).

The incorporation of silica fume into the binder decreases the C/S ratio of the binder, and once the portlandite is consumed, the C/S ratio of the C-S-H decreases and can reach 0.9 (Codina et al. 2008). The pH decreases with the addition of silica fume. Tests carried out on cement pastes made with OPC of very high alkalinity (pH 13.9) showed that the pH of the interstitial solution decreases by 0.5 units following the addition of 10% silica fume, and by 1 unit when the addition is 20% (of the total binder mass) (Page et Vennesland 1983).

Fly ash-based cements

Fly ash is collected in electrostatic or mechanical flue gas cleaning installations of coal-fired power plants (Taylor 1997). It consists of aluminosilicate phases (mass fraction of 60 to 90%) and non-reactive crystalline minerals. Their chemical composition and reactivity vary according to the fuel used (Malhotra et Mehta 2002). The pozzolanic reaction of fly ash is slow (Taylor, Mohan, et Moir 1985, 85; Taylor 1997). Due to their low calcium content, C-S-H formed from binders incorporating fly ash have a lower C/S ratio than Portland cement hydrates (Sakai et al. 2005). Therefore, as with silica fume cements, the pH of the pore solution decreases as the amount of fly ash incorporated increases (Shehata, Thomas, et Bleszynski 1999). Furthermore, the substitution of part of the cement by fly ash induces a decrease in the concentration of Na^+, K^+ and OH^- ions in the interstitial solution of the hardened material (Diamond 1981; Nixon et al. 1986; Canham, Page, et Nixon 1987).

Slag-based cements

Blast-furnace slag is a by-product of the production of cast iron which is quenched by spraying with water (Taylor 1997). It is a latent hydraulic material, i.e. it has hydraulic properties when activated and consists mainly of 4 oxides: CaO, SiO_2, Al_2O_3 and MgO (Wang et Scrivener 1995). When mixed with Portland cement, it is the portlandite formed by hydration of the clinker that activates the hydration of the slag by increasing the alkalinity.
In addition to the phases usually present in OPC, the presence of magnesium in slag leads to the formation of hydrotalcite and M-S-H (Brew et Glasser 2005a). The amount of portlandite and the C/S ratio value of C-S-H in a slag-based cement is lower than that produced by OPC hydration (Taylor, Mohan, et Moir 1985; Duchesne et Bérubé 1995). The C/S of C-S-H decreases as the proportion of slag in the binder increases, from 1.8 for OPC to 1.1 - 1.2 in the extreme case of a cement paste containing only alkali-activated slag (Richardson et Groves 1992).

More information about the influence of additions on the microstructural and mechanical properties of the cement pastes are proposed in the sections 1.1.3 and 1.1.4.

In low-pH/low-CO_2 cement pastes, C-S-H is the main phase. The following section provides a review of the literature on the chemical and crystallographic properties of C-S-H.

1.1.2. Chemical and crystallographic properties of C-S-H

1.1.2.1. C-S-H production

For research purposes, in order to identify the chemical, mineralogical, microstructural and mechanical properties of C-S-H, C-S-H suspensions and pastes can be used. The manufacturing process of synthetic C-S-H influences the structure of C-S-H. Accordingly, to recover the C-S-H of real cementitious pastes, the determination of the target C/S ratio and identification of the method that gives the closest structure to that observed in the real cementitious paste, is needed. C-S-H suspensions (Haas 2012; Roosz 2016) allow for a very accurate C/S ratio and very fast hydration given the large amount of water available (water/solid = 50). This method allows chemical, kinetic and thermodynamic characterization of C-S-H but shows limitations in the mechanical characterization of C-S-H and the identification of structural changes during degradation. For this, cohesive pastes are needed. Kangni-Foli (Kangni-Foli 2019) developed a manufacturing process to produce cohesive C-S-H pastes based on mixing C_3S, colloidal silica, superplasticizer and demineralised water (w/b between 0.5 and 0.78 depending on the C/S).

Numerous researchers have studied C-S-H and have sought to characterise them. Several notations have been defined according to their chemical, mechanical and micro-structural properties (Table 1-2).

Table 1-2: Classifications of C-S-H according to their chemical, mechanical and micro-structural properties by different authors

Chemical classification			
C-S-H (I)	C-S-H (II)	C/S<1.5 = C-S-H (I), C/S>1.5 = C-S-H (II)	(Taylor 1964)
C-S-H (B)	C-S-H (A)	C-S-H (A)= supersaturated with portlandite (high C/S)	(Jennings 1986)
C-S-H (α) et C-S-H (β)	C-S-H (γ)	C-S-H(α) : 0.66<C/S<1 - in solution 2 mmol/L < [CaO] < 3 mmol/L - C-S-H(β) : 1<C/S<1.5 - in solution 3 mmol/L < [CaO] < 22 mmol/L - C-S-H(γ) : C/S>1.5 - in solution 22 mmol/L < [CaO] < 30 mmol/L	(Lecoq 1993)
Mechanical and microstructural classification			
OP C-S-H	IP C-S-H	OP C-S-H = Outer Products IP C-S-H = Inner Products	(Richardson 2000; 1999; Richardson et al. 1994)
LD C-S-H	HD C-S-H	LD C-S-H = low-density C-S-H HD C-S-H = high-density C-S-H	(Jennings 2000; Thomas et Jennings 2006)

1.1.2.2. Chemical classification

The classification based on the chemical properties of C-S-H has evolved over time. Taylor (Taylor 1964) distinguished two types of C-S-H according to their C/S ratio: C-S-H(I) and C-S-H (II). Jennings (Jennings 1986) drew two equilibrium curves (A) and (B) (Figure 1-1). These two curves correspond to two types of C-S-H and their thermodynamic equilibrium in solution. Curve (A), was associated with the C-S-H supersaturated in portlandite, i.e. with high Ca/Si ratio. The notation C-S-H(α), C-S-H(β) and C-S-H(γ) was given after the work of Lecoq (Lecoq 1993). Three types of C-S-H were distinguished according to their C/S ratio, or equivalently by the concentration of calcium in solution. This notation was taken up by Haas (Haas 2012) to create a thermodynamic model. In 2004, Nonat (Nonat 2004) condensed the previous notations and compared them. According to Nonat, Lecoq's C-S-H(β) would correspond to Taylor's C-S-H(I) and Jennings' C-S-H(A) curve. The C-S-H(α) could correspond to the 14 Å-tobermorite of Taylor. On the other hand, the C-S-H(γ) do not have any equivalence. Indeed, Nonat highlights the presence of tobermorite residues in the X-ray diffractograms which excludes the analogy with C-S-H(II) which are jennite and not tobermorite (Taylor 1964). Jennings' C-S-H(B) curve would also not be consistent with C-S-H(γ).

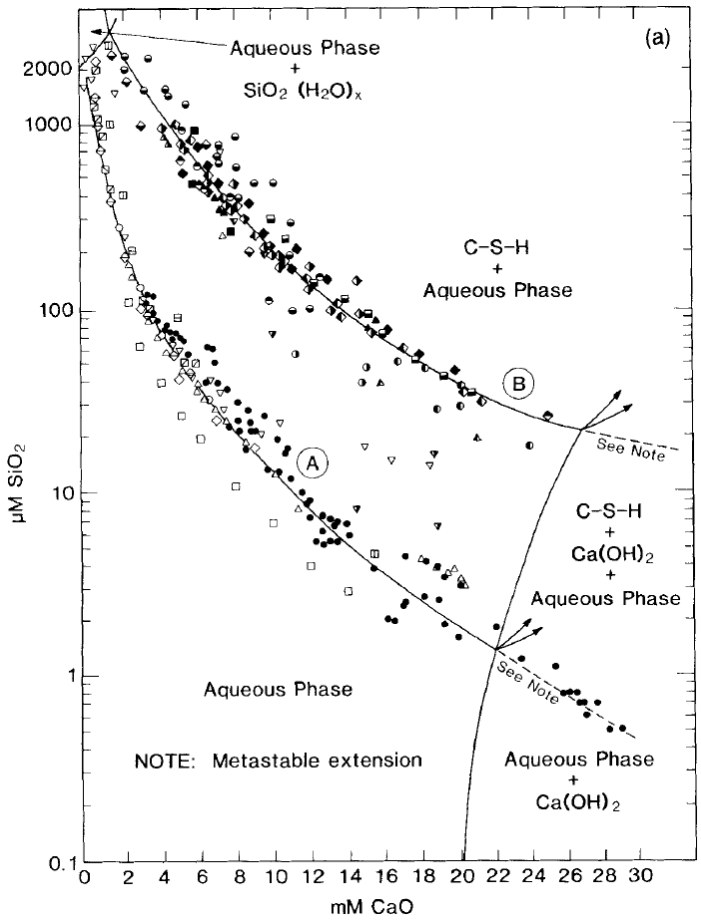

Figure 1-1: Curve of SiO_2 concentration versus CaO concentration in aqueous phase (Jennings 1986)

1.1.2.3. Thermodynamic constants

To model the behaviour of concrete in chemically aggressive environments, the chemical and thermodynamic properties of the hydrated phases of the cement paste are needed. Several thermodynamic databases exist (Blanc et al. 2012; Hummel et al. 2002; Wolery 1992, 3) and have been enriched over time to include phases produced during material degradation (M-S-H for example) (Roosz 2016). In the case of Thermoddem, the database commonly used with the Hytec reactive transport code, about ten C-S-H without aluminium incorporation and about fifteen with, have been defined according to their C/S ratio. Table 1-3 lists the properties of C-S-H without aluminium. It should be noted that Thermoddem's C-S-H are defined with two moles of SiO_2 for one mole of C-S-H.

Table 1-3 : Thermodynamic properties considered for C-S-H after the database Thermoddem 2020 (V1.10, Code version 1.07_2.06)

C/S	Name	Equation	logK (25°C)	density (kg/m³)
0.7	C0.7SH	$1.4\ Ca^{2+} + 2\ H_4SiO_4 \underset{\rightarrow}{\leftarrow} (CaO)_{1.4}.(SiO_2)_2.(H_2O)_{1.93} + 0.67\ H_2O + 2.8\ H^+$	-17.796	2291.49
0.8	C0.8SH	$1.6\ Ca^{2+} + 2\ H_4SiO_4 \underset{\rightarrow}{\leftarrow} (CaO)_{1.6}.(SiO_2)_2.(H_2O)_{2.18} + 0.22\ H_2O + 3.2\ H^+$	-21.184	2299.1
0.9	C0.9SH	$1.8\ Ca^{2+} + 2\ H_4SiO_4 + 0.11\ H_2O \underset{\rightarrow}{\leftarrow} (CaO)_{1.8}.(SiO_2)_2.(H_2O)_{2.31} + 3.6\ H^+$	-25.247	2327
1	C1SH	$2\ Ca^{2+} + 2\ H_4SiO_4 + 0.40\ H_2O \underset{\rightarrow}{\leftarrow} (CaO)_2.(SiO_2)_2.(H_2O)_{2.4} + 4\ H^+$	-29.474	2358.12
1.1	C1.1SH	$2.2\ Ca^{2+} + 2\ H_4SiO_4 + 0.75\ H_2O \underset{\rightarrow}{\leftarrow} (CaO)_{2.2}.(SiO_2)_2.(H_2O)_{2.55} + 4.4\ H^+$	-33.758	2379.59
1.2	C1.2SH	$2.4\ Ca^{2+} + 2\ H_4SiO_4 + 1.19\ H_2O \underset{\rightarrow}{\leftarrow} (CaO)_{2.4}.(SiO_2)_2.(H_2O)_{2.79} + 4.8\ H^+$	-38.095	2388.54
1.3	C1.3SH	$2.6\ Ca^{2+} + 2\ H_4SiO_4 + 1.57\ H_2O \underset{\rightarrow}{\leftarrow} (CaO)_{2.6}.(SiO_2)_2.(H_2O)_{2.97} + 5.2\ H^+$	-42.473	2414.86
1.4	C1.4SH	$2.8\ Ca^{2+} + 2\ H_4SiO_4 + 1.91\ H_2O \underset{\rightarrow}{\leftarrow} (CaO)_{2.8}.(SiO_2)_2.(H_2O)_{3.11} + 5.6\ H^+$	-46.935	2447.24
1.5	C1.5SH	$3\ Ca^{2+} + 2\ H_4SiO_4 + 2.26\ H_2O \underset{\rightarrow}{\leftarrow} (CaO)_3.(SiO_2)_2.(H_2O)_{3.26} + 6\ H^+$	-51.442	2477.78
1.6	C1.6SH	$3.2\ Ca^{2+} + 2\ H_4SiO_4 + 2.61\ H_2O \underset{\rightarrow}{\leftarrow} (CaO)_{3.2}.(SiO_2)_2.(H_2O)_{3.41} + 6.4\ H^+$	-55.989	2506.15

1.1.2.4. Structure

The literature proposes two main representations of the C-S-H structure:

- The first, initially proposed by Taylor (Taylor 1986), is based on the existence of two phases with crystal structures close to either tobermorite or jennite. The evolution of the C-S-H structure towards one or the other of the two phases depends on the C/S ratio. In both phases, the layers are separated by a hydrated interspace that may contain cations.
- The other representation, put forward by Richardson (Richardson 2008; 2014), is based on a single form of tobermorite in which, with increasing C/S, portlandite would intercalate. Figure 1-2 (a) shows a C-S-H layer when all Si bridging sites are occupied. Figure 1-2 (b) represents the different sites considered and their notation (figure after (Grangeon et al. 2016)).

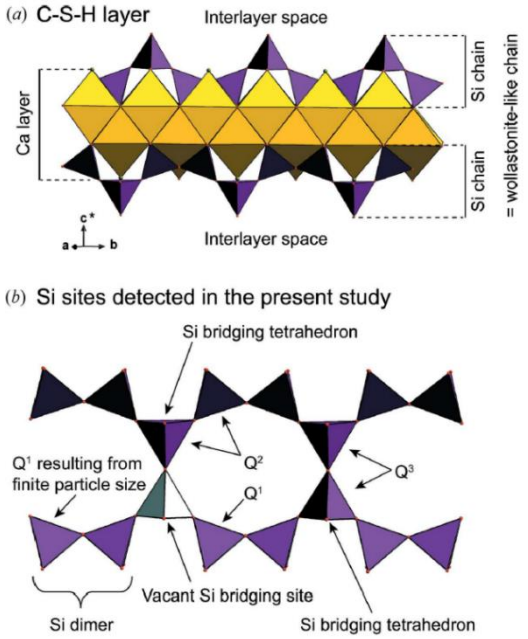

Figure 1-2 : (a) Sketch of the structure of a C-S-H layer in the tobermorite hypothesis, (b) Illustration of the sites (and their notation) observable on the chain. According to (Grangeon et al. 2016)

Grangeon (Grangeon et al. 2016) agreed with the second hypothesis and proposes a mechanism for structure evolution as a function of C/S, illustrated in Figure 1-3.

The structure of the C-S-H is a turbostratic[1] and nanocrystalline tobermorite evolving with the C/S ratio. At low C/S ratio, the silicon chain is complete (no vacancies). For 0.6<C/S<0.87, the increase in the ratio implies an increase in the inter-layer distance, depolymerisation, with notably a decrease in the occupation of the bridging sites and the intercalation of calcium between the layers. For 0.87<C/S<1.4, the phenomenon continues but the calcium interlayer can polymerise, possibly into the interlayer space, to form a structure that has many structural similarities with portlandite ($Ca(OH)_2$).

[1]. Describing a crystal structure in which basal planes have slipped out of alignment

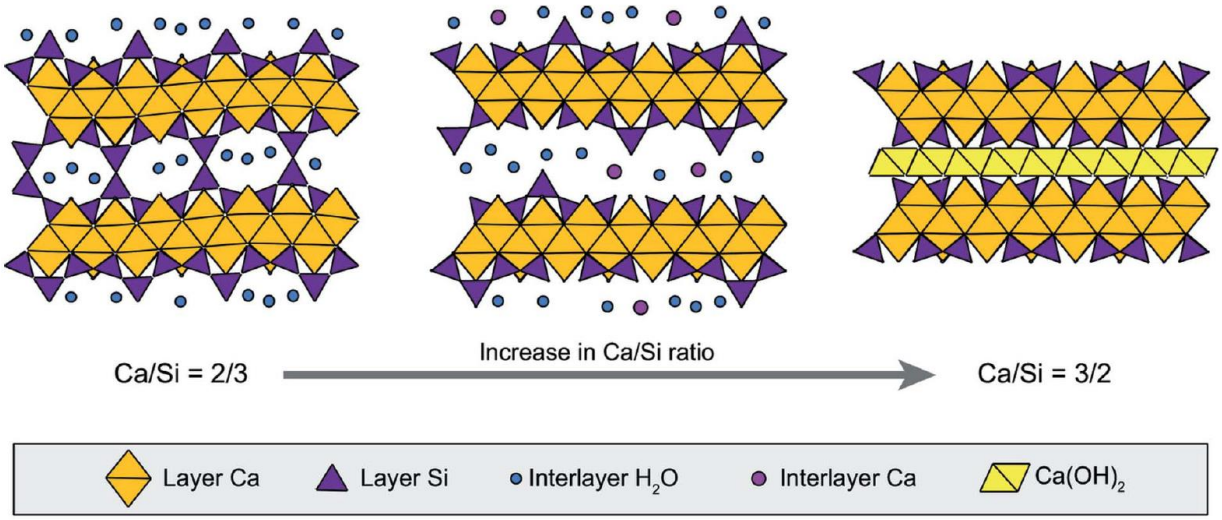

Figure 1-3 : Illustration of the mechanism of evolution of the C-S-H structure as a function of the C/S ratio according to (Grangeon et al. 2016)

1.1.3. Microstructure of the cement paste

For the same water/binder (w/b) ratio, compared to OPC, after a certain period of hydration, cements with additions show a refinement of the pore structure and a lower diffusion coefficient, for silica fume (Gleize, Müller, et Roman 2003; Dureković 1995; Hooton 1993; Bentz et al. 2000), fly ash (Fu et al. 2002; De Gutiérrez, Delvasto, et Talero 2000; Linderoth, Johansson, et Wadsö 2020) or slag (Hooton 1986; Xi, Siemer, et Scheetz 1997; Shi 1996) type additions. With silica fume, to really improve microstructure (and mechanical strength), silica fume must be dispersed in the mix. If this condition is not fulfilled, no improvement is observed (Yajun et Cahyadi 2003). At early age, the porosity is higher than for OPC. From the pozzolanic reaction between silica fume or fly ash with hydrated lime, C-S-H are later formed in the paste capillary voids and at later age (28 days old), the porosity is lower than for OPC (Marsh, Day, et Bonner 1985; Day et Marsh 1988; Gleize, Müller, et Roman 2003).

Cement paste consists of hydrates, a small amount of remaining anhydrous species (clinker, silica fume for example) and pores. Two types of porosity can be distinguished: capillary porosity and hydrates internal porosity (as internal porosity of C-S-H (Muller 2014)). Figure 1-4 illustrates the four levels of microstructure usually considered in cement pastes (Nguyen 2017; Jennings et al. 2007; Thomas et Jennings 2006; Chen et al. 2010). The C-S-H gel is considered to form the matrix of the hydrated paste in common mechanical homogenisation schemes (Constantinides et Ulm 2004; Hu et al. 2019). The 4 levels are:

- **Level 0:** This is the smallest scale. It can be the molecules of C-S-H in the cement paste. At this scale, the greatest heterogeneity corresponds to the distance between the molecules forming the C-S-H. This one depends on the model and the C/S ratio considered.
- **Level 1:** It is an intermediate level. In the cementitious paste, it is the floc of globules for C-S-H.
- **Level 2**: The globule flocs associate in a more or less dense manner to create high density C-S-H (HD C-S-H) or low-density C-S-H (LD C-S-H) (described in the following section). The high- and low-density C-S-H form the C-S-H gel.

- **Level 3**: This is the highest scale considered here. It is the cementitious paste, consisting not only of the C-S-H gels but also of other hydrates or non-hydrated particles such as clinker as well as pores.

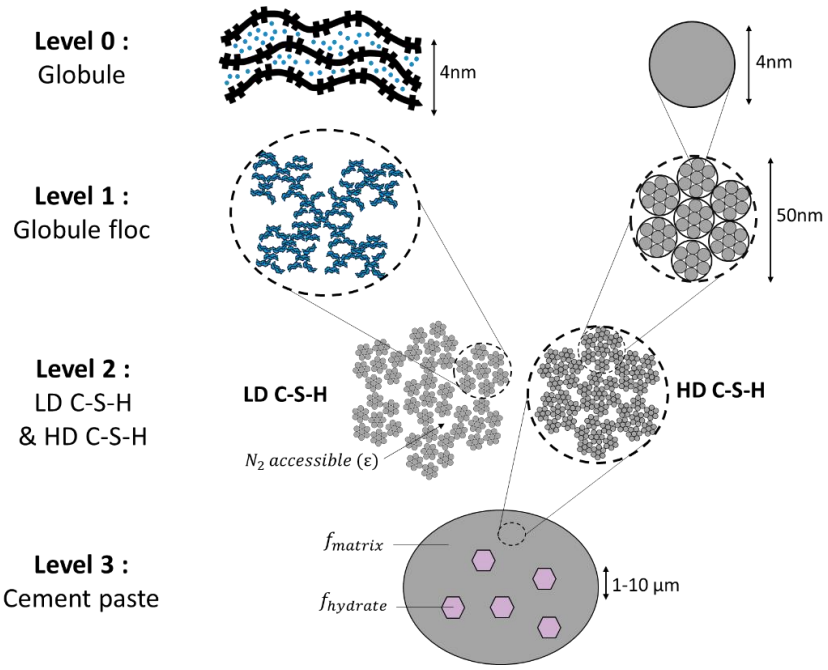

Figure 1-4 : Four-level microstructure of the cement paste, adapted from (Jennings et al. 2007; Thomas et Jennings 2006; Chen et al. 2010)

Two types of C-S-H are distinguished by their location within the paste and their assumed formation process. In 1998, Thomas and Jennings (Thomas, Jennings, et Allen 1998) highlighted the formation of two C-S-H morphologies during the cement hydration. During the first days of hydration, high surface area C-S-Hs are rapidly formed filling the entire free pore space. Subsequently, lower surface area C-S-H form. Richardson (Richardson 2000; 1999; Richardson et al. 1994) introduces the notation C-S-H_{int} (or C-S-H_{inner}) and C-S H_{ext} (or also C-S-H_{outer}). When the cement paste hydration begins, C_3S and C_2S react with water. This reaction takes place at the surface of the grains and a layer of C-S-H forms around the grain, the so-called "outer" C-S-H (or C-S H_{ext}). They have a laminated structure and form rapidly. In a second step, water diffuses into the C-S-H_{ext} layer and causes the formation of C-S-H inside the outer layer. These are the inner C-S-Hs (C-S-H_{int}). These have a honeycomb structure and form more slowly. The two images in Figure 1-5 illustrate the structure observed by Béjaoui (Béjaoui et al. 2006) in both cases. This denomination of C-S-H was used by Stora (Stora 2007) to designate the different phases useful in his model.

Figure 1-6 (Richardson 2004) shows the boundary between the two species.

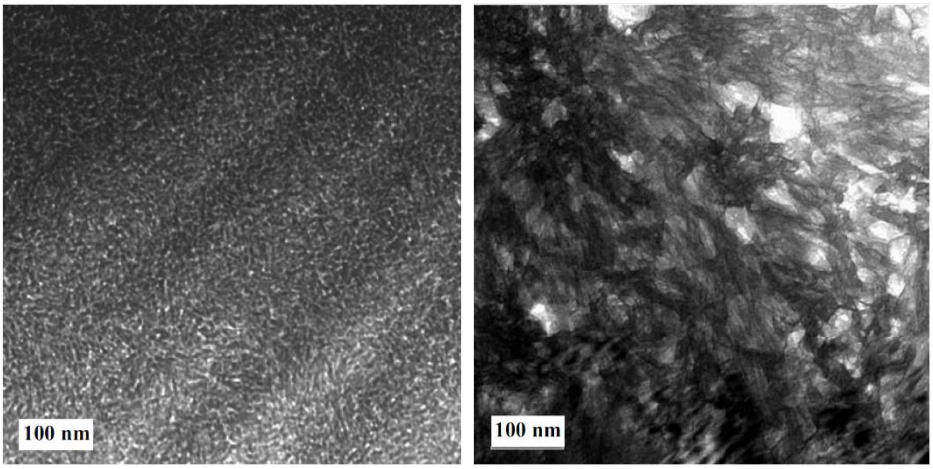

Figure 1-5 : Images of the microstructure of C-S-H obtained by Transmission electron microscopy (TEM). On the left, C-S-H^{int} for a CEM I with w/c=0.25. On the right, C-S-H^{ext} for a CEM I with w/c=0.32 (Béjaoui et al. 2006)

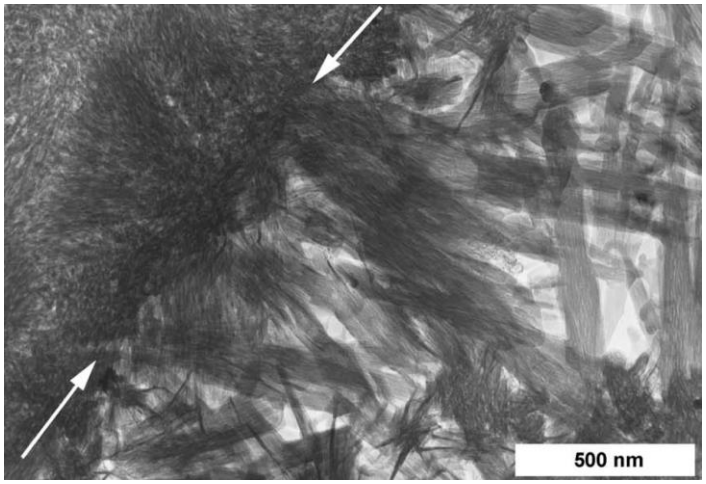

Figure 1-6 : Illustration of the structure (by TEM) of outer and inner C-S-H in a C_3S paste with w/c=0,4 stored for 8 years at 20°C. The two white arrows indicate the border between C-S-H^{int} (top left) and C-S-H^{ext} (Richardson 2004)

In a similar way, Jennings (Jennings 2000; Thomas et Jennings 2006) differentiates high density (HD) and low density (LD) C-S-H (corresponding respectively to C-S-H_{inner} and C-S-H_{outer}). The diagram in Figure 1-7 (Thomas et Jennings 2006) illustrates the difference in porosity between the two types put forward by Jennings. The difference in density observed according to the type of C-S-H implies different intrinsic porosities of C-S-H. According to Souyris (Souyris 2012), C-S-H LDs have an intrinsic porosity (d<12 nm) of 28% and C-S-H HDs a porosity of 13%. Statistical nanoindentation tests (see 1.1.4.1) on an OPC paste with w/b=0.5 showed proportions of 67% LD C-S-H and 33% HD C-S-H (Constantinides et Ulm 2004).

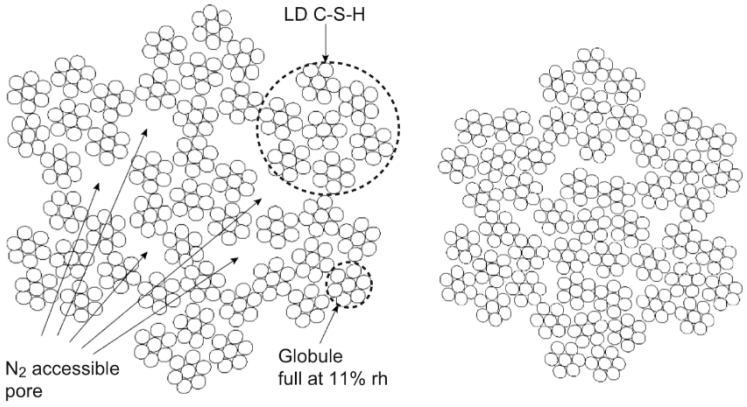

Figure 1-7 : Schematic representation of LD C-S-H (left) and HD C-S-H (right) (Thomas et Jennings 2006)

1.1.4. Determination of the mechanical properties of the cement paste phases

The mechanical properties of the cement paste depend on the pore structure and the mechanical properties of the mineralogical phases. As detailed in the previous section, with the incorporation of additions, the pore structure is refined and the mechanical properties in the long term are generally higher. As the hydration of Supplementary Cementitious Material (SCM) is longer than that of the clinker, the mechanical properties of blended cement at young age are lower than those of an OPC but in the long term they are generally higher (28-90 days) (Cheng-yi et Feldman 1985; Fu et al. 2002; Xi, Siemer, et Scheetz 1997; Shi 1996).

To determine the mechanical properties of the cement paste phases, small-scale mechanical tests, such as nano-indentation test, can be carried out.

1.1.4.1. Indentation

Indentation is a method for identifying the local mechanical properties of a heterogeneous material. For the cement paste, it allows to determine the mechanical properties of hydrates and anhydrous species. Indentation is based on the contact between a hard material with known mechanical properties (the indenter), and the material under investigation whose properties are unknown. The depth of penetration is measured continuously during the loading process. A stress/ depth curve is obtained (Figure 1-8). The elastic indentation modulus (E_{IT}) of the material can be determined from the slope of the unloading of the indentation curve, considering that the Poisson's ratio of the material is known. E_{IT} is expressed as:

$$E_{IT} = \frac{(1-\nu^2)*E_r*E_i}{E_i-E_r*(1-{\nu_i}^2)} \text{ with } E_r = \frac{\sqrt{\pi}*S}{2*\sqrt{A_c}} \quad (1\text{-}1)$$

with:

- E_i the modulus of elasticity of the indenter
- E_r the reduced modulus of elasticity
- E_{IT} the modulus of elasticity of the material under investigation
- ν the Poisson coefficient of the tested material
- ν_i the Poisson coefficient of the indenter
- S the contact stiffness of the upper part measured experimentally during the unloading phase of the test
- A_c the projected contact area

Figure 1-9 illustrates the experiment. A_c is estimated from the contact depth noted h_c. In the case of a Berkovich tip, $A_c/h_c^2 = 24{,}50$ (Maciejak et Aubert 2007; Nguyen 2017) and h_c is expressed by :

$$h_c = h_{max} - \frac{\varepsilon * P_{max}}{S} \tag{1-2}$$

with

$$\varepsilon = \frac{2}{\pi}.(\pi - 2) \tag{1-3}$$

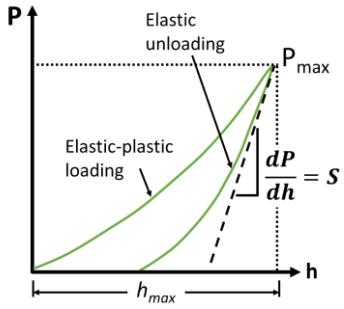

Figure 1-8: Typical load-depth curves in nano-indentation experiment, adapted from (Fu et al. 2018)

P_{max} and h_{max} are the maximal load and depth respectively. The indentation modulus reflects the properties of the material within the interaction volume directly underneath and around the indent (illustrated in yellow on Figure 1-9). The interaction volume depends on the applied load and the indented depth (h_{max}). It extends, in the shallow subsurface, to 3-4 times the indented depth (h_{max}) (Ulm et al. 2010; Constantinides et Ulm 2004; Trtik, Münch, et Lura 2009). When indentation is performed on hardened cement pastes, the material response and mechanical properties that are measured depend on the properties and volume fractions of the different hydrated and non-hydrated phases present in the interaction volume (C-S-H, portlandite, ettringite, clinker, porosity etc.). The higher the applied load, the higher the indented depth and the larger the interaction volume. A larger proportion of porosity is then included in the measuring points and, for a homogeneous material, the indentation modulus decreases (Hu et al. 2020). Figure 1-9a and c correspond to a smaller interaction volume (yellow on the figure) than the characteristic length (D) of the biggest inhomogeneity at the level considered. Figure 1-9b and d correspond to a bigger interaction volume than the characteristic length of the biggest inhomogeneity at the level considered. For an indented depth of about 100 nanometres, the test is called nanoindentation. For indented depths of around ten microns, the test is called microindentation.

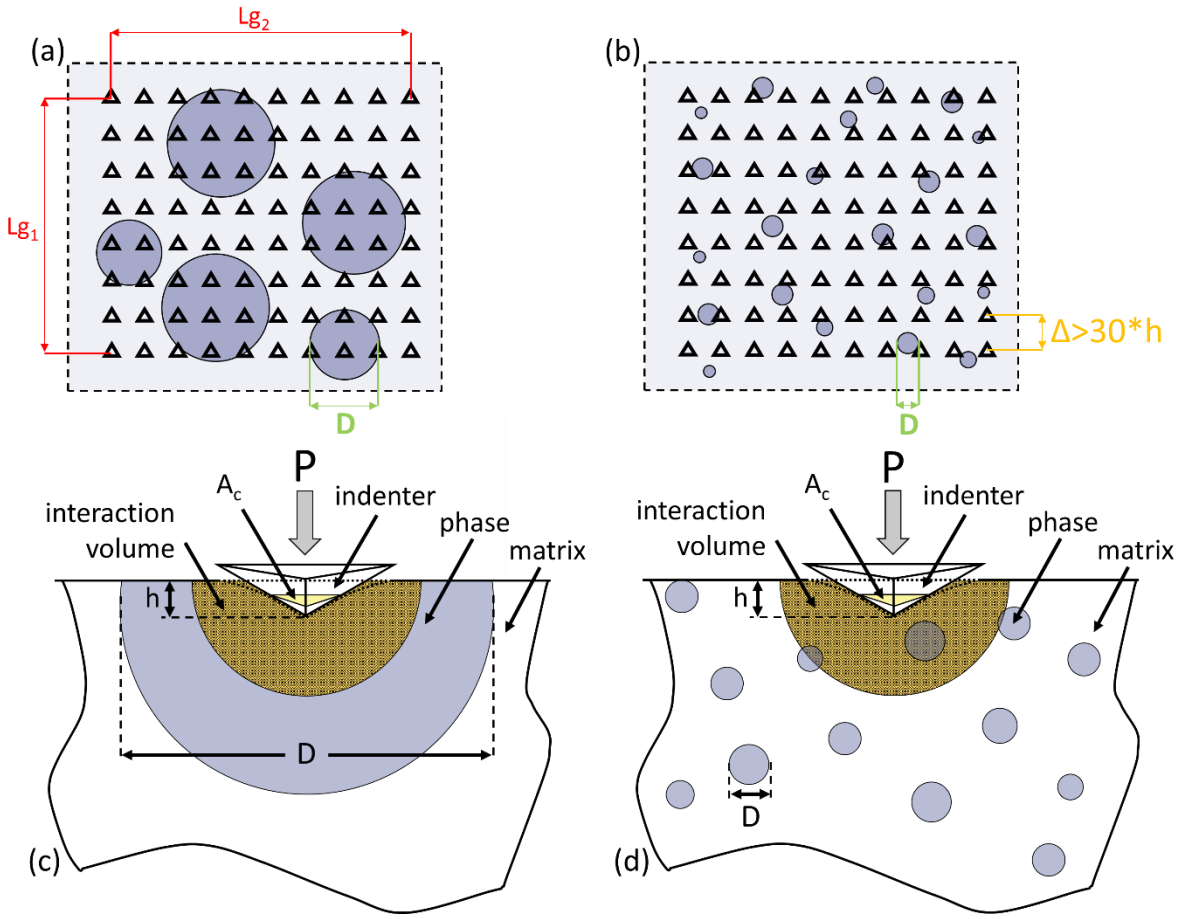

Figure 1-9: Grid indentation and indenter scheme on a heterogeneous system where the probed microvolume (cross-hatched regions below the indenter) is either (a-c) smaller or (b-d) larger than the characteristic length scale, D, of the phase of interest. The triangles correspond to the indents. Other symbols are defined in the text. Adapted from (Nguyen 2017; Ulm et al. 2010; Chen et al. 2010)

Over time, the indentation method has evolved. Initially, the indents were placed manually on already determined phases in order to characterise them mechanically (Hughes et Trtik 2004; Mondal, Shah, et Marks 2007; Chen et al. 2010). This method is still used for homogeneous materials or when coupled with SEM/EDS. The most commonly used method today is based on a statistical analysis of the E and H properties obtained on an indentation grid. The phases are identified a posteriori by discriminating their mechanical properties through deconvolution approaches (Constantinides et Ulm 2004; Nguyen 2017; Ulm et al. 2007; Vandamme 2008).

To carry out a statistical analysis, a high number of indents placed randomly with regards to the materials' heterogeneity (typically using a grid) have to be carried out. The choice of the experimental parameters; indentation depth, point spacing and grid size, requires knowledge of the dimensions of the phases to be characterised. Figure 1-9a gives an example of a grid made on inhomogeneous materials where the depth of the indent (h) is much smaller than the dimensions of the phase (D), i.e. $h \ll D$. Lg_1 and Lg_2 are the dimensions of the grid, Δ is the distance between indents and D is the characteristic dimension of the smallest phase.

According to Constantinides (Constantinides 2006; Constantinides et al. 2006), the indentation depth must be between two bounds for the results to be representative of the phase to be characterised. The mechanical properties of the hydrated and anhydrous phases of the cement

paste correspond to level 2 phases (see Figure 1-4) and the indentation depth should be in the following range:

$$d_1 \ll h \leq d_3/10 \quad (1\text{-}4)$$

with d_1 et d_3 the characteristic sizes of the heterogeneities at level 1 and level 3 (Nguyen 2017). At level 1, the heterogeneity to be considered is the size of a globule of C-S-H, i.e. 5.6 nm (Jennings 2000). At level 3, the size of the heterogeneity (C-S-H gel) is around 2 µm.

The spacing of the measurements depends on the indentation depth. In order to avoid the overlapping of elastic domains perturbed by two neighbouring points, it is recommended to take Δ>30*h (Nguyen 2017). However, in order to correctly measure the possible property and phase gradient, the spacing need to be not too high. Spacings observed in the scientific literature for cement pastes are illustrated in Table 1-4.

For a heterogeneous material, the grid must be larger than the characteristic size of the largest phase in level 3. For cement paste, the largest phase corresponds to unhydrated clinker (10 µm) (Nguyen 2017). In addition, the size of the grid is dependent on the number of points and the spacing defined previously. Table 1-4 shows all the experimental parameters used for cement pastes. The load applied by the nanoindentation tip has the shape of a trapezium defined by its charging speed (v_L), unloading speed (v_U) and holding time (t_H). The charging and discharging speed are taken as identical by all researchers listed in the table.

Table 1-4 : Referencing the spacings and sizes of the nanoindentation grids used for cement pastes. v_L and v_U charge and unloading rates respectively, t_H force holding time.

References	Indentation depth (nm)	Spacing Δ (µm)	Grid size (no. of indents)	Grid size $Lg_1 x Lg_2$ (µm²)	$v_L=v_U$ (mN/min)	t_H (s)
(Constantinides et Ulm 2007)	167±53	10	10x10	90x90	3	5
(Zhu et al. 2007)	300-400	10	15x15	140x140	-	30
(Davydov, Jirásek, et Kopecký 2011)	150-600	20	20x20	380x380	60	30
(da Silva, Němeček, et Štemberk 2013)	200	8	16x18	120x136	12	10
(Vandamme et Ulm 2013)	200±45	20	20x20	380x380	12	180
(Nguyen 2017)	200	10	20x20	190x190	12	5

The mechanical properties are determined by means of the load-unload curves at each point and a distribution of Young's modulus and hardness is plotted. In heterogeneous materials, the distribution may show several broad peaks, indicating the presence of several phases with different mechanical properties. To distinguish the different phases and determine their proportion, a deconvolution scheme is performed.

The nanoindenter allows the local determination of mechanical properties based on precise measurements of force and tip displacement. The nanoindentation test is performed on supposedly perfectly smooth surfaces. In reality, this is not possible, especially for cementitious materials which have a significant porosity. The samples are rough. Polishing limits the irregularities on the surface, but the surface condition is still not perfectly smooth and this influences the determination of the contact surface (Nguyen 2017).

1.1.4.2. Scaling up

Several types of nano indenters exist. Depending on the chosen indenter (NHT^3, UNHT^3 etc.), the force control range changes, influencing the indented depth and the diameter of the impacted area. The NHT^3 nano-indenter (Anton Paar), for example, allows the mechanical properties of the paste to be determined on a small scale, from that of C-S-H gel (h = 200 nm) to that of cement paste (h=10-15 µm). Thus, depending on the set strength/depth of the nanoindenter, the impacted area may comprise part of the paste porosity. In order to determine the intrinsic mechanical properties of a phase, without the porosity, it is then necessary to perform a mechanical homogenisation. The three main homogenisation schemes are described below.

Diluted distribution scheme

The dilute distribution scheme is based on the results of Eshelby in 1957 (Eshelby et Peierls 1957). In this scheme, the material considered consists of a matrix surrounding different heterogeneities. If the volume fractions of the phases are small and the heterogeneities are sufficiently far apart, then the heterogeneities can be considered as isolated and embedded in an infinite matrix. In this case, the interactions between these heterogeneities can be neglected. According to several authors, the use of the diluted scheme is only relevant if the proportion of inclusion does not exceed 10% (Benhamida et al. 2005; Xu 2004).

Mori-Tanaka scheme

This scheme was described by Mori & Tanaka in 1973 (Mori et Tanaka 1973). The Mori-Tanaka approximation assumes that the inclusions are embedded in an infinite medium having the properties of the matrix. The deformation considered at infinity corresponds to the average deformation of the matrix, as in the diluted scheme. However, the deformation of the matrix is, with this scheme, influenced by the presence of the inclusions which is not the case in the diluted scheme. The Mori-Tanaka scheme can for example be applied on concrete, considering the matrix as the cementitious paste and the inclusions the aggregates. In two dimensions, the Mori-Tanaka scheme can be simplified by the following equations (Bary 2008) :

$$k_{eff} = \left(k_m + \frac{4}{3}\mu_m \sum_{j=1}^{n} \Phi_j \frac{k_j - k_m}{k_j + \frac{4}{3}\mu_m} \right) \left(1 - \sum_{j=1}^{n} \Phi_j \frac{k_j - k_m}{k_j + \frac{4}{3}\mu_m} \right)^{-1} \quad (1\text{-}5)$$

$$\mu_{eff} = \left(\mu_m + H_m \sum_{j=1}^{n} \Phi_j \frac{\mu_j - \mu_m}{\mu_j + H_m} \right) \left(1 - \sum_{j=1}^{n} \Phi_j \frac{\mu_j - \mu_m}{\mu_j + H_m} \right)^{-1} \quad (1\text{-}6)$$

$$H_m = \frac{\mu_m \left(\frac{3}{2} k_m + \frac{4}{3}\mu_m \right)}{k_m + 2\mu_m} \quad (1\text{-}7)$$

With k_{eff} and μ_{eff} the effective compressibility and shear moduli, k_m, μ_m, k_j, μ_j the compressibility and shear moduli of the matrix and of each inclusion respectively, Φ_j the volume proportion of each inclusion.

Self-consistent scheme

The self-consistent scheme was introduced in the literature by Hershey (Hershey 1954) for a polycrystalline type material, and then reformulated by Hill (Hill 1965) for the material with elliptical inclusions. This scheme differs from the two approximations presented above by the

definition of its VER. It is considered here that each element (matrix or inclusion) is immersed in a homogeneous medium comprising all phases, which is called the Equivalent Homogeneous Medium (EHM). The deformations around the VER are equal to the effective macroscopic deformation of the composite. The self-consistent model requires the solution of a system of two equations ((1-8) and (1-9)) with implicit solutions. This resolution is obtained at each hydration step by a numerical method of the Newton Raphson type (Bernard, Ulm, et Lemarchand 2003).

$$K_{hom}^{est} = \frac{\sum_{r=1}^{n} f_r K_r \left(1 + \alpha_0^{est}\left(\frac{K_r}{K_{hom}^{est}} - 1\right)\right)^{-1}}{\sum_{r=1}^{n} f_r \left(1 + \alpha_0^{est}\left(\frac{K_r}{K_{hom}^{est}} - 1\right)\right)^{-1}} \quad (1\text{-}8)$$

$$\mu_{hom}^{est} = \frac{\sum_{r=1}^{n} f_r \mu_r \left(1 + \beta_0^{est}\left(\frac{\mu_r}{\mu_{hom}^{est}} - 1\right)\right)^{-1}}{\sum_{r=1}^{n} f_r \left(1 + \beta_0^{est}\left(\frac{\mu_r}{\mu_{hom}^{est}} - 1\right)\right)^{-1}} \quad (1\text{-}9)$$

$$\alpha_0^{est} = \frac{3K_{hom}^{est}}{3K_{hom}^{est} + 4\mu_{hom}^{est}} \quad (1\text{-}10)$$

$$\beta_0^{est} = \frac{6(K_{hom}^{est} + 2\mu_{hom}^{est})}{5(3K_{hom}^{est} + 4\mu_{hom}^{est})} \quad (1\text{-}11)$$

With K_{hom}^{est}, μ_{hom}^{est}, K_r, μ_r the compressibility and shear moduli of the medium and of each phase respectively, f_r the volume proportion of each phase.

1.1.4.3. Mechanical properties of main hydrates and anhydrous species of the cement paste

The mechanical properties of the main cement paste phases have been determined by nanoindentation. Table 1-5 goups the Young's modulus and hardness values for C-S-H, portlandite, ettringite and unhydrated clinker.

Different studies focused on high and low density (or inner and outer) C-S-H mechanical properties. In 2004, Constantinides and Ulm (Constantinides et Ulm 2004) defined two types of C-S-H based on their nanoindentation properties; corresponding to LD C-S-H and HD C-S-H. In 2007, Mondal defined a third phase which has greater mechanical properties. It is called ultra high density C-S-H (UHD C-S-H). Although its notation seems to indicate that it is C-S-H, Chen et al. (Chen et al. 2010) show that it is rather a very fine mixture of HD C-S-H and portlandite.

Table 1-5 shows that the values measured vary from one study to another. Several parameters can explain these differences. Firstly, the measurement method is different for the first two studies in the table compared to the last six. The measurement points are chosen manually and the values presented are derived from around ten indents. For the other studies, it is a statistical study where a deconvolution is performed. It therefore depends on the number of clusters considered. Figure 1-10 illustrates the deconvolution procedure. 4 phases are identified. Nguyen (Nguyen 2017) associates the first phase (blue) with LD C-S-H, the second phase (yellow) with HD C-S-H, the third phase (red) with UHD C-(S)-H and the last phase with unhydrated clinker.

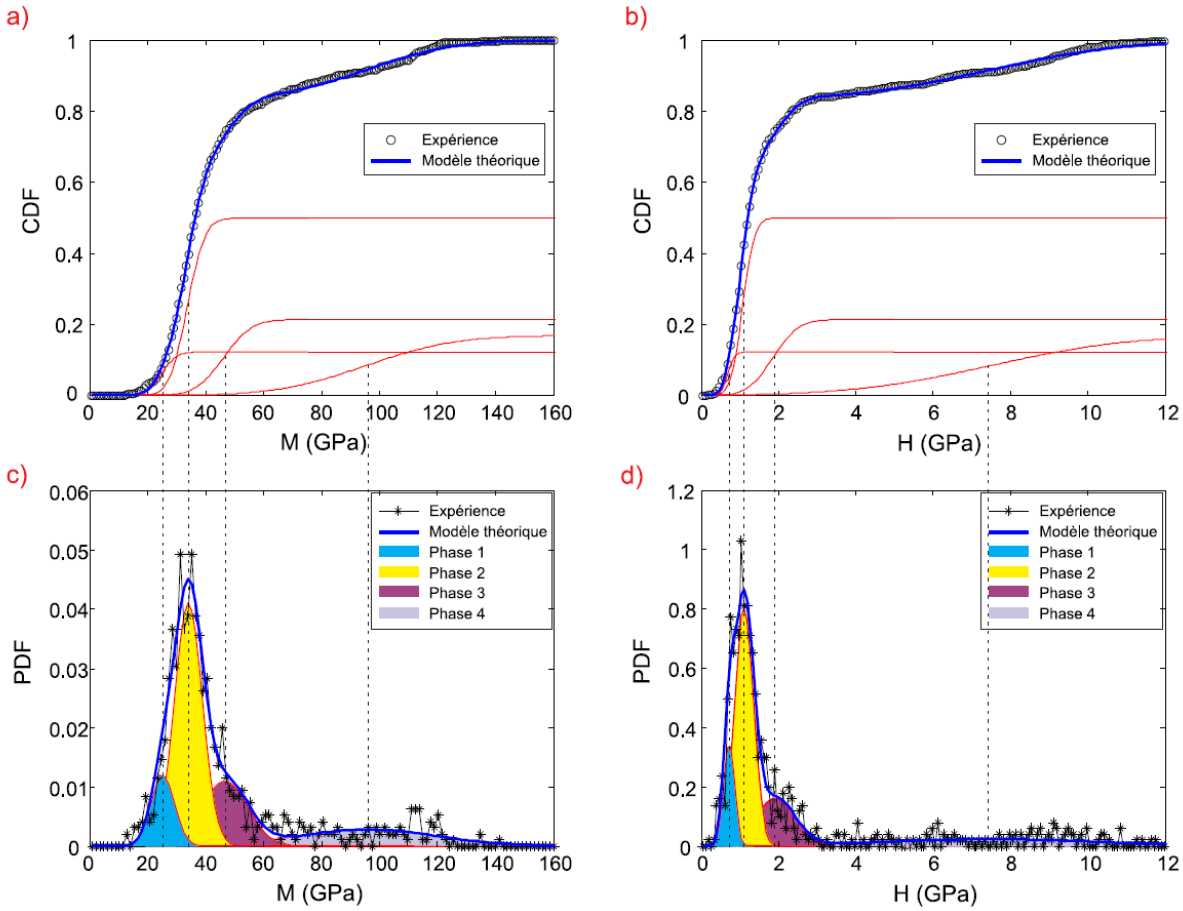

Figure 1-10 : Illustration of the deconvolution technique of 4 Gaussian distributions for w/c=0.28 (Nguyen 2017). a) represents the cumulative distribution function (CDF) corresponding to the Young modulus whose probability density function (PDF) is illustrated in figure c), b) represents the CDF corresponding to the hardness whose PDF is shown in figure d)

Furthermore, the indented depth differs from one study to another implying a different interaction volume. The higher the interaction volume, the higher the porosity taken into account and vice versa. Moreover, the w/b is not always the same, so the porosity is not always the same. Finally, the length of time and the method of storage of the samples can vary the mineralogy, the microstructure and the properties of the paste.

In conclusion, the Young's modulus of C-S-H depends on the type of C-S-H considered, the size of the interaction volume and the w/b ratio. The value to be considered depends on its use.

Table 1-5: Young modulus (E) and hardness (H) of cement phases. (C-S-H are separated in different phases: inner (IP) and outer (OP) / low (LS), medium (MS) and high stiffness (HS) / low (LD), high (HD) and ultra-high density (UHD). When defined, Poisson's coefficient is equal to 0.24.

References	w/b	Paste Conservation	Phase	E(GPa)	H(GPa)	Method	h(nm)
(Hughes et Trtik 2004)	0.45	1 month in water	OP C-S-H	25.74±10.84	0.88±0.36	Manual + Microscope	1500
			IP C-S-H	22.97	0.88		
			Portlandite	29.05±9.95	1±0.43		
(Mondal, Shah, et Marks 2007)	0.45	1 month in water at 25°C	LS C-S-H	22.89±0.76	0.93±0.11	Manual + Microscope	250-500
			MS C-S-H	31.16±2.51	1.22±0.07		
			HS C-S-H	41.45±1.75	1.43±0.29		
			Anhydrous	122.2±7.85	6.67±1.23		
(Yang et Guo 2011)	-	-	Ettringite	20.27±1.21	0.207±0.003	Manual + Microscope	100
(Chen et al. 2010)	0.2	1 year of sealed hydratation	OP C-S-H	~44	~1.3	Statistical Nanoind + Microscope	310
			IP/I C-S-H	~50	~1.7		
(Constantinides et Ulm 2004)	0.5	27 days in lime water at 20°C	LD C-S-H	21.7±2.2	-	Statistical Nanoind.	300-500
			HD C-S-H	29.4±2.4	-		
			Portlandite	38±5	-		
(Zhu et al. 2007)	0.35	28 days in lime water at 20°C ± 3°C	LD C-S-H	23.4±3.4	0.73±0.15	Statistical Nanoind.	300-400
			HD C-S-H	31.4±2.1	1.27±0.18		
			HD C-S-H	31.0±4.0	-		
(Constantinides et Ulm 2007)	0.5	5 months	LD C-S-H	18.2±4.2	0.45±0.14	Statistical Nanoind.	170
			HD C-S-H	29.1±4	0.83±0.18		
			Portlandite	40.3±4.2	1.31±0.23		
(Vandamme et Ulm 2009)	0.3	-	LD C-S-H	23.7±5.9	0.68±0.18	Statistical Nanoind.	200-450
			HD C-S-H	36.1±3.4	1.01±0.16		
(Vandamme et Ulm 2013)	0.4	-	LD C-S-H	23.03±4.48	0.561±0.121	Statistical Nanoind.	200
			HD C-S-H	31.35±3.84	0.812±0.131		
(Nguyen 2017)	0.28	-	LD C-S-H	24.7-28.6	0.70-0.84	Statistical Nanoind.	200
			HD C-S-H	32.9-36.0	1.05-1.20		
			UHD C-(S)-H	41.5-47.5	1.60-1.90		
			Clinker	78.7-90.9	5.58-6.82		

1.2. Degradation of cementitious materials in contact with Mg-bearing environments

1.2.1. Ionic composition of aqueous media of Mg-bearing environments

During contact between concrete and an aqueous medium, a chemical degradation may occur. When contact takes place between an aqueous medium and the pore water of the concrete, an imbalance is created if the two media have different compositions and/or pH. Under the effect of the gradient of concentration, diffusion takes place between the two media and some phases will dissolve while others precipitate depending on the value of their solubility. Magnesium is contained in several environments with which civil engineering structures may exposed to. Table 1-6 shows the chemical composition of some Mg-bearing waters (natural ground waters, soft water, synthetic solutions used in laboratory experiments).

Table 1-6 : Chemical composition of groundwater, soft water or sea water in the studies. NA=not available. The data is taken from : * (Dauzères et al. 2014), ** (Alonso et al. 2017), *** (Rosenqvist et al. 2017) and * (Jakobsen, De Weerdt, et Geiker 2016)***

Localisation	pH	T (°C)	mmol/L											
			Na	K	Ca	Mg	Sr	Cl	S	Si	Fe	C	F	Al
Natural groundwater*	7.1	25	45.6	1	7.4	6.7	0.2	41	15.6	0.2	0.03	NA	NA	NA
Experimental solution*	7.1	25	45.6	1	7.4	6.7	0.2	40.7	45.6	-	-	NA	NA	NA
Groundwater - Granite**	9	NA	0.38	0.01	0.18	8^{e-4}	NA	0.01	0.08	0.16	NA	0.39	0.22	NA
Interstitial water - Bentonite**	7.4	NA	91.3	0.38	12.7	16.0	NA	112.8	13.1	-	NA	2.18	-	NA
River Ångermanälven (1969–2013)***	6.93	NA	0.1	0.01	0.1	0.03	NA	NA	0.03	0.05	4^{e-3}	0.11	NA	2^{e-3}
Atlantic****	NA	NA	457	9.72	10.0	55.5	NA	536	27.8	NA	NA	2.33	NA	NA
Fjord of Trondheim****	NA	NA	478	9.72	10.7	54.7	NA	595	30.9	NA	NA	1.67	NA	NA
Baltic sea****	NA	NA	93	1.79	1.2	10.7	NA	110	17.8	NA	NA	-	NA	NA

Magnesium in natural waters is found with other ions (Cl^-, SO_4^{2-}, CO_3^{2-} for example). Several reactions with the cementitious matrix take place at the same time. Concrete leaching, and the reactions induced by chlorides, carbonates and sulphates attacks on cementitious materials has already been well studied in the literature. There is fewer information regarding the attack by magnesium on concrete. The next section provides a short review of the literature on the effect of these different ions on cement matrices.

1.2.2. Effect of model environments (single compound solutions) on cement matrices

1.2.2.1. Pure water and ammonium nitrate solution

The effect of leaching on the chemo-mechanical behaviour of cementitious material has been studied by many authors (Kamali, Moranville, et Leclercq 2008; Jain et Neithalath 2009; Carde, François, et Torrenti 1996; Wan et al. 2013; Nguyen et al. 2007; Bes 2019).

The aggressive solution in these studies is either pure (demineralised) water or ammonium nitrate solution, which is used to accelerate the degradation. As shown by Kamali (Kamali, Moranville, et Leclercq 2008) on cement pastes, the use of ammonium nitrate increases the rate of deterioration by around 5 times.

For any type of cement paste, when the cement paste is immersed in pure water or ammonium nitrate solution, leaching takes place. A progressive dissolution of the different phases of the cementitious matrix takes place (in order: portlandite, AFm, AFt), in parallel with the decalcification and dissolution of C-S-H followed by the secondary precipitation of hydrotalcite and silico-aluminous gel (Carde, François, et Torrenti 1996; Faucon et al. 1996). As a result, the porosity increases and the mechanical properties decrease (Carde, François, et Torrenti 1996; Jain et Neithalath 2009; Wan et al. 2013; Bes 2019).

The mineralogical composition and microstructural properties influence the degradation kinetics and the chemical property gradients. As the w/b ratio increases, the porosity of the sound material and the diffusion coefficient increase (Kamali, Moranville, et Leclercq 2008). Materials with a high w/b ratio show greater leaching depth. Cements with SCM (such as silica fume, ash, slag etc.), show lower degradation rates (Kamali, Moranville, et Leclercq 2008). The reasons are (i) the decrease in porosity due to a refinement of the granular skeleton, (ii) the limited presence (or absence) of portlandite which usually increases the leaching kinetics (Kamali, Moranville, et Leclercq 2008) and (iii) the aluminium incorporation which enhances the stability of C-S-H resulting in a slowdown of their dissolution (Faucon et al. 1998).

As shown by (Carde, François, et Torrenti 1996; Jain et Neithalath 2009), for Ordinary Portland Cement (OPC) pastes, the increase in porosity and loss of mechanical properties following leaching is mainly due to the dissolution of portlandite, the effect of decalcification of C-S-H being negligible. For highly substituted cement pastes, as there is little or no portlandite, it is the decalcification of the C-S-H, which is progressive from the core of the material to the surface, that is responsible for the increase in porosity and the loss of mechanical properties (Carde, François, et Torrenti 1996; Bes 2019).

A chemical shrinkage phenomenon, related to the decalcification (decalcification shrinkage), is observed when the C/S of C-S-H is reduced below ~ 1.2. It could be due to structural changes in C–S–H at Ca/Si ~ 1.2 and eventually to the decomposition of C–S–H into silica gel (Chen, Thomas, et Jennings 2006).

1.2.2.2. CO_2

Carbon dioxide is naturally present in the atmosphere and in some environments its relative pressure may be high (underground - geological disposal of nuclear waste for example (Dauzeres et al. 2016)). Chemical reactions, associated to carbonation, take place between atmospheric carbon dioxide (CO_2) and the calcium bearing phases of hydrated cement leading to the precipitation of calcium carbonate ($CaCO_3$) (Parrott 1990). The drop in pH (from 12.5 à 8.5, (Escadeillas et Hornain 2008)) induced by portlandite dissolution can lead to steel depassivation and can trigger active corrosion under low moisture content and oxygen availability (Bertolini et al. 2013). At high moisture contents the pores will be partially filled with water and restrict ingress of carbon dioxide (Parrott 1990). The corrosion of the steel of the reinforcements, intended to take

up the internal tensile forces in the concrete, then jeopardises the mechanical properties of reinforced concrete (Escadeillas et Hornain 2008).

If carbonation is a source of degradation of reinforced concrete when it reaches the reinforcement coating zone, this natural ageing phenomenon can also be beneficial for the OPC concrete. Indeed, the formation of calcium carbonate ($CaCO_3$) partially seals the porosity of the cementitious material, making it less permeable to aggressive agents as sulphate ions, chlorides, and more generally, aggressive waters such as sea water, sulphated or Mg-bearing waters, etc (Dauzères et al. 2014).

There are several polymorphs of calcium carbonate ($CaCO_3$): calcite, aragonite, vaterite and amorphous calcium carbonate. Amorphous calcium carbonate has been observed by Black (Black et al. 2007) as the first carbonation product formed. Auroy (Auroy et al. 2018) showed that the carbonation of portlandite and ettringite generates calcite and aragonite respectively and that vaterite is issued from C-S-H carbonation. Under normal condition, calcite is the most stable polymorph (Black et al. 2007) and in the long term, vaterite, aragonite and amorphous calcium carbonate are transformed into calcite (Šauman 1971).

In new binders with additions, the content of portlandite may be very low and C-S-H may become the main species to carbonate. Kangni-Foli (Kangni-Foli et al. 2021) studied the influence of C-S-H carbonation on the microstructure of cementitious materials and the protective role of portlandite. He produced model cement pastes composed either only of portlandite and C-S-H or only C-S-H and achieved an accelerated carbonation experiment at 3% CO_2 (25°C, 55% RH). According to his study, C-S-H is the main contributor of porosity change during carbonation of the cement paste. A shrinkage phenomenon, similar to the one induced by leaching (Chen, Thomas, et Jennings 2006), has been observed on pre-dried samples (195 days in a 25°C, RH=55% climatic chamber before test). Carbonation shrinkage is associated with the decalcification of C-S-H. The presence of portlandite provide indirect protection from cracking induced by carbonation.

1.2.2.3. Chlorides

Chloride ions can come from the concrete itself (formerly use of chloride-containing admixtures for reinforced concrete) or from outside (de-icing salts or sea salt in marine environments etc) (Bamforth, Price, et Emerson 1997; Glass et Buenfeld 2000). When chloride ions penetrate into concrete matrix from external environments, some of them react with hydration products in cement and form bound chloride, and others remain in pore solution as free chloride which can further move inward (Hou, Li, et Wang 2018; Martín-Pérez et al. 2000). The progression of chloride ions depends on the conditions of saturation of the concrete, exposure to the environment containing the chloride ions and fixing capacity of the matrix. Chloride ions penetrate the cementitious matrix much faster when the concrete is subjected to wet/dry cycles than when it is saturated (Francy 1998). The use of fillers decreases the porosity (open porosity and pore size distribution). The penetration of chloride ions is consequently reduced.

Corrosion of reinforced concrete steels can be initiated or enhanced by chloride ions. In this case, the depassivation of the steel is initiated when the chloride penetration front crosses the concrete cover and the chloride concentration reaches the threshold value (Glass et Buenfeld 2000). The thesis focuses on the cement paste. Therefore, the impact of chlorides on steel corrosion will not be detailed.

Besides the effect of chloride on corrosion, chloride can bound to hydration products (C-S-H, portlandite, ettringite (AFt), aluminate-ferrite-monosubstituent phases (AFm), etc) either by a chemically combination or by physically adsorption (Ipavec et al. 2013; Florea et Brouwers 2012). C-S-H can adsorb massive chlorides due to its large specific area (Chang et al. 2019; Beaudoin, Ramachandran, et Feldman 1990; Zhou et al. 2016). Some experiments with high concentrations of $MgCl_2$ (up to 15wt% (Yang et al. 2020), 20wt% (Xie, Dang, et Shi 2019) and 26.7wt% (Qiao et al. 2018)), have been performed and showed that new salts and species are formed (Friedel's salt,

brucite, magnesium oxychloride, and/or secondary calcium oxychloride). The recrystallisation of salts when the concrete is subjected to drying/wetting cycles can cause cracking and damage to the concrete (Neville 1995; Pigeon 2014; Escadeillas et Hornain 2008).

The addition of fly ash and slag in the binder increase the chloride binding capacity of hydrated cements due to the increased amount of aluminium in the binder and the facilitated formation of Friedel salts. On the contrary, addition of silica fume reduces the content of aluminium in the binder and therefore decreases chloride binding (Ipavec et al. 2013).

1.2.2.4. Sulphates

The action of sulphates is associated with the internal sulphate attack (ISA) and external sulphate attack (ESA). In the first case, the source of sulphates is a phase of the material (aggregates or cement paste). In the second case, sulphates come from the external environment. As the magnesium environments correspond to external sulphate attack, only the latter will be developed here.

ESA is a pathology due to a high concentration of sulphates in contact with the concrete. Sulphates can be found in several forms: solid (gypsum soils), liquid (natural water percolating through soils and solutions of various origins), or gaseous (atmospheric pollution by SO_2) (Escadeillas et Hornain 2008). ESA occurs in a moist, sulphate-concentrated environment with sufficient permeability for the penetration of sulphate ions. Without one of these three elements, the sulphate ions cannot diffuse and the attack does not take place (Collepardi 2003).

The attack is characterised by two mechanisms. Firstly, the calcium present in the portlandite and C-S-H is leached out. The release of Ca^{2+} ions allows the formation of gypsum ($CaSO_4.2H_2O$). (Santhanam, Cohen, et Olek 2002a; 2003b). In a second stage, ettringite is formed. It results from the reaction of gypsum (more or less dissociated into SO_4^{2-} and Ca^{2+} ions) with the calcium aluminates of the binder (anhydrous aluminates: C_3A, C_4AF or hydrated aluminuates: C_4AH_{13} or calcium monosulfoaluminate) (Santhanam, Cohen, et Olek 2002a; 2003b; Escadeillas et Hornain 2008). Gypsum and ettringite formation can cause expansion in volume and cracks (Santhanam, Cohen, et Olek 2001; 2002a). The composition of the binder plays an important role in the effect of sulphate attack. If the binder contains no aluminium (C_3S), only gypsum is formed. For OPC, both gypsum and ettringite are formed (Santhanam, Cohen, et Olek 2003a). More cracking for the OPC mortar than C_3S mortar has been observed because no ettringite is observed in the second case. The effect of additions has also been studied (Santhanam, Cohen, et Olek 2002a). Replacing part of the cement with silica fume (10%) or metakaolin (20%) reduces the expansion. In the magnesium sulphate solution, the silica fume paste exhibited the lowest expansion.

Different types of zones are formed one after the other, from the sound zone to the surface. They depend on the type of aggressive solution. With sodium sulphate solution, three distinct zones are formed. Zone 1 is the chemically unaltered zone (sound zone), zone 2 is composed of gypsum around aggregates and in pores, and ettringite within the paste, zone 3 is a cracked and highly deteriorated surface zone. With magnesium sulphate solution, a external layer of brucite and gypsum forms on the surface and prevents the free passage of the external solution into the mortar. Gypsum and ettringite form just below this external layer. In severely deteriorated areas, where the brucite layer is cracked, M-S-H takes the place of C-S-H (Santhanam, Cohen, et Olek 2002a).

1.2.2.5. Magnesium

Several studies have investigated the impact of $MgCl_2$ and $MgSO_4$ solutions on cementitious materials. The presence of magnesium, as discussed previously (1.2.2.4), can modify the zonation of external sulphate attack. As $MgSO_4$ impact has already been dealt with previously, this section focuses on the impact of $MgCl_2$. Several concentrations of $MgCl_2$ in the aggressive solution were tested: from 4.3wt% to 26.7wt% (Qiao et al. 2018), from 0wt% to 15wt% (Yang et al. 2020) and from 1wt% to 20wt% (Xie, Dang, et Shi 2019) i.e. from 100 to 3100 mmol/L.

The presence of magnesium causes the formation of magnesium phases: brucite, magnesium oxychloride (when chlorides are also present), hydrotalcite and M-S-H (Qiao et al. 2018; Xie, Dang, et Shi 2019). Dissolution of portlandite ($Ca(OH)_2$) makes OH^- ions available allowing the formation of brucite ($Mg(OH)_2$) (Yang et al. 2020). The use of $MgCl_2$ decreases the pH of the aggressive solution (Xie, Dang, et Shi 2019) and as M-S-H are stable at lower pH than C-S-H (7.5-11.5 for M-S-H versus 10-12.5 for C-S-H), M-S-H are formed (Qiao et al. 2018; Bernard et al. 2017a). Brucite forms as a layer on the surface (Xie, Dang, et Shi 2019) while M-S-Hs replace C-S-Hs, within the cement paste (Qiao et al. 2018). Hydrotalcite is observed in small quantities although modelling predicts it to be present in larger quantities (Yang et al. 2020).

These studies were conducted on OPC (Yang et al. 2020; Xie, Dang, et Shi 2019; Qiao et al. 2018) or fly-ash substituted pastes (Qiao et al. 2018). The C/S ratio of these pastes is therefore high. As the presence of portlandite is associated to high pH of the pore solution, the formation of brucite is favoured against M-S-H. It is expected that the reduction of the C/S ratio consumes all or part of the portlandite and modifies the phenomenon. There is a lack of studies on this aspect. Two studies on low C/S cementitious materials in contact with magnesium have been carried out by Bernard (Bernard et al. 2017a; Bernard, Dauzères, et Lothenbach 2018a).

The first study consisted of (i) synthesising C-S-H (C/S=0.8) and (ii) placing the wet C-S-H in a $MgCl_2$ or MgO solution to see which species precipitate (Bernard et al. 2017a). The addition of $MgCl_2$ lowers the pH and destabilise the C-S-H which are decalcified, and M-S-H are formed. On the other hand, the addition of MgO increases the pH and leads to the formation of brucite and M-S-H. The dissolution kinetics of brucite is low. Consequently, brucite can be observed experimentally whereas models predict only M-S-H.

The second study consisted of bringing two discs into contact, one consisting of C-S-H (C/S=0.8) and the other of M-S-H (M/S=0.8), both synthesised in suspension form and then compacted (Bernard, Dauzères, et Lothenbach 2018a). To ensure saturation of the samples, at each end of the discs a solution in equilibrium, with the C-S-H and M-S-H respectively, was placed. This study investigated the mechanism of formation of M-S-H, validating the theory that M-S-H is formed from the dissolution of C-S-H.

1.2.2.6. Summary

Magnesium environments contain many ions whose respective effects have been studied in the last 30 years, with the exception of the effect of magnesium where the literature is limited to a few studies. These studies are moreover concentrated on OPC. However, the new binders, in particular the low-pH ones considered for geological disposal of radioactive waste, exhibit a different mineralogy. It is expected that the absence of portlandite will modify the reaction mechanisms of magnesium attack and it seems necessary to study the impact of magnesium independently of other ions. In the absence of such a study, the next section proposes to study the impact of real magnesium environments on cementitious materials, especially materials with low C/S ratios to investigate the main mechanisms of magnesium attack on these materials.

1.2.3. Effect of real environments (multi-ionic aqueous media) on cement matrices

1.2.3.1. Deep geological repository environment

In the context of the Cigéo project, in the contact zones between the rock and the concrete (see Figure 1 in General introduction), the use of low-pH concretes is envisaged in order to limit the impact of the concrete on the clay of the host rock and the swelling clay used to close the galleries (Dauzeres et al. 2010; Gaucher et Blanc 2006; Savage et al. 2007).

The pore water contained in the host rocks planned for geological disposal may contain magnesium (see first 4 lines of Table 1-6) and will come into contact with the concrete. The

magnesium concentrations in both cases are of the same order of magnitude; 6.7 mmol/L in the first case (Dauzères et al. 2014) versus. 16.1 mmol/L in the second case (Fernández et al. 2017; Alonso et al. 2017).

Degradation of concrete at rock contact can be divided into several zones. According to Calvo (García Calvo et al. 2010), 3 zones can be observed in the solid during contact between a low-pH concrete and groundwater. The first, in the heart of the sample, is the sound zone. The second zone, closer to the surface, is a decalcified zone (0.25<C/S<0.6). The last zone, at the surface, is enriched in magnesium and chloride. Mg and Cl- ions seem to be incorporated in the solid phases (C-S-H for the most part).

In 2014, Dauzères (Dauzères et al. 2014) studied these zones in more detail on two types of concrete, a low-pH and a CEM I-based concrete. According to him, the degradation could be divided in section according to the following scheme (Figure 1-11):

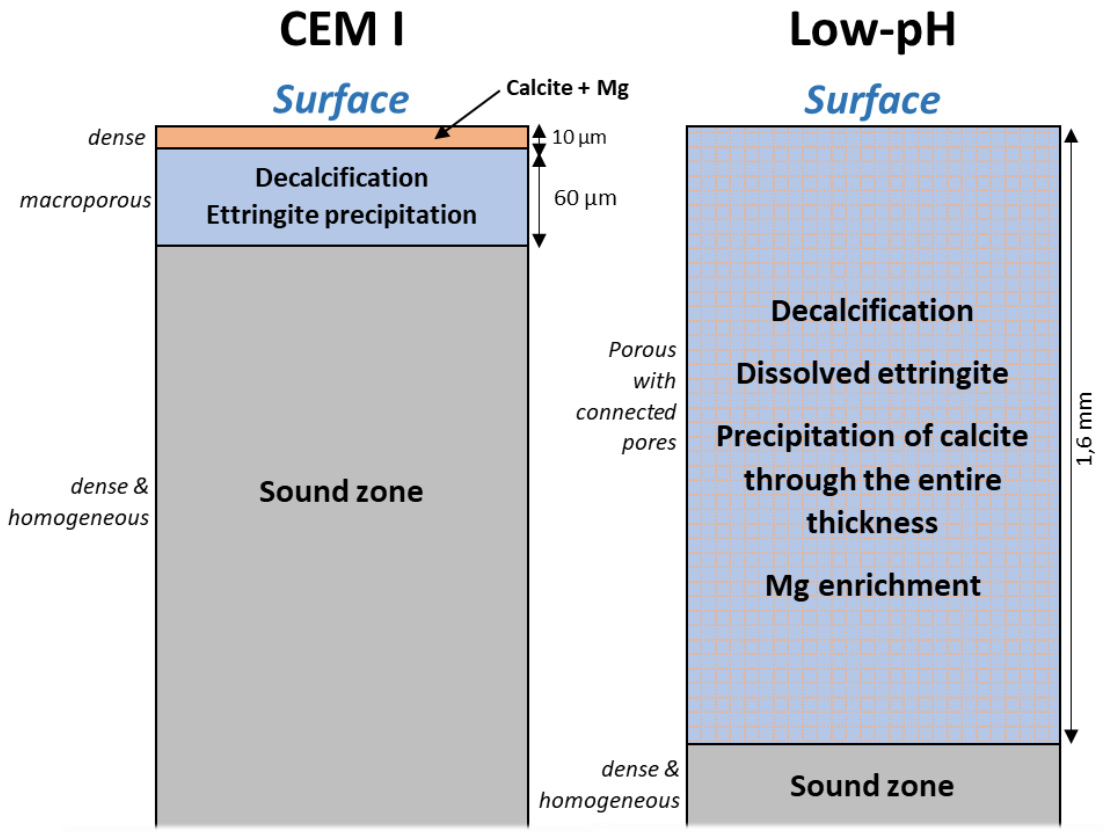

Figure 1-11 : Schematic representation of the degradation on two types of concrete after 5 months in water that replicates groundwater concentrations, after (Dauzères et al. 2014)

A magnesium attack is observed on both pastes. For CEM I, the external layer seems to be enriched in Mg, creating a Mg-calcite layer. After 5 months, the layer consists of 3% Mg (atomic %). For low-pH, below the amorphous silica and calcite, M-C-S-H or M-S-H mixed with C-S-H can be observed. This shows that M-S-H gel formation is possible, even at low Mg concentration (6.7 mmol/L see Table 1-6).

In the case of contact between some bentonites and concrete, Fernández (Fernández et al. 2017) proposes a decomposition of the magnesium attack in several stages, based on his in situ laboratory study (Dauzères 2010; Fernández et al. 2004; Sánchez et al. 2006). It would be characterised initially by the dissolution of part of the magnesium-rich minerals in the bentonite, such as montmorillonite. This is followed by the precipitation of secondary minerals such as

brucite. An unknown magnesium phase is also observed in this study. Several structures and compositions have been proposed for this phase. For some researchers, the phase they observe corresponds to C-S-H in which magnesium atoms would be incorporated or M-C-S-H (Alonso et al. 2017; Dauzères et al. 2014; García Calvo et al. 2010). The structure remains broadly the same; the phase appears amorphous.

1.2.3.2. Rivers and streams

Soft water naturally contains magnesium in small amounts (~0.05 mmol/L). Despite the limited amount of magnesium, M-S-H is observed. Rosenqvist (Rosenqvist et al. 2017) investigates the alteration of a dam after 55 years of exposure. The composition of the water is shown in Table 1-6 in row 5. Several areas of the dam are analysed. On the surface, the concrete is abraded. Deep in the water, the temperature change does not cause a freeze-thaw cycle or abrasion. It is this area that is most representative of the effect of soft water on the concrete.

Climatic conditions play a major role in degradation. The work of Rosenqvist et al. (Rosenqvist et al. 2017) confirms this assertion. The deeper the concrete under water, the greater the hydrostatic pressure. The water no longer enters the concrete only by capillary suction, but is also pushed by the hydrostatic pressure. Thus, as more water enters the concrete, the decalcification of the C-S-H increases and the concrete appears more degraded at greater depths.

Like deep geological repository, concrete degradation is divided into several zones. Figure 1-12 illustrates the layout of the zones and the associated phenomena. Figure 1-13 shows the evolution of the chemical composition of the cement paste in these zones.

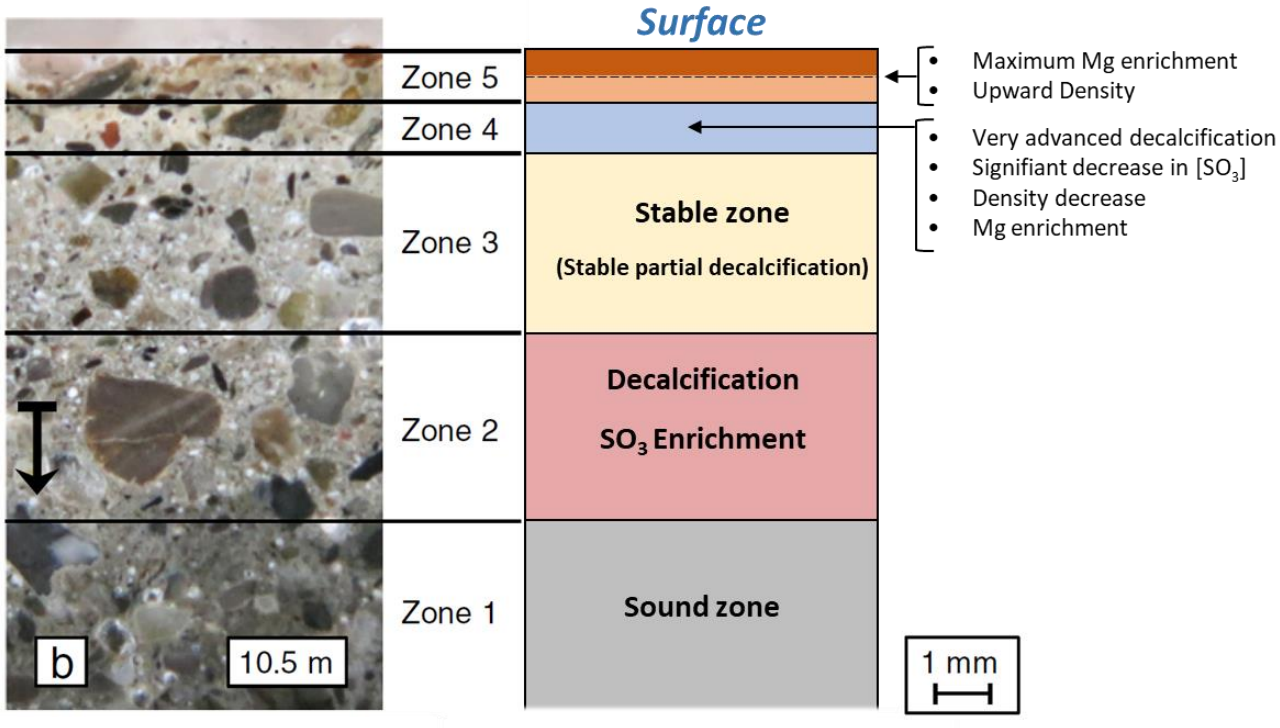

Figure 1-12 : Illustration of the degraded sample at 10.5m depth in a dam and identification of the zones adapted from (Rosenqvist et al. 2017)

The arrow corresponds to the marker from which the phenolphthalein was reacted.

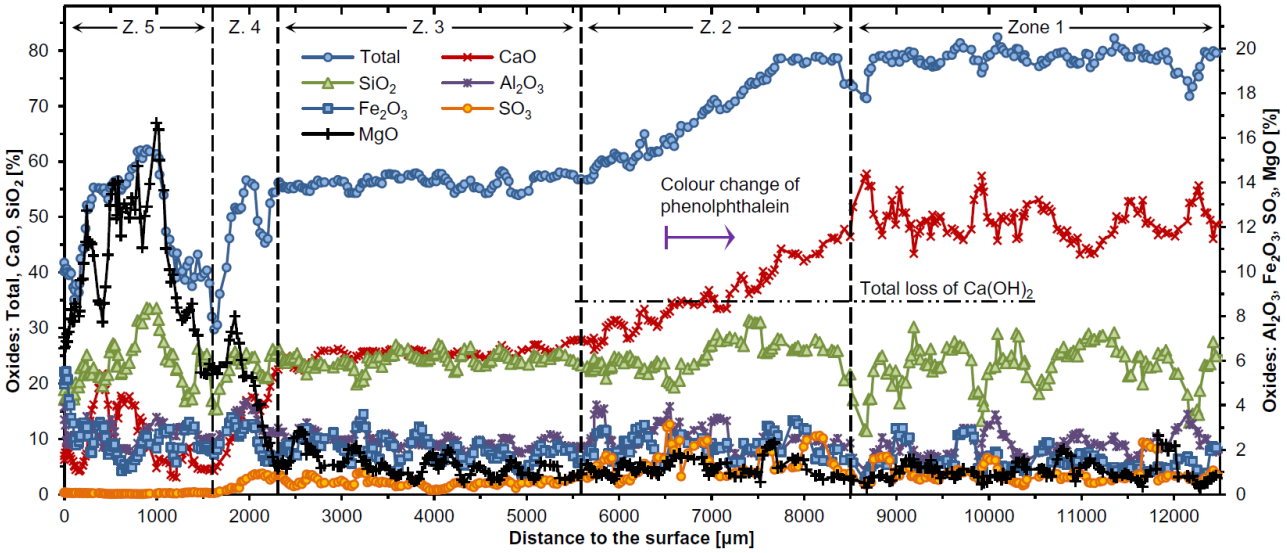

Figure 1-13 : Composition of cement paste in concrete at 10.5 m depth (of a dam) as a function of distance from the upstream face, by microprobe, after (Rosenqvist et al. 2017). The horizontal line represents the theoretical limit of total portlandite loss in the cement paste.

The first zone is the sound zone (Z1). Zone 2 (Z2) shows a decalcification and an enrichment, with respect to the sound zone, in SO_3. From the sound zone, there is a dissolution of the portlandite and a partial decalcification of the C-S-H, in parallel with a dissolution of the AFt and AFm phases. An intermediate zone (Z3) joins the magnesium-rich zone at the surface. In this zone (Z4), decalcification is maximal and the SO_3 concentration is low. The concentration of magnesium in the solid does not vary in the same way depending on the depth at which the coring is carried out. At medium depth (10.5m), magnesium enrichment is highest in the middle of the Mg-rich zone (Z5), whereas at great depth (18.5m) it is highest at the surface.

The degraded areas show increased porosity and degraded mechanical properties. This is consistent with calcium leaching and decalcification. The major mineral changes are localised near the surface.

1.2.3.3. Marine environment

Jakobsen (Jakobsen 2013) published a study of 18 concretes exposed to cold sea water in Denmark (at Rødby Harbor) for 6 months to 2 years. The composition of the water is given in the last lines of Table 1-6. The very broad study allows comparison of the degradation on several types of concrete (CEM I or CEM III). According to the chemical analysis, the degradation can be divided into 3 zones. The first is decalcified, carbonated and rich in magnesium. The second is rich in sulphur and the last in chloride. After 6 months, these three zones are already observable and become more refined over time. Apart from one formulation, no concrete contains brucite. This concrete contains 15% fly ash (FA) and is partially covered with brucite after 2 years. For the others, the first zone shows no brucite and consists almost entirely of Si and Mg. For two concretes, it is hydrotalcite. For the others, it is M-S-H.

In 2015, De Weerdt and Justnes (De Weerdt et Justnes 2015) adopted a different methodology. In order to study the effect of seawater on phase assembly, they crushed cement paste and place it in seawater. They were looking to see how the ions in the seawater change the structure of the concrete. The methodology adopted allowed the acceleration of phase development but analysis of the depth of degradation is not possible.

The ground paste is enriched in magnesium, sulphur and chloride (twice as much as the others). At the same time, it leaches calcium and potassium. Massive decalcification results in a loss of mass. Degradation leads to dissolution of portlandite, decalcification (partial or total) of C-S-H, formation of gypsum and calcium carbonates with the leached calcium.

Magnesium-rich particles appear. The authors state that these are largely M-S-H that would have been formed by substitution of Mg with Ca through partial decalcification of C-S-H. Contrary to Lerouge (Lerouge et al. 2017), De Weerdt and Justnes reject the hypothesis of a precipitation of M-S-H from hydrated silicate and decide on M-S-H produced by the substitution of Ca by Mg. They based their opinion on the morphology of Mg-rich particles observed in BSE (back-scattered electrons). Indeed, they appear very similar to Ca-rich particles except that they are very rich in Mg. The M-S-H observed in this study varies from M/S=0.9 to 2.5. The high M/S observed could be attributed to a fine mixture of brucite with M-S-H. For M/S ratios below 1, the author proposes that these are partially decalcified C-S-H where calcium is substituted by magnesium. In addition, aluminium appears to be incorporated into the M-S-H (Al/Mg=0.2), and decalcified C-S-H and M-S-H can incorporate chlorides.

In 2016, Jakobsen (Jakobsen, De Weerdt, et Geiker 2016) completed his research with a paper on 21 degraded concretes at 9 locations in Denmark and Norway in seawater. The exposure lasts between 2 years and 34 years.

These concretes all show degradation in three zones, as shown above. These are the same zones: the magnesium enrichment zone, the sulphur zone and finally the chloride zone. The order of the zones is independent of age, location and binder composition. No macroscopic damage is observed in the studied concretes. Figure 1-14 (Jakobsen, De Weerdt, et Geiker 2016) illustrates this zonation by detailing the species present and the evolution of chloride, magnesium, calcium and sulphur concentrations.

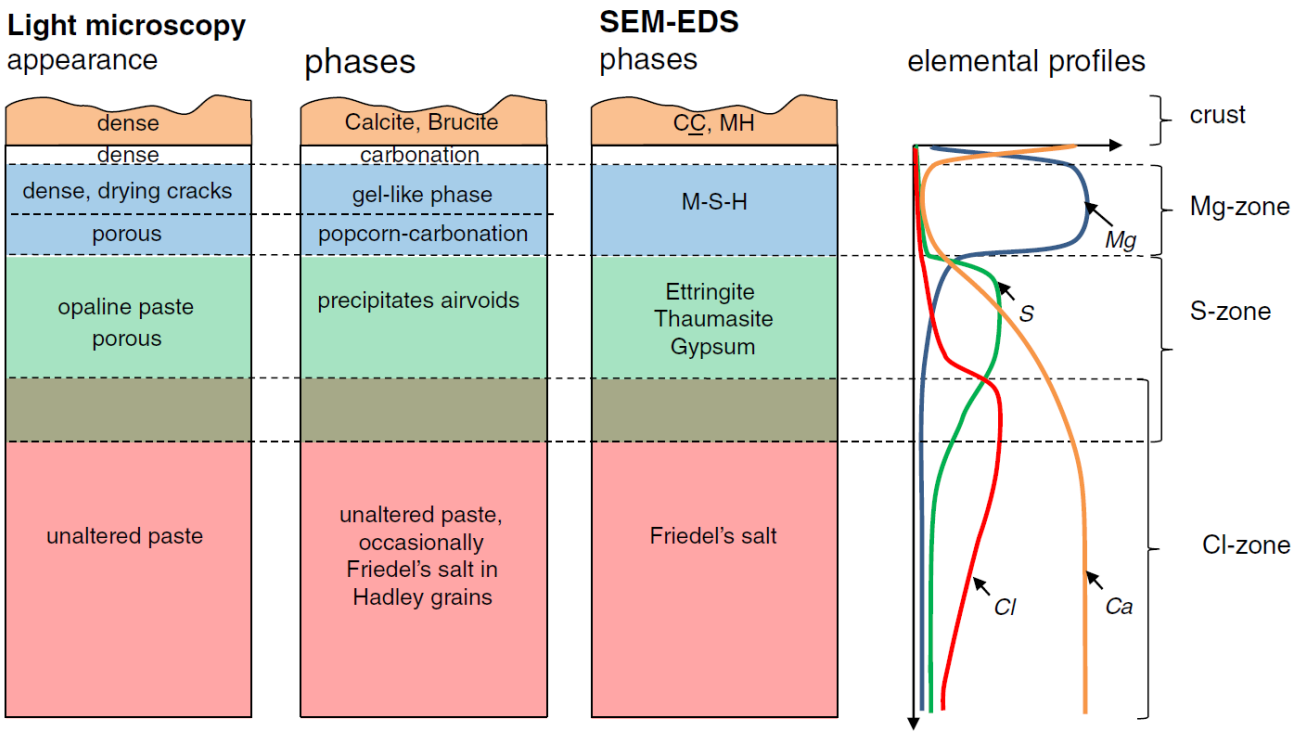

Figure 1-14 : Schematic overview of the different zones and the corresponding observations using light microscopy and SEM-EDS of a concrete exposed to see water (Jakobsen, De Weerdt, et Geiker 2016)

For most concretes, an increase in porosity is observed at the surface. Only the concretes with a calcite external layer do not show this increase. For most concretes, the magnesium and sulphur rich zones are located in the area of increased porosity, indicating that the volume of the sulphur and magnesium rich phases is insufficient to compensate for the leaching.

In addition, in some specimens brucite precipitates. It is mixed with the calcite layer which is embedded in the cracks. In the magnesium-enriched zone, the main phase is M-S-H. This zone shows strong leaching and decalcification. The morphological similarities between M-S-H and C-S-H and the indication that M-S-H are only visible when strong decalcification takes place, could lead to the idea that M-S-H are formed by substitution of Ca by Mg. However, the author refutes this assumption based on the research of Nied (Nied et al. 2016) and Roosz (Roosz et al. 2015) who expose that the structure of M-S-Hs differs greatly from that of C-S-Hs, even showing that they cannot be formed with an ion exchange between Mg and Ca. Like Lerouge (Lerouge et al. 2017), Jakobsen rejects the hypothesis of magnesium incorporation into C-S-H and positions herself in favour of M-S-H precipitation from fully decalcified C-S-H. M-S-H then replaces decalcified C-S-H and the M-S-H rich zones are often porous. The low cohesion of the zone and erosion can cause this zone to split with the rest of the paste and decompose in water.

For concrete with a calcite external layer, no M-S-H is detected. This seems to show that this calcite layer prevents the formation of M-S-H. In some specimens, a particular morphology of M-S-H is observed, called "magnesium freckles". The origin of this morphology is not known. Sometimes, brucite is integrated between M-S-H sheets. Overall, M-S-H is observed systematically while brucite is observed on only some specimens and integrated in the calcite layer or in cracks as in the deep geological repository environment (1.2.3.1).

Finally, as no macroscopic damage is visible, it seems that the phase change does not lead to major spalling. However, it should be noted that the specimens studied are from the intact parts

of the structures. Therefore, they do not take into account any errors in positioning that may have occurred or inhomogeneities.

Depending on the environment, the mechanisms associated with magnesium attack differ. In soft water, for example, despite the observed magnesium enrichment, neither brucite nor hydrotalcite is observed. This difference with the marine studies can be explained by the difference in water composition. River water has a low Mg and Ca content compared to sea water. The leaching of calcium is therefore very strong, preventing the formation of brucite or gypsum. At the same time, this favours the formation of M-S-H.

1.2.3.4. Summary

The consequences of a magnesium attack will be different for a low-pH binder than for a OPC. The composition of the binder influences the pH and the concentration of ions in repository, which shifts the equilibrium of the solid phases. For a freshly hydrated CEM I binder, the pH of the pore repository can reach 13.5 due to the concentration of alkalis (Lothenbach et Winnefeld 2006; Vollpracht et al. 2016). For a low-pH binder, the pH can drop to around 11 (Codina 2007).

During a magnesium attack, in the case of standard concretes (CEM I), a protective magnesium calcite external layer is formed limiting/preventing the precipitation of M-S-H (Dauzères et al. 2014; Rosenqvist et al. 2017; Jakobsen 2013). This calcite layer protects the concrete by covering the surface and limiting diffusion effects.

Moreover, the presence of portlandite delays the decalcification of C-S-H. Indeed, the latter is the first to dissolve (Alonso et al. 2017; Dauzères et al. 2014; Fernández et al. 2017).

In the case of low-pH concretes, where portlandite is absent (Dauzères et al. 2014; García Calvo et al. 2010; Lerouge et al. 2017), decalcification is faster and surface porosity is increased. In the absence of a calcite layer, diffusion phenomena are accelerated and decay depths are greater. For example, in the work of Dauzères et al. (Dauzères et al. 2014), portlandite is dissolved to a depth of 100 µm after 5 months for a CEM I whereas for a low-pH, decalcification extends to 1.5 mm depth. The formation of M-S-H is therefore facilitated with the use of low-pH binders.

Over time, several formation processes have been proposed by researchers. The formation of M-S-H has always been linked to C-S-H. As early as 1995, d'Espinose de la Caillerie (d'Espinose de la Caillerie, Kermarec, et Clause 1995) studied a magnesium silicate formed from an impregnation of silica with an aqueous Mg^{2+} repository. They then discovered the formation of a hydrated magnesium silicate, an M-S-H. They proposed two possible formation mechanisms. On the one hand, it could be a dissolution-precipitation phenomenon where the solubility of the silica is not altered but the Mg^{2+} ions combine with soluble silica and precipitate into a less soluble and more hydrated species. On the other hand, it could be a situation where the adsorption of magnesium on the surface disturbs the chemical environment of the silicon atoms and weakens the Si-O bonds.

The precipitation-dissolution hypothesis is opposed to a substitution phenomenon of calcium by magnesium in C-S-H. The substitution process was initially supported by researchers (Alonso et al. 2017; Dauzères et al. 2014; De Weerdt et Justnes 2015; Fernández et al. 2017; García Calvo et al. 2010). However, the work of Lothenbach (Lothenbach et al. 2015), studying the interaction between C-S-H and M-S-H, suggests the impossibility of calcium substitution by magnesium in C-S-H given the difference in ion size. Subsequently, Dauzères, Jakobsen, De Weerdt and Lerouge (Dauzeres et al. 2016; Jakobsen, De Weerdt, et Geiker 2016; Lerouge et al. 2017) support the hypothesis of M S H formation by precipitation-dissolution.

The consensus is that the formation process can be defined as a dissolution-precipitation mechanism that can be divided into several steps.

In a first step, the concrete comes into contact with a magnesium source, e.g. $MgCl_2$ or magnesium ions. This causes decalcification of the C-S-H, the calcium is leached out and an amorphous silica

phase is formed. Magnesium ions can then bind with the amorphous silica and precipitate as M-S-H. An intermediate zone consists of both C-S-H, M-S-H and amorphous silica. Magnesium ions must penetrate and diffuse through the M-S-H layer to reach the amorphous silica and continue the formation of M-S-H.

Often the precipitation of M-S-H is accompanied by the precipitation of other species, depending on the surrounding environment, climatic conditions, exposure time and concrete mix. In natural waters, magnesium is not the only source of degradation (Dauzères et al. 2014; Rosenqvist et al. 2017; Jakobsen, De Weerdt, et Geiker 2016).

When concrete comes into contact with an aqueous medium, multi-ionic chemical degradation can take place. In the case of a magnesium-containing medium containing magnesium (soft water, sea water, clay rock), the action of sulphates, chlorides and/or carbonates is accompanied by a magnesium attack. Concrete becomes enriched in magnesium within its cement paste. The formation of several magnesium-containing species has been observed. One of these species, M-S-H, forms deep in the paste and takes the place of a binding phase, C-S-H. In order to determine the influence of the magnesium attack on the mechanical properties of the concrete, it is necessary to know the chemo-mechanical properties of the M-S-H and to carry out a scaling up by taking into account the associated microstructural modifications of the cement paste. For this purpose, it is necessary to know the chemical, microstructural and mechanical properties of C-S-H, as well as the ones of M-S-H.

1.2.4. Properties of phases resulting from chemical degradation

1.2.4.1. Decalcified C-S-H and amorphous silica

As presented in 1.2.2.1, Ca leaching of the cement paste implies the dissolution of portlandite and the decalcification of C-S-H. Different studies were conducted to determine the decalcification mechanism of C-S-H and its influence on the microstructural and mechanical properties of the C-S-H.

Liu (Liu et al. 2019) shows that the decalcification of C-S-H corresponds to a decrease in the C/S ratio of C-S-H and their polymerization. He studied synthetized C-S-H leached in NH_4NO_3 solutions with increasing concentration to study different decalcification states. According to the NMR results, the proportion of Q^1 site decreases and those of Q^2, Q^3, and Q^4 sites gradually increase with the decalcification and the decrease of C/S ratio of C-S-H. He proposes the scheme in Figure 1-15 to illustrate the mechanism. At the beginning, the interlayer is leached and in parallel, the silicon chain linkage increase. For higher decalcification states, C-S-H crosslinking is observed. As long as C-S-H maintains its tobermorite-like layer structure during decalcification, the intralayer Ca does not leach out. Further decalcification takes place by a complete dissolution of C-S-H and formation of amorphous silica.

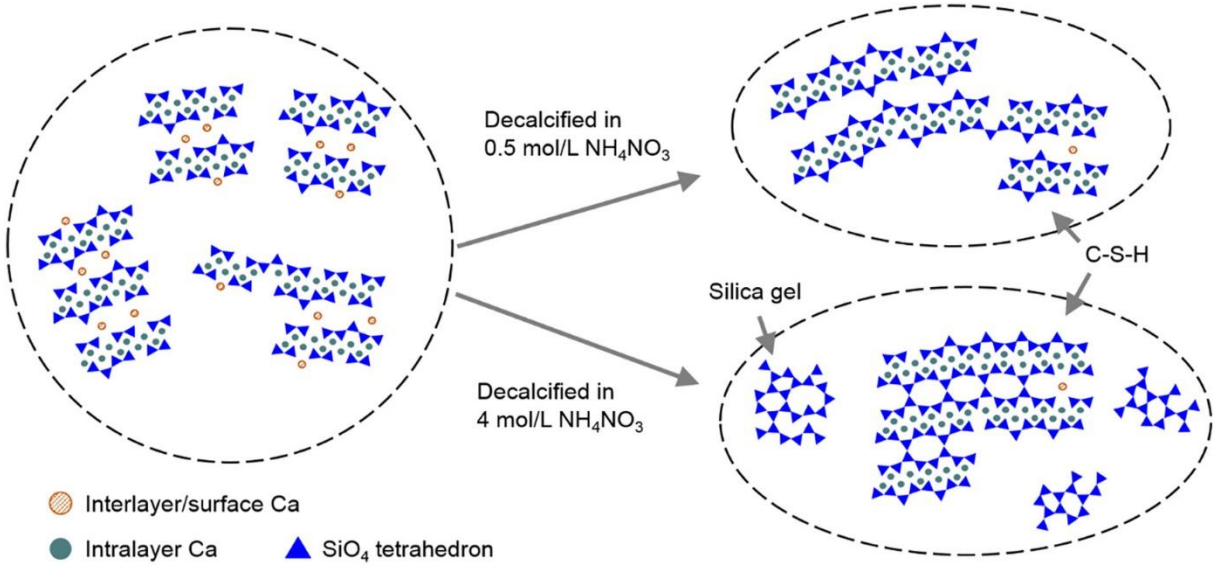

Figure 1-15: Illustration of the atomistic structural evolution of C-S-H undergoing decalcification using NH_4NO_3 solution (Liu et al. 2019)

Constantinides (Constantinides et Ulm 2004) studied the mechanical properties of leached C-S-H by nanoindentation. As detailed in 1.1.2.4 and 1.1.4.3, two types of C-S-H are defined depending on their formation process, density and mechanical properties : LD and HD C-S-H. Ca leaching leads to a loss of their intrinsic elasticity, but the volume fractions of the two types of C-S-H in the cement paste are not affected, suggesting that Ca leaching occurs homogeneously in the C-S-H matrix. The indentation modulus of LD C–S–H drops from 21.7 GPa to 3.0 GPa, and the indentation modulus of HD C–S–H drops from 29.4 GPa to 12.0 GPa after cement paste was placed in 6 mol/L NH_4NO_3 for 5 months.

When the decalcification of C-S-H is complete, only a silica gel remains. Like the C-S-H, the silica gel is considered porous. According to Snel and Zemnukhova (Snel 1984a; 1984b; Zemnukhova et al. 2015), its intrinsic porosity is 70%. No indentation has been performed on it. According to Bes' work (Bes 2019), upon pure leaching of a low-pH paste, the C/S in the degraded zone falls below the C-S-H limit value (0.6-0.7). The degraded zone could therefore be considered as consisting of a silica gel. Bes obtains mechanical properties after homogenization in this zone of $0.1*E_{sound}$, i.e. equal to about 1.2 GPa. Consequently, the Young's modulus of amorphous silica could be considered as egal to 1.2 GPa.

1.2.4.2. Hydrotalcite and Brucite

Brucite and hydrotalcite are two magnesium phases that are formed during the magnesium attack of cementitious materials (Qiao et al. 2018; Xie, Dang, et Shi 2019; Jakobsen 2013; Jakobsen, De Weerdt, et Geiker 2016).

In magnesium attack, brucite ($Mg(OH)_2$) forms on the surface of the cementitious material as a external layer. It limits the diffusion of ions contained in the environment towards the cement matrix and the diffusion of cement cations towards the outside (Santhanam, Cohen, et Olek 2002a; Jakobsen, De Weerdt, et Geiker 2016). Brucite is studied in the context of the production of novel cement systems for waste encapsulation that would form with a pH of around 10 (Zhang, Cheeseman, et Vandeperre 2011; Zhang, Vandeperre, et Cheeseman 2014) or to develop a alkali-activated industrial by-products to reduce the production of Portland cement in many civil engineering applications (Wang et al. 2018). In this case, the brucite does not precipitate as a layer on the surface of the material but forms within the paste with M-S-H. In these pastes, brucite is a transitional hydration product that will react with silica to form M-S-H. Thus, these intrinsic properties have not been studied.

Hydrotalcite is both a phase that can be formed during the hydration of cement with slag (Brew et Glasser 2005a) and during the magnesium attack of cementitious materials (Jakobsen 2013). Hydrotalcite is formed within the degraded zone during the magnesium attack of cementitious materials (Jakobsen 2013). Hydrotalcite is a Mg and Al based layered double hydroxide solid with an isomorphic substitution of Mg^{2+} by Al^{3+} in the brucite-like sheet. The main layer can have a variable Mg/Al ratio (Richardson 2013; Mills et al. 2012) and different interlayer anions can be contained in the interlayer (Mills et al. 2012). Consequently, the structure and composition of hydrotalcite evolve according to the Mg/Al ratio and the anions which can be contained in its interlayer. Hydrotalcite can be written as $[Mg_{1-x}\,Al_x\,(OH)_2]^{x+}\,[A_{x/n}{}^{n-}\,mH_2O]^{x-}$ with $0 < x < 0.33$; "A" indicates the presence of anions such as OH^-, Cl^-, $NO3^-$, CO_3^{2-}, SO_4^{2-}, in the interlayer (Miyata 1983; Bernard et al. 2022). Hydrotalcite group is also named layered double hydroxides (LDHs) or hydrotalcite-like compounds (HTlc) (Goh, Lim, et Dong 2008). A representation of its structure is given in Figure 1-16. Its behaviour is not yet well known and is the subject of research, particularly with regard to the incorporation of ions into its interlayer (Bernard et al. 2022). While its chemical and mineralogical properties are well studied (powder X-ray diffraction, Fourier transform infrared spectroscopy, Raman spectroscopy, thermogravimetry, scanning electron microscopy, nuclear magnetic resonance etc.), its mechanical properties are currently unknown (Goh, Lim, et Dong 2008).

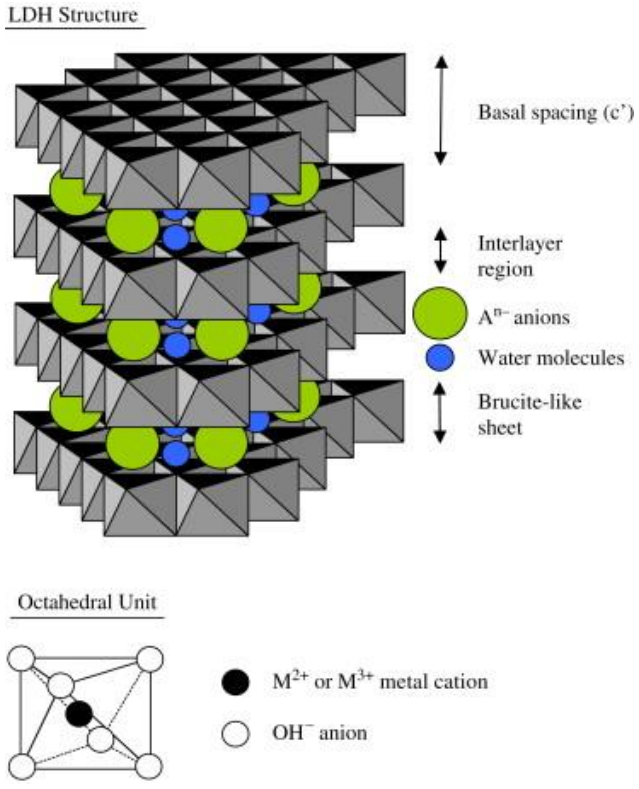

Figure 1-16: Schematic representation of the LDH structure (Goh, Lim, et Dong 2008)

1.2.4.3. M-S-H

The formation of M-S-H has been observed during the magnesium attack of cementitious materials within the paste (Qiao et al. 2018; Xie, Dang, et Shi 2019; Santhanam, Cohen, et Olek 2002b; Alonso et al. 2017; Dauzères et al. 2014; García Calvo et al. 2010; Jakobsen 2013; Rosenqvist et al. 2017; De Weerdt et Justnes 2015; Jakobsen, De Weerdt, et Geiker 2016). To identify the chemical, mineralogical, microstructural and mechanical properties of M-S-H, M-S-H suspensions and pastes have been produced by researchers.

Initially, M-S-H was synthesised by suspension in a large volume of demineralised water. This made it possible to determine the chemical, mineralogical and thermodynamic properties of M-S-

H. To study the mechanical properties of M-S-H, cohesive pastes of M-S-H are required. Recently, the first M-S-H pastes have been made by greatly decreasing the water-to-solid (w/s) mass ratio. Table A-1 (Appendix A) shows the protocols and main results of researchers who have made M-S-H in the laboratory.

1.2.4.3.1. M-S-H identification via TGA and XRD

M-S-H are hydrated magnesium silicates whose notation is derived from the cementitious notation, as for C-S-H. M-S-Hs do not have a fixed stoichiometry and are defined by the ratio Mg/Si or M/S.

M-S-H are identified by X-ray diffraction (XRD) and thermogravimetric analysis (TGA). In XRD, M-S-H do not produce peaks but bulges due to their semi-amorphous nature. A maximum of 6 humps has been observed by different researchers. In 1995, d'Espinose de la Caillerie (d'Espinose de la Caillerie, Kermarec, et Clause 1995) identified two humps at 2.59Å and 1.525Å. In 2005, Brew and Glasser (Brew et Glasser 2005b) identified an additional bulge at 3.6-3Å. In 2015, Roosz (Roosz et al. 2015) identified three more. Table 1-7 lists the different M-S-H specific humps identified by the authors over time and Figure 1-17 shows the diffractograms obtained.

Table 1-7 : Identification of M-S-H by XRD, observed humps

Article	**Angle 2Θ [CuKα]**					
	19.7	26.7	35	54	59.9	71
(d'Espinose de la Caillerie, Kermarec, et Clause 1995) [CoKα]			2.59 Å		1.525 Å	
(Brew et Glasser 2005b)		3.6 – 3.0 Å	2.6 – 2.3 Å		1.6 – 1.5 Å	
(Zhang, Vandeperre, et Cheeseman 2014)		X	X		X	
(Roosz et al. 2015)	X		X	X	X	X
(Nied et al. 2016)	X	X	X		X	
(Bernard et al. 2017b)	X	X	X		X	
(Bernard et al. 2018)	X	X	X	X	X	

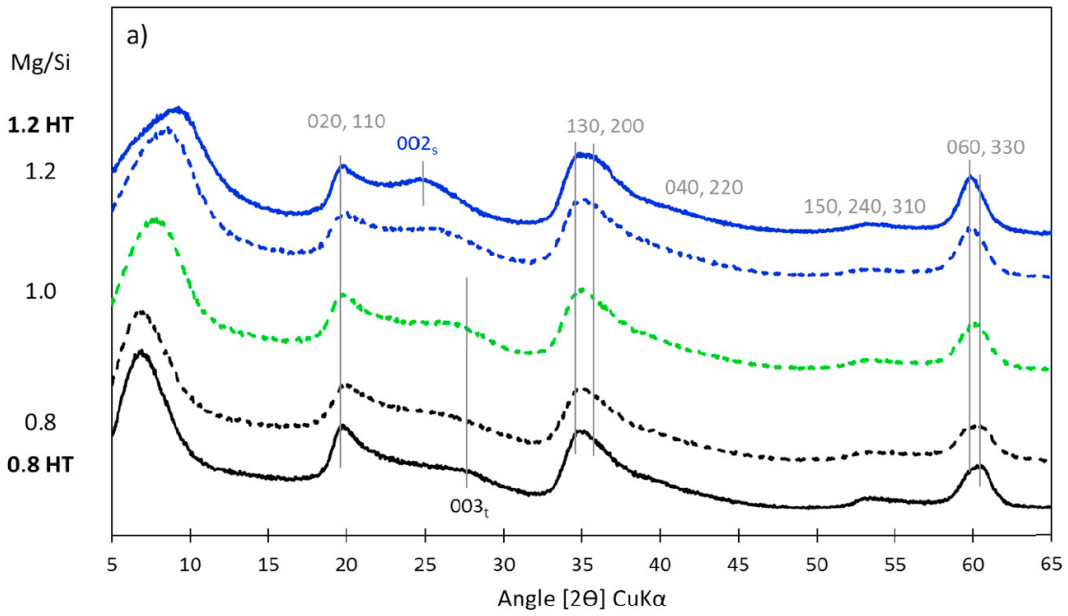

Figure 1-17 : Diffractograms associated to M-S-H synthesized by Bernard (Bernard et al. 2019). HT corresponds to hydrothermally synthesised samples.

The identification of M-S-H is validated by TGA. Three mass losses are observed (Mitsuda et Taguchi 1977; Zhang, Cheeseman, et Vandeperre 2011; Lothenbach et al. 2015; Nied et al. 2016; Bernard et al. 2017b) :

- Between 30°C and 280°C, the unbound or loosely bound water in the M-S-H creates the first significant mass loss.
- Between 280°C and 750°C, a weaker but more extensive hump is observed. These are the hydroxyl groups bound to the Mg^{2+} ions in the M-S-H.
- Between 750°C and 840°C, a last hump, similar to the previous one, is observed. It corresponds to the loss of the silanol groups of M-S-H.

In addition, the presence of brucite is revealed by a mass loss centred around 400°C.

Figure 1-17 corresponds to the TGA carried out on the M-S-H as in Figure 1-18. It illustrates the mass losses listed above.

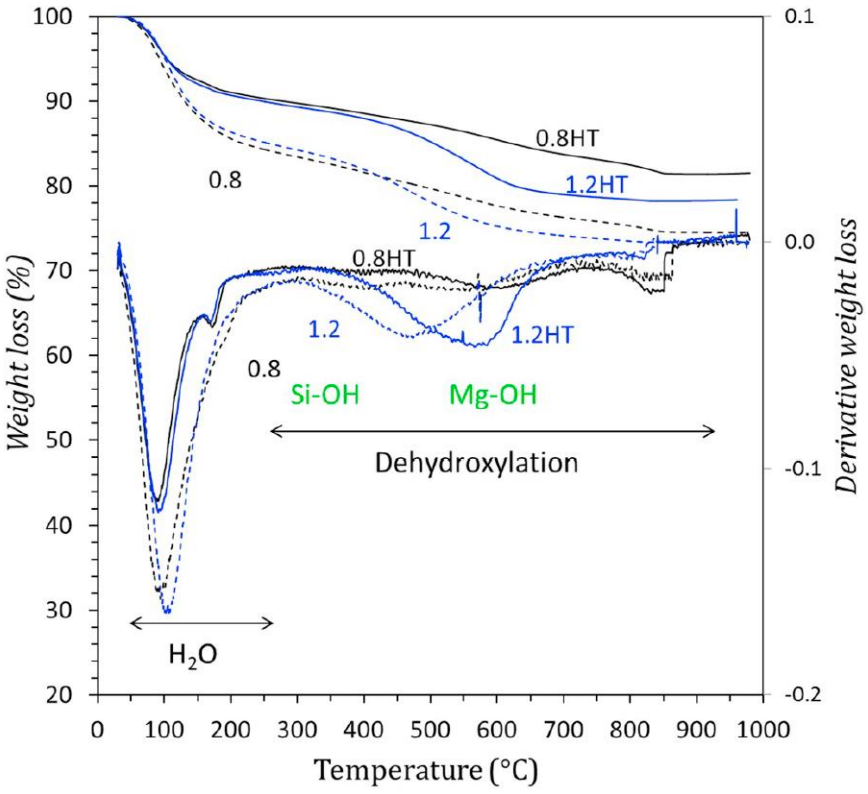

Figure 1-18 : Thermogravimetric analysis of M-S-H synthesised by Bernard (Bernard et al. 2019). HT corresponds to samples synthesized hydrothermally.

1.2.4.3.2. Structure and porosity

Many studies have focused on the structure of M-S-H in an attempt to approximate it to a known structure.

In 1995, D'Espinose de la Caillerie (d'Espinose de la Caillerie, Kermarec, et Clause 1995) discovered a phase during the impregnation of silica with an aqueous solution of Mg^{2+}. They defined it as hydrated magnesium silicates and observed two humps in XRD. These broad peaks on the diffractograms induce an amorphous phase which they define as a gel similar to a very disordered phyllosilicate. For them, the structure of M-S-H does not take the form of layers.

In 2005, Brew and Glasser (Brew et Glasser 2005b) agreed with d'Espinose de la Caillerie on the definition of M-S-H as a gel. They point out a poorly crystalline phyllosilicate structure that varies with the M/S ratio. For M/S around 0.6, it would be a structure close to sepiolite. For M/S around 0.75, it would be a kind of talc and for 0.8<M/S<0.9, it would be a mixture of two nanometric crystalline phases embedded in a relatively amorphous matrix, close to 2:1 and 1:1 phyllosilicates. Increasing the hydration time and the M/S ratio improves the local structural order.

In 2015, Roosz (Roosz et al. 2015) based his model on talc. The structure would be lamellar and turbostratic. The author tries several models of the M-S-H structure in order to find the structure that gives the closest XRD results to reality. To do this, he varies several parameters, notably :

- The **parameters a, b et c of the meshes.** In the end, he opts for a = 5.313, b = 9.191 Å and c = 9.46 Å.
- The **average size of the coherent scattering domain** in the ab plane is refined to 1.5 nm.
- Several **angles of rotation of the tetrahedra** are tested. Finally, the one that gives the best results is **7.1°.**

- The **percentage occupancy of the Si sites**. This occupancy varies from 100%, with full silica sheets (M/S= 0.75), to 80%, with a lack of silicon tetrahedra, which is in agreement with an M/S=1.2 ratio.

Finally, Roosz deduced that M-S-H correspond to nanocrystalline and turbostratic phyllosilicates, whose layer charge comes mainly from vacancies in the tetrahedral Si sites.

In 2015, Lothenbach (Lothenbach et al. 2015) confirmed that M-S-Hs have a sheet structure. The contrast with the silica dreierketten structure of C-S-H is clear. Lothenbach also highlights the large amount of chemically bound water in M-S-H.

In 2016, Nied (Nied et al. 2016) investigates the influence of the M/S ratio on the structure of M-S-H and the amount of bound water present. He shows that increasing the M/S ratio implies increasing the bound water present in M-S-H. He proposes two structures for M-S-H: either a sheet structure with gaps or broken chains, as put forward by (Roosz et al. 2015) or in double (triple) chain form as in anthophyllite. The silicate sheets would be connected by octahedrally coordinated layers of Mg^{2+} ions and similar to the structure of talc, antigorite or jimthompsonite. According to Nied, M-S-H shows two phyllosilicate structures: a talc-like structure at low M/S and a serpentine-like structure at higher M/S. As the ratio increases, the silicate network depolymerises.

In the same year, Tonelli (Tonelli et al. 2016) observed M-S-H in the SEM. The M-S-H have a homogeneous morphology at the microscopic scale and globular at higher magnification. The images show that the globule groups are smaller than 30 nm. The results seem to show a coexistence between a "talc-like" structure and a "chrysotile-like" structure. The molar ratio between these two phases is 1:1.

In 2018, Zhang (Zhang et al. 2018) observed how M-S-Hs form. M-S-Hs grow on the surface of the particles and come into contact with the solution. However, they do not grow into the space between the formed gel and the silica grains, leading to the formation of a shell-like structure.

In 2019, Bernard (Bernard et al. 2019) also investigates the structure of M-S-H. The authors support the hypothesis of a silicate sheet structure with small ordered regions. For low M/S ratios such as 0.8, the structure would be 2:1 phyllosilicate like talc or stevensite. For higher M/S ratios such as 1.2, the structure would be more of a 1:1 phyllosilicate like antigorite. M-S-H contains between 1 and 2.5 molecules of H_2O per silicon, which is much more water than talc. The water in M-S-H is present both as adsorbed water and in the structure as H_2O and hydroxyl groups. M-S-H would then behave like swelling clays such as saponite or montmorillonite. The total amount of water in M-S-H increases significantly with relative humidity and seems to fill the microporosity of the particles. This increase in water content with relative humidity would be consistent with the XRD observation that the inter-sheet distance increases with relative humidity.

The tests revealed the presence of exchangeable cations (mainly Mg^{2+}) on the surface of M-S-H, the amount of which increases with pH. This indicates a deprotonation of the silanol groups of M-S-H and an increase of the negative surface charge with pH.

The specific surface area (SSA_{BET}) of M-S-H is very high and decreases as the M/S ratio increases. Thus, M/S=0.8; 1 and 1.2 correspond to surfaces of 406, 315 and 194 m^2/g after 3.3 years of hydration. These high surface areas are comparable to those of synthetic clay materials where macro, meso and microscopic pores are present. It has been shown that the specific surface area of such materials increases with increasing w/s. The authors therefore believe that this high surface area value is due to dilution and that in confined atmospheres the specific surface areas would be lower.

In conclusion, the studies carried out so far on M-S-H have made it possible to describe their structure in order to better predict their properties. From the beginning, their structure was associated with that of phyllosilicates. Over time, several kinds of phyllosilicates have been put

forward and the consensus that seems to have developed is the existence of a silicate sheet structure that evolves with the M/S ratio, as for C-S-H with C/S. At low M/S, the structure would be 2:1 phyllosilicate like talc and at higher M/S, 1:1 phyllosilicate like antigorite. Increasing the M/S ratio causes depolymerisation into silicon, increasing the gaps in the structure. Thus, M-S-H would be nanocrystalline and turbostratic phyllosilicates, whose layer charge comes mainly from vacancies in the tetrahedral Si sites. As M-S-Hs act as swelling clay, increasing relative humidity increases the water content of M-S-Hs as well as the interlayer distance.

1.2.4.3.3. Interaction with calcium

Several researchers have investigated the possibility of calcium incorporation in M-S-H and magnesium incorporation in C-S-H.

In 2005, Brew and Glasser (Brew et Glasser 2005b) pointed out the very different structure and chemistry of C-S-H and M-S-H. On the one hand it is a very dense chain structure, on the other hand a sheet structure. Based on their different structure, the two gels, M-S-H and C-S-H, are not miscible. The authors state that analyses in the literature reporting Ca in M-S-H gels and Mg in C-S-H gels probably result from the physical inability to resolve intimate fine-grained mixtures of two gels. In 2015, Lothenbach (Lothenbach et al. 2015) agreed on the immiscibility of the two phases. Two observations support their statement. Firstly, as pointed out by Brew and Glasser, the structure of the two gels is very different. Secondly, M-S-H contains more bound water than C-S-H. Substitution of Ca by magnesium in C-S-H would be unlikely given the different size of Ca^{2+} (1.1 Å) and Mg^{2+} (0.8 Å). On the other hand, there could be a small incorporation of Mg in C-S-H and Ca in M-S-H (2-4% at.).

In 2018, Bernard (Bernard et al. 2018; Bernard, Dauzères, et Lothenbach 2018a) investigated the possibility of calcium incorporation into M-S-H and magnesium into C-S-H. When small amounts of calcium were added during the synthesis of M-S-H, calcium uptake by M-S-H was demonstrated. Indeed, the calcium present in the precipitated solid phases was not in the form of C-S-H and the structure of the solid phase was that of M-S-H. The introduced calcium could be in two forms: as cations on the surface of M-S-H to balance with the negative charges of M-S-H or incorporated more deeply. Thus, M-(C)-S-H would correspond to an M-S-H phase containing small amounts of adsorbed and/or incorporated calcium.

For samples with high calcium and low magnesium, there appeared to be no incorporation of Mg into C-S-H. The pH and low Mg concentration indicated the separate precipitation of M-S-H and C-S-H. The results showed that all the magnesium present appeared to be in the M-(C)-S-H phase. Thus, incorporation of Ca into M-S-H is possible.

1.2.4.3.4. Thermodynamics and kinetics

In the majority of studies of synthetic M-S-H, the raw materials for their manufacture are silica fume and MgO. Most studies produce M-S-H suspensions. The few researchers who wanted to make M-S-H pastes ran into the problem of the rheology of the mixture. Indeed, it has been established that MgO powder requires a lot of water. This problem is notably encountered by Zhang in 2014 (Zhang, Vandeperre, et Cheeseman 2014). According to their study, the hydration time of a paste based on MgO, silica fume and demineralised water is very long and the strength very low. To improve the fluidity of the mixture, the researcher adds sodium hexametaphosphate (NaHMP). The NaHMP reduces the w/s, which improves the mechanical strength.

The formation mechanism of M-S-H from silica fume and MgO is a slow process that lasts at least 2 years at 20°C (Bernard et al. 2017b). Several researchers (Bernard et al. 2017b; Tonelli et al. 2016; Zhang et al. 2018; Zhang, Vandeperre, et Cheeseman 2014) observe that M-S-H is not the majority phase during the initial contact between MgO, silica fume and water at 20°C. Silica fume dissolves more slowly than MgO reacts. The silica fume particles dissolve slowly forming a layered structure, with cavities: M-S-H forms on the surface of the particles. MgO thus initially forms

mostly brucite. In the article by (Zhang et al. 2018) the XRD results show that after 7 days, MgO is the main crystalline phase. At 28 days, all the MgO has reacted to form brucite and M-S-H. Thereafter, the brucite is consumed and reacts with amorphous silica to form M-S-H. After 90 days, brucite still remains as it is slowly consumed. After 300 days, the brucite is replaced by M-S-H. This shows that it is the dissolution of brucite that limits the formation of M-S-H. As M-S-H formation is slow, Bernard (Bernard et al. 2019) leaves some of his samples to hydrate for over three years.

In 2017, Bernard (Bernard et al. 2017b) investigates the influence of temperature on the formation of M-S-H. At 50°C and 70°C, the appearance of M-S-H is faster and the structure and M/S ratios achieved are the same.

A consequence of the very slow hydration reaction of M-S-H is the tightening of M/S ratios in the short term. Several authors (Bernard et al. 2019; 2017b; Brew et Glasser 2005b; Nied et al. 2016) found actual M/S ratios far from the target ratios, tightening to around 1. Bernard showed in 2017 (Bernard et al. 2017b) that the M/S ratios loosen over time and that this is due to the slow reaction. In their study, in the simultaneous presence of silica and brucite, the M-S-H that formed have an M/S≈1. It is only after a long exposure time that M-S-H with larger M/S (0.8 to 1.3) are formed. In 2019, Bernard (Bernard et al. 2019) also showed that the older the samples get, the more ordered their structure becomes.

Tonelli (Tonelli et al. 2017) and Zhang (Zhang et al. 2018) split the hydration kinetics into several phases. Tonelli divides the hydration into 3 periods, as for usual cementitious pastes: the initial induction period, an acceleration period and a final period where the hydration is strongly reduced. Zhang joins Tonelli with 4 periods:

- a **pre-induction period** (0-1^{rst} day) followed by a **dormant period** (1^{rst}- 10th days) :
- As soon as the MgO comes into contact with water, it is rapidly consumed and the pH value of the solution reaches about 11. Brucite precipitates on the surface of the MgO grains and the high pH value inhibits further hydration. Dissolution of the silica fume accelerates with time and M-S-H forms on the surface of the silica grains. The formation of M-S-H is limited by the formation of brucite.
- an **acceleration period** (10th-30th days) : the pH is reduced and the concentration of magnesium and silicate in solution increases, favouring the formation of M-S-H. The brucite itself is transformed into M-S-H
- a **stable period** (30th – 300th days) : The rate of M-S-H formation gradually increases as the dissolution rate of the silica fume increases. The M-S-H grows on the surface of the particles and comes into contact with the solution.

Based on these findings, researchers are trying to model the formation of M-S-H in order to take into account the magnesium attack in the models. For this purpose, solubility constants are calculated by Nied and Bernard (Bernard et al. 2017b; Nied et al. 2016).

In 2018, Roosz (Roosz et al. 2018) determined the thermodynamic properties of the three species M-S-H, C-S-H and C-A-S-H: free enthalpy, enthalpy, entropy, heat capacity, molar volume, equilibrium constant. It also seeks to determine the domains of stability and predominance of the three species. Figure 1-19 shows the diagrams proposed by Roosz. The M-S-H are located in the same zone as the phases with low C/S ratio. The M-S-H are thus in the high silica activity zone of the diagram corresponding to environments with decalcified C-S-H phases and low pH, typical characteristics of altered and carbonate zones, as experimentally observed (Dauzères 2010). M-S-H with M/S=1.2 are less and less stable with increasing temperature, their predominance range is strongly reduced at 100°C.

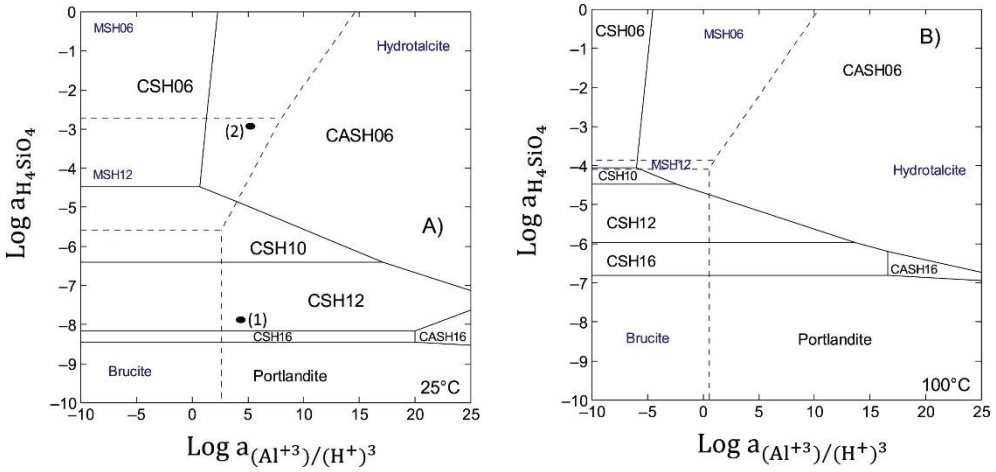

Figure 1-19 : Stability diagram of M-S-H, C-S-H, C-A-S-H systems and associated minerals a) at 25°C and b) at 100°C according to (Roosz et al. 2018)

In 2017, Bernard (Bernard et al. 2017a) brought C-S-H into contact with two solutions based on MgO or $MgCl_2$. The author determines the stability domains of C-S-H and M-S-H as a function of pH. For a pH of 9.6 to 11.5 and a low C/S ratio, C-S-H are stable. The addition of $MgCl_2$ decreases the pH which leads to decalcification of C-S-H (decrease in C/S) and formation of M-S-H. The addition of MgO leads to an increase in pH from 10 to 11.5 as well as in the C/S ratio in the C-S-H, i.e. shorter silicate chains. The M-S-H appear to be stable for 7.5<pH<11.5.

The determination of thermodynamic and kinetic properties allows to feed models such as Hytec (Bernard, Dauzères, et Lothenbach 2018a) where the magnesium attack can thus be taken into account.

Table 1-8 shows the thermodynamic properties of M-S-H considered when using the Hytec reactive transport code. No study has been achieved to study the influence of M/S ratio of the density values and density presented were calculated by Bernard from M-S-H volumes (Bernard et al. 2018). One difference that persists between the model and the experimental is the presence of brucite whereas the model does not predict it. Indeed, thermodynamically, M-S-H are more stable but the reaction of formation of M-S-H is so slow that experimentally brucite is observed until long times. Bernard's work (Bernard et al. 2019) tends to show that in the long term, brucite is dissolved and precipitates with amorphous silica to form mainly M-S-H. It seems therefore that the magnesium attack can be integrated into computational codes and the prediction of behaviour during contact between clay and a low-pH, such as carbonation or leaching.

Table 1-8 : Thermodynamic properties considered for M-S-H in the work of Bernard (Bernard et al. 2017b)

M/S	Name	Equation	logK (25°C)	density (kg/m³)
0.78	MSH-078	$0.78\,Mg^{2+} + 1\,H_4SiO_4 + 0.26\,H_2O \underset{\rightarrow}{\leftarrow} (MgO)_{0.78}.(SiO_2)_1.(H_2O)_{1.48} + 1.56\,H^+$	-7.25	2000
0.83	MSH-083	$0.83\,Mg^{2+} + 1\,H_4SiO_4 + 0.33\,H_2O \underset{\rightarrow}{\leftarrow} (MgO)_{0.83}.(SiO_2)_1.(H_2O)_{1.5} + 1.66\,H^+$	-7.90	2000
1	MSH-100	$1\,Mg^{2+} + 1\,H_4SiO_4 + 0.6\,H_2O \underset{\rightarrow}{\leftarrow} (MgO)_1.(SiO_2)_1.(H_2O)_{1.6} + 2\,H^+$	-10.43	2000
1.3	MSH-130	$1.3\,Mg^{2+} + 1\,H_4SiO_4 + 2.1\,H_2O \underset{\rightarrow}{\leftarrow} (MgO)_{1.3}.(SiO_2)_1.(H_2O)_{2.8} + 2.6\,H^+$	-14.96	2000

1.2.4.3.5. Mechanical properties

Two research teams (Zhang, Vandeperre, et Cheeseman 2014; Sonat et Unluer 2019) performed mechanical tests on M-S-H paste specimens. For this purpose, they made pastes by adding NaHMP.

In 2014, Zhang (Zhang, Vandeperre, et Cheeseman 2014) showed that as the w/s ratio decreased, the mechanical strength increased. Moreover, the strength also increased with time, even beyond 90 days showing that the hydration was long. With a w/s of 0.4; the paste reached a strength of 70 MPa after 28 days. The author concluded by saying that the M-S-H paste seemed to have the potential to create strong products. However, the pastes all showed the presence of brucite and unhydrated MgO. Over time, the peaks decreased in intensity in favour of significant M-S-H humps. The lower the w/s ratio, the longer it took for these two species to disappear. The pastes were therefore not exclusively composed of M-S-H.

Sonat and Unluer (Sonat et Unluer 2019), on the other hand, used rice husk ash (RHA) as a source of silica to make M-S-H within pastes. Two types of RHA were tested: crystalline (RHA-c) and amorphous (RHA-a). In addition, samples with microsilica were made for comparison. NaHMP was used to fluidise the mixture (1% mass of solid). The w/s ratio was 0.55. The results showed that the samples with crystalline RHA gave the lowest compressive strengths (about 10 MPa after 56 days). Indeed, the only phase that was created with RHA-c was brucite, which had no binding properties. For the other silica sources (MS and RHA-a), M-S-H was formed. The use of RHA-a allowed high mechanical strengths to be obtained more quickly (22 MPa after 3 days and 34 MPa after 7 days). In the long term, however, the highest strength values were obtained with microsilica (47 MPa after 56 days). The objective of the researchers had been achieved; the use of rice husk ash was a good way to reuse waste materials, as long as only the amorphous part is used.

The influence of NaHMP on the structure of M-S-H and other hydrated phases has been studied by several authors (Hesaraki, Zamanian, et Moztarzadeh 2009; Jia et al. 2016; Tonelli et al. 2019). Although it led to a better rheological behavior and the formation of M-S-H over brucite (due to the adsorption of phosphate species on MgO, which inhibits the nucleation of the $Mg(OH)_2$), the formation of secondary phases (such as $[6MgOH^+ \cdot (PO_3)_6^{6-}]$) (Jia et al. 2016; Tonelli et al. 2019) and minor changes in the structure of M-S-H gels have been observed (Hesaraki, Zamanian, et Moztarzadeh 2009; Tonelli et al. 2019). NaHMP could thus cause chemical and mineralogical differences between in situ precipitated M-S-H and synthetized M-S-H.

In conclusion, the mechanical tests carried out were not performed on pastes consisting entirely of M-S-H or comparable to M-S-H formed during a magnesium attack. Further tests on M-S-H pastes are needed to mechanically characterise M S H.

1.2.4.3.6. Conclusion

The mechanism for the formation of M-S-H from silica fume and MgO is a slow process. The silica fume dissolves more slowly than the MgO reacts, forming brucite in the first instance. Subsequently, the brucite is consumed and reacts with the amorphous silica to form M-S-H. Its dissolution drives the formation of M-S-H. Increasing the temperature from 20°C to 50°C or 70°C accelerates the precipitation of M-S-H.

M-S-H is, like C-S-H, a weakly crystallised phase. The consensus structure of M-S-H is a silicate sheet structure that evolves with the M/S ratio, as for C-S-H with C/S. Increasing the M/S ratio causes depolymerisation into silicon, increasing the gaps in the structure. M-S-H are thought to be nanocrystalline, turbostratic phyllosilicates, whose layer charge comes mainly from vacancies in the tetrahedral Si sites. As M-S-Hs act as swelling clay, increasing relative humidity increases the water content of M-S-Hs as well as the interlayer distance.

The determination of the thermodynamic properties of M-S-H allowed the models to be improved. The stability and dominance domains of the M-S-H - C-S-H - C-A-S-H system confirm that M-S-H

are stable in environments with decalcified C-S-H phases and low pH, typical characteristics of altered and carbonate zones, as experimentally observed (Dauzeres et al. 2010).

M-S-H are hydrates that form during a magnesium attack by dissolution of C-S-H and precipitation of M-S-H. They are observed during contact between cementitious materials and different environments: soft water, sea water or pore water in rocks for geological disposal of radioactive waste. The thermodynamic, kinetic and structural properties of M-S-H have been established, but the mechanical properties of M-S-H resulting from magnesium attack remain unknown. In order to integrate M-S-H into mechanical models for predicting the properties of cement paste and concrete, it is necessary to determine these properties. An identification of the local mechanical properties associated with a mechanical homogenisation could allow to calculate them.

Summary and research objectives

The aim of the literature review was to explain the background, evaluate the current technical and scientific knowledge in order to position this thesis work on the interactions between Mg-bearing environments and the low-carbon, low-pH cementitious materials constituting the concrete structure.

The first part of this study described the properties of cement pastes with and without additions. The incorporation of additions in cement modifies the mineralogy, microstructure and mechanical properties of cement pastes. When the C/S of the paste is sufficiently low, no portlandite remains. A review of the chemical, mineralogical, microstructural and mechanical properties of C-S-H was then proposed. The nanoindentation technique, used in the literature to determine the mechanical properties on a small scale, was explained, followed by an introduction to microindentation and mechanical homogenisation.

The second part of this study was devoted to the degradation of cementitious materials in Mg-bearing environments. The complexity of the different environments and the interaction of different ions was highlighted. A short summary of the model underwater attacks was proposed and showed the lack of information about the effect of magnesium attack alone. In real environments (dams, marine structures, deep geological disposal), studies show that the effect of magnesium attack is very different for Portland cement-based material (CEMI) and substituted materials with a much lower C/S (e.g. low-pH). On low-pH pastes, the magnesium enrichment is deep and M-S-H is formed. On Portland cement (CEMI) based pastes, the presence of portlandite seems to cause brucite formation. However, in the long term and/or when the protective external layer is torn off (e.g. by freeze-thawing on dams), M-S-Hs start to form. M-S-H formation therefore becomes a phenomenon to be considered in the safety of facilities. Knowledge about M-S-H is limited. The chemical, mineralogical and thermodynamic properties have already been studied, but the microstructural and mechanical properties have not been studied.

In order to provide knowledge in this area, this thesis aims to answer several objectives and questions:

(i) Understanding of the reaction mechanisms of magnesium attack and M-S-H formation in low-calcium cementitious matrices

Under which conditions are M-S-H favoured over brucite in degraded cementitious pastes?

What is the formation process of M-S-H?

(ii) Studying the influence of M-S-H formation on the cement paste properties

Does the structure of C-S-H influence the structure of M-S-H formed by degradation?

What is the influence of M-S-H formation on the mechanical and microstructural properties of cementitious materials?

Is the pattern of decalcification of C-S-H that takes place in pure leaching similar to that which takes place in the formation of M-S-H?

(iii) Proposal of microstructural and mechanical data of M-S-H that can be integrated in chemo-mechanical models.

What are the intrinsic properties of M-S-H?

Can the properties obtained on M-S-H pastes be transposed to those of a degraded cement paste?

Can we predict the properties of degraded cement pastes in a magnesium environment?

In order to address answers to these questions, the thesis is structured as follows:

Chapter 2 summarizes the the syntheses methods and the main analytical techniques used. It also proposes a short analysis of the chemical behaviour of different cementitious pastes in $MgCl_2$ solution in order to select those pastes that can form, by degradation of the cementitious material, M-S-H rapidly and in a sufficient depth to perform mechanical tests.

Chapter 3 is devoted to the production of pure and cohesive M-S-H pastes and their chemical, mineralogical, microstructural and mechanical characterization.

Chapter 4 proposes a multi-physics characterization of a low-pH model cement paste exposed to 5 mM and 50 mM $MgCl_2$ solution.

Chapter 5 presents a comparison with the effect of pure leaching on the same paste.

Finally, chapter 6 concludes with an analysis of a low-pH industrial paste under magnesium attack to see the differences that can exist between the model paste and a real paste.

A general conclusion is proposed at the end of the manuscript, together with a reflection on the perspectives resulting from this work.

CHAPTER 2. MULTI-PHYSICS CHARACTERIZATION STRATEGY

Introduction

In low-carbon, low-pH binders, in the long term, the portlandite is fully consumed and the C-S-H tends to equilibrate at low C/S ratios. In the literature, the behaviour of these binders in Mg-bearing environments is different from that of unsubstituted cements. While for Portland-based cementitious materials the magnesium attack is characterised by the formation of a protective brucite external layer, for low C/S cementitious materials, the absence of portlandite changes the thermodynamic equilibrium and brucite no longer precipitates, but M-S-H, whose microstructural and mechanical properties are unknown, is formed. The formation of M-S-H is associated with deep Mg enrichment and decalcification of C-S-H. The use of highly substituted binders is constantly increasing.

In structures made from Portland cement, for long service lives (dams, marine structures etc.), the brucite that initially forms may dissolve or be pulled out (e.g. freeze/thaw phenomenon) or magnesium may eventually diffuse through the brucite external layer. In any case, for long lifetimes, M-S-H formation is also observed (Rosenqvist et al. 2017; Jakobsen, De Weerdt, et Geiker 2016).

To assess the safety of various civil engineering structures that may come (or are already) into contact with magnesium environments, it is necessary to better understand the behaviour of these low C/S binders in the context of degradation with magnesium. For this, it is necessary to have representative model binders without the need to wait for years of curing. This chapter proposes several approaches to achieve low C/S ratios and no portlandite cementitious pastes:

- Production of C_3S and silica-based model pastes (already used in the literature to study the carbonation of C-S-H (Kangni-Foli 2019; Kangni-Foli et al. 2020; 2021))
- Production of silica-enriched model cement pastes: CEMI with a low proportion of C_3A (to have few aluminates) associated with silica
- Use of “industrial” silica and slag-enriched cement pastes: CEMI with silica fume and slag (T3)

The first part of this chapter is devoted to the analytical techniques implemented in this thesis on sound and homogeneous materials and to the multiphysics characterization developed in this work for the characterization of degraded samples. The second part presents the selection process of the low-pH materials used in the subsequent degradation. The manufacture of different low C/S cementitious pastes and control high C/S cementitious pastes is detailed. The comportment of these pastes in magnesium solution has been tested to select pastes that form M-S-H and that will be used for degradation in the thesis. A chemical simulation via a reactive transport code (Hytec) is used to discuss the experimental results.

2.1. Characterization methods

2.1.1. Polishing protocol

Polished sections (EpoFix-based) were made for (i) microprobe and (ii) microindentation and SEM/EDS characterizations. The polishing protocol (Table 2-1) for the microprobe was performed without lubricant, only with compressed air to remove dust from the sheet. Only degraded cementitious pastes were prepared for microprobe. The polished sections were rinsed with ethanol after each step and were held against the abrasive paper by hand. For SEM/EDS and microindentation, two polishing protocols were used: one for M-S-H (Table 2-2) and one for cement pastes (Table 2-3). For sound cementitious samples, all 7 steps (Table 2-3) are performed. For degraded samples, due to the fragility of the sample, only steps 1 to 5 are performed. Longer and finer polishing caused particles to break off in the degraded area, creating scratches and holes. In addition to this, a cracking phenomenon occurred, which made the surface of the degraded samples and the M-S-H pastes very rough and not flat. It was then impossible to perform

nanoindentation tests (indented depth of 300nm). The force had to be increased to 200mN, corresponding to microindentation tests (indented depth of about 10 um). All products used for polishing are from Struer. The polisher used is the Struers LaboPol-2.

Table 2-1: Polishing protocol of sections for microprobe (EPMA)

Step	Abrasive Paper	Speed (rd/min)	Time (min)	Abrasive Product
1	800	250	3–4	SiC
2	1200	250	3	SiC
3	4000	250	2	SiC

Table 2-2: Polishing protocol of M-S-H pastes sections for SEM/EDS.

Step	Abrasive Paper	Retention Strength	Speed (rd/min)	Time (min)	Abrasive Product	Lubricant + Rinsing Agent
1	240	30 N	500	1–3		Ethanol
2	1200	30 N	250	1		Ethanol
3	2000	30 N	250	1		Ethanol
4	4000	30 N	250	1		Ethanol
5	3 µm	Manual	250	5	DP-Suspension-A 3 µm (diamond)	Ethanol
6	1 µm	Manual	250	5	DP-Suspension-A 1 µm (diamond)	Ethanol

Table 2-3: Polishing protocol of cement paste sections for SEM/EDS and nano or micro-indentation

Step	Abrasive Paper	Retention Strength	Speed (rd/min)	Time (min)	Abrasive Product	Lubricant + Rinsing Agent
1	500	30 N	250	2–4	SiC	Ethanol
2	800	30 N	250	30s	SiC	Ethanol
3	1200	30 N	250	1	SiC	Ethanol
4	2000	30 N	250	1min30	SiC	Ethanol
5	4000	30 N	250	6-8	SiC	DP-Lubricant Brown
6	MD-Dur (3 µm)	30 N	250	8	DP-Suspension-A 3 µm (diamond)	DP-Lubricant Yellow
7	MD-Dur (1 µm)	30 N	250	9	DP-Suspension-A 1 µm (diamond)	DP-Lubricant Yellow

2.1.2. Characterization technics used for homogeneous materials

2.1.2.1. Mineralogical and Chemical Analyses

X-ray diffraction analyses were performed on powders obtained by crushing the samples, either on a Malvern Panalytical Empyrean instrument, a PANalytical X'Pert Pro operating at 40 kV and 40 mA (Sorbonne Université, Jussieu, Paris, France) with a Cu anti-cathode (λ~1.54 Å), a D8 Advance Bruker operating at 40 kV and 40 mA (LMDC, Toulouse, France) with a Cu anti-cathode (λ~1.54 Å), or a Malvern PANalytical Aeris (IRSN, Fontenay-aux-Roses, France) operating at 600 W, 40 kV and 15 mA, with a Cu anti-cathode (λ~1.54 Å). The scanning region was in the range 2Θ = 5°–70° with either: (i) a step size of 0.0131, for a total duration of 4 h (Jussieu, Paris, France); (ii) a step size of 0.020, for a total duration of 2 h (LMDC, Toulouse); or (iii) a step size of 0.0109, for a total duration of 20 min (IRSN, Fontenay-aux-Roses, France). X-ray diffractograms were plotted against the 2Θ angle, noted [2Θ] CuKα. Table A-2 (Appendix A) lists the instruments used for each M-S-H sample analyzed. All cementitious materials were analyzed on Malvern PANalytical Aeris (IRSN, Fontenay-aux-Roses, France).

Thermogravimetric analyses were carried out under argon flux on non-dried powdered M-S-H samples and cementitious samples (30–40 mg) with a Mettler TGA 2 instrument (LMDC, Toulouse, France) and a heating rate of 10 °C/min from ambient temperature to 980 °C. The powders used for the test were obtained by crushing a cross section of the sample to 80 µm. The amount of $Mg(OH)_2$ was quantified from the weight loss around 420 °C (335–455 °C) using the stepwise method (Lothenbach, Durdziński, et De Weerdt 2016) and calculated according to Equation (2-1):

$$\text{wt\%brucite}_{\text{dry}} = \frac{\text{water loss (brucite)}}{\text{100-water loss}_{\text{H}_2\text{O (25–550 °C)}}} \times \frac{\text{M}_{\text{brucite}}}{\text{M}_{\text{H}_2\text{O}}} \times 100 \qquad (2\text{-}1)$$

where wt% $brucite_{dry}$ corresponds to the weight percentage of brucite for 100 g of dry mass (g/100 g) and water losses are expressed in weight percentages. $M_{brucite}$ is the molar mass of $Mg(OH)_2$ (equal to 58.32 g/mol) and M_{H2O} is the molar mass of water (equal to 18.02 g/mol). The relative error on the brucite content was ±5–10% (Lothenbach, Durdziński, et De Weerdt 2016).

Solid chemical characterizations were carried out with an energy-dispersive spectrometry (EDS) system adapted to a scanning electron microscope (SEM; Hitachi S3500N, IRSN, Fontenay-aux-Roses, France). The system comprised two EDS Brücker SDD detectors working at 15 kV and a working distance of 16.8 mm. Observations were performed on a polished section (Table 2-2) coated with a gold-palladium alloy (277 Å thick).

Microscopic imagery was carried out with the same instrument on fractures coated with a thin gold-palladium layer (92 Å thick) at 25 kV. The working distance depended on the sample and its geometry.

2.1.2.2. Microstructure Analyses

Different types of microstructure analyses were conducted. Figure 2-1 illustrates the porosity characterization techniques used as a function of pore range associated with the dimensional range of solids and pores in hydrated cement and M-S-H pastes. The porosity characterization of the pastes was carried out by combining several techniques. Pore distribution from 2.5 nm to 0.1 mm was determined by nitrogen physisorption and MIP. The open porosity of the samples was measured by autoradiography, MIP (Φ_M), saturation of the material with water (Φ_W), and by means of a calculation (Φ_H) from the bulk (ρ_{bulk}) and true densities (ρ_{true}). X-ray microtomography was used to observe the distribution of unreacted silica particles in the pastes.

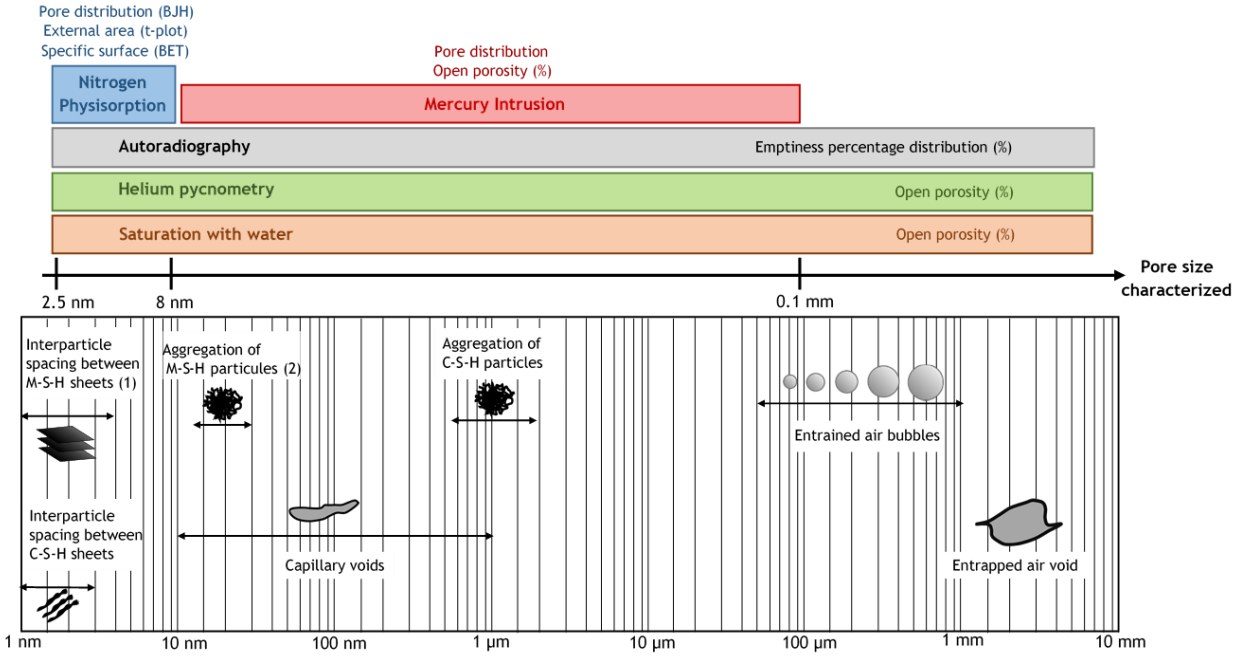

Figure 2-1: Representation of porosity characterization techniques as a function of pore range associated with the dimensional range of solids and pores in an M-S-H paste (adapted from Mehta and Monteiro (Mehta et Monteiro 2005)). (1) After Bernard (Bernard et al. 2019) and (2) after Tonelli (Tonelli et al. 2016).

M-S-H samples were analyzed by X-ray microtomography using two different devices: SkyScan 1272 and SkyScan 1173 (Bruker microCT N.V, Fontenay-aux-Roses, France). A spatial resolution of 15 µm was obtained for a sample size of approximately 5 cm3. The parameters of the X-ray tube (100 kV, 100 mA) were set to optimize the contrast between the different phases and the

pores. An angular step of 0.3° was used to acquire radiographs (total acquisition time of approximately 9 h).

Autoradiographic analyses were conducted on 1.5 cm × 1.5 cm × 2 cm samples made from colloidal silica. Samples were impregnated with C-14-methylmethacrylate (C-14-MMA) tracer solution, filling the connected porosity. The polymerization process was induced by gamma irradiation in order to fix the tracer to the open pore space. Samples were cut, polished and exposed on storage phosphor imaging plates (IPs) for 1–3 days. After exposure, the IPs were scanned using a FUJI-FLA 5100 digital scanner with a resolution of 1200 dpi and a 16-bit image depth to obtain the autoradiographs of the impregnated samples. The scanning resolution of the film was 10 µm. Quantification of porosity is based on the assumption that optical densities on autoradiographs are proportional to the content of the decaying tracer isotope in the material (Sardini et al. 2006; Hellmuth, Siitari-Kauppi, et Lindberg 1993; Hellmuth, Lukkarinen, et Siitari-kauppi 1994; Sammaljärvi et al. 2016; Lalan et al. 2019). First, the optical densities of the autoradiographs are calculated. All intensity values or grey levels in the subdomains (pixels) are converted into the corresponding optical densities, which in turn are converted into activities with calibration curves measured for each exposure. Finally, the activities are converted into porosities by taking into account the beta attenuation and the true density of the samples (measured by helium pycnometry) (Sammaljärvi et al. 2016). Several PMMA standards of known C-14 activities are needed to convert the grey values of each pixel into porosity values (Sammaljärvi et al. 2012; 2016; Lalan et al. 2019; Delayre et al. 2020). The uncertainty of the C-14-PMMA autoradiography has been empirically determined to be approximately 10% (Sammaljärvi et al. 2016). Three samples with colloidal silica—one for every M/S—were analyzed of which one broke during impregnation (M/S = 1), making it impossible to analyze this ratio. The sample with M/S = 1.3 was divided into two parts, allowing for two analyses.

Nitrogen sorption isotherms were measured using a Micromeritics 3Flex 3500 (Norcross, GA, USA) instrument equipped with version 4.05 of the 3Flex software (IRSN, Fontenay-aux-Roses). Prior to the analysis, the samples were reduced into pieces of approximately 0.2 cm^3 and placed in a freeze dryer (Crios-50, Cryotec, IRSN, Fontenay-aux-Roses, France) for a least 5 days. For cementitious materials, a freeze drying (by adding liquid nitrogen and allowing sublimation through the pressure of the freeze dryer) has been processed. They were then degassed (i.e., heated at 45 °C under a vacuum in a sample cell) in the instrument for 4 h to remove water and other physically adsorbed volatile material from the surface of the sample. The samples underwent nitrogen adsorption and desorption for approximately 20 h. Three measurements were carried out on each sample. The specific surface area (SSA_{BET}) of the samples was calculated by applying the Brunauer-Emmett-Teller (BET) equation in the p/p_0 range 0.05–0.2. External surface area (SSA_{ext}) and total pore volume were calculated from the t-curve (obtained from the equations fitted on Aerosil 200 in (Galarneau et al. 2018)) for $p/p_0 < 0.8$, between 7 and 10 Å on the second slope (Galarneau et al. 2018; de Boer et al. 1966). Figure 2-2 illustrates the t-curve of one sample with the slopes and calculation parameters. $SSA_{meso + ext}$ corresponds to the mesopore + external surface areas and to the SSA_{BET}. The pore distribution was obtained from the desorption isotherm with the Barrett-Joyner-Halenda (BJH) method (Barrett, Joyner, et Halenda 1951).

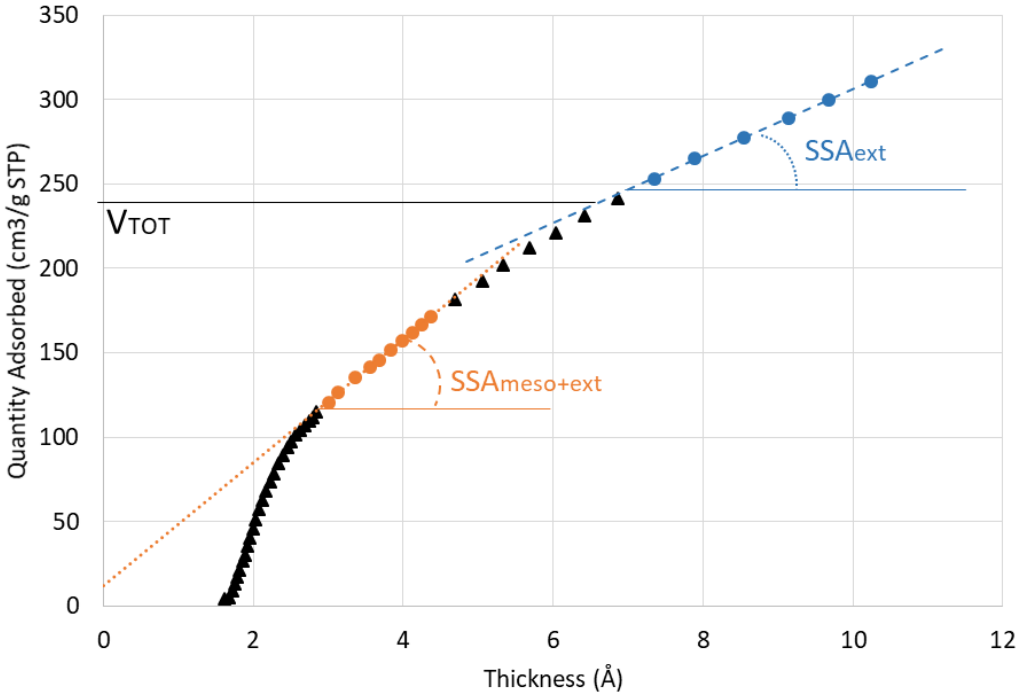

Figure 2-2: Illustration of the t-plot on an M-S-H paste highlighting the external surface area (SSA_{ext}), the pore volume (V_{TOT}), and the total specific surface area ($SSA_{meso+ext}$), which corresponds to the specific surface area calculated with BET (after Galarneau et al. (Galarneau et al. 2018)).

Mercury intrusion porosimetry was performed with an AutoPore IV 9500 porosimeter from Micromeritics (LMDC, Toulouse, France). The samples underwent the same pre-treatment as for nitrogen physisorption. After a pre-equilibrium step to fill the gaps between the sample and the chamber wall at 3 KPa, the pressures on mercury were automatically and stepwise raised to 413.69 MPa. The MIP gives information on the porosity for d > 10 nm approximately (Φ_{MIP}) and on the pore diameter of the structure.

Bulk density and water porosity were measured in two different ways, at the LMDC and at the IRSN.

The determination, at IRSN, of the bulk density of the sound material (ρ_{bulk}) was carried out by measuring the pressure induced by the immersion of the sample in kerosene according to Archimedes' principle following the method initially proposed by Monnier et al. (Monnier, Stengel, et Fies 1973) and included in the AFNOR standard X31-505 (AFNOR 1992). The samples remained 4 hours in kerosene before weighing.

Water content measurements were carried out at IRSN by weighing before and after heating at 105°C until constant weight was reached. Water absorption of samples was determined by an immersion in MilliQ-water for 24 hours followed by a heating at 105°C until constant weight was reached. The open porosity (Φ_w) was determined by the following equation:

$$\phi_W = \frac{m_{water}}{m_{total}} * \frac{\rho_{bulk}}{\rho_{water}} \qquad (2\text{-}2)$$

with ρ_{bulk} the bulk density of the material, ρ_{water}=1g/cm^3, m_{water} the mass of water in the saturated sample and m_{total} the total mass of the sample after heating at 105°C.

For comparison, for the cementitious materials, the bulk density was also determined by immersion in water during the water porosity protocol at LMDC according to the procedure

recommended by the AFPC-AFREM (Hornain 2007; Ollivier 1997; AFGC 2004). The samples were placed in a desiccator for 4 hours under vacuum. They were then immersed in water, under vacuum, for 24 hours. The samples were then subjected to hydrostatic weighing (m_{im}) and weighing out of the water (m_{air}). The samples were placed in an oven at 105°C until the mass no longer changed. A final weighing was performed to obtain the dry mass (m_{dry}). The bulk density (ρ_{bulk}) and the porosity (Φ_w) were determined by the following equations:

$$\rho_{bulk} = \frac{m_{dry}}{m_{air} - m_{im}} * \rho_{water} \quad (2\text{-}3)$$

$$\phi_W = \frac{m_{air} - m_{dry}}{m_{air} - m_{im}} \quad (2\text{-}4)$$

True density was measured with two different devices, at the LMDC and at the IRSN. A pycnometer (Micrometrics, AccuPyc II 1340 – IRSN, Fontenay-aux-Roses) was used to determine the true density (ρ_{true}) of the samples at IRSN. The volume of the samples of known mass was determined from the pressure change of helium in a calibrated volume. Measurement were done in modules of 10 cm^3 on a set of sized pieces of 0.2 cm^3. 15 cycles of introduction and extraction of helium have been operated. At LMDC, the true density was measured on an Ultrapyc 5000 pycnometer (Anton Paar, LMDC, Toulouse). The test protocol used is similar. M-S-H samples' true density was only measured at IRSN. The open porosity (Φ_H) was calculated with Equation (2-5) :

$$\phi_H = 1 - \frac{\rho_{bulk}}{\rho_{true}} \quad (2\text{-}5)$$

where ρ_{bulk} is the bulk density of the material and ρ_{true} is the true density of the material.

2.1.2.3. Mechanical characterization

Compression test

In order to determine the macroscopic Young modulus of sound cementitious samples, compression tests were conducted on 100 kN capacity MTS machine (MTS Systems – LMDC, Toulouse, France) with a 10kN sensor, on samples of 3*2*1cm^3 of the sound materials with a speed of 2 µm/s. A gauge was glued on each of the 4 faces of the samples in order to have a precise measurement of the deformation.

Indentation

Nanoindentation tests were carried out with a nano-indenter (NHT³, Anton Paar ® —IRSN, Fontenay-aux-Roses, France) with a Berkovich tip on polished section of the sound cementitious samples (same polishing protocol as for SEM/EDS, see Table 2-2, Appendix A). The nanoindentation tests were depth and force controlled (Max depth = 300 nm, Loading rate = 12 mN/min, Pause = 10 s). To avoid the influence of one indentation on the other, the tests should be separated by a minimum distance (Δ). The recommended distance to avoid overlapping of the elastic domains of each indentation is at least 30 times the maximum depth (Nguyen 2017). Accordingly, a grid of 35*35 indents was made, each indent separated by 10 µm.

Microindentation tests were carried on the M-S-H samples and sound cement pastes (for comparison). They were force controlled (Max load = 200 mN, Loading rate = 100 mN/min, Pause = 10 s). Several grids of 4*14 indents were made. In these tests, the penetration depth was about 10 µm, so the indents were spaced 300 µm apart.

2.1.3. Multi-physic characterization developed for materials with properties' gradient

2.1.3.1. A multi-physics characterization

Magnesium attack influences different properties: chemical, mineralogical, microstructural, and mechanical ones. Several types of characterizations are necessary to understand the behaviour of the material in this environment. As it is observed in leaching ((Carde et François 1997; Wan et al. 2013; Wan, Li, et Sun 2013; Faucon et al. 1998)), a gradient of properties is expected, and it is not possible to characterize the changes in properties with macroscopic techniques. It is necessary to characterize the degradation locally and/or using inverse analysis to identify some properties. A multi-physic characterization procedure is proposed, based on chemical, mineralogical, microstructural and mechanical characterizations along the degradation profile (Figure 2-3).

Chemical (EDS, microprobe) and mechanical (microindentation) analyses were carried out on polished sections giving direct access to a property profile along the sample. The mineralogy of the degradation was obtained by successive abrasion of the surface and XRD at each abrasion. The microstructural properties were determined along the degradation by microtomography and autoradiography. Micro-tomography allows to obtain the material microstructural properties in 3D while autoradiography allow a 2D visualization of the material properties (as EDS and microindentation). The other three microstructural characterization techniques (N_2 Physisorption, MIP, Water porosity) require the use of whole pieces of material. After degradation, as soon as the samples were taken out of the tank, the boundary between the degraded and the sound zone was visible to the naked eye. The degraded area showed a yellow/brown coloration (Figure 2-4a).

During the preparation of the samples or during the tests, as soon as the water was removed from the samples, cracks appeared. These cracks were located at the limit between the sound zone and the degraded zone (Figure 2-4b) and within the degraded zone, perpendicular to the surface (Figure 2-4c). It was thus possible to separate the sound zone from the degraded one to obtain samples from each zone. Samples were polished at the interface to limit residue from the other zone. An illustration of the location of cracks in relation to the chemical degradation front is proposed on Figure 2-5.

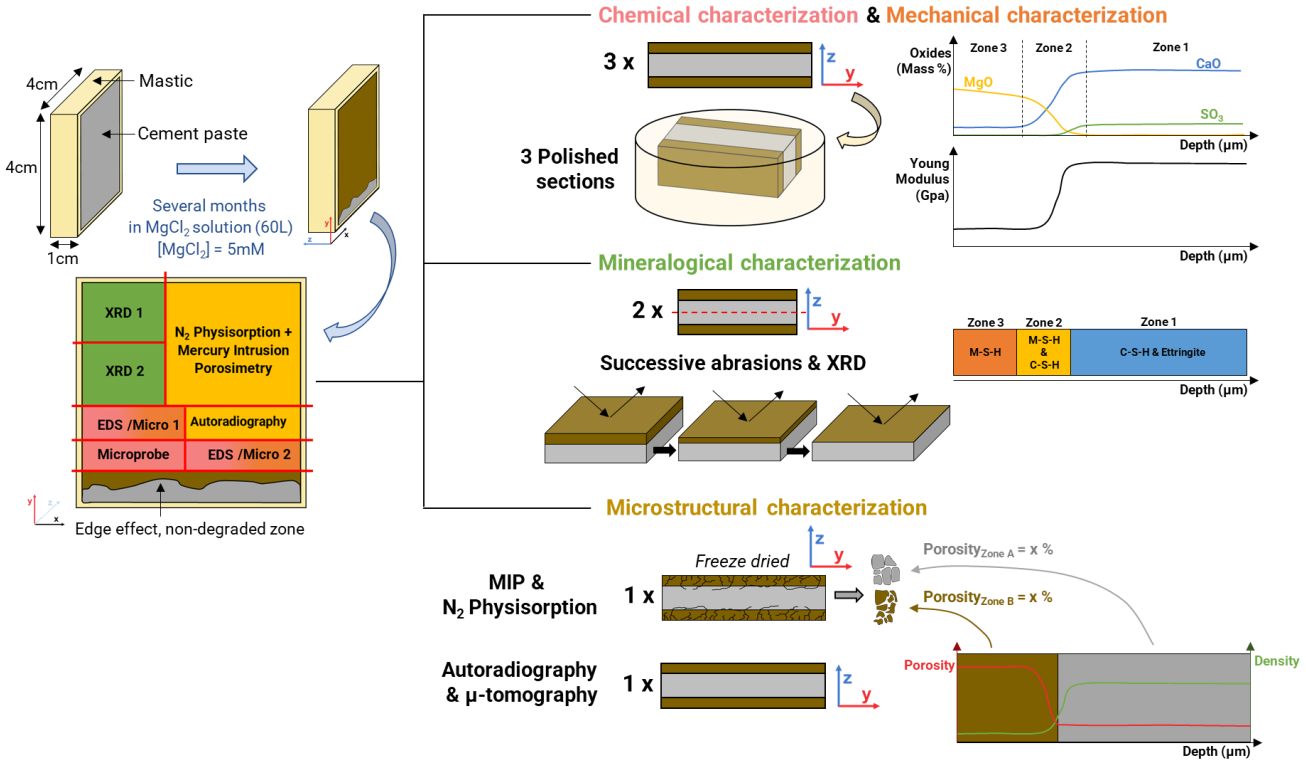

Figure 2-3: Schematic representation of the multi-physics characterization

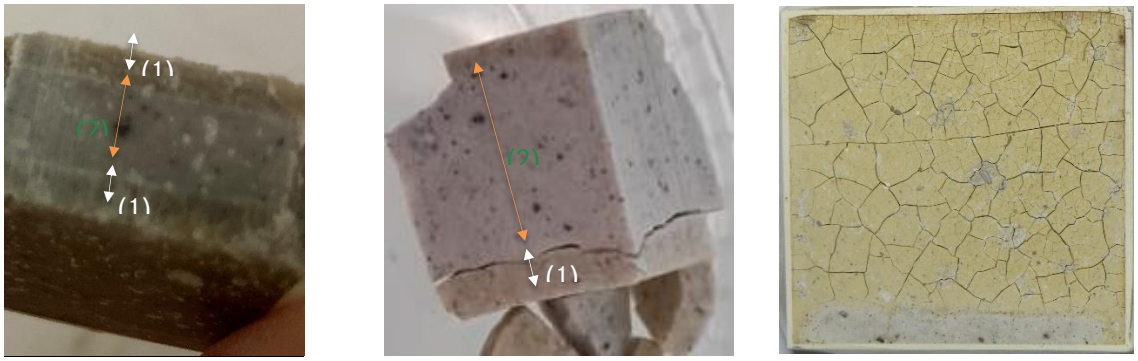

(a) (b) (c)

Figure 2-4: Visual observation of the Mg enriched zone (1) and the sound zone (2) on a still humid sample (a) and illustration of the shrinkage that occurs at the junction of the two zones on a dry sample (b - profile) and (c – face).

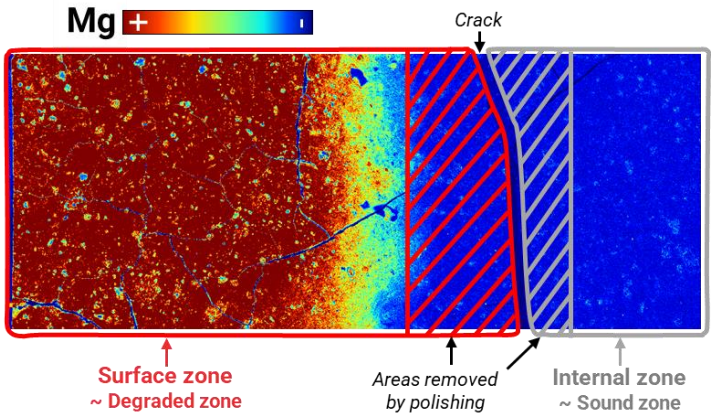

Figure 2-5: Illustration of the samples prepared for MIP and N_2 Physisorption on Mg EDS mapping

Chemo-mechanical compatibility

To ensure comparability between chemical and mechanical results, the same polished section was used for both tests (EDS and microindentation) and the same areas were studied. To identify the areas observed by EDS, a specific protocol was developed (Figure 2-6). First, the polished section was passed under the indenter to make a grid of indents (Figure 2-6: 1^{rst} step), in the resin, next to the sample. Then the section was coated with carbon (or gold palladium) and entered the SEM. Several zones were chosen, according to their chemical and mechanical interest (Figure 2-6: 2nd step). The presence of longitudinal and transverse cracks regards to the surface made it necessary to choose areas between two transverse cracks (perpendicular to the surface). Elemental mappings were performed in each of these areas. The longer the sample was degraded, the deeper the degradation front was, requiring the realization of several maps next to each other (1 to 4). Then, the sample was placed under the indenter. The previously selected areas were identified owing to the locations of the previously indents (Figure 2-6: 1^{rst} step) in the resin and some remarkable patterns (cracks in the material, bubbles in the resin etc.). Several grids of 4*4 indents

were made to cover all the zones (Figure 2-6: 3rd step). The choice of the indentation parameters was based on tests on sound material and a section of degraded material to optimize the indentation force from which the spacing between the indents and therefore the size of the grid derived. Finally, during the post-treatment, the mechanical results were compared to the chemical results (Figure 2-6: 4th step).

The use of these different analytical methods allows to obtain chemical, microstructural and mechanical property profiles along the sample.

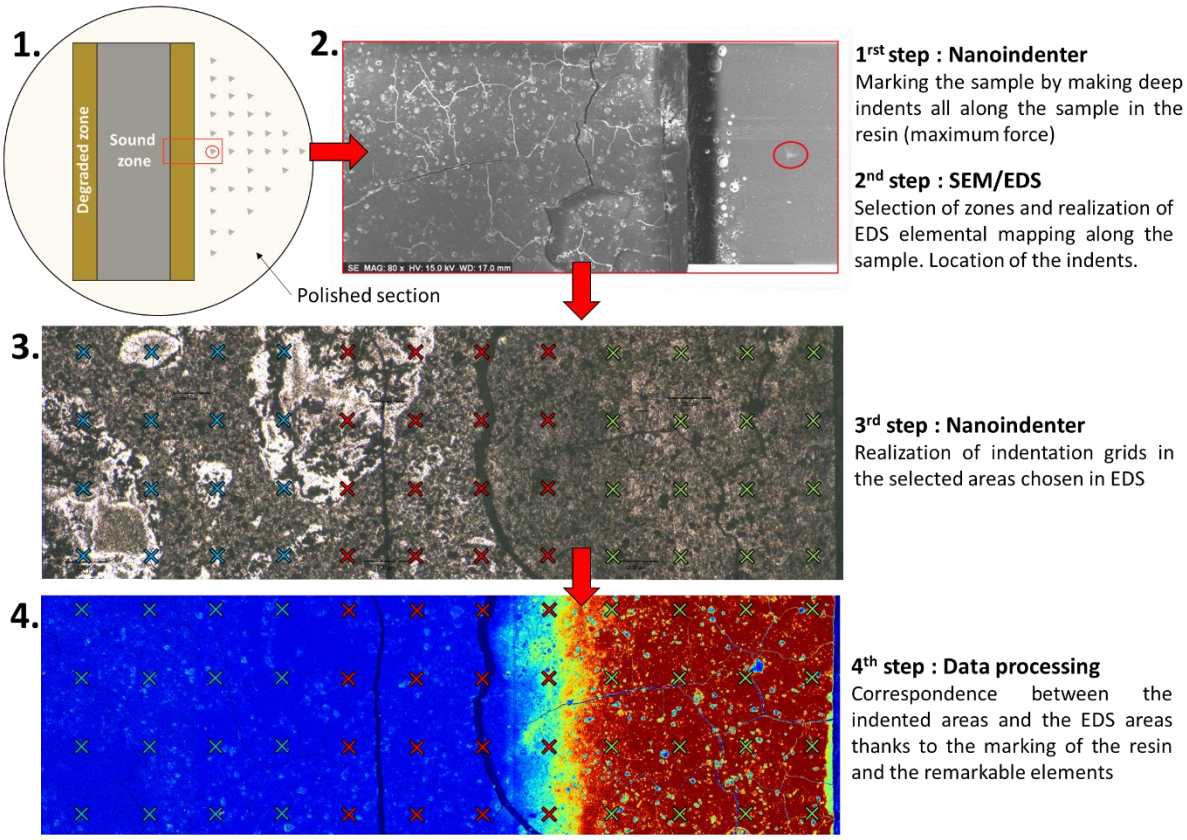

Figure 2-6: Scheme of coupled chemo-mechanical analysis protocol

2.1.3.2. Mineralogical and chemical analyses

X-Ray Diffraction (XRD) analyses were performed on an Malvern Panalytical Aeris (IRSN, Fontenay-aux-Roses) operating at 600W, 40 kV and 15 mA, with a Cu anti-cathode (λ~1.54 Å) on solids obtained by cutting the degraded samples and polishing successively the surface to characterize the degraded depth. The scanning region was in the range 2Θ from 5° to 70° with a step size of 0.0109, for a total duration of 20 min (IRSN, Fontenay-aux-Roses).

Solid chemical characterizations were carried outwith the same device as for homogeneous samples. Observations were performed on a polished section coated with gold-palladium alloy (277 Å thick) or carbon alloy (300 Å). The elemental maps were obtained by making hyper-spectral images of a duration of 1h47 on a surface of 1536x1152 µm (magnification x80) with a digital resolution of 3 µm. M/S and C/S intensity ratios were obtained, for each distance to the surface (x), by averaging the intensity of Mg/Si and Ca/Si of each column of pixels (384 pixels by column).

In addition, tests were performed on a Cameca SXFive microprobe (Centre de micro caractérisation Raimond Castaing – UMS 3623, Toulouse, France), operating at 15 kV and 20 nA, equipped with 5 WDS spectrometers and with an analysis volume of about 5 μm^3. Calibrations were carried out before each series of analyses on synthetic natural controls. The analysed points were chosen one by one to avoid residual anhydrous grains. The microprobe expresses the

concentrations of each element in the probed volume as a mass percentage of material (voids excluded). For cementitious materials, these mass percentages are conventionally expressed as mass percentage of associated oxides. The sum of the oxides is usually around 75%. The complement to 100% is largely attributed to bound water in the hydrated phases of the cement matrix (C-S-H, M-S-H etc.). 1 or 2% can be attributed to carbon in the form of CO_2 or heavy metals. In the sound part of the samples, even if the measuring points are chosen, it can happen that anhydrous grains invisible to the eye are found and in this case the total can exceed 75% (Bertron et al. 2009; Giroudon 2021).

2.1.3.3. Microstructure analyses

Different types of microstructure analyses were conducted to obtain information of the evolution of microstructure along the degradation (X-ray microtomography, autoradiography) and average values on selected zones (N_2 physisorption, mercury intrusion, water porosity, bulk density measurements).

X-ray microtomography

Small pieces (~100 mm^3) of the degraded samples were cut and placed under parafilm directly at the exit of the degradation tanks. The samples were then analysed by X-ray microtomography using a SkyScan 1272 (Bruker microCT N.V, Fontenay-aux-Roses). The samples remained under parafilm throughout the test. A spatial resolution of 2 µm was obtained. The parameters of the X-ray tube (100 kV, 100 mA) were set in order to optimize the contrast between the different phases and the pores. An angular step of 0,1° was used to acquire radiographs (total acquisition time: about 20 h).

Nitrogen physisorption

Nitrogen sorption isotherms were measured according to the same protocol as the homogeneous cement pastes.

Mercury intrusion

Mercury intrusion porosimetry (MIP) was performed according to the same protocol as the homogeneous cement pastes. The samples underwent the same pre-treatment as for nitrogen physisorption.

Follow-up (visual) cracking test

In order to visualise the shrinkage phenomenon that appears on some degraded samples, a follow-up (visual) cracking test was carried out. The degraded samples were placed under parafilm directly at the exit of the degradation tanks until the test (1 to 2 weeks). The follow-up cracking test consisted of taking high-resolution photos (with a Nikon® D810) at regular intervals (181 photos every 30 seconds, then 61 photos every 2 minutes, then photos every 20 minutes until the end of the test) while the sample was left in the open air in a controlled atmosphere room (20°C, RH=50%). Initially, only the front side is left in the open air, the other side is left under parafilm. After 24 hours, the sample is cut in two for the profile test (Figure B-5, Appendix B).

2.1.3.4. Mechanical characterization

For the degraded samples, due to the shrinkage phenomenon and the high porosity in the degraded zone, the sample was not flat enough to perform nanoindentation tests. Consequently, the indentation force was increased until the tests were no longer impacted by the roughness of the sample. The tests are named microindentation tests. They were force controlled (Max load = 200 mN, Loading rate = 100 mN/min). Several grids of 4*14 indents were made. In these tests, the penetration depth was about 10 µm, so the indents were spaced 300 µm apart.

2.1.4. Modelling tools

2.1.4.1. Chemical simulation (HYTEC)

Chemical simulations were performed with a reactive transport code, HYTEC (Van der Lee et al. 2003). The aim is not to perform predictive simulations but to use simulation as an analytical tool to identify the nature of the material exchanges between the cementitious material and the magnesium environment and to better understand the differences in mechanisms and kinetics between magnesium attack and pure leaching. No code development is done in this work.

HYTEC is a code developed for geochemical transport problems in saturated media. It allows to take into account geochemical heterogeneities and variations of physical parameters generated by mineralogical evolutions. The HYTEC code solves the chemical-transport problem by coupling CHESS chemical equilibrium code with a R2D2 transport module (Van der Lee et al. 2003).

The geochemical speciation code CHESS (Van der Lee 1998) controls the chemical reactions. This code performs calculations at thermodynamic equilibrium but kinetics can also be taken into account but need to be added manually. In this manuscript, no reaction kinetics will be included. This may result in larger degraded depths than in reality. It controls all phases of the system: minerals, solutions, aqueous and gaseous species etc. The calculations are based on a thermodynamic database. This database contains all the data necessary to solve the thermodynamic calculations: basic species, aqueous species, minerals and gaseous species. The equilibrium constants (K) of all reactions between species are specified. All equilibrium calculations are solved by an iterative Newton-Raphson method. The mineral species considered in the simulations are listed in Table 2-4. It has been shown that the properties of C-S-H and M-S-H depend on the ratio of C/S and M/S (see 1.1.2 and 1.2.4.3). The software and database do not allow the creation of a species with a variable composition. Therefore, several C-S-H and M-S-H were discretised according to their C/S and M/S ratio. As presented before (1.2.4.2), the composition of hydrotalcite evolves according to the Mg/Al ratio. In the Thermoddem 2020 (V1.10, Code version 1.07_2.06) database, the present hydrotalcite corresponds to a Mg/Al ratio of 2:1. This is what will be considered in the Hytec modelling.

Table 2-4 : Thermodynamic properties of mineral phases considered for the database

Name	Equation	logK (25°C)	density (kg/m³)	Ref
C0.7SH	$1.4\ Ca^{2+} + 2\ H_4SiO_4 \underset{\rightarrow}{\leftarrow} (CaO)_{1.4}.(SiO_2)_2.(H_2O)_{1.93} + 0.67\ H_2O + 2.8\ H^+$	-17.796	2291.49	1
C0.8SH	$1.6\ Ca^{2+} + 2\ H_4SiO_4 \underset{\rightarrow}{\leftarrow} (CaO)_{1.6}.(SiO_2)_2.(H_2O)_{2.18} + 0.22\ H_2O + 3.2\ H^+$	-21.184	2299.1	1
C0.9SH	$1.8\ Ca^{2+} + 2\ H_4SiO_4 + 0.11\ H_2O \underset{\rightarrow}{\leftarrow} (CaO)_{1.8}.(SiO_2)_2.(H_2O)_{2.31} + 3.6\ H^+$	-25.247	2327	1
C1SH	$2\ Ca^{2+} + 2\ H_4SiO_4 + 0.40\ H_2O \underset{\rightarrow}{\leftarrow} (CaO)_2.(SiO_2)_2.(H_2O)_{2.4} + 4\ H^+$	-29.474	2358.12	1
C1.1SH	$2.2\ Ca^{2+} + 2\ H_4SiO_4 + 0.75\ H_2O \underset{\rightarrow}{\leftarrow} (CaO)_{2.2}.(SiO_2)_2.(H_2O)_{2.55} + 4.4\ H^+$	-33.758	2379.59	1
C1.2SH	$2.4\ Ca^{2+} + 2\ H_4SiO_4 + 1.19\ H_2O \underset{\rightarrow}{\leftarrow} (CaO)_{2.4}.(SiO_2)_2.(H_2O)_{2.79} + 4.8\ H^+$	-38.095	2388.54	1
C1.3SH	$2.6\ Ca^{2+} + 2\ H_4SiO_4 + 1.57\ H_2O \underset{\rightarrow}{\leftarrow} (CaO)_{2.6}.(SiO_2)_2.(H_2O)_{2.97} + 5.2\ H^+$	-42.473	2414.86	1
C1.4SH	$2.8\ Ca^{2+} + 2\ H_4SiO_4 + 1.91\ H_2O \underset{\rightarrow}{\leftarrow} (CaO)_{2.8}.(SiO_2)_2.(H_2O)_{3.11} + 5.6\ H^+$	-46.935	2447.24	1
C1.5SH	$3\ Ca^{2+} + 2\ H_4SiO_4 + 2.26\ H_2O \underset{\rightarrow}{\leftarrow} (CaO)_3.(SiO_2)_2.(H_2O)_{3.26} + 6\ H^+$	-51.442	2477.78	1
C1.6SH	$3.2\ Ca^{2+} + 2\ H_4SiO_4 + 2.61\ H_2O \underset{\rightarrow}{\leftarrow} (CaO)_{3.2}.(SiO_2)_2.(H_2O)_{3.41} + 6.4\ H^+$	-55.989	2506.15	1
Ettringite	$6\ Ca^{2+} + 2\ Al^{3+} + 3\ {SO_4}^{2} + 38\ H_2O \underset{\rightarrow}{\leftarrow} Ca_6Al_2(SO_4)_3(OH)_{12}.26H_2O + 12\ H^+$	-56.958	1766.96	1
Portlandite	$Ca^{2+} + 2\ H_2O \underset{\rightarrow}{\leftarrow} Ca(OH)_2 + 2\ H^+$	-22.809	2241.44	1
Amorphous silica	$H_4SiO_4 \underset{\rightarrow}{\leftarrow} SiO_2(am) + 2\ H_2O$	2.714	2071.90	2
Calcite	$Ca^{2+} + HCO_3^- \underset{\rightarrow}{\leftarrow} CaCO_3 + H^+$	-1.847	2709.89	1
MSH-078	$0.78\ Mg^{2+} + 1\ H_4SiO_4 + 0.26\ H_2O \underset{\leftarrow}{\rightarrow} (MgO)_{0.78}.(SiO_2)_1.(H_2O)_{1.48} + 1.56\ H^+$	-7.25	2300[a]	2
MSH-083	$0.83\ Mg^{2+} + 1\ H_4SiO_4 + 0.33\ H_2O \underset{\leftarrow}{\rightarrow} (MgO)_{0.83}.(SiO_2)_1.(H_2O)_{1.5} + 1.66\ H^+$	-7.90	2300[a]	2
MSH-100	$1\ Mg^{2+} + 1\ H_4SiO_4 + 0.6\ H_2O \underset{\leftarrow}{\rightarrow} (MgO)_1.(SiO_2)_1.(H_2O)_{1.6} + 2\ H^+$	-10.43	2300[a]	2
MSH-130	$1.3\ Mg^{2+} + 1\ H_4SiO_4 + 2.1\ H_2O \underset{\leftarrow}{\rightarrow} (MgO)_{1.3}.(SiO_2)_1.(H_2O)_{2.8} + 2.6\ H^+$	-14.96	2300[a]	2
Brucite	$Mg^{2+} + 2\ H_2O \underset{\rightarrow}{\leftarrow} Mg(OH)_2 + 2\ H^+$	-17.112	2367.84	1
Hydrotalcite	$4\ Mg^{2+} + 2\ Al^{3+} + 17\ H_2O \underset{\rightarrow}{\leftarrow} Mg_4Al_2(OH)_{14}(H_2O)_3 + 14\ H^+$	-73.735	1949.91	1

1 = Thermoddem 2020 (V1.10, Code version 1.07_2.06)
2 = Bernard (Bernard et al. 2017b; Bernard, Dauzères, et Lothenbach 2018a) except for the densities that have been determined in this work in Chapter 3 (3.3.3). No trend was observed on the influence of the M/S ratio on the density and the value considered is an average of the values obtained on the M-S-H pastes.

The transport is simulated by the R2D2 module. This module is coded in finite elements and allows for 1D and 2D calculations in diffusive and/or convective transport. The transport equation (2-6) of a chemical species in water saturated media, without convective phenomenon, can be written as:

$$\frac{\partial \omega C_i^{sol}}{\partial t} = \mathrm{div}\left(D * \overrightarrow{\mathrm{grad}}.\, C_i^{sol}\right) - \frac{\partial \omega C_i^{p}}{\partial t} \qquad (2\text{-}6)$$

where ω is the porosity, C_i^{sol} the mobile fraction in the chemical component C_i, C_i^{p} the immobile fraction incorporating component C_i (precipitate), and D the effective diffusion coefficient.

When porosity is considered variable, a retroactive law varies the porosity as a function of phase volume and the diffusion coefficient can be porosity dependent if Archie's law is used (Lagneau 2013).

2.1.4.2. Analytical homogenisation technique for mechanical properties determination

A method has been developed to calculate the mechanical properties along the degradation of cement pastes from chemical properties and data about the sound sample (see 4.5). Figure 4-26 represents the method. The first step consists of combining microprobe and XRD data to determine molar profiles of the hydrated phases along the degradation. The second step consists of converting the molar profiles to volume proportions of hydrated phases thanks to the molar volume of the phases. The total volume (hydrates volume and capillary porosity) is considered constant. By combining the variation of volume of the solid and the porosity determined on the sound sample, the variation of the capillary porosity is simulated. The last steps consist to determine the homogenised properties of the degraded at each degradation depth from the volume proportion of each phase and their mechanical properties. This method is also used for the homogeneous sound materials (only one calculation point).

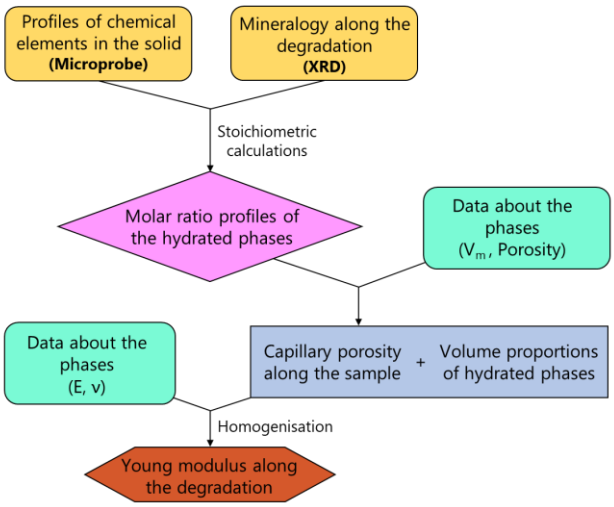

Figure 2-7 : General scheme of the method

2.2. Selection of cementitious materials

To better understand of the reaction mechanisms of magnesium attack and M-S-H formation in low-calcium cementitious matrices, several cementitious materials have been produced: Portland cement pastes (called CEMI or OPC) as control samples, C_3S based pastes and low-pH cement pastes (T3 and CEMI-sil-col).

2.2.1. Production of cementitious pastes

2.2.1.1. CEMI industrial paste

CEMI pastes were produced by the mixing of Portland cement (CEMI) and distilled water (milli-Q water). The Portland cement was a CEMI 52,5 N CE PM-ES-CP2 NF, coming from Val d'Azergues (Table 2-5). The pastes were prepared by mechanical mixing (rotation speed between 140 rd/min and 285 rd/min during 8 min, 450W). The proportions are given in Table 2-6. The mineralogical composition of the cement is as follows: 64.4% C3S, 1.4% C3A, 15.3% C_4AF. The product data sheet is available in Appendix H.

Table 2-5 : Oxides proportions in CEM I 52,5 N CE PM-ES-CP2 NF, coming from Val d'Azergues

Oxides	SiO_2	Al_2O_3	Fe_2O_3	CaO	MgO	K_2O	Na_2O	SO_3	TiO_2	MnO	P_2O_5	CO_2
Proportion (%)	20.6	3.60	5.00	64.3	0.70	0.70	0.20	2.70	ND	ND	0.40	0.90

Table 2-6: Mix proportions for CEMI paste

Sample name	g		w/b
	CEMI	MilliQ-water	
CEMI	1790	716	0.4

2.2.1.2. Industrial low-pH cement (T3)

Low-pH cement pastes (called T3) were produced by the mixing of a silica fume, a cement (CEMIII A), distilled water (milli-Q water) and superplasticizer. The formulation is among those considered by Codina et al. (Codina et al. 2008) to be compatible with an underground waste repository environment and is called T3. The notation will be kept in this work. The silica fume was CONDENSIL® S95 DM, provided by CONDENSIL®. The superplasticizer was CHRYSO®Fluid Optima 175, provided by Chryso France®. The cement was a CEMIII A 52.5 L CE PM-ES-CP1 NF, coming from Rombas (Table 2-7). It is made up of 36% clinker and 64% slag.

Table 2-7 : Oxides proportions in CEMIII A 52.5 L CE PM-ES-CP1 NF, coming from Rombas

Oxides	SiO_2	Al_2O_3	Fe_2O_3	CaO	MgO	K_2O	Na_2O	SO_3	TiO_2	MnO	P_2O_5
Proportion (%)	29.4	8.9	1.3	49.9	4.7	0.67	0.41	2.6	0.5	0.2	ND

Before the mixing with water and superplasticizer, the cement and silica fume were placed in TURBULA® mixer for 30min. Then the pastes were mechanically mixed (rotation speed between 140 rd/min and 285 rd/min during 8 min, 450W). The proportions are given in Table 2-8.

Table 2-8: Mix proportions of T3 cement paste

Sample name	g				Sp/b	w/b
	CEMIIIA	Silica fume	MilliQ-water	Superplasticizer (dry extract)		
T3	585.8	282.1	373.3	9	1.5%	0.43

Several batches were made. One before the start of the thesis and another during the thesis. The batch performed before the thesis allows for a more thorough hydration of the paste.

2.2.1.3. Model paste with colloidal silica (CEMI-sil-col)

Model cement pastes (called CEMI-sil-col) were produced by the mixing of a colloidal silica, a Portland cement (CEMI), distilled water (milli-Q water) and superplasticizer. The colloidal silica was Rheomac AS 150 (also called Mastermatrix 150), provided by BASF® in the form of an aqueous suspension (dry extract = 52 ± 2.5%). The Portland cement was also the CEMI 52,5 N CE PM-ES-CP2 NF, from Val d'Azergues. The superplasticizer was CHRYSO®Fluid Optima 175, provided by Chryso France®.

The pastes were prepared by mechanical mixing (rotation speed between 140 rd/min and 285 rd/min during 8 min, 450W). The w/b ratio and the superplasticizer content were optimized in regard to the workability of the mix (w/b=0.65). The proportions are given in Table 2-9.

Table 2-9: Mix proportions of CEMI-sil-col cement paste

Sample name	g				Sp/b	w/b
	CEMI	Rhéomac AS 150	MilliQ-water	Superplasticizer (dry extract)		
CEMI_sil-col	590.5	621.7	275.1	10.56	1.2%	0.65

2.2.1.4. Model paste based on C_3S and silica

Pure C_3S-based pastes (also named C-S-H pastes) were produced by the mixing of a colloidal silica, C_3S provided by Septodont®, distilled water (milli-Q water) and superplasticizer. The colloidal silica and superplasticizer were the same as for previous mix.

The protocol was adapted from the work of Kangni-Foli on C-S-H pastes (Kangni-Foli 2019). The pastes were prepared by mechanical mixing (rotation speed between 140 rd/min and 285 rd/min during 8 min, 450W). The w/b ratio and the superplasticizer content were optimized in regard to the workability of the mix. Two mixes were made for C/S=1.3 (P1 and P2) to test two addition rates of silica and superplasticizer to match the rheology. As mix two (P2) was too liquid and mix one (P1) a little too viscous, the mix for C/S=1 was adapted to obtain an ideal rheology. The proportions are given in Table 2-10.

Table 2-10: Mix proportions of C_3S-based pastes

Sample name	g				Sp/b	w/b
	C_3S	Rhéomac AS 150	MilliQ-water	Superplasticizer (dry extract)		
CS_3	1385.5	-	692.8	-	0%	0.50
CS_1-3_P1	770.15	530.3	356.1	48.6	4.7%	0.60
CS_1-3_P2	770.8	530.3	356.4	34.9	3.4%	0.60
CS_1	640	672.9	297.2	59.3	6.1%	0.65

2.2.2. Mineralogy of sound pastes

The mineralogy of the cementitious pastes has been study by XRD (Figure 2-8) and TGA (Figure 2-9).

The composition of cementitious pastes, and especially the presence of portlandite, influences the pH of the pore solution of the cementitious paste (Sumra, Payam, et Zainah 2020; Codina et al. 2008). For highly silica-substituted cementitious pastes such as T3, CEMI-sil-col or C_3S-based pastes (C_3S and colloidal silica-based pastes), the portlandite can be entirely consumed during hydration allowing the pH to be lowered to 11. However, the consumption of all the portlandite may take a long time and some of it may remain in the short term. This can be observed in C_3S-based pastes. After 100 days of hydration, the portlandite signal is still observable on the X-Ray diffractograms (Figure 2-8a). As the pastes are mainly composed of C-S-H, although some portlandite remains, it can be observed in the XRD. The TGA performed in parallel confirms these results (Figure 2-9a). For the C_3S based paste with C/S=3, as for CEMI based one, the presence of portlandite, which is expected, is well reflected by the weight loss around 500°C. The paste that shows the least amount of portlandite is the C/S=1.3 P1 paste.

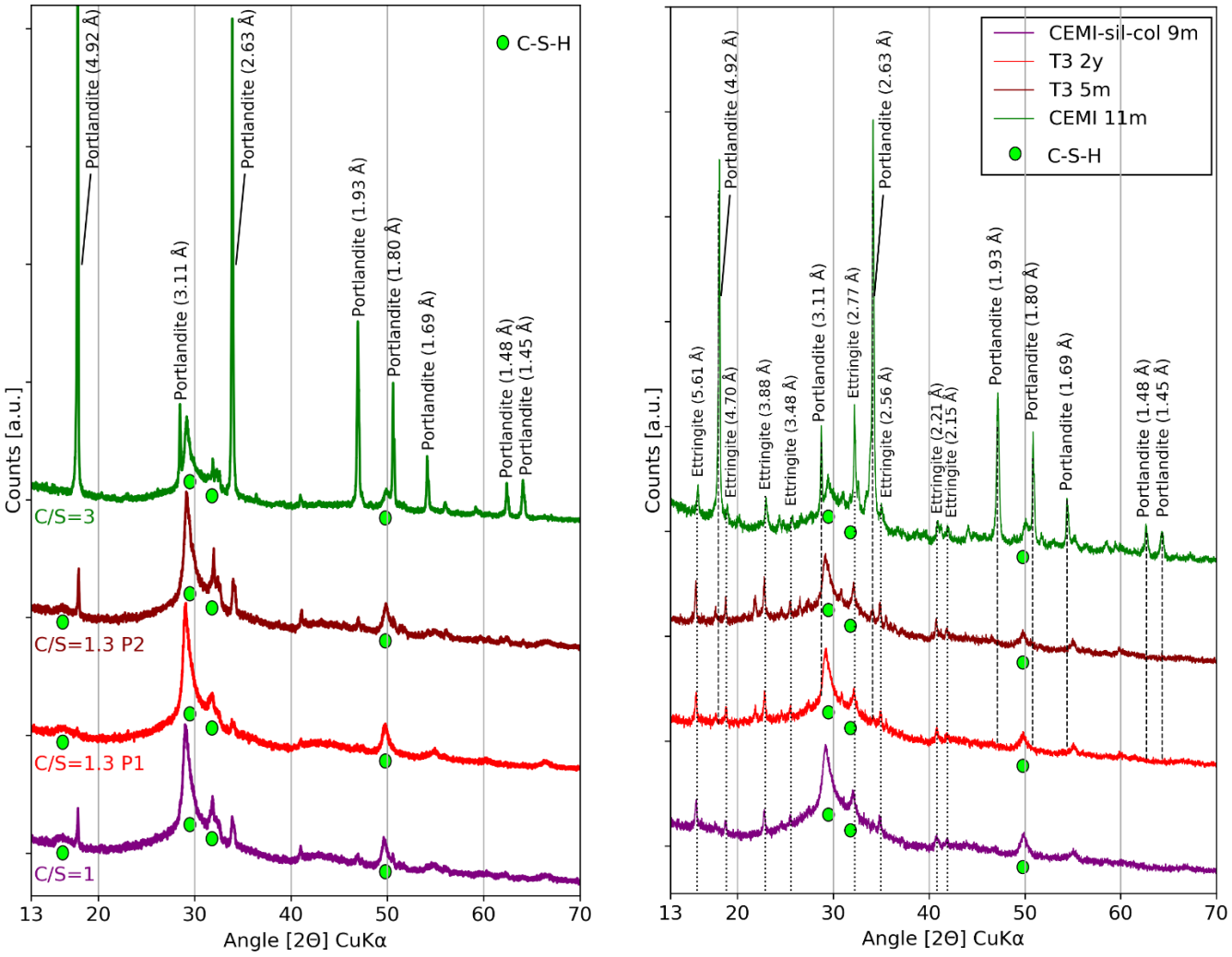

Figure 2-8 : X-Ray diffractograms of (a) C_3S based pastes with 3 different C/S after 3.5 months of hydration and (b) cement pastes: three low-pH pastes (T3 and CEMI-sil-col) and one Portland paste (CEMI) hydrated for 2 years, 5 months, 9 months and 11 months respectively

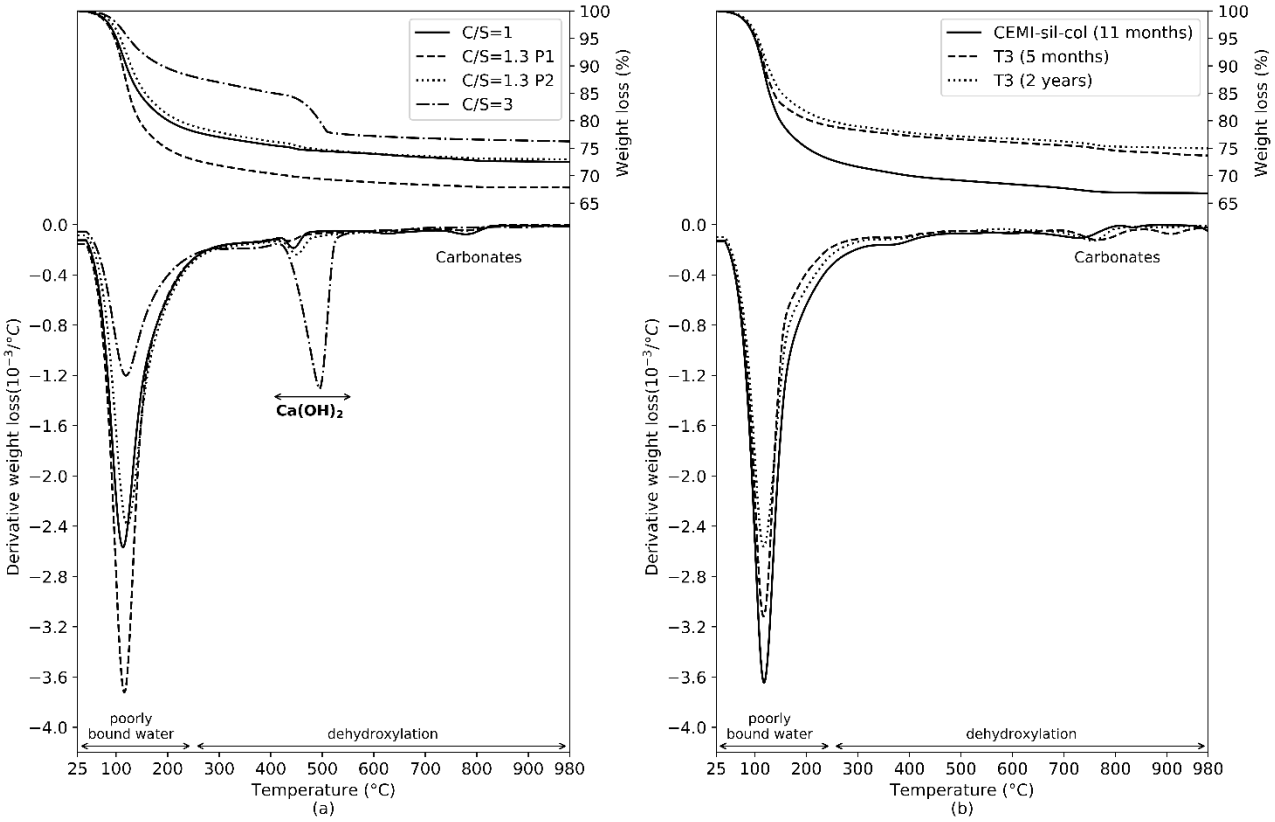

Figure 2-9 : TGA results of (a) C_3S based pastes with 3 different C/S after 3.5 months of hydration and (b) cement pastes: three low-pH pastes (T3 and CEMI-sil-col) and one Portland paste (CEMI) hydrated for 2 years, 5 months, 9 months and 11 months respectively

Model paste, based on CEMI and colloidal silica, has a proportion of silica equivalent to low-pH cement (T3) (C/S of the paste of 0.94 and 1.0 respectively) which is theoretically sufficient to have no portlandite. In XRD (Figure 2-8a), due to the presence of other hydrates such as ettringite and other species provided by silica fume (quartz, cristobalite), the portlandite signal is more difficult to observe at low concentrations. The presence or absence of portlandite can be better seen with TGA. From the XRD (Figure 2-8b) and TGA (b), there does not appear to be any residual portlandite in the 2-year-old T3 sample, the 5-month-old T3 sample or the 11-month-old CEMI-sil-col sample.

By adding silica and decreasing the C/S ratio, the amount of portlandite is minimised although it is still detectable by XRD and TGA for the C_3S-based model pastes. To test their behaviour in contact with magnesium, a degradation test in a $MgCl_2$ solution was carried out and is detailed in the next sections.

2.2.3. Simplified degradation test procedure for material selection

At the end of their manufacture, the pastes were kept under endogenous conditions until the beginning of the degradation procedure (see Table 2-11). Samples of 4*4*1 cm^3 were cut, coated with sealant on the sides of 4*1 cm^2 to force unidirectional degradation.

To make a first selection of materials, the degradation protocol used is simpler than the one finally applied for the thesis (less handling) (see 4.1.2). The degradation solution is not renewed. For the formulations retained after the first series of tests, the solution is renewed regularly.

The samples were immersed in 5 or 50 mmol/L $MgCl_2$ solutions in containers of different capacities (0.6 L to 60 L) for several weeks to several months. Table 2-11 presents the degradation

protocol for the different pastes tested and the mineralogy of the degraded zone observed on XRD. For infinite volume protocol, the solutions were constantly agitated and renewed every two months. At the end of each exposure time, one to two samples were taken, cut out and prepared for various characterization tests.

As shown by Table 2-11, immersion in $MgCl_2$ solution did not give the same minerology of the degraded zone depending on the paste tested. In order to explain the difference, some characterizations have been achieved on the degraded samples and will be exposed in the next part.

Table 2-11: Protocol of immersion of the pastes in $MgCl_2$ solutions associated with the mineralogy of the degraded zone observed on XRD

	Type of paste	Volume (L)	[$MgCl_2$] concentration (mmol/L)	Hydration time (m=months, y=years)	Degradation time (w=weeks, m=months)	Mineralogy of the degraded zone
Finite volume – no renewal of the solution	**CEMI**	2	5	10.5m	1m	Brucite
			50		1m	Brucite
	T3	2	50	6m	1m	Brucite
					4m	Brucite
	C/S=1,3 P2	20	5	3m	2w	Brucite
					1m	Brucite + Calcite
			50		2w	Brucite
					1m	Brucite
	C/S=1	2	50	5.5m	2.5w	Brucite
		After polishing, put back in bottle for 2 months more			2.5w+2m	Brucite
		2	50 + [$NaCO_3$] = 2		2.5w	Brucite
		After polishing, put back in bottle for 2 months more			2.5w+2m	Brucite + Calcite
	CEMI-sil-col	2	50	9.5m	1m	MSH + CSH
					4m	MSH + CSH
	T3	0,6	5	>2y	2m	MSH + CSH
			50		2m	MSH + small amount of CSH
Infinite volume	**C/S=1,3 P1**	60	5	3.8m	3m	CSH + small amount of brucite and M-S-H
					6m	CSH + small amount of brucite and M-S-H

2.2.4. Analysis of the mineralogy and chemistry of 4 cementitious materials under magnesium attack

2.2.4.1. Portland cement pastes

Tests were carried out on portland cement paste. Two sections of CEMI were placed in 5 mM and 50 mM $MgCl_2$ for 1 month. The result is similar to the literature. A thick layer of brucite forms on the surface. The presence of brucite on the surface of the samples can be seen in the diffractograms (Figure 2-11 XRD). For CEMI placed in 50 mM $MgCl_2$ for one month (b), brucite is predominant at the surface and in a thickness of at least 135 µm. For CEMI with a lower $MgCl_2$ concentration (5 mM) (a), brucite also precipitates but the ratio of brucite to C-S-H peak intensity is much lower. The higher the $MgCl_2$ concentration, the higher the amount of brucite for the same sound paste. Calcium leaching is very important (Figure 2-11 EDS and profiles). The higher the concentration of Mg in solution, the more significant the leaching. Due to the presence of portlandite, the initial Ca/Si intensity ratio ($C/S_{intensity} \approx 2.8$) is high. The CEMI paste with 50 mM of $MgCl_2$ only shows the degraded zone. The leaching is so deep that the sound zone does not appear, but the sound zone can be considered as identical as the one of CEMI with 5 mM (same C/S). The higher the calcium leaching from the paste, the higher the brucite layer. Portlandite ($Ca(OH)_2$) releases OH^- ions when it dissolves, which facilitates the formation of brucite ($Mg(OH)_2$). This predominance of brucite over other magnesium phases can also be explained by the pH associated with the presence of portlandite. According to the pH-driven predominance diagram (Figure 2-10) proposed by Bernard (Bernard et al. 2017b), brucite and M-S-H coexist for a pH above 10.1. From a concentration of about 0.1 mM in Mg, depending on the pH, brucite takes over. The M/S intensity ratio (Figure 2-11 Profiles) should tend towards infinity when brucite is present but as observed in the XRD diffractograms (Figure 2-11 XRD), other phases (C-S-H) persist and the EDS interaction bulb is too large to discriminate hydrates. The proposed profiles are made using columns of pixels. Thus, the value of the M/S ratio during brucite precipitation reaches a high but not infinite value.

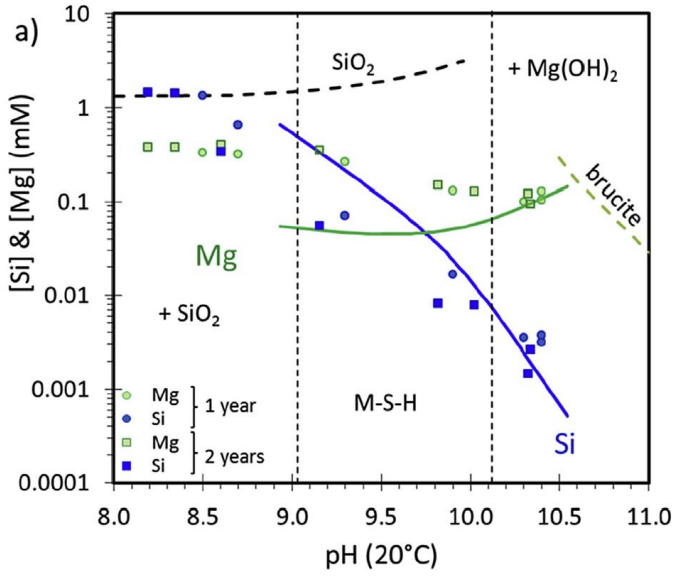

Figure 2-10 : Magnesium (light green symbols) and silicon (dark blue, black or red symbols) concentrations as a function of pH at 20°C after 1 year (circles) and 2 years (squares). Lines indicate calculated solubility of amorphous SiO2, M-S-H and brucite. Vertical lines separate the area where i) silica + M-S-H, ii) M-S-H only and iii) M-S-H + brucite are present. (Bernard et al. 2017b)

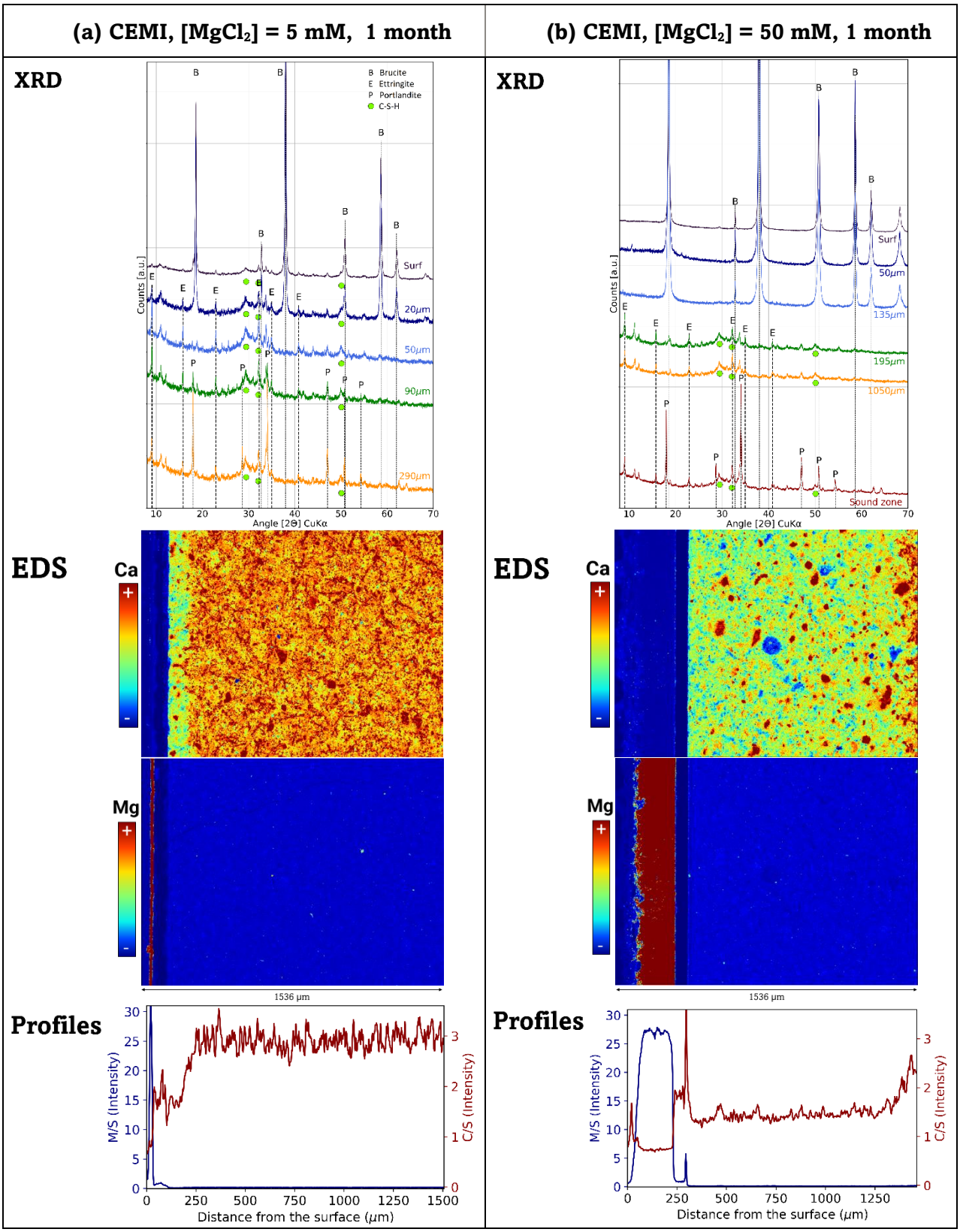

Figure 2-11: Results on the Portland cement pastes (hydrated during 10.5 months) degraded in 5 mM (a) and 50 mM (b) $MgCl_2$ solution during 1 month. From top to bottom : X-Ray diffractograms along the degradation, Ca & Mg EDS Cartographies and C/S and M/S Intensity profiles determined from EDS maps

2.2.4.2. Industrial low-pH cement paste

The low-pH cementitious pastes produced during the thesis fulfil the conditions for the formation of M-S-H and the absence of brucite according to the simulation. However, the sample placed for four months in 50 mM $MgCl_2$ shows only the presence of brucite (Figure 2-12a XRD). The EDS maps in Mg and Ca as well as the M/S and C/S intensity profiles are shown in Figure 2-12b and c respectively. The M/S and C/S profiles are derived from the EDS maps and correspond to intensity ratios and not atomic ratios. They are made by averaging the pixels per column. According to the EDS mapping (Figure 2-12b) and the M/S profile (Figure 2-12c), a layer with a high concentration of magnesium forms on the surface. This agrees with the brucite formation process observed in the literature (Dauzères et al. 2014); brucite forms as a layer on the surface of the sample (1.2.3). The formation of the brucite layer, filling the porosity, similar to that of a calcite layer, limits the diffusion of Mg ions, even with a small thickness. This prevents a deep Mg enrichment of the paste and the formation of M-S-H. The rest of the sample is then protected. No calcium leaching is observed. The brucite layer detached when the sample was put under vacuum. This disbonding is visible on the EDS maps and in the M/S and C/S profiles by the presence of an increase in the C/S ratio near the surface. This is an artefact due to the presence of a hole between the brucite layer and the rest of the sample as no increase in calcium is visible on the EDS maps.

As literature (Dauzères 2010) showed the formation of M-S-H on this type of cementitious materials, the same type of paste, prepared 2 years earlier (2018) was tested under similar conditions to verify this result. The aim is to see if the hydration time influences the type of phases that are formed under magnesium attack. In the first case presented, the sample was produced about 6 months before the test. The degradation time of the second paste tested is therefore 4 times longer. Two sections of the paste hydrated for 2 years has been put in 5 mM and 50 mM $MgCl_2$ solution for 2 months. Results are displayed in Figure 2-13. No signals associated with brucite are visible on the diffractograms. At the surface of the samples, 4 main humps (19.7, 26.7, 35, 54 and 59.9 [2θ] CuKα, see 1) associated with the presence of M-S-H (Bernard et al. 2019; Roosz et al. 2015) are observable. A zone of coexistence between M-S-H and C-S-H appears, from the surface to a variable depth depending on the Mg concentration (115 µm to 290 µm). Several peaks of low intensity appear on the diffractograms at about 11, 22 and 35.7 [2θ] CuKα. According to (Lojka et al. 2020), this would correspond to the formation of a magnesium oxychloride ($Mg_2(OH)_3Cl.4H_2O$) in small quantities. As the aggressive solution is composed of $MgCl_2$, the formation of magnesium oxychloride seems possible but unlikely because the $MgCl_2$ concentration is low. Indeed, it is only at high concentration of MgCl2 (≥5 wt% or ≥250 mmol/L) that chloride-based phases are formed (Yang et al. 2020; Xie, Dang, et Shi 2019; Qiao et al. 2018; Sutter et al. 2006). Some peaks (11 and 22 [2θ] CuKα) could also correspond to the formation of hydrotalcite but this does not explain the peak around 35.7. Hydrotalcite ($Mg_6Al_2CO_3(OH)16{\cdot}4H_2O$) is a magnesium phase which has also been observed with M-S-H during magnesium attack of cement pastes (Codina et al. 2008; Jenni et al. 2014; Kobayashi, Takahashi, et Kawabata 2021). Its presence would be consistent, and it would explain where the aluminium initially present in ettringite goes in the leached zone. This second hypothesis being more probable, it is the hydrotalcite which will be considered thereafter as being at the origin of the peaks. As in the sound pastes (Figure 2-8b and Figure 2-9b), in the sound zones of the degraded pastes no portlandite is visible.

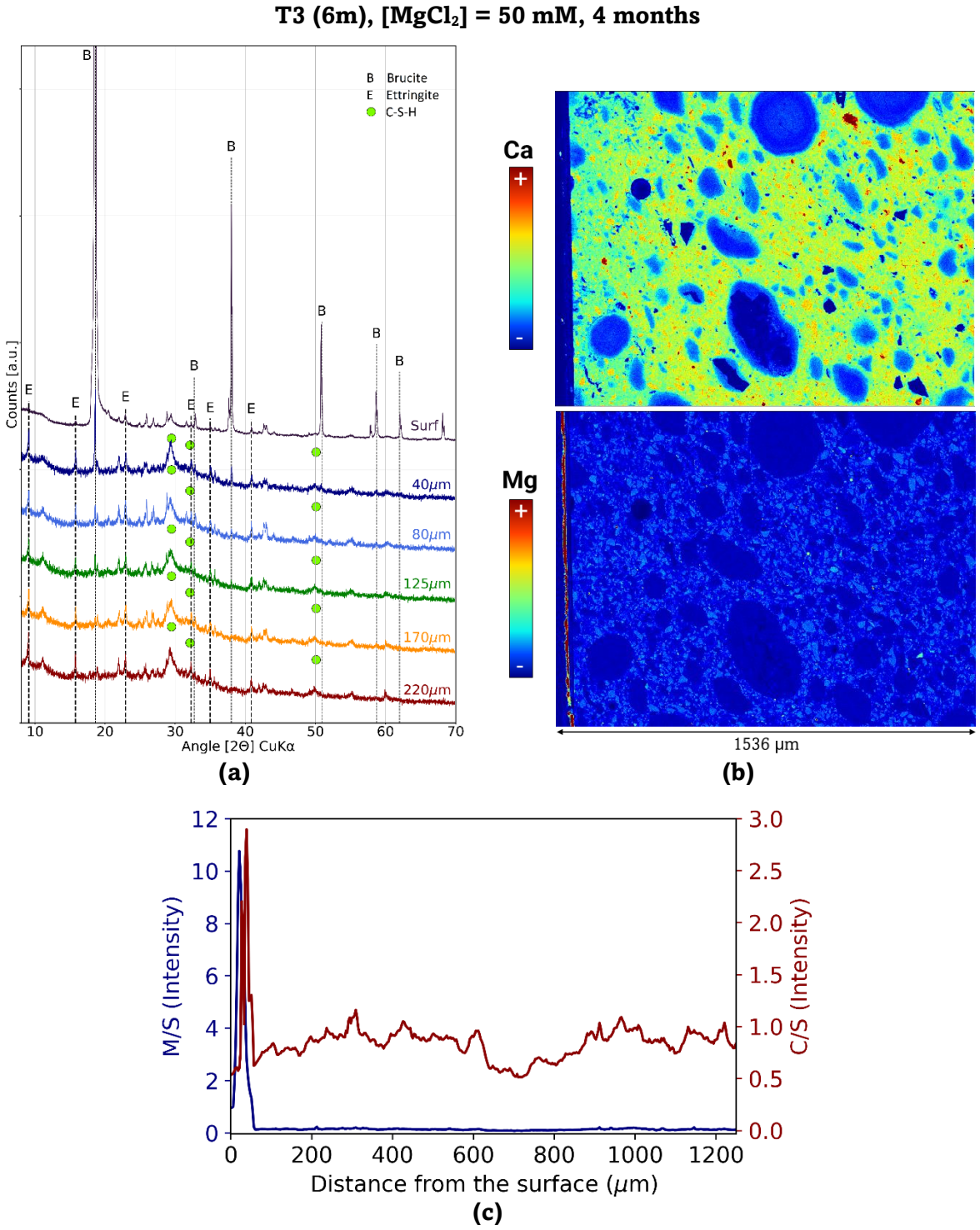

Figure 2-12: Results on the T3 cement paste (hydrated during 6 months) degraded in 50 mM $MgCl_2$ solution during 4 months. (a) X-Ray diffractograms along the degradation, (b) Ca & Mg EDS Cartographies and (c) C/S and M/S Intensity profiles determined from EDS maps

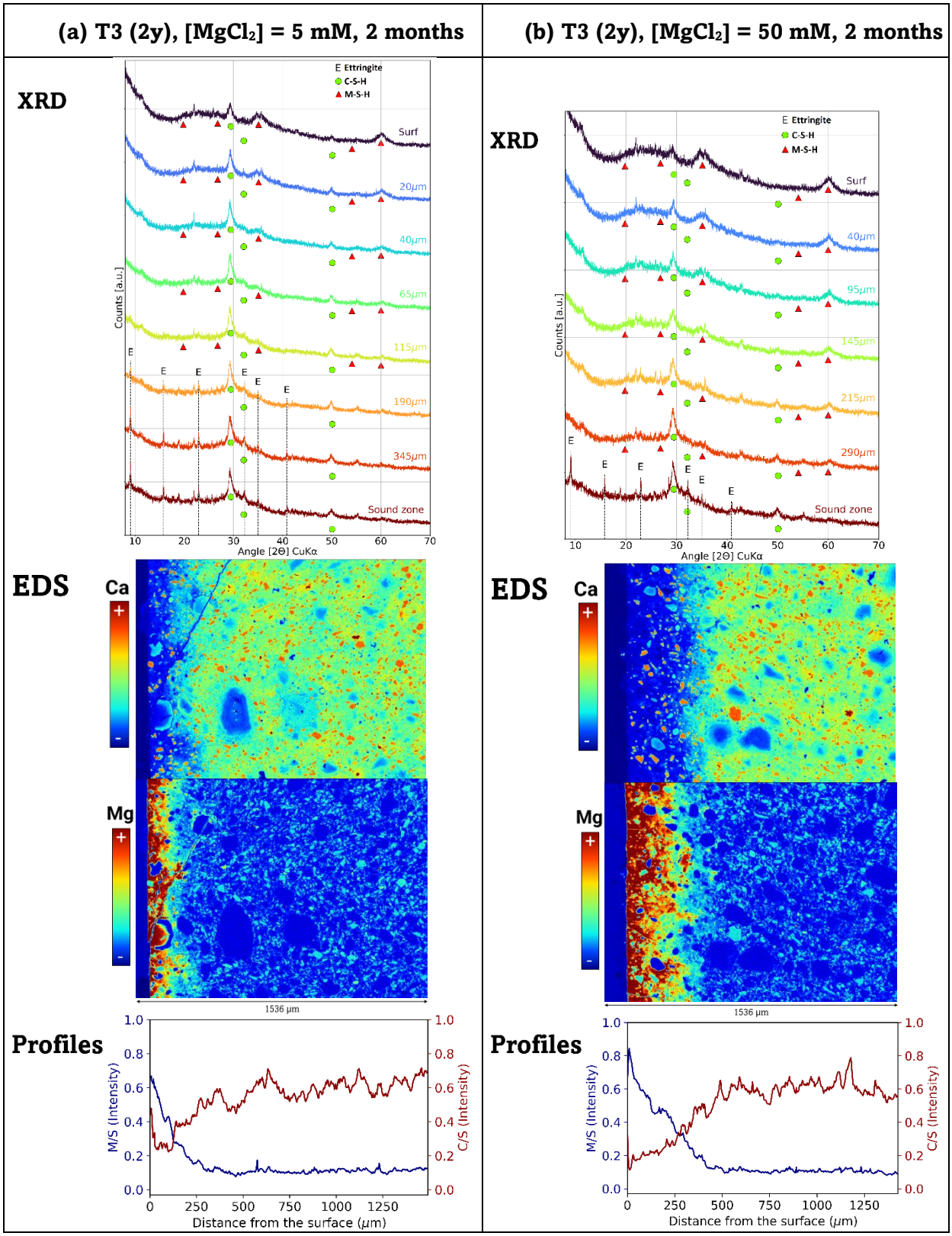

Figure 2-13: Results on the T3 cement paste (hydrated during 2 years) degraded in 5 mM (a) and 50 mM (b) $MgCl_2$ solution during 2 months. From top to bottom : X-Ray diffractograms along the degradation, Ca & Mg EDS Cartographies and C/S and M/S Intensity profiles determined from EDS maps

The EDS maps (Figure 2-13 - EDS) show deep magnesium enrichment in parallel with calcium leaching (200 to 400 µm thick). Despite the initial non-uniform distribution of Ca and Si, the degradation front is homogeneous along the surface. The M/S and C/S ratios along the degradation (Figure 2-13 - Profiles) confirm the observations made on the EDS maps. The magnesium signal increases when the calcium signal decreases. The slope of the Ca evolution is similar to that of magnesium. The enrichment is not abrupt but progressive. The maximum value of the M/S ratio, reached at the surface, is about 0.6 to 0.8. It was seen earlier that when brucite ($Mg(OH)_2$) precipitates, the M/S ratio reaches much higher values (over 10). With M-S-H, the atomic ratio reaches 0.78 to 1.3 in the literature (Bernard et al. 2017b) which explains a much lower value of the ratios in intensity when brucite is absent and M-S-H is formed.

Thus, for a paste of the same formulation but with a longer hydration, the magnesium phases that precipitate are not the same. T3 pastes are produced from cement, slag and silica fume. The hydration reaction is therefore longer than for standard cements (1.1.1). In addition, the non-homogeneous distribution of silica may make the silica available gradually and not directly. It is possible that for the 6-month-old paste, even if no portlandite signal is visible on XRD and TGA (Figure 2-8 and Figure 2-9), hydration is not sufficiently advanced and that C-S-H with high C/S ratio coexist with amorphous silica.

To study this effect, a chemical simulation has been performed on HYTEC. Simulations were carried out in two steps: a first part devoted to a hydration calculation of 4 different pastes and a second part devoted to their degradation. The database used is that of Thermoddem 2020 (V1.10, Code version 1.07_2.06) associated with the values of the magnesium phases proposed by Bernard in 2017 (see Table 2-4). The 4 selected pastes differ in the amount of silica added to the cement. Paste A is composed only of hydrated CEMI while in pastes B, C and D the amount of silica increases gradually. The aim was to obtain a paste with a small amount of portlandite (B) and a paste without portlandite but with a C/S at the limit of portlandite precipitation (C).

Table 2-12 gives the results of the hydration calculation for each of the pastes.

Table 2-12 : Hydration results on HYTEC

Mix name		**A**	**B**	**C**	**D**
% of colloïdal silica in the binder		0	23.5	24	34.5
w/b		0.4	0.6	0.6	0.65
C/S		**3.34**	**1.67**	**1.65**	**0.94**
Hytec results - Hydratation					
pH		11.9835	12.1245	11.6	10.5323
Ionic Strenght		1.0185	0.55629	0.536	0.397013
Solids (g/L)	Portlandite	588.71	1.6636	0	0
	Ettringite	133.04	102.08	102.1	95.805
	C1.6SH	812.47	995.19	981.3	0
	C1SH	0	0	0	722.94
	C0.8SH	0	0	14.332	0
	C0.7SH	0	0	0	304.94
molal	Na[+]	0.092	0.054	0.054	0.044
	K[+]	0.204	0.12	0.118	0.096

After the hydration calculation, the results were used to simulate degradation. The porosity considered for paste A is lower (0.4) than for paste B, C and D (0.5) due to the addition of silica in

the latter. The simulation is carried out in 1D, with a thickness of 5 mm of the sample. A surface boundary condition is applied to the left of the sample; at x=0, the sample is considered to be in contact with a solution of constant $MgCl_2$ concentration (5 mM).

No kinetics are considered in the simulation for solid-liquid exchanges; the interstitial solution in each cell is in equilibrium with the solid phases. The solid phases considered in the calculation are the phases initially present (C-S-H – C/S=1.6 to 0.7, Ettringite, Portlandite) and the phases resulting from degradation (Hydrotalcite, M-S-H – M/S=0.78 to 1.30, Brucite) (see Table 2-4).

The diffusion properties are identical for all ionic species and are considered constant ($D = 1.0^{e-11}$ m^2/s) as there is not enough data to take into account the effect of mineralogical changes (precipitation, dissolution, decalcification) on the transport properties. Porosity is considered constant. In reality, brucite can block the porosity, slowing down the diffusion. Not taking into account a variable porosity therefore may lead to an overestimation of the degradation kinetics but for this simulation, only the species formed are discussed, not the degraded depth.

The degradation time considered is 4 months. The results are shown in Figure 2-14 and Figure 2-15. In Figure 2-14, the phase C-S-H corresponds to the sum of all C-S-H defined by different C/S ratios in Hytec. To visualise the decalcification, Figure 2-15 represents the M/S and C/S ratios along the degradation calculated from the molar concentration of all phases. Several observations can be made.

- 3 of the 4 pastes show the presence of brucite, M-S-H and hydrotalcite at the surface (A, B and C). These pastes have a high C/S ratio and a pH above 11.5. Pastes A and B, initially contain portlandite and the pH is around 12. In contact with a magnesium solution, the high pH causes the formation of brucite. Thermodynamically, the formation of M-S-H seems possible. However, the porosity closure associated with the formation of a brucite external layer is not taken into account (cf constant porosity hypothesis). The calculations could therefore allow for the diffusion of magnesium ions when in reality this is not possible, resulting in the formation of M-S-H.
- Paste C, although not containing portlandite, has a high pH. It contains a large amount of C-S-H with C/S=1.6. On contact with the magnesium solution, the high pH value also causes the formation of brucite. This simulation shows that even if there are no signals associated with portlandite in XRD, it is possible that the pH of the pore solution is still too high if hydration is not finalised and C-S-H with high C/S ratios persist. It is then possible to form brucite, even in the absence of portlandite.
- Sound paste D has a much lower C/S ratio than the others and consists only of C-S-H with low C/S ratios and ettringite. As a result, the pH is much lower than the other pastes (10.5). On contact with the magnesium solution, only M-S-H and hydrotalcite are formed.

The simulations agree with the hypothesis based on the experimental results. The absence of portlandite is not sufficient to prevent the creation of a brucite layer. It is also necessary to have C-S-H with low C/S ratios in order to lower the pH sufficiently to leave the brucite stability range. This confirms the previous results on the two low-pH cementitious pastes (T3). The "young" paste is not yet re-equilibrated and, locally, C-S-H with high C/S ratios may be present (as observed by El Bitouri on low-pH cement pastes, (El Bitouri et al. 2016)). To be representative of long-term behaviour, low-pH model cement pastes must therefore have a low and homogeneously distributed C/S. Next section (2.2.4.3) will present the experimental results on these pastes.

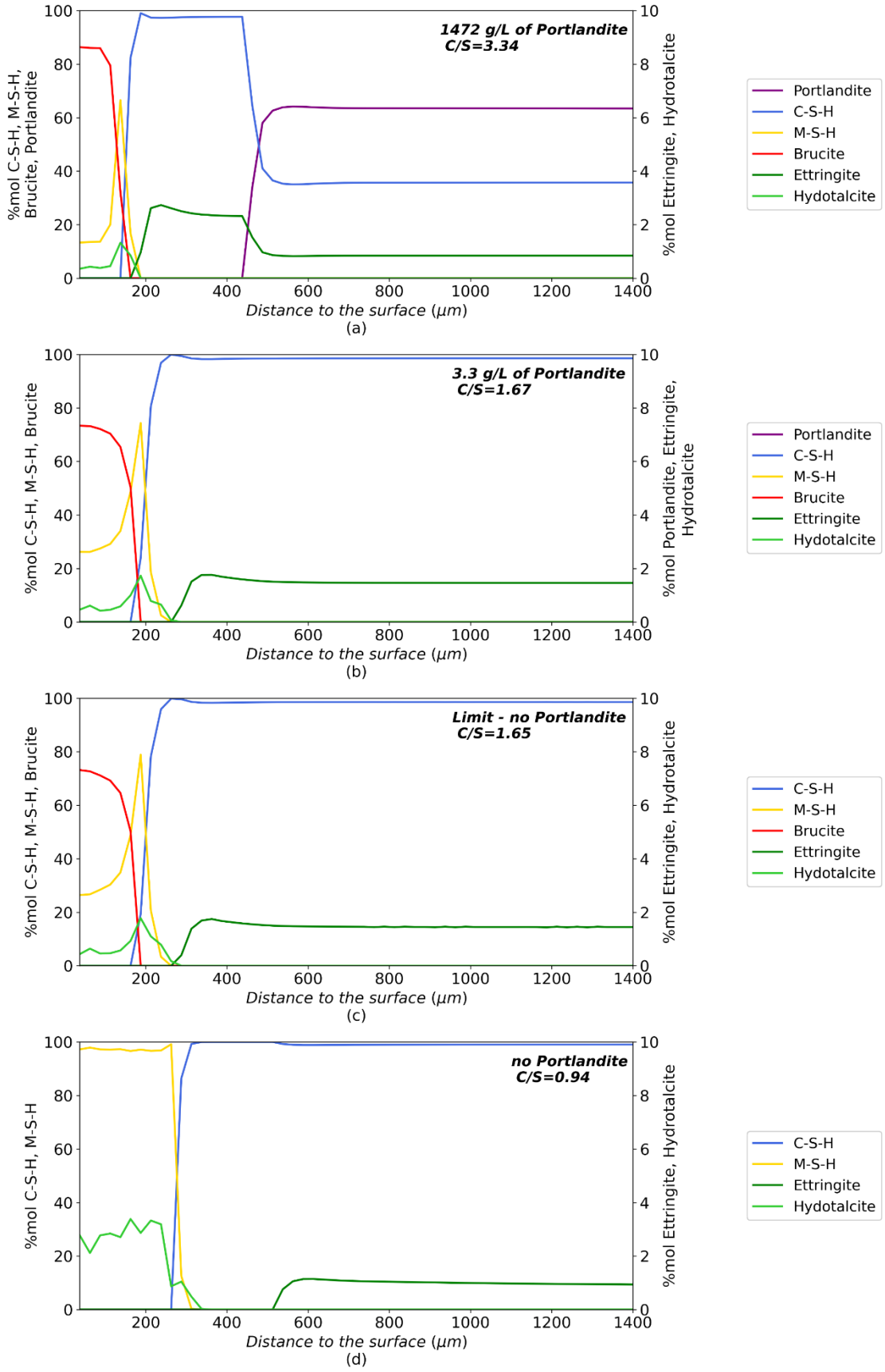

Figure 2-14 : Hytec simulation of a 1D degradation with 5 mM of $MgCl_2$. (a), (b), (c) and (d) corresponds to simulations for the cement pastes A, B, C and D of Table 2-12

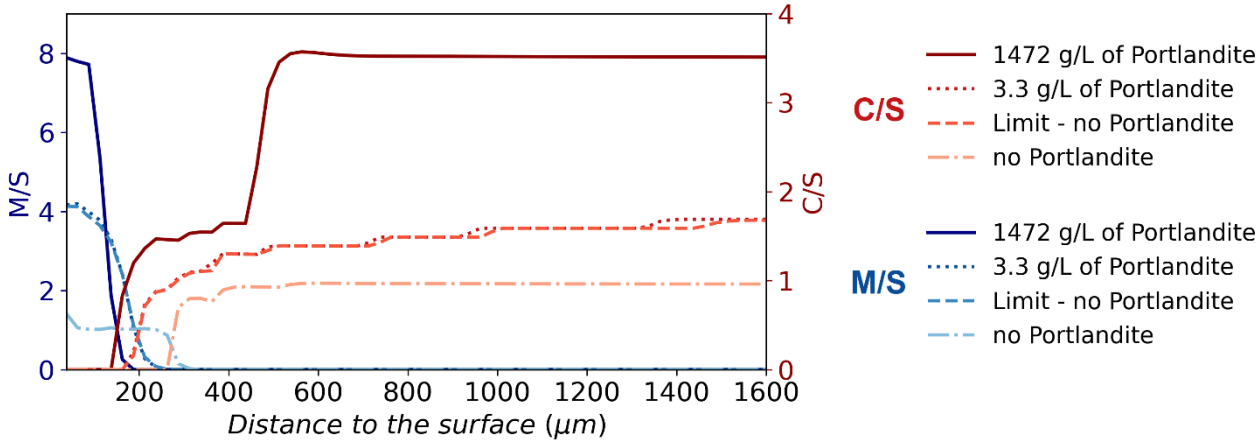

Figure 2-15 : M/S and C/S calculated along the degradation from the Hytec simulation results

2.2.4.3. Model cement pastes

1.2.4.3.7. C_3S-based pastes

Degradation tests were performed on C_3S-based pastes with C/S ratios less than 1.3. C_3S-based paste with C/S=1 have been placed in 50 mM $MgCl_2$ for 2.5 weeks (Figure 2-16a), C_3S-based paste with C/S=1.3 (P2) have been placed in 5 mM and 50 mM $MgCl_2$ during 1 month (Figure 2-16 b and c respectively).

Despite the amount of silica in the mix, all the C_3S-based pastes studied, initially showed some portlandite (Figure 2-8). After contact with $MgCl_2$ solutions, results show the presence of brucite in small or large quantities (Figure 2-16 XRD Figure 2-17).

As before for the CEMI pastes (Figure 2-11 - XRD), the higher the magnesium concentration in solution, the higher the amount of brucite appears to be for the same sound C_3S-based paste (higher brucite/C-S-H ratio for Figure 2-16 c than for b). For the C_3S-based paste with C/S=1.3 (P2) placed in 5 mM $MgCl_2$ during 1 month, calcium leaching appears on both the Ca EDS map and the C/S profile (Figure 2-16b). For the paste with C/S=1 (Figure 2-16a), weak leaching is also visible in the magnesium-enriched zone. Although brucite appears on the diffractograms, no magnesium external layer is visible. Magnesium enrichment is more gradual, the maximum M/S (Intensity) is low (about 1.0). As the degradation time is very short, it is possible that brucite precipitates first because of the presence of traces of portlandite in the sound paste. Soon, all the portlandite dissolves and it is possible to precipitate M-S-H (Jakobsen, De Weerdt, et Geiker 2016). As the time frame is short and M-S-H is a semi-amorphous species like C-S-H in contrast to brucite, its presence in small quantities is not visible in XRD.

In conclusion, the two C_3S-based pastes (C/S=1 and C/S=1.3 (P2)), showed potential for M-S-H formation if the Mg concentration stay low and if the degradation lasts longer.

Accordingly, the C_3S-based paste with the lowest portlandite content according to XRD and TGA (C/S=1.3 (P1), see Figure 2-8 and Figure 2-9), was placed in an “infinite” volume (60L renewed every 2 weeks) of 5 mM $MgCl_2$ solution for several months. Figure 2-17 (XRD) and Figure 2-18 (EDS) exhibit the results after 3 months and 6 months of degradation. Over time the amount of brucite on the surface decreases. After 6 months, it is hardly visible on the diffractograms (Figure 2-17b). In addition, humps can be associated with the presence of M-S-H. A progressive and deep enrichment of the paste in Mg is observable on EDS maps (Figure 2-18). On the 3 months degraded paste, the influence of the distribution of silica and calcium in the paste on the formation of the magnesium phases appears clearly (Figure 2-18a). On the upper part of the map, a small external layer enriched in Mg has precipitated at the location of a calcium cluster, probably corresponding

to brucite. On the lower part, at the level of a silica cluster, a deep and progressive enrichment is visible, probably corresponding to M-S-H. Thus, for the paste in Figure 2-18a, although the EDS does not show a brucite external layer, it is possible that a small part of the sample passed to XRD contains a small portion with a thin brucite layer, explaining the weak signal observed in XRD (Figure 2-17a). The beginning of a zone with a brucite layer can be seen at the bottom of the map.

In conclusion, the production of C_3S-based pastes from C_3S and colloidal silica does not allow a homogeneous distribution of silica and calcium. As the C_3S used is very fine (D_{50}=15-20 µm), as is the colloidal silica, the mixture solidifies instantly without sufficient agitation and/or without sufficient superplasticizer. This results in the formation of calcium and silica clusters and an inhomogeneity of C/S ratios within the paste. These conditions are favourable for the formation of brucite. As time is limited, it is not possible to allow the pastes to hydrate any longer and it is therefore not possible to use these pastes in the thesis project.

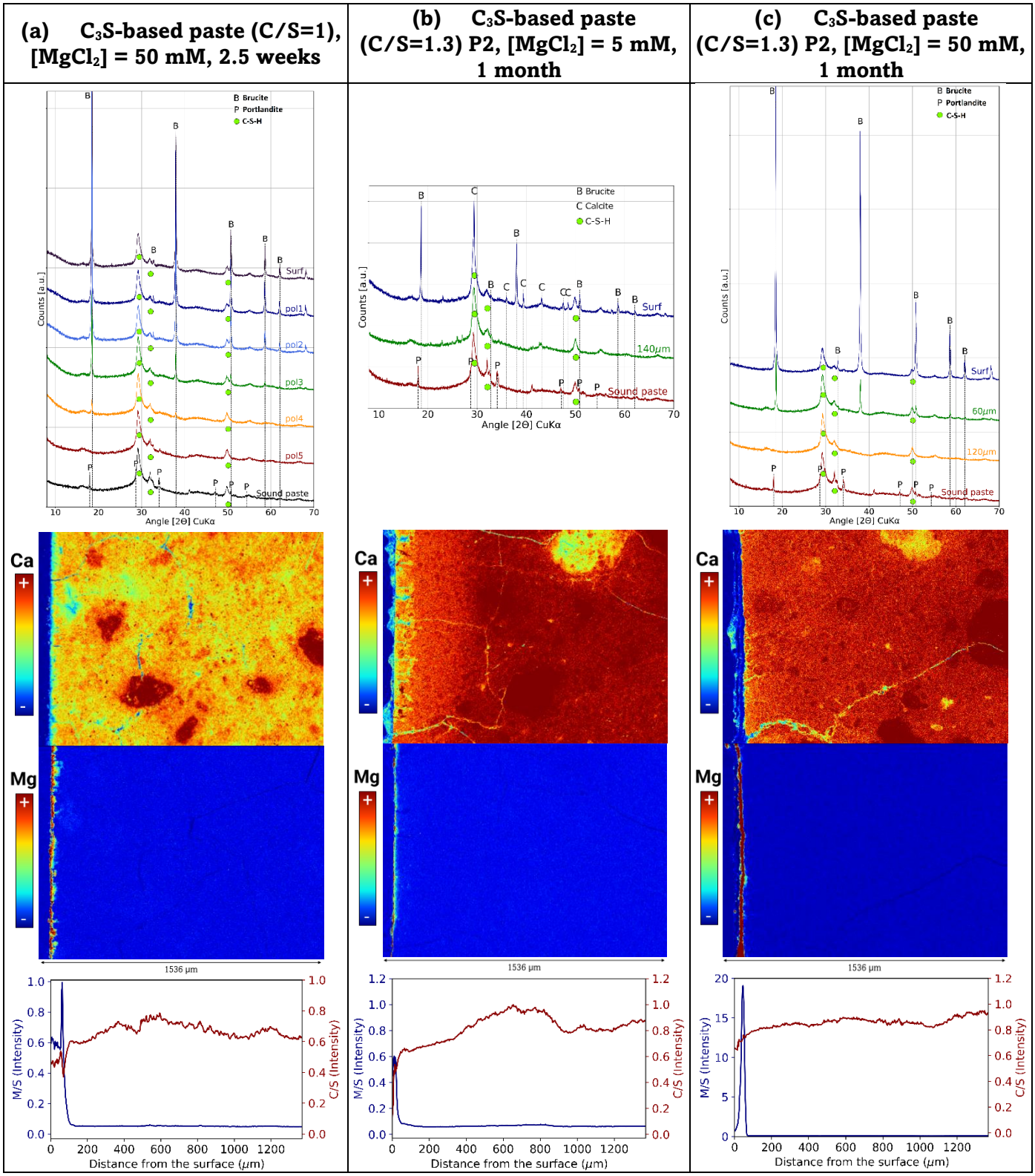

Figure 2-16: Results on three C_3S-based pastes: (a) C/S=1 and [$MgCl_2$] = 50 mM during 2.5 weeks, (b) C/S=1.3 (P2) and [$MgCl_2$] = 5 mM during 1 month and (c) C/S=1.3 (P2) and [$MgCl_2$] = 50 mM during 1 month. From top to bottom: X-Ray diffractograms along the degradation, Ca & Mg EDS Cartographies and C/S and M/S Intensity profiles determined from EDS maps

(a) C_3S-based paste (C/S=1.3) P1, [$MgCl_2$] = 5 mM, 3 months, "Infinite" volume

(b) C_3S-based paste (C/S=1.3) P1, [$MgCl_2$] = 5 mM, 6 months, "Infinite" volume

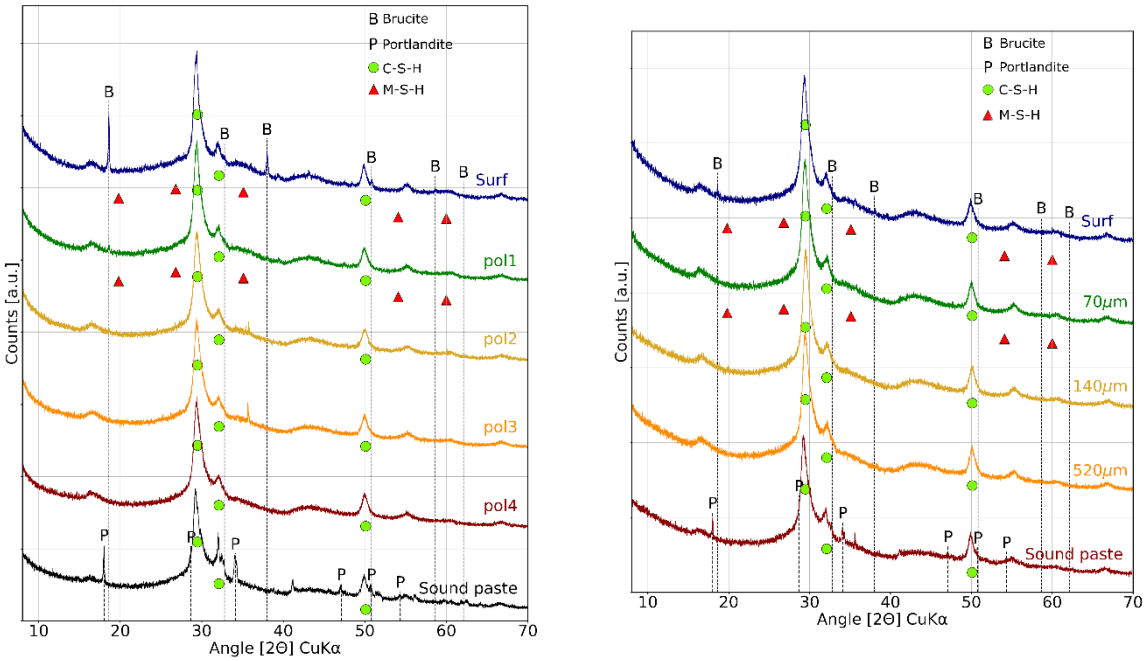

Figure 2-17 : X-Ray diffractograms along the degradation of a C_3S-basedpaste (C/S=1.3, P1) placed in infinite 5 mM $MgCl_2$ solutions for 3 months (a) and 6 months (b)

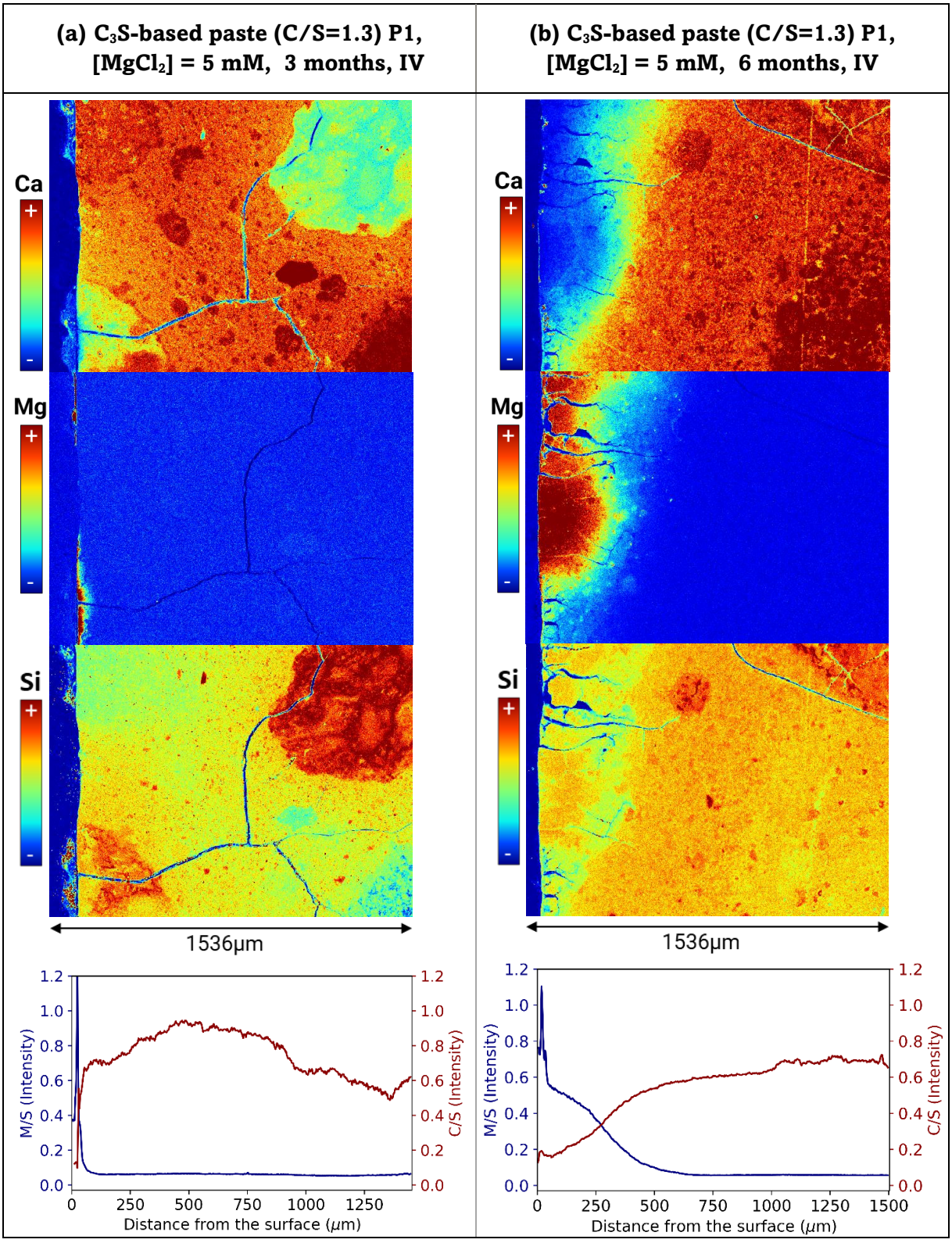

Figure 2-18 : Ca, Mg & Si EDS Cartographies of a C_3S-basedpaste (C/S=1.3, P1) placed in infinite 5 mM $MgCl_2$ solutions (IV=Infinite volume) for 3 months (a) and 6 months (b) and M/S and C/S EDS profiles associated

1.2.4.3.8. CEMI-sil-col

The paste made from CEMI and colloidal silica was placed in 50 mM $MgCl_2$ during 1 month (Figure 2-19a) and 4 months (Figure 2-19b).

As before, the CEMI-sil-col placed in 50 mM $MgCl_2$ for 1 and 4 months was one of the first samples on which the successive abrasion XRD protocol was tested, and the depth abraded is not known.

No signal associated with brucite is visible on the diffractograms (Figure 2-19 XRD). At the surface of the samples, 4 main humps associated with the presence of M-S-H are observable. As for the T3 sample (Figure 2-13), a zone of coexistence between M-S-H and C-S-H appears, from the surface to a variable depth depending on the degradation time. EDS maps (Figure 2-19 EDS) show deep magnesium enrichment in parallel with calcium leaching (200 to 400 µm thick).

The initial distribution of silica and calcium is homogeneous (Figure 2-19 - EDS), in contrast to industrial low-pH pastes (Figure 2-13) and C_3S-based pastes (Figure 2-18). For the 1 month degraded sample, the Mg enrichment and Ca leaching are uniform in the material (Figure 2-19a), on contrary to the 4 months degrades sample for which the observed degradation front is not homogeneous along the surface (Figure 2-19b). This can be due to the lack of homogenisation of the solution, which is small in volume, over a period twice as long as for T3 (4 months against 2 months) or the initial heterogeneity of the porous media of the cement paste.

The M/S and C/S ratios along the degradation (Figure 2-19 - Profiles) confirm the observations made on the EDS maps. The magnesium signal increases when the calcium signal decreases. The results are similar to those of the T3 pastes hydrated for 2 years (Figure 2-13).

In conclusion, the paste based on cement and colloidal silica is well suited for further study of the effect of M-S-H formation and magnesium attack on low-pH binders. Its distribution is homogeneous and the mineralogical phases are reduced (C-S-H and ettringite only according to XRD, see Figure 2-8b) due to the low amount of C_3A (1.4%). This paste can be considered as a model paste which will simplify the study of the degradation phenomena.

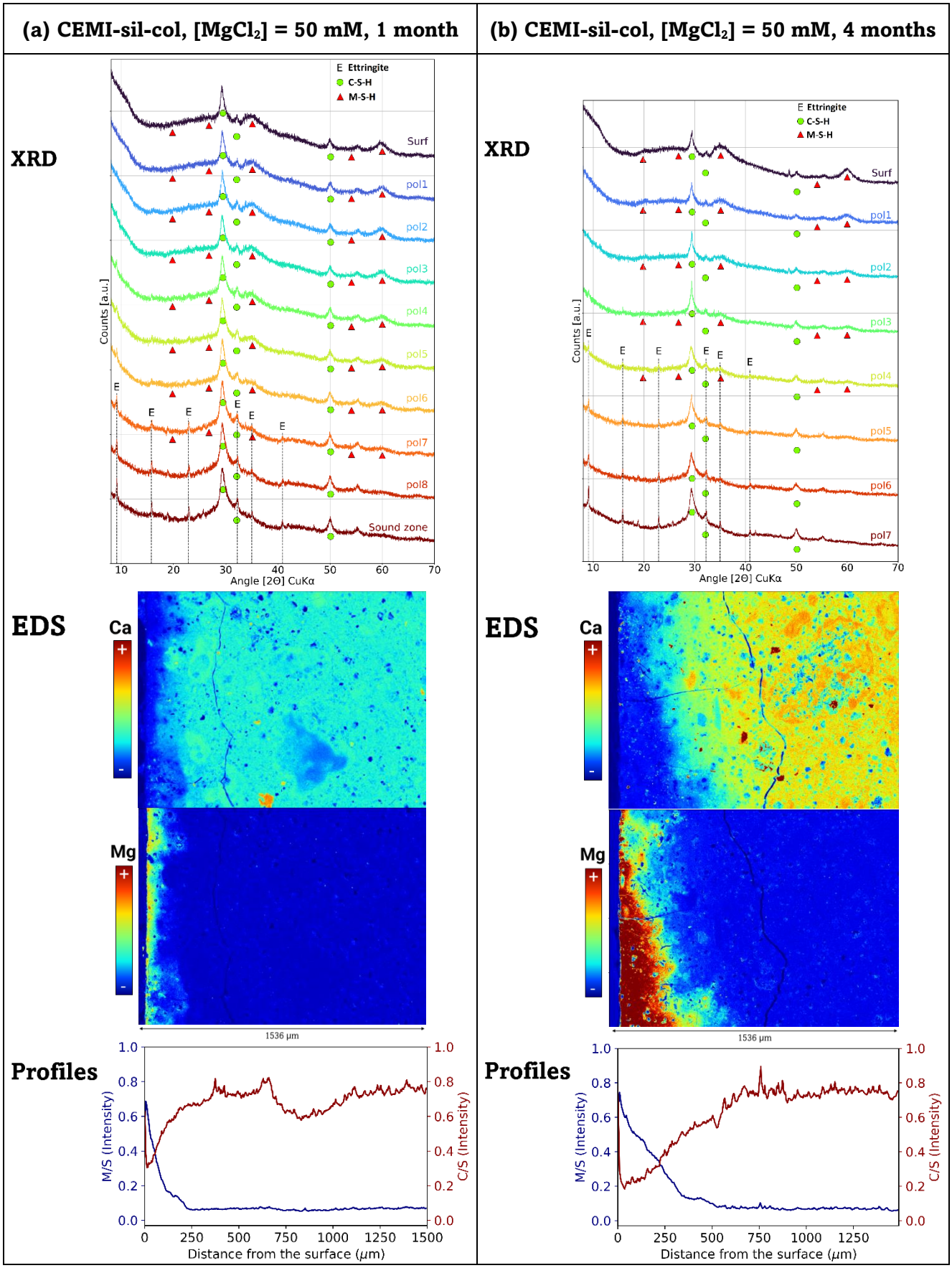

Figure 2-19: Results on the low-pH model cement paste (hydrated during 9.5 months) degraded in 50 mM $MgCl_2$ solution during 1 month (a) and 4 months. From top to bottom : X-Ray diffractograms along the degradation, Ca & Mg EDS Cartographies and C/S and M/S Intensity profiles determined from EDS maps

Conclusion

In conclusion, magnesium attack can lead to the formation of several magnesium phases: brucite, M-S-H and hydrotalcite. Brucite precipitates as an external layer and, like calcite, limits the diffusion of ions afterwards. It forms preferentially to the other magnesium phases when the pH of the pore solution of the cement matrix is high, i.e. when the material contains portlandite. However, even in the absence of portlandite, in some materials with long hydration times, such as substituted cements (low pH), if magnesium attack occurs too quickly after manufacture, brucite will precipitate. When the pH of the pore solution falls below 12 (absence of portlandite), M-S-H is preferentially formed. On XRD, as it is an amorphous phase, it is difficult to detect if it forms in the cementitious matrix in small quantities. On EDS, their formation can be identified by a progressive and deep enrichment in Mg in parallel with Ca leaching. The two fronts coincide perfectly. In the case of sound cementitious pastes containing a small amount of portlandite, the concentration of magnesium in solution greatly influences the predominance of one phase over the other. At 50 mM, brucite forms a layer limiting the formation of M-S-H. At 5 mM, M-S-Hs are able to form. However, the initial presence of portlandite causes some brucite to form in some places and the formation of M-S-H is slower.

To study the mechanical properties of degraded M-S-H, it is necessary to form only M-S-H and to have sufficient degraded depth to perform micro-indentation tests in the degraded zone. For this purpose, two cementitious pastes were selected: the T3(2y) paste and the CEMI-sil-col paste. Both pastes showed the possibility of forming M-S-H, even at 50 mM $MgCl_2$. They are both low-pH pastes but differ in their mineralogical composition and distribution. The CEMI-sil-col paste can be considered as a model low-pH cementitious paste; it consists only of C-S-H and ettringite according to XRD and has a very homogeneous Ca and Si distribution. The T3 paste is made from CEM III and silica fume. As a result, its initial Ca and Si distribution is heterogeneous and its mineralogical composition is more complex. The study of the properties of M-S-H from these two pastes will allow a better identification of the intrinsic properties of M-S-H.

CHAPTER 3. CHEMICAL AND MICROSTRUCTURAL PROPERTIES OF DESIGNED COHESIVE M-S-H PASTES

Introduction

One of the objectives of this thesis is to determine the intrinsic microstructural and mechanical properties of M-S-H. For this purpose, it is necessary to have a material consisting exclusively of M-S-H and on which indentation tests can be performed. The preparation of pure cohesive M-S-H pastes faces two main obstacles: (i) the difficulty to obtain cohesive pastes with representative porosity and microstructure that allow the physical and mechanical characterization of in situ, experimentally observed M-S-H; and (ii) the difficulty to obtain materials containing only M-S-H phases within a reasonable time (a few months). The manufacture of M-S-H pastes is complicated because of the high need of water of MgO powder and researchers tend to use sodium hexametaphosphate (NaHMP) as a superplasticizer. However, this may cause minor changes in the structure of M-S-H gels and a new manufacturing protocol is needed.

This chapter aims to develop a protocol for producing cohesive pastes of M-S-H with high purity and different magnesium to silicon (M/S) ratios, and to microstructurally and mechanically characterize them to further the knowledge on the intrinsic properties of M-S-H. The first part of the chapter is dedicated to the development and comparison of four different protocols for the production of cohesive M-S-H pastes (with different M/S ratios). The two parameters modified throughout the protocols are the source of silica (silica fume and colloidal silica) and the curing temperature (20 °C and 50 °C). Two types of mixing —mechanical and manual— are tested. In the second part of the chapter, the selected M-S-H pastes are characterized by X-ray diffraction (XRD), thermogravimetric analysis (TGA), microtomography, and energy-dispersive X-ray spectroscopy (EDS). The morphology of the M-S-H pastes is observed with a scanning electron microscope (SEM). Microstructure and porosity characterizations are performed by autoradiography, mercury intrusion porosimetry (MIP), water saturation and helium pycnometry.

This chapter was published in MDPI, Materials in 2022 (Dewitte et al. 2022). The previous chapter (2.1.1) defined the analytical techniques used in this chapter.

3.1. Materials

3.1.1. Raw Materials

M-S-H pastes were produced by mixing a source of silica (silica fume or colloidal silica), magnesium (MgO, to be precise) and distilled water (Milli-Q® water). The silica fume (CONDENSIL S95 DM), composed of 95% SiO2 and with a specific surface of 22 m^2/g, was provided by Condensil®. The silica fume was sieved at 315 μm prior to its use in manufacturing M-S-H. The colloidal silica (Rheomac AS 150, also called Masterma-trix 150) was provided by BASF® as an aqueous suspension (dry extract = 52 ± 2.5%).

The magnesium was MgO provided by VWR® (VWR International S.A.S, 1 rue d'Aurion, Rosny-sous-Bois, France), with a content of MgO (on the calcined product) >97% and a loss on ignition of 8%.

The superplasticizer (CHRYSO®Fluid Optima 175) was provided by Chryso France® (ZI du Sauvoy, 5 Rue de la Bizière, 77165 Saint-Soupplets, France).

3.1.2. Preparation of M-S-H samples

The preparation of pure cohesive M-S-H pastes faces two main obstacles: (i) the difficulty to obtain cohesive pastes with representative porosity and microstructure that allow the physical and mechanical characterization of in situ, experimentally observed M-S-H; and (ii) the difficulty to obtain materials containing only M-S-H phases within a reasonable time (a few months).

Concerning the first aspect, two protocols for manufacturing M-S-H pastes have been developed in the literature to meet the high need of water of MgO powder (Zhang, Vandeperre, et Cheeseman

2014), either using a high water/binder ratio (w/b = 2) (Tonelli et al. 2016; 2017) or sodium hexametaphosphate (NaHMP), a superplasticizer (0.025–0.3 g in 10 g of water, with 0.4 < w/b < 0.8) (Zhang, Vandeperre, et Cheeseman 2014; Sonat et Unluer 2019). As detailed in 1.2.4.3.5, the use of NaHMP can cause chemical and mineralogical differences between in situ precipitated M-S-H and synthetized M-S-H. At high w/b ratios, the structure could be modified. Excess of water results in the modification of the porous network through the creation of pores, air voids, etc., which alters species diffusion. Moreover, high porosity weakens the material and complicates mechanical characterization.

Concerning the second aspect, literature on M-S-H suspension synthesis has shown that the mechanism of M-S-H formation from the reaction between silica fume and MgO is a slow process that lasts at least 2–3 years at 20 °C (d'Espinose de la Caillerie, Kermarec, et Clause 1995; Bernard et al. 2019). Several researchers (Bernard et al. 2017b; Zhang et al. 2018; Zhang, Vandeperre, et Cheeseman 2014; Tonelli et al. 2016) have reported that M-S-H are not the only phase formed during the initial contact between MgO, silica fume and water at 20 °C. Silica fume dissolves more slowly than MgO reacts, leading to thermodynamic conditions favorable to brucite formation (low silicon concentration in the solution). Brucite is subsequently consumed, reacting with the amorphous silica to form M-S-H. This process leads to a very long synthesis. This problem can be circumvented by increasing the curing temperature as shown by Bernard (Bernard et al. 2017b), who obtained M-S-H suspensions cured at 50 °C or 70 °C comparable to those cured at 20 °C but with a shorter hydration time. Bernard et al. showed that a cure at 50 °C or 70 °C on M-S-H suspensions seemed to reduce the content of brucite and improved the reaction to the advantage of M-S-H. The effect appeared to be the same at 50 °C and 70 °C.

Consequently, in this thesis, M-S-H pastes were prepared according to a protocol adapted from Tonelli et al. (Tonelli et al. 2016). In Tonelli's study, silica fume and MgO were mixed at 20 °C with an MgO/SiO_2 (M/S) atomic ratio of 1 and a w/b ratio of 2. In the present study, the optimal w/b ratio (i.e., the lowest value to maintain sufficient workability without using a superplasticizer) was sought to favor a more cohesive paste, without segregation and with lower porosity. We carried out two thermal curing protocols to try to maximize the formation of M-S-H in the pastes. The source of silica was varied to accelerate the reactivity and improve the homogeneity of the mix (increasing the specific surface area of the reagents). Three different M/S were selected following the work of Bernard et al. (Bernard 2017): 0.78, 1 and 1.3, as detailed in Table 1. The first campaign consisted of mixes of MgO, silica fume and Milli-Q water with a w/b of 1. For the second campaign, silica fume was replaced by colloidal silica and superplasticizer was used to improve the workability of the mix. Two mixing methods—mechanical (noted E; rotation speed 140–285 rd/min for 10 min, 450 W) and manual (noted M; 5 min)—were tested. Analysis of the chemical composition and microstructure of M-S-H pastes with different mixing techniques, w/b ratios and therefore porosities provided a wider range of data likely comparable to M-S-H formed by precipitation in cementitious materials. All pastes with silica fume were mechanically mixed. For pastes with colloidal silica, both types of mixing were tested for every M/S. The w/b ratio and the superplasticizer content were modified to improve the workability of the mix for manually mixed pastes (w/b = 1.45).

Table 3-1: Mix proportions. Sp/b represents the mass percentage of superplasticizer against binder

Type of Silica	M/S	T (°C)	Sample Name	g				Sp / b	w / b
				MgO	Silica Fume	Milli-Q-Water	Superplasticizer (Dry Extract)		
Silica fume	0.78	20	MS_0-78_SF_T20	176.4	336.9	513.8	0	0	1
		50	MS_0-78_SF_T50						
	1	20	MS_1_SF_T20	208.7	309.2	522.2	0	0	1
		50	MS_1_SF_T50						
	1.3	20	MS_1-3_SF_T20	242.8	278.1	526.3	0	0	1
		50	MS_1-3_SF_T50						
Type of silica	**M/S**	**T (°C)**	**Sample name**	**g**				**Sp / b**	**w / b**
				MgO	**Rheomac AS 150**	**Milli-Q-water**	**Superplasticizer (dry extract)**		
Colloidal silica	0.78	20	MS_0-78_CS_T20_M	63.2	241.3	145.8	8.94	4.9%	1.45
		50	MS_0-78_CS_T50_M						
	0.78	50	MS_0-78_CS_T50_E	241.1	920.3	312.5	47.4	6.8%	1.1
	1	50	MS_1_CS_T50_M	71.7	213.3	151.5	9.18	5.1%	1.45
	1	20	MS_1_CS_T20_E	292.5	872.7	292.7	45.1	6.2%	1
		50	MS_1_CS_T50_E						
	1.3	20	MS_1-3_CS_T20_M	119.8	274.3	235.1	7.14	2.8%	1.45
		50	MS_1-3_CS_T50_M						
	1.3	50	MS_1-3_CS_T50_E	331.7	760.8	403	38.25	5.4%	1.1

Two curing protocols were carried out for each type of silica and M/S ratio. Half of the samples were put in a sealed box with water (to keep relative humidity close to 100%, no water bath) and placed in a climatic chamber at 50 °C. The other half was put in a box with water and left at ambient temperature.

An abbreviated notation has been implemented to identify M-S-H pastes with respect to their manufacturing protocol. It begins with "MS" followed by the M/S ratio, the type of silica used (SF for silica fume and CS for colloidal silica), the temperature of curing, and finally the type of mixing (for the pastes with colloidal silica; E for mechanically mixed and M for manually mixed). For instance, MS_0-78_CS_T20_M matches the samples made with an M/S ratio of 0.78, colloidal silica, cured at ambient temperature (20 °C ± 2 °C) and mixed manually (Table 3-1).

3.2. Chemical and Microstructural Characterization of M-S-H as a Function of Design and Curing Protocols

3.2.1. Influence of the Type of Silica

Images of X-ray microtomography analyses (Figure 3-1) and EDS mappings (Figure 3-2 and Figure 3-3) showed that switching the silica source from silica fume to colloidal silica resulted in a better distribution of the particles and a higher homogeneity of the hydrated paste, irrespective of the curing temperature.

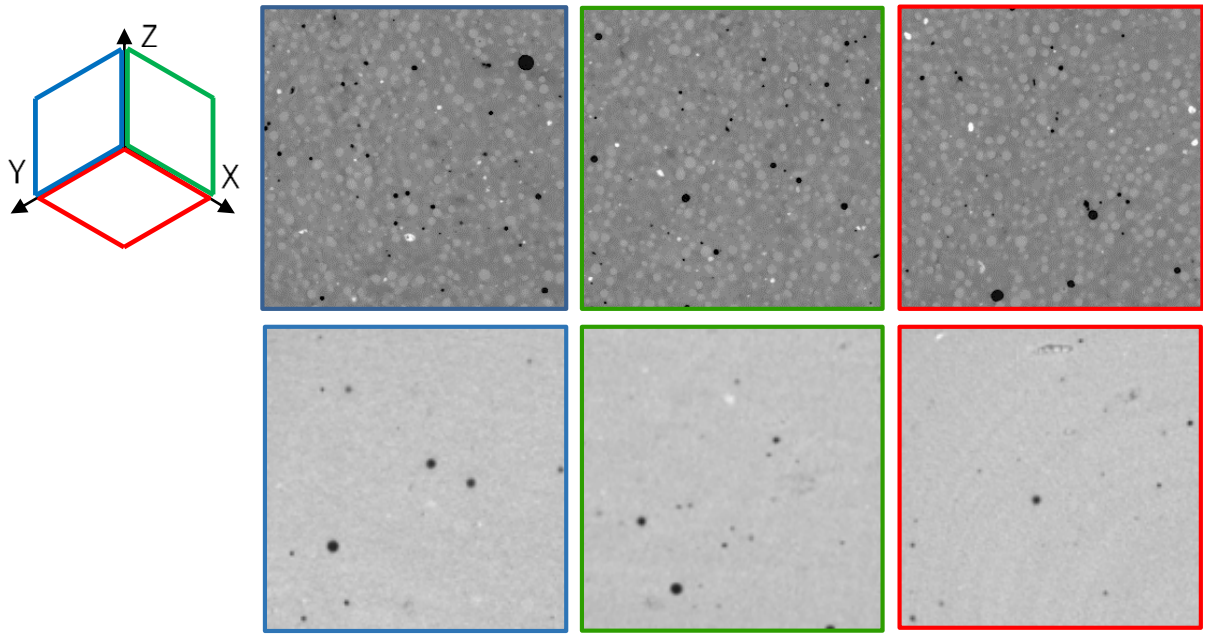

Figure 3-1: Tomography images: MS_1_SF_T50_21d (line 1) and MS_1_CS_T20_3d (line 2). The three columns correspond to three observations surfaces presented on the left by three colors (Y-Z=blue, Z-X=green, Y-X=red).

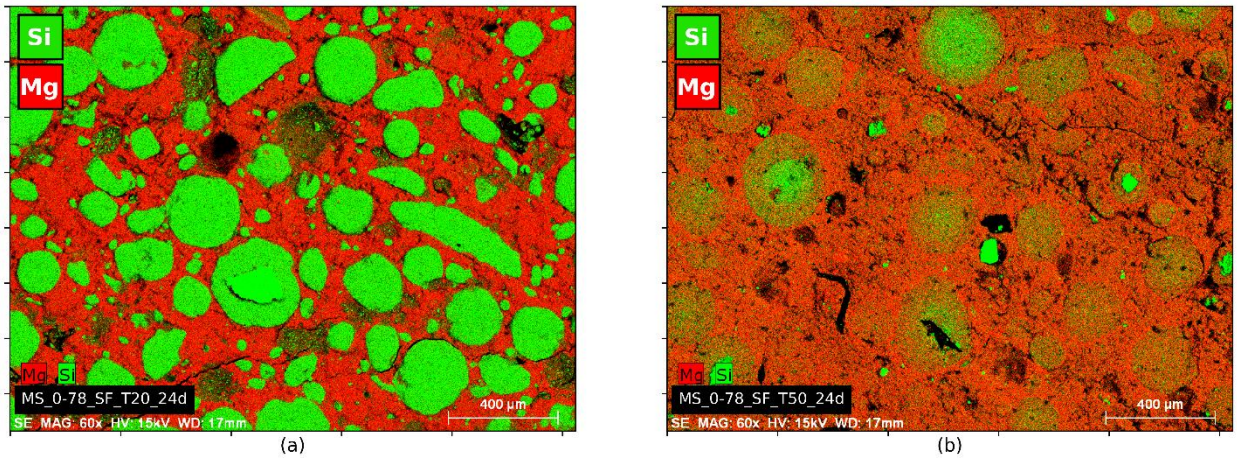

Figure 3-2: EDS images of M-S-H pastes with M/S = 0.78 and silica fume after 24 days of hydration. (a) curing at 20 °C; (b) curing at 50 °C.

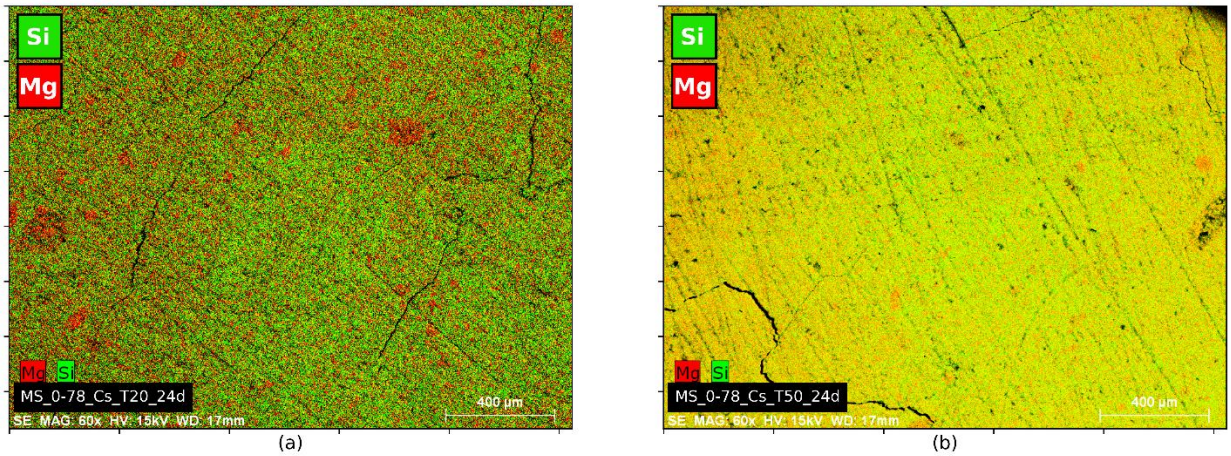

Figure 3-3: EDS images of M-S-H pastes with M/S = 0.78 and colloidal silica after 24 days of hydration. (a) curing at 20 °C; (b) curing at 50 °C.

EDS mappings (Figure 3-2 and Figure 3-3) obtained from the pastes cured at 20 °C show the effect of the silica type on the size of the cluster of unreacted silica. The average cluster size was 200 µm for silica fume and 25 µm for colloidal silica. The latter resulted in a better dispersion of silica particles within the Mg-matrix, improving the homogeneity of the paste (even if this distribution does not allow to evaluate whether the dispersed silica has already reacted with MgO).

Furthermore, the raw colloidal silica did not contain crystallized phases (such as quartz or cristobalite) but only amorphous silica. This was confirmed by the absence of the corresponding peaks (Table 3-2) on the X-ray diffractograms of colloidal silica pastes (Figure 3-4b), although quartz peaks were observed on the X-ray diffractograms of silica fume pastes (Figure 3-4a).

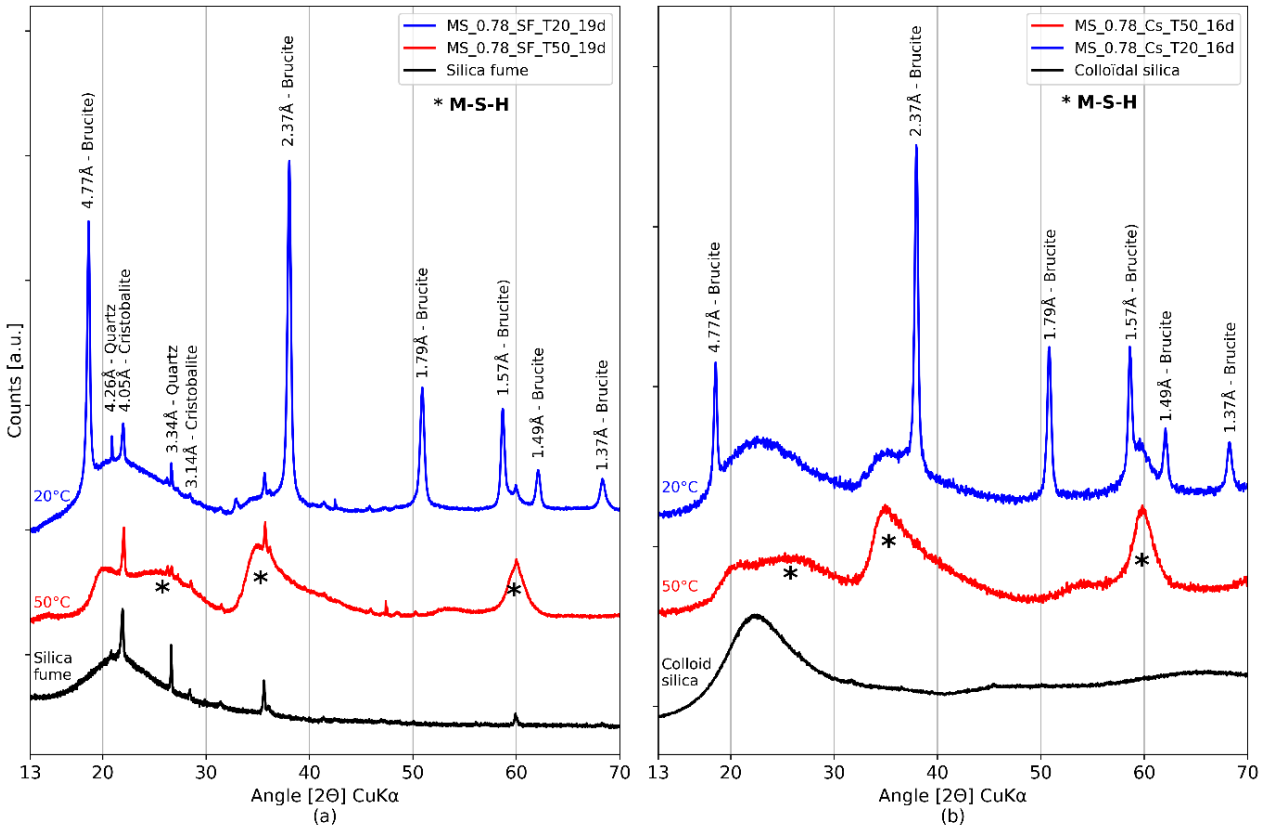

Figure 3-4: X-ray diffractograms of M-S-H pastes with M/S = 0.78. Comparison between the four protocols after two weeks of hydration. (a) Pastes with silica fume and M/S=0,78 after 19 days of hydration at 20°C (blue) or 50°C (red) (b) Pastes with colloidal silica and M/S=0,78 after 16 days of hydration at 20°C (blue) or 50°C (red).

Table 3-2: Indexing of X-ray peaks for quartz, cristobalite, brucite, amorphous silica, and M-S-H.

References	Species	Unit	Peaks Indexing					
COD 96-901-0145 and COD 96-900-9687	Quartz and cristobalite	Å	4.26	4.05	3.34	3.14		
		[2Θ] CuKα	20.85	21.92	26.65	28.39		
Bernard et al. (Bernard et al. 2017b)	Brucite	Å	4.76	2.74	2.37	1.79	1.57	1.50
		[2Θ] CuKα	18.6	32.7	38	50.9	58.7	62
Data of Figure 3-2	Amorphous silica	Å	4.04					
		[2Θ] CuKα	22					
Bernard et al. (Bernard et al. 2019) and Roosz et al. (Roosz et al. 2015)	M-S-H	Å	4.43	3.42	2.56	1.70	1.54	
		[2Θ] CuKα	20	26	35	54	60	

In conclusion, the use of colloidal silica led to improved homogeneity and purity, i.e., in terms of presence of M-S-H only, of the pastes.

3.2.2. Influence of the curing temperature

Pastes prepared with silica fume. Mg and Si EDS mapping of M-S-H pastes with M/S = 0.78 and silica fume are shown in Figure 3-2. The samples used for the tests originated from the same mix and were cured for 24 days at 20 °C or 50 °C.

Areas rich in silicon and poor in magnesium were observed for the 20 °C curing (Figure 3-2a). These areas correspond to residual unreacted silica fume clusters. At this temperature, the reaction of MgO with silica fume was slow and did not result in a homogeneous M-S-H paste at the time of observation. At 50 °C (Figure 3-2b), orange regions on the mapping correspond to a mix of Mg- and Si-containing phases, with an equivalent intensity of these elements. The matrix was enriched in silicon and the remains of the clusters were enriched in magnesium. This paste was more homogeneous than the paste cured at 20 °C.

In order to evaluate the mineralogical composition of the paste, XRD (Figure 3-4a) analyses were performed.

The sample cured at 20 °C contained brucite and amorphous silica (Figure 3-4a). The presence of M-S-H was detected but their formation was likely limited by the initial formation of brucite, at least at the tested ages (d'Espinose de la Caillerie, Kermarec, et Clause 1995; Bernard et al. 2019). For the 50 °C curing, no characteristic peak of brucite was visible and the amorphous silica seemed to have been consumed (the associated hump disappeared). Conversely, M-S-H humps were clearly observable (as M-S-H are a semi-amorphous phase, only broad peaks or humps are observed). The five M-S-H humps observed by Bernard et al. and Roosz et al. (Roosz et al. 2015; Bernard et al. 2019), including three main humps (Nied et al. 2016; Tonelli et al. 2016; Li et al. 2014) (~20, 26, 35, 54, 60 [2θ] CuKα) were present in the sample cured at 50 °C. The same observations were made for the other M/S pastes tested in the present study.

Pastes prepared with colloidal silica. Mg and Si EDS mapping of M-S-H pastes with M/S = 0.78 and colloidal silica are shown in Figure 3-3. As for the sample with silica fume, brucite was visible on X-ray diffractograms after 16 days of 20 °C curing (Figure 3-4b) while only M-S-H humps were present at 50 °C. The pastes with colloidal silica considered for this analysis were mechanically mixed, except for M/S = 1 for practical reasons (not produced at the same time). EDS mapping (Figure 3-3a,b) showed a better distribution of magnesium and silicon in the paste cured at 50 °C than in the paste cured at 20 °C. The clusters observed at 20 °C were reduced considerably at 50 °C, dropping from a diameter of 25 µm to a few microns.

In conclusion, the thermal curing at 50 °C resulted in a more homogeneous paste. Pastes showed a lower content of brucite at this temperature than pastes cured at 20 °C. No brucite was observed for the pastes with an M/S ratio equal to 0.78, even after only 16 days of curing for pastes designed with colloidal silica (Figure 3-4b).

To produce M-S-H with different M/S ratios, with properties comparable to those observed in synthesis (on suspensions) (Nied et al. 2016; Roosz et al. 2015; Bernard et al. 2019) and with the highest content of M-S-H and the lowest content of impurities, the suggested method is a protocol with colloidal silica and 50 °C thermal curing.

3.2.3. Formation of M-S-H

The kinetics of M-S-H formation have been studied on M-S-H suspensions at 20 °C, 50 °C and 70 °C by Bernard (Bernard 2017) and at 20 °C, 30 °C and 40 °C by Szczerba (Szczerba et al. 2013). The purpose of this section is to compare the observations and conclusions between suspensions and pastes. The phenomena and kinetics of diffusion of ionic species—and the accessibility to water for reagents through already formed hydrate layers—are different between suspensions and cohesive pastes. Bernard et al. produced M-S-H suspensions by mixing magnesium oxide and silica fume with ultrapure water (water/solid ratio of 45) (Bernard et al. 2019; Bernard 2017). Figure 3-5 presents X-ray diffractograms of M-S-H pastes made with silica fume with M/S = 1 and M/S = 1.3 after 19 and 91 days of curing at 20 °C or 50 °C.

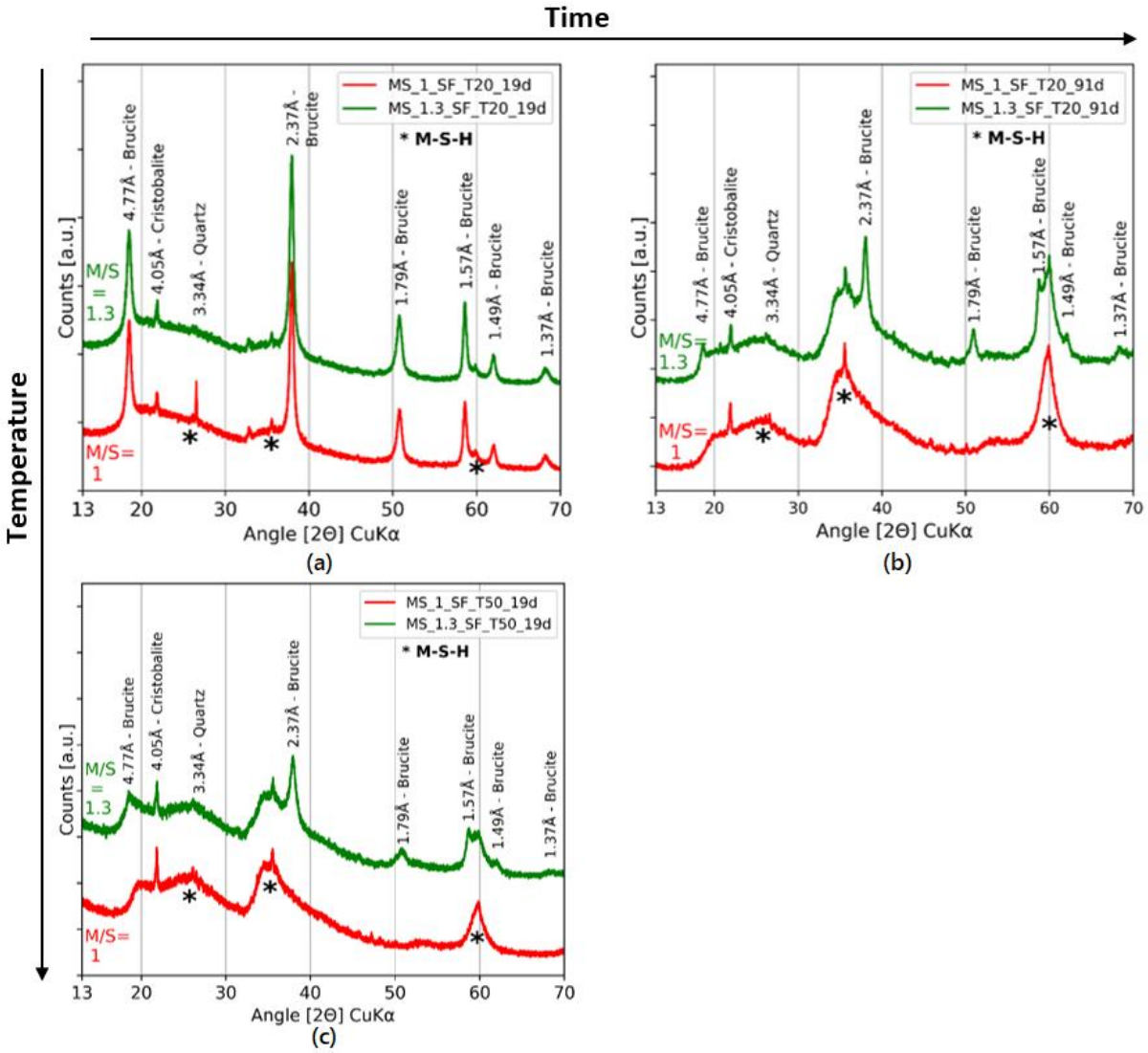

Figure 3-5: X-ray diffractograms of pastes with silica fume after 19 (a) or 91 days (b) with 20 °C curing, and with 50 °C curing after 19 days (c).

The precipitation of brucite was not impeded by curing at 50 °C for the two sources of silica. Brucite was observed on the XRD for M/S = 1.3 after 19 days of hydration at 50 °C (silica fume; Figure 3-5c). In addition, the M/S ratio seemed to influence the persistence of brucite. The higher the ratio, the longer the brucite remained present. Brucite was observed for high (M/S = 1.3) but not low (M/S ≤ 1) M/S ratios after either 19 days of thermal curing at 50 °C or 91 days at 20 °C (Figure 3-5).

This result was in agreement with the observations of Bernard on M-S-H suspensions (Bernard 2017). In that study, no brucite was observed in M-S-H suspensions at M/S < 1.0 cured at 50 °C or 70 °C after the same hydration time (91 days), while at 20 °C some brucite was observed, indicating a faster formation of M-S-H at higher temperatures. For M/S ≥ 1.2, brucite was still observed even after one year at 50 °C and 70 °C. The presence of residual brucite was thus linked to the M/S ratio. The higher the M/S ratio, the longer the presence of brucite. It should be noted that TGA on pastes with colloidal silica no longer showed the presence of brucite after 5 months for all the M/S ratios in the present study. This result is presented in Section 3.3.2.

The effect of thermal curing could be twofold in that it may: (i) accelerate the dissolution of SiO_2 and MgO and the diffusion of ionic species, and (ii) shift thermodynamic equilibria. Bernard

(Bernard 2017) stated that temperature had a significant influence on the kinetics of M-S-H formation and their solubility, having observed a faster M-S-H formation at higher temperatures. The magnesium and silicon concentrations at 50 °C and 70 °C reached equilibrium with M-S-H faster than at 20 °C. According to Bernard's work, the thermodynamic equilibrium of brucite was modified with the curing temperature. More Mg was needed in solution at 50 °C than at 20 °C to form brucite. Brucite only formed in the short term for low M/S ratios with SiO_2 dissolving and diffusing over time. The ratio in solution decreased, becoming more favourable to M-S-H and less to brucite (which dissolved).

In conclusion, the formation of M-S-H pastes from MgO and SiO_2 (silica fume or colloidal silica) is a slow process that can be accelerated by thermal curing. As expected, the higher the M/S ratio, the longer the brucite is present.

3.3. In-Depth Characterization of Colloidal Silica M-S-H Pastes with Different M/S Ratios

As detailed in the previous section, the protocol with colloidal silica and a 50 °C curing yielded the highest content of M-S-H and the lowest content of other species. In this section, the samples analysed originate from this protocol exclusively. Two types of mixing were tested, mechanical and manual. Three M/S ratios were studied: 0.78, 1 and 1.3. The pastes considered for Sections 3.3.1 and 3.3.2 were MS_0-78_CS_T50_M, MS_1_CS_T50_E and MS_1-3_CS_T50_M.

3.3.1. Morphology of M-S-H

The morphology of M-S-H pastes was observed by SEM on fractured samples (Figure 3-6), proving to be similar to the morphology reported by Tonelli et al. (Tonelli et al. 2016). M-S-H did not show crystalline facies but rather aspects of gel with globular chains. M-S-H showed high porosity at high magnification (Figure 3-6c), as we will discuss in Section 3.3.3.

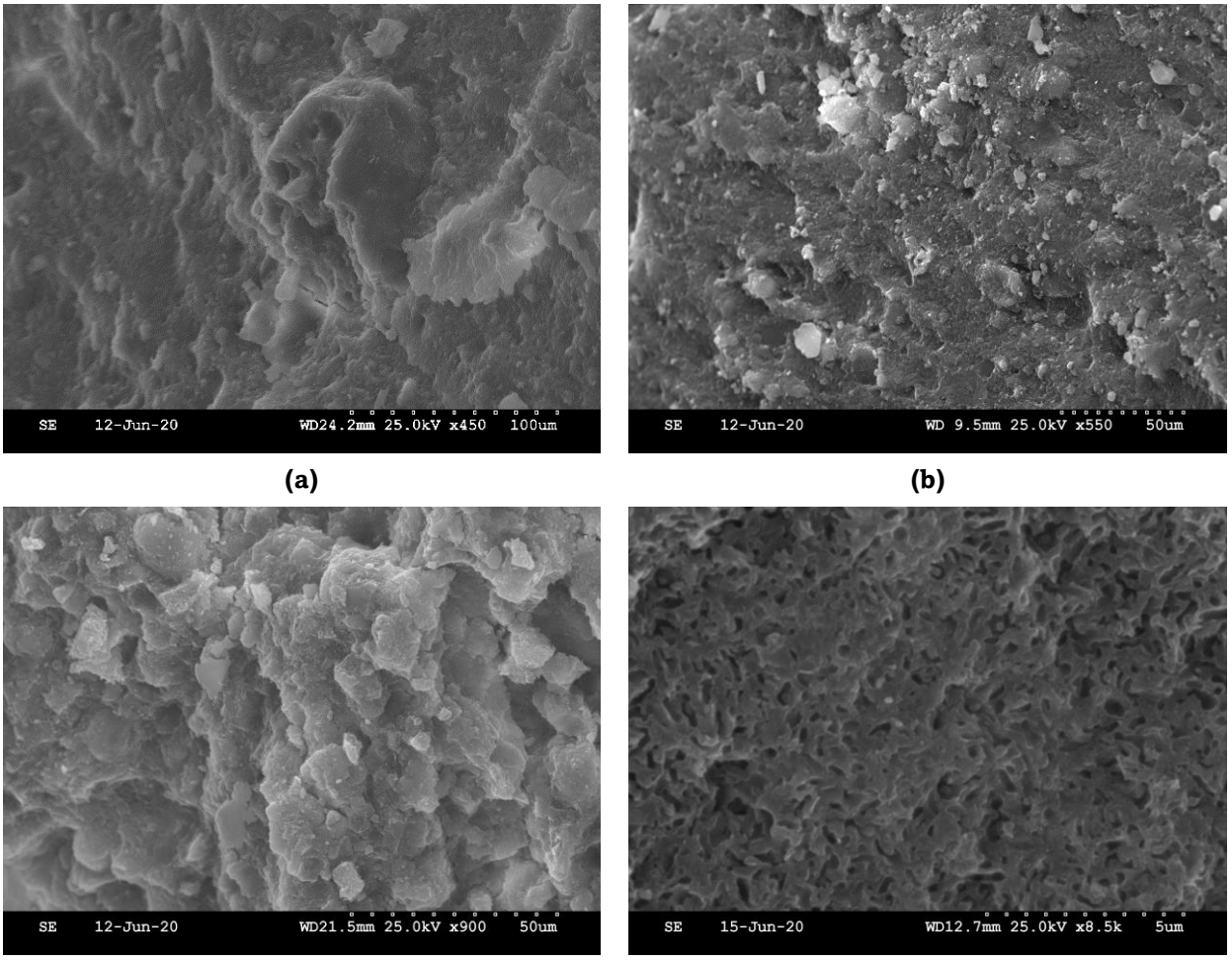

Figure 3-6: Fresh facture images on SEM of colloidal silica pastes with a 50 °C curing after 4.5 months of hydration: (a) and (c) M/S = 1.3, (b) M/S = 0.78 and (d) M/S = 1.

3.3.2. Solid Composition

X-ray diffractograms of three M-S-H pastes are presented in Figure 3-7. The humps of M-S-H (see Table 3-2 for positions) were observed on all diffractograms (Nied et al. 2016; Tonelli et al. 2016; Li et al. 2014). No brucite peaks were identifiable. The proportion of second broad reflection (~26 [2θ] CuKα) relative to the rest of the diffractogram increased along with the M/S ratio, as was the case for diffractograms of M-S-H suspensions of Bernard (dashed lines in Figure 3-7) (Bernard et al. 2019). The first broad reflection (20 [2θ] CuKα) simultaneously decreased, indicating a rearrangement of the structure as the M/S ratio increased. As proposed by Bernard, the first broad reflection would be linked to a structure similar to talc (a natural analogue of M-S-H) while the second broad reflection would be linked to serpentine. Thus, the X-ray diffractograms indicated a rearrangement of the structure with the increase in M/S, from a talc-like structure to serpentine, as Nied et al. observed in 2016 (Nied et al. 2016).

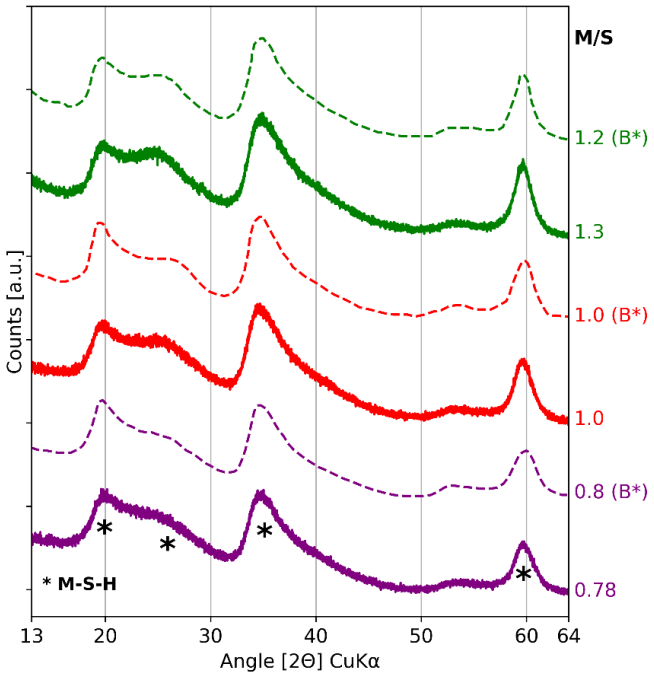

Figure 3-7: X-ray diffractograms of three M-S-H pastes with colloidal silica after 4.5 months of a 50 °C curing and three M-S-H suspensions synthetized by Bernard et al. (Bernard et al. 2019) (dashed lines, noted B*). Manual mixing was used for pastes M/S = 0.78 and M/S = 1.3; mechanical mixing was used for M/S = 1.

The TGA curves of M-S-H pastes and the derivative weight losses are shown in Figure 3-8. Brucite (400–420 °C) was absent. The three water loss regions expected for M-S-H were observable. The first water (30–280 °C) loss region was linked to H_2O (poorly bounded) loss in M-S-H.

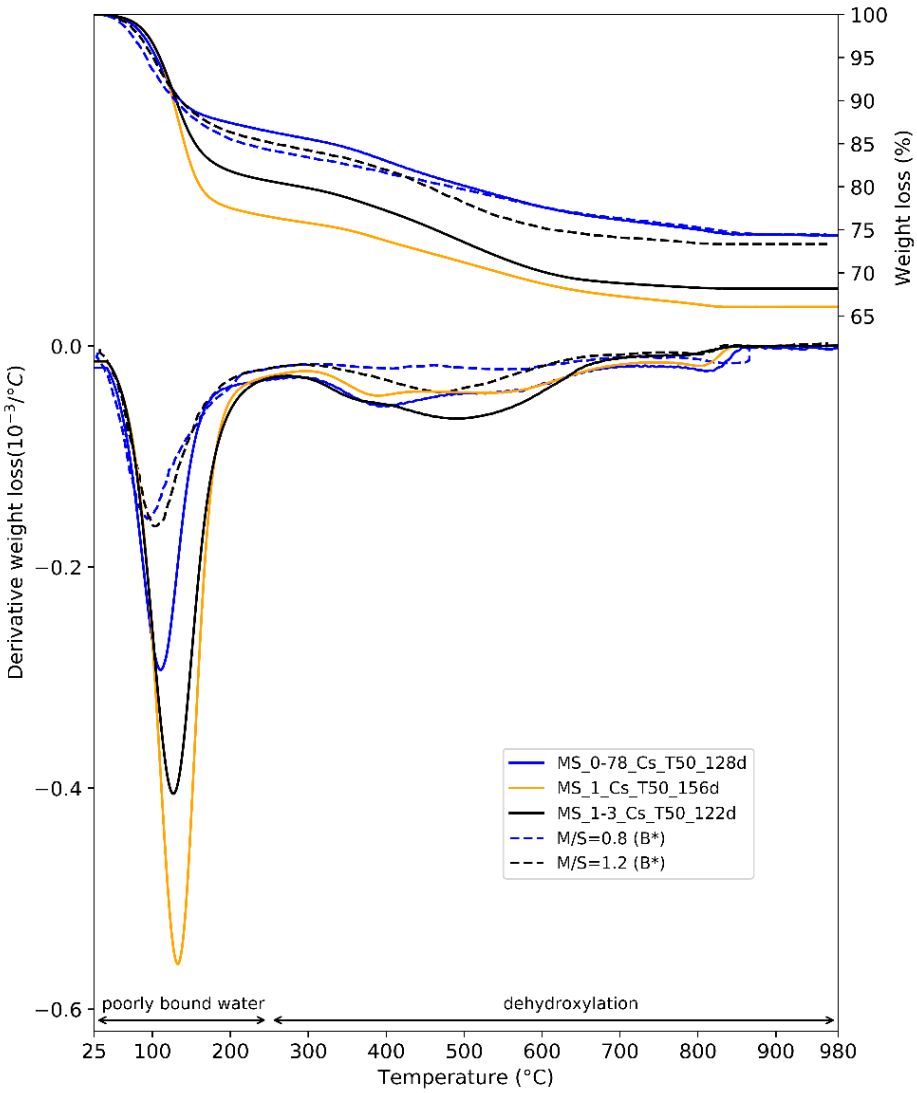

Figure 3-8: TGA results of three M-S-H pastes with colloidal silica after 4.5 months of a 50 °C curing and two M-S-H suspensions synthetized by Bernard et al. (Bernard et al. 2019) (dashed lines, noted B*). Manual mixing was used for pastes M/S = 0.78 and M/S = 1.3; mechanical mixing was used for M/S = 1.

The second and third water losses have been attributed to silanol and/or magnesium hydroxyl groups in M-S-H, but they may also comprise water present as a monolayer on the M-S-H surface (Nied et al. 2016; Bernard et al. 2019; Lothenbach, Durdziński, et De Weerdt 2016). Their attribution is controversial. Table 3-3 recaps the views and assumptions of various authors. The structure of M-S-H has been compared to that of many phyllosilicates (sepiolite, talc, etc.) (Nied et al. 2016; Roosz et al. 2015; Brew et Glasser 2005b; Lothenbach et al. 2015; Bernard et al. 2019). Nied et al. (Nied et al. 2016) suggested that the weight loss between 280 °C and 750 °C corresponds to hydroxyl groups with Mg^{2+}, while the one between 750 °C and 840 °C would be linked to silanol groups on M-S-H. In the case of synthetic talc, Dumas et al. (Dumas et al. 2013) attributed the weight loss (150–450 °C) to silanol (Si–OH) and magnesium (Mg–OH) hydroxides on the sheet edges. The next loss (450–750 °C) would be linked to the dehydroxylation of small particles, whereas the high temperature loss (750–850 °C) would correspond to the dehydroxylation of bigger particles and the formation of enstatite and silica. For Bernard et al. (Bernard et al. 2019), and according to the work of Zhuravlev (Zhuravlev 2000) on amorphous

silica, the weight loss around 390 °C (observable in Figure 3-8 on curves M/S = 0.78, 0.8 and 1) would match the dehydroxylation of silanol groups (on the surface) while the weight loss at 500 °C would be related to dehydroxylation of Mg–OH in M-S-H. Moreover, the removal of internal OH groups of silanols happened at around 900 °C.

Table 3-3: Different attributions of weight losses in TGA for M-S-H or correlated phases.

Author	Species Concerned	Temperature and Phase Associated to Weight Losses		
Lothenbach et al. (Lothenbach, Durdziński, et De Weerdt 2016)	M-S-H	270–700 °C hydroxyl groups in M-S-H		
Nied et al. (Nied et al. 2016)	M-S-H	280–750 °C Mg–OH in M-S-H		750–840 °C Si-OH in M-S-H
Dumas et al. (Dumas et al. 2013)	talc	150–450 °C Mg–OH and Si–OH	450–750 °C small particles	750–850 °C big particles
Zhuralev (Zhuravlev 2000)	amorphous silica	190–400 °C vicinal bridged OH groups of silanols	400–900 °C geminal OH groups of silanols	900–1200 °C complete removal of all OH groups
Bernard et al. (Bernard et al. 2019)	M-S-H	390 °C surface Si–OH in M-S-H	500 °C Mg–OH in M-S-H	900–1200 °C internal Si–OH in M-S-H

The position shared by the authors quoted is the following: (i) the weight losses between 200 °C and 800 °C for M-S-H systems are linked to the dehydroxylation of a hydroxyl group in M-S-H, and (ii) the potential offsets of the losses are linked to the evolution of the structure of M-S-H. With regard to the type of hydroxyl groups associated with each temperature, the most recent and documented assumption (Bernard et al. (Bernard et al. 2019)) was chosen.

The second water loss region between 280 °C and 750 °C differed with the M/S ratio (Figure 3-8). For M/S = 0.78 and M/S = 1, the second hump was located in the same place, while for M/S = 1.3 the second hump was shifted to the right. The offset of the hump (400–500 °C) resulting from the increase in M/S from 0.78–1 to 1.3 also appeared on the TGA on M-S-H suspensions from Bernard et al. and Nied et al. (Nied et al. 2016; Bernard et al. 2019). The height of the last water loss region between 750 °C and 840 °C also evolved with the M/S. The amount of bound water increased along with the magnesium content. As the weight loss around 400 °C has been associated to surface Si–OH and the weight loss around 500 °C to Mg–OH in M-S-H (Bernard et al. 2019), the offset of the hump would indicate the formation of more Mg–OH groups with the increase in M/S. For M/S = 1.3, the broader weight loss around 500 °C covered the weight loss around 400 °C of M/S = 0.78 and M/S = 1, indicating that the amount of surface Si–OH groups remains stable. Conversely, the decrease in height of the weight loss peak around 800 °C as M/S increases would indicate a decrease in the internal Si–OH content of M-S-H. Thus, the internal structure of M-S-H would evolve with M/S.

The structure of M-S-H has been compared to that of many phyllosilicates (sepiolite, talc, etc.) and characterized as a sheet structure evolving with the M/S (Nied et al. 2016; Roosz et al. 2015; Brew et Glasser 2005b; Lothenbach et al. 2015; Bernard et al. 2019). The silicate sheets would be linked

by layers of octahedral-coordinated Mg^{2+} ions (Nied et al. 2016), with water present both as adsorbed water and in structure as H_2O and hydroxyl groups (Bernard et al. 2019). As the X-ray diffractograms (Figure 3-7) illustrate, the interlayer distance decreases while M/S in M-S-H increases (Bernard et al. 2019), as is the case for C-S-H when the calcium to silicon (C/S) ratio increases (Grangeon et al. 2016). According to the TGA results (Figure 3-8), this reduction of the interlayer distance would be associated with the formation of Mg–OH in M-S-H, with internal silanol groups being reduced. The evolution mechanism of the M-S-H structure with the variation of M/S would then be similar to that of the C-S-H with the variation of C/S. A possible parallel could be inferred between the Ca–OH that forms between the chains of Ca–Si and the Mg–OH that would form between the layers of Mg–Si as C/S or M/S increase.

The two analyses allowed to describe the pastes as composed only of M-S-H. The evolution of the structure with M/S appeared in the XRD and TGA. Talc-like characteristics were observed at low M/S, while serpentine-like reflections were associated with high M/S. Moreover, we detected an increase in the Mg–OH content of M-S-H as M/S increased.

3.3.3. Microstructure and Porosity

Several techniques were used to characterize the microstructure and porosity of M-S-H pastes. Figure 2-1 illustrates the panel of porosity characterizations associated with the dimensional range of solids and pores in an M-S-H paste. In this section, we propose the characterization of the porous structure starting from the smallest (physisorption) to the largest scale (water saturation). Since the mixing protocol and the w/b could influence the structure and porosity of a paste, the tests were carried out on both pastes with manual (noted M, w/b ~ 1.45) and mechanical (noted E, w/b ~ 1.1) mixing. The results presented correspond to pastes MS_0-78_CS_T50_M/E, MS_1_CS_T50_E, and MS_1-3_CS_T50_M/E.

Figure 3-9 shows the N2 adsorption-desorption isotherms of M-S-H samples made with M/S = 0.78, M/S = 1.0 and M/S = 1.3, mixed manually (Figure 3-9b) or mechanically (Figure 3-9a). The mixing protocol and the w/b seemed to influence the form of the isotherm at relative pressures >0.7 (for both the adsorption and desorption curves). The mechanical mixing—associated to a lower w/b—resulted in a smoother desorption for very high relative pressures and a lower adsorbed quantity. In the range p/p0 = {0; 0.7} the mixing process and w/b had no influence, probably due to the creation of “bigger” pores with manual mixing (where the w/b was higher). The internal structure of M-S-H remained the same since low pressures were not affected.

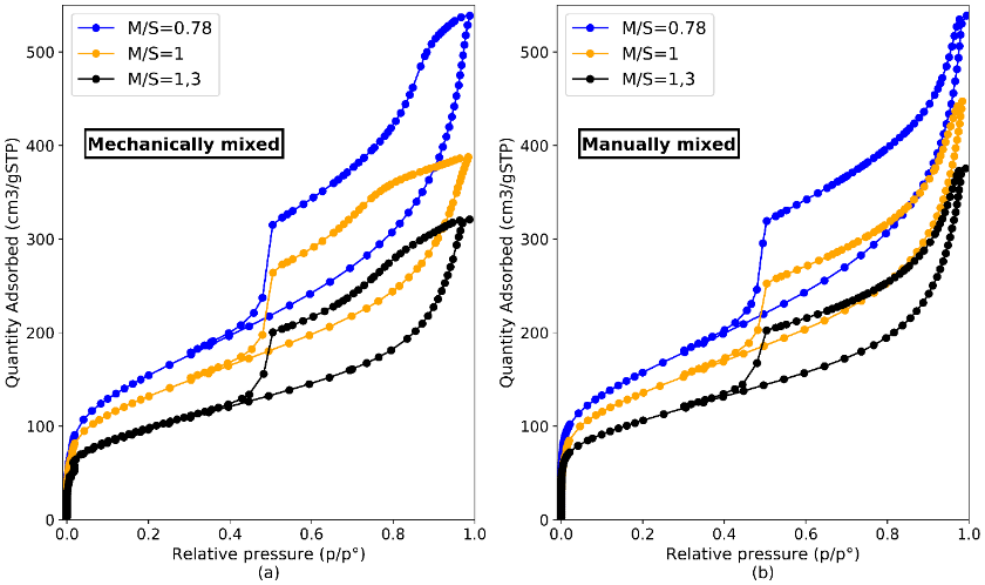

Figure 3-9: N_2 adsorption-desorption isotherms of M-S-H samples with M/S = 0.78, M/S = 1.0 and M/S = 1.3, mixed mechanically (a) or manually (b).

Figure 3-10 illustrates the different types of isotherms and hysteresis loops following the IUPAC classification (Sing 1985). The isotherms presented a hysteresis loop characteristic of a Type IV isotherm according to this classification. The adsorption part of the Type IV isotherm could be attributed to a monolayer-multilayer adsorption. The initial vertical slope at low p/p0 was characteristic of the presence of microporosity (equivalent diameter between 0.4 nm and 2 nm).

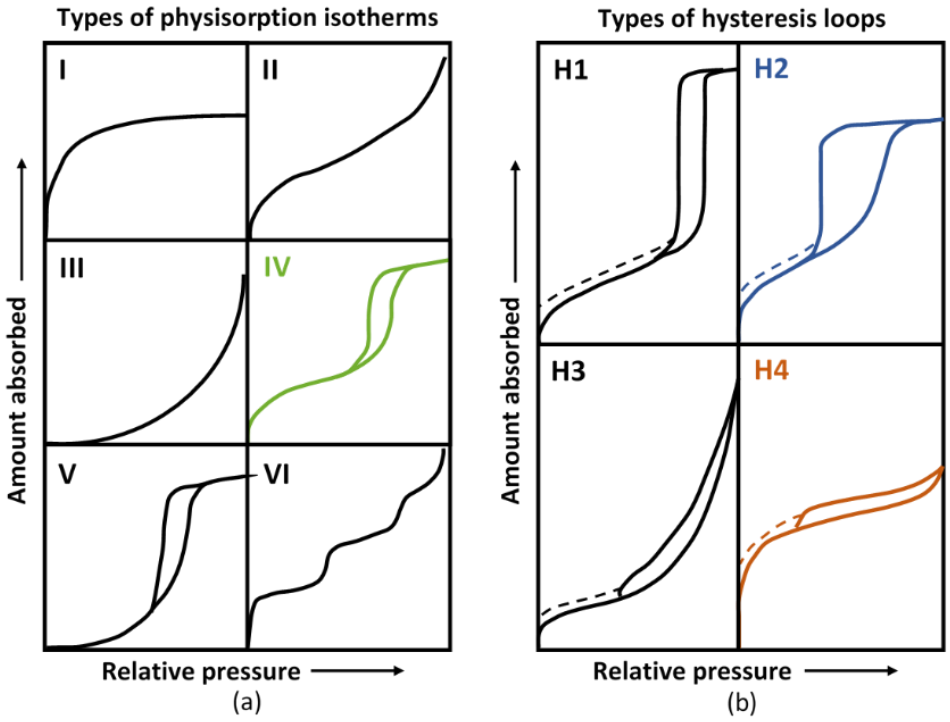

Figure 3-10: Types of physisorption isotherms (a) and hysteresis loops (b) (after Sing (Sing 1985)).

Hysteresis has been associated with capillary condensation taking place in mesopores (2–50 nm in diameter) (Bernard et al. 2019). M-S-H pastes made by mechanical mixing (lowest w/b), exhibited hysteresis comparable to H4 types with a small portion of the curve (on desorption at high p/p_0) which would correspond to H2 type. The Type H4 loop is associated with narrow slit-like pores while the Type H2 is harder to interpret and is often associated with pore size and a not well-defined shape (Sing 1985). The form of the high pressure hysteresis for mechanically mixed pastes could therefore relate to the presence of specific bottleneck-shaped pores (Bardestani, Patience, et Kaliaguine 2019). Overall, the structure we observed corresponded to plate-like materials with mesopores. The shape of the isotherms—especially of manually mixed pastes (highest w/b)—resembled that of synthetic saponite-like materials prepared by traditional hydrothermal crystallization at 513 K with H_2O/SiO_2 = 50 by Bisio et al. (Bisio et al. 2008). The form of the hysteresis was also similar to that of the M-S-H suspensions synthesized by Bernard (Bernard et al. 2019) under hydrothermal treatment (180 °C for 4 days).

According to Figure 3-9, the M/S ratio of M-S-H pastes appeared to influence the amount of N_2 adsorbed: the lower the M/S, the higher the total N_2 adsorbed.

The specific surface areas calculated with BET (SSA_{BET}) on M-S-H pastes hydrated from 2 (mechanically mixed) to 7.5 months (manually mixed; M/S = 1 is an exception, as it was hydrated for 2.5 months) are displayed in Table 3-4. Figure 3-11 illustrates the evolution of the specific surface as a function of the M/S ratio and the mixing protocol. Bernard's data obtained on synthetic suspensions (Bernard et al. 2019) are plotted in blue and green.

Table 3-4: Average specific surfaces and volume calculated for M-S-H pastes (colloidal silica and thermal cure at 50 °C) using BET and t-plot methods from nitrogen isotherms.

	Mechanically Mixed			**Manually Mixed**		
M/S	0.78	1	1.3	0.78	1	1.3
w/b	1.1	1	1.1	1.45	1.45	1.45
Age (days)	70	50	70	230	70	230
Average specific surface area BET (m^2/g)	556.7	475.2	345.3	562.9	488.2	381.6
Medium uncertainty	1.2	0.8	1.1	0.8	1.1	0.6
Standard deviation	11.7	3.7	6.6	8.7	8.1	3.0
External average specific surface area (t-plot) (m^2/g)	416.6	296.8	230.6	394.9	314.6	249.8
Standard deviation	6.5	1.8	7.4	26.3	5.4	9.5
V_{tot} (cm^3/g)	230.0	193.5	142.3	235.0	198.3	158.3
Standard deviation	5.0	2.1	2.5	5.0	2.9	2.9
Pore volume (cm^3/g)	0.355	0.299	0.220	0.363	0.307	0.245

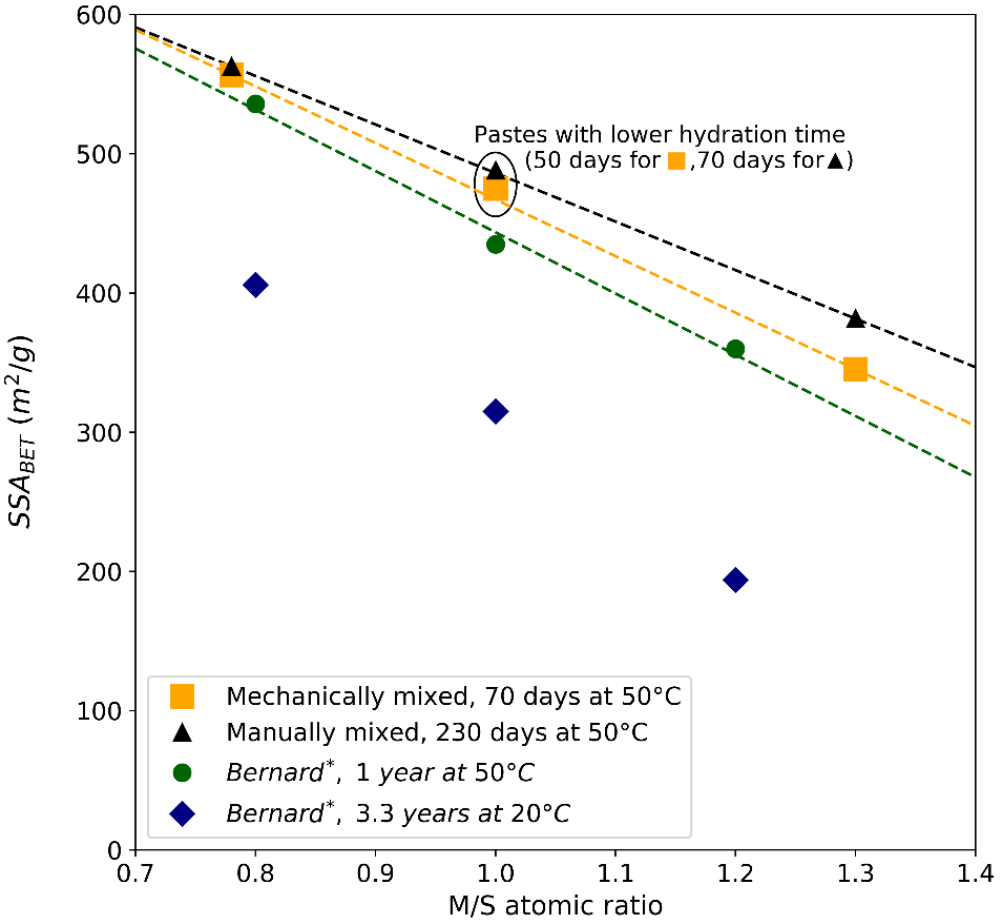

Figure 3-11: Specific surface area (SSA_{BET}) found in M-S-H pastes as a function of the M/S atomic ratio and of the mixing protocol. The dotted lines are the trend lines from the mechanically mixed (orange), manually mixed (black) and *Bernard et al. (Bernard et al. 2019) measurements (green: M-S-H suspensions equilibrated for 1 year at 50 °C; blue: M-S-H suspensions equilibrated for 3.3 years at 20 °C).

High SSA_{BET} were close to large surface areas reported by Bernard (Bernard et al. 2019) for suspensions with a similar curing (1 year at 50 °C). As expressed by Bernard, specific surfaces were much lower for samples cured for 3.3 years at 20 °C due to a longer hydration time. Over time, the porous network could evolve. Initially, magnesium phases are formed upon contact between water and magnesium oxide and/or silica. As is the case with inner C-S-H (Richardson 1999), denser M-S-H could gradually be formed in the inner layer of reacted silica fume clusters, which would result in finer porosity, lower specific surface areas and lower pore volumes. In the case of M-S-H pastes with colloidal silica, no silica clusters were formed, reducing the possibility of a more dense M-S-H formation.

Contrary to Bernard's hypothesis, according to which M-S-H forms in non-diluted systems or might exhibit a smaller SSA in field experiments, the experiments presented in this thesis proved that M-S-H pastes showed similar specific surfaces to suspensions, both cured at 50 °C. The specific surface seemed independent of the mixing protocol for low M/S ratios (0.78 and 1). The SSA_{BET} decreased with the M/S ratio in M-S-H with a slightly different slope from that of Bernard's data. At high M/S (M/S = 1 and M/S = 1.3), a gap arose between the data of Bernard, the data for manual mixing (w/b = 1.45) and the data for mechanical mixing (w/b = 1.1). The measurement uncertainty and the standard deviation (obtained by repeating the test) are too low to explain the difference in value between the protocols for these M/S values. High M/S ratios seem to be more

affected by curing time and type of mixing. As for the effect of the mixing protocol at high M/S—highlighted in Section 3.2.2—the high content of MgO compared to SiO_2 implies a slower consumption of brucite. This could explain a different low-scale organization of the material between the pastes, following the initial brucite content (brucite is a crystallized phase, as opposed to M-S-H). The consumption of brucite to form M-S-H in a hardening shape could produce a different porous network.

Pore volumes and SSA_{ext} are plotted in Figure 3-12. As was the case with SSA_{BET}, the values measured were higher than those of Bernard on suspensions equilibrated for 3.3 years at 20 °C (Bernard et al. 2019). No value was presented by Bernard on samples equilibrated for 1 year at 50 °C. SSA_{ext} and pore volumes were notably high for all our samples, implying a high content of micro- and mesopores. A clear trend was visible with the evolution of the M/S ratio. An increase in M/S implied a decrease in external surface area and pore volume. The porosity of samples with high M/S ratios (M/S = 1.3) seemed to contain less micro- and mesopores than the porosity of samples with low M/S ratios (M/S = 0.78).

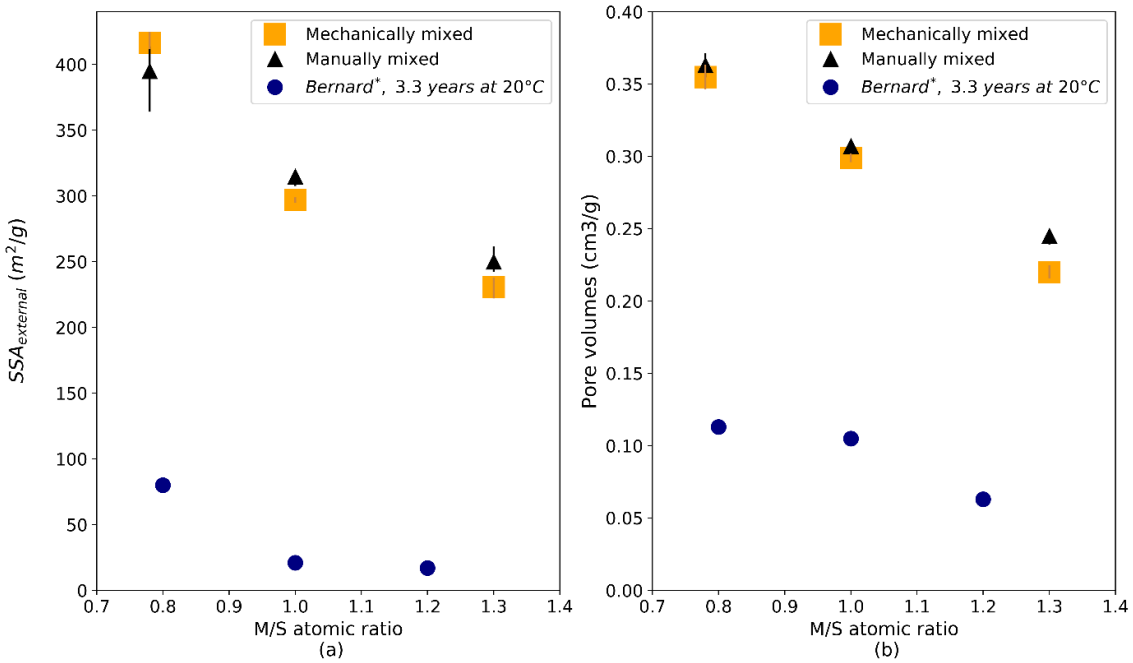

Figure 3-12: SSA_{ext} (a) and pore volumes (b) obtained by t-plot in M-S-H pastes as a function of the M/S atomic ratio and of the mixing protocol. *Bernard et al. measurements (in blue) correspond to M-S-H suspensions equilibrated for 3.3 years at 20 °C.

The pore size distribution between 2.5 and 8 nm—according to the BJH method—is shown in Figure 3-13. All samples showed a peak around 4 nm. The incremental pore volume (cm^3/g) increased as the M/S atomic ratio decreased, confirming that the M-S-H pastes with high M/S contained less micro- and mesopores than the pastes with lower M/S. The common location of the peak and the similar appearance of the curves indicated that the mixing protocol and the w/b did not influence this range of pores.

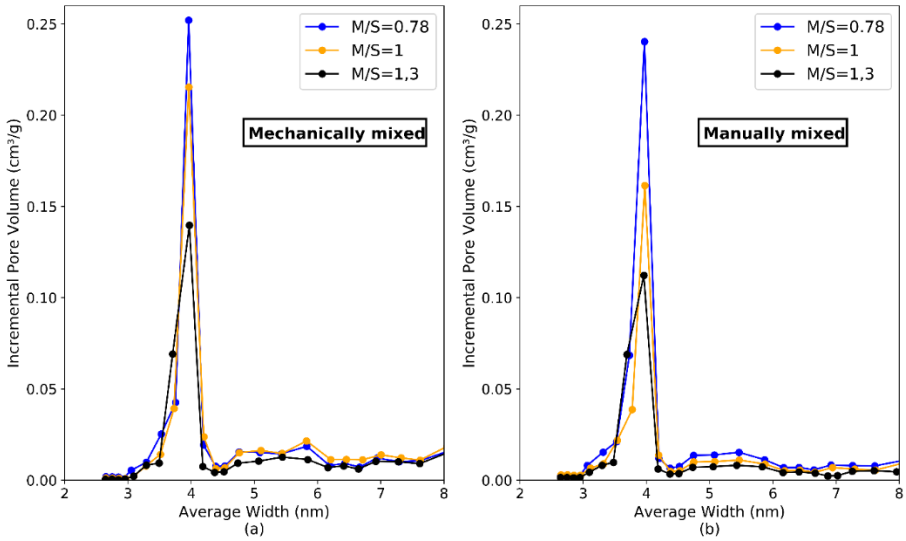

Figure 3-13: Pore size distribution by N_2 physisorption (calculated from the BJH method in desorption) of M-S-H samples with M/S = 0.78, M/S = 1.0 and M/S = 1.3, mixed mechanically (a) or manually (b).

In order to characterize the pore size distribution at the higher scale, MIP was used. The pore size distribution between 8 and 4 × 105 nm is shown in Figure 3-14. The pastes manually mixed showed a family of small pores between 8 and 10 nm with a high peak centered at 26 nm, while the mechanically mixed pastes only exhibited a family of pores with a mean value centered at 9 nm. A manual mixing associated to a high w/b (1.45) therefore influenced the size and distribution of the mesopores by creating supplementary capillary pores (26 nm in diameter). The porosity values (Table 3-5) obtained with MIP will be discussed in the following sections.

Table 3-5: Porosity of the M-S-H pastes according to MIP, kerdane and helium pycnometry, autoradiography, and water porosity.

		Mechanically Mixed			**Manually Mixed**		
	M/S	0.78	1	1.3	0.78	1	1.3
	w/b	1.1	1	1.1	1.45	1.45	1.45
	Age (days)	120	430	120	430	120	430
MIP	Porosity (%)	46.54	39.71	39.17	46.83	46.38	-
Kerdane and helium pycnometry	Bulk density (g/cm^3)	0.83	0.88	0.84	0.75	0.67	0.71
	True density (g/cm^3)	2.23	2.30	2.22	2.30	2.34	2.31
	Porosity (%)	62.86	61.78	61.89	67.60	71.39	69.17
Auto-radiography	Porosity (%)- Aged of 180 days	-	-	-	75.2	-	66.4
Water Porosity	Porosity (%)	77.62	70.08	71.03	86.14	78.79	74.69

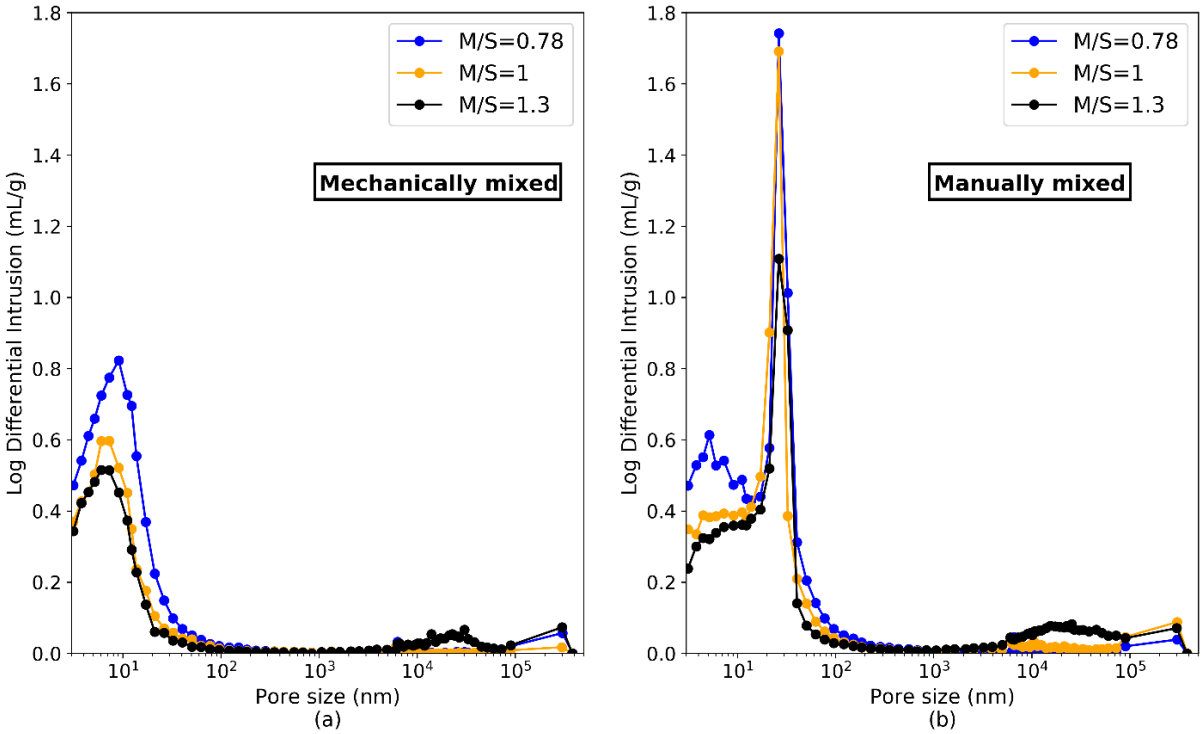

Figure 3-14: Pore size distribution by mercury intrusion porosimetry (MIP) of M-S-H samples with M/S = 0.78, 1.0 and 1.3, mixed mechanically (a) or manually (b).

Autoradiography was useful for establishing a link between the pore distribution and the overall porosity of the material, since it provides a 2D image of void percentage on samples and a histogram of the void percentage distribution. Autoradiography analyses were carried on three samples (one for M/S = 0.78 and two for M/S = 1.3). Figure 3-15a–c show the autoradiography maps. A cracking phenomenon—similar to shrinkage—appeared in the samples (Figure 3-15b,c) as soon as water was removed from them by drying, vacuum, etc. This experimental perturbation did not prevent us from analyzing the porosity of the samples through the extraction of cracks and bubbles by deconvolution of the porosity histograms. The histograms associated with the maps (Figure 3-15d–f) show the distribution of the void ratio (porous areas and cracks). In the histograms—where all kinds of features were taken into account—the highest values approximately reach 100%. For M/S = 1.3, three Gaussian distributions were used to reproduce the histogram. For M/S = 0.78, only one Gaussian distribution was necessary. The characteristics of the Gaussian distributions are displayed in the histogram (Figure 3-15d–f). For M/S = 1.3, the first Gaussian distribution with μ = 58% (sample 1) or μ = 56.4% represented more than 80% of the histogram. The two other Gaussian distributions—with μ = 72% and μ = 89% (sample 1) or μ = 68.9% and μ = 85%—would correspond to bubbles and cracks. The removal of cracks corresponded to considering only the first Gaussian for each histogram. The average value of the porosity obtained by further treatment would then be 57.2% for M/S = 1.3 and 67.5% for M/S = 0.78.

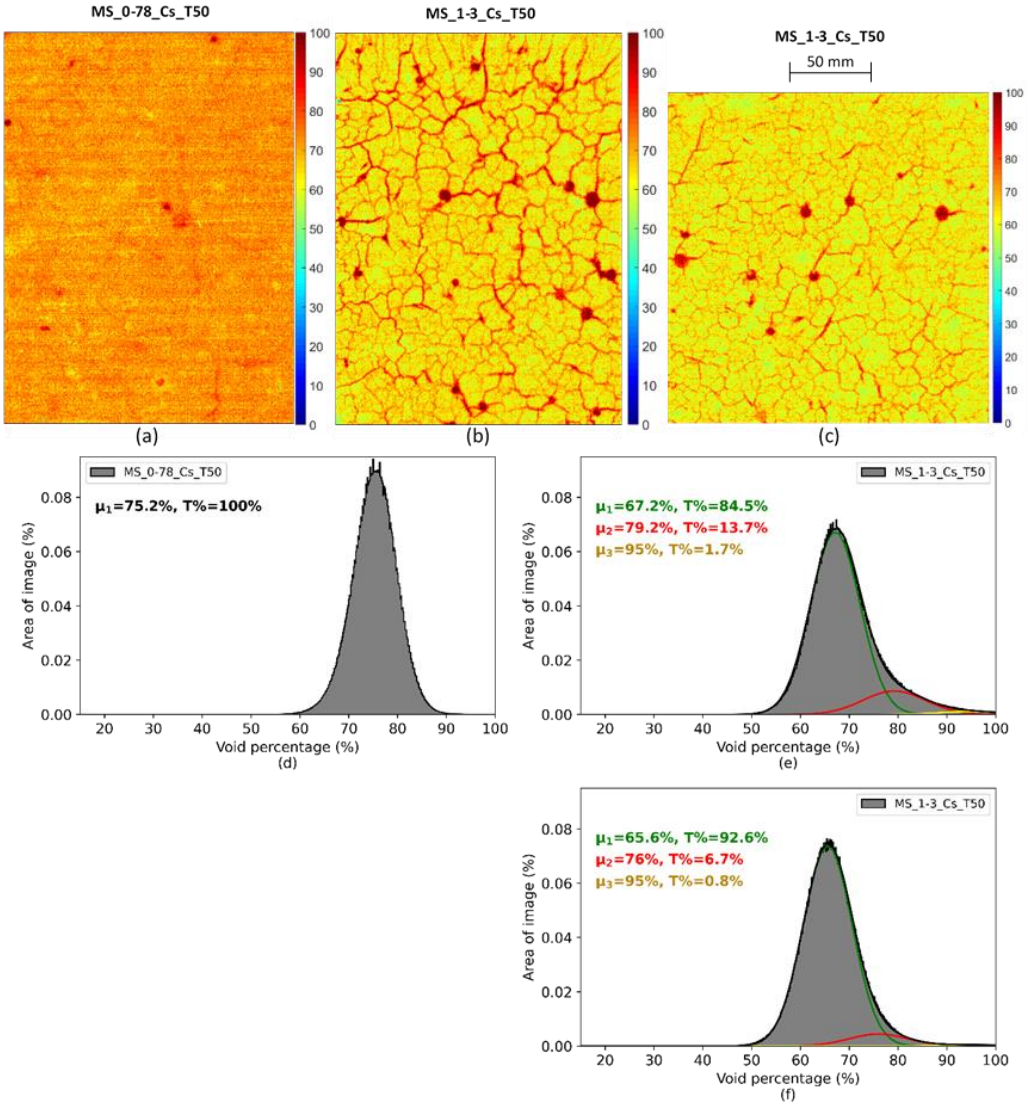

Figure 3-15: Autoradiography maps of M-S-H manually mixed pastes (a) M/S = 0.78; (b,c) M/S = 1.3 and associated porosity histograms and deconvolution—(d) for (a), (e) for (b) and (f) for (c). μ is the mean of the phase and T% corresponds to the percentage of the phase into the total histogram.

The M/S-dependent effect on cracking was observed in the autoradiography maps. As explained in Section 4.3 and observed in Figure 3-15, the sample with M/S = 1.3 showed numerous bubbles and cracks. The sample with M/S = 1 cracked during impregnation while the samples with M/S = 0.78 did not show large cracks. According to Figure 3-13, the samples in question did not exhibit any difference in low-scale pore distribution, except for the amount of N_2 adsorbed. Thus, the difference in the cracking pattern was not due to the finer distribution of the pores. While the pastes with the lowest M/S (M/S = 0.78) were the most porous, they underwent the least cracking. Preferential and faster cracking appearing for high M/S could therefore be linked to lower mechanical properties of the material. For the same capillary pressure, if one material is more brittle than another, then it will crack more easily.

Autoradiography and MIP provided a first idea of the total open porosity of the material. Other measurements were carried out in order to obtain a clearer picture of the porosity of the pastes (Table 3-5). The lowest porosity value was obtained with MIP, followed by the values acquired

with helium pycnometry and kerdane, autoradiography and water porosity. These observations can be explained by the range and type of pores considered depending on the test.

MIP explored only the connected porosity; while pores >8 nm were taken into account, large defects (air bubbles and very open cracks) were ignored. The porosity values obtained by helium pycnometry correspond to the open porosity, including cracks and bubbles. Autoradiography measured the connected porosities, with air bubbles and cracks being removed during post-processing (smallest visible pores = 10 µm). Water porosity took into account the connected porosity, bubbles and cracks. The latter is therefore the largest measured value. Moreover, the 105 °C drying protocol used for water porosity may consume certain hydrates, resulting in a potential small overestimation of the actual porosity. As each method had its limitations, it was interesting to combine them all to characterize the material.

A general trend could still be observed. Manually mixed pastes had a slightly higher porosity (10% more) than mechanically mixed ones (these results were consistent with the higher w/b ratio used for manual mixing). Overall, the porosity of these pastes was high. The influence of the M/S ratio on the overall porosity was difficult to assess because the pastes were very porous (due to the high w/b ratio imposed). C_3S-based pastes cast with a similar protocol (colloidal silica) also have a high porosity, close to 60% according to Kangni-Foli (Kangni-Foli 2019). The effect of mixing and w/b disappeared only on a smaller scale. According to Bernard (Bernard et al. 2020), the molar volume of M-S-H increases with increasing M/S. It is expected that the higher the solid molar volume, the lower the pore volume (Shah et Scott 2021). This observation can be found in our study through N_2 physisorption and MIP. The more the M/S increases, the more the absorbed amounts of N_2 and Hg and the specific surface area decrease, thus indicating a higher mesoporosity. On a larger scale, the porosities measured by the different techniques show this same trend. The pastes were mainly mesoporous, with a small amount of micropores and some defects appearing on a larger scale (bubbles due to mixing and cracks due to pre-treatments).

The microstructure of M-S-H pastes was characterized in this study. On a smaller scale, at the level of silica sheets (Figure 2-1), physisorption analyses described the material as a highly porous phase with plate-like micropores and mesopores. The increase in M/S implied a decrease in the quantity of N_2 adsorbed, as well as a reduction of the specific surface (SSA_{BET}), the SSA_{ext} and the micro- and mesopore volume. At the level of capillary pores to clusters of globules of M-S-H (Figure 2-1), MIP was used to distinguish the effect of the mixing protocol. Mechanically mixed pastes exhibited a mesopore family around 10 nm, while manual mixing also created a high amount of mesopores around 30 nm. The mechanical mixing—which lasted longer and used a higher speed and strength—helped reduce the w/b, leading to a denser paste with less porosity. On a larger scale, porosity measurement protocols provided information about open porosity. On autoradiography maps, we observed the formation of cracks as soon as the water was removed from the samples. This mechanism highlighted the mechanical strength and sensibility of M-S-H in a relatively humid environment. The removal of cracks and bubbles from histograms of porosity showed the high open porosity of the pastes (approximately 60% for manually mixed pastes). This high value was supported by other characterization methods, although the porosity measurements were influenced by pre- or post-treatment of the samples. Drying at 105 °C after water saturation and bulk density measurements could lead to the calcination of hydrates, resulting in an overestimated porosity. Overall, the open porosity of M-S-H pastes could be considered to be 70% for manually mixed pastes and 62% for mechanically mixed pastes, with this percentage increasing as the M/S ratio decreases.

Similar to C-S-H, the M-S-H phase possess internal porosity. To determine the intrinsic porosity of M-S-H, the porosity measurements (water porosity, MIP, bulk density) were compiled on mechanically mixed pastes.

2 types of porosity, the intrinsic M-S-H (or C-S-H) gel porosity (Φ_{gel}) and the capillary porosity (Φ_{cap}), were calculated from the experimental data. MIP is considered to correspond to the porosity for pores with diameter superior to 10nm (d>10nm) (Renhe, Baoyuan, et Zhongwei 1990) while water porosity allows to consider all the open porosity (intrinsic porosity of semi-amorphous and amorphous species included, as C-S-H and M-S-H) (0<d<10nm + d>10nm). By combining these two porosity measurements with a bulk density measurement, it is possible to determine the Φ_{gel} (0<d<10nm) and Φ_{cap} (d>10nm). The expressions for the porosities are as follows:

$$\Phi_{gel} = \frac{V_{p_{0<d<10nm}}}{V_s + V_{p_{0<d<10nm}}} \quad (3\text{-}1)$$

$$\Phi_{cap} = \frac{V_{p_{d>10nm}}}{V_{app}} \quad (3\text{-}2)$$

$$V_{app} = \frac{m_{tot}}{\rho_{bulk}} \quad (3\text{-}3)$$

$$V_S = V_{app} - V_{p_{0<d<10nm}} - V_{p_{d>10nm}} \quad (3\text{-}4)$$

$$V_{p_{d>10nm}} = V_{app} * \Phi_{MIP} \quad (3\text{-}5)$$

$$V_{p_{0<d<10nm}} = V_{app} * (\Phi_w - \Phi_{MIP}) \quad (3\text{-}6)$$

with V_{app} the apparent volume, m_{tot} the total mass of the volume considered, V_s the solid volume, $V_{p_{0<d<10nm}}$ and $V_{p_{d>10nm}}$ the pore volume for pores of diameter between 0 and 10 nm and above 10 nm respectively.

These assumptions and equations have been tested on the low-pH model cement pastes mainly composed of C-S-H and are conclusive ($\Phi_{gel} \approx 0.28$ as for LD C-S-H in literature (Souyris 2012)).

For M-S-H pastes, calculations are based on data for mechanically mixed colloidal silica-based pastes cured at 50°C (first 3 columns in Table 3-5). According to the calculations, Φ_{gel} of M-S-H is egal to 58.1%, 50.4% and 52.4% for M/S=0.78, M/S=1 and M/S=1.3 respectively.

The calculation of the molar volume of M-S-H is performed according to the following calculation:

$$V_m = V_m{}^{chem} * \frac{1}{1 - \Phi_{gel}} \quad (3\text{-}7)$$

With V_m the apparent molar volume of the phase and $V_m{}^{chem}$ the chemical molar volume (or true molar volume).

The molar volume calculated from the equation (3-7) is displayed in Table 3-6.

Table 3-6: M-S-H intrinsic porosity and molar volume determined on M-S-H pastes

		M-S-H (M/S=0.78)	M-S-H (M/S=1)	M-S-H (M/S=1.3)
Molar volume (cm^3/mol)	Basic unit	57 [1]	63 [2]	71 [1]
	Gel	136 [4]	127 [4]	149 [4]
Gel porosity (%)		58.1% [3]	50.4% [3]	52.4% [3]

Numbers corresponds to the source of the values : 1=(Bernard et al. 2020), 2=adapted from (Bernard et al. 2020), 3=calculated by equation (3-1), 4=calculated by equation (3-7)

3.3.4. Elastic properties

Due to the shrinkage phenomenon discussed earlier (3.3.3), the mechanical characterization of the M-S-H pastes was complicated. To perform indentation tests, a flat surface is required (see 1.1.4.1). The shallower the indented depth, the flatter the surface of the sample must be. As the indenter used did not allow for testing in a humid atmosphere, the samples cracked during the tests. Thus, the force was increased to 200 mN, corresponding to an indented depth of about 10 µm, and only the samples with M/S=0.78 and M/S=1 yielded results. For M/S=1.3, the shrinkage was far too great. As for the determination of the intrinsic porosity of M-S-H, the mechanical properties were determined from the results of the mechanically mixed paste. The results of microindentation on the M-S-H pastes are presented in Table 3-7. The Poisson coefficient considered is 0.24.

Table 3-7 : Young modulus (GPa) of M-S-H pastes determined by microindentation, ν=0.24

M/S	0.78	1
Number of values	127	65
Standard deviation	0.55	0.47
Median	2.83	1.67
Mean	2.88	1.60

The microindentation results can be used to determine the intrinsic mechanical properties of M-S-H via reverse mechanical homogenisation. The M-S-H paste is composed from the M-S-H phase and the capillary porosity (46.5% and 39.7% for M/S=0.78 and M/S=1 respectively). The homogenized elastic properties of M-S-H pastes can be evaluated according to the intrinsic properties of M-S-H phase using a Mori-Tanaka scheme, in saturated drained conditions. In this scheme, the volume fraction of matrix (M-S-H) and inclusion (capillary porosity) are known and the elastic properties of the M-S-H phase are unknown. Calculations are made in drained conditions and the properties of porosity are thus considered equal to zero. The value of the Poisson's coefficient of M-S-H is considered like that of C-S-H (0.24). The intrinsic elastic properties of M-S-H determined by the calculation are 7.9 GPa and 3.7 GPa for M/S=0.78 and M/S=1 (Table 3-8). The number of successfully completed indents is low (127 and 65 for M/S=0.78 and M/S=1 respectively). The variation in Young's modulus observed with increasing M/S ratio cannot be confirmed. This could be due to a greater sensitivity to shrinkage. Further testing would be required to comment on the effect of the M/S ratio.

Table 3-8 : M-S-H intrinsic mechanical properties determined on M-S-H pastes

	M-S-H (M/S=0.78)	M-S-H (M/S=1)
E (GPa)	7.9 ± 1.5	3.7 ±1.1
ν	0.24*	0.24*
k (GPa)	5.06 ± 0.97	2.37 ± 0.7
μ (GPa)	3.19 ± 0.60	1.49 ± 0.44

*not known considered equal to C-S-H
k and μ are the incompressibility and shear moduli. They are calculated from E and ν.

Conclusion

This chapter focused on the chemical, microstructural and mechanical properties of cohesive M-S-H pastes. Four protocols to obtain cohesive and homogenous M-S-H pastes—without brucite or other species—were tested in this study. The increase in curing temperature (20–50 °C) accelerated the consumption of brucite and favoured the formation of M-S-H, with colloidal silica enabling a better distribution of particles than silica fume. The higher the M/S ratio, the longer the brucite was present. The protocol of choice for M-S-H manufacturing therefore involves colloidal silica and MgO with w/b = 1 and mechanical mixing (140–285 rd/min rotation for 10 min), followed by a thermal cure at 50 °C for 50 days (minimum recommended).

X-ray diffraction and thermogravimetric analyses indicated a rearrangement of the structure—from talc-like structure to serpentine—as M/S increased, linked to a decrease in the interlayer distance and an increase in the Mg–OH content in M-S-H. The evolution of the M-S-H structure would be similar to that of the C-S-H. A parallel could be drawn between the Ca–OH that forms between the chains of Ca–Si and the Mg–OH that would form between the layers of Mg–Si as C/S or M/S increase.

The porosity of M-S-H pastes was studied from the level of entrained air bubbles and voids to the level of silica sheets. On a large scale, the combination of different characterization methods made it possible to quantify the total, open porosities of the pastes. Mechanical mixing reduced the open porosity from 70% (manual mixing) to 62%. This value changed along with the M/S ratio in that the higher the ratio, the lower the porosity. On a smaller scale—from the capillary pores to the level of clusters of M-S-H globules—manual mixing resulted in an additional family of pores (around 30 nm) that mechanically mixed pastes did not have, the latter only showing a family of mesopores centered on 10 nm. The finer porosity of the mechanically mixed pastes can be explained by the reduction in w/b due to increased mixing speed and power, which leads to denser and less porous pastes. On the smallest scale studied in this article (silica sheets), it seemed that the specific surface area and the amount of porosity increased when the M/S ratio decreased, while the size of the pores remained unaltered. M-S-H comprise a highly porous phase with plate-like micro- and mesopores and are sensitive to changes in humidity.

Microstructural and mechanical characterizations have allowed the determination of the intrinsic elastic properties and porosity of M-S-H. M-S-H are much more porous than C-S-H (55% compared to about 28% for C-S-H (Souyris 2012)) and their Young modulus are much lower (5 GPa on average compared to 22 GPa according to the literature (Nguyen 2017; Constantinides et Ulm 2004; Zhu et al. 2007; Jennings et al. 2007; Constantinides et Ulm 2007; Vandamme et Ulm 2009; 2013)). It remains to validate these properties on M-S-H from degradation.

CHAPTER 4. CHEMO-MECHANICAL CHARACTERIZATION OF LOW PH MODEL CEMENT PASTES IN MG-BEARING ENVIRONMENTS

Introduction

The previous chapter focused on the chemical and microstructural properties of cohesive M-S-H pastes. The determined properties of M-S-H are those of synthetic M-S-H. To ensure that these microstructural and mechanical data of M-S-H can be integrated in chemo-mechanical models, it is necessary to verify that the determined properties are consistent with those of a cementitious material under magnesium attack.

For this purpose, a first verification step is the degradation of a cementitious material with a simple mineralogy and a homogeneous Ca and Si distribution. As developed in chapter 2, a low-pH model paste, consisting of CEM I and colloidal silica, was produced. The analysis of the magnesium attack of this model cement paste will allow a better understanding of the reaction mechanisms of magnesium attack and M-S-H formation in low-calcium cementitious matrices and to study the influence of M-S-H formation on the cement paste properties.

This chapter is devoted to the study of this low-pH model paste under magnesium attack. The first part proposes an analysis of the influence of the magnesium attack on the chemical, microstructural and mechanical properties of the cement paste. The second part proposes the study of the influence of the Mg concentration on the reaction mechanism and on the properties of the cement paste. The last part proposes to test the validity of the microstructural and mechanical properties of M-S-H determined on pure M-S-H pastes in Chapter 3. For this purpose, the method detailed in Chapter 2 (2.1.4.2) is implemented. It allows, based on microprobe data, XRD and the porosity of the sound material, to simulate the homogenised mechanical properties along the degradation.

4.1. Materials and methods

4.1.1. Raw materials and preparation of model cement samples

Low-pH model cement pastes were produced by the mixing of a colloidal silica, a Portland cement (CEMI), distilled water (milli-Q water) and superplasticizer. The colloidal silica was Rheomac AS 150 (also called Mastermatrix 150), provided by BASF® in the form of an aqueous suspension (dry extract = 52 ± 2.5%). The Portland cement was a CEMI 52,5 N CE PM-ES-CP2 NF, from Val d'Azergues (cement's oxide composition provided in Table 4-1). The superplasticizer was CHRYSO®Fluid Optima 175, provided by Chryso France®.

Model cement pastes were prepared by mechanical mixing (rotation speed between 140 rd/min and 285 rd/min during 8 min, 450W). The water/binder (w/b) ratio and the superplasticizer content (Sp/b) were optimized in regard to the workability of the mix (w/b=0.65). The proportions are given in Table 4-2.

Table 4-1: Oxides proportion in cement

Oxides	SiO_2	Al_2O_3	Fe_2O_3	CaO	MgO	K_2O	Na_2O	SO_3	P_2O_5	CO_2
Proportion (%)	20.6	3.60	5.00	64.3	0.70	0.70	0.20	2.70	0.40	0.90

Table 4-2: Mix proportions

Sample name	Mass (g)				Sp/b	w/b
	CEMI	Rhéomac AS 150	MilliQ-water	Superplasticizer (dry extract)		
CEMI_sil-col	590.5	621.7	275.1	10.56	1.2%	0.65

4.1.2. Degradation procedure

Several magnesium solutions have been used in the literature as model media ($MgSO_4$, MgO and $MgCl_2$). The use of $MgSO_4$ is excluded for this study because (i) the sulphate ions would cause changes in the cement paste in addition to the magnesium attack and (ii) its use causes the formation of an external layer of brucite, which is to be avoided (Santhanam, Cohen, et Olek 2002a) (see 1.2.2.4). In 2017, Bernard (Bernard et al. 2017a) tested the use of $MgCl_2$ and MgO and showed that the addition of $MgCl_2$ lowers the pH and allow the formation of M-S-H. On contrary, the addition of MgO increase the pH and leads to the formation of brucite (see 1.2.2.5). Moreover, the action of chlorides is mainly its participation in the corrosion of steel reinforcement. It is only at high concentrations (>100 mmol/L) that chloride-based phases are formed (see 1.2.2.3). Consequently, the aggressive solution in this study was made from $MgCl_2$.

At the end of their manufacture, the pastes were kept under endogenous conditions for 11 months. Then, samples of 4*4*1 cm^3 were cut, coated with sealant (Resoltech®, Mastic EPOXY 3030 / 3036) on the 4*1 cm^2 sides in order to impose unidirectional degradation. The samples were immersed in 5 or 50 mmol/L $MgCl_2$ solutions in 60 L closed tanks for 2, 4 and 6 months. The solutions were constantly agitated and renewed regularly (black vertical lines on Figure 4-1). At the end of each exposure time, one or two samples were taken out of the tanks, cut out and prepared for the various characterization tests. The pH of the tanks was measured before and after the renewing (black vertical lines on Figure 4-1). The pH of the renewal solution is between 5.4 and 5.8. This depends on the time allowed for the solution to equilibrate with the CO_2 in the air before the samples are placed in it and water is taken (between few hours to two days).

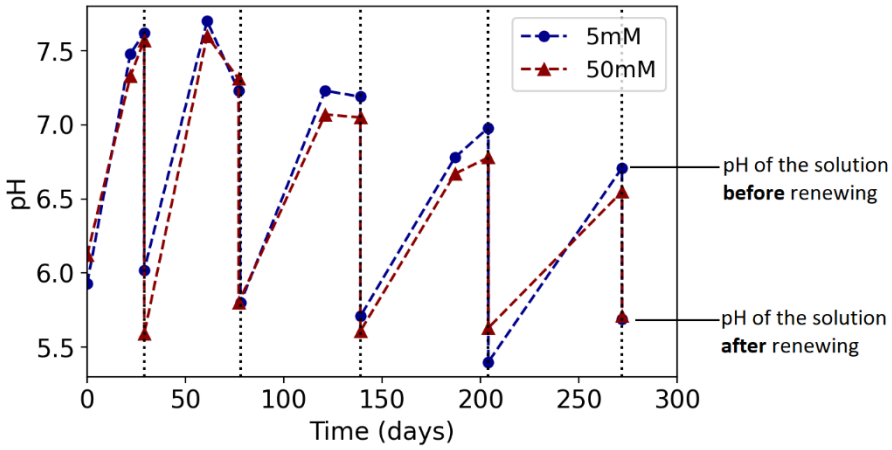

Figure 4-1: pH of the 60L of magnesium solution (5 and 50 mmol/L) as a function of time

The multi-physics characterization techniques used are detailed in Chapter 2 (2.1.3).

4.2. Properties of sound paste

4.2.1. Mineralogical and chemical properties

The elemental composition and the experimental C/S ratio of the sound zone of the degraded sample (see Figure 4-7) has been measured by microprobe. An average of 40 points in the sound zone was taken to determine the values associated with the sound material (Table 4-3). The experimental C/S ratio (0.90±0.05) is consistent with the theoretical ratio (0.94) calculated from the quantities of raw materials.

Table 4-3: Oxides proportions in the sound zone of the paste

Oxides	CaO	SiO_2	Al_2O_3	Fe_2O_3	SO_3	MgO	Cl	TiO_2	Na_2O	P_2O_5	Total
Mean (%)	32.42	38.82	1.63	2.63	1.49	0.24	0.08	0.13	0.08	0.38	77.88
Standard deviation (%)	1.35	1.10	0.22	0.33	0.45	0.14	0.01	0.05	0.01	0.44	2.02

XRD analyses performed on flat sections of the sound material (Figure 4-2) showed few crystallised phases. The only phases detected are C-S-H and ettringite. No portlandite nor anhydrous phase are detected. The indexing of the X-ray peaks for the C-S-H (green circles) phases is based on (Bernard et al. 2018).

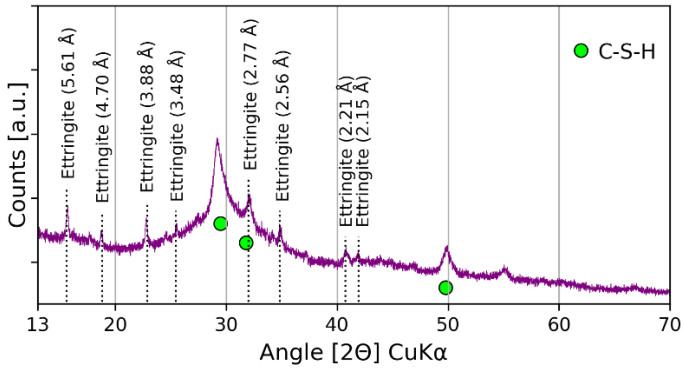

Figure 4-2: X-ray diffractograms of the sound paste (low-pH model cement paste).

4.2.2. Microstructural properties

Microstructural properties were determined on the sound sample by MIP, Water porosity, N_2 Physisorption and apparent density measurements. Table 4-4 summarizes the results. It appears that the water porosity determined by the two methods are similar. As expected, the water porosity is the highest porosity (because of the drying at 105°C which can remove some of the bound water), followed by the MIP porosity since it does not take into account the small pores.

Table 4-4: Microstructural properties of the sound sample

	ρ_{bulk}		Φ_w		Φ_{MIP}	Pore volume (cm^3/g)	Specific surface (m^2/g)
Place - Method	IRSN (Kerdane)	LMDC (Water)	IRSN	LMDC	LMDC	IRSN (N_2 Physisorption)	
Mean	1.191	1.086	52.4%	50.5%	35.5%	0.092	36.2
Standard deviation	0.004	0.022	0.8%	1.0%	0.15%	0.001	1.5

4.2.3. Elastic properties

Microindentation and nanoindentation were performed on the sound sample. To calculate the Young Modulus from the experiment, it is necessary to know the Poisson's ratio (equation (1-1)). The Poisson's ratio considered for these tests is 0.24, as usually for C-S-H matrix in cement pastes

(Constantinides et Ulm 2004; Mondal, Shah, et Marks 2007). Figure 6-2a shows the distribution of results. Table 4-5 groups the statistical calculations on the data after the removal of outliers by the interquartile method (Barbato et al. 2011; Vinutha, Poornima, et Sagar 2018). If a data item does not fall within the range [Q1-1.5*Interquartile; Q3+1.5*Interquartile], then it is considered an outlier and is removed.

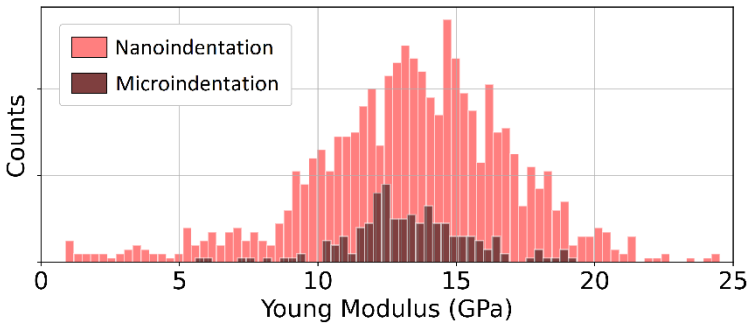

Figure 4-3: Young modulus determined on the sound low-pH model cement paste via nanoindentation (depth = 300 nm) in red and microindentation (F = 200 mN, depth ≈10 µm) in black

Table 4-5: Statistical calculations on micro and nanoindentation results

Type of indentation	Micro	Nano	Macro
Number of values	256	1164	2 x 3
Median	12.4 GPa	13.6 GPa	10.5 GPa
Mean	10.0 GPa	13.6 GPa	11.4 GPa
Standard Deviation	6.1 GPa	3.2 GPa	1.6 GPa

In microindentation, as the indented depth is high (depth ≈ 10 µm), the determined mechanical properties includes a large part of porosity while nanoindentation (depth = 300 nm) mainly considers solid phases and their intrinsic porosity proportions (Constantinides et Ulm 2004; Hu et al. 2020). Therefore, the values in nanoindentation are higher than those in microindentation. The results of the macroscopic mechanical tests (obtained on 2 samples with 3 strain gauges for each) and the microindentation results are similar. It seems that microindentation allows to approach the macroscopic Young's modulus.

In nanoindentation tests, the diameter of the impacted area is egal to 1.8 to 2.4 µm (6 to 8 times the indented depth, see 1.1.4.1). Although the interaction volume is much smaller than in microindentation, a part of porosity is taken into account in the interaction volume. The amount of porosity included in this volume depends on the formation mechanism of the C-S-H and the properties of the paste. As observed in XRD (Figure 4-2), the cement pastes are mainly composed of C-S-H and ettringite, and nanoindentation should reflect their mechanical properties. The C-S-H gel seems to exhibit weaker mechanical properties than in the literature (around 22 GPa) (Constantinides et Ulm 2004; Zhu et al. 2007; Jennings et al. 2007; Constantinides et Ulm 2007; Vandamme et Ulm 2009; 2013). This gap between the literature and the experimental observations could be due to a different formation process because of the use of colloidal silica and/or higher w/b ratio (0.65) than OPC (w/b<0.5) characterized in literature. LD and HD C-S-H properties defined in literature are measured on OPC and not on low C/S cement pastes (see 1.1.4.3). The formation process of LD C-S-H complies with the hydration process of this paste. The LD C-S-H form first during the hydration around the grains, forming a gangue. High Density C-S-H (HD C-S-H) usually forms in a second time from the remaining grains within the LD C-S-H gangues

(Richardson 1999; 2000; Richardson et al. 1994). If the silica grains are not large enough and hydration is not rapid, as in this case, the formation of HD C-S-H may not take place. Increasing the porosity can also increase the porosity of the interaction volume and decrease the measured elastic properties.

4.3. Magnesium attack on low-pH model cement paste

4.3.1. Overall properties

Figure 4-4 shows the multi-physics characterization of a sample immersed for 6 months in the 5 mmol/L $MgCl_2$ solution.

To visualize the degradation front and characterize the chemical evolution in the degraded samples, SEM/EDS analyses were performed. Figure 4-4 (a) shows the EDS Ca and Mg maps. The surfaces exposed to magnesium attack are on the right and left. It appears that in conjunction to a strong leaching of calcium, an enrichment of magnesium took place in the paste from 0 to 1700 µm. Cracking appears on the EDS maps, as discussed in 2.1.3.1. The estimative depth of the degradation front observed on the EDS maps was plotted on each part of the figure (vertical dashed lines at 1700 µm depth).

In addition, microprobe analyses along the degradation were performed. Figure 4-4 (b) shows the major oxide profiles. The same graph is available is full page in Appendix B (Figure B-1). As in the case of other types of attack leading to leaching (Bertron et al. 2009), analyses showed that the leaching front of sulphate species was an indicator of the beginning of the highly degraded zone. A drop in the sulphur signal was observed by microprobe (Figure 4-4 (b)) around 1750 µm which corresponded to the limit of the decalcification zone. From the core of the specimen to the surface in contact with the aggressive solution, three zones could be distinguished:

- **the sound zone** (Z1) from the core to 1750 µm from the surface
- **a transition zone** (Z2) between 1100 and 1750 µm. The Ca signal decreases while the Mg signal increases.
- **a zone strongly decalcified and enriched in Mg** (Z3). The Ca signal remains constant and egal to 5wt% while the Mg signal continues to increase.

X-ray micro-tomography analyses (Figure 4-4 (c)) were carried out in order to visualize the evolution of the apparent density in the sample volume along the degradation. The density presented here is the signal intensity at each point (value related to the absorption coefficient of the material) normalized to the maximum value of the sample. Micro-tomography results show two zones of different apparent densities, one in the core and one corresponding to the external zone in contact with the aggressive solution with a density twice as low. The spatial boundary between the two corresponds to the boundary observed on the EDS map and on the microprobe profile between zone 2 and zone 1. Since apparent density is inversely proportional to porosity, this suggested that the degraded zone, despite the formation of Mg-bearing solid phases, has a higher porosity than the sound zone. The formation of Mg-bearing solid phases did not appear to fill the porosity induced by decalcification of C-S-H.

After 6 months of immersion in $MgCl_2$ solution, microindentation was performed to characterize the Young's modulus of the paste as a function of the distance from the surface (approximately 16 indents for each distance x). Figure 4-4 (d) shows the results after 6 months of degradation at 5 mmol/L. The Young's modulus observed in the sound zone on these samples (17 months aged) was similar to the Young's modulus measurements on the sound samples presented in section 4.2 (13 months aged). A significant decrease in elastic mechanical properties was observed in the magnesium-enriched zone. Just after the end of the Mg enrichment front, a lower Young's

modulus value was observed, corresponding to the cracks observed between the degraded and the sound zone (highlighted by the grey bands on the figure).

The following sections propose a more detailed analysis of the phenomena.

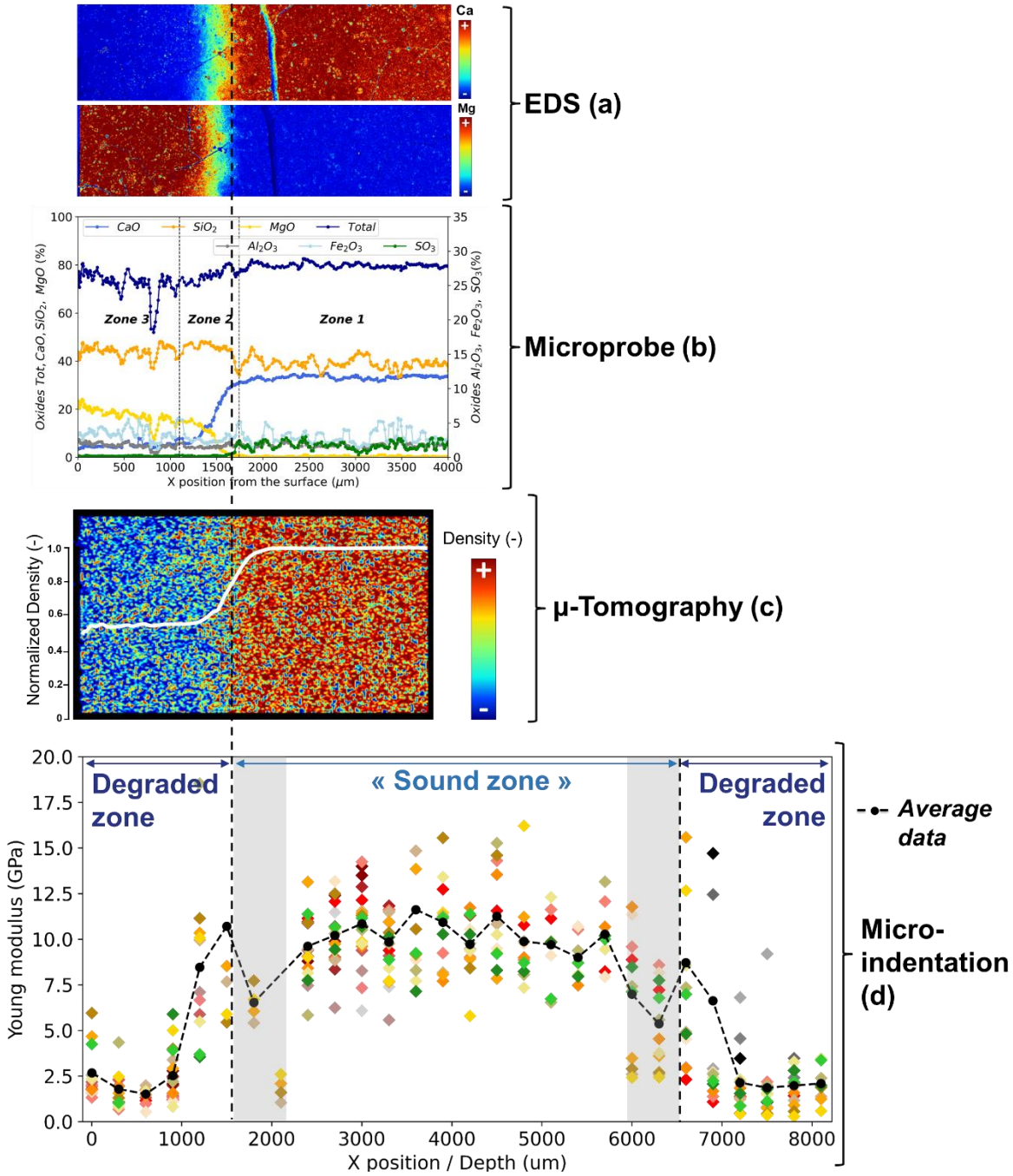

Figure 4-4: Multi-physics characterization of model cement paste immerged during 6 months in a solution with [$MgCl_2$] = 5 mmol/L, (a) EDS Ca and Mg maps, (b) Microprobe, (c) microtomography and (d) microindentation

4.3.2. Magnesium enrichment and zonation

Samples were taken from the solution and analysed at different exposure times (2, 4 and 6 months). Figure 4-5 shows the EDS magnesium and calcium maps. Figure 4-6 shows the profiles of Ca/Si and Mg/Si intensity ratios calculated from the EDS elemental mappings. The curves are obtained by averaging the ratios of intensities of the elements (Ca/Si and Mg/Si) by columns of pixels. Profiles of molar M/S and C/S ratios (Figure 4-7) according to the distance from the exposed surface were obtained from the microprobe profiles for the sample degraded for 6 months in a solution with 5 mmol/L of $MgCl_2$.

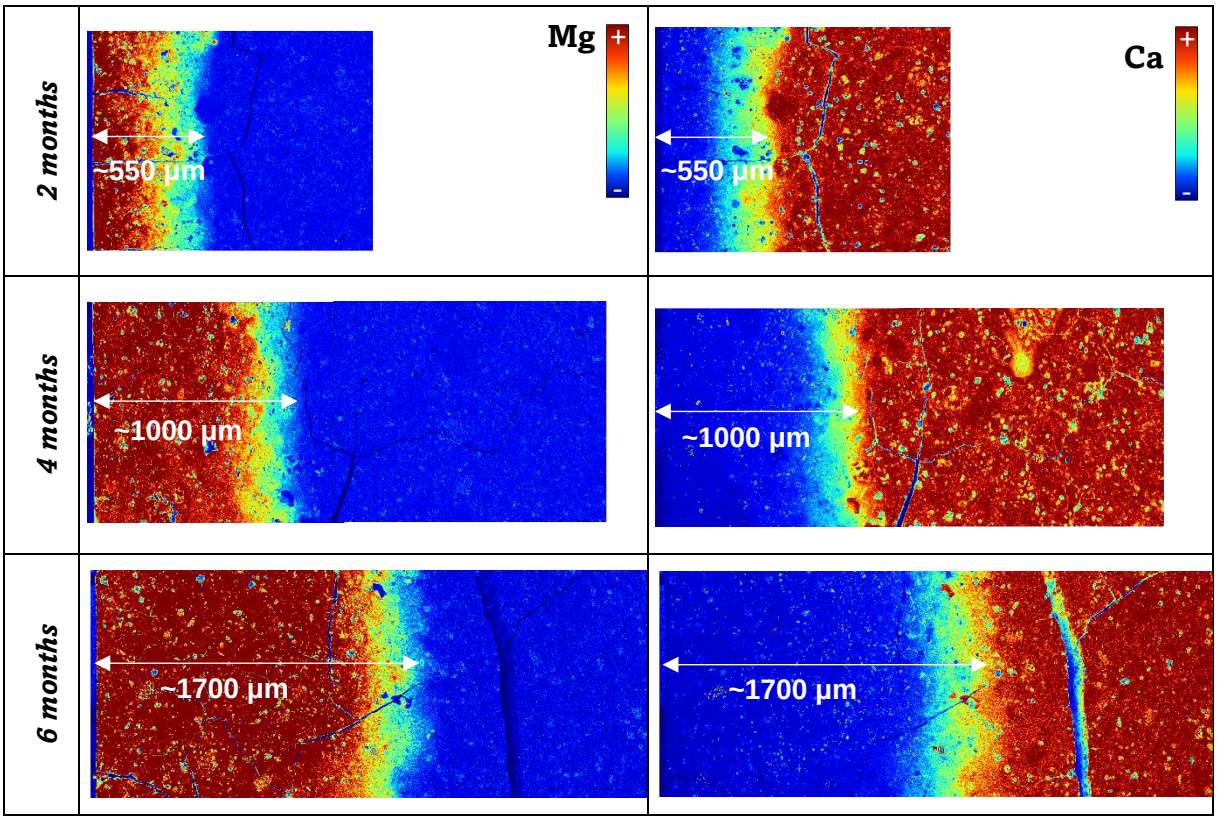

Figure 4-5: Elemental maps (EDS) in calcium and magnesium of a low-pH model cement paste placed in a solution with [$MgCl_2$] = 5 mmol/L for 2, 4 or 6 months

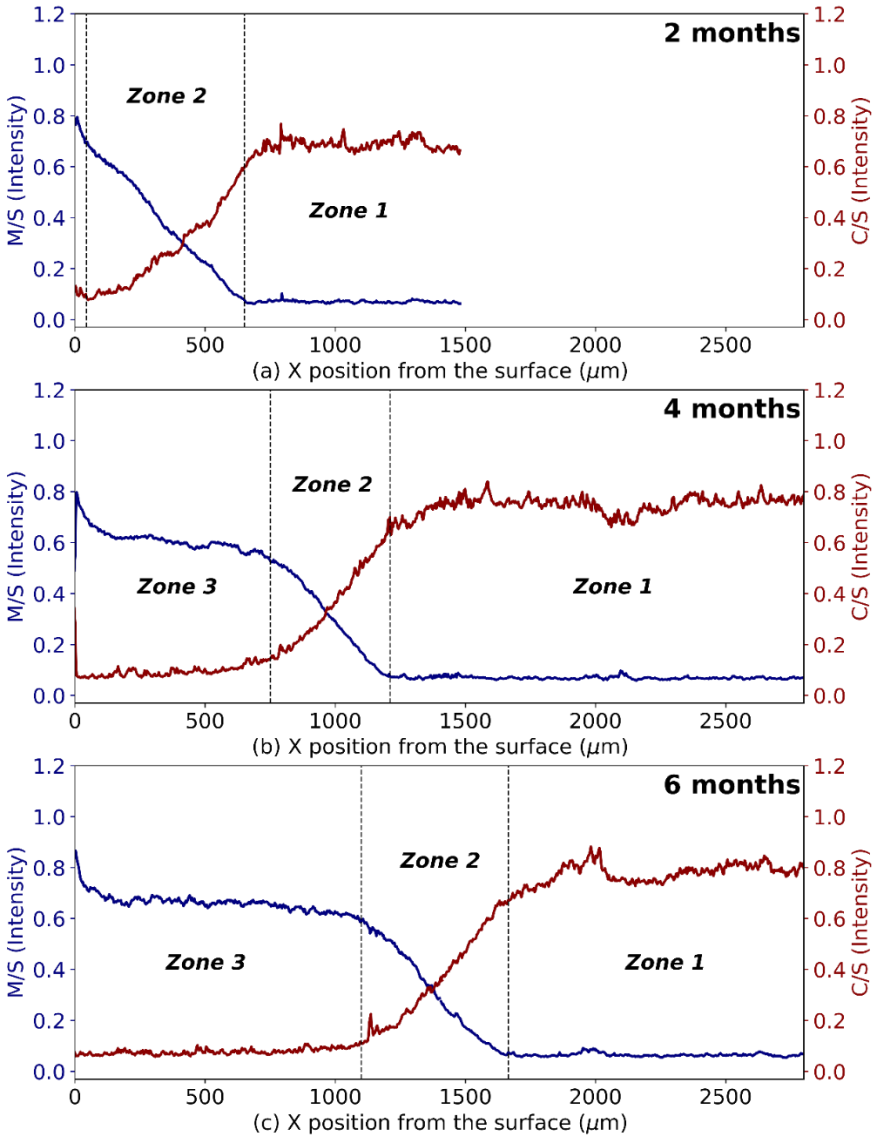

Figure 4-6: M/S and C/S intensity ratios calculated from solid chemical composition (EDS) of a low-pH model cement paste immersed in solution with [$MgCl_2$] = 5 mmol/L for 2 months (a), 4 months (b) or 6 months (c) according to the distance to the surface of the specimen

It should be noted that the M/S (Intensity) ratio in the sound zone is about 0.1, whereas the cement used only contains 0.7% MgO (Table 2-5). The intensity associated with a chemical element at a point (x,y) in the material corresponds to the area under the curve of the EDS spectrum at the emission line of the chemical element concerned, acquired at that point (x,y). In order to comment on the value (and not its evolution), it is necessary to refer to quantitative analyses. As these are intensity ratios, the value is not quantitative and needs to be corrected via a quantification method (e.g. Phi-Rho-Z (Packwood et Brown 1981)) which requires the acquisition of controls, not available at the time of testing. In addition, background noise is not subtracted. Thus, the lower the intensity, the more the calculated intensity (from the Gaussian) is impacted by background noise. To discuss quantitative values, a microprobe was made and is shown in Figure 4-7.

A Mg enrichment of the cement paste, in parallel with Ca leaching, appears on EDS maps (Figure 4-5). In the literature, the presence of brucite corresponds to the formation of a Mg-rich external layer while the formation of M-S-H corresponds to an enrichment of the paste (Dauzeres et al.

2016; Jakobsen, De Weerdt, et Geiker 2016; Lerouge et al. 2017). From Figure 4-5 and Figure 4-6, no Mg layer is visible on the surface of the specimens. The Mg enrichment occurs in the paste which is consistent with M-S-H formation. Moreover, the enrichment is progressive within the paste. The depth of the magnesium-enriched zone (Z3) increased with time. For each degradation time, the M/S ratio systematically reaches 0.8 at the surface. Thus, when the maturity is short, the slope of the M/S curve is higher. As the degradation time increases, the M/S reaches a fixed value (0.7) in the middle of zone 3.

Figure 4-7 shows the microprobe results, after correction of the signal with respect to silica. Only the 6 months degraded sample was studied by microprobe. As shown by Bertron (Bertron et al. 2009), the silicon content can be used for the correction method of microprobe data. Quantification by microprobe only analyses the solid. Thus, some of the elements are not quantified (notably H). The results give the quantities of elements, relative to the quantity of solid analysed in the volume of the interaction bulb. Silicon correction, similar to titanium correction, allows to obtain the absolute variation of the specimen's chemical composition in the altered zone. The mass percentages of the oxides presented are therefore corrected against the silicon signal. A smoothing of the data is proposed for future calculations (lines).

Zone 1 corresponding to the sound zone, showed a plateau of C/S at 0.9 and M/S at 0.05. The amount of Mg in the sound zone was negligible, consistent with the content of MgO in the cement (0.70%). The atomic C/S ratio obtained from microprobe analyses is consistent with the theoretical one of the model pastes, the Ca/Si ratio of the mix being 0.94 (section 4.2). Zone 2, corresponding to the transition zone, showed a linear decrease of C/S in conjunction with a linear growth of M/S. In the degraded zone (Z3), the atomic M/S ratio increases slower until it reaches a ratio of 0.8 at the surface. As the surface is approached, the slope of the M/S curve increases, indicating a higher Mg enrichment of the paste in direct contact with the solution. It should be noted that the C/S and M/S ratios correspond to the ratio between all the calcium or magnesium and all the silicon present in the solid phase, which can therefore correspond to a mixture of several species (amorphous silica, M-S-H etc.). In the literature, the stable M-S-H with the lowest M/S ratio is 0.78 [4]. The values obtained in the degraded zone require further discussion depending on the mineralogy observed in XRD (Figure 4-8).

The Al signal remained constant along the degradation (Figure 4-7). Since the Al signal does not drop in the degraded area, this means that there are solid phases that capture the Al released from the dissolved ettringite and that this may be a Mg-Al phase, or an incorporation of Al into the silica gel and/or MSH. This will be discussed in section 4.3.3 and 4.5.2 on the basis of stoichiometric considerations, literature data and XRD results.

No enrichment in chloride and no variation in Fe content was observed (Figure 4-4 for Fe and Figure B-2 in Appendix B for Cl). Therefore, chloride does not seem to bind to the matrix (as will be confirmed by XRD).

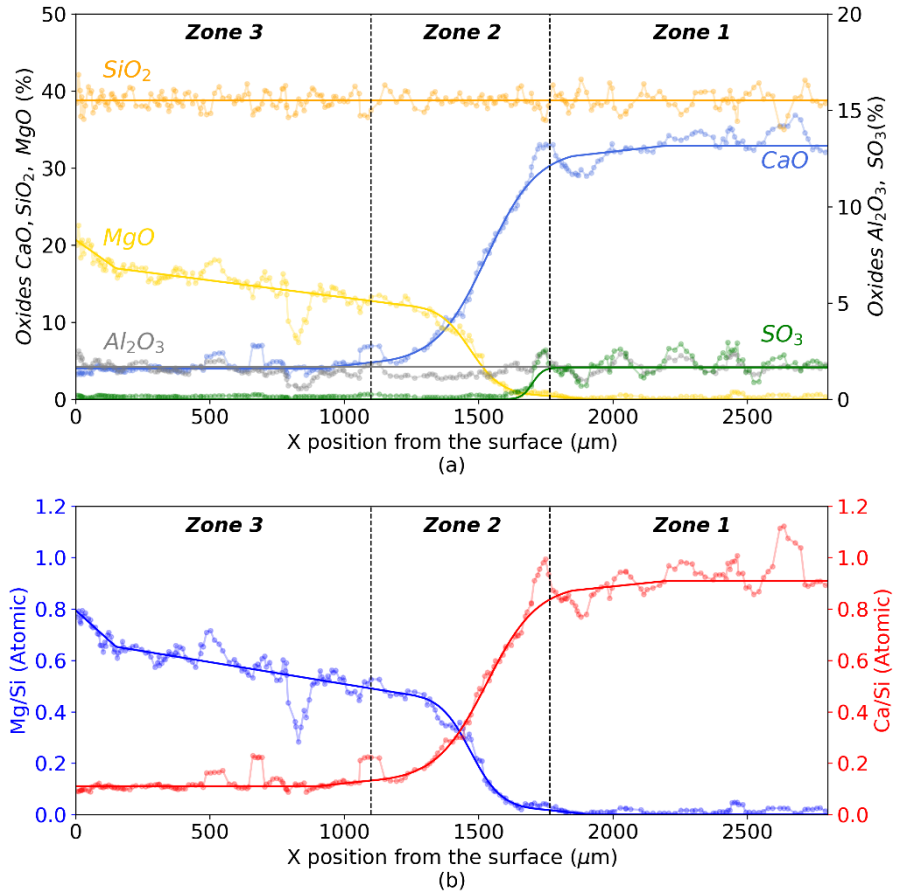

Figure 4-7: (a) Chemical composition of oxides of a low-pH model cement paste, immersed in solution with [$MgCl_2$]=5 mmol/L for 6 months according to the distance to the surface of the specimen (analysis by electron microprobe, corrected), (b) M/S and C/S atomic ratios calculated from (a). The lines represent an approximation of the signal for future calculations.

4.3.3. Mineralogy of the magnesium enriched zone

The mineralogical composition of the paste as a function of distance from the surface exposed to the $MgCl_2$ solution was characterized by XRD (Figure 4-8). The indexing of the X-ray peaks for the C-S-H (green circles) and M-S-H (red triangles) phases is based on (Bernard et al. 2018).

Three zones can be defined according to their mineralogical composition, the location of the limits between these zones changing as the reaction progresses. (i) In the sound zone, the paste is mostly composed of C-S-H and some ettringite. No peaks associated with portlandite is visible, consistent with the sound paste (4.2). (ii) In the intermediate zone, M-S-H and C-S-H coexist. (iii) In the outer zone, X-Ray diffractograms display only the humps associated with M-S-H. No brucite was detected in this zone.

It should be noted that the distances to the surface in Figure 4-8 were measured with a digital measuring device to an accuracy of 0.001 mm at one point in the material and only give an indication of the actual distance because the material abrasion was carried out by hand. Thus, the XRD observations are to be compared with the EDS and microprobe observations. For example, the beginning of the sound zone will be considered as the place where the sulphur and calcium signal reaches its maximum value.

By linking the EDS, microprobe and XRD results, it appears that the three zones observed in XRD corresponds quite well to the zones observed in EDS. The sound zone, composed of C-S-H and ettringite, corresponds well to zone 1 in EDS (Z1 Figure 4-6). The intermediate zone, composed of C-S-H and M-S-H, coincides with the transition zone in EDS (Z2 Figure 4-6). Finally, the Mg-enriched zone, consisting of M-S-H corresponds to zone 3 in EDS (Z3 Figure 4-6). For the 4-month degraded sample, the intermediate zone consisting of M-S-H and C-S-H seems to start earlier in XRD than in EDS. Indeed, the linear increase of Ca and the linear decrease of Mg in EDS (750 µm) start later than the appearance of the first C-S-H signals (170 µm). This difference could be explained by a soft increase of the Ca signal not considered in the definition of zone 2 in EDS. Even if the amount of calcium does not increase significantly, if the threshold value of Ca concentration in solution is exceeded, C-S-H might be present. In conclusion, the degraded zone corresponds to the formation of M-S-H in parallel with the decalcification of C-S-H. Over time, the mineralogy of zone 3 remained the same. The diffractograms at the surface of the degraded samples are similar for all three time periods. Only the depth of degradation increases.

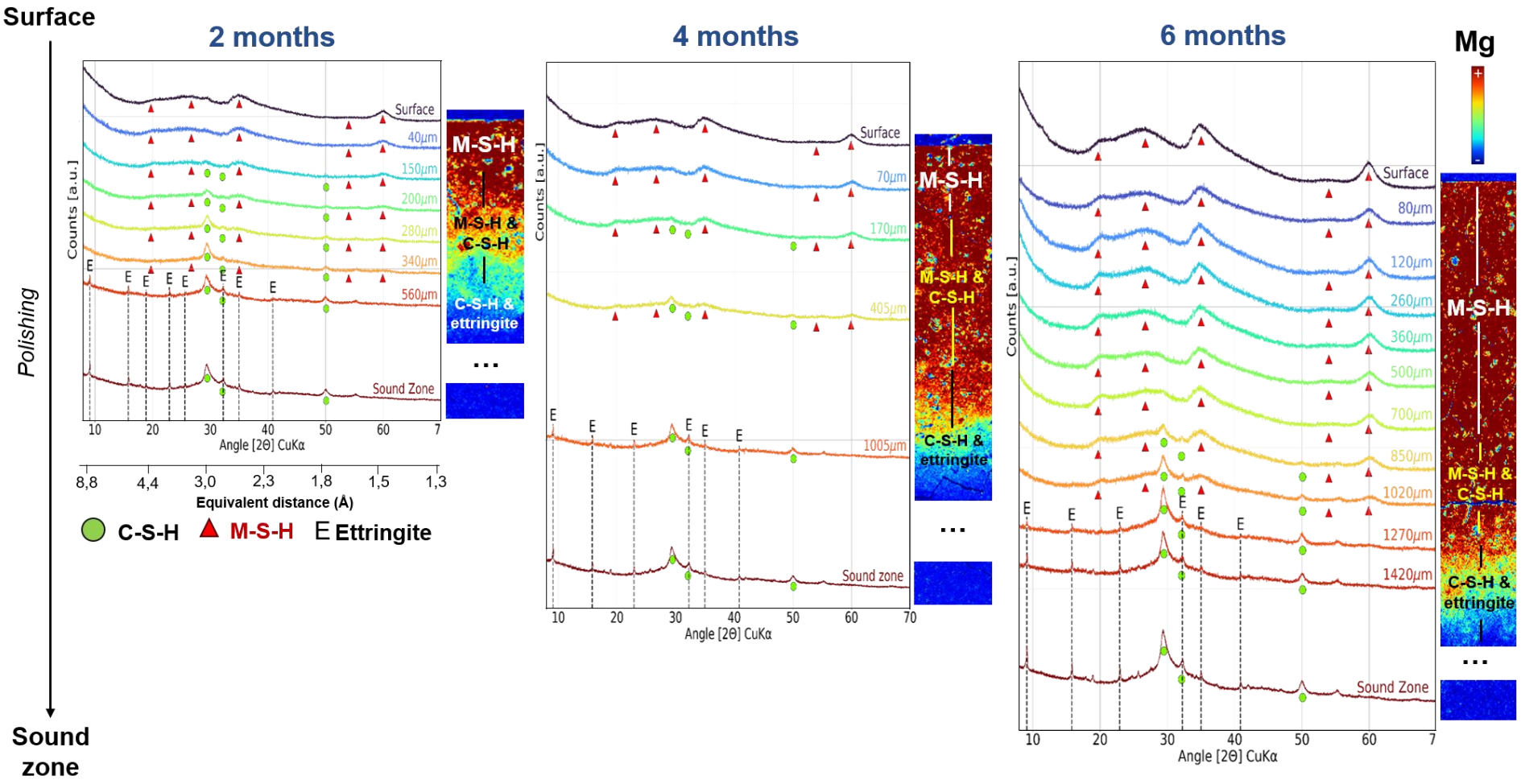

Figure 4-8: X-Ray diffractograms along the degradation of a low-pH model cement paste placed in a solution with [MgCl2] = 5 mmol/L for 2, 4 and 6 months associated to EDS maps.

Figure 4-9 proposes a diagram summarizing the degraded and intermediate thicknesses and the mineralogical phases present in each zone bases on EDS and XRD characterizations (Figure 4-6 and Figure 4-8). The mineralogical phases displayed in each zone are the majority phases. C-S-H may be present in small quantities in the degraded zone (Z3), close to the transition zone (Z2).

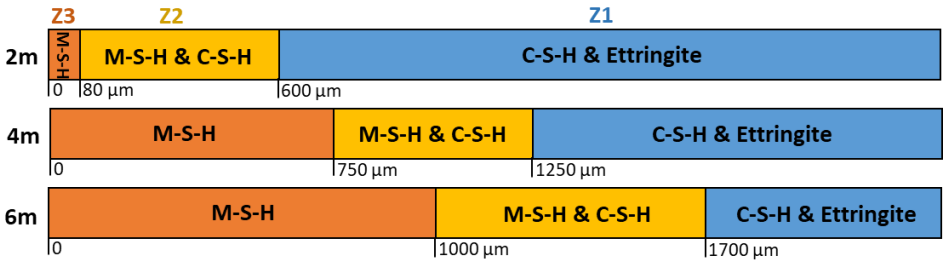

Figure 4-9: Schematic representation of the chemistry of the degraded samples issued from XRD and EDS analyses

At the surface of the 6-month degraded sample, the microprobe shows an M/S ratio of 0.78 consistent with the possible stoichiometries of M-S-H according to Bernard (Bernard et al. 2018; Bernard, Dauzères, et Lothenbach 2018b). The Mg signal decreases not only within zone 2 but also along zone 3. In zone 3, no C-S-H is detected in XRD. As the M/S ratio is less than 0.78 - the lowest M/S ratio to guarantee M-S-H stability - the presence of an amorphous siliceous solid phase not detected by x-ray seems likely, as in pure leaching (Bes 2019).

In addition, the microprobe reveals calcium in the degraded area. As the microprobe detects only the elements contained in the solid, this indicates that calcium remained in the solid phase and raised questions about the integration of calcium in the solid phases. The C/S molar ratio measured in microprobe reaches 0.1 (Figure 4-7). The calcium would therefore be in the M-S-H and/or in the amorphous siliceous phase. In the literature (Brew et Glasser 2005b; Bernard et al. 2018; Bernard, Dauzères, et Lothenbach 2018b), it is admitted that calcium can be integrated in M-S-H in small quantities (M-C-S-H with M/S=0.78 and C/S=0.05 up to 0.1). Bes observed, during pure leaching of a cementitious paste, Ca in the amorphous silica with a C/S≈0.1 ratio (Bes 2019).

As the microprobe is quantitative, it is possible to perform stoichiometric calculations to see if there are any assumptions that explain this solid calcium. First the quantity of M-S-H is calculated from the amount of magnesium. Then, the silicon remaining is considered to correspond to amorphous silica (AS). The silica signal increased when approaching the transition zone (Z2). It is coherent with the phenomenon of dissolution-precipitation where a dissolution on C-S-H is expected, creating a Si gel before the precipitation of M-S-H thanks to the Mg diffusion (Dauzeres et al. 2016; Jakobsen, De Weerdt, et Geiker 2016; Lerouge et al. 2017). The following calculations are performed in the first 900 microns:

$$n_{MSH} = \frac{n_{Mg}}{0.78} \quad (4\text{-}1)$$

$$n_{AS} = n_{Si} - n_{MSH} \quad (4\text{-}2)$$

With n_{MSH} and n_{AS} the quantities of M-S-H and amorphous silica respectively, n_{Mg} and n_{Si} the quantities of Mg and Si determined from microprobe respectively.

Figure 4-10a shows the results of the stoichiometric calculations performed. Several assumptions for the incorporation of calcium into the two solid phases (M-S-H and amorphous silica) were tested and are illustrated in Figure 4-10b. The figure shows the amount of calcium remaining after the incorporation hypothesis considered. The four assumptions are as follows:

- H1: no incorporation of calcium in either M-S-H or amorphous silica.
- H2: incorporation of calcium into M-S-H only, at C/S_{MSH}=0.05.
- H3: incorporation of calcium at C/S_{MSH}=0.05 and C/S_{AS}=0.1 in M-S-H and amorphous silica respectively.
- H4: incorporation of calcium at C/S_{MSH}=0.11 and C/S_{AS}=0.11 in M-S-H and amorphous silica respectively.

The amount of remaining calcium ($Ca_{remaining}$) is calculated according to the equation:

$$Ca_{remaining} = n_{Ca} - \frac{C}{S_{MSH}} * n_{MSH} - \frac{C}{S_{AS}} * n_{AS} \quad (4\text{-}3)$$

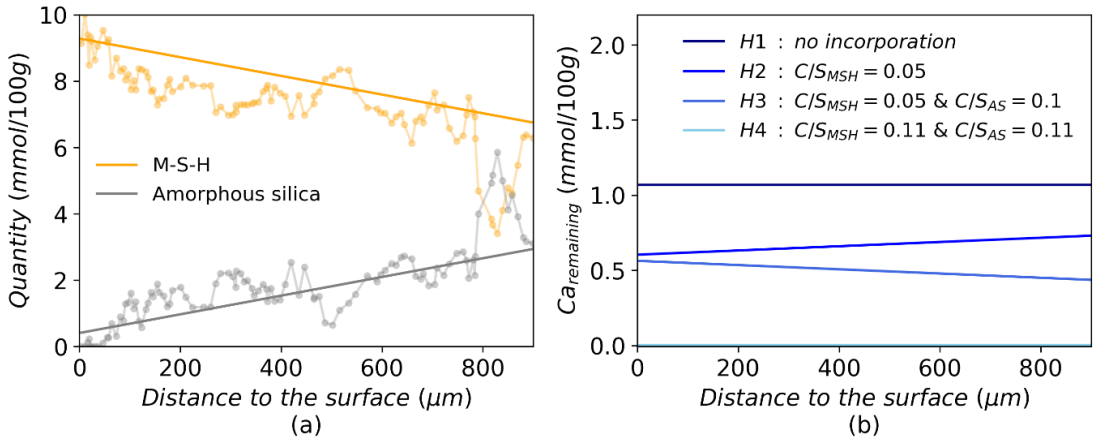

Figure 4-10: Simulation of the quantities of M-S-H and amorphous silica (a) and the remaining amounts of Ca following four hypothesis of Ca incorporation (H1, H2, H3 and H4)

In the case of the first three assumptions, unintegrated calcium remained (Figure 4-10b). Only the last case (H4), where the C/S in M-S-H and amorphous silica is increased to 0.11, allow to integrate all the calcium. Thus, it appears that the M-S-H formed contains some calcium, as does the amorphous silica.

The signal of aluminium remained stable in zone 3 in microprobe, indicating that this element also remained in the solid phase. As no aluminium-based phases are detected in XRD in the degraded area, this means either that aluminium phases are present in too small quantities to be detected by XRD, or that the aluminium is incorporated in an amorphous phase (silica gel, CSH and/or M-S-H). It is accepted that M-S-H, like C-S-H, can incorporate aluminium ions (Bernard et al. 2020). The formation of a silico aluminous gel can also explain the presence of aluminium ions (Roosz et al. 2022). Another possibility is the formation of hydrotalcite ($Mg_6Al_2CO_3(OH)_{16}{\cdot}4H_2O$). Hydrotalcite is a magnesium phase which has also been observed with M-S-H during magnesium attack of cement pastes (Codina et al. 2008; Jenni et al. 2014; Kobayashi, Takahashi, et Kawabata 2021). If the hydrotalcite is embedded in the M-S-H, its XRD signal could be so weak compared to that of the M-S-H that its contribution could be considered as noise. A weak bulge, which could correspond to hydrotalcite, can be observed on the sample degraded for 6 months around 11 [2θ] CuKα (Wiyantoko et al. 2015).

In conclusion, the contact between a $MgCl_2$ solution and the model cement paste created a magnesium enrichment of the paste, characterized by the formation of M-S-H, associated with a decalcification of C-S-H and a leaching in sulphur. Aluminium didn't leach out, but the sound paste

didn't contain much aluminium (3.6% of the cement, Table 4-1). The degraded depth was consequent (2 mm) after 6 months making possible the microstructural and mechanical characterization of M-S-H formed within a magnesium paste, without disturbance of other mineralogical species.

4.3.4. Microstructural properties

4.3.4.1. Cracking pattern of degraded sample in contact with partially dried atmosphere

As soon as the degraded samples dried, by any process (natural drying, vacuum drying, freeze drying, etc.), cracks were formed at the boundary between the degraded and the sound zone, as well as perpendicularly to the attacked surface, within the degraded zone. To study this phenomenon, its kinetics and to see if it was due to the material rather than to the presence of M-S-H, a follow-up (visual) cracking test upon exposure of the samples to the air, with high quality photos taken at regular intervals was carried out on the samples placed in $MgCl_2$ solutions (5 mM and 50 mM) (see Appendix B, Figure B-5 for an illustration of the technique).

Figure 4-11 shows the results for a sample placed 9 months in the 5 mM solution. Initially, the surface is wet because it has just come out of the parafilm in which the section was stored. The test was carried out in two different axes, from the front and from the side (see Appendix B, Figure B-5 for illustration of the method). The test was first carried out from the front, keeping the opposite side in parafilm, and then the section was cut to carry out the profile test. In the profile photos (top right of each image), the left side is the previously dried side and is therefore already cracked and very clear. The side to be observed is the one on the right. When the degraded area dries, it becomes lighter. The photos show that the first cracks appeared very quickly. As early as 1', cracks appeared at the bottom of the section (front view). The cracks propagated and then became denser. After 3 hours, the cracks opened more and more and after 8 hours, the degraded area had no cohesion. This could be due to the high intrinsic porosity of the M-S-H (Chapter 3) and/or to the juxtaposition of two zones (sound zone and degraded zone) with very different chemical, microstructural and mechanical properties.

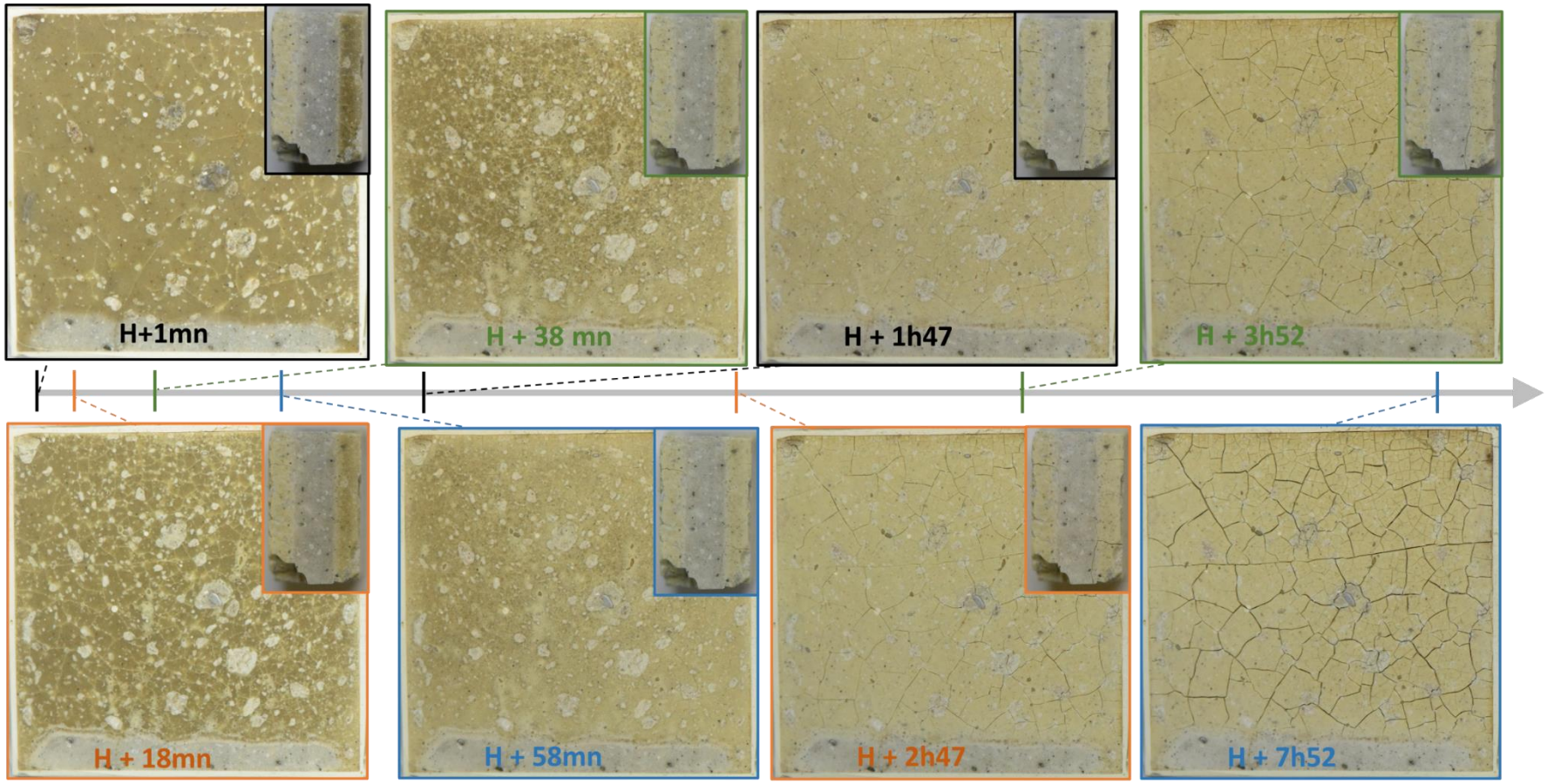

Figure 4-11: Follow-up (visual) cracking test during exposure to a controlled atmosphere (20°C, RH=50%) on the samples placed in 5 mM $MgCl_2$ solution during 9 months (H is the moment of the sample removal from the solution and exposition to laboratory controlled atmosphere)

4.3.4.2. Microstructural mapping

The microstructure of the samples along the degradation was studied by micro-tomography. The tests were performed only on the 6-month degraded sample (Figure 4-4-middle and Figure 4-13).

The micro-tomography analysis of degraded samples gives access, after reconstruction and choice of a Region of Interest (ROI), to a 3D image of the signal intensity variation in the sample (Figure 4-12). The reconstruction is based on the assembly of 2D planes acquired by the system while the sample is rotating. The 2D image proposed in Figure 4-4, corresponds to a section of the 3D volume, considered after data analysis as representative of the sample. To realize a 1D density profile (Figure 4-13), the intensity is averaged on each plane parallel to the surface exposed to the $MgCl_2$ solution. As the intensity is linked to the density of the sample, to obtain a normalized density, the highest point of the curve is considered as the base value and the average of each plane is divided by this value.

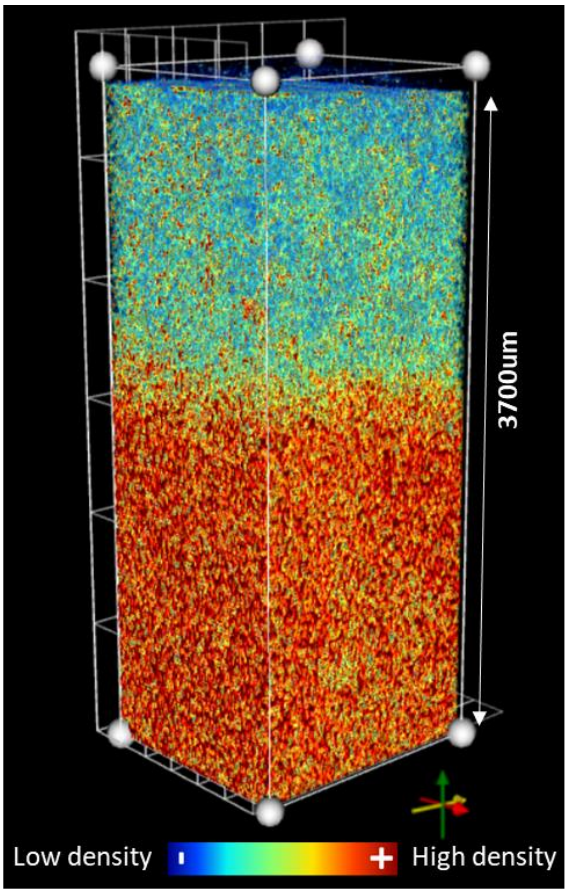

Figure 4-12: 3D visualisation of the density after micro-tomography measurements for CEM I paste with colloidal silica, immersed in solution with [$MgCl_2$] = 5 mmol/L for 6 months

As the density is inversely proportional to the porosity, the analyses indicate that the degraded zone is more porous than the sound zone. This increase of porosity could be due to the calcium leaching that takes place in parallel with the magnesium enrichment (Figure 4-6). The decalcification of solid paste (Figure 4-6 and Figure 4-7) is known to induce porosity increase (Carde et François 1999; Wan et al. 2013; Kamali et al. 2004) but the magnesium enrichment observed seems to allow the formation of one or more phases that could compensate the increase. This compensation is not observed here so the high porosity in the degraded zone could be due to higher intrinsic porosity of the magnesium formed phases (or lower density) than that of the C-

S-H and ettringite. If they are M-S-H, it would be possible that like the C-S-H, low density M-S-H exist and that in this configuration it is the low density M-S-H that predominates.

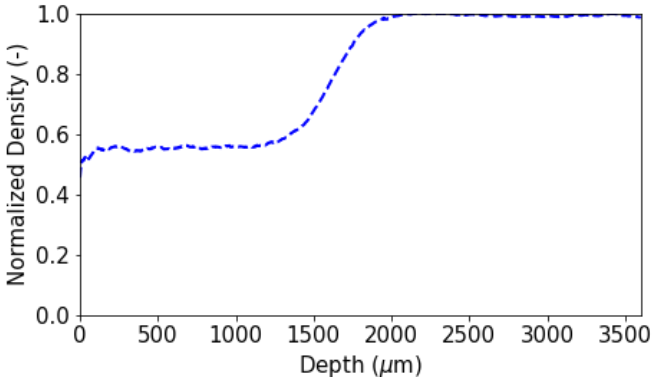

Figure 4-13: Density profile of the degraded sample after micro-tomography characterization

4.3.4.3. Pore characterization of the magnesium enriched zone

The characterization was carried out on the degraded zone by taking and polishing pieces of samples between 0 and 1700 µm degraded for 6 months, corresponding to zone 2 and 3 (Figure 2-5). The microstructure at low scale had been studied by N_2 Physisorption (Table 4-6and Figure 4-14). Results will be compared to those of M-S-H pastes produced and characterized previously (see Chapter 3).

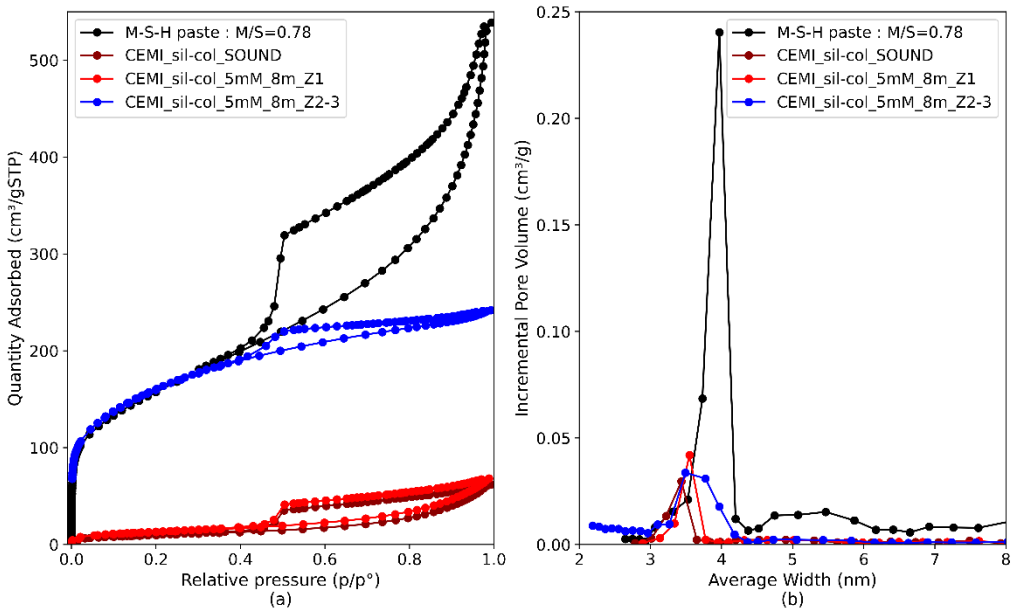

Figure 4-14 : (a) N_2 adsorption-desorption isotherms of the sound zone and degraded zone, compared to a pure M-S-H paste (M/S=0.78) (Dewitte et al. 2022) and (b) Associated pore size distributions (BJH). Z1 = Zone 1 (sound zone) of the degraded paste, Z2-3 = Assembly of zones 2 and 3 (enriched in Mg) of the degraded paste

Table 4-6 : Average Specific Surface B.E.T (m^2/g) determined by N_2 Physisorption of the sound model cement paste, a degraded sample and a M-S-H paste (see Chapter 3)

Type of sample	Sound model cement paste	Degraded model cement paste		M-S-H paste, M/S=0.78
Zone	-	Sound Zone (Z1)	Surface (Z2-Z3)	-
Average Specific Surface B.E.T (m^2/g)	36.2	53.2	571.1	562.9

Figure 4-14a shows that the degraded zone (Z2-Z3 EDS – light blue curves) had a much higher specific surface area (Table 4-6) and a higher adsorbed amount (Figure 4-14) than the sound zone (red curves), indicating a higher porosity and confirming the observations made in micro-tomography and autoradiography. The sound part of the sample had similar properties to the sound sample (both BJH and isotherms). The specific surface of the sound sample is lower than the one of the sound zone (Z1) of the degraded sample. Such a difference could be due to (i) the presence of a small part of Z2-Z3 in Z1, (ii) the increased hydration of the degraded sample in the sound zone (during degradation, the sample is saturated, and it can allow further hydration in the sound zone resulting in the formation of more C-S-H gel with an intrinsic porosity – d<10nm) (see section 4.4.3.1 for more detailed discussion). The value remains of the same order of magnitude and the shape of the BJH and the isotherm validate the preparation of the samples. The degraded zone (Surface, Z2-Z3) had, at small scale (p/p_0<0.4), similar properties to the M-S-H pastes (same specific surface, similar isotherm curve at the beginning). For higher p/p_0 (p/p_0>0.4), the M-S-H paste showed a larger porosity (a divergence of the sorption/desorption isotherm) than the surface of the degraded model cement paste (Z2-Z3). This could be related to the higher w/b of the M-S-H paste (1.1 vs 0.65) and/or the presence of other phases resulting from the degradation in the degraded zone (amorphous silica for example). The peak in BJH for the degraded sample wasn't placed at the exact same location as for M-S-H pastes. The peak broadened and extended from its initial position (sound sample, 3.5 nm) to the position of the peak observed on the M-S-H pastes (4 nm). This could be caused by the presence of part of the transition zone (Z2) in the "Surface" sample (Z2-Z3).

In conclusion, the degraded zone - enriched in Mg, was well constituted of M-S-H, showing an increased porosity compared to the sound zone, despite the formation of M-S-H. The microstructural properties observed in the Mg-enriched zone at low scale (p/p_0), showed similarities with those of synthetic M-S-H pastes.

4.3.5. Elastic properties mapping

To study the mechanical properties of the material according to the degradation, it was necessary to have a sufficiently enriched thickness (>1000 µm). Thus, only the samples degraded for 6 months were characterized. Figure 4-15 shows the indentation grids performed on the degraded sample for 6 months (the yellow box corresponds to a 4x4 indent on a 1.2x1.2 mm^2 zone), the associated Mg EDS maps (a) and the mechanical results (b). The phenomenon of cracking (see 4.3.4.1) when exposed to air makes this characterisation difficult (indentation in the room's environment, therefore "drying").

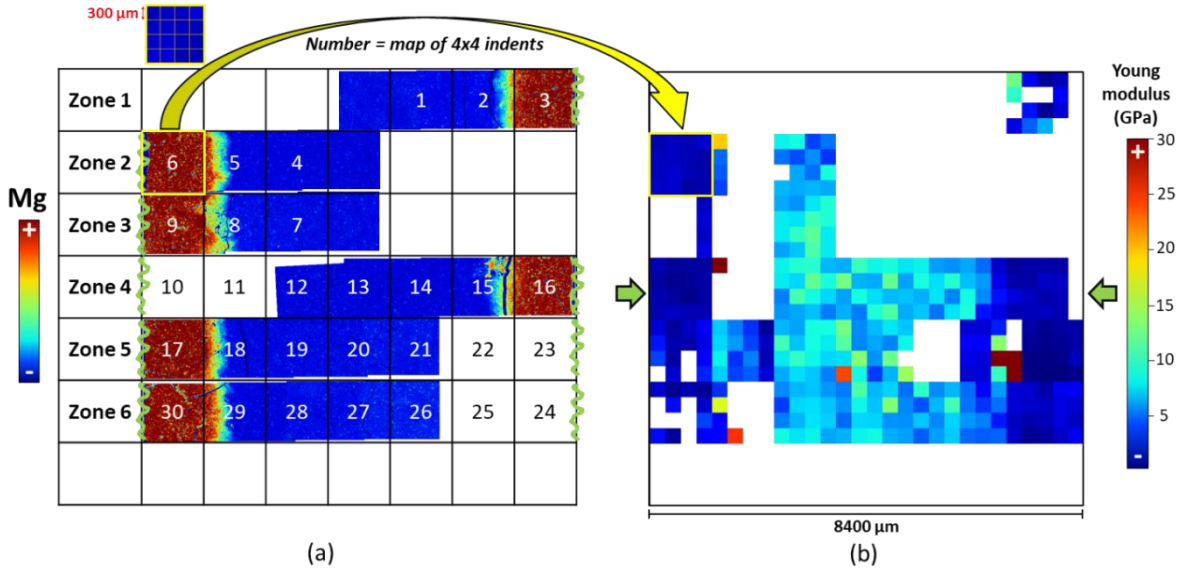

Figure 4-15: 2D illustration of the microindentation data, (a) Localisation of 4x4 indents grids on Mg EDS Maps and (b) Young Modulus results (GPa)

As shown on Figure 4-15 some indents, performed on zones 3, 5, 9, 10, 16, 17, 22, 23, 30, 29, did not yield results. This is due to several factors:

- To the surface not being quite flat. Because of the shrinkage phenomenon that creates an overhang on one of the two sides during cracking, the indenter may not succeed in reaching the sample, arriving at the end of the piston (no curve). Figure 4-16 presents an example of a degraded zone in SEM. The location of the indents made in this zone have been marked with green crosses. The difference in level of the surface is visible by the difference in brightness. Furthermore, due to the fragility of the sample, with the impregnation protocol used, it was not possible to polish the sample for a long time and finely without losing material and polluting the polishing sheet. The material remains on the sheet and causes scratches to the sample.
- To the high porosity. Depending on where the Adjustment Depth Offset (ADO) is made, i.e. where the distance between the sample and the indenter is initially measured, the measuring point can be either much lower than the standard or much higher. In the first case, the piston reaches the end of its stroke (no curve). In the second case, the contact point is not good, the curve becomes unusable (non-linear curve). To limit these effects, an approach distance to the indenter is defined. The indenter then goes up higher than what the ADO recommends. As this adds a lot of time to the measurement, it is necessary to find an optimum and there are still some points that cannot be measured.
- to the weak properties of the sample. The sample can fracture at the point where the indenter presses during the measurement, resulting in a non-evaluable curve (stall and stop of the measurement).

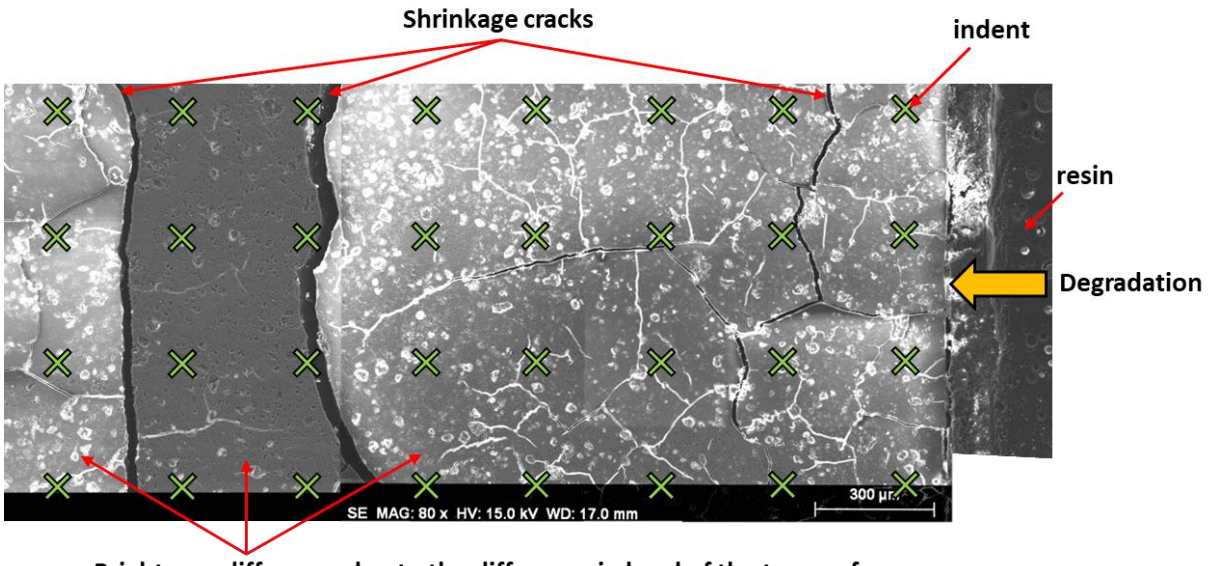

Figure 4-16: SEM Image of the degraded sample and the associated location of indents (Green crosses)

Moreover, it appears on the 2D representation of the results (Figure 4-15b) that there are outliers. Figure 4-4 (bottom) shows the brut data obtained along the degradation while Figure 4-17 shows the results after removing the outliers. Outliers were excluded using the interquartile range method (see 4.2 – Mechanical properties). The dispersion of the data is displayed via the mean, the median and the standard deviation (greyed beam) on Figure 4-17. The upper part of the figure shows the number of points kept for each x-position.

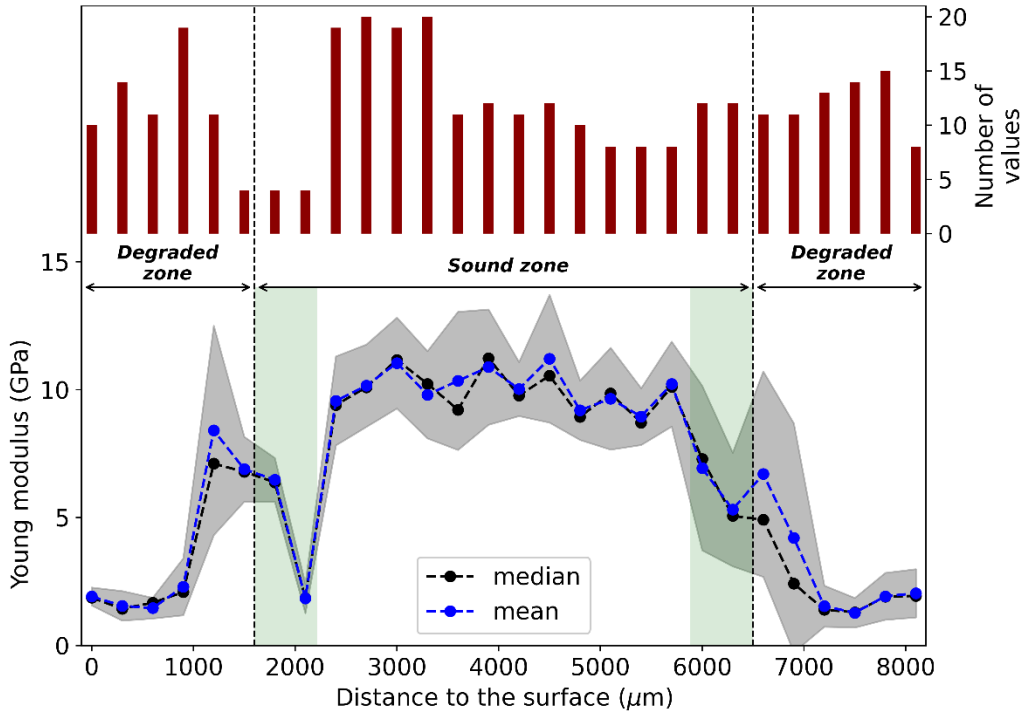

Figure 4-17: Microindentation data without outliers, cracking zones are underlined in green

The sound zone (Z1) had mechanical properties similar to those of the sound sample. In the degraded zone, the mechanical properties were greatly diminished. The green areas on the graph correspond to the areas where cracks appeared, implying a sharp drop in Young's modulus. The cracking of the sample implied the elevation of one side of the sample and an extended disturbed area (see 2.1.3.1). The number of points where the results were valid in the left cracking zone (zones 5, 8, 11, 18 and 29 on figure 11 - 1600<x<2200 µm) were indeed much lower than in the other locations and cannot be considered as representative (while 20 indents were performed, only about 4 were successful).

The decrease in Young's modulus was progressive before reaching a plateau around 3 GPa towards the surface and follows the trend of Ca and Mg profiles in the paste observed by micropobe and EDS at the same degradation time.

The E_{deg}/E_{sound} is equal to 16%. In pure leaching, for low-pH cementitious pastes with w/b=0.5, the macroscopic E/E_{sound} ratio is about 38% after 90 days of pure leaching (Bes 2019). According to Bes' homogenization work, this gives a E_{deg}/E_{sound} ratio of 10%. The macroscopic Young's modulus (E) corresponds to the properties measured by macroscopic compression test on the whole degraded sample, while E_{sound} corresponds to that of the sound sample. E_{deg} corresponds to the mechanical properties of the degraded area only, obtained by homogenisation (Bes 2019). The loss of modulus observed in the case of magnesium attack of our model paste is thus similar to that of pure leaching on a low-pH cementitious paste. It seems that the formation of M-S-H does not compensate for the loss of properties due to leaching.

In conclusion, the model pastes showed a homogeneous magnesium enrichment of the cement paste associated with calcium and sulphur leaching. This Mg enriched and Ca and S leached zone had a lower density, a higher porosity and much lower mechanical properties than the sound zone.

4.4. Effect of the magnesium concentration on the degradation of low-pH model cement paste

In the previous section, the phenomenology of magnesium attack on a model low-pH paste was studied for a magnesium concentration of 5 mmol/L. Real environments have a magnesium concentration that can vary between 0.05 mmol/L (Rosenqvist et al. 2017) and 50 mmol/L (Jakobsen, De Weerdt, et Geiker 2016). In order to study the impact of magnesium concentration on the magnesium attack of low-pH and low-CO_2 pastes, a study was carried out on the same pastes as above with a magnesium concentration of 50 mmol/L. The multi-physics characterization performed is the same as for the 5 mM degraded samples. A similar figure as for the sample degraded during 6 months in 5 mM (Figure 4-4), with the main techniques, is available for the sample degraded during 6 months in a solution with [$MgCl_2$] =50 mmol/L in Appendix C, Figure C-1.

4.4.1. Influence of the Mg concentration on the mineralogy of degraded samples

The mineralogical composition of the paste as a function of distance from the surface exposed to the $MgCl_2$ solution was characterized by XRD (Figure 4-18 for the 6 months degraded sample and Appendix C, Figure C-3 for other). As for the 5 mM, the magnesium attack leads to the formation of M-S-H. The same 3 zones can be defined:

- **A sound zone**. The paste is mostly composed of C-S-H and some ettringite. No peaks associated with portlandite are visible, consistent with the purpose of the model paste.
- **A transition zone**. The results show a coexistence of signals associated with M-S-H and C-S-H.
- **A Mg enriched zone**. X-Ray diffractograms displays only the humps associated with M-S-H, like those obtained on the synthetic M-S-H. No brucite was detected.

The only difference in mineralogy with 5 mM samples observed is the appearance of peaks on the surface diffractogram. A very weak signal (at 11 and 22 [2θ] CuKα or 8.0 Å and 4.0 Å) can be observed and would correspond to the presence of hydrotalcite ($Mg_6Al_2CO_3(OH)_{16}{\cdot}4H_2O$) or a magnesium oxychloride ($Mg_2(OH)_3Cl.4H_2O$) in very small quantities (see 2.2.4). The increase in $MgCl_2$ concentration from 5 mM to 50 mM could be the reason for the appearance of the species.

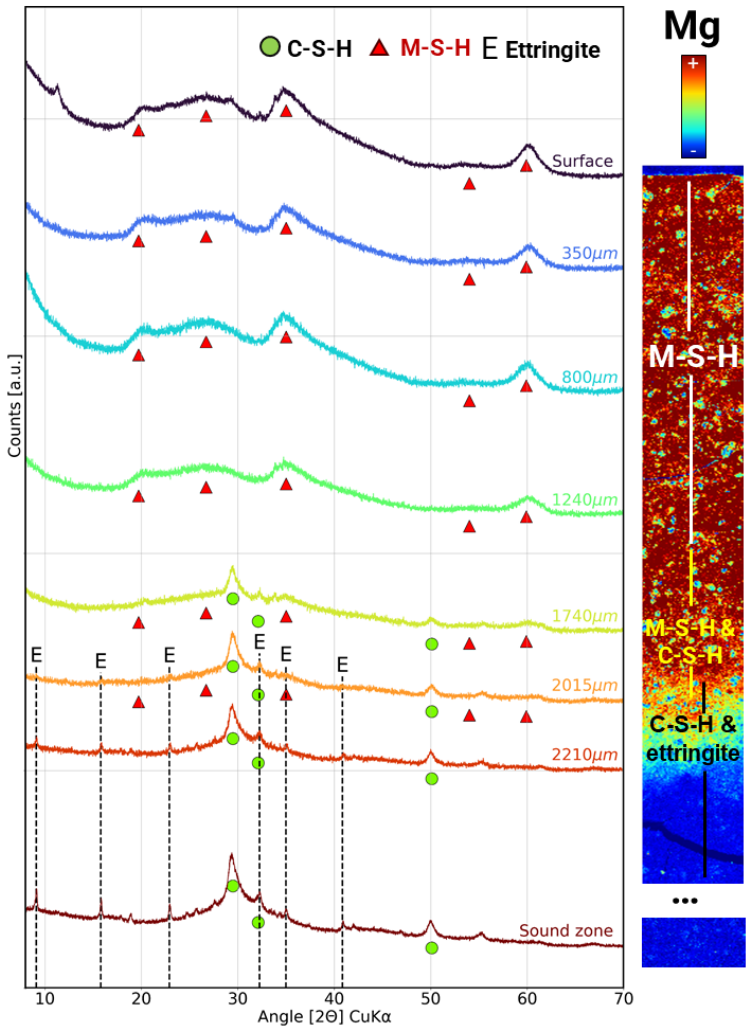

Figure 4-18: X-Ray diffractograms along the degradation of a CEMI paste with colloidal silica placed in a solution with [$MgCl_2$] = 50 mmol/L for 6 months associated to Mg EDS maps.

^{29}Si MAS NMR has been achieved on the 5 mM and 50 mM degraded samples (during 9 and 11 months respectively). As for N2 Physisorption, the degraded samples were separated in two parts: the degraded zone (equivalent to Z2-3 in EDS) and the sound zone (Z1). The results are presented on Figure 4-19. The ^{29}Si MAS NMR spectra of the M-S-H paste with M/S=0.78 (E) (see Chapter 3) has been added to compare.

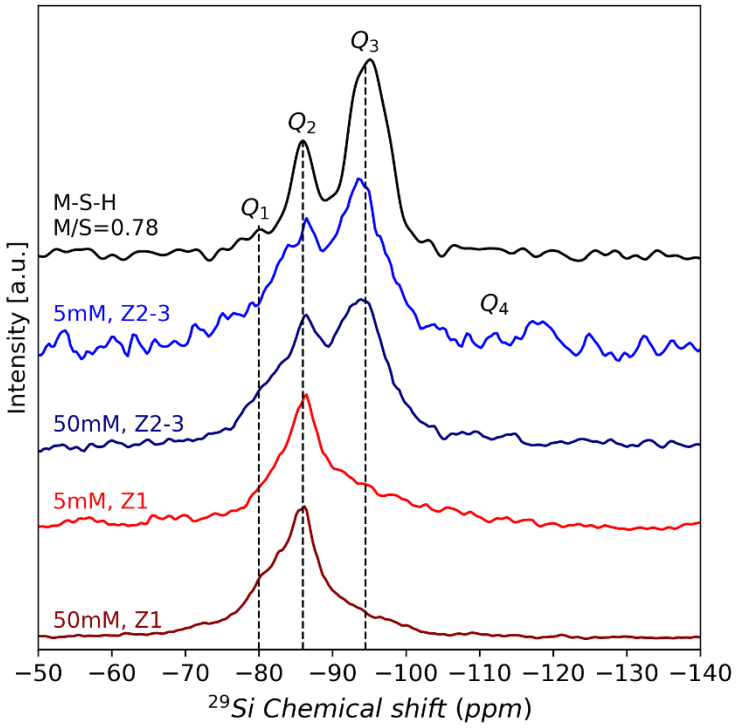

Figure 4-19: ^{29}Si MAS NMR spectra of the zones 1 and zones 2-3 of the samples degraded at 5 mM and 50 mM (during 9 and 11 months respectively) compared to ^{29}Si MAS NMR spectra of M-S-H pastes (M/S=0.78)

First, the spectra of the samples degraded at 5 mM or 50 mM are similar. In the sound zone, the main peak is Q_2, consistent with the dreiketten form of C-S-H (Klur et al. 1998). It is accompanied by Q_1 and Q_3 peaks. Q_1 corresponds to the end-chain tetrahedra of C-S-H while Q_2 corresponds to the in-chain tetrahedra and Q_3 to bonding in the interlayer space of the silica chains. Because the C/S is low, the intensity of Q_2 regarding Q_1 is high. The chain is longer when C/S increase. There appears to be no Q_4, so no unconsumed amorphous silica in the sound zone.

In the degraded zone (Z2-3), 4 peaks appear. The most important one is associated with Q_3. As shown at the top of Figure 4-19, in M-S-H the most important peak is of the Q_3 type because of its sheet-like structure (Bernard et al. 2017b). The predominance of this peak in the degraded area, where XRD confirmed the presence of M-S-H, validates the sheet structure of M-S-H formed by degradation. The higher intensity of peaks Q_1 and Q_2 than for the M-S-H paste is due to the residual presence of C-S-H in the transition zone (Z2). Finally, a hump in the Q_4 area is visible. It corresponds to the presence of amorphous silica (Klur et al. 1998; Bernard et al. 2017b). Thus, NMR shows that magnesium attack at 5 mM and 50 mM of $MgCl_2$ results not only in the formation of M-S-H but also in the formation of amorphous silica, which is difficult to observe in XRD when there are M-S-H because the humps are located at the same place.

In conclusion, the mineralogy is similar for degradation at 5 or 50 mM $MgCl_2$. In the degraded zone, ettringite and C-S-H dissolve and M-S-H and amorphous silica are formed. At 50 mM, it is possible that hydrotalcite is formed in addition to M-S-H.

4.4.2. Effect of the Mg concentration on the progression of the reaction

Microprobe has been performed on the sample placed 6 months in the 50 mM $MgCl_2$ solution. The results are similar to that of the sample degraded for 6 months in 5 mM $MgCl_2$ solution (Figure 4-7). A similar Figure as for the 5 mM sample, after correction of the signal with respect to silica, is available in Appendix C, Figure C-5.

A comparison with the M/S and C/S atomic ratios profiles of the 5 mM sample is proposed in Figure 4-20. The degradation zone of the 50 mM sample is 1000 µm deeper than that of the 5 mM. The degradation zone observed with the microprobe is more extensive than that observed by the other techniques (Appendix C, Figure C-1). This may be due to two factors. On the one hand, the degradation is not quite uniform in the degraded section and the microprobe sample is not the same as the EDS/microindentation sample. On the other hand, the microprobe sample, as with the 5 mM, spent three months under resin before being tested, without the water being removed from the sample. Due to the high concentration for the 50 mM $MgCl_2$ sample, it is possible that the Mg concentration in the pore solution remained high enough to continue to diffuse and degrade the material. The C/S measured on the 50 mM sample is overall a bit lower than the one of the 5 mM sample. Within the degraded zone, for the 5 mM sample, the M/S ratio is steadily increasing until the surface while the M/S ratio shows a plateau around 0.6 for the 50 mM. The M/S value reached at the surface is the same (0.75) for both samples and it is likely that for a longer degradation time, if the front extends, the M/S ratio also plateaus for the 5 mM.

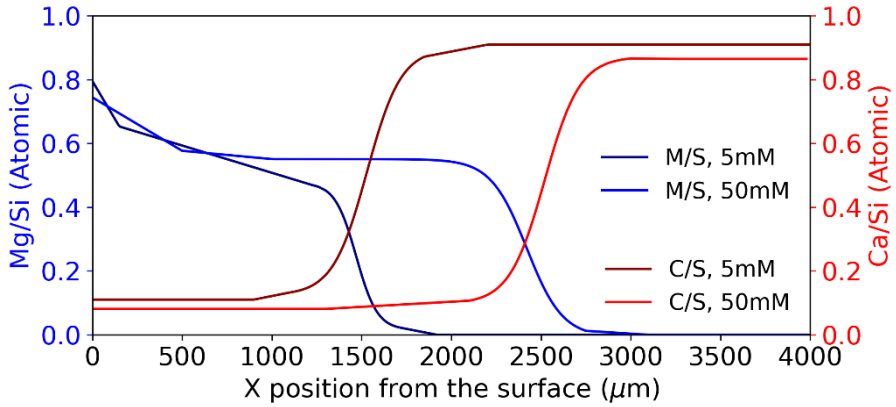

Figure 4-20: M/S and C/S atomic ratios trends calculated from microprobe data of a CEM I paste with colloidal silica, immersed in solution with [$MgCl_2$] = 5 and 50 mmol/L for 6 months

Only the 6 months degraded sample (50 mM) was analysed with microprobe. To visualise the evolution of the M/S and C/S ratios with time, samples were taken and analysed with SEM/EDS at different degradation times (2, 4 and 6 months). Figure 4-21 shows Ca/Si and Mg/Si ratios in intensity calculated from the EDS elemental mappings. Data from the 5 mM degraded samples are overlaid, in lighter colours, on the 50 mM data. As for the 5 mM samples, the degradation front increase with time (Figure 4-21). For a short degradation time (2 months), the degraded depth is the same for both $MgCl_2$ concentrations, while for the longer degradation times, samples degraded to 50 mM show a greater degraded depth than the 5 mM.

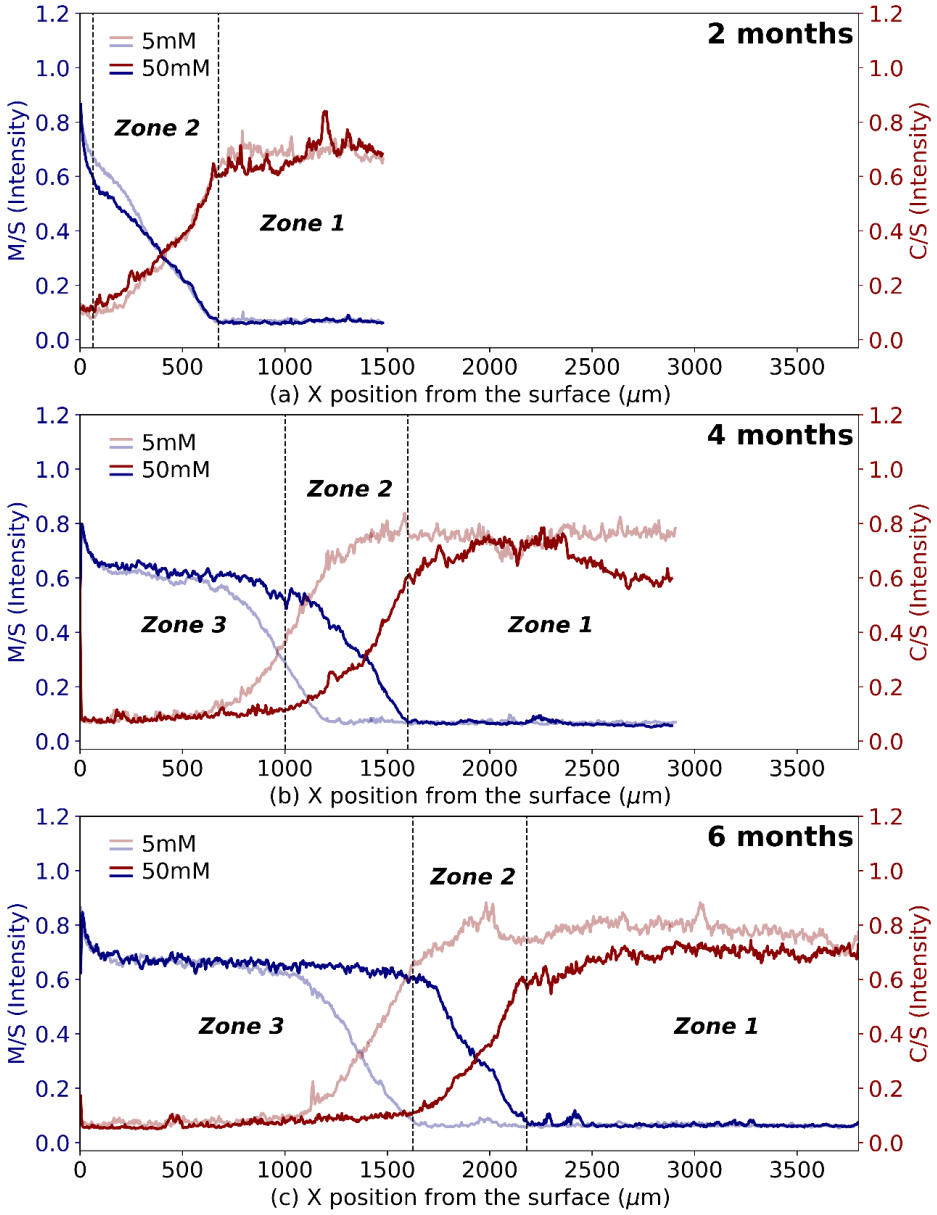

Figure 4-21: M/S and C/S intensity ratios calculated from solid chemical composition (EDS) of a CEM I paste with colloidal silica, immersed in solution with [$MgCl_2$] = 5 mmol/L or 50 mmol/L for 2 months (a), 4 months (b) or 6 months (c) according to the distance to the surface of the specimen

The difference in degraded depth between 5 mM and 50 mM increases with time. Although the Mg concentration is 10 times higher for the 50 mM, the depth of the front of the 50 mM samples is only 1.3 times that of the 5 mM samples. The relation between the degraded depth and the square root of time √t (Figure 4-22) shows a linear evolution for both cases, meaning that the kinetics of the magnesium attack of the cement paste is governed by a diffusion process and can be described using Fick's law. The trend line for 50 mM shows a higher slope than for 5 mM. This suggests an increasing difference between the degraded depths at 5 mM and 50 mM.

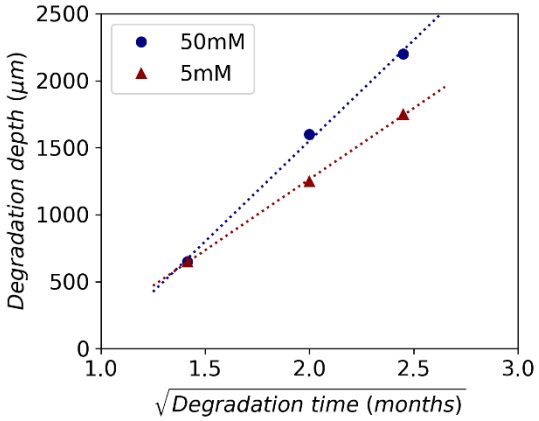

Figure 4-22: Illustration of the degraded depth (defined as the depth of Mg enrichment – limit of Z1 in Figure 4-21) against the square root of the degradation time (months). Doted lines correspond to trendlines.

4.4.3. Influence on the microstructure and mechanical properties

4.4.3.1. Microstructure

The microstructure of the sample degraded at 50 mM during 6 months was studied by micro-tomography. The 1D density profile is presented in Figure 4-23. The density profile of the sample degraded during 6 months in 5 mmol/L has been added to the figure to compare. 2D and 3D visualisations are available in Appendix C (Figure C-6 and Figure C-7).

As for the 5 mM sample, 3 zones can be defined: a low density zone (0-1700 µm), a transition zone (1700-2600 µm) and a denser zone (from 2600 µm) and correspond respectively to the degraded zone (Z3-EDS), the transition zone (Z2-EDS) and the sound zone (Z1-EDS). While the 5 mM sample shows a stable density value in the degraded zone (Figure 4-23), the 50 mM sample shows a gradual drop in density in the last 500 µm before reaching the surface. Moreover, the decrease in relative density between the sound and degraded zones is much greater for the 50 mM than for the 5 mM (0.4 versus 0.55). It seems that the increase in Mg concentration not only amplifies the depth of magnesium enrichment and calcium and sulfur leaching, but also implies a different microstructure. Density and porosity being inversely proportional, the porosity of the degraded zone is greater than that of the sound zone and the 50 mM shows a slightly greater porosity than the 5 mM in the degraded zone with a slightly different appearance. For the 50 mM, the increase in porosity in the first 500 µm could correspond to amorphous silica formation. Indeed, without the silica correction, the silica and total microprobe signal decreases for 0<x<500 µm (Figure C-1) indicating an increase in the water content of the material (Bertron et al. 2009), as does the density measured by micro-tomography (Figure C-1 and Figure 4-23). This is also in agreement with the NMR observation of silica in the degraded zone (presence of Q^4, Figure 4-19).

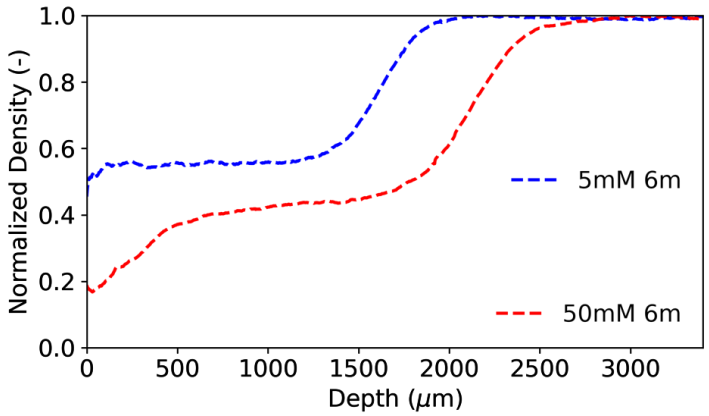

Figure 4-23: Normalized density after micro-tomography measurements for CEM I paste with colloidal silica, immersed in solution with [$MgCl_2$] = 5 mmol/L or 50 mmol/L for 6 months

The microstructure at low scale had been studied by N_2 Physisorption (Appendix C, Figure C-8 and Table C-1). The pattern of isotherms and pore size distribution (BJH) is the same as for 5 mM samples. The sound zone (Z1) has a similar specific surface area to that of the sound sample, the isotherm and pore size distribution are identical. The degraded zone (Z2-3) shows a similar specific surface area (532 m^2/g) as the 5 mM degraded zone (571.1 m^2/g) and as M-S-H (562.9 m^2/g).

The microstructure at larger scale had been studied by MIP (Table 4-7 and Figure 4-24). The sound sample shows a hump around 10 nm that doesn't appear in the sound zone of the degraded sample, but the global look is similar to that of the sound zone. Concerning the porosity value exhibited in Table 4-7, the sound zone of the degraded sample has a lower porosity than the sound sample. The sound sample, used to perform the degradation test, was kept under parafilm until the degradation test started. As discussed in section 4.3.4.2, during the degradation, the sections were immersed in tanks of $MgCl_2$ solution, thus under water, unlike the rest of the sound samples which were returned under parafilm. One of the differences between the sound zone of the degraded sample and the sound sample is therefore the 4 months spent under water in the degraded sample. It is possible that the degradation acted as an underwater cure for the material and that the remaining anhydrous reacted and plugged some of the porosity. This would explain the lower capillary porosity (d>10nm) in the sound zone than in the sound material and the higher specific surface area observed by N_2 Physisorption (2<d<10nm). The capillary pore network would be partly filled by the formation of C-S-H so the capillary porosity would decrease but as C-S-H have an intrinsic porosity (d<10nm), the specific surface observed in N_2 Physisorption (2<d<10nm) would increase.

For the pore sizes below 100 nm, no big difference appears between the sound zone and the degraded zone of the degraded sample. The degraded area shows, in contrast to the sound area, the presence of pores whose size is between 0.5 µm and 5 µm. Moreover, for the largest pore diameters, the intrusion volume is very large, probably due to the presence of cracks, not present in the sound zone, which fill up. As suggested by the micro-tomography results, the porosity of the degraded zone is much higher than that of the sound zone (44% against 30.2%).

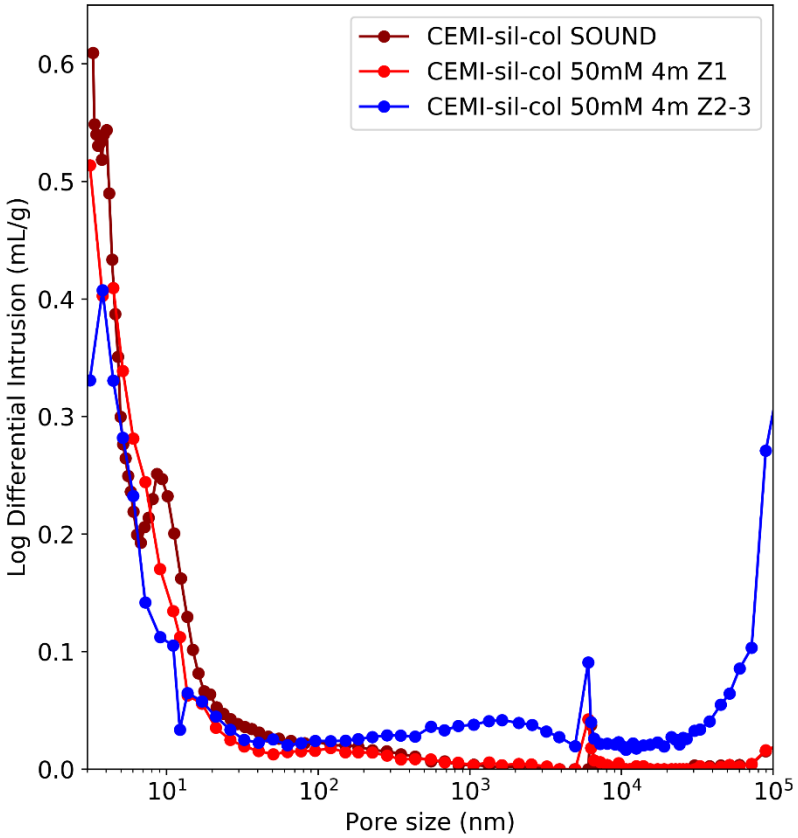

Figure 4-24: Pore size distribution by mercury intrusion porosimetry (MIP) of the sound zone and degraded zone of the degraded sample (50 mM) during 4 months, compared to the sound sample. Z1 = Zone 1 (sound zone) of the degraded paste, Z2-3 = Assembly of zones 2 and 3 (enriched in Mg) of the degraded paste (50 mM)

Table 4-7 : Porosity determined by MIP of the sound model cement paste and a degraded sample

Type of sample	Sound model cement paste	Degraded model cement paste	
Zone	-	Sound Zone (Z1)	Degraded Zone (Z2-Z3)
Porosity (%)	35.6	30.2	44.0

In conclusion, the analysis of the microstructure of the degraded zone at different scales showed that the structure of the degraded M-S-H is similar to that of the synthetic M-S-H (Dewitte et al. 2022; Bernard et al. 2019). The structure is sheet-like. The porosity of the degraded zone for pore diameters below 10 nm is very high compared to that of the sound zone. This is in agreement with the previously calculated high intrinsic porosity of M-S-H (>50%) (3.3.3). On a larger scale, the capillary porosity appears to be similar between the sound and degraded zones. Only the porosity associated with pore diameters greater than 0.5 µm appears to be higher. This could correspond to the presence of cracks created by the shrinkage phenomenon.

As with the sample placed in 5 mM $MgCl_2$, a drying shrinkage phenomenon is visible. The same test as for the 5 mM sample (Figure 4-11, 4.3.4.1) was carried out and Figure C-4 (Appendix C) shows the results.

4.4.3.2. Elastic properties

As for the 5 mM (Figure 4-17), several grids of 4x4 indents were made along the degradation. Figure 4-25 shows the results after the removing of outliers using interquartile method. In the cracking area on the left, no measurement points worked. On the surface on the right, only three points worked and show a strong dispersion. Below 5 measurement points, the reliability of the values can be questioned. The values for x=3000 µm and x=8100 µm should not be considered.

As for the 5 mM (Figure 4-17), the Young's modulus decreases strongly from the sound zone to the degraded zone. Here, the modulus oscillates between 4 and 5 GPa while for the 5 mM the Young's modulus went down to 2.5 GPa. Although the density observed in the degraded zone of the 50 mM is lower than that of the 5 mM (Figure 4-23), the mechanical properties observed are of the same order of magnitude, or even a little higher. In the degraded zone, the measured Young's modulus again shows a plateau. The degraded zone shows stable chemical, microstructural and mechanical properties, except near the surface where the magnesium signal increases, and the density decreases.

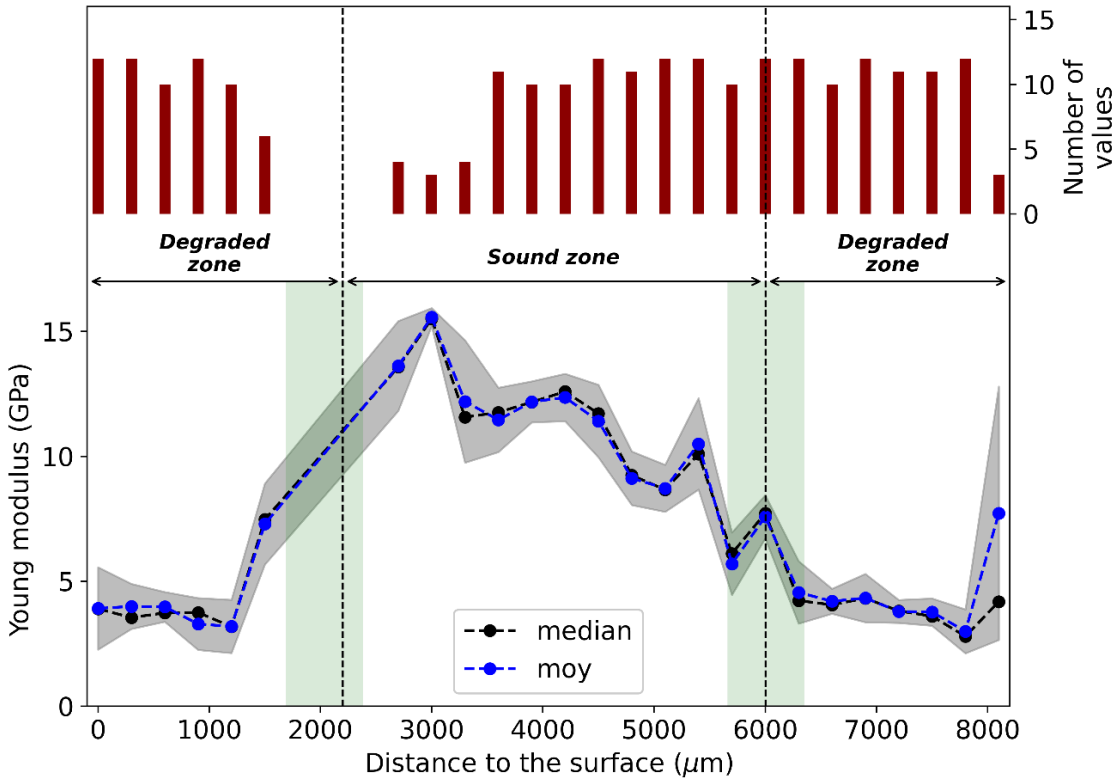

Figure 4-25: Microindentation data without outliers of the model cement paste degraded during 6 months in 50 mM of $MgCl_2$, cracking zones are underlined in green

Overall, it appears that the gradient of chemical, microstructural, and mechanical properties is similar between 5 mM and 50 mM. The contact of the sample with a 50 mM solution of $MgCl_2$ caused a strong enrichment in magnesium accompanied by a leaching in calcium and sulfur. The Mg enriched zone shows a density 2.5 times lower than the sound zone and the measured Young's modulus is 2.5 times lower than the sound zone. The 50 mM shows a more extensive degradation front, greater porosity but comparable mechanical properties.

In conclusion, the effect of magnesium concentration on the magnesium attack of a low-pH model paste showed that the phenomenology is similar but not identical. The dissolved and formed phases are the same. The impact on the microstructural and mechanical properties is close. The M-S-H formed appear to have the same M/S ratio and the same microstructure. With a

concentration of 50 mM of $MgCl_2$, the porosity of the degraded zone is slightly higher, but the mechanical properties are similar. The increase of the magnesium concentration in solution has mainly an impact on the depth of the degradation front. While the Mg concentration increases by a factor of 10, the degradation front does not. The kinetics seem to change. As the degradation time increases, the difference in degraded depth between the two concentrations increases.

4.5. From chemical properties to microstructural and elastic properties

The previous sections have presented the chemical, microstructural and mechanical characterization of low-pH model cement pastes under magnesium attack. The magnesium attack on these low C/S pastes corresponds to the formation of a zone strongly enriched in Mg and leached in Ca and S, associated with the formation of M-S-H and the dissolution of C-S-H. The mechanical properties of this zone are very low (2.5 - 5 GPa) and are in agreement with the properties measured on the M-S-H pastes. However, this observation remains qualitative. To verify that the M-S-H porosity and Young's modulus data determined in Chapter 3 can be used in models for predicting the behaviour of cementitious materials under magnesium attack, a method for calculating the mechanical properties of degraded model paste samples was developed. This method uses microprobe and XRD data of the degraded samples, combined with the microstructural (V_m, porosity) and mechanical (E, ν) properties of the identified mineralogical phases and the porosity of the sound material. The next sections detail the method.

4.5.1. Method

The method is described in detail in 2.1.4.2. As a reminder, the general scheme of the method is as follows (Figure 4-26).

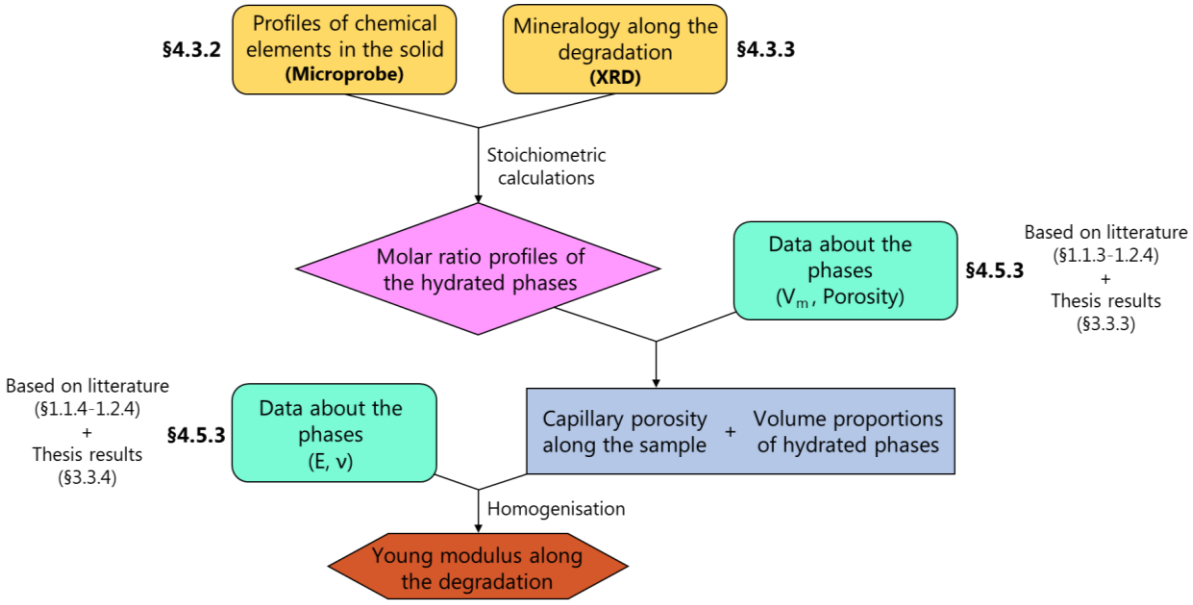

Figure 4-26 : General scheme of the method

Microprobe and XRD data allow to obtain molar profiles of the hydrated phases along the degradation. To get to the mechanical and physical properties of the paste, it is necessary to know the elementary properties of the phases (intrinsic porosity of the phase, molar volumes and elastic properties - E and ν) and combine it with a homogenisation model.

4.5.2. Determination of the molar proportions of the mineralogical phases

The microprobe tests performed along the degradation profiles (Figure 5-3, Figure 4-7 and Figure C-5, Appendix C for the 0 mM, 5 mM and 50 mM degraded samples respectively) allow to calculate the molar proportions of elements in solid phases. XRD (Figure 5-2, Figure 4-8 and Figure 4-18 for 0 mM, 5 mM and 50 mM respectively) showed that the solid phases observed in the sound and degraded pastes were M-S-H, hydrotalcite, amorphous silica, C-S-H and ettringite. For the implementation of the calculations, the most complex case in terms of mathematical resolution (with the most mineralogical phases) was considered. It concerns the two pastes under magnesium attack. The method was therefore carried out using data from the sample placed in 5 mM $MgCl_2$ for 6 months.

Two phases, hydrotalcite ($Mg_6Al_2CO_3(OH)_{16}{\cdot}4H_2O$) and ettringite ($Ca_6Al_2(SO_4)_3(OH)_{12}{\cdot}26H_2O$), have a fixed stoichiometry. The three others (M-S-H, C-S-H and amorphous silica) can integrate a variable quantity of magnesium, calcium and aluminium.

The initial C/S ratio of the paste being low (0.9), the C-S-H formed have a C/S of about 0.85 because of the presence of ettringite. Thus, when the paste leaches calcium, it can be considered that they are destabilized and dissolve (Perlot 2005). Indeed, according to the equilibrium curve provided by Perlot (Perlot 2005), below C/S=0.8, the C-S-H dissolve and for a C/S in the solid lower than 0.3, no C-S-H remain. It is the amorphous silica which takes over. In order to fully consume the aluminium observed in microprobe and in agreement with the literature (Al/Si up to 0.05) (Roosz et al. 2018), it is considered that C-S-H contain aluminium up to Al/Si=0.03. As discussed before (4.3.3), the amorphous silica integrates a part of the calcium observed in the solid (C/S_{AS}=0.11), the considered M-S-H have a ratio M/S=0.78 and also integrates a part of the calcium (C/S_{MSH}=0.11).

Based on these considerations, the molar quantity of elements (measured by microprobe) in solid phases can be defined as followed:

$$n_{Al} = 2 * \mathrm{n_{Aft}} + 2 * \mathrm{n_{Ht}} + 0.03 * \mathrm{n_{CSH}} \quad (4\text{-}4)$$

$$n_S = 3 * n_{Aft} \quad (4\text{-}5)$$

$$n_{Mg} = 6 * n_{Ht} + 0.78 * n_{MSH} \quad (4\text{-}6)$$

$$\mathrm{n_{Si}} = \mathrm{n_{MSH}} + \mathrm{n_{CSH}} + \mathrm{n_{AS}} \quad (4\text{-}7)$$

$$n_{Ca} = 0.11 * n_{MSH} + 0.9 * n_{CSH} + 0.11 * n_{AS} + 6 * n_{Aft} \quad (4\text{-}8)$$

With Ht for hydrotalcite, AFt for ettringite, MSH for M-S-H, CSH for C-S-H and AS for amorphous silica.

In the system of equation ((4-4) to (4-8)), the quantities of elements ($n_i/\Sigma n_i$) in the solid phases is known along the degradation profile (m_i/m_{total} measured by microprobe, see Figure 4-7a, and converted in mol_i/mol_{total}) and the unknown are the molar quantity of the 5 solid phases : Ettringite

(AFt), Hydrotalcite (Ht), C-S-H, M-S-H, amorphous silica (AS). Stoichiometric calculations have thus been performed by inversing the system. Results are given in Figure 4-27.

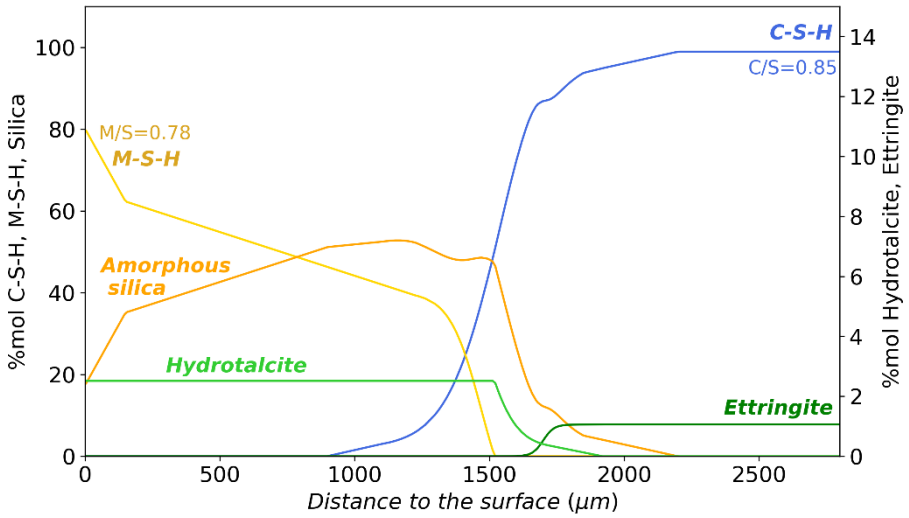

Figure 4-27 : Molar proportions ($n_i/\Sigma n_i$) of the phases by stoichiometric calculations of a low-pH model cement paste immersed during 6 months in 5 mM of $MgCl_2$ according to the distance to the surface

To carry out the method of determining mechanical properties from chemical data (Figure 4-26) on the degraded model cement paste, it is necessary to know the microstructural and mechanical properties of all hydrated phases in the degraded zone.

4.5.3. Determination of the microstructural and mechanical properties of the initial and newly formed solid phases

Sound paste phases

C-S-H is a semi-amorphous phase with an internal microstructure (Figure 4-28). They are made of globules of about 4 nm in diameter which, by associating, form globule flocs and then what is called low-density or high-density C-S-H. Within the floc of globules and between globules, a porosity is formed, it is the intrinsic porosity of C-S-H.

In section 4.2, it was observed that the C-S-H formed in the low-pH model pastes during nanoindentation measurements had lower elastic properties than in the literature. This difference can be explained by the inclusion of porosity in the nanoindentation interaction volume that is not purely intrinsic to the gel. In the homogenization calculation, the C-S-H phase corresponds to the C-S-H gel that incorporates only the intrinsic porosity. Thus, the properties of the C-S-H considered in the previously detailed method are those of the LD C-S-H and are grouped in Table 4-8.

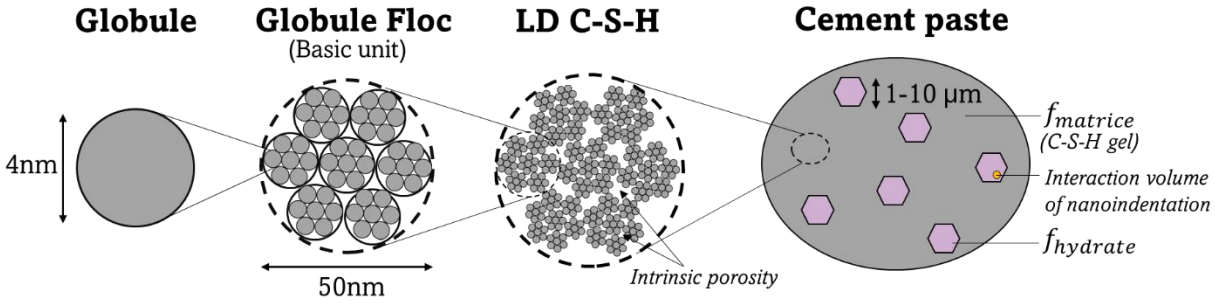

Figure 4-28: Microstructure of the C-S-H phase

The porosity of the C-S-H gel (Φ_{gel}) is considered equal to 28%. The calculation of the molar volume of C-S-H is performed according to the following calculation:

$$V_m = {V_m}^{chem} * \frac{1}{1 - \Phi_{gel}} \quad (4\text{-}9)$$

With V_m the apparent molar volume of the phase and ${V_m}^{chem}$ the chemical molar volume (or true molar volume).

The results are displayed in Table 4-8. Since ettringite has no internal porosity, the data from the literature are directly reported in the table.

Table 4-8: Properties of the sound paste phases considered for homogenisation

		LD C-S-H	Ettringite
Molar volume (cm^3/mol)	Basic unit	72.7 [1]	725 [5]
	Gel	101 [3]	
Gel porosity (%)		28% [2]	-
E (GPa)		22 [4]	20 [6]
ν		0.24 [4]	0.24*
k (GPa)		14.1	12.82
µ (GPa)		8.9	8.06

*not known considered equal to C-S-H
Numbers corresponds to the source of the values :
1=(Tennis et Jennings 2000),
2=(Souyris 2012),
3=calculated from 1 and 2,
4=(Nguyen 2017; Constantinides et Ulm 2004; Zhu et al. 2007; Jennings et al. 2007; Constantinides et Ulm 2007; Vandamme et Ulm 2009; 2013),
5=(Min et Mingshu 1994; Kothari et Takahashi 2022; Adenot 1992; Tennis et Jennings 2000),
6=(Yang et Guo 2011)

Phases resulted from degradation

As discussed in 4.3.3, 3 phases can be considered in the degraded zone : M-S-H, amorphous silica (or silica gel), and hydrotalcite.

Intrinsic mechanical and microstructural properties considered for M-S-H are those of M-S-H with M/S=0.78 determined previously in Chapter 3.

Amorphous silica is also considered to be a gel with an intrinsic porosity of 70% (Snel 1984a; 1984b; Zemnukhova et al. 2015). Its molar volume is calculated accordingly (Table 3-6). According to Bes' work, upon pure leaching of a low-pH paste, the C/S in the degraded zone falls below the C-S-H limit value (0.6-0.7). The degraded zone could therefore be considered as consisting of a silica gel. Bes obtains mechanical properties after homogenization in this zone of $0.1*E_{sound}$, i.e. equal to about 1.2 GPa. Consequently, the amorphous silica considered in this study will have for Young's modulus this value (Table 3-6).

Like ettringite, hydrotalcite has no internal porosity and data from the literature are directly reported in Table 3-6.

Table 4-9: Properties of the phases, resulting from degradation, considered for homogenisation (data for M-S-H in bold issued from Chapter 3)

		M-S-H (M/S=0.78)	Amorphous silica	Hydrotalcite
Molar volume (cm^3/mol)	Basic unit	57 [1]	29 [2]	219 [7]
	Gel	**136**	96.7 [3]	
Gel porosity (%)		**58.1%**	70% [4]	-
E (GPa)		**7.9**	1.2[5]	20**
ν		0.24*	0.19[6]	0.24*
k (GPa)		5.06	0.65	12.82
μ (GPa)		3.19	0.5	8.06

*not known considered equal to C-S-H
** not known considered equal to ettringite
Numbers corresponds to the source of the values : 1=(Bernard et al. 2020), 2=(Bernard et al. 2020), 3=calculated from 2 and 4, 4=(Snel 1984a; 1984b; Zemnukhova et al. 2015), 5=(Bes 2019), 6=(Arnold, Boccaccini, et Ondracek 1996) , 7=(Bernard et al. 2022)
k and μ are calculated from E and ν.

4.5.4. Calculated mineralogical, microstructural and mechanical evolutions

The microprobe and mineralogical assumptions allowed to determine the molar ratios of the different phases (Figure 4-27). To carry out a mechanical homogenization, it is necessary to know the volume proportions of each phase in the solid (f_i) and the capillary porosity (Φ_{cap}) along the degradation. f_i is expressed by:

$$f_i(\%) = \frac{v_i}{V_{TOT_S}} \quad (4\text{-}10)$$

with

$$v_i = n_i * V_{m_i} \quad (4\text{-}11)$$

$$f_i(\%) = \frac{v_i}{V_{TOT_S}} \tag{4-10}$$

and

$$V_{TOT_S} = \sum_i v_i \tag{4-12}$$

With the v_{TOTs} the total volume of solid, intrinsic porosity of the phases included, v_i and V_{mi} are the volume and molar volume of the phases (intrinsic porosity included) respectively.

As quantitative values of the porosity in the degraded zone are unsure, the capillary porosity (Φ_{cap}) will be calculated from the molar volume (V_m) and quantity of each phase (n_i), coupled to the properties of the sound zone. For further discussions, the global porosity (Φ_{tot}) will also be calculated. Figure 4-29 shows the phases considered in the study. No phase can be considered as a matrix since their proportions evolve along the degradation. Consequently, the grey phase (a) corresponds to an assembly of all phases (b).

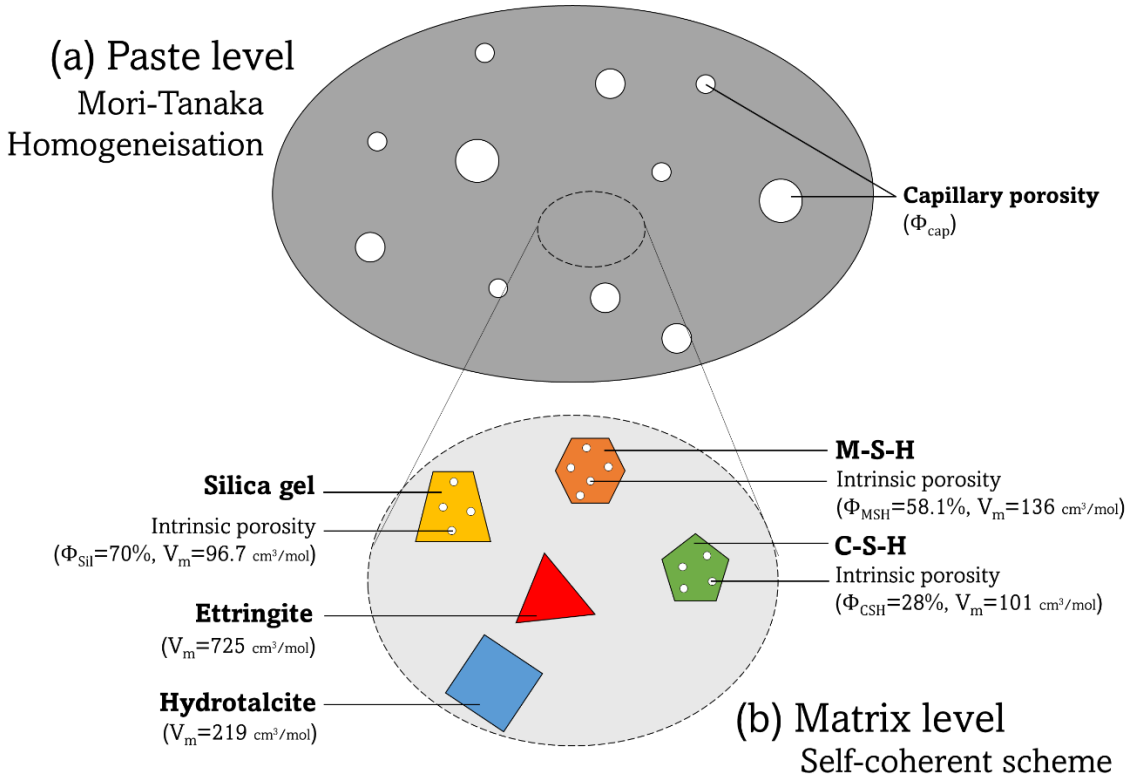

Figure 4-29: Illustration of the phases considered for calculations and their properties

The total porosity and the capillary porosity can be expressed by equations (4-13) and (4-14) :

$$\Phi_{tot} = \frac{\Phi_{MSH} * V_{MSH} + \Phi_{CSH} * V_{CSH} + \Phi_{Sil} * V_{Sil} + \Phi_{cap}.V_{app}}{V_{app}} \tag{4-13}$$

$$\Phi_{cap} = 1 - \frac{V_{TOT_S}}{V_{app}} \tag{4-14}$$

Φ_{MSH} , Φ_{CSH} and Φ_{Sil} are the gel porosity of M-S-H, C-S-H and amorphous silica respectively and were previously defined in Table 4-8 and Table 4-9. V_{MSH} , V_{CSH} and V_{Sil} are the volume of M-S-H, C-S-H and amorphous silica respectively and are calculated from equation (4-11). V_{TOT_S} is the total volume of solid, intrinsic porosity of the phases included, calculated by (4-12). V_{app} is the apparent volume and is unknown. Its determination is based on the assumption that there is no chemical shrinkage and that V_{app} is constant along the sample.

In the sound zone, as shown by XRD, the paste is composed of C-S-H, ettringite and capillary porosity. The system of two equations defined before becomes:

$$\Phi_{tot_{sound}} = \Phi_w = \frac{\Phi_{CSH} * V_{CSH(sound)} + \Phi_{cap_{sound}} . V_{app}}{V_{app}} \quad (4\text{-}15)$$

$$\Phi_{cap_{sound}} = 1 - \frac{V_{TOT_{S(sound)}}}{V_{app}} \quad (4\text{-}16)$$

In the sound zone, $\Phi_{tot_{sound}}$ can be considered equal to the water porosity of the sound sample (Φ_w= 51.5%, see 4.2.2). Thus, only two unknowns ($\Phi_{cap_{sound}}$ and V_{app}) remain and the system can be solved.

The resulting volume proportions of each phase are shown in Figure 4-30.

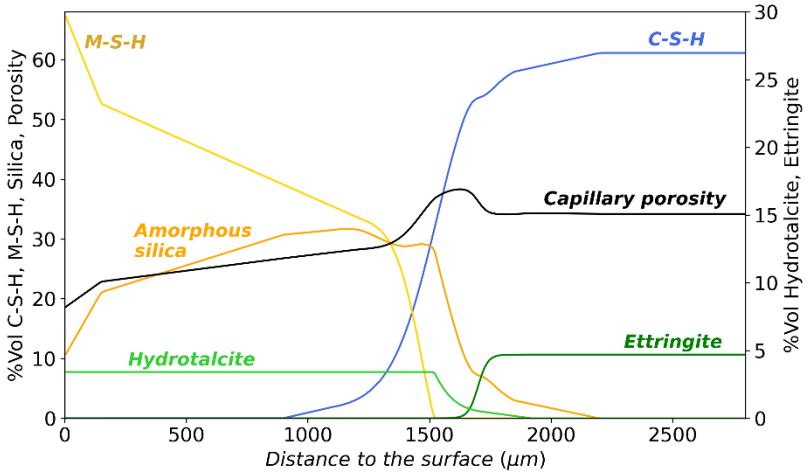

Figure 4-30: Calculated volume proportions of the mineralogical phases of a low-pH model cement paste immersed during 6 months in 5 mM of $MgCl_2$ according to the distance to the surface

Mechanical homogenization was performed in two steps under drained conditions (k and μ equal to 0 for the porosity). In the first step, as no solid phase can be defined as a matrix along the entire sample, the self-consistent scheme was applied to all solid phases (including intrinsic porosity of the phases) as in Figure 4-29 (b). Moreover, in the transition zone (Z2), no phase is in the majority. Inclusions are considered spherical. The obtained homogenized solid phase properties are then used in a second homogenization scheme, Mori-Tanaka, where the solid phase is considered as matrix and the capillary porosity as inclusion as in Figure 4-29 (a). The homogenized Young's modulus calculated and the experimental results (microindentation) are displayed in Figure 4-31.

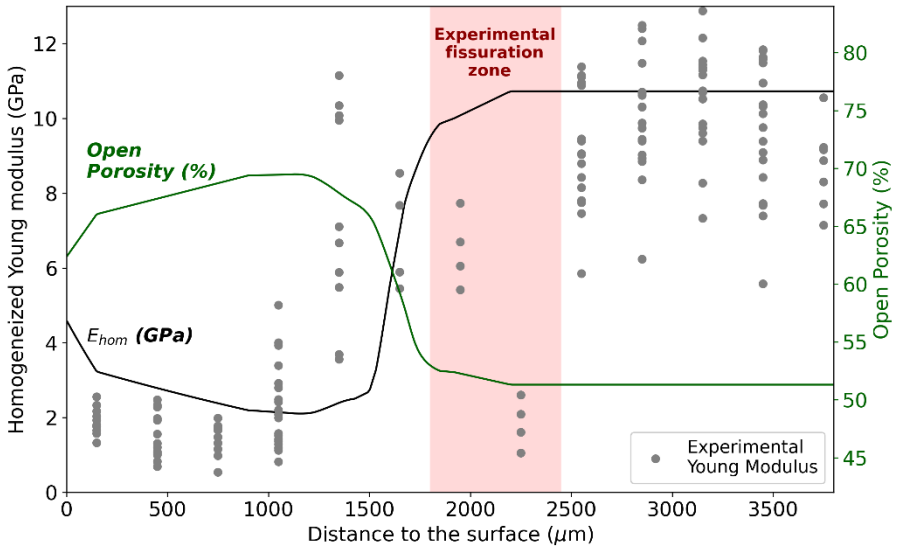

Figure 4-31 : Determination of the homogenised properties of a low-pH model cement paste immersed during 6 months in 5 mM of $MgCl_2$ according to the distance to the surface

First, the experimental cracking zone observed in microindentation did not appear in the microprobe results (Figure 4-7), so the abrupt loss of mechanical properties (1800-2400 µm) does not appear in the mechanical homogenization. Moreover, the calculated porosity and mechanical properties show an increase (respectively decrease) shifted by about 250 µm compared to the experimental data. Although shifted, the Young's modulus decrease in the transition zone follows the same slope as the experimental data. The degraded zone and the sound zone show close calculated and real values, validating the data considered in the model. In the degraded zone (0-900 µm), as the strong cracking in this zone (Figure 4-16) is not considered in the calculations, the calculated Young's modulus is slightly higher than the one observed experimentally and the open porosity decreases at the approach of the surface when the amorphous silica decreases and the quantity of M-S-H increases (Figure 4-30) when in reality this is not the case (Figure 4-4 - Microtomography).

The Φ_{deg}/Φ_{sound} ratio (68%/51.5%=1.32) is of the same order of magnitude as that observed by Bes (Bes 2019) on his leached low-pH cement pastes (61%/49.2%=1.24). The higher relative increase observed here, could be due to the different nature of the degradation (magnesium attack against pure leaching) and phases in the degraded zone.

The same method has been applied on the sample placed during 6 months in 50 mM of $MgCl_2$. All calculation assumptions are the same as for 5 mM except for the C/S ratio in M-S-H and amorphous silica. The value used to ensure that all calcium is consumed in the degraded zone is increased from 0.11 to 0.085. The C/S of C-S-H is egal to 0.842 for the 50 mM sample against 0.845 for the 5 mM. Figure 4-32 shows the results obtained at each stage of the method. The results are very similar to those for 5 mM. As magnesium showed a plateau in microprobe, the plateau is found for M-S-H (Figure 4-32a). The micro-indentation data agree with the homogenisation data. As with the 5 mM, the only difference is the shift of a few hundred microns in the Young's modulus drop. As the microprobe already showed a shifted degradation front compared to the other methods, this is not surprising. Thus, the data of the phases considered for homogenisation allows to find satisfactorily the microindentation results.

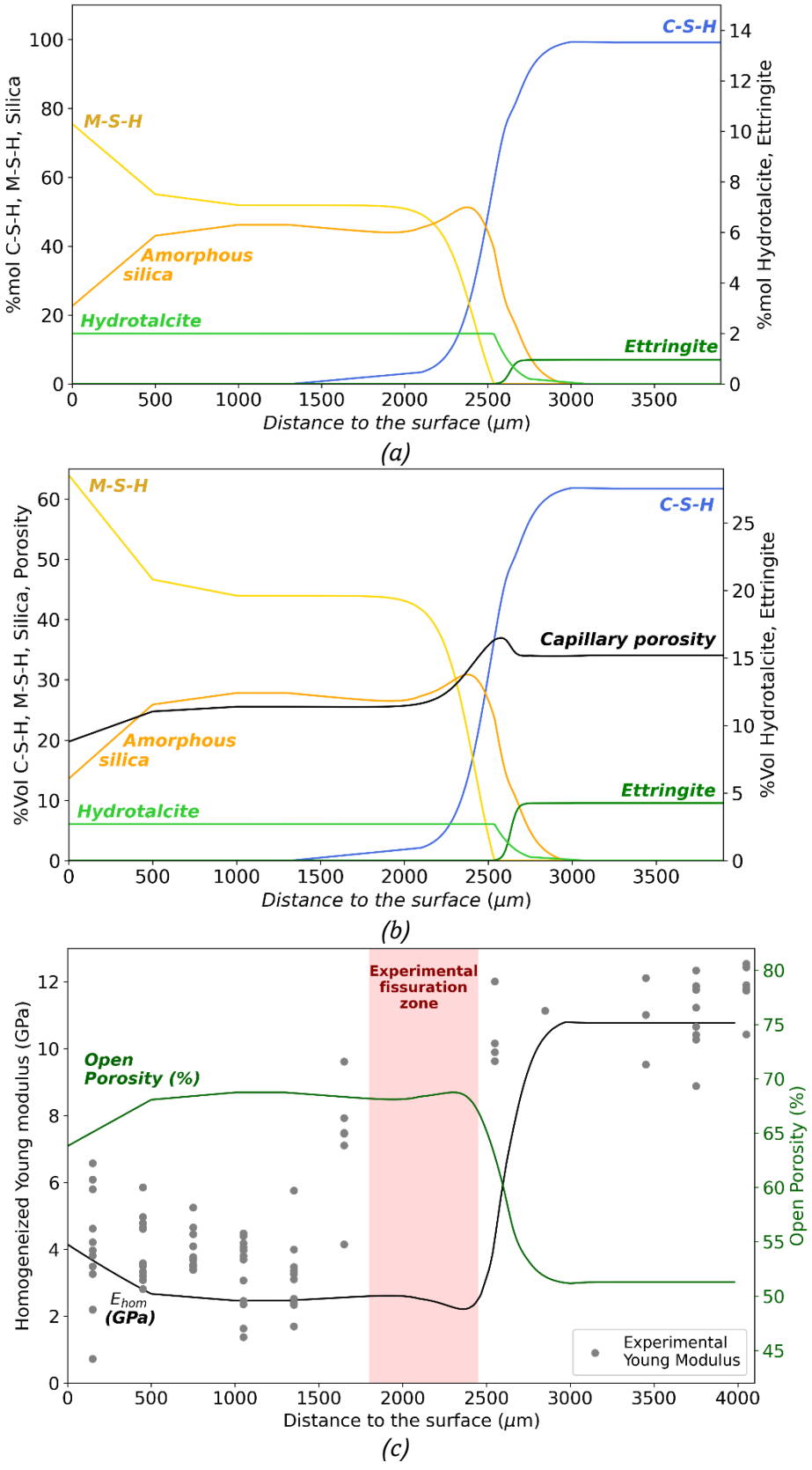

Figure 4-32: Calculated molar proportions (a) and volume proportions (b) of the phases and homogenised properties of the degraded sample according to the distance to the surface (c) of a low-pH model cement paste immersed during 6 months in 50 mM of $MgCl_2$

Conclusion

Chemo-mechanical and microstructural characterizations were performed on model cement pastes composed by CEM I and colloid silica with low Ca/Si ratio (Ca/Si=0.9), chemically representative of low-pH cement pastes, placed in 5 mM $MgCl_2$ solution for 2, 4 and 6 months. EDS and microprobe analyses showed a homogeneous and extensive degradation front, corresponding to a strong magnesium enrichment (Mg/Si=0.8) and a strong leaching of calcium and sulphur. Mg enrichment resulted in M-S-H formation. In the most magnesium enriched zone, calcium remained present in low proportion (Ca_{total}/Si_{total}=0.1) without the signal of a calcium containing hydrate being visible in XRD. After simulation, it seems that the most likely explanation is the incorporation of some calcium in the M-S-H and amorphous silica.

The Mg-enriched zone showed lower density (micro-tomography) and thus higher porosity than the sound zone. The density and porosity followed the calcium and magnesium signal. When Mg increased and Ca decreased, density decreased according to a comparable sigmoid. The Mg-enriched zone had similar microstructural properties to those previously determined on pure M-S-H pastes (N_2 Physisorption) and showed a low residual Young's modulus (15-20% of sound zone modulus). It remains to be determined whether this drop in mechanical property is less than that associated with leaching alone. In addition, the appearance of cracks at the interface of the sound and degraded areas complicated the analysis, especially for the making of XRD by successive abrasions. The surfaces of the polished sections were not completely flat, making microindentation tests difficult. It seemed that these shrinkage properties were intrinsic to M-S-H, the same phenomenon having been observed on pure M-S-H pastes. In tidal areas, where the concrete undergoes cycles of immersion, emersion, this property could explain the loss of material on the surface (Rosenqvist et al. 2017). However, the magnesium attack never occurs alone. Waters contain other ions, notably sulphates, and several attacks take place at the same time. Moreover, this material is a model material, presenting the worst possible case to study only the properties of the M-S-H (to include them in the mechanical models), without any external perturbation. In reality, the M-S-H will not be alone, which may limit the observed shrinkage.

The samples degraded either at 5 mM or 50 mM of $MgCl_2$ showed the same global properties. The mineralogy of the degraded zone is similar. At 50 mM, a small amount of hydrotalcite seems to precipitate in addition to the M-S-H. The same deep Mg enrichment is observable, accompanied by a sulphur and calcium leaching. Only the degraded depth is higher for the 50 mM. At 50 mM, the density is slightly lower than for 5 mM in the degraded zone indicating a slightly higher porosity. The elastic properties of the degraded zone are low, as for 5 mM.

A simulation of the mechanical properties of the model cement pastes degraded for 6 months in 5 and 50 mmol/L of $MgCl_2$ was performed based on the chemical and microstructural experimental properties and by integrating the previously determined mechanical properties of M-S-H into the model. By combining the microindentation results on pure M-S-H pastes with mechanical homogenization, values for the properties of M-S-H were proposed (for M/S=0.78, Φ_{gel} =58.1%, E=7.9 GPa and for M/S=1, Φ_{gel} =50.4%, E=3.71 GPa). The simulation result was compared with the experimental results obtained by microindentation. The intrinsic mechanical properties of the M-S-H could thus be validated (see 3.3.4).

CHAPTER 5. COMPARISON OF THE REACTION MECHANISMS OF MAGNESIUM ATTACK AND PURE LEACHING ON A LOW-PH MODEL CEMENT PASTE

Introduction

In the previous chapter, the impact of magnesium attack on the chemical, mineralogical, microstructural and mechanical properties of a model cementitious paste was investigated, thus fulfilling part of first thesis objective (Understanding of the reaction mechanisms of magnesium attack and M-S-H formation in low-calcium cementitious matrices). The reaction mechanism of magnesium attack on low C/S binders was discussed. It was shown that magnesium attack on low C/S model cementitious matrices results in an enrichment of Mg within the paste in parallel with a leaching of S and Ca, to a depth of up to 2 mm after 6 months of immersion in $MgCl_2$ solution. M-S-H is formed while ettringite and C-S-H dissolve and/or decalcify. When the degradation time is sufficient (4 to 6 months), the degraded zone presents an extended zone (Z3, thickness of the zone between 600 and 1600 µm depending on the concentration of Mg in solution) where the quantity of Ca in the solid reaches a constant and very low value (4wt%). This zone with very degraded microstructural and mechanical properties raises questions about the comparison of these effect of degradation with the one observed in pure leaching conditions. To answer these questions, a second study was carried out by placing the paste in pure water for 4 months. The first part of this chapter is devoted to this. The same multi-physics analysis is performed and the experimental results are compared. The second part of this chapter proposes, based on a chemical simulation, to discuss the effect of magnesium in the aggressive solution on the chemistry and mineralogy of the degraded zone as well as on the kinetics of decalcification and dissolution of C-S-H.

5.1. Experimental comparison between leaching and magnesium attack

5.1.1. Degradation procedure

2 samples were prepared in the same way as for magnesium attack (4.1.2) and immersed in a 3L milli-Q water tank. The pH was maintained by a pH controller set to 7 using hydrochloric acid (HCl) diluted to 0.25 mol/L. As soon as the volume of acid added reached 30 mL, the 3L solution was renewed. In order to reproduce the pH conditions in the tanks with magnesium (Figure 4-1), the pH of the renewal solution was lowered to about 5.6. The pH and HCl volume added were measured continuously (Figure 5-1).

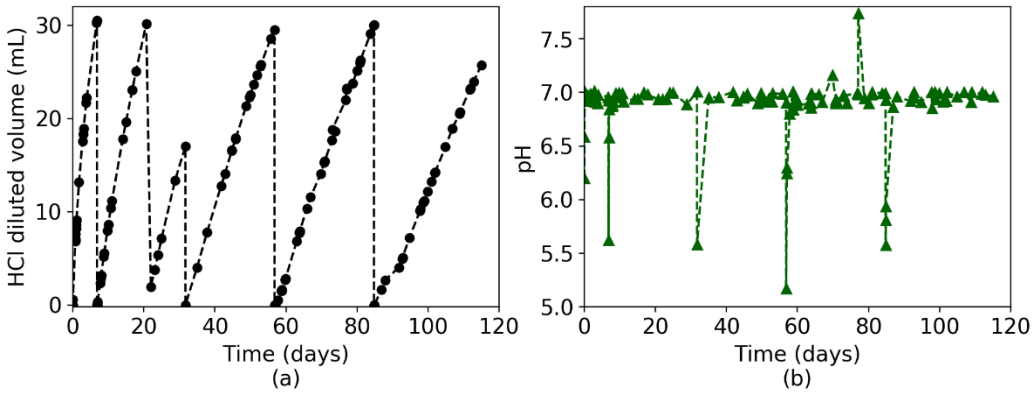

Figure 5-1: HCl volume injected (a) and pH (b) evolution as a function of time in the leaching experiment

The multi-physics characterization performed is the same as for the 5 mM and 50 mM degraded samples. A similar overall figure, with the main techniques, is available for the sample put in pure water during 4 months in Appendix D, Figure D-1.

5.1.2. Effect of the leaching on the chemical properties of low-pH model paste

The mineralogical composition of the paste as a function of distance from the surface exposed to pure water during 4 months was characterized by XRD (Figure 5-2a). For comparison, XRD results of the sample exposed to 5mM $MgCl_2$ solution during 4 months has been added (Figure 5-2b). Calcium EDS mapping was positioned alongside to visualise the evolution of the mineralogy along the sample. Two zones appear. The beginning of the sound zone appears as soon as the ettringite signal returns, i.e. at 575 µm. Before that, it is the degraded zone. In the degraded area, a hump around 30 [2θ] CuKα becomes bigger as it approaches the surface. It corresponds to the formation of amorphous silica. The C-S-H gradually decalcify and form amorphous silica.

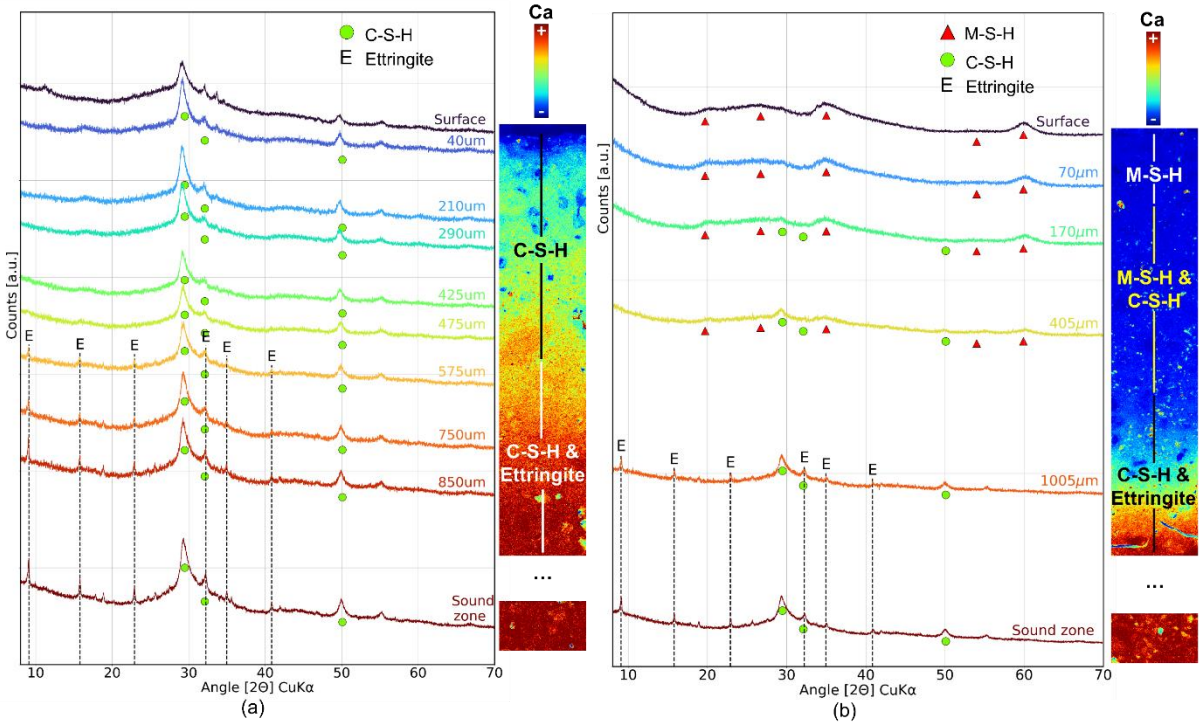

Figure 5-2: X-Ray diffractograms along the degradation associated to Ca EDS map of a CEMI paste with colloidal silica placed (a) in pure water for 4 months and (b) in 5 mM $MgCl_2$ for 4 months

The microprobe results (Figure 5-3) show a progressive Ca leaching, coherent with a progressive decalcification of the C-S-H. The microprobe curves were corrected against silicon content (Figure 5-3a) and profiles of atomic M/S and C/S ratios (Figure 5-3b) along the degradation were obtained from the microprobe profiles.

The Ca signal decreases from 1100 µm to 0 µm. Two zones can be defined, the sound zone (Z1) from the core to 1100 µm and the degraded zone (Z2) from 1100 µm to the surface. The degraded zone corresponds to the zone where Ca and S signals decrease. Although the XRD shows the presence of ettringite as early as 575 µm (confirmed in microprobe because SO3 falls to 0 only around 550 µm, see Figure 5-3), the sound zone is defined as a zone with stable mineralogy and chemical composition. As the calcium signal is not stable before 1100 µm, the boundary of the sound zone is considered to be 1100 µm.

On the raw data, before correction against silica content (Appendix D, Figure D-1 – Microprobe), at the surface, in the last 150 µm, all signals drop sharply. This would correspond to the end of the solid. The remaining material would only be a kind of waterlogged silica gel. As the sound paste

consists only of C-S-H and ettringite according to the XRD, it is expected that calcium and sulphur leaching will dissolve the only phases present and weaken the paste. XRD confirm this hypothesis. With the silica correction, the abrupt signal loss at the surface disappears.

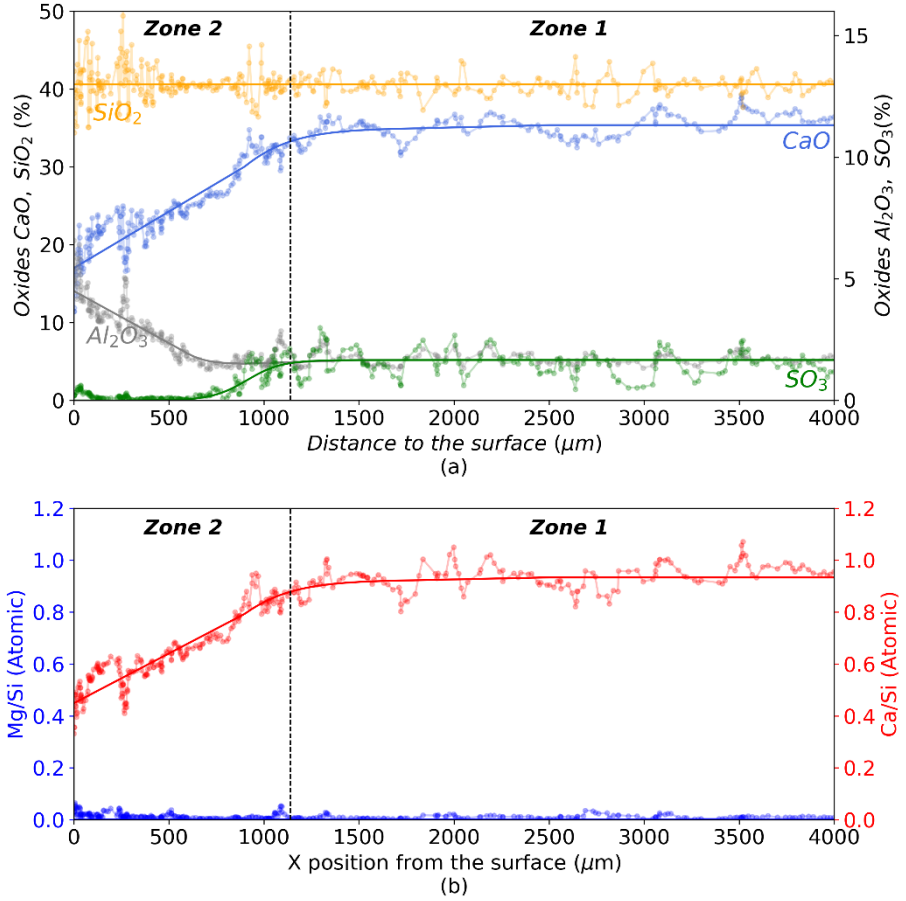

Figure 5-3: (a) Chemical composition of oxides of a low pH model cement paste, immersed in pure water for 4 months according to the distance to the surface of the specimen (analysis by electron microprobe, corrected), (b) M/S and C/S atomic ratios calculated from (a). The lines represent an approximation of the signal for future calculations.

Calcium leaching is progressive and linear throughout Z2. The C/S decreases from about 0.9 to 0.45. As the cement contains only a very small amount of magnesium and the pure water contains no magnesium, the M/S ratio is 0 throughout the sample. In contrast to the magnesium attack carried out with $MgCl_2$ previously (Figure 4-7), the aluminium signal increases in zone 2. For the paste exposed to 50 mM $MgCl_2$, the Al signal increased slightly as it approached the surface, but the phenomenon was limited to the last 250 µm, while the degraded area measured about 2700 µm (Appendix C, Figure C-5). On the data without silica reprocessing (Appendix D, Figure D-1 – Microprobe), not only the Al_2O_3 signal increases in zone 2 but also that of Fe_2O_3 and SiO_2. Fe, Al and Si being stable in an neutral medium, these increases may be linked with the relative character of the quantification (Bertron et al. 2009). As calcium and sulphur are leached out, the other non-leached elements take a larger part of the total mass. Moreover, the sound zone showed constant contents of Al_2O_3, Fe_2O_3 and SiO_2 contents. No migration of aluminium, iron or silicon from solid phases of the sound zone to the degraded zone could have generated these increases. While the samples degraded with 5 mM and 50 mM of $MgCl_2$ show a minimum C/S ratio of about 0.1, the minimum ratio in the leached sample (0 mM) is 0.45. The presence of magnesium causes a higher Ca leaching. In addition, the shape of the C/S curve is very different.

As the microprobe analysis weren't performed at the same time on the magnesium attack samples (5 mM and 50 mM), the degraded depth observed in microprobe cannot be compared (6 months for magnesium attack and 4 months for pure water). EDS maps and C/S and M/S profiles of each sample degraded either at 0 mM (pure water), 5 mM or 50 mM during 4 months are compared in Figure 5-4 and Figure 5-5 respectively.

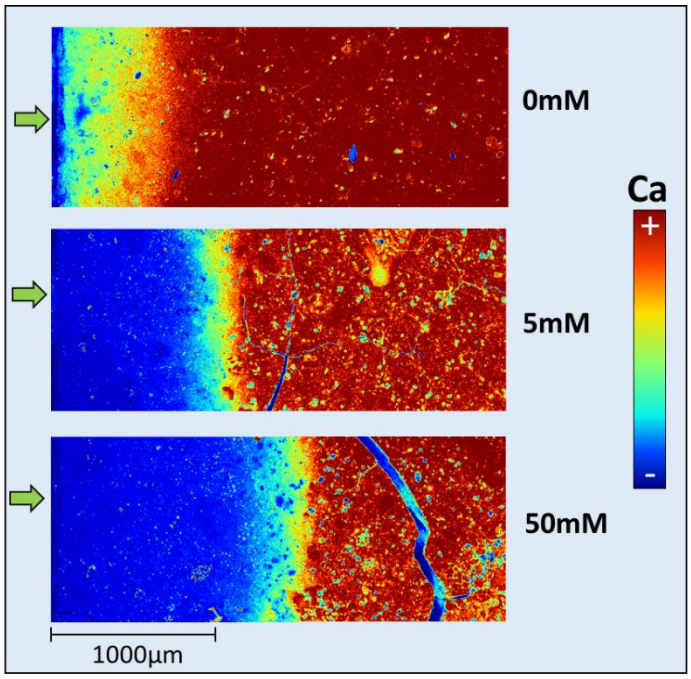

Figure 5-4: Calcium EDS cartographies of low pH model cement pastes immerged during 4 months in pure water (0 mM), 5 mM and 50 mM of $MgCl_2$

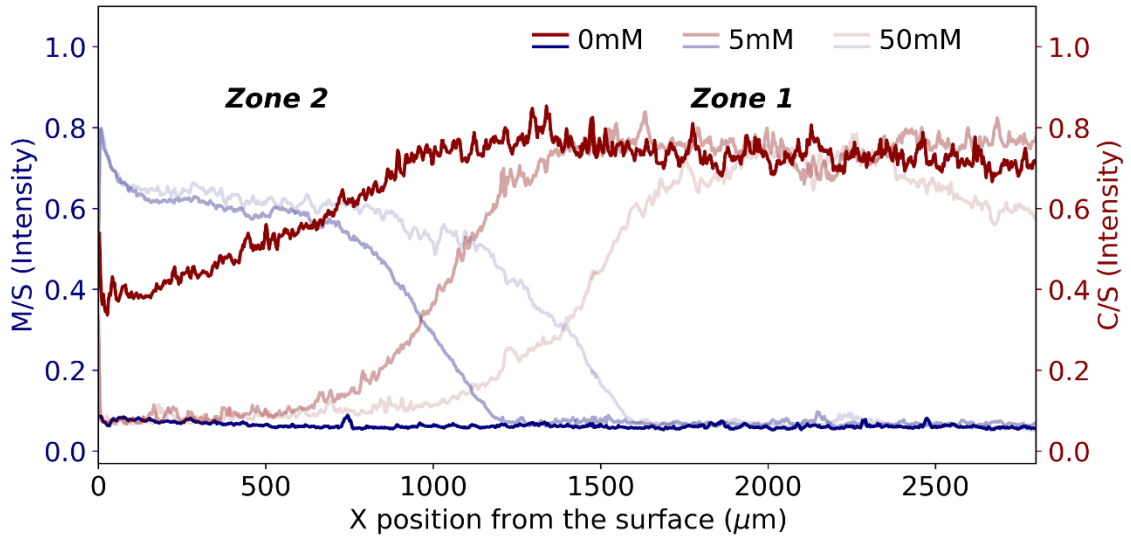

Figure 5-5: M/S and C/S intensity ratios calculated from solid chemical composition (EDS) of a low pH model cement paste, immersed during 4 months either in pure water (0 mM) or in a solution with [$MgCl_2$] = 5 mmol/L (5 mM) or 50 mmol/L (50 mM) according to the distance to the surface of the specimen

The appearance of the EDS curves is similar to those observed in the microprobe, only the degradation depth is different. Figure 5-4 shows the visual difference of aspect of the Ca leaching

in the three cases. The two pastes subjected to magnesium attack, either at 5 mM or 50 mM $MgCl_2$, show a zone where the Ca signal is very weak (blue zone). No such zone is observed for the leached sample (0 mM). Looking at the associated C/S profiles (Figure 5-5), for pure leaching, the C/S (Intensity) decreases linearly down to 0.4 with a slope of about $4.1x10^{-4}$ μm^{-1}. For magnesium attack, the C/S decreases faster. The slope is about $11x10^{-4}$ μm^{-1}, and the C/S then reaches a stable value over the remaining 62.5% of the degraded area (Z2-3). Furthermore, the degraded depth increases with the magnesium concentration. It increases from 1100 µm without magnesium to 1200 µm with 5 mM $MgCl_2$ and to 1600 µm with 50 mM $MgCl_2$. Thus the magnesium attack (with $MgCl_2$ solution) causes a deeper and stronger leaching of calcium than when in contact with pure water.

5.1.3. Effect of the leaching on the microstructure and mechanical properties

5.1.3.1. Cracking pattern of degraded sample in contact with partially dried atmosphere

A follow-up (visual) cracking test upon exposure of the samples to the air was carried out under the same conditions (RH=50%, T=20°C) as for the magnesium attacked samples (Figure 4-11 in 4.3.4.1 and Figure C-4 in Appendix C) to see if the shrinkage observed in magnesium attacked samples (during 9 months) is also observable on the leached samples (during 4 months). All images, for the 0 mM sample, are available in Appendix D, on Figure D-4. To compare the results, Figure 5-6 shows images of the 0 mM, 5 mM and 50 mM sections after 7h52 of exposure to the air. For the 0 mM sample, some small cracks appeared but with a much smaller crack opening than the one observed for the samples under magnesium attack. Even if the sample was left for 23h in the open air, no large cracking developed (Appendix D, Figure D-4). Differential shrinkage induced cracking is greatly increased in the case of magnesium attack. In the case of pure leaching, the property gradient is progressive, whereas for the pastes under magnesium attack, two zones with different chemical, microstructural and mechanical properties are bound together by a short transition zone. Moreover, high sensitivity to drying has already been observed in M-S-H pastes (see 3.3.3). At the level of dams, a loss of material as well as a magnesium enrichment has been observed on the surface of concrete immersed in fresh water (Rosenqvist et al. 2017).

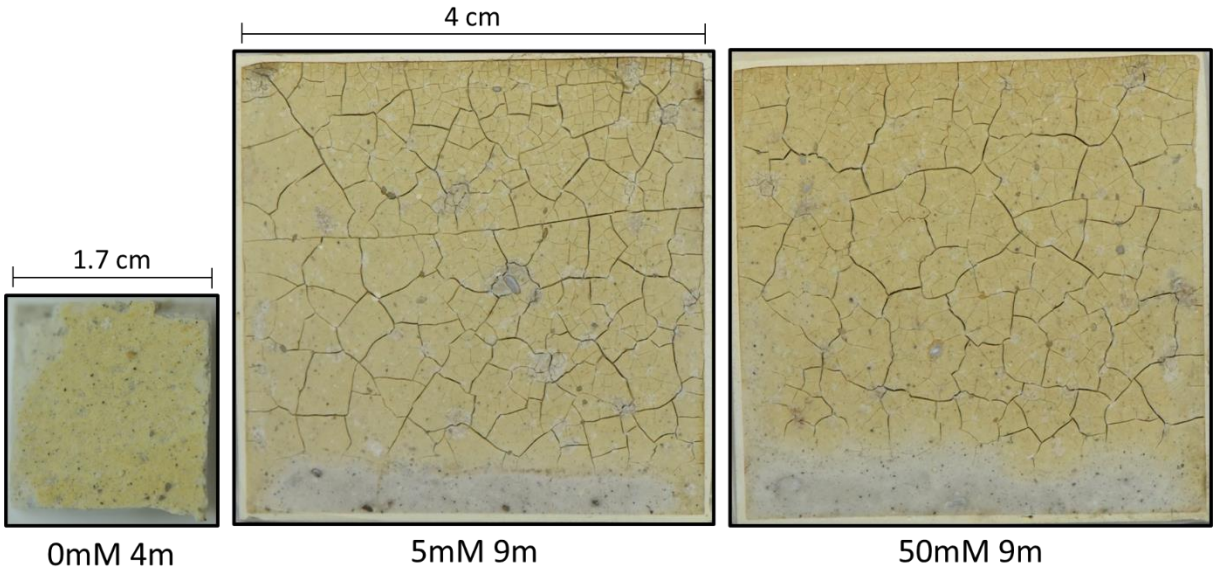

Figure 5-6: Pictures from follow-up (visual) cracking test after 7h52 of exposure to the air (20°C, RH=50%) of the 5 mM and 50 mM samples degraded during 9 months and 0 mM sample during 4 months

5.1.3.2. Microstructural properties

The microstructure of the sample along the degradation was studied by micro-tomography (Figure 5-7). The 3D and the 2D visualisations are available in Appendix D (Figure D-2 and Figure D-3). The density profile (Figure 5-7) shows a decrease in density and thus an increase in porosity in two parts. The second part, close to the surface, has a sharp slope. It corresponds to the zone observed in the microprobe where the total mass percentages decrease and corresponds to a sort of very porous siliceous gel (Appendix D, Figure D-1 – Microprobe). Considering that the density of the sound zone is the same for all degraded sample, regardless of the magnesium concentration, is possible to compare the relative loss of density between the magnesium attack and the leaching experiment.

For the 5 mM, the normalised density in the degraded zone is 0.55 while for the 50 mM it is 0.4. For the pure leached sample (0 mM), the density does not show a plateau in the degraded zone. As in EDS and microprobe results, the density slopes down to 0.5 and then sharply down to 0.2. Although the minimum value reached (0.5) is similar to that of the magnesium attack pastes, the absence of a plateau and the presence of a progressive and gentle density gradient promises better mechanical properties.

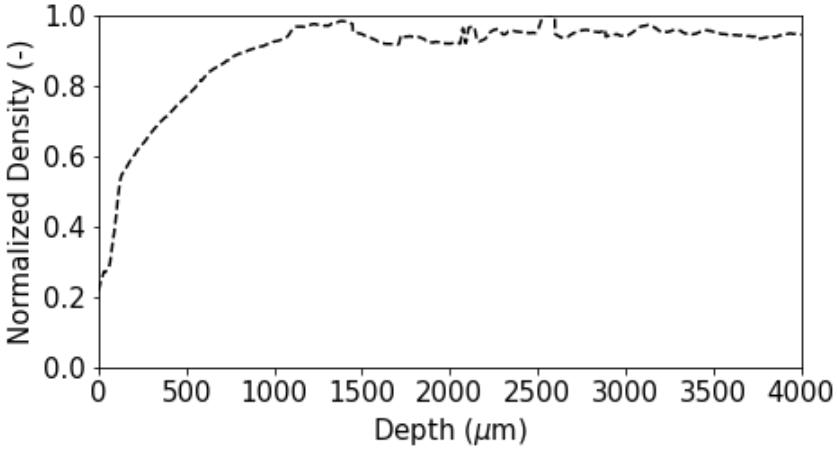

Figure 5-7: Normalized density after micro-tomography measurements for CEM I paste with colloidal silica, immersed in pure water for 4 months

The microstructure at low scale had been studied by N_2 Physisorption (Figure 5-8 and Table 5-1). As before, the isotherm, pore size distribution (BJH) and specific surface area of the sound zone are similar to those of the sound sample. The degraded zone shows a high specific surface area (Table 5-1) compared to the sound zone but lower than the degraded zones with 5 mM and 50 mM $MgCl_2$ (around 550 m^2/g). On the other hand, the amount adsorbed for $p/p_0>0.4$ (Figure 5-8a) is much greater than for the two magnesium attacks, corresponding to the presence of larger pores in greater quantities. This is reflected in the pore distribution (BJH) (Figure 5-8b). A first peak appears around 3.8 nm, as for the 5 mM and 50 mM degraded samples and then the curve remains higher than that of the 5 mM and 50 mM degraded samples for the upper pores. Pure leaching seems to create larger pores in the degraded zone than magnesium attack. The formation of M-S-H seems to fill some of the porosity created by decalcification and dissolution of C-S-H and ettringite. It would be necessary to carry out a mercury porosity test to see if this observation is true for pore diameters larger than 8 nm. Due to the small degraded thickness, the amount of degraded zone was not sufficient to perform both nitrogen physisorption and MIP in this study.

Table 5-1: Average Specific Surface B.E.T (m^2/g) determined by N_2 Physisorption of the sound model cement paste, a degraded sample and a M-S-H paste

Type of sample	Sound model cement paste	Leached model cement paste	
Zone	-	Sound Zone (Z1)	Degraded zone (Z2-Z3)
Average Specific Surface B.E.T (m^2/g)	36.2	46.0	362.8

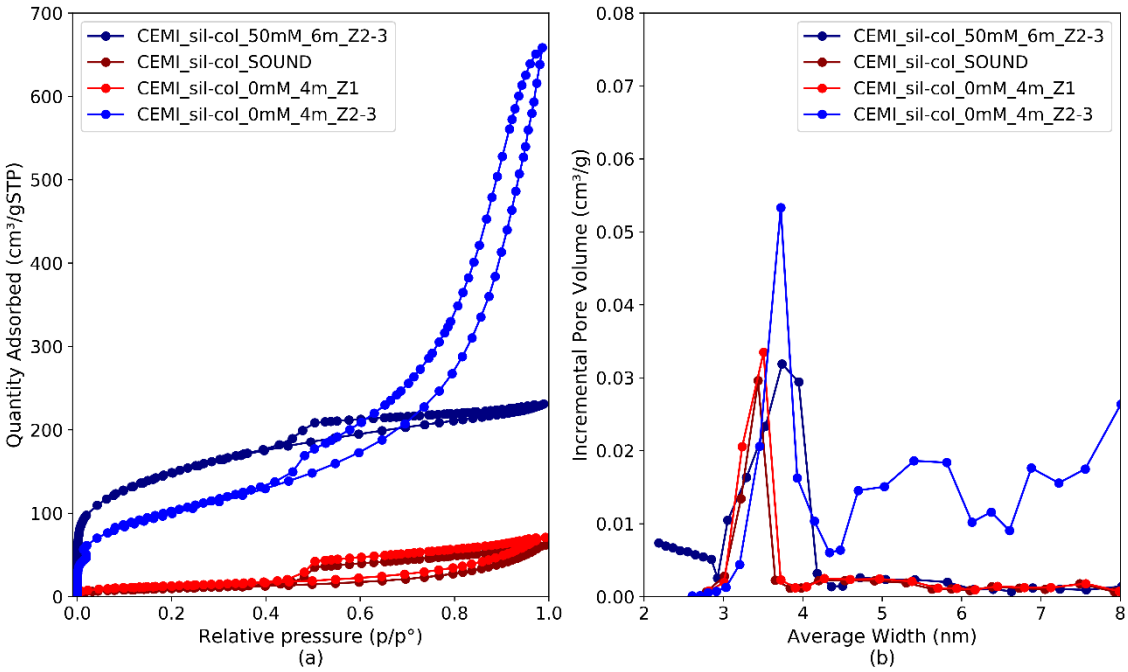

Figure 5-8: (a) N_2 adsorption-desorption isotherms of the sound zone and degraded zone of the leached sample, compared to a pure M-S-H paste (M/S=0.78) (Dewitte et al. 2022) and (b) Associated pore size distributions (BJH). Z1 = Zone 1 (sound zone) of the degraded paste, Z2-3 = Assembly of zones 2 and 3 (enriched in Mg) of the degraded paste (50 mM)

5.1.3.3. Elastic properties

As for the 5 mM and 50 mM degraded samples, microindentation was performed to determine the mechanical properties along the degradation of the leached sample (0 mM). Figure 5-9 shows the results after removing of the outliers by interquartile method.

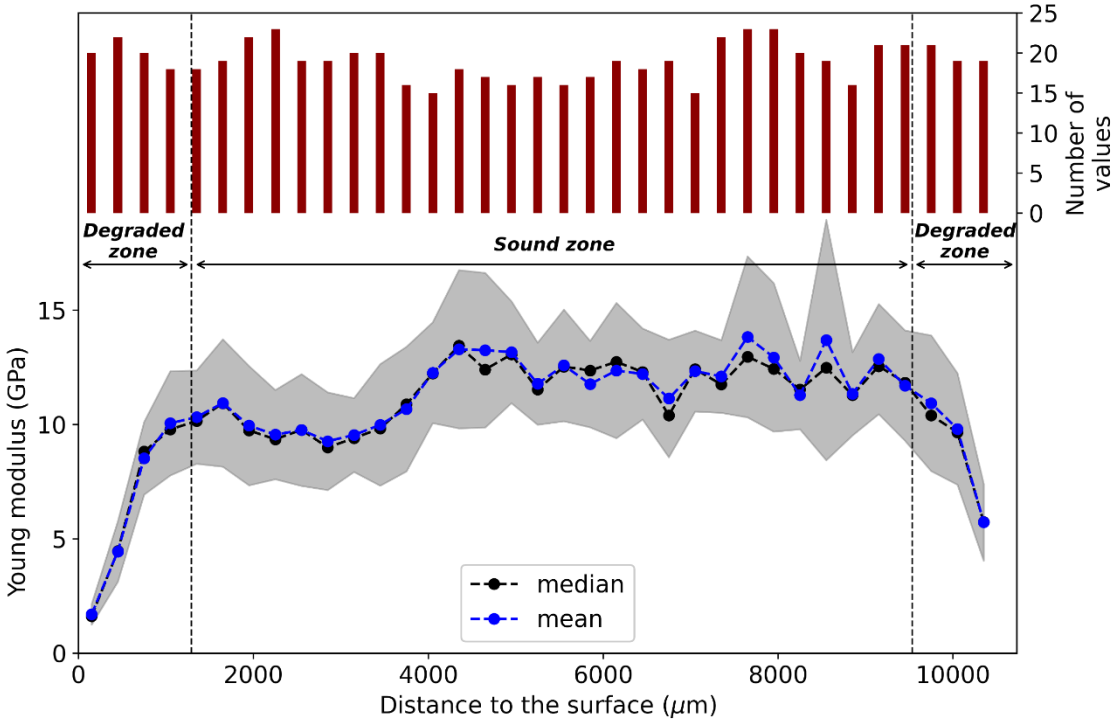

Figure 5-9: Microindentation data without outliers of the model cement paste immersed in pure water during 4 months

The number of successful indents of the last column (10650 µm) is not sufficient (6 indents) and are not represented on the graph. It appears that the mechanical properties follow the same trend as the calcium and density profiles. The Young's modulus decreases in the degraded area until it reaches about 2 GPa. While the C/S at the surface of the leached sample is 4 times higher than that of the magnesium attacked samples, the mechanical properties are similar (around 2.5 GPa). The amount and structure of the remaining (decalcified) C-S-H in the degraded zone for the pure leached sample (0 mM), does not allow to keep good mechanical properties. The properties of the residual C-S-H (in pure leaching) appear to be similar to those of the M-S-H formed (in magnesium attack). Furthermore, it shows that decalcification of C-S-H has an important part in the observed decrease of mechanical properties.

In conclusion, the pure leaching of the low-pH model pastes showed a progressive decalcification from the sound zone to the surface of the sample. The microstructural and mechanical properties follow the same trend, the increase in porosity and the loss of mechanical properties are progressive. On the contrary, during the magnesium attack of the same pastes, the samples show the presence of two zones (Z1 and Z3) with stable but very different chemical, microstructural and mechanical properties. The Mg-enriched zone (Z3) has a very low proportion of calcium, no C-S-H is detected in contrast to the degraded zone under pure leaching. The transition between the two zones is rapid and a shrinkage phenomenon causes detachment at the junction of the two zones once the sample is placed in an unsaturated environment. Thus, although the depth of the degraded zone is similar for the leached sample and the sample under magnesium attack (5 mM), the behaviour and properties of the degraded zone are weaker in the case of magnesium attack. Furthermore, as the magnesium concentration increases, the depth of the degradation front increases. Although M-S-H are formed and replace C-S-H during magnesium attack, their presence does not counteract decalcification. Magnesium attack on the low pH model cement pastes is even more detrimental than pure leaching. It increases the degraded depth and causes the formation of a homogeneous degraded zone with the lowest microstructural and mechanical properties observed in pure leaching.

The method of determining mechanical properties from microprobe and XRD data (see 2.1.4.2 and 4.5) was applied to the leached paste in order to verify its validity in the case of another type of attack. The mineralogical composition of the degraded sample in pure leaching is much simpler than for magnesium attack. Only three phases are considered: ettringite, C-S-H and amorphous silica. The C/S ratio in the sound zone of the leached sample (0 mM) is slightly higher than in the sound zones of 5 mM and 50 mM (0.934 versus 0.9) (see Figure 4-7 and Figure 5-3). The C/S ratio of C-S-H was therefore modified accordingly in the code and considered equal to 0.864. To consume all the species, the C/S ratio of the silica was taken to be 0.085 (as for the 50 mM). In the sound zone, $Al/Si_{amorphous\ silica}$=0 and Al/Si_{CSH}=2.85%. In the degraded zone, as the aluminium signal increases as it approaches the surface, the Al/Si ratio in the amorphous silica and C-S-H increases as it approaches the surface. The Al/Si value considered in C-S-H and amorphous silica is the same. It varies from 0 to 12% in order to integrate all aluminium detected on microprobe (Figure 5-3). The integration of aluminium does not change the molar or volume percentage of the phases. This is an attempt to incorporate the aluminium observed in the microprobe without influence on the mechanical calculations. Figure 5-10 shows the results.

When calcium is leached out and C-S-H decalcifies, it is considered in the simulation that the amount of C-S-H decreases since only one C/S ratio is considered (Figure 5-10a). The remaining silica is then present as amorphous silica. As amorphous silica has a high intrinsic porosity, the capillary porosity (Figure 5-10b) does not increase much while the total porosity increases from 51% to 70% (Figure 5-10c). Mechanical homogenisation gives similar results to those obtained by microindentation. This time, no x-shift is visible between the microindentation data and the simulation. The loss of elasticity is located at the same point. The data of the phases considered for homogenisation allows to find satisfactorily the microindentation results.

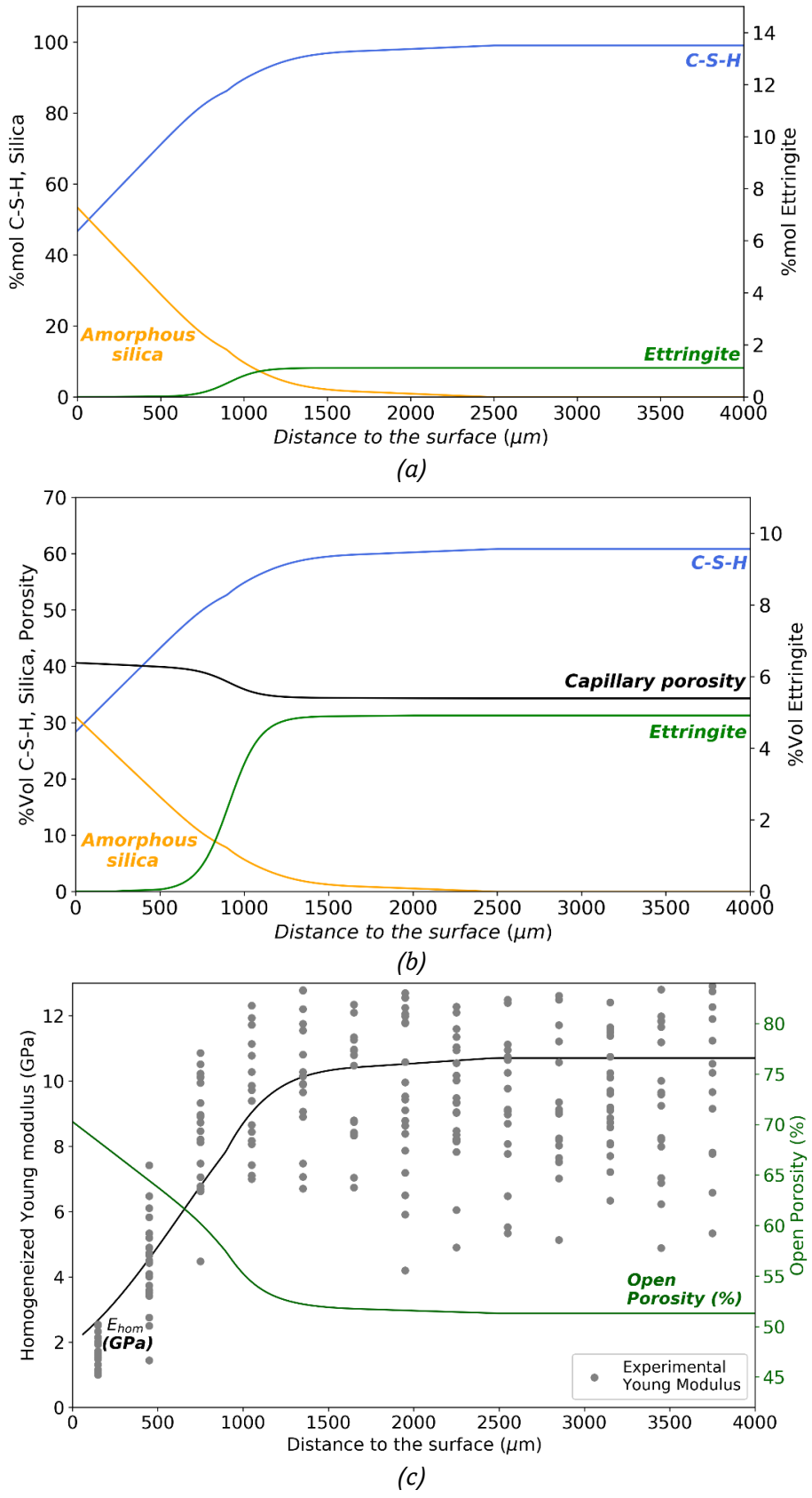

Figure 5-10: Calculated molar proportions (a) and volume proportions (b) of the phases and homogenised properties of the degraded sample according to the distance to the surface (c) of a low-pH model cement paste immersed during 4 months in pure water

5.2. Discussion on the reaction mechanisms of magnesium attack compared to leaching

The previous sections have shown a difference in kinetics (different degraded depth) and reaction mechanism (different appearance of the degraded zone) between pure leaching and magnesium attack depending on the Mg concentration in solution. This section proposes a discussion on the reaction mechanisms based on HYTEC simulations varying the type of aggressive solution and observing the solid phases and the composition of the pore solution.

5.2.1. Chemical composition of the sound sample

To carry out a chemical simulation of the degradation of low-pH model cement pastes, it is first necessary to determine the initial composition of the material. According to the formulation, the concentration of oxides in the mixing preparation is the following:

Table 5-2: Oxides concentration in the mixing paste

Oxide	SiO_2	Al_2O_3	CaO	SO_3
Concentration (mmol/L_{paste})	7861.3	231.7	7391.5	217.3

According to the XRD (4.2.1), two types of phases are present: C-S-H and ettringite. For the calculation, the presence of residual, non-hydrated C_4AF is also considered. Thus, the four main oxides presented above are driven by the four mineralogical phases considered.Two types of C-S-H are considered because the C/S ratio is 0.85 (see figure) and the C-S-H in the database are incremented in steps of 0.1. It is therefore necessary to consider two C-S-H with different ratios. According to a pre-calculation with Hytec, the most thermodynamically stable C-S-H is for C/S=1. Consequently, the second C-S-H considered is with C/S=0.7. But it would have been perfectly possible to consider C-S-H with ratios C/S=0.8 and 0.9. The C-S-H concentrations would then become 2327 mmol/L for C/S=0.8 and 1603.7 mmol/L for C/S=0.9 (see Table 5-3).

To integrate the results of stoichiometric calculations into the reactive transport code (Hytec), the C-S-H considered are those of Thermoddem. Thus one mole of C-S-$H_{Thermoddem}$ corresponds to two moles of H_4SiO_4, or two moles of C-S-H in the usual considerations. The results of the stoichiometric calculations are given in the second row of the Table 5-3 (Concentration mmol/L). In Hytec, such a mineralogy gives a pH of 11.15 and a Ca^{2+} concentration in solution of 2.0 mmol/L. The last row gives the results in g/l_{paste}, i.e. taking into account the porosity of the paste (0.515). In the simulation, C_4AF is considered inert facing leaching (Matte et al. 2000).

Table 5-3: Model low-pH cement paste composition according to stoichiometric calculations

Mineralogical phase	Ettringite	C-S-H (C/S=1)	C-S-H (C/S=0,7)	C_4AF
Concentration (mmol/L)	72.4	1844.8	2085.9	86.9
g/l_{paste}	176.5	987.1	979.8	ND

5.2.2. Simulation hypotheses

Several degradation simulations were carried out. The geometry of the simulation is illustrated in Figure 5-11.

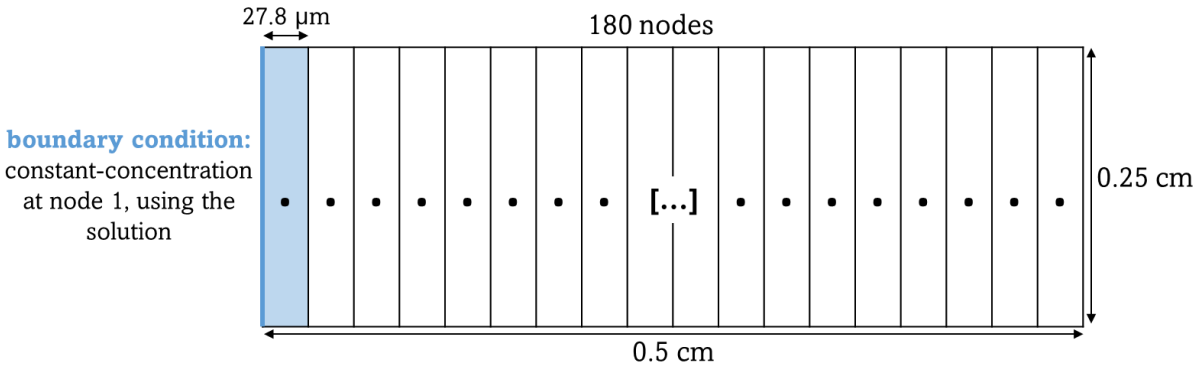

Figure 5-11: Geometry of the simulation

3 study cases were simulated, by changing the composition of the solution:

(a) Solution = pure water (0 mM)
(b) Solution = pure water + $MgCl_2$ at 5 mM (called 5 mM)
(c) Solution = pure water + $MgCl_2$ at 50 mM (called 50 mM)

To reproduce the conditions of the real tests (see Figure 4-1), the equilibrium with ambient CO_2 was considered in the boundary condition (fugacity=4.10^{-4} in the solution), allowing to obtain the same pH (5.8).

The transport is simulated with a constant diffusion coefficient along the degradation profile (hypothesis susceptible to underestimate the degradation kinetic as porosity and thus diffusion coefficient is increased). The value is obtained considering a porosity of 51.5% (Φ_w, see 4.2.2) using the equation proposed by (Mainguy et al. 2000) : $D = \exp(9.95\phi - 29.08) = 4 \cdot 10^{-11} m^2/s$.

5.2.3. Discussion

5.2.3.1. Comparison with experimental results

The results of the simulation after 4 months of degradation are presented in Figure 5-12 (Mineralogical composition according to the distance to the surface) and Figure 5-13 (M/S and C/S molar ratios in the solid according to the distance to the surface). For easier comparison, the M/S and C/S intensity ratios calculated from EDS were added on the Figure 5-13. All the figures that will be presented hereafter plot the properties of the mesh from the second cell (exclusion of the cell corresponding to the aggressive solution).

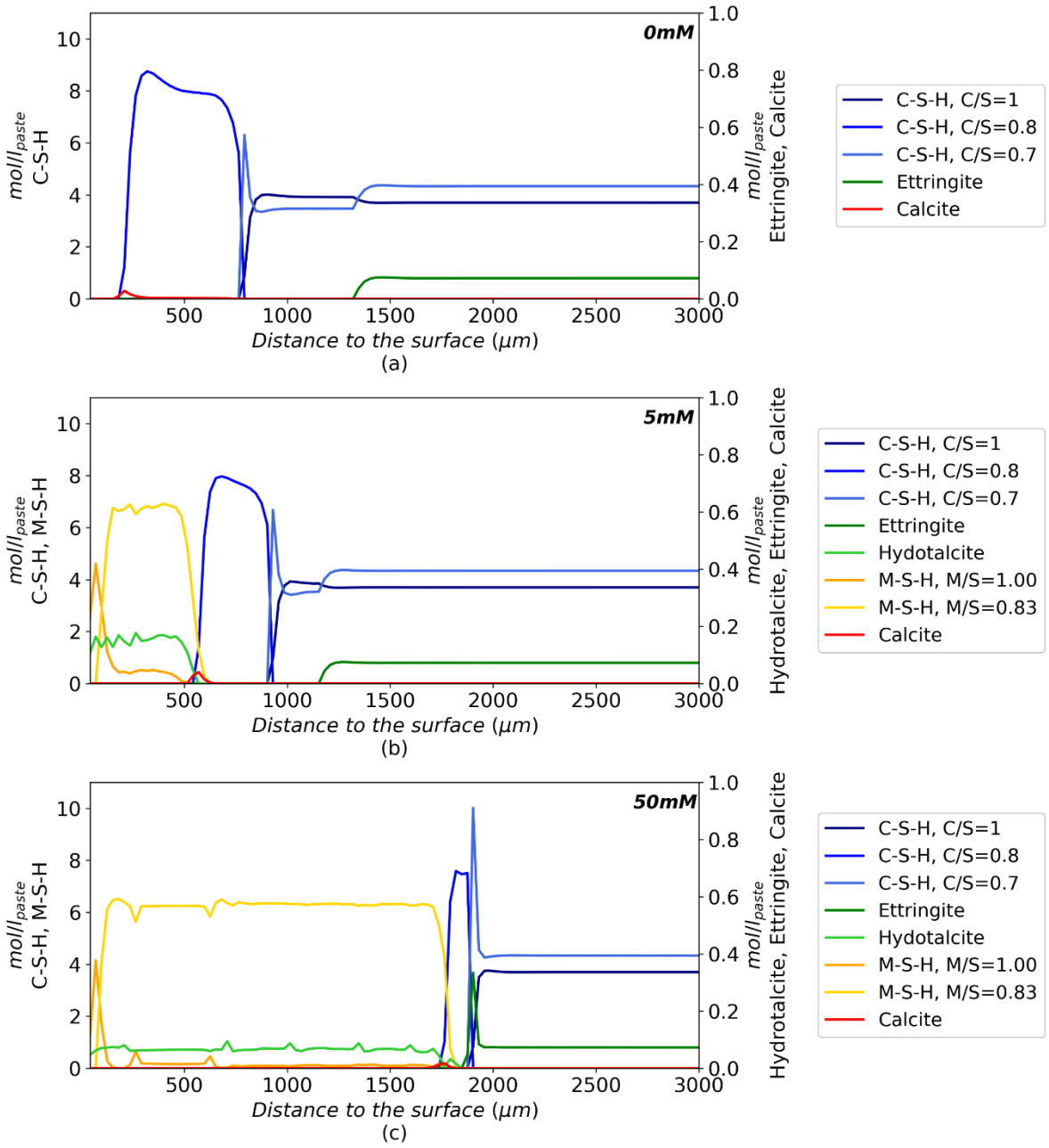

Figure 5-12: Hytec simulation of a 1D degradation of model low-pH cement paste in contact with (a) pure water (0 mM), (b) a solution of 5 mM of $MgCl_2$ and (c) 50 mM of $MgCl_2$ during 4 months

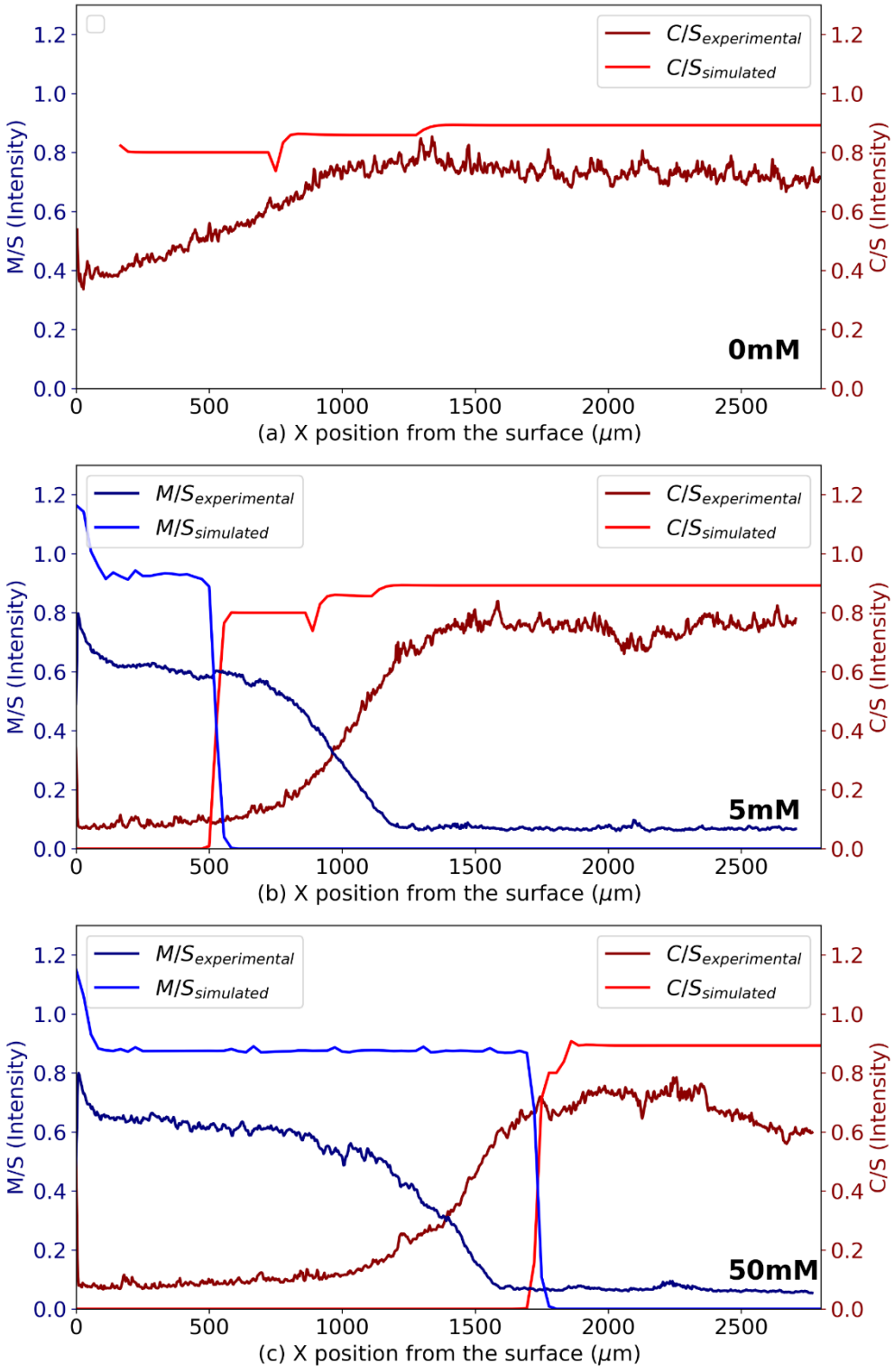

Figure 5-13: M/S and C/S (in the solid) calculated along the degradation from the Hytec simulation results (Molar ratios) and experimental EDS results (Intensity ratios) of model low-pH cement paste in contact with (a) pure water (0 mM), (b) a solution of 5 mM of $MgCl_2$ and (c) 50 mM of $MgCl_2$ during 4 months

Two types of zones can be defined: the "sound zone", in which all the concentrations of the mineralogical phases keep a constant value, and the degraded zone, from the surface (left) to the sound zone. The depth of the degradation front, according to this definition, is reported in Table 5-4. The evolution of the degraded depth and the kinetics will be discussed in the next section (5.2.3.2).

Table 5-4: Degradation depth according to the simulation of the three cases after 4 months of degradation

Case number	a	b	c
$MgCl_2$ concentration	0 mM	5 mM	50 mM
Simulation, *minimal depth for a sound C/S*	1400 µm	1250 µm	1950 µm
Experiments, *minimal depth for a sound C/S (EDS)*	1100 µm	1250 µm	1600 µm

Several types of mineralogical species are formed: magnesium phases (M-S-H and hydrotalcite) and calcite. Although not observed experimentally, calcite precipitates in the simulation due to the presence of CO2 in the aggressive solution. C-S-H and ettringite dissolve much more abruptly than in reality (Figure 4-30, Figure 4-32 and Figure 5-10).

As shown in Table 5-4, the depth of the degradation front is greater in the simulation than in reality. Only the sample degraded in 5 mM $MgCl_2$ shows a similar simulated and experimental depth (1250 µm). Although the depth of the degradation front is similar for the simulated and experimental 5 mM, the appearance of the degraded zone is different.

In the case of leaching, the silica gel is not stable (it does not form), therefore (i) C-S-H are only destabilised when the calcium concentration is very low and (ii) there is a zone where there is no solid phase. The thermodynamic constant of the silica gel considered does not therefore seem to be appropriate.

In both cases (pure leaching and magnesium attack), the simulation does not show a transition zone (with progressive decalcification of C-S-H and/or progressive magnesium enrichment). This can be seen in the C/S profile for the pure leached sample (0 mM) (Figure 5-13a). While in the experiments the C/S reaches 0.4 at the surface (Figure 5-10), in the simulation the lowest C/S is 0.75 and then suddenly all the C-S-H are dissolved. For both magnesium attack simulations, as soon as C-S-H are destabilised, M-S-H are formed instead (Figure 5-13b and c). Furthermore, no amorphous silica is formed as for the pure leached simulation, whereas experimentally it is (see NMR, Figure 4-19).

This is due to two factors: (i) no kinetics for dissolution and precipitation of species were considered and (ii) it is an equilibrium calculation, the more stable phase precipitates, and the non-stable phase dissolves. As C-S-H is defined as a set of independent phases with a fixed C/S ratio, the C/S ratio follows the evolution of the phases that form. In the absence of amorphous silica, the lowest C/S is that of the lowest C-S-H. As raised previously, the thermodynamic constant of the silica gel considered does not therefore seem appropriate.

Beyond the degraded depth, which depends on the simulation hypotheses, the simulation does not therefore make it possible to account for the progressive decalcification and Mg enrichment observed experimentally.

5.2.3.2. Effect of $MgCl_2$ on leaching kinetics

The simulations also allow to evaluate the evolution of the concentration of ions in solution and the pH in the different cases of study were studied. It appears on Figure 5-14 that Cl^- ions diffuse

throughout the sample. It is important to note that no adsorption of Cl^- on C-S-H was taken into account in the simulation (no easy way to introduce a sorption isotherm in the commercial version of HYTEC) which leads to an overestimation of the penetration kinetic of Cl^-.

While usually the Ca^{2+} concentration in equilibrium with C-S-H of low C/S ratios in the pore solution is about 2 mmol/L (Roosz et al. 2018; Chen et al. 2004), it appears that during the magnesium attack, the Ca^{2+} concentration, even within the "sound" zone, increases. The higher the Mg concentration in the aggressive solution, the higher the Ca^{2+} equilibrium concentration in the "sound zone".

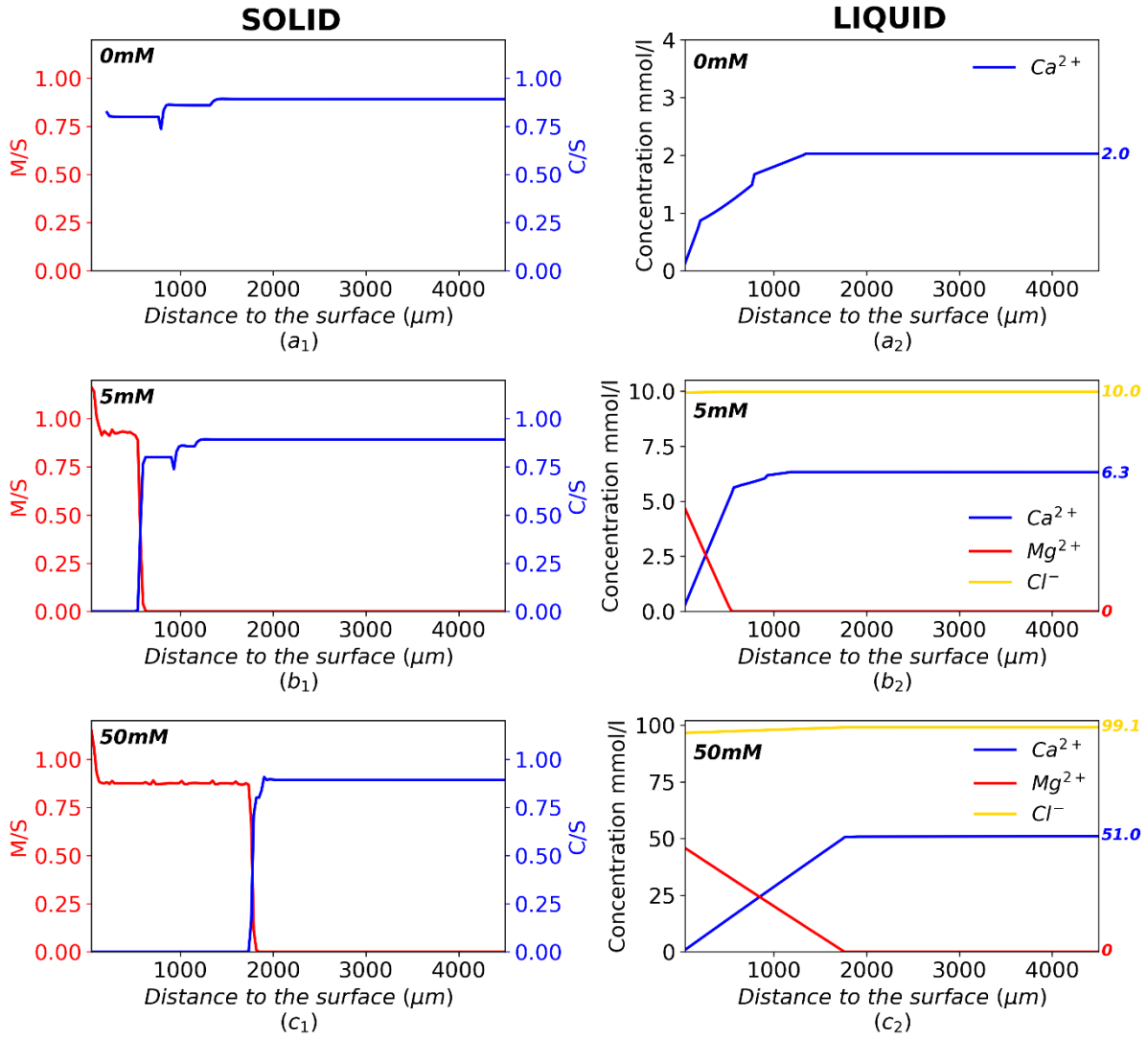

Figure 5-14: (a_1, b_1, c_1) M/S and C/S (in the solid) calculated along the degradation from the Hytec simulation results and (a_2, b_2, c_2) Ca^{2+}, Mg^{2+} and Cl^- concentration in the poral solution (liquid) of the simulation cases a, b and c (4 months of degradation)

To see if the origin of the increase in Ca^{2+} concentration is due to the presence of Mg^{2+} and Cl^- ions alone in the aggressive solution, three more study cases were simulated, by changing the species available in the database (magnesium phases are no longer allowed to form):

(d) Solution = pure water + $MgCl_2$ at 5 mM, precipitation of Mg phases not allowed (called 5 mM, No Mg phases allowed)

(e) Solution = pure water + $MgCl_2$ at 50 mM, precipitation of Mg phases not allowed (called 50 mM, No Mg phases allowed)
(f) Solution = pure water + NaCl at 100 mM (called 100 mM NaCl)

The results of the simulation (Mineralogical composition according to the distance to the surface) after 4 months of degradation are available in Appendix G (Figure G-1).

If the aggressive solution consists of NaCl (at 100 mmol/L to respect the Cl^- concentration) and no more $MgCl_2$, the Ca^{2+} concentration decreases to 3.4 mmol/L (Figure 5-15 (f_2)).

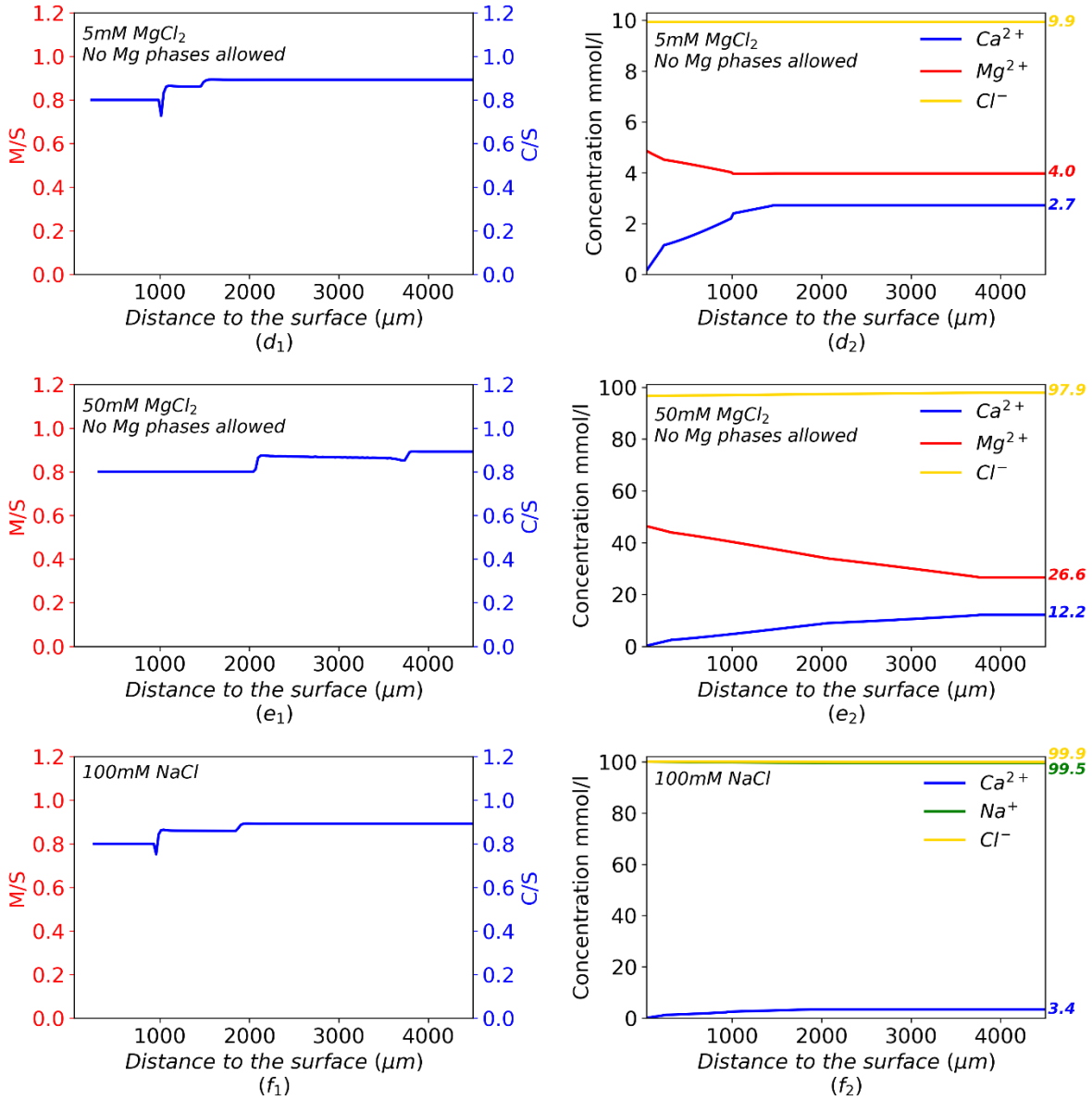

Figure 5-15: (d_1, e_1, f_1) M/S and C/S (in the solid) calculated along the degradation from the Hytec simulation results and (d_2, e_2, f_2) Ca^{2+}, Mg^{2+}, Na^+ and Cl^- concentration in the poral solution (liquid) of the simulation cases d, e and f (4 months of degradation)

If the $MgCl_2$ concentration is maintained but precipitation of the magnesium phases is no longer allowed (cases (d) and (e)), the Ca^{2+} concentration in solution (Figure 5-14) is higher (2.7 and 12. 2 for 5 mM and 50 mM $MgCl_2$ respectively) than that with NaCl (3 mmol/L for 100 mM NaCl) and in the absence of ions (pure leaching, case (a), 2 mmol/L) but it remains significantly lower than that observed when M-S-H precipitates (6.3 and 51 mmol/L for 5 mM and 50 mM $MgCl_2$

respectively). Thus, it appears that the presence of magnesium ions and the formation of M-S-H changes the thermodynamic equilibrium. For C-S-H to be in equilibrium in the presence of magnesium, the Ca^{2+} concentration must increase. This increase is related to the evolution of the pH. In the presence of $MgCl_2$, the pH of the sound zone decreases (Figure 5-16). The decrease in pH is all the greater when the formation of magnesium phases is possible. The pH of the aggressive solution (not plot on Figure 5-16) is around 5.6 (5.61 for 0mM and 100mM NaCl, 5.60 for 5mM and 5.58 for 50mM).

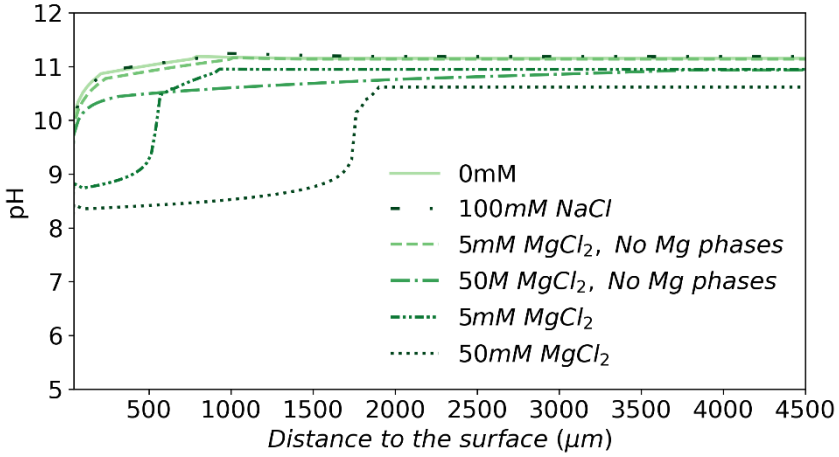

Figure 5-16: pH along the degradation from the Hytec simulation results after 4 months of degradation

When the Mg concentration of the aggressive solution is multiplied by 10 (50 mM), the simulation predicts a degraded depth for the sample placed in 50 mM $MgCl_2$ that is 1.5 times greater than that with 5 mM $MgCl_2$, whereas in reality, the degraded depth is only 1.3 times greater.

Several factors may explain the gap between the simulated and real degraded depth. The first is the absence of consideration of dissolution-precipitation kinetics (solid-liquid interaction). This includes both reaction kinetics and micro-diffusion kinetics in the intrinsic porosity. As the transport properties in M-S-H are not known, it would have been necessary to randomly choose a value, which in addition can evolve over time. A second cause is the lack of consideration of the variation of porosity. No retroaction law was used to link the variation of volume, porosity and diffusion coefficient. Indeed, the law available on Hytec is Archie's law. It is mainly the effect on the capillary porosity that is taken into account, whereas in our case, the capillary porosity is rather stable (Figure 4-30) while the total porosity (Figure 4-31) increases a lot. It would therefore be more likely an evolution of the hydrate porosity. The law did not seem to be adapted.

As the simulation does not take into account precipitation/dissolution kinetics, the simulation tends to overestimate the degraded depth. The increase in degraded depth with increasing Mg concentration in the aggressive solution is attributable to the increase in ionic strength, the decrease in pH and consequently a change in the thermodynamic equilibrium of C-S-H involving an increase in Ca^{2+} concentration in the pore solution. Furthermore, the increase in Mg concentration does not alter the M/S ratio of the M-S-H formed both in simulation (Figure 5-14 (a_1) to (e_1)) and experimentally (Figure 4-20 and Figure C-5, Appendix C).

Conclusion

The effect of pure leaching was compared to the effect of magnesium attack on a low-pH cement model paste. Pure leaching was performed by placing samples in pure water for 4 months. Chemical, microstructural and mechanical characterizations were compared to those of the magnesium attacked pastes (5 mM and 50 mM). Pure water causes a progressive Ca and S

leaching from the core of the material to the surface. The porosity of the degraded zone increases progressively to the surface, in parallel with a decrease in elastic properties. The degraded depth is slightly lower than that of magnesium attack with 5 mM $MgCl_2$. Although the degraded depth is similar, the appearance of the degraded zone and its averaged properties are clearly superior to those during magnesium attack. The magnesium attack is much more detrimental than pure leaching, despite the replacement of C-S-H by M-S-H. As shown in a chemical simulation, increasing the magnesium concentration disturbs the thermodynamic equilibrium of C-S-H. The ionic strength and Ca^{2+} concentration in the pore solution (even within the sound zone) increase which accelerates the calcium leaching kinetic.

CHAPTER 6. MAGNESIUM ATTACK ON INDUSTRIAL LOW-PH PASTE

Introduction

The last two chapters (Chapter 4 and Chapter 5) were devoted to the study of the magnesium attack of a low-pH model cement paste and the comparison with the effect of pure water. The study showed that the magnesium attack on this type of material corresponded to the formation of M-S-H and that it resulted in the decrease of mechanical properties and the increase of porosity. The reaction mechanism of the formation of M-S-H and its kinetics were investigated. It appears that magnesium attack is more detrimental than pure leaching on materials with low C/S ratio because it causes the formation of a large zone where C-S-H are completely absent unlike pure leaching where the decalcification of C-S-H is smooth and progressive. The microstructural and mechanical data of M-S-H, determined in Chapter 3, were validated on the degraded model materials. To verify that the reaction mechanism of the magnesium attack and the formed M-S-H have similar properties on more complex materials, this chapter proposes a study on a low-pH industrial paste placed in a magnesium environment. The formulation of this low-pH paste (named T3) is similar to the one foreseen for the project of nuclear waste geological disposal in a clayey rock in France (Cigéo) and was already introduced in Chapter 2. It had shown a non-homogeneous distribution of calcium and silica as well as a more complex mineralogy than the low-pH model cement paste.

The low-pH paste has been produced by mixing CEM III A with silica fume. At the end of their manufacture, the pastes were kept under endogenous conditions for 2 years. Then, cylindric samples (diameter=3cm, thickness=1cm) were cut, coated with sealant on the lateral side to allow unidirectional degradation. The samples were immersed in 50 $MgCl_2$ solutions in 60 L closed tanks for 4 months. The solutions were constantly agitated and renewed every two months. At the end of the exposure time, two samples were taken, cut out and prepared for the various characterization tests.

6.1. Properties of the sound sample

6.1.1. Mineralogical and chemical properties

The theoretical C/S ratio, based on the quantities of raw materials, is 0.71. The XRD performed (Figure 6-1) on the sound material showed the presence of ettringite and C-S-H. Portlandite was absent.

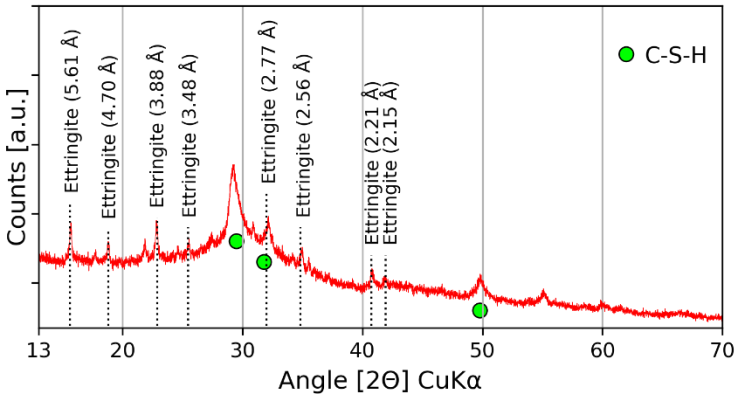

Figure 6-1: X-ray diffractograms of the sound paste after 2 years of hydration.

6.1.2. Microstructural properties

Microstructural properties were determined by several methods (Helium pycnometry, Water porosity, MIP, N_2 Physisorption, Microtomography and Autoradiography, see 2.1.3 for more details) on the sound sample. Table 6-1 summarizes the results.

Table 6-1: Microstructural properties of the sound sample

	ρ_{true}		ρ_{bulk}		Φ_w	Φ_H		Φ_{MIP}	Specific surface (m^2/g)
Place - Method	IRSN (Helium)	LMDC (Helium)	IRSN (Kerdane)	LMDC (Water)	LMDC	IRSN	LMDC	LMDC	IRSN (N_2 Physisorption)
Mean	1.673	1.722	1.394	1.286	40,6%	16.68%	25.36%	33.8%	10.7
Standard deviation	0.005	0.040	0.005	0.019	0,7%	0.4%	1.7%	0.15%	0.3

The water porosity is the highest porosity (because of the drying at 105°C which can remove some of the bound water), followed by the MIP porosity since it does not take into account the smaller pores. In contrast to the low-pH model cement pastes, the helium porosity is lower than the MIP porosity. Indeed, according to Table 4-4 in Chapter 4.2.2 and Figure F-8 in Chapter Appendix E, for low-pH model pastes, the helium porosity is higher than that in MIP.

Several authors have studied the influence of the measurement method on the open porosity values. It has been consistently observed that porosity measured by water saturation is the highest and tends to overestimate the actual porosity (Feldman 1972; Marsh, Day, et Bonner 1985; Krus, Hansen, et Künzel 1997). Krus (Krus, Hansen, et Künzel 1997) explains this by the fact that water is a highly polar liquid that can slip between the mineral layers of the material (e.g. in C-S-H), widening the distances between them and creating new pore spaces. He observes that the helium porosity and MIP porosity of five different type of cement pastes (Ordinary Portland Cement pastes with or without few additions at different w/b ratios) are 2-3 times lower than the water porosity.

Tracz (Tracz 2016) proposed in 2016 a further study on the influence of the w/b ratio and the type of cement on the porosity calculated by the following three methods: Water saturation, Helium pycnometry and MIP. He finds that the measured water porosity is significantly higher than that measured by MIP and helium pycnometry. He shows that helium pycnometry gives higher porosity values than those obtained by MIP for all the w/b tested and the three cement types (CEMI, CEMII and CEMIII). The difference between the open porosity evaluated by mercury intrusion porosimetry and that measured by helium pycnometry could be explained by the fact that the cement paste contains pores smaller than the minimum size of accessibility of mercury, which therefore cannot be identified by MIP but which can be reached by the smaller nitrogen molecules. For blended pastes with significant pozzolanic reaction, helium porosity tends to give lower results than MIP (Marsh, Day, et Bonner 1985; Day et Marsh 1988). A comparison of porosities measured by mercury porosimetry and helium pycnometry indicates a clear difference in behaviour between fly ash and ordinary cement pastes. This difference can be explained by pore blocking which only occurs in fly ash pastes (Day et Marsh 1988). There would be a discontinuity in pore structure that occurs in ash pastes but not in ordinary pastes. This discontinuity can be thought of as blockages that form when pozzolanic reaction products enter porous channels normally capable of supporting flow. These blockages render large volumes of the pore structure inaccessible to fluids that are introduced at a relatively low pressure, such as helium. Upon mercury intrusion, however, mercury is forced into the paste at high pressure; mercury is able to break through these blockages and enter otherwise inaccessible pore volumes.

The T3 paste studied here is composed of slag and silica fume. It was shown that long term reactions occur in this binder leading to the production of C-S-H at long term by internal chemical rebalance. Similar blockages are likely to occur.

In the case of low-pH model pastes, the only addition is silica which is in colloidal form. The reaction is accelerated compared to pastes with silica fume and from the experimental results, it does not seem that blockages are formed.

The difference between the real density and Φ_H values measured at LMDC and IRSN could be explained by a different helium intrusion pressure (between 1 and 1.25 bar at LMDC and 1.36 bar at IRSN) and different protocol of apparent density measurement (with Kerdane at IRSN and water at LMDC). The porosity value considered for future discussions is the water porosity.

6.1.3. Mechanical properties

Nanoindentation and microindentation were performed on the sound sample. As detailed in 2.1.2.3, nanoindentation has been performed at a depth of 300 nm and microindentation with a force of 200 mN (depth ≈10 µm). In nanoidentation, 6300 indents were made but only 4845 were sucessfull and kept after exclusion of outliers. In microindentation, 416 points were realized and 240 points were sucessfull and kept after exclusion of outliers. The tests on the T3 paste are more difficult and less successful than on the model paste because of the presence of clusters of silica fume which generates a less good flatness of the sample and a difference in level and hardness between the clusters and the matrix. The amount of indents retained is less than that for the model paste (23% of failed or outliers indents for the T3 paste against 5% for the model paste in nanoindentation). Figure 6-2 shows the distribution of results.

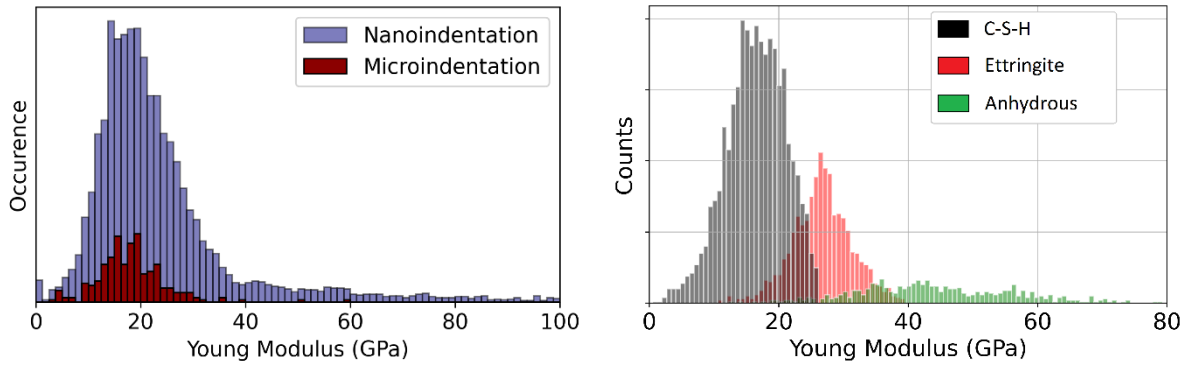

Figure 6-2: (a) Young modulus determined on the sound paste via indentation (b) deconvolution of the data of nanoindentation presented in (a).

Table 6-2: Deconvolution results on the nanoindentation data of the sound paste

Deconvolution n°	0	1	2
µ	16.5	25.6	45.4
σ	4.9	5.2	13.7
Weight	61.2%	26.9%	11.9%

A deconvolution was performed on the nanoindentation data (Figure 6-2). Three types of phases with different mechanical properties can be expected: ettringite around 20 GPa (Yang et Guo 2011), C-S-H between 18 and 27 GPa (Nguyen 2017; Constantinides et Ulm 2004; Zhu et al. 2007; Jennings et al. 2007; Constantinides et Ulm 2007; Vandamme et Ulm 2009; 2013) and anhydrous beyond 30 GPa (Hughes et Trtik 2004; Nguyen 2017). Thus, 3 clusters have been defined and deconvoluted (Table 6-2). Cluster 0 centered around 16.5 GPa would represent low-density C-S-H. Cluster 1 would correspond to ettringite. Finally, the last cluster (2) would correspond to anhydrous phases like silica fume or slag (E=101 GPa, (Königsberger et al. 2021)).

The values obtained in micro-indentation are in agreement with the nano-indentation data. They are slightly lower because they take into account the porosity of the material. The mean Young Modulus is 18.15 ± 6.7 GPa.

6.2. Determination and analysis of property gradients

6.2.1. Overall properties

A multi-physics characterization was performed on the degraded samples (see 2.1.3). This procedure has been developed to combine different types of analyses, especially EDS, microprobe, microtomography and microindentation to have access to the evolution of mineralogical properties along the depth of the sample and the consequences on the microstructure and mechanical properties. It has already been used in the previous chapters (Chapter 4 and Chapter 5) on the low-pH model cement degraded pastes. Figure 6-3 shows the results.

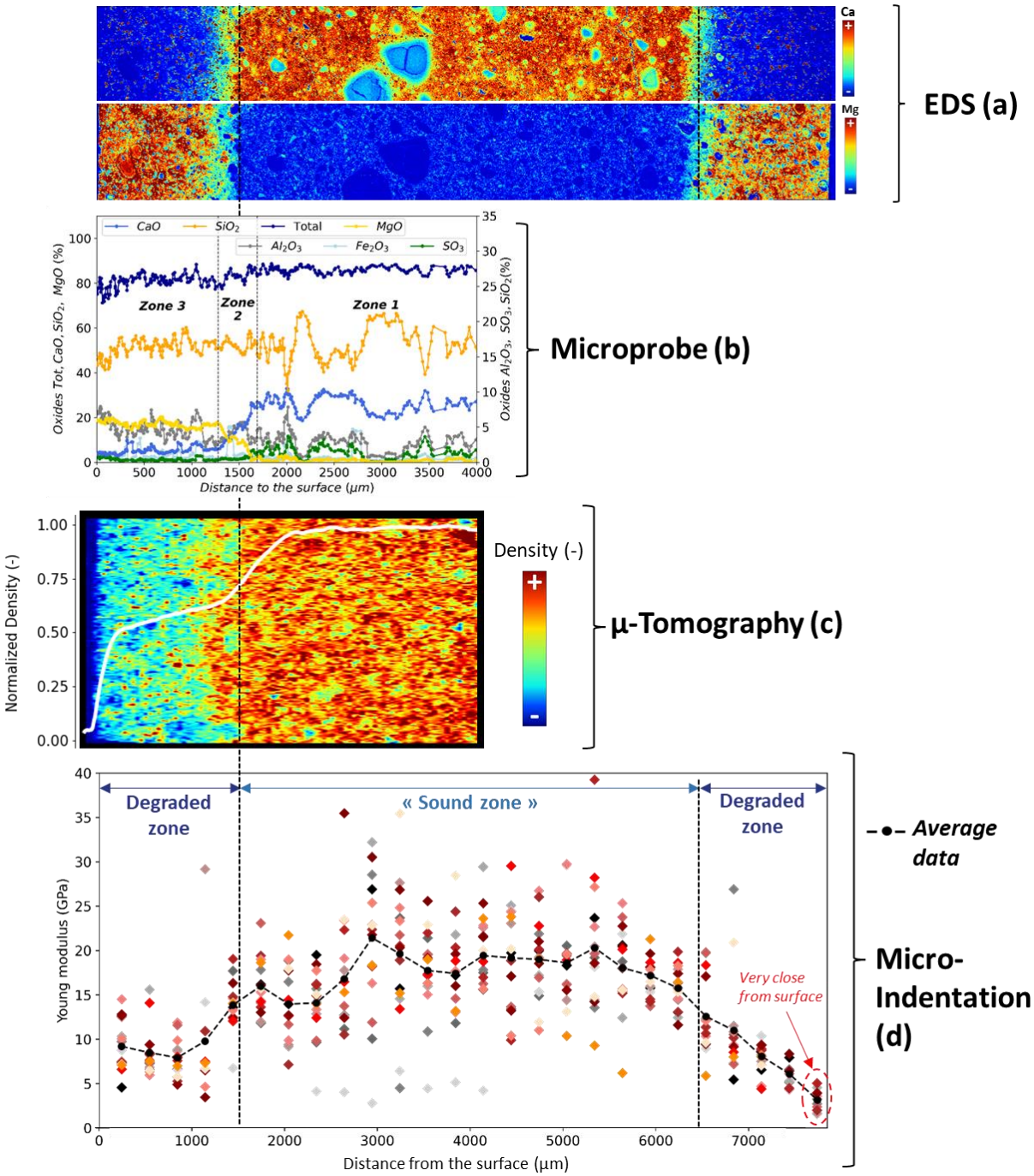

Figure 6-3 : Multi-physics characterization of a low-pH industrial cement paste immersed during 4 months in 50 mM $MgCl_2$

To visualize the degradation front and characterize the chemical evolution in the degraded samples, SEM/EDS analysis was performed. Figure 6-3 (a) shows the elemental EDS maps in Ca and Mg. It appears that in parallel to a strong leaching of calcium, an enrichment of magnesium took place in the paste. The estimative depth of the degradation front observed with EDS mapping was plotted on each part of the figure (vertical dashed lines at 1500 µm depth).

In addition, microprobe analyses along the degradation were performed. Figure 6-3 (b) shows the major oxide profiles (different scale for the 3 minorities Al_2O_3, Fe_2O_3 and SO_3). The results are comparable to those of the model paste (Mg enrichment of the paste in parallel with S and Ca leaching). The degraded depth after 4 months in the 50mM concentrated $MgCl_2$ solution is

between 1700 µm (Microprobe) and 1500µm (EDS) for T3 paste compared to 1600 µm (EDS) for the low-pH model cement paste under the same conditions (Figure 4-6). The degraded depth is similar while T3 is slightly less porous (40.6% vs. 51.5% in water porosity).

X-ray micro-tomography (Figure 6-3 (c)) was conducted in order to visualize the evolution of the density and by extension the porosity along the degradation. As for the low-pH model cement pastes exposed to magnesium attack (Chapter 4, Figure 4-23), the Mg-enriched zone shows a lower density.

Microindentation was performed to characterize the Young's modulus of the paste as a function of distance from the surface (approximately 20 indents for each x). Figure 6-3 (d)) shows the results after 4 months of degradation at 50 mmol/L. The Young's modulus observed in the sound zone on these samples was around 18 GPa. A significant decrease in elastic mechanical properties was observed in the magnesium-enriched zone, as for the low-pH model cement pastes. The following sections propose a more detailed analysis of the phenomena. As illustrated by the red circle on Figure 6-3 (d)), the last column of indents was very close from surface and Young modulus could be underestimated.

6.2.2. Magnesium enrichment and zonation

Chemical analysis by SEM/EDS and microprobe was performed on the degraded samples. Figure 6-4 shows the EDS maps performed from one degraded side to another. 4 elements mapping are displayed: calcium, magnesium, silicon and sulphur. The Ca/Si and Mg/Si ratios in intensity calculated from the EDS elemental mappings are presented on the bottom of Figure 6-4. The silica cluster around 3000 µm have not been taken into account in the calculation.

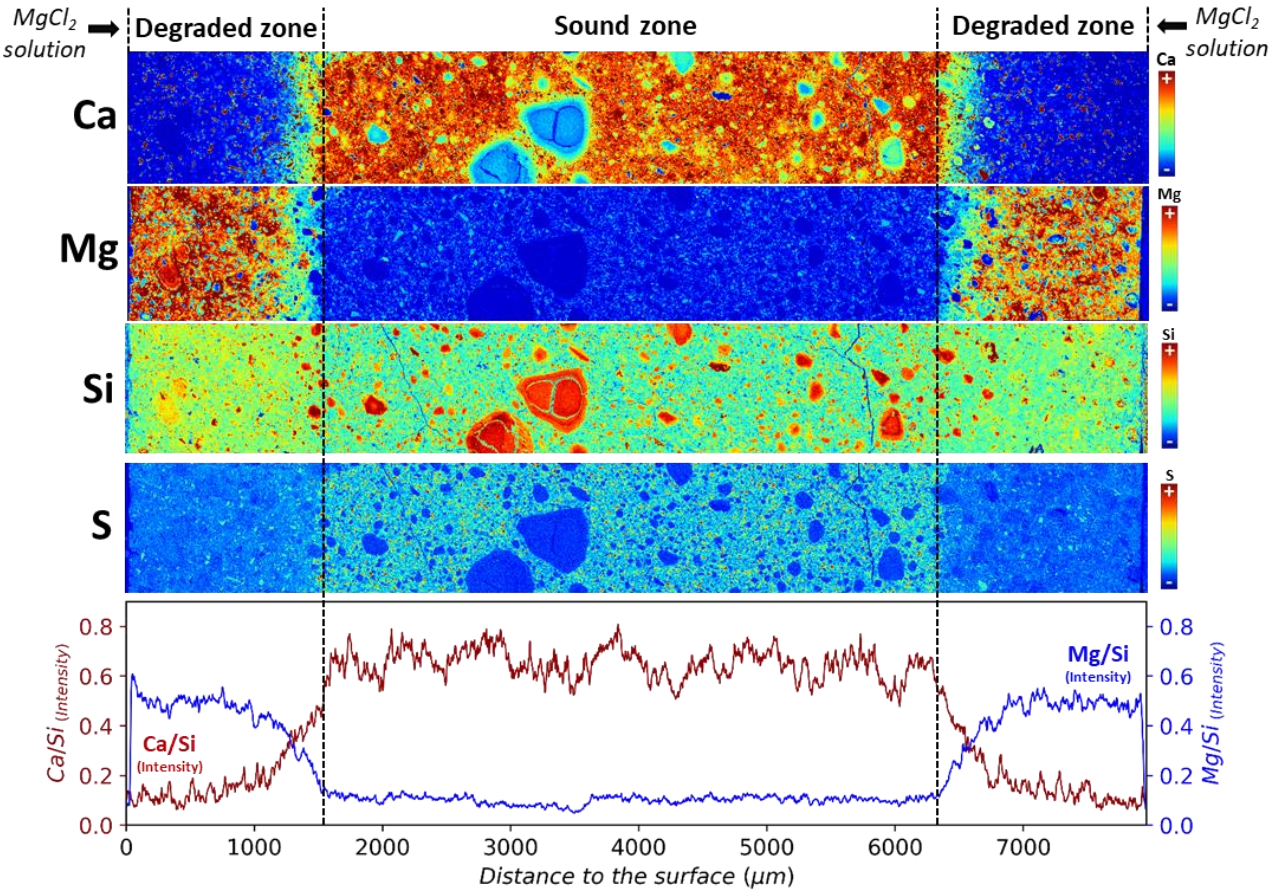

Figure 6-4 : Elemental maps (EDS) in Ca, Mg, Si and S of a low-pH industrial cement paste immersed during 4 months in 50 mM $MgCl_2$ and M/S and C/S intensity ratios calculated from solid chemical composition (EDS)

Several observations can be made based on EDS (Figure 6-4). The cement paste is enriched in magnesium, in parallel with a calcium leaching. No Mg external layer is visible in the tests. The Mg enrichment is deep and progressive within the paste, which is consistent with M-S-H formation. Magnesium preferentially binds to the location of former silicon clusters. The degraded area shows the presence of calcium clusters which would correspond to the slag embedded in the binder. Sulphur mapping shows that the depth leached in sulphur is the same as that leached in Ca and enriched in Mg.

Figure 6-5 shows the microprobe results after correction of the signal (Bertron et al. 2009) (see Chapter 4) with respect to silica and the resulting M/S and C/S atomic ratios profiles. When silica clusters are present, this correction may not be appropriate because silica clusters are difficult to avoid with the microprobe and may cause the amount of silica in the sound zone to vary. The correction, from a moving average, leads to artificially erase a real inhomogeneity on silica in the sound zone. Therefore, the strong Ca decreases observed between 2050 µm and 2300 µm are not interpreted as related to silica clusters. Trend curves, based on sigmoids, were defined from the experimental data (dots) and are displayed in the figure (lines). Several observations can be made based on microprobe (Figure 6-5).

As for the low-pH model cement paste (Chapter 4.4.1, Figure 4-4), the amount of aluminum on the surface is slightly higher than in the sound area. This increases may be linked with the relative character of the quantification (Bertron et al. 2009). As calcium and sulphur are leached out, the other non-leached elements take a larger part of the total mass. No variation in Fe and Cl was observable (see Figure 5-3 in Chapter 5 or Figure E-4 in Appendix E for Fe, see Figure E-2 and

Figure E-3 in Appendix E for Cl). As in the case of other types of attack leading to leaching (Bertron et al. 2009), analyses showed that the leaching front of sulphate species was an indicator of the beginning of the degraded zone. A drop in the sulphur signal was observed by microprobe (Figure 6-3 (b)) around 1700 µm which corresponded to the limit of the decalcification zone. 3 zones could be distinguished:

- **the sound zone (Z1)** from 1700 µm
- **the transition zone (Z2)** between 1250 and 1700 µm. The Ca signal decreased while the Mg signal increased.
- **the zone strongly enriched in Mg (Z3)**. The Ca signal was stable but not zero while the Mg signal continued to increase but more slowly. This could correspond to the incorporation of calcium in M-S-H or in the silica gel.

Zone 1 corresponding to the sound zone, showed a plateau of C/S (Atomic) at 0.6 and M/S at 0.02. The amount of Mg in the sound zone was negligible. The atomic C/S ratio observed is lower than the theoretical one of the sound paste, the C/S ratio of the mixture being 0.71 (6.1.1). The micropore measurement points were chosen outside the anhydrous. However, the cement used in this paste contains 64% slag. On EDS (Figure 6-4), in the degraded zone, clusters with a high concentration of calcium can be observed. They correspond to the clusters of slag which are also present in the sound zone, even if they are less visible. The non-homogeneous distribution of chemical elements could explain this under estimation of the C/S ratio in microprobe.

Zone 2, corresponding to the transition zone, showed a linear decrease of C/S (Atomic) in parallel with a linear growth of M/S. In the degraded zone (Z3), the atomic M/S ratio increases more slowly until it reaches a ratio of 0.6 at the surface. It should be noted that the C/S and M/S ratios correspond to the ratio between all the calcium or magnesium and all the silicon present in the solid phase, which can therefore correspond to a mixture of several species (amorphous silica, M-S-H etc.).

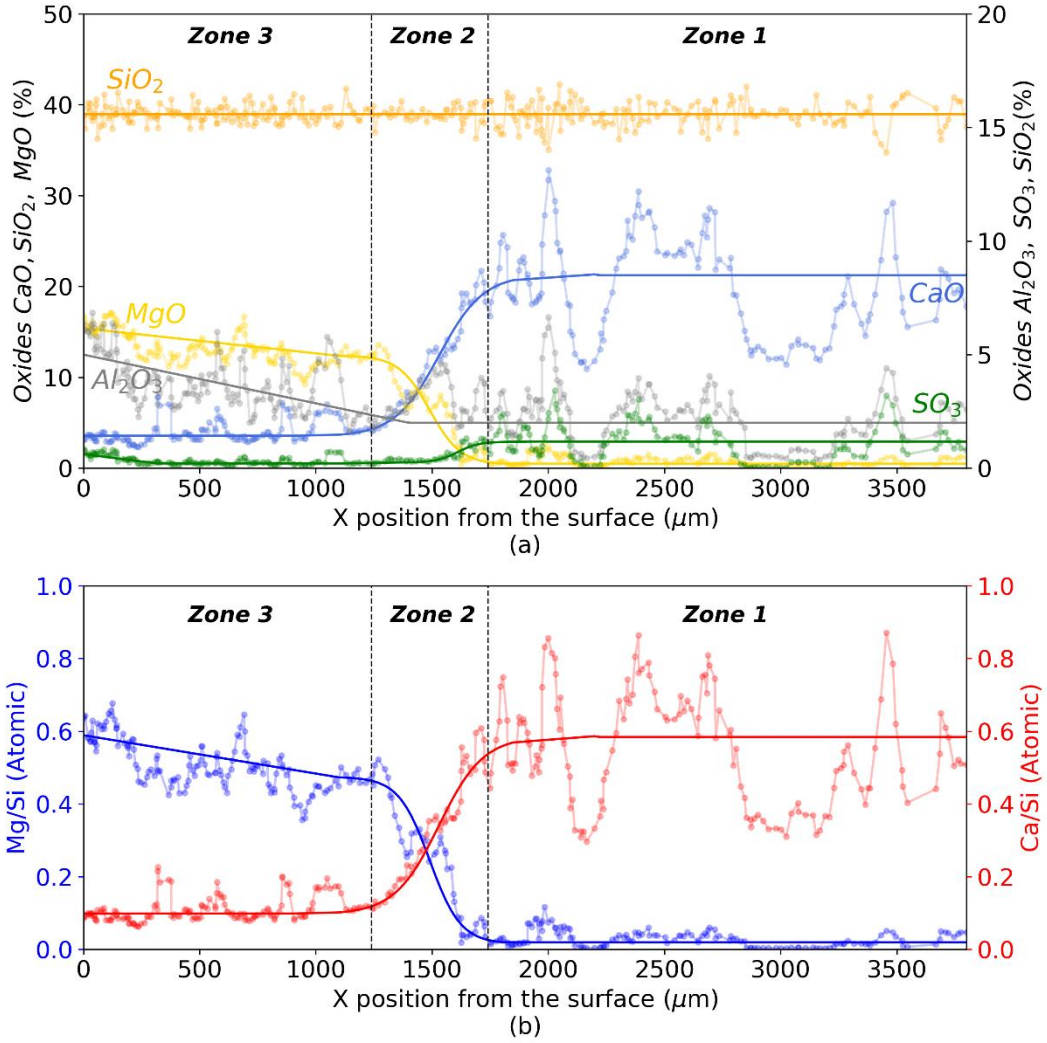

Figure 6-5 : (a) Chemical composition of oxides of a low-pH industrial cement paste immersed during 4 months in 50 mM $MgCl_2$ according to the distance to the surface of the specimen (analysis by electron microprobe, corrected), (b) M/S and C/S atomic ratios calculated from (a). The lines represent an approximation of the signal for future calculations.

The molar M/S ratio at the surface is 0.6 compared to 0.8 for the low-pH model pastes (Figure 4-20). This lower value may be due to a higher amount of silica in the industrial material. The theoretical C/S ratio, based on the quantities of raw materials, is 0.71 for the T3 against 0.94 for the model pastes and the C/S ratio of the sound zone (excluding silica clusters) is 0.6 compared to 0.9 for the low pH model pastes.

The mineralogical composition of the paste as a function of distance from the surface exposed to the $MgCl_2$ solution was characterized by XRD (Figure 6-6). The indexing of the X-ray peaks for the C-S-H (green circles) and M-S-H (red triangles) phases is based on (Bernard et al. 2018).

As for the low-pH model cement pastes (Chapter 4), 3 zones can be defined according to their mineralogy.

- A sound zone (from 1600 µm). The paste was mostly composed of C-S-H and ettringite. No peaks associated with portlandite were visible, consistent with the low C/S.
- An intermediate zone (1000-1600 µm). The results showed a coexistence of signals associated with M-S-H and C-S-H.

- A Mg-enriched zone (0-1000 µm). X-Ray diffractograms displays only the bulges associated with M-S-H, like those obtained on the synthetic M-S-H and the peaks linked to quartz (initially in silica fume). No brucite was detected.

It should be noted that the distances to the surface in Figure 6-6 were measured with a digital measuring device to an accuracy of 0.001 mm at one point in the material and only give an indication of the actual distance because the material abrasion was carried out by hand. Thus, the XRD observations are to be compared with the EDS and microprobe observations. For example, the beginning of the sound zone will be considered as the place where the sulphur and calcium signal reaches its maximum value.

By linking the EDS, microprobe and XRD results, it appeared that the three zones observed in EDS corresponded quite well to the zones observed in XRD. The sound zone, composed of C-S-H and ettringite, corresponded to zone 1 in EDS (Z1 Figure 6-5). The intermediate zone, composed of C-S-H and M-S-H, is a bit larger than the transition zone in EDS (Z2 Figure 6-5). Finally, the Mg-enriched zone, consisting of M-S-H corresponded to zone 3 in EDS (Z3 Figure 6-5). The linear increase of Ca and the linear decrease of Mg in EDS (1250 µm) started later than the appearance of the first C-S-H signals (950 µm). This difference could be explained by a soft start of the Ca signal not considered in the definition of zone 2 in EDS and/or by the measurement error of the abraded thickness. Even if the amount of calcium didn't increase significantly, if the threshold value of Ca concentration in solution was exceeded, C-S-H might be present. Thus, zone 2 would rather start around 1000 µm. In conclusion, the degraded zone corresponded well to the formation of M-S-H in parallel with the decalcification of C-S-H.

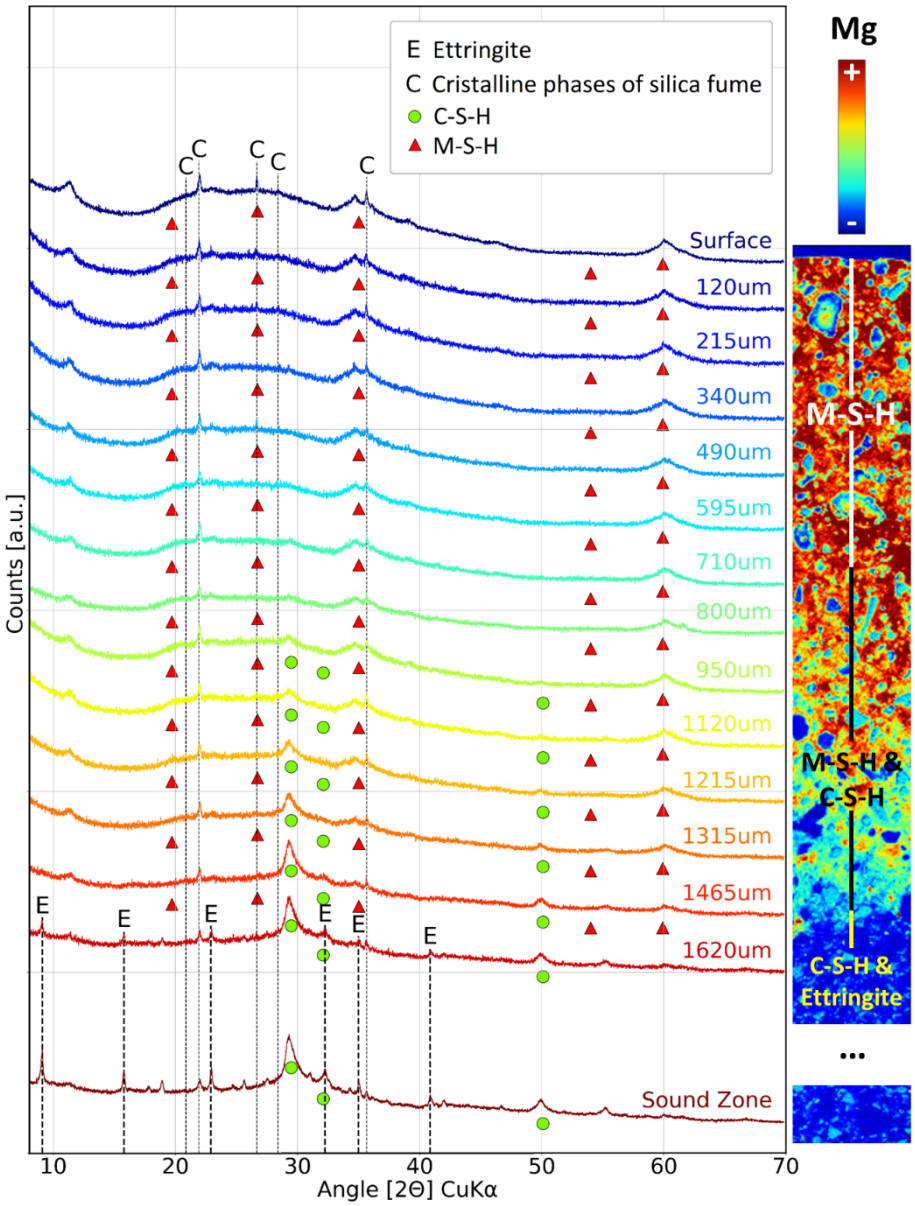

Figure 6-6 : X-Ray diffractograms along the degradation of T3 low-pH cement paste placed in a solution with [$MgCl_2$]=50 mmol/L for 4 months

The magnesium attack causes a Mg enrichment of the paste similar to that of the low-pH model cement pastes (see Chapter 4 and Chapter 5). The chemical zonation of the degradation is the same. The degraded area has broadly the same mineralogy. The differences are related to the initial Ca and Si heterogeneity of the material which leads to heterogeneity in the Mg distribution.

In conclusion, the contact between a $MgCl_2$ solution and the T3 low-pH cement paste created a magnesium enrichment of the paste, characterized by the formation of M-S-H, associated with a decalcification of C-S-H and a leaching in sulphur. The degraded depth was consequent (1700 µm) after 4 months making possible the microstructural and mechanical characterization of M-S-H formed within a cement paste.

6.2.3. Microstructural properties

6.2.3.1. Microstructural mapping

The microstructure of the sample along the degradation was studied by micro-tomography (Figure 6-8 and Figure 6-7) and autoradiography (Figure 6-9) as for the low-pH model cement pastes (4.3.4.2, 4.4.3.1 and 5.1.3).

Density

The micro-tomography analysis of degraded samples gives access, after reconstruction and choice of a Region of Interest (ROI), to a 3D image of the signal intensity variation in the sample (Figure 6-7c). The reconstruction is based on the assembly of 2D planes acquired by the system while the sample is rotating. The 2D images proposed in Figure 6-3 (c) and Figure 6-7 (a and b), corresponds to a section of the 3D volume, considered after data analysis as representative of the sample.

On the 2D and 3D maps, the impact of the presence of silica fume appears. Less dense areas appear, comparable in size to the larger silica clusters observed by EDS. In EDS (Figure 6-4), around x=6000 µm, the size is about 220 µm against 240 µm in micro-tomography (Figure 6-7). In the degraded area, the position of the old silica clusters appears much less clearly. Slightly darker areas appear at the bottom of the sample in the 3D visualisation.

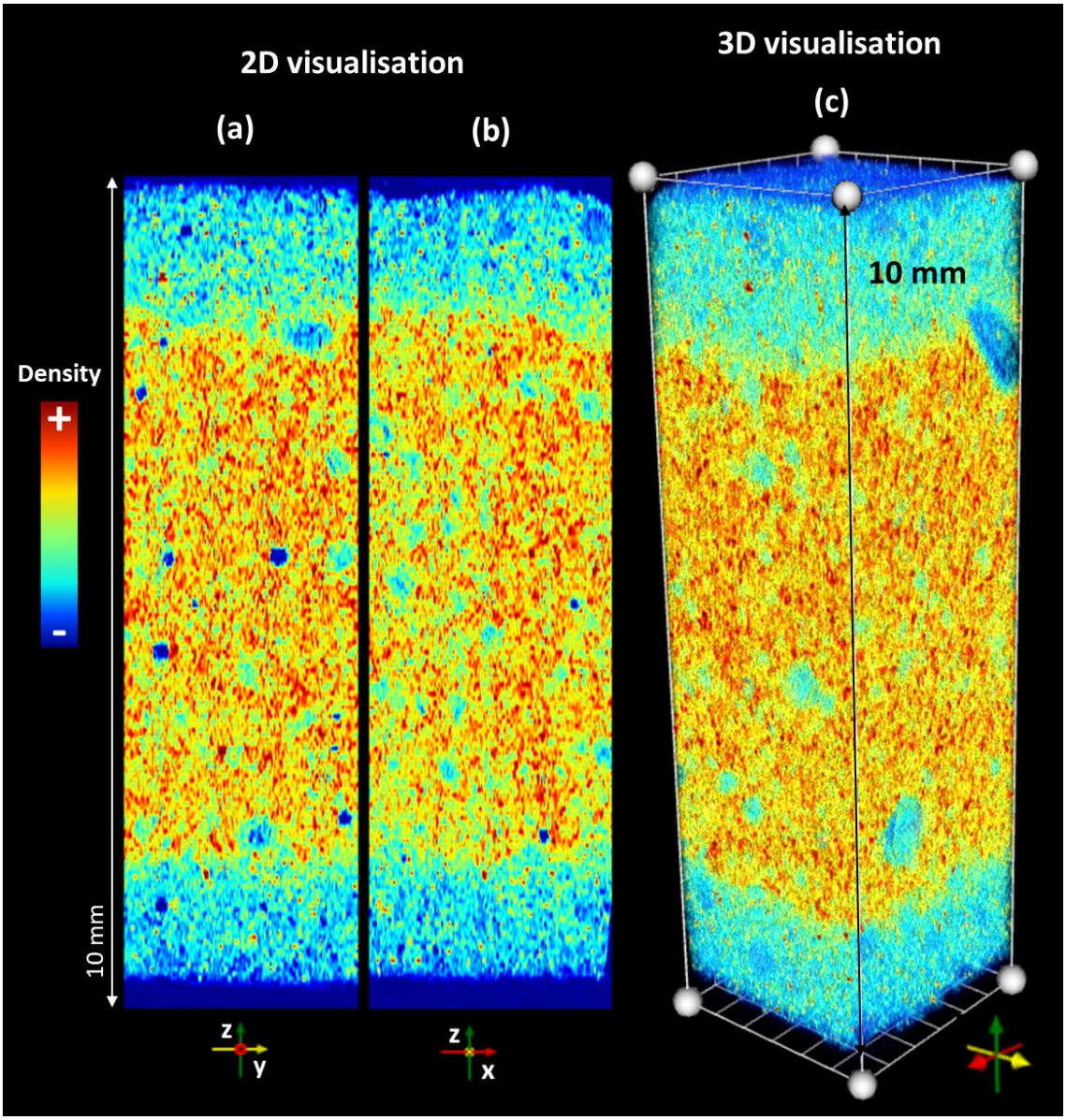

Figure 6-7 : 2D density maps on x plane (a) and y plane (b) and 3D visualisation of the density (c) of a low-pH industrial cement paste immersed during 4 months in 50 mM $MgCl_2$ after micro-tomography

To realize a 1D density profile, the intensity is averaged on each plane parallel to the surface exposed to the $MgCl_2$ solution. As the intensity is linked to the density of the sample, to obtain a normalized density, the highest point of the curve is considered as the base value and the average of each plane is divided by this value (Figure 6-8). The boundary of the sound zone previously observed by microprobe and EDS has been drawn on the micro-tomography profile.

Near the surface, the density decreases drastically (grey bands on Figure 6-8). This is partly due to the fact that the attacked surface is not completely horizontal and flat on the 2D maps and the 3D visualisation. When the 1D profile is calculated at the surface, the value obtained therefore considers a part of the void.

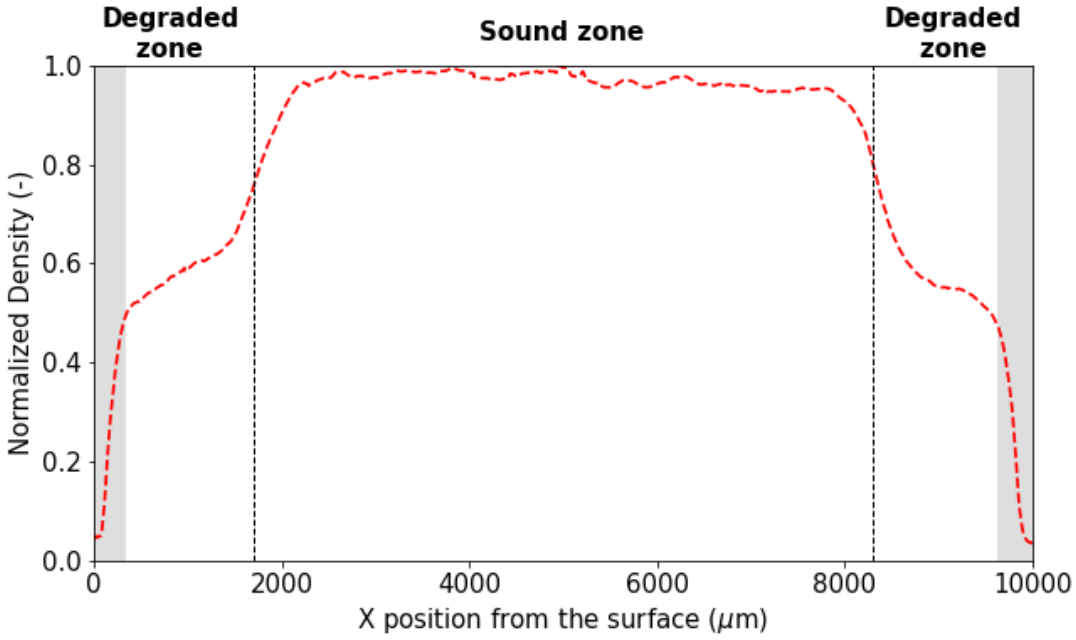

Figure 6-8 : Density profile of of a low-pH industrial cement paste immersed during 4 months in 50 mM $MgCl_2$ after micro-tomography characterization and limits (dotted lines) of the sound zone according to microprobe and EDS

Porosity

To obtain a porosity mapping, the literature has shown that it is possible to use the autoradiography method (Lalan et al. 2019). This technique requires the samples to be completely dry in order to allow the penetration of the radioactive marker. As presented in Appendix F, this method could not be used satisfactorily on the low-pH model cement paste because it was not possible to properly dry the degraded samples without observing a detachment of the degraded zone. The porosity measured in the sound zone of the low-pH model cement pastes was much lower than that measured by other techniques (MIP, water porosity, helium pycnometry) (Figure F-8).

The same problem appears for the low-pH industrial (T3) degraded cement. While the measured water porosity is 40.6%, the MIP porosity is 33.8% and the helium porosity is about 20% (Table 6-1), the autoradiography gives a value of 5% in the "sound" zone (A1) for a density ($\rho_{r\text{-}sound}$) of 1.7. However, the porosity measured in the degraded area (A3) seems to be correct for the low-pH model cement paste due to rapid drying of the degraded area (Chap. 4.4.1). The same phenomenon is expected for T3.

A zone A2, almost as wide as the degraded zone, is visible. It corresponds to a 15% porosity plateau on the porosity profile (Figure 6-9a). It has an intermediate porosity between the porosity of the "sound" zone (A1) and the degraded zone (A3). Based on the width of the zone and the corresponding depth, it is not the transition zone observed in the other techniques (Figure 6-4). The transition zone observed in EDS and microprobe would rather be included in the A1 zone. In micro-tomography, this zone does not appear in the density variation (Figure 6-8). According to Figure 6-10, the demarcation observed in autoradiography (a), is not found when the sample is observed with the naked eye (b). Moreover, when looking at the whole sample, it is observed that the intermediate porosity zone seems to go around the sample and does not respect the degradation direction. This supports the theory that the tracer did not completely penetrate the material. The porosity of the A1 zone would then be underestimated and would rather correspond to that of the A2 zone, i.e. approximately 15%. The porosity of the sound zone would then be more

consistent. Currently, the porosity in the A1 zone is 5%, which is extremely low, especially compared to the values of other techniques (Table 6-1).

In the degraded area (A3), the porosity is between 50 and 70%, i.e. higher than that measured in the sound sample by the different techniques (Table 6-1). A thin and highly porous layer appears on the surface. This observation can be seen in micro-tomography, especially in the 3D visualisation of the density. A very weakly dense zone appears at the bottom of Figure 6-7c.

In conclusion, by correlating micro-tomography and autoradiography with EDS, it appears that the degraded zone has a much higher porosity than the sound zone.

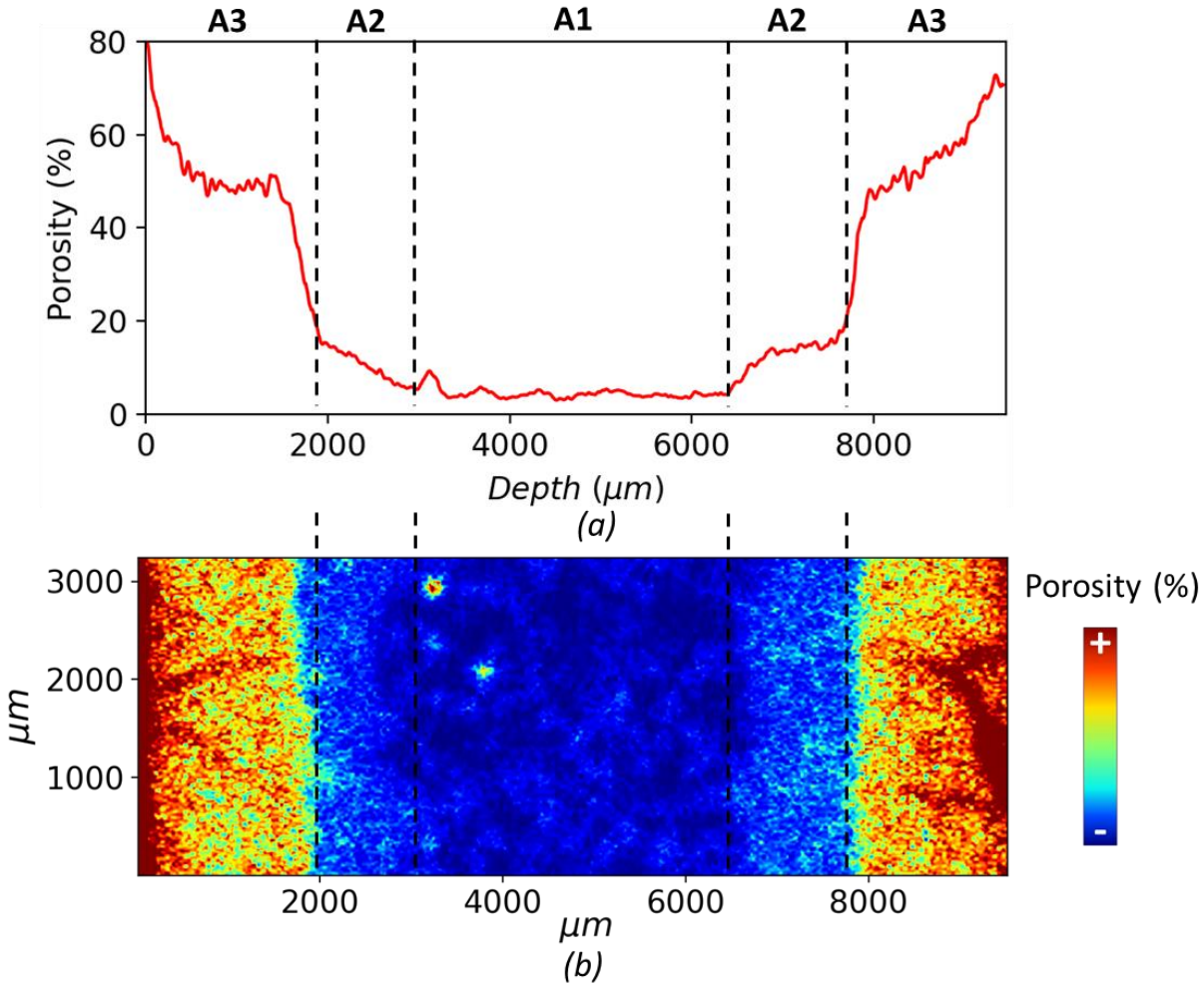

Figure 6-9 : Porosity profile (a) and porosity map (b) of a low-pH industrial cement paste immersed during 4 months in 50 mM $MgCl_2$ after autoradiography characterization

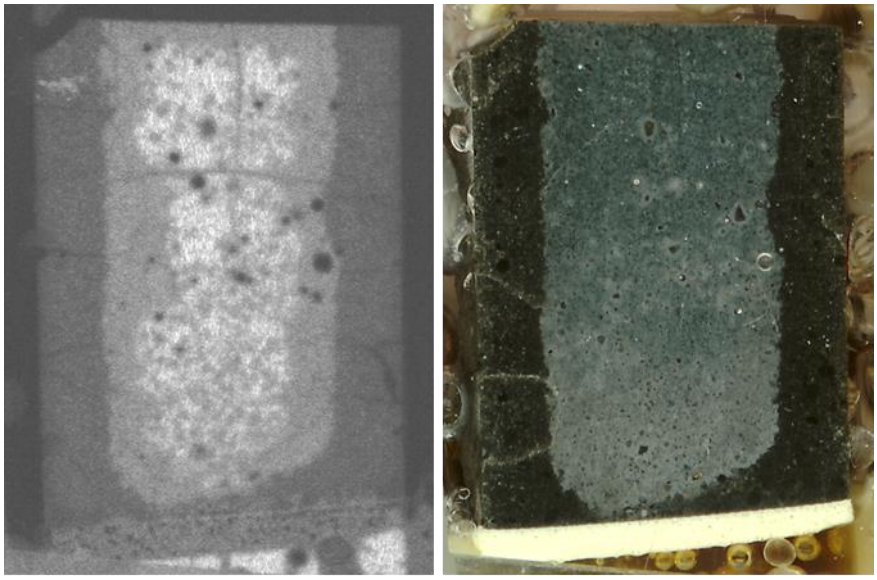

Figure 6-10 : (a) Grey levels of autoradiography of the degraded sample and (b) scan of the corresponding section (naked eye)

6.2.3.2. N_2 Physisorption

The microstructure at low scale had been studied by N_2 Physisorption (Table 6-3 and Figure 6-12). The characterization was carried out on the degraded zone by removing and polishing pieces of samples between 0 and 1700 µm degraded for 4 months, corresponding to part of zone 2 and 3 (Figure 6-5 and Figure 6-11).

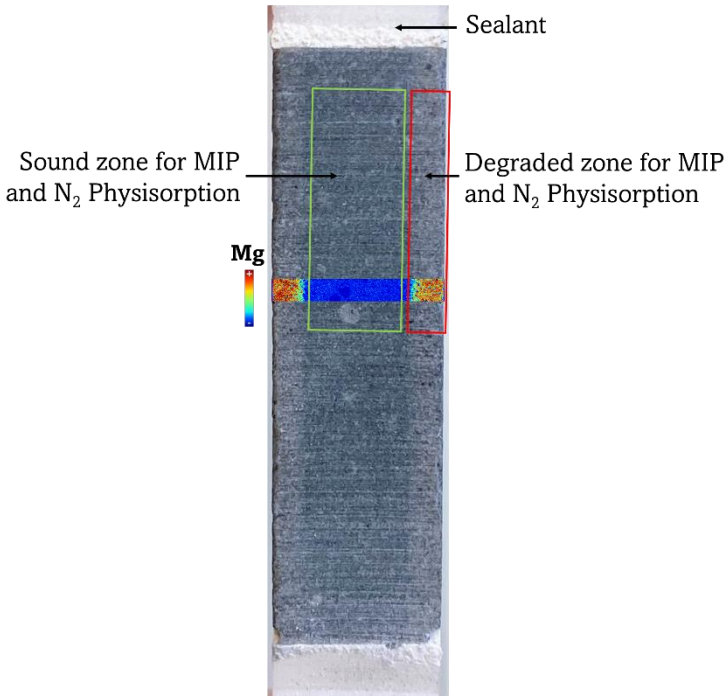

Figure 6-11: Illustration of the zones for MIP and N_2 Physisorption

Table 6-3 : Average Specific Surface B.E.T (m^2/g) determined by N_2 Physisorption of the degraded sample (low-pH industrial cement paste immersed during 4 months in 50 mM $MgCl_2$) and a M-S-H paste.

Type of sample	Sound T3 paste	Degraded T3 paste (50mM 4m)		M-S-H paste, M/S=0.78	Degraded CEMI-sil-col
Zone	-	Sound Zone (Z1)	Degraded zone (Z2-Z3)	-	Degraded zone (Z2-Z3)
Average Specific Surface B.E.T (m^2/g)	10.7	23.7	315.8	562.9	532.1

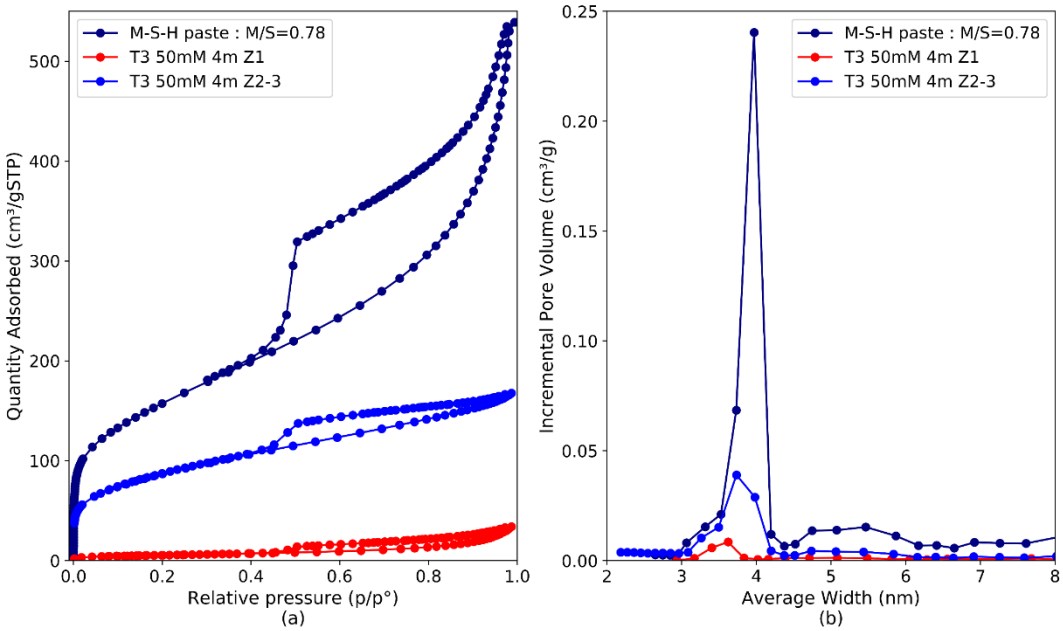

Figure 6-12 : (a) N_2 adsorption-desorption isotherms of the sound zone (Z1) and degraded zone (Z2-3), compared to a pure M-S-H paste (M/S=0.78) (Dewitte et al. 2022) and (b) Associated pore size distributions (BJH). Z1 = Zone 1 (sound zone) of the degraded paste, Z2-3 = Assembly of zones 2 and 3 (enriched in Mg) of a low-pH industrial cement paste immersed during 4 months in 50 mM $MgCl_2$

Figure 6-12a and Table 6-3 shows that the degraded zone (Z2-Z3 EDS) had a much higher specific surface area and a higher adsorbed amount than the sound zone, indicating a higher porosity and confirming the observations made in micro-tomography and autoradiography. The specific surface area of the sound zone is similar to that of the sound sample (10.7 vs. 23.7 m^2/g), as well as the pore size distribution pattern and the isotherm (Appendix E, Figure E-1). As a result, the sample preparation protocol seems consistent.

The degraded zone (Surface, Z2-Z3) had, at small scale (p/p_0<0.4), intermediate properties between the sound zone and the M-S-H paste. The specific surface is high but lower than the one of M-S-H and the slope of the isotherm at the beginning is less than the one of M-S-H. The peak in BJH for the degraded zone is almost 5 times lower than the one for M-S-H pastes but is placed at a similar location as for M-S-H pastes. The peak broadened and extended from its initial position (sound sample, 3.5 nm) to the position of the peak observed on the M-S-H pastes (4 nm). This could indicate an intermediate pore structure between the sound zone and the M-S-H paste, perhaps caused by the presence of part of the transition zone (Z2) in the degraded zone.

The specific surface of the degraded zone of the T3 paste is lower than that of the model paste (50 mM 6 months) (Table 6-3). This may be due to the presence in the degraded zone of other phases than M-S-H, more dense/less porous than M-S-H. On the XRD, crystalline silica fume phases appear in the degraded zone and on the EDS maps calcium clusters seem to correspond to the residual presence of slag.

6.2.3.3. MIP

The porosity and pore distribution at larger scale have been determined by MIP (Figure 6-13 and the porosity accessible to mercury has been determined on the degraded zone (Z2-3) (Table 6-4) and appears to be 15% higher than that of the sound zone. The degraded area shows a slightly higher proportion of pores whose size is between 0.1 µm and 1 µm but the rest of the pore size distribution is similar. The porosity associated with large pores (MIP, d > 8 nm) is therefore not greatly modified in contrast to that of micropores (B.E.T, 2 nm < d < 8 nm). The formation of M-S-H seems to imply a similar capillary porosity distributed slightly differently but a higher intrinsic hydrate porosity. This would be in agreement with the properties determined on pure M-S-H pastes. While C-S-H has an intrinsic porosity of 28%, that of M-S-H would be more around 50% (3.3.3).

The pore size distribution curve (Figure 6-13) of the sound zone shows two humps for d=20-30 nm and d=100-300 nm. A fine modification of the pore distribution is observed without significant modification of the total capillary porosity.

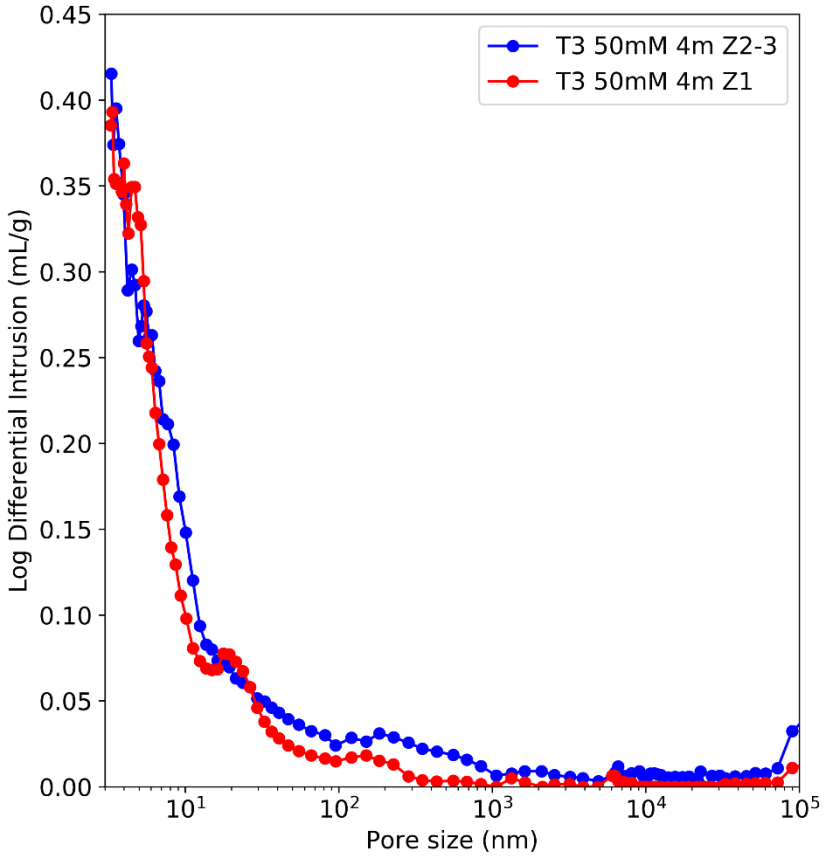

Figure 6-13 : Pore distribution after MIP of the degraded (Z2-3) and sound zones of a low-pH industrial cement paste immersed during 4 months in 50 mM $MgCl_2$

The porosity accessible to mercury has been determined on the degraded zone (Z2-3) (Table 6-4) and appears to be 15% higher than that of the sound zone. The porosity associated with large pores (MIP, d > 8 nm) is therefore not greatly modified in contrast to that of micropores (B.E.T, 2

nm < d < 8 nm). The formation of M-S-H seems to imply a similar capillary porosity distributed slightly differently but a higher intrinsic hydrate porosity.

Table 6-4 : Porosity after MIP measurements of the sound paste, the degraded (Z2-3) and sound zone of a low-pH industrial cement paste immersed during 4 months in 50 mM $MgCl_2$

Type of sample	Degraded T3 paste	
Zone	Sound Zone (Z1)	Degraded zone (Z2-Z3)
Porosity (%)	27.1	31.2

In conclusion, the degraded zone - enriched in Mg, was well constituted of M-S-H, showing an increased total open porosity compared to the sound zone, despite the formation of M-S-H. The capillary porosity is similar, although slightly differently distributed, while the porosity associated with micropores and thus hydrates is higher. This is consistent with the intrinsic porosity of M-S-H being almost twice that of C-S-H. The microstructural properties observed in the Mg-enriched zone, showed similarities with those of synthetic M-S-H pastes but can't be resumed as a M-S-H zone. Other phases should be present to explain the difference in B.E.T surface and BJH distribution. As the paste contains initially large amount of silica fume clusters, remaining silica can be present and not seen in XRD as it is amorphous. Moreover, calcium clusters corresponding to initially to slag are still observable in EDS in the degraded zone. The more varied microstructure, chemistry and initial mineralogy of T3 than for the model paste, implies the coexistence of M-S-H with other phases and thus a lesser influence of M-S-H formation on microstructural and mechanical properties.

6.2.4. Elastic properties mapping

A mechanical properties mapping has been achieved via microindentation. Figure 6-14a illustrates the position of indents on the sample (indenter camera pictures) and Figure 6-14b presents the 2D results associated. The EDS zones boundaries have been plotted (white lines).

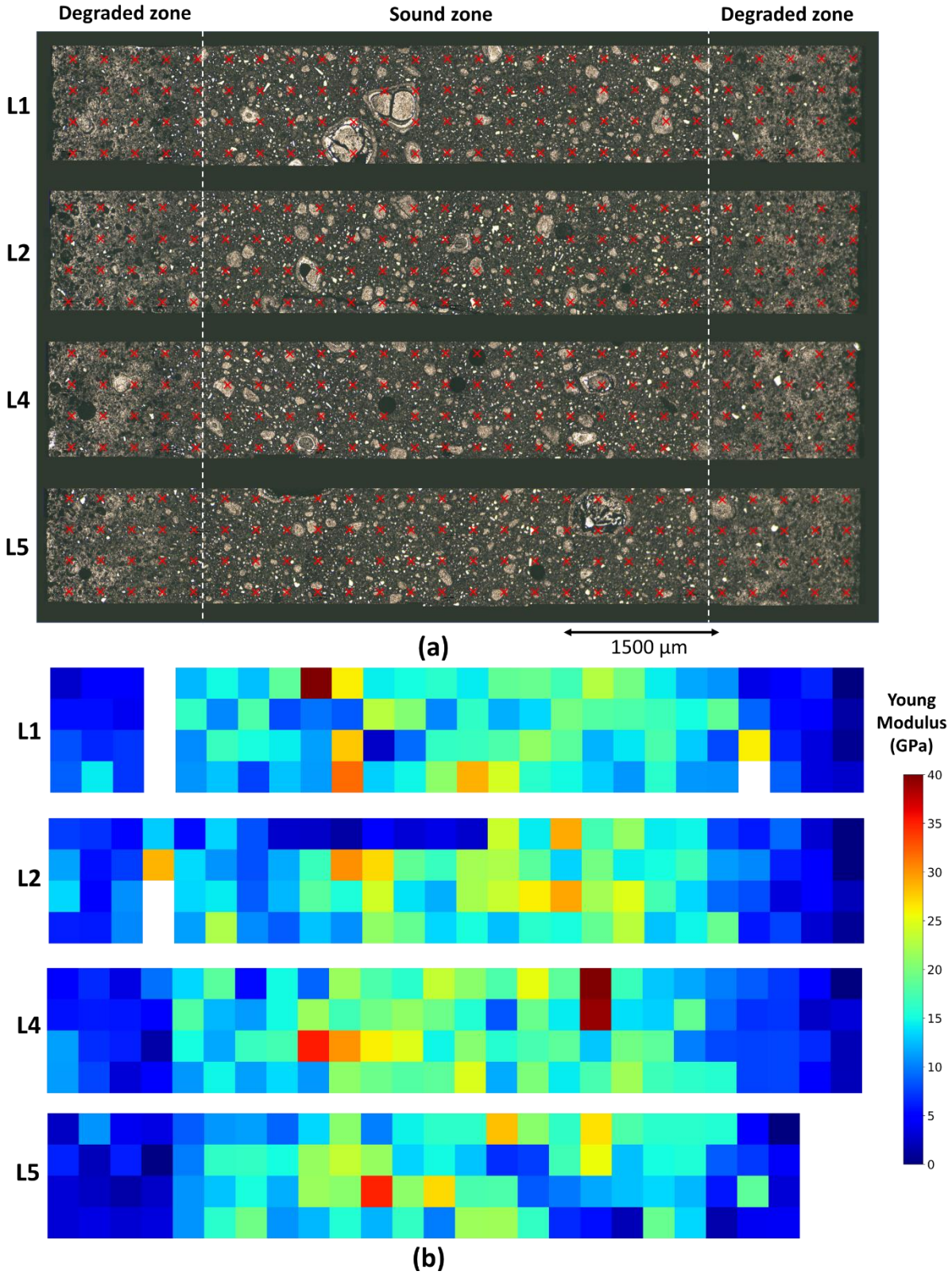

Figure 6-14 : 2D illustration of the microindentation data, (a) Localisation of indents on the sample via the nano-indenter microscope and (b) Young Modulus results (GPa) of a low-pH industrial cement paste immersed during 4 months in 50 mM $MgCl_2$

The dispersion of the raw data (Figure 6-3 (d)) is greater for T3 than for the model paste (Figure 4-4) due to the presence of heterogeneities. In the sound zone, clusters of silica fume are visible on the indenter pictures (Figure 6-14a). When the indent is in the middle of a silica fume cluster, the measured value is very high because silica fume is in silica condensed form and contain quartz. Therefore clusters have high mechanical properties. When the indent is made on the edge of a cluster, the measured value is low (or without result), probably because of the difference in strength and level (z-height) between the cluster and the cement matrix. For this type of material, it is all the more necessary to repeat the measurements in order to carry out a statistical study of the results.

Figure 6-15 shows the results obtained according to the distance of surface after removing of the outliers. As for other tested pastes in Chapter 4 and Chapter 5, outliers were excluded using the interquartile range method. The dispersion of the data is displayed via the mean, the median and the standard deviation (greyed beam) on Figure 6-15. The upper part of the figure shows the number of points kept for each x-position. As illustrated in Figure 6-3 (Overall properties - 6.2.1) and in Figure 6-14, the last column of indents made was too close to the surface. The data will therefore not be considered and has not been plotted in Figure 6-15.

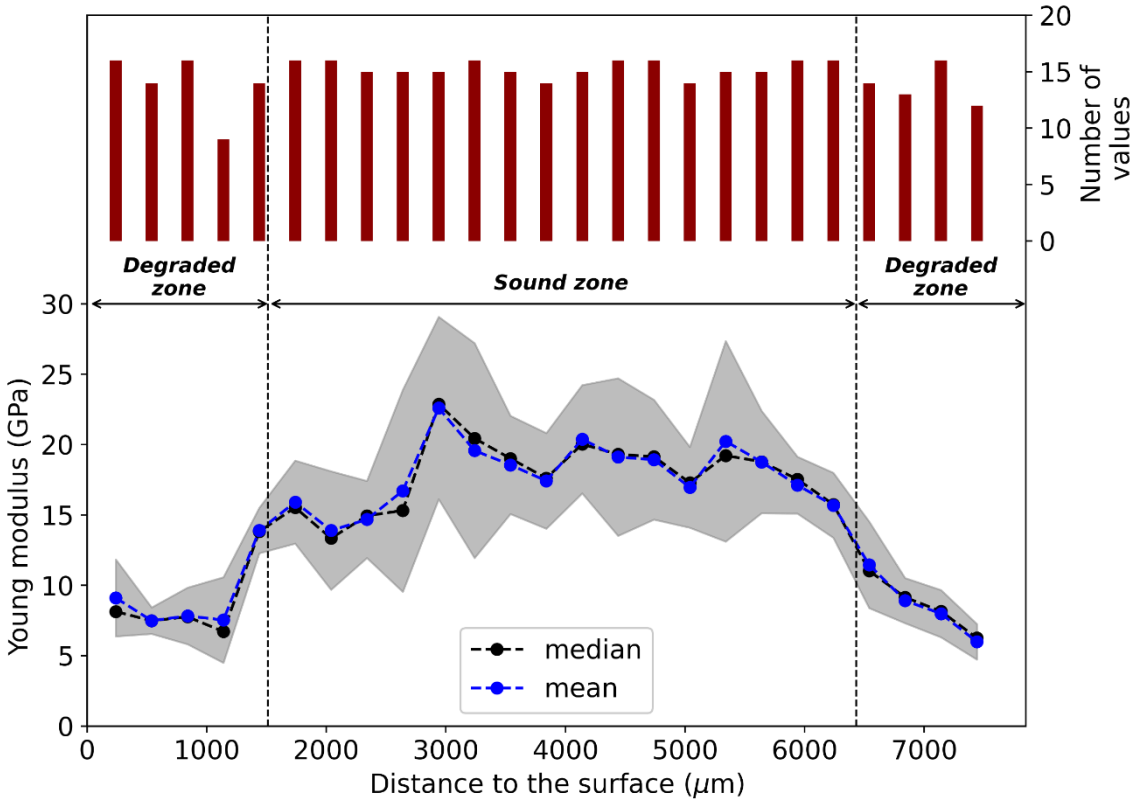

Figure 6-15 : Microindentation data without outliers along the degradation of a low-pH industrial cement paste immersed during 4 months in 50 mM $MgCl_2$

The sound zone (Z1) has a Young Modulus around 20 GPa. In the degraded zone, the mechanical properties are greatly diminished.

The E_{deg}/E_{sound} (8/18 GPa) is equal to 45%. For the low-pH cement model paste exposed 4 months to 50 mM of $MgCl_2$, the ratio was about 15% (Appendix C, Figure C-2). The T3 industrial cementitious paste shows a lower loss of mechanical properties than the model paste. While the depth of the Ca-leached and Mg-enriched zone is comparable (at 4 months, the front for 50 mM $MgCl_2$ (EDS) is 1600 µm for the model paste versus 1500 µm for T3), the mechanical properties are better preserved for the T3. This difference may be due to the non-homogeneous distribution of initial Si and Ca, to the presence of other phases such as slag or to a lower initial porosity. The

presence of these non-degraded phases could limit the impact of M-S-H formation on the mechanical properties of the degraded zone.

Conclusion

The T3 paste is a cementitious paste representative of the low-pH concrete foreseen for the Cigéo underground geological repository for radioactive waste project in clayey rock. It is made from clinker, slag and silica fume with a relatively low w/c (0.43). It is a paste with a complex mineralogy and a heterogeneous distribution of calcium and silicon due to the use of slag and silica fume which form clusters. The paste was put in contact with a 50 mM $MgCl_2$ solution for 4 months in order to understand, in an accelerated way, the magnesium attack that takes place during the contact between clay and concrete, without taking into account other chemical attacks (Carbonation etc.). This magnesium attack is characterised by the enrichment of the paste in magnesium in parallel with a leaching of calcium and sulphur. It corresponds to the formation of M-S-H, the decalcification/dissolution of C-S-H and dissolution of Aft phases. The degradation front is deep (1700 µm in 4 months). The degraded zone shows a higher porosity than the sound zone despite the formation of M-S-H. The capillary porosity is approximately the same in the degraded and sound zone while the microporosity is higher. As the measured intrinsic porosity of M-S-H is about 50% compared to 28% for C-S-H, when M-S-H replaces C-S-H, it is logical that the microporosity increases. The mechanical properties measured by microindentation show that the degraded zone has a Young's modulus reduced by half compared to the sound zone. This reduction in properties is probably due to the poor microstructural and mechanical properties of M-S-H. Replacing a phase with a porosity of 28% and a Young's modulus of about 20 GPa with a phase with a porosity of 50% and a Young's modulus of about 6 GPa, necessarily implies a reduction in the macroscopic mechanical properties.

In the study of the low-pH model paste (CEMI-sil-col), made from CEMI and colloidal silica, the measured microstructural and mechanical properties of the degraded paste were much lower than those of T3. The sound paste was this time homogeneous and composed only of C-S-H and ettringite. In contact with the $MgCl_2$ solution, at 5 mM or 50 mM, the findings were the same. The magnesium attack causes the leaching of calcium and sulphur, dissolving the only two phases observed in XRD. The degraded zone is then only made up of M-S-H. The poor microstructural and mechanical properties of M-S-H are not compensated by any other phase, greatly impacting the properties of the degraded sample. In the case of T3, the heterogeneous distribution, the low w/c and the presence of other phases such as slag limit the impact of M-S-H formation on the microstructural and mechanical properties of the material. The very significant shrinkage phenomenon observed on the model pastes is limited on T3. Fine cracks appear but the degraded zone does not detach from the sound zone and the cracks do not open up afterwards.

In conclusion, the analysis of the magnesium attack on T3 confirms what was observed on the model paste. The magnesium attack is characterised by the dissolution of C-S-H and ettringite, as well as by the formation of M-S-H during the contact between a low-pH paste/concrete and an environment containing magnesium. As M-S-H has much lower microstructural and mechanical properties than C-S-H, the replacement of C-S-H by M-S-H does not maintain good mechanical and microstructural properties. Even if a new, semi-amorphous phase is formed, the mechanical properties of the paste are significantly reduced during magnesium attack.

GENERAL CONCLUSION

The objectives of this thesis work were (i) to identify precisely the reaction mechanisms of magnesium attack and M-S-H formation in low-calcium cementitious matrices, (ii) to study the influence of M-S-H formation on microstructural and mechanical properties and (iii) to propose microstructural and mechanical data of M-S-H that can be integrated in chemo-mechanical models.

To achieve these objectives, the approach of the thesis has been divided into three stages, as shown in Figure 2. The first step consisted in the production and characterisation of pure and cohesive M-S-H pastes in order to determine the microstructural and mechanical properties of M-S-H. The second step was the phenomenological analysis of the formation of M-S-H during the magnesium attack of a model cementitious low-pH material. The simplified mineralogical composition and the initial homogeneous distribution of the material allowed the formation of a zone entirely composed of M-S-H and amorphous silica. The formation mechanism of M-S-H and the properties of the degraded zone have been compared with those of synthetic M-S-H. Finally, the last step was devoted to the analysis of the magnesium attack on an industrially manufactured, (i.e. non-model), low-pH cementitious material. The mineralogy of such paste is more complex and the initial Ca and Si distribution is not homogeneous resulting in different M-S-H formation mechanisms and different degraded mechanical properties. The comparison with the results on the low-pH model cement paste allowed to discuss these differences and to better understand the impact of the magnesium attack on the low-pH cementitious materials.

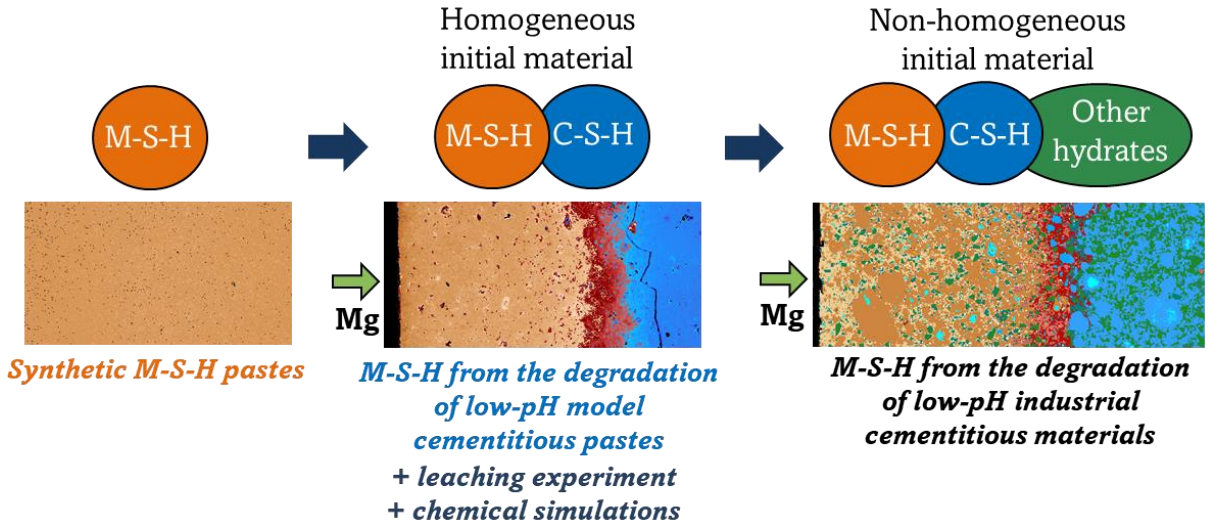

Figure 2: Schematic representation of the structure of the thesis

The work has been achieved through the development of a multi-physics characterization method. The analysis of the results issued from this characterisation was carried out through a dialogue with analytical modelling (homogenisation for microstructural and elastic properties evolutions) and numerical modelling (with HYTEC code for the chemical phenomena).

The literature review presented at the beginning of the manuscript raised some knowledge gaps on magnesium attack in low-pH or low-carbon binders where portlandite is absent, especially on the properties of M-S-H. The conclusion of this review raised a series of questions which this work has sought to answer and whose main conclusions are summarised below.

General conclusion

In which conditions are M-S-H favoured over brucite in degraded cementitious pastes? What is the formation process of M-S-H?

M-S-H seems preferentially formed against brucite, when the pH of the pore solution is below 10.6 according to the HYTEC simulations performed in this work. This is the case for low C/S ratio pastes with a hydration time of more than about 10 months to 2 years depending on the type of silica. Without long hydration, not all the portlandite and/or high ratio C-S-H that forms initially is consumed and brucite forms. In the case of civil engineering constructions, the expected service life of the structures is long and if low-pH or low-carbon binders are used, the formation of M-S-H is extremely likely. It has already been observed in different environments, e.g. for dams in contact with fresh water, for marine structures and for structures in contact with clay (deep geological disposal for radioactive wastes).

The structure of the degraded zone during the magnesium attack observed by ^{29}Si NMR was sheet-like, in agreement with the process of dissolution of C-S-H and then precipitation of M-S-H described in the literature.

On contact with the $MgCl_2$ solution, the cement pastes showed a large zone consisting entirely of M-S-H and amorphous silica followed by a zone where M-S-H and C-S-H coexist. Increasing the magnesium concentration did not seem to change the M/S ratio of the M-S-H formed but it increased significantly the degraded depth (1750 µm for the 5mM and 2200 µm for the 50mM after 6 months of degradation).

What are the intrinsic properties of M-S-H? Can the properties obtained on M-S-H pastes be transposed to those of a degraded cement paste?

The validity of the properties determined on M-S-H pastes was tested via a mechanical homogenisation scheme, using mineralogical and chemical data of the low-pH cementitious paste under magnesium attack. The results validate the intrinsic properties determined on M-S-H pastes.

M-S-H are a highly porous phase with plate-like micro- and mesopores and are very sensitive to changes in humidity. Shrinkage has been observed both in the pure M-S-H pastes and in the degraded zone of the pastes under magnesium attack. The intrinsic modulus of elasticity of M-S-H is in the order of 6 GPa (3.7- 7.9 GPa depending on the M/S ratio). Like C-S-H, M-S-H has an intrinsic porosity, of about 55% (against 28% for C-S-H).

Does the structure of C-S-H influence the structure of M-S-H formed by degradation?

No evidence for this hypothesis has been found. Structural analysis of the degraded zone was observed by ^{29}Si NMR. Due to the residual presence of C-S-H in the degraded zone, it was not possible to discuss this point. However, the structure and initial mineralogy of the cement paste influence the microstructural and mechanical properties of the Mg enriched zone (M-S-H). For the low-pH model paste, the distribution of silica and calcium was homogeneous and the mineralogy very simple (composed of ettringite and C-S-H). The porosity of the paste was already high (51.5%) and during the formation of the M-S-H, no phase initially present remained within the highly Mg enriched zone. Since M-S-H and amorphous silica have a high intrinsic porosity, the porosity of the degraded zone was very high. The elastic properties of the degraded zone directly matched those of the M-S-H pastes. For the industrial low-pH paste, the mineralogy was more complex and the phases were not evenly distributed due to the use of slag and silica fume which formed clusters. The porosity of the paste was lower (40.6%). During the formation of M-S-H, the shrinkage phenomenon was less pronounced than for the model paste and the porosity of the degraded zone was lower. Finally, the mechanical properties remained low but higher than those observed for the model paste.

General conclusion

What is the influence of M-S-H formation on the mechanical and microstructural properties of cementitious materials?

Two types of low-pH cement pastes (Low-pH model cement paste based on CEMI and colloidal silica, and low-pH industrial cement paste based on CEMI, slag and silica fume) were immersed in $MgCl_2$ solutions during several months. In contact with $MgCl_2$, the pastes showed a strong magnesium enrichment in parallel with calcium and sulphur leaching, characterised by the dissolution of C-S-H and ettringite in parallel with the formation of M-S-H and amorphous silica. The zone corresponding to the formation of M-S-H showed a strong weakening of the mechanical properties and an increase in porosity. For the low-pH model cement paste (CEMI-sil-col), the microscopic Young modulus decreased from 11.5 GPa to 4-2.5 GPa. For the low-pH industrial cement paste (T3), the microscopic Young modulus decreased from 18 GPa to 8 GPa.

The formation of M-S-H did not maintain high microstructural and mechanical properties. On the contrary, their formation caused a strong weakening of the matrix.

Is the pattern of decalcification of C-S-H that takes place in pure leaching similar to that which takes place in the formation of M-S-H?

The low-pH model cement paste was subjected to both attacks and the results after 4 months of degradation were compared. At low $MgCl_2$ concentration (5 mmol/L), the degradation depth was similar to pure water degradation but while the pure leaching of the paste led to a smooth and progressive decalcification of the C-S-H, the magnesium attack led to an extended and highly leached zone where the M-S-H was the main phase. As the mechanical properties of the M-S-H are low, the degraded zone in the case of magnesium attack had lower mechanical properties than the degraded zone in the case of pure leaching. However, at the surface, the mechanical properties were similar in both degradation conditions. As a conclusion, for low-CO_2 binders (with very low C/S ratios) the exposure to $MgCl_2$ solution was more detrimental than pure leaching. The high concentrations of $MgCl_2$ (50 mmol/L) increased the degradation rate and the mechanical properties in the degraded zone of the Mg attacked samples were lower.

One possible explanation for this difference in degradation rate is the increase in Ca^{2+} concentration in the sound zone observed numerically. During magnesium attack, the equilibrium of C-S-H with Ca^{2+} ions in solution is modified. The concentration of Ca^{2+} ions in the pore solution is equal to that of Mg^{2+} ions in the aggressive solution.

Can we predict the properties of degraded cement pastes in a magnesium environment?

From the determination of the microstructural and mechanical properties of M-S-H, it is now possible to integrate M-S-H into chemical and mechanical prediction models. For go further, it would be interesting to determine the associated diffusion coefficient.

In conclusion, the thesis has provided knowledge in several areas.

A new multi-physics characterisation method for materials undergoing degradation was proposed and could be used in other types of attack. Combined with mechanical homogenisation, it has made it possible to test hypotheses and properties on the constituent phases of degraded materials.

The results on very low-CO_2/ low-pH materials undergoing degradation have enriched the data on mineralogy, degradation profiles, microstructural and mechanical properties associated with magnesium attack and leaching on this type of binder.

This thesis allowed to determine the properties (M-S-H gel structure, internal porosity, molar volume and elastic properties) of one of the phases resulting from magnesium attack of cementitious pastes (M-S-H). These properties can be used to integrate M-S-H into predictive simulations of concrete/magnesium interactions, such as in the context of deep geological disposal of radioactive waste, dams or marine structures.

Finally, this thesis provided data comparing $MgCl_2$ attack to leaching, allowing the transposition of macroscopic models of water degradation to the case of $MgCl_2$ degradation. This thesis highlights the interest to consider the magnesium attack for the long-term durability of low-pH cementitious materials in geological disposal environment. The work showed that the effect of magnesium attack on low-pH is different from that on Ordinary Portland Cement pastes and that magnesium attack cannot be neglected on this type of material. It highlights that, with the increasing use of low-CO_2 materials in civil engineering structures, the transposition of degradation phenomena observed on ordinary concrete (OPC or cement with C/S higher than 1.2) to the behaviour of low-CO_2, low-pH concrete may not be possible.

OUTLOOKS

This work provides important information for the understanding of the mechanism and influence of magnesium attack on low-carbon/low-pH cementitious materials. However, some points remain to be investigated.

Short-term outlooks

The structure of the M-S-H resulting from degradation could not be studied independently of the rest of the mineralogical species of the degraded zone (in the present study, NMR was carried out on the total degraded zone, thus integrating a part of C-S-H). Consequently, the study didn't allow to see if the structure of C-S-H influence the structure of M-S-H formed by degradation. In order to do so, it is necessary to characterize by NMR the degraded zone of a low-pH model cement sample with a very significant degraded depth (1 year of degradation at 50mM $MgCl_2$ for example) in order to be able to dissociate the first part of the zone with only M-S-H from the rest of the degraded zone.

Only the model pastes were subjected to pure leaching. In order to complete the analysis, it would be necessary to observe the behaviour of the industrial low-pH paste under pure leaching. This would allow to see if, as for the magnesium attack, the industrial paste maintains better properties than the model material and if the more "severe" degradation effect of $MgCl_2$, compared to leaching, is also observed on a real material for which the siliceous sites have a different distribution and accessibility.

In addition, the analytical method used to determine elastic properties from microprobe data has not been applied to the industrial low-pH paste. In order to see if this method is also applicable on more complex materials, the data from the thesis (on T3 paste) can be used to adapt the method to a non-homogeneous material.

In real environments, M-S-H is not the only magnesium phase that form during magnesium attack of low-pH pastes. The presence of hydrotalcite has also been noted in the paste. Its chemical and mineralogical properties are already the object of research because hydrotalcite has the capacity to integrate ions in its interlayer and is considered to remove harmful oxyanions such as arsenate, chromate, phosphate, etc. from contaminated waters (Goh, Lim, et Dong 2008). To complete the database on magnesium phases resulting from magnesium attack, it would be interesting to determine the microstructural and mechanical properties of hydrotalcite.

It has been observed that the mechanical properties of C-S-H measured on the low-pH pastes are lower than those in the literature where the measurements are made on Ordinary Portland Cement (OPC) pastes. To study the impact of the C/S ratio on the mechanical properties of C-S-H, it is considered to use the C_3S and colloidal silica-based pastes made during the thesis and not used due to insufficient hydration. Several C/S ratios having been achieved (C/S=1, C/S=1.3 and C/S=3), statistical nanoindentation tests would allow to discuss this point.

Medium and long-term outlooks

The multi-physics characterization developed in the thesis allowed to observe the impact of degradation on chemical, mineralogical, microstructural and mechanical properties along the sample. This characterization method can be applied to other types of attack (sulphates for example) to complete the knowledge on low-CO_2/low-pH binders to see if the impact of other attacks on cementitious materials is also modified when the C/S ratio is low.

The multi-physics method could be extended to characterize the evolution of transfer properties during degradation. The characterization of transfer properties on gradient materials is challenging because no small-scale measurement techniques (comparable to microindentation for the measurement of elastic properties) have been so far developed for this purpose. A methodology should be developed to measure the diffusion coefficient on materials with a gradient of properties and coupled it with a homogenization method on the diffusion properties (as the method described by Stora et al. (Stora, Bary, et He 2008)).

In addition, the microindentation performed only provided access to the elastic properties of the tested materials. In order to estimate the creep, plasticity or fracture limit of M-S-H, it would be necessary to develop a method for exploiting the indentation results and/or to produce materials that hold together sufficiently to perform macroscopic tests.

M-S-H properties and magnesium attack kinetics data could be used in a structure-wide model linking chemistry and mechanics to account for magnesium attack. Similar to the integration of leaching acceleration when using ammonium nitrate, it could be considered to propose a leaching accelerating model based on the magnesium concentration in solution.

GLOSSARY

ANDRA: French National Agency for Radioactive Waste Management

Cementitious notation: C = CaO, M = MgO, S = SiO_2, A = Al_2O_3, F = Fe_2O_3, H = H_20

Cigéo: Centre industriel de stockage géologique (Industrial geological disposal centre)

C-S-H: calcium silicate hydrates

EDS: Energy Dispersive X-ray Spectroscopy

HLW: high-level waste

ILW-LL: long-lived intermediate-level waste

LLW-LL: low-level long-lived waste

MH: brucite

MIP: Mercury Intrusion Porosimetry

M-S-H: magnesium silicate hydrates

OPC: Ordinary Portland Cement

SCM: Supplementary Cementitious Material

SEM: Scanning Electron Microscope

URL: Underground Research Laboratory

XRD: X-Ray Diffraction

REFERENCES

Adenot, Frédéric. 1992. « Durabilite du beton : caracterisation et modelisation des processus physiques et chimiques de degradation du ciment ». These de doctorat, Orléans. https://www.theses.fr/1992ORLE2001.

AFGC. 2004. « Maîtrise de la durabilité vis-à-vis de la corrosion des armatures et de l'alcali-réaction : Etat de l'art et Guide pour la mise en œuvre d'une approche performantielle et prédictive sur la base d'indicateurs de durabilité ». Documents scientifiques et techniques. CONCEPTION DES BÉTONS POUR UNE DURÉE DE VIE DONNÉE DES OUVRAGES. Association Française de Génie Civil (AFGC). https://www.afgc.asso.fr/app/uploads/2007/10/Indicateurs-durabilite.pdf.

AFNOR. 1992. « Méthode de détermination du volume apparent et du contenu en eau des mottes ». Norme X31-505. https://www.boutique.afnor.org/norme/x31-505/qualite-des-sols-methodes-physiques-methode-de-determination-du-volume-apparent-et-du-contenu-en-eau-des-mottes/article/863490/fa027222.

Alonso, María Cruz, José Luis García Calvo, Jaime Cuevas, María Jesús Turrero, Raúl Fernández, Elena Torres, et Ana I. Ruiz. 2017. « Interaction Processes at the Concrete-Bentonite Interface after 13 Years of FEBEX-Plug Operation. Part I: Concrete Alteration ». *Physics and Chemistry of the Earth, Parts A/B/C*, Mechanisms and Modelling of Waste-Cement and Cement-Host Rock Interactions, 99 (juin): 38-48. https://doi.org/10.1016/j.pce.2017.03.008.

ANDRA. 2019. « Inventaire national des matières et déchets radioactifs ». Les essentiels 2019.

Arnold, M., A. R. Boccaccini, et G. Ondracek. 1996. « Prediction of the Poisson's Ratio of Porous Materials ». *Journal of Materials Science* 31 (6): 1643-46. https://doi.org/10.1007/BF00357876.

Auroy, Martin, Stéphane Poyet, Patrick Le Bescop, Jean-Michel Torrenti, Thibault Charpentier, Mélanie Moskura, et Xavier Bourbon. 2018. « Comparison between Natural and Accelerated Carbonation (3% CO2): Impact on Mineralogy, Microstructure, Water Retention and Cracking ». *Cement and Concrete Research* 109 (juillet): 64-80. https://doi.org/10.1016/j.cemconres.2018.04.012.

Bamforth, P. B., W. F. Price, et Mary Emerson. 1997. *An International Review of Chloride Ingress into Structural Concrete*. Contractor Report (Transport Research Laboratory (Great Britain)). Edinburgh: Transport Research Laboratory.

Barbato, G., E. M. Barini, G. Genta, et R. Levi. 2011. « Features and performance of some outlier detection methods ». *Journal of Applied Statistics* 38 (10): 2133-49. https://doi.org/10.1080/02664763.2010.545119.

Bardestani, Raoof, Gregory S. Patience, et Serge Kaliaguine. 2019. « Experimental Methods in Chemical Engineering: Specific Surface Area and Pore Size Distribution Measurements—BET, BJH, and DFT ». *The Canadian Journal of Chemical Engineering* 97 (11): 2781-91. https://doi.org/10.1002/cjce.23632.

Barrett, Elliott P., Leslie G. Joyner, et Paul P. Halenda. 1951. « The Determination of Pore Volume and Area Distributions in Porous Substances. I. Computations from Nitrogen Isotherms ». *Journal of the American Chemical Society* 73 (1): 373-80. https://doi.org/10.1021/ja01145a126.

Bary, B. 2008. « Simplified Coupled Chemo-Mechanical Modeling of Cement Pastes Behavior Subjected to Combined Leaching and External Sulfate Attack ». *International Journal for Numerical and Analytical Methods in Geomechanics* 32 (14): 1791-1816. https://doi.org/10.1002/nag.696.

« Basics of the Final Disposal ». 2020. Posiva. 20 avril 2020. http://www.posiva.fi/en/final_disposal/basics_of_the_final_disposal.

Beaudoin, J. J., V. S. Ramachandran, et R. F. Feldman. 1990. « Interaction of Chloride and C□S□H ». *Cement and Concrete Research* 20 (6): 875-83. https://doi.org/10.1016/0008-8846(90)90049-4.

Béjaoui, Syriac, Benoît Bary, Serge Nitsche, Damien Chaudanson, et Cécile Blanc. 2006. « Experimental and modeling studies of the link between microstructure and effective diffusivity of cement pastes ». *Revue Européenne de Génie Civil* 10 (9): 1073-1106. https://doi.org/10.1080/17747120.2006.9692906.

Benhamida, A., I. Djeran-Maigre, H. Dumontet, et S. Smaoui. 2005. « Clay Compaction Modelling by Homogenization Theory ». *International Journal of Rock Mechanics and Mining Sciences*, Rock Physics and Geomechanics, 42 (7): 996-1005. https://doi.org/10.1016/j.ijrmms.2005.05.021.

Bentz, D. P, O. M Jensen, A. M Coats, et F. P Glasser. 2000. « Influence of Silica Fume on Diffusivity in Cement-Based Materials: I. Experimental and Computer Modeling Studies on Cement Pastes ». *Cement and Concrete Research* 30 (6): 953-62. https://doi.org/10.1016/S0008-8846(00)00264-7.

Bernard, E., B. Lothenbach, C. Cau-Dit-Coumes, I. Pochard, et D. Rentsch. 2020. « Aluminum Incorporation into Magnesium Silicate Hydrate (M-S-H) ». *Cement and Concrete Research* 128 (février): 105931. https://doi.org/10.1016/j.cemconres.2019.105931.

References

Bernard, Ellina. 2017. « Magnesium silicate hydrate (M-S-H) characterization : temperature, calcium, aluminium and alkali ». *http://www.theses.fr*. Thesis, Bourgogne Franche-Comté. http://www.theses.fr/2017UBFCK025.

Bernard, Ellina, Alexandre Dauzères, et Barbara Lothenbach. 2018a. « Magnesium and Calcium Silicate Hydrates, Part II: Mg-Exchange at the Interface "Low-PH" Cement and Magnesium Environment Studied in a C-S-H and M-S-H Model System ». *Applied Geochemistry* 89 (février): 210-18. https://doi.org/10.1016/j.apgeochem.2017.12.006.

———. 2018b. « Magnesium and Calcium Silicate Hydrates, Part II: Mg-Exchange at the Interface "Low-PH" Cement and Magnesium Environment Studied in a C-S-H and M-S-H Model System ». *Applied Geochemistry* 89 (février): 210-18. https://doi.org/10.1016/j.apgeochem.2017.12.006.

Bernard, Ellina, Barbara Lothenbach, Céline Cau-Dit-Coumes, Christophe Chlique, Alexandre Dauzères, et Isabelle Pochard. 2018. « Magnesium and Calcium Silicate Hydrates, Part I: Investigation of the Possible Magnesium Incorporation in Calcium Silicate Hydrate (C-S-H) and of the Calcium in Magnesium Silicate Hydrate (M-S-H) ». *Applied Geochemistry* 89 (février): 229-42. https://doi.org/10.1016/j.apgeochem.2017.12.005.

Bernard, Ellina, Barbara Lothenbach, Christophe Chlique, Mateusz Wyrzykowski, Alexandre Dauzères, Isabelle Pochard, et Céline Cau-Dit-Coumes. 2019. « Characterization of Magnesium Silicate Hydrate (M-S-H) ». *Cement and Concrete Research* 116 (février): 309-30. https://doi.org/10.1016/j.cemconres.2018.09.007.

Bernard, Ellina, Barbara Lothenbach, Fabien Le Goff, Isabelle Pochard, et Alexandre Dauzères. 2017a. « Effect of Magnesium on Calcium Silicate Hydrate (C-S-H) ». *Cement and Concrete Research* 97 (juillet): 61-72. https://doi.org/10.1016/j.cemconres.2017.03.012.

Bernard, Ellina, Barbara Lothenbach, Daniel Rentsch, Isabelle Pochard, et Alexandre Dauzères. 2017b. « Formation of Magnesium Silicate Hydrates (M-S-H) ». *Physics and Chemistry of the Earth, Parts A/B/C*, Mechanisms and Modelling of Waste-Cement and Cement-Host Rock Interactions, 99 (juin): 142-57. https://doi.org/10.1016/j.pce.2017.02.005.

Bernard, Ellina, Wolfgang Jan Zucha, Barbara Lothenbach, et Urs Mäder. 2022. « Stability of Hydrotalcite (Mg-Al Layered Double Hydroxide) in Presence of Different Anions ». *Cement and Concrete Research* 152 (février): 106674. https://doi.org/10.1016/j.cemconres.2021.106674.

Bernard, Olivier, Franz-Josef Ulm, et Eric Lemarchand. 2003. « A Multiscale Micromechanics-Hydration Model for the Early-Age Elastic Properties of Cement-Based Materials ». *Cement and Concrete Research* 33 (9): 1293-1309. https://doi.org/10.1016/S0008-8846(03)00039-5.

Bertolini, Luca, Bernhard Elsener, Pietro Pedeferri, Elena Redaelli, et Rob B. Polder. 2013. *Corrosion of Steel in Concrete: Prevention, Diagnosis, Repair*. John Wiley & Sons.

Bertron, A., G. Escadeillas, P. de Parseval, et J. Duchesne. 2009. « Processing of Electron Microprobe Data from the Analysis of Altered Cementitious Materials ». *Cement and Concrete Research* 39 (10): 929-35. https://doi.org/10.1016/j.cemconres.2009.06.011.

Bes, Thomas. 2019. « Etude du comportement des bétons bas-PH sous sollicitations chimiques ». These de doctorat, Toulouse 3. https://www.theses.fr/2019TOU30337.

Bisio, C., G. Gatti, E. Boccaleri, L. Marchese, G. B. Superti, H. O. Pastore, et M. Thommes. 2008. « Understanding Physico–Chemical Properties of Saponite Synthetic Clays ». *Microporous and Mesoporous Materials*, Workshop on Innovative Applications of Layered Materials: From Catalysis to Nanotechnology, 107 (1): 90-101. https://doi.org/10.1016/j.micromeso.2007.05.038.

Black, Leon, Chris Breen, Jack Yarwood, Krassimir Garbev, Peter Stemmermann, et Biliana Gasharova. 2007. « Structural Features of C–S–H(I) and Its Carbonation in Air—A Raman Spectroscopic Study. Part II: Carbonated Phases ». *Journal of the American Ceramic Society* 90 (3): 908-17. https://doi.org/10.1111/j.1551-2916.2006.01429.x.

Blanc, Ph., A. Lassin, P. Piantone, M. Azaroual, N. Jacquemet, A. Fabbri, et E. C. Gaucher. 2012. « Thermoddem: A Geochemical Database Focused on Low Temperature Water/Rock Interactions and Waste Materials ». *Applied Geochemistry* 27 (10): 2107-16. https://doi.org/10.1016/j.apgeochem.2012.06.002.

Boer, J. H. de, B. C. Lippens, B. G. Linsen, J. C. P. Broekhoff, A. van den Heuvel, et Th. J. Osinga. 1966. « Thet-Curve of Multimolecular N2-Adsorption ». *Journal of Colloid and Interface Science* 21 (4): 405-14. https://doi.org/10.1016/0095-8522(66)90006-7.

Brew, D. M. R., et F. P. Glasser. 2005a. « The Magnesia–Silica Gel Phase in Slag Cements: Alkali (K, Cs) Sorption Potential of Synthetic Gels ». *Cement and Concrete Research* 35 (1): 77-83. https://doi.org/10.1016/j.cemconres.2004.03.016.

Brew, D. R. M., et F. P. Glasser. 2005b. « Synthesis and Characterisation of Magnesium Silicate Hydrate Gels ». *Cement and Concrete Research* 35 (1): 85-98. https://doi.org/10.1016/j.cemconres.2004.06.022.

References

Buffo-Lacarrière, Laurie, Alain Sellier, Anaclet Turatsinze, et Gilles Escadeillas. 2011. « Finite Element Modelling of Hardening Concrete: Application to the Prediction of Early Age Cracking for Massive Reinforced Structures ». *Materials and Structures* 44 (10): 1821-35. https://doi.org/10.1617/s11527-011-9740-y.

Caillerie, Jean-Baptiste d'Espinose de la, Maggy Kermarec, et Olivier Clause. 1995. « 29Si NMR Observation of an Amorphous Magnesium Silicate Formed during Impregnation of Silica with Mg(II) in Aqueous Solution » 99: 17273-81.

Canham, I., C. L. Page, et P. J. Nixon. 1987. « Aspects of the Pore Solution Chemistry of Blended Cements Related to the Control of Alkali Silica Reaction ». *Cement and Concrete Research* 17 (5): 839-44. https://doi.org/10.1016/0008-8846(87)90046-9.

Carde, Christophe, et Raoul François. 1997. « Effect of the Leaching of Calcium Hydroxide from Cement Paste on Mechanical and Physical Properties ». *Cement and Concrete Research* 27 (4): 539-50. https://doi.org/10.1016/S0008-8846(97)00042-2.

———. 1999. « Modelling the Loss of Strength and Porosity Increase Due to the Leaching of Cement Pastes ». *Cement and Concrete Composites* 21 (3): 181-88. https://doi.org/10.1016/S0958-9465(98)00046-8.

Carde, Christophe, Raoul François, et Jean-Michel Torrenti. 1996. « Leaching of Both Calcium Hydroxide and C-S-H from Cement Paste: Modeling the Mechanical Behavior ». *Cement and Concrete Research* 26 (8): 1257-68. https://doi.org/10.1016/0008-8846(96)00095-6.

Chang, Honglei, Pan Feng, Kai Lyu, et Jian Liu. 2019. « A Novel Method for Assessing C-S-H Chloride Adsorption in Cement Pastes ». *Construction and Building Materials* 225 (novembre): 324-31. https://doi.org/10.1016/j.conbuildmat.2019.07.212.

Chen, J. J, Luca Sorelli, Matthieu Vandamme, Franz-Josef Ulm, et Gilles Chanvillard. 2010. « A Coupled Nanoindentation/SEM-EDS Study on Low Water/Cement Ratio Portland Cement Paste: Evidence for C–S–H/Ca(OH)2 Nanocomposites ». *Journal of the American Ceramic Society* 93 (5): 1484-93. https://doi.org/10.1111/j.1551-2916.2009.03599.x.

Chen, J. J, J. J Thomas, et Hamlin M. Jennings. 2006. « Decalcification Shrinkage of Cement Paste ». *Cement and Concrete Research* 36 (5): 801-9. https://doi.org/10.1016/j.cemconres.2005.11.003.

Chen, Jeffrey J., Jeffrey J. Thomas, Hal F. W. Taylor, et Hamlin M. Jennings. 2004. « Solubility and Structure of Calcium Silicate Hydrate ». *Cement and Concrete Research*, H. F. W. Taylor Commemorative Issue, 34 (9): 1499-1519. https://doi.org/10.1016/j.cemconres.2004.04.034.

Cheng-yi, Huang, et R. F. Feldman. 1985. « Influence of Silica Fume on the Microstructural Development in Cement Mortars ». *Cement and Concrete Research* 15 (2): 285-94. https://doi.org/10.1016/0008-8846(85)90040-7.

Codina, M. 2007. « Les bétons bas pH : formulation, caractérisation et étude à long terme ». *http://www.theses.fr*. Thesis, Toulouse, INSA. http://www.theses.fr/2007ISAT0029.

Codina, M., C. Cau-dit-Coumes, P. Le Bescop, J. Verdier, et J. P. Ollivier. 2008. « Design and Characterization of Low-Heat and Low-Alkalinity Cements ». *Cement and Concrete Research* 38 (4): 437-48. https://doi.org/10.1016/j.cemconres.2007.12.002.

Collepardi, M. 2003. « A State-of-the-Art Review on Delayed Ettringite Attack on Concrete ». *Cement and Concrete Composites*, Concrete Durability, 25 (4): 401-7. https://doi.org/10.1016/S0958-9465(02)00080-X.

Constantinides, G. 2006. « Invariant Mechanical Properties of Calcium-Silicate-Hydrates (C-H-S) in Cement-Based Materials : Instrumented Nanoindentation and Microporomechanical Modeling ». Thesis, Massachusetts Institute of Technology. https://dspace.mit.edu/handle/1721.1/34377.

Constantinides, G., K. S. Ravi Chandran, F. -J. Ulm, et K. J. Van Vliet. 2006. « Grid Indentation Analysis of Composite Microstructure and Mechanics: Principles and Validation ». *Materials Science and Engineering: A* 430 (1): 189-202. https://doi.org/10.1016/j.msea.2006.05.125.

Constantinides, G., et Franz-Josef Ulm. 2004. « The Effect of Two Types of C-S-H on the Elasticity of Cement-Based Materials: Results from Nanoindentation and Micromechanical Modeling ». *Cement and Concrete Research* 34 (1): 67-80. https://doi.org/10.1016/S0008-8846(03)00230-8.

———. 2007. « The Nanogranular Nature of C–S–H ». *Journal of the Mechanics and Physics of Solids* 55 (1): 64-90. https://doi.org/10.1016/j.jmps.2006.06.003.

Dauzeres, A., G. Achiedo, D. Nied, E. Bernard, S. Alahrache, et B. Lothenbach. 2016. « Magnesium Perturbation in Low-PH Concretes Placed in Clayey Environment—Solid Characterizations and Modeling ». *Cement and Concrete Research* 79 (janvier): 137-50. https://doi.org/10.1016/j.cemconres.2015.09.002.

Dauzères, A., P. Le Bescop, C. Cau-Dit-Coumes, F. Brunet, X. Bourbon, J. Timonen, M. Voutilainen, L. Chomat, et P. Sardini. 2014. « On the Physico-Chemical Evolution of Low-PH and CEM I Cement Pastes Interacting with

References

Callovo-Oxfordian Pore Water under Its in Situ CO2 Partial Pressure ». *Cement and Concrete Research* 58 (avril): 76-88. https://doi.org/10.1016/j.cemconres.2014.01.010.

Dauzeres, A., P. Le Bescop, P. Sardini, et C. Cau Dit Coumes. 2010. « Physico-Chemical Investigation of Clayey/Cement-Based Materials Interaction in the Context of Geological Waste Disposal: Experimental Approach and Results ». *Cement and Concrete Research* 40 (8): 1327-40. https://doi.org/10.1016/j.cemconres.2010.03.015.

Dauzères, Alexandre. 2010. « Etude expérimentale et modélisation des mécanismes physico-chimiques des interactions béton-argile dans le contexte du stockage géologique des déchets radioactifs ». *http://www.theses.fr*. Thesis, Poitiers. http://www.theses.fr/2010POIT2289.

Davydov, D., M. Jirásek, et L. Kopecký. 2011. « Critical Aspects of Nano-Indentation Technique in Application to Hardened Cement Paste ». *Cement and Concrete Research* 41 (1): 20-29. https://doi.org/10.1016/j.cemconres.2010.09.001.

Day, Robert L., et Bryan K. Marsh. 1988. « Measurement of Porosity in Blended Cement Pastes ». *Cement and Concrete Research* 18 (1): 63-73. https://doi.org/10.1016/0008-8846(88)90122-6.

De Gutiérrez, R., S. Delvasto, et R. Talero. 2000. « Permeability Properties of Cement Mortars Blended with Silica Fume, Fly Ash, and Blast Furnace Slag ». *ASTM Special Publication* Marine Corrosion in Tropical Environments (STP 1399): 190-96.

De Weerdt, K., et H. Justnes. 2015. « The Effect of Sea Water on the Phase Assemblage of Hydrated Cement Paste ». *Cement and Concrete Composites* 55 (janvier): 215-22. https://doi.org/10.1016/j.cemconcomp.2014.09.006.

Delayre, C., J. Sammaljärvi, S. Billon, E. Muuri, P. Sardini, et M. Siitari-Kauppi. 2020. « Comparison of Phosphor Screen Autoradiography and Micro-Pattern Gas Detector Based Autoradiography for the Porosity of Altered Rocks ». *Scientific Reports* 10 (1): 9455. https://doi.org/10.1038/s41598-020-65791-7.

Dewitte, Charlotte, Alexandra Bertron, Mejdi Neji, Laurie Lacarrière, et Alexandre Dauzères. 2022. « Chemical and Microstructural Properties of Designed Cohesive M-S-H Pastes ». *Materials* 15 (2): 547. https://doi.org/10.3390/ma15020547.

Diamond, Sidney. 1981. « Effects of Two Danish Flyashes on Alkali Contents of Pore Solutions of Cement-Flyash Pastes ». *Cement and Concrete Research* 11 (3): 383-94. https://doi.org/10.1016/0008-8846(81)90110-1.

Duchesne, J., et M. A. Bérubé. 1995. « Effect of Supplementary Cementing Materials on the Composition of Cement Hydration Products ». *Advanced Cement Based Materials* 2 (2): 43-52. https://doi.org/10.1016/1065-7355(95)90024-1.

Dumas, Angela, François Martin, Christophe Le Roux, Pierre Micoud, Sabine Petit, Eric Ferrage, Jocelyne Brendlé, Olivier Grauby, et Mike Greenhill-Hooper. 2013. « Phyllosilicates Synthesis: A Way of Accessing Edges Contributions in NMR and FTIR Spectroscopies. Example of Synthetic Talc ». *Physics and Chemistry of Minerals* 40 (4): 361-73. https://doi.org/10.1007/s00269-013-0577-5.

Dureković, A. 1995. « Cement Pastes of Low Water to Solid Ratio: An Investigation of the Porosity Characteristics under the Influence of a Superplasticizer and Silica Fume ». *Cement and Concrete Research* 25 (2): 365-75. https://doi.org/10.1016/0008-8846(95)00022-4.

El Bitouri, Y., L. Buffo-Lacarrière, A. Sellier, et X. Bourbon. 2016. « Modelling of Chemo-Mechanical Behaviour of Low PH Concretes ». *Cement and Concrete Research* 81 (mars): 70-80. https://doi.org/10.1016/j.cemconres.2015.12.005.

Escadeillas, G., et H. Hornain. 2008. « Chap 12 : La durabilité des bétons vis-a-vis des environnements chimiquement agressifs ». In *La durabilité des bétons*, JP Ollivier, A. Vichot.

Eshelby, John Douglas, et Rudolf Ernst Peierls. 1957. « The determination of the elastic field of an ellipsoidal inclusion, and related problems ». *Proceedings of the Royal Society of London. Series A. Mathematical and Physical Sciences* 241 (1226): 376-96. https://doi.org/10.1098/rspa.1957.0133.

Faucon, P, F Adenot, J. F Jacquinot, J. C Petit, R Cabrillac, et M Jorda. 1998. « Long-Term Behaviour of Cement Pastes Used for Nuclear Waste Disposal: Review of Physico-Chemical Mechanisms of Water Degradation ». *Cement and Concrete Research* 28 (6): 847-57. https://doi.org/10.1016/S0008-8846(98)00053-2.

Faucon, P., P. Le Bescop, F. Adenot, P. Bonville, J. F. Jacquinot, F. Pineau, et B. Felix. 1996. « Leaching of Cement: Study of the Surface Layer ». *Cement and Concrete Research* 26 (11): 1707-15. https://doi.org/10.1016/S0008-8846(96)00157-3.

Feldman, R. F. 1972. « DENSITY AND POROSITY STUDIES OF HYDRATED PORTLAND CEMENT » 3 (1). https://trid.trb.org/view/97449.

References

Fernández, A. M, B Baeyens, M Bradbury, et P Rivas. 2004. « Analysis of the Porewater Chemical Composition of a Spanish Compacted Bentonite Used in an Engineered Barrier ». *Physics and Chemistry of the Earth, Parts A/B/C*, Water Geochemistry and Hydrogeology, 29 (1): 105-18. https://doi.org/10.1016/j.pce.2003.12.001.

Fernández, Raúl, Elena Torres, Ana I. Ruiz, Jaime Cuevas, María Cruz Alonso, José Luis García Calvo, Enrique Rodríguez, et María Jesús Turrero. 2017. « Interaction Processes at the Concrete-Bentonite Interface after 13 Years of FEBEX-Plug Operation. Part II: Bentonite Contact ». *Physics and Chemistry of the Earth, Parts A/B/C*, Mechanisms and Modelling of Waste-Cement and Cement-Host Rock Interactions, 99 (juin): 49-63. https://doi.org/10.1016/j.pce.2017.01.009.

Florea, M. V. A., et H. J. H. Brouwers. 2012. « Chloride Binding Related to Hydration Products: Part I: Ordinary Portland Cement ». *Cement and Concrete Research* 42 (2): 282-90. https://doi.org/10.1016/j.cemconres.2011.09.016.

Francy, Olivier. 1998. « Modelisation de la penetration des ions chlorures dans les mortiers partiellement satures en eau ». These de doctorat, Toulouse 3. https://www.theses.fr/1998TOU30219.

Fu, Jia, Siham Kamali-Bernard, Fabrice Bernard, et Marilyne Cornen. 2018. « Comparison of Mechanical Properties of C-S-H and Portlandite between Nano-Indentation Experiments and a Modeling Approach Using Various Simulation Techniques ». *Composites Part B: Engineering* 151 (octobre): 127-38. https://doi.org/10.1016/j.compositesb.2018.05.043.

Fu, Xinghua, Zhi Wang, Wenhong Tao, Chunxia Yang, Wenping Hou, Youjun Dong, et Xuequan Wu. 2002. « Studies on Blended Cement with a Large Amount of Fly Ash ». *Cement and Concrete Research* 32 (7): 1153-59. https://doi.org/10.1016/S0008-8846(02)00757-3.

Gaboreau, S., D. Prêt, E. Tinseau, F. Claret, D. Pellegrini, et D. Stammose. 2011. « 15 Years of in Situ Cement–Argillite Interaction from Tournemire URL: Characterisation of the Multi-Scale Spatial Heterogeneities of Pore Space Evolution ». *Applied Geochemistry* 26 (12): 2159-71. https://doi.org/10.1016/j.apgeochem.2011.07.013.

Galarneau, Anne, Dirk Mehlhorn, Flavien Guenneau, Benoit Coasne, Francois Villemot, Delphine Minoux, Cindy Aquino, et Jean-Pierre Dath. 2018. « Specific Surface Area Determination for Microporous/Mesoporous Materials: The Case of Mesoporous FAU-Y Zeolites ». *Langmuir* 34 (47): 14134-42. https://doi.org/10.1021/acs.langmuir.8b02144.

García Calvo, J. L., A. Hidalgo, C. Alonso, et L. Fernández Luco. 2010. « Development of Low-PH Cementitious Materials for HLRW Repositories: Resistance against Ground Waters Aggression ». *Cement and Concrete Research* 40 (8): 1290-97. https://doi.org/10.1016/j.cemconres.2009.11.008.

Gaucher, Eric C., et Philippe Blanc. 2006. « Cement/Clay Interactions – A Review: Experiments, Natural Analogues, and Modeling ». *Waste Management*, Mechanisms and Modeling of Waste/Cement Interactions, 26 (7): 776-88. https://doi.org/10.1016/j.wasman.2006.01.027.

Giroudon, Marie. 2021. « Evaluation des interactions entre biodéchets en digestion anaérobie et matériaux cimentaires à base de différents liants en vue d'une meilleure durabilité des structures de méthanisation ». These de doctorat, Toulouse, INSA. http://www.theses.fr/2021ISAT0001.

Glass, G K, et N R Buenfeld. 2000. « Chloride-Induced Corrosion of Steel in Concrete ». *Progress in Structural Engineering and Materials* 2 (4): 448-58. https://doi.org/10.1002/pse.54.

Gleize, P. J. P., A. Müller, et H. R. Roman. 2003. « Microstructural Investigation of a Silica Fume–Cement–Lime Mortar ». *Cement and Concrete Composites* 25 (2): 171-75. https://doi.org/10.1016/S0958-9465(02)00006-9.

Goh, Kok-Hui, Teik-Thye Lim, et Zhili Dong. 2008. « Application of Layered Double Hydroxides for Removal of Oxyanions: A Review ». *Water Research* 42 (6): 1343-68. https://doi.org/10.1016/j.watres.2007.10.043.

Grangeon, S., F. Claret, C. Roosz, T. Sato, S. Gaboreau, et Y. Linard. 2016. « Structure of Nanocrystalline Calcium Silicate Hydrates: Insights from X-Ray Diffraction, Synchrotron X-Ray Absorption and Nuclear Magnetic Resonance ». *Journal of Applied Crystallography* 49 (3): 771-83. https://doi.org/10.1107/S1600576716003885.

Haas, Jérémy. 2012. « Etude expérimentale et modélisation thermodynamique du système CaO-SiO2-(Al2O3)-H2O ». *http://www.theses.fr*. Thesis, Dijon. http://www.theses.fr/2012DIJOS058.

Hellmuth, K. -H., M. Siitari-Kauppi, P. Klobes, K. Meyer, et J. Goebbels. 1999. « Imaging and Analyzing Rock Porosity by Autoradiography and Hg-Porosimetry/X-Ray Computertomography—Applications ». *Physics and Chemistry of the Earth, Part A: Solid Earth and Geodesy* 24 (7): 569-73. https://doi.org/10.1016/S1464-1895(99)00081-2.

Hellmuth, K. H., M. Siitari-Kauppi, et A. Lindberg. 1993. « Study of Porosity and Migration Pathways in Crystalline Rock by Impregnation with 14C-Polymethylmethacrylate ». *Journal of Contaminant Hydrology*, Chemistry and Migration of Actinides and Fission Products, 13 (1): 403-18. https://doi.org/10.1016/0169-7722(93)90073-2.

References

Hellmuth, Karl-Heinz, Juuso Sammaljärvi, Marja Siitari-Kauppi, Jean-Charles Robinet, et Paul Sardini. 2021. « STED Nanoscopy – A Novel Way to Image the Pore Space of Geological Materials ». *Journal of Microscopy* 283 (2): 151-65. https://doi.org/10.1111/jmi.13016.

Hellmuth, K.-H., S. Lukkarinen, et M. Siitari-kauppi. 1994. « Rock Matrix Studies with Carbon-14-Polymethylmethacrylate (PMMA); Method Development and Applications ». *Isotopenpraxis Isotopes in Environmental and Health Studies* 30 (1): 47-60. https://doi.org/10.1080/00211919408046712.

Hershey, A. V. 1954. « The Elasticity of an Isotropic Aggregate of Anisotropic Cubic Crystals ». *Journal of Applied Mechanics* 21 (3): 236-40. https://doi.org/10.1115/1.4010899.

Hesaraki, S., A. Zamanian, et F. Moztarzadeh. 2009. « Effect of Adding Sodium Hexametaphosphate Liquefier on Basic Properties of Calcium Phosphate Cements ». *Journal of Biomedical Materials Research Part A* 88A (2): 314-21. https://doi.org/10.1002/jbm.a.31836.

Hill, R. 1965. « A Self-Consistent Mechanics of Composite Materials ». *Journal of the Mechanics and Physics of Solids* 13 (4): 213-22. https://doi.org/10.1016/0022-5096(65)90010-4.

Hooton, R. D. 1986. « Permeability and Pore Structure of Cement Pastes Containing Fly Ash, Slag and Silica Fume ». *Blended Cements, ASTM* STP 897: 128-43.

———. 1993. « Influence of Silica Fume Replacement of Cement on Physical Properties and Resistance to Sulfate Attack, Freezing and Thawing, and Alkali-Silica Reactivity ». *Materials Journal* 90 (2): 143-51. https://doi.org/10.14359/4009.

Hornain, Hugues. 2007. *GranDuBé: grandeurs associées à la durabilité des bétons*. Presses des Ponts.

Hou, Dongshuai, Tao Li, et Pan Wang. 2018. « Molecular Dynamics Study on the Structure and Dynamics of NaCl Solution Transport in the Nanometer Channel of CASH Gel ». *ACS Sustainable Chemistry & Engineering* 6 (7): 9498-9509. https://doi.org/10.1021/acssuschemeng.8b02126.

Hu, Zhangli, Adrien Hilaire, Julien Ston, Mateusz Wyrzykowski, Pietro Lura, et Karen Scrivener. 2019. « Intrinsic Viscoelasticity of C-S-H Assessed from Basic Creep of Cement Pastes ». *Cement and Concrete Research* 121 (juillet): 11-20. https://doi.org/10.1016/j.cemconres.2019.04.003.

Hu, Zhangli, Mateusz Wyrzykowski, Michele Griffa, Karen Scrivener, et Pietro Lura. 2020. « Young's Modulus and Creep of Calcium-Silicate-Hydrate Compacts Measured by Microindentation ». *Cement and Concrete Research* 134 (août): 106104. https://doi.org/10.1016/j.cemconres.2020.106104.

Hughes, John J., et Pavel Trtik. 2004. « Micro-Mechanical Properties of Cement Paste Measured by Depth-Sensing Nanoindentation: A Preliminary Correlation of Physical Properties with Phase Type ». *Materials Characterization*, EMABM 2003: 9th Euroseminar on Microscopy Applied to Building Materials, 53 (2): 223-31. https://doi.org/10.1016/j.matchar.2004.08.014.

Hummel, W., U. Berner, E. Curti, F. J. Pearson, et T. Thoenen. 2002. « Nagra/PSI Chemical Thermodynamic Data Base 01/01 ». *Radiochimica Acta* 90 (9-11): 805-13. https://doi.org/10.1524/ract.2002.90.9-11_2002.805.

Ipavec, Andrej, Tomaž Vuk, Roman Gabrovšek, et Venčeslav Kaučič. 2013. « Chloride Binding into Hydrated Blended Cements: The Influence of Limestone and Alkalinity ». *Cement and Concrete Research* 48 (juin): 74-85. https://doi.org/10.1016/j.cemconres.2013.02.010.

Jain, Jitendra, et Narayanan Neithalath. 2009. « Analysis of Calcium Leaching Behavior of Plain and Modified Cement Pastes in Pure Water ». *Cement and Concrete Composites* 31 (3): 176-85. https://doi.org/10.1016/j.cemconcomp.2009.01.003.

Jakobsen, Ulla Hjorth. 2013. « Microstructural surface deterioration of concrete exposed to seawater; results after 2 years exposure », 10-14.

Jakobsen, Ulla Hjorth, Klaartje De Weerdt, et Mette R. Geiker. 2016. « Elemental Zonation in Marine Concrete ». *Cement and Concrete Research* 85 (juillet): 12-27. https://doi.org/10.1016/j.cemconres.2016.02.006.

Jenni, A., U. Mäder, C. Lerouge, S. Gaboreau, et B. Schwyn. 2014. « In Situ Interaction between Different Concretes and Opalinus Clay ». *Physics and Chemistry of the Earth, Parts A/B/C*, Mechanisms and Modelling of Waste-Cement and Cement-Host Rock Interactions, 70-71 (janvier): 71-83. https://doi.org/10.1016/j.pce.2013.11.004.

Jennings, Hamlin M. 1986. « Aqueous Solubility Relationships for Two Types of Calcium Silicate Hydrate » 69 (8): 614-18.

———. 2000. « A Model for the Microstructure of Calcium Silicate Hydrate in Cement Paste ». *Cement and Concrete Research* 30 (1): 101-16. https://doi.org/10.1016/S0008-8846(99)00209-4.

Jennings, Hamlin M., J. J Thomas, Julia S. Gevrenov, Georgios Constantinides, et Franz-Josef Ulm. 2007. « A Multi-Technique Investigation of the Nanoporosity of Cement Paste ». *Cement and Concrete Research*,

References

Cementitious Materials as model porous media: Nanostructure and Transport processes, 37 (3): 329-36. https://doi.org/10.1016/j.cemconres.2006.03.021.

Jia, Yuan, Baomin Wang, Zhenlin Wu, Junnan Han, Tingting Zhang, Luc J. Vandeperre, et Chris R. Cheeseman. 2016. « Role of Sodium Hexametaphosphate in MgO/SiO2 Cement Pastes ». *Cement and Concrete Research* 89 (novembre): 63-71. https://doi.org/10.1016/j.cemconres.2016.08.003.

Juenger, Maria, John L. Provis, Jan Elsen, Winnie Matthes, R. D. Hooton, Josée Duchesne, Luc Courard, et al. 2012. « Supplementary Cementitious Materials for Concrete: Characterization Needs ». *MRS Online Proceedings Library (OPL)* 1488. https://doi.org/10.1557/opl.2012.1536.

Kamali, Siham, M Moranville, E Garboczi, S Prené, et B Gérard. 2004. « Hydrate dissolution influence on the Young's modulus of cement pastes ». In . https://framcos.org/FraMCoS-5/kamali.hydrate.pdf.

Kamali, Siham, Micheline Moranville, et Stéphanie Leclercq. 2008. « Material and Environmental Parameter Effects on the Leaching of Cement Pastes: Experiments and Modelling ». *Cement and Concrete Research* 38 (4): 575-85. https://doi.org/10.1016/j.cemconres.2007.10.009.

Kangni-Foli, E., S. Poyet, P. Le Bescop, T. Charpentier, F. Bernachy-Barbé, A. Dauzères, E. L'Hôpital, et J. -B. d'Espinose de Lacaillerie. 2021. « Carbonation of Model Cement Pastes: The Mineralogical Origin of Microstructural Changes and Shrinkage ». *Cement and Concrete Research* 144 (juin): 106446. https://doi.org/10.1016/j.cemconres.2021.106446.

Kangni-Foli, E., S. Poyet, P. Le Bescop, T. Charpentier, F. Bernachy-Barbé, A. Dauzères, E. L'Hôpital, M. Neji, et J. -B. d'Espinose de Lacaillerie. 2020. « Model Synthetic Pastes for Low PH Cements ». *Cement and Concrete Research* 136 (octobre): 106168. https://doi.org/10.1016/j.cemconres.2020.106168.

Kangni-Foli, Ekoé. 2019. « Apport de matériaux cimentaires modèles à la description des cinétiques de carbonatation de bétons bas-pH : conséquences sur la microstructure le transport de gaz et les déformations ». *http://www.theses.fr*. http://www.theses.fr/s172446.

Klur, Ivan, Benoît Pollet, Joseph Virlet, et André Nonat. 1998. « C-S-H Structure Evolution with Calcium Content by Multinuclear NMR ». In *Nuclear Magnetic Resonance Spectroscopy of Cement-Based Materials*, édité par Pierre Colombet, Hélène Zanni, Arnd-Rüdiger Grimmer, et Piero Sozzani, 119-41. Berlin, Heidelberg: Springer. https://doi.org/10.1007/978-3-642-80432-8_8.

Kobayashi, Mari, Keisuke Takahashi, et Yuichiro Kawabata. 2021. « Physicochemical Properties of the Portland Cement-Based Mortar Exposed to Deep Seafloor Conditions at a Depth of 1680 m ». *Cement and Concrete Research* 142 (avril): 106335. https://doi.org/10.1016/j.cemconres.2020.106335.

Königsberger, Markus, Luis Zelaya-Lainez, Olaf Lahayne, Bernhard L. A. Pichler, et Christian Hellmich. 2021. « Nanoindentation-probed Oliver-Pharr half-spaces in alkali-activated slag-fly ash pastes: Multimethod identification of microelasticity and hardness ». *Mechanics of Advanced Materials and Structures* 0 (0): 1-12. https://doi.org/10.1080/15376494.2021.1941450.

Kothari, Chirayu, et Yuya Takahashi. 2022. « The Effect of Heat Treatment on the Kinetics of the Delayed Ettringite Formation – An Improved Chemo-Thermal-Hygral Model ». *Construction and Building Materials* 331 (mai): 127358. https://doi.org/10.1016/j.conbuildmat.2022.127358.

Krus, M., K. K. Hansen, et H. M. Künzel. 1997. « Porosity and Liquid Absorption of Cement Paste ». *Materials and Structures* 30 (7): 394-98. https://doi.org/10.1007/BF02498561.

Lagneau, Vincent. 2013. « Modélisation des couplages entre réactions géochimiques et processus hydrodynamiques en milieu poreux-applications au stockage de CO2 et à l'exploitation d'uranium ». Doctoral dissertation. Université Pierre et Marie Curie-Paris VI).

Lalan, Philippines, Alexandre Dauzères, Laurent De Windt, Juuso Sammaljärvi, Danièle Bartier, Isabelle Techer, Valéry Detilleux, et Marja Siitari-Kauppi. 2019. « Mineralogical and Microstructural Evolution of Portland Cement Paste/Argillite Interfaces at 70 °C – Considerations for Diffusion and Porosity Properties ». *Cement and Concrete Research* 115 (janvier): 414-25. https://doi.org/10.1016/j.cemconres.2018.09.018.

Langan, B. W., K. Weng, et M. A. Ward. 2002. « Effect of Silica Fume and Fly Ash on Heat of Hydration of Portland Cement ». *Cement and Concrete Research* 32 (7): 1045-51. https://doi.org/10.1016/S0008-8846(02)00742-1.

Lauch, Kim-Séang, Vinciane Dieryck, et Valérie Pollet. 2016. « The Use of Ternary Cements to Reduce the Environmental Impact of Concrete ». *RILEM Technical Letters* 1 (décembre): 88-93. https://doi.org/10.21809/rilemtechlett.2016.19.

Lecoq, X. 1993. « Etude de l'hydratation à concentration contrôlée du silicate tricalcique Ca 3 SiO 5 et des caractéristiques de ses produits de réaction ».

Lerouge, Catherine, Stéphane Gaboreau, Sylvain Grangeon, Francis Claret, Fabienne Warmont, Andreas Jenni, Veerle Cloet, et Urs Mäder. 2017. « In Situ Interactions between Opalinus Clay and Low Alkali Concrete ». *Physics*

References

and Chemistry of the Earth, Parts A/B/C, Mechanisms and Modelling of Waste-Cement and Cement-Host Rock Interactions, 99 (juin): 3-21. https://doi.org/10.1016/j.pce.2017.01.005.

Li, Zhaoheng, Tongsheng Zhang, Jie Hu, Yue Tang, Yanfei Niu, Jiangxiong Wei, et Qijun Yu. 2014. « Characterization of Reaction Products and Reaction Process of MgO–SiO2–H2O System at Room Temperature ». *Construction and Building Materials* 61 (juin): 252-59. https://doi.org/10.1016/j.conbuildmat.2014.03.004.

Linderoth, O., P. Johansson, et L. Wadsö. 2020. « Development of Pore Structure, Moisture Sorption and Transport Properties in Fly Ash Blended Cement-Based Materials ». *Construction and Building Materials* 261 (novembre): 120007. https://doi.org/10.1016/j.conbuildmat.2020.120007.

Liu, Lin, Can Sun, Guoqing Geng, Pan Feng, Jiaqi Li, et Rainer Dähn. 2019. « Influence of Decalcification on Structural and Mechanical Properties of Synthetic Calcium Silicate Hydrate (C-S-H) ». *Cement and Concrete Research* 123 (septembre): 105793. https://doi.org/10.1016/j.cemconres.2019.105793.

Lojka, Michal, Ondřej Jankovský, Adéla Jiříčková, Anna-Marie Lauermannová, Filip Antončík, David Sedmidubský, Zbyšek Pavlík, et Milena Pavlíková. 2020. « Thermal Stability and Kinetics of Formation of Magnesium Oxychloride Phase 3Mg(OH)2·MgCl2·8H2O ». *Materials* 13 (3): 767. https://doi.org/10.3390/ma13030767.

Lothenbach, B., D. Nied, E. L'Hôpital, G. Achiedo, et A. Dauzères. 2015. « Magnesium and Calcium Silicate Hydrates ». *Cement and Concrete Research* 77 (novembre): 60-68. https://doi.org/10.1016/j.cemconres.2015.06.007.

Lothenbach, Barbara, Paweł Durdziński, et Klaartje De Weerdt. 2016. « Chapter 5 : Thermogravimetric Analysis ». In *A Practical Guide to Microstructural Analysis of Cementitious Materials*, 177-212. CRC Press.

Lothenbach, Barbara, et Frank Winnefeld. 2006. « Thermodynamic Modelling of the Hydration of Portland Cement ». *Cement and Concrete Research* 36 (2): 209-26. https://doi.org/10.1016/j.cemconres.2005.03.001.

Maciejak, Olek, et Pascal Aubert. 2007. « Mesure de dureté par nano-indentation ». Text. Ref : TIP155WEB - « Nanosciences et nanotechnologies ». Editions T.I. | Techniques de l'Ingénieur. 2007. 10 octobre 2007. https://www.techniques-ingenieur.fr/base-documentaire/innovation-th10/nanosciences-concepts-simulation-et-caracterisation-42194210/mesure-de-durete-par-nano-indentation-nm7200/.

Mainguy, Marc, Claire Tognazzi, Jean-Michel Torrenti, et Frédéric Adenot. 2000. « Modelling of Leaching in Pure Cement Paste and Mortar ». *Cement and Concrete Research* 30 (1): 83-90. https://doi.org/10.1016/S0008-8846(99)00208-2.

Malhotra, V. M., et P. K. Mehta. 2002. « High-Performance, High-Volume Fly Ash Concrete: Materials, Mixture Proportioning, Properties, Construction Practice, and Case Histories », août. https://www.osti.gov/etdeweb/biblio/20464963.

Marsh, B. K., R. L. Day, et D. G. Bonner. 1985. « Pore Structure Characteristics Affecting the Permeability of Cement Paste Containing Fly Ash ». *Cement and Concrete Research* 15 (6): 1027-38. https://doi.org/10.1016/0008-8846(85)90094-8.

Martín-Pérez, B, H Zibara, R. D Hooton, et M. D. A Thomas. 2000. « A Study of the Effect of Chloride Binding on Service Life Predictions ». *Cement and Concrete Research* 30 (8): 1215-23. https://doi.org/10.1016/S0008-8846(00)00339-2.

Matte, V., M. Moranville, F. Adenot, C. Richet, et J. M. Torrenti. 2000. « Simulated Microstructure and Transport Properties of Ultra-High Performance Cement-Based Materials ». *Cement and Concrete Research*, Papers presented at the Symposium on « Transport Properties and Microstructure of Cement-Based Systems », 30 (12): 1947-54. https://doi.org/10.1016/S0008-8846(00)00288-X.

Mehta, P., et Paulo J. M. Monteiro. 2005. *Concrete : Microstructure, Properties, and Materials: Microstructure, Properties, and Materials*. McGraw Hill Professional.

Mills, S. J., A. G. Christy, J.-M. R. Génin, T. Kameda, et F. Colombo. 2012. « Nomenclature of the Hydrotalcite Supergroup: Natural Layered Double Hydroxides ». *Mineralogical Magazine* 76 (5): 1289-1336. https://doi.org/10.1180/minmag.2012.076.5.10.

Min, Deng, et Tang Mingshu. 1994. « Formation and Expansion of Ettringite Crystals ». *Cement and Concrete Research* 24 (1): 119-26. https://doi.org/10.1016/0008-8846(94)90092-2.

Mitchell, D. R. G., I. Hinczak, et R. A. Day. 1998. « Interaction of Silica Fume with Calcium Hydroxide Solutions and Hydrated Cement Pastes ». *Cement and Concrete Research* 28 (11): 1571-84. https://doi.org/10.1016/S0008-8846(98)00133-1.

Mitsuda, T., et H. Taguchi. 1977. « Formation of Magnesium Silicate Hydrate and Its Crystallization to Talc ». *Cement and Concrete Research* 7 (3): 223-30. https://doi.org/10.1016/0008-8846(77)90083-7.

References

Miyata, Shigeo. 1983. « Anion-Exchange Properties of Hydrotalcite-Like Compounds ». *Clays and Clay Minerals* 31 (4): 305-11. https://doi.org/10.1346/CCMN.1983.0310409.

Mondal, Paramita, Surendra P. Shah, et Laurence Marks. 2007. « A Reliable Technique to Determine the Local Mechanical Properties at the Nanoscale for Cementitious Materials ». *Cement and Concrete Research* 37 (10): 1440-44. https://doi.org/10.1016/j.cemconres.2007.07.001.

Monnier, G., P. Stengel, et J.C. Fies. 1973. « Une méthode de mesure de la densité apparente de petits agglomérats terreux. Application à l'analyse des systèmes de porosité du sol ». *Ann. Agron.* 24 (5): 533-45.

Mori, T, et K Tanaka. 1973. « Average Stress in Matrix and Average Elastic Energy of Materials with Misfitting Inclusions ». *Acta Metallurgica* 21 (5): 571-74. https://doi.org/10.1016/0001-6160(73)90064-3.

Muller, Arnaud Charles Albert. 2014. « Characterization of Porosity & C-S-H in Cement Pastes by ^{1}H NMR ». Lausanne: EPFL. https://doi.org/10.5075/epfl-thesis-6339.

Neji, M., A. Dauzères, A. Grellier, J. Sammaljärvi, O. Tikkanen, et M. Siitari-Kauppi. 2022. « Comparison of the Chemo-Mechanical Behavior of Low-PH Cement Exposed to Calcareous Water and to Argillite Pore Water ». *Applied Geochemistry*, juillet, 105392. https://doi.org/10.1016/j.apgeochem.2022.105392.

Neville, Adam. 1995. « Chloride Attack of Reinforced Concrete: An Overview ». *Materials and Structures* 28 (2): 63-70. https://doi.org/10.1007/BF02473172.

Nguyen, D. L. 2017. « Nouvelle méthodologie d'identification des propriétés mécaniques locales d'un matériau hétérogène par nanoindentation : application aux matériaux du génie civil ». *http://www.theses.fr*. Thesis, Paris Est. http://www.theses.fr/2017PESC1028.

Nguyen, V. H., H. Colina, J. M. Torrenti, C. Boulay, et B. Nedjar. 2007. « Chemo-Mechanical Coupling Behaviour of Leached Concrete: Part I: Experimental Results ». *Nuclear Engineering and Design* 237 (20): 2083-89. https://doi.org/10.1016/j.nucengdes.2007.02.013.

Nied, Dominik, Kasper Enemark-Rasmussen, Emilie L'Hopital, Jørgen Skibsted, et Barbara Lothenbach. 2016. « Properties of Magnesium Silicate Hydrates (M-S-H) ». *Cement and Concrete Research* 79 (janvier): 323-32. https://doi.org/10.1016/j.cemconres.2015.10.003.

Nixon, P J, C L Page, R Bollinghaus, et I Canham. 1986. « The effect of a Pfa with a high total alkali content on pore solution composition and alkali silica reaction ». *Magazine of Concrete Research* 38 (134): 30-35. https://doi.org/10.1680/macr.1986.38.134.30.

Nonat, André. 2004. « The Structure and Stoichiometry of C-S-H ». *Cement and Concrete Research*, H. F. W. Taylor Commemorative Issue, 34 (9): 1521-28. https://doi.org/10.1016/j.cemconres.2004.04.035.

———. 2008. « Chap 2 : L'hydratation des ciments ». In *La durabilité des bétons*, JP Ollivier, A. Vichot.

Ollivier, J.-P. 1997. « Les résultats croisés AFREM pour la détermination de la masse volumique apparente et de la porosité accessible à l'eau des bétons ». Compte rendu des Journées techniques AFPC-AFREM « Durabilité des bétons ». Toulouse: Laboratoire matériaux et durabilité des constructions. https://books.google.fr/books?hl=fr&lr=&id=0hUQMCJG9q0C&oi=fnd&pg=PA17&dq=Grandub%C3%A9+porosit%C3%A9+%C3%A0+l%27eau&ots=0rlkJ2M8G-&sig=QjIf4Ljfg2XGW9mYIAuKpp0aXyY#v=onepage&q=Grandub%C3%A9%20porosit%C3%A9%20%C3%A0%20l'eau&f=false.

Packwood, R. H., et J. D. Brown. 1981. « A Gaussian Expression to Describe ϕ(Pz) Curves for Quantitative Electron Probe Microanalysis ». *X-Ray Spectrometry* 10 (3): 138-46. https://doi.org/10.1002/xrs.1300100311.

Page, C. L., et Ø. Vennesland. 1983. « Pore Solution Composition and Chloride Binding Capacity of Silica-Fume Cement Pastes ». *Matériaux et Construction* 16 (1): 19-25. https://doi.org/10.1007/BF02474863.

Parrott, L. J. 1990. « Damage Caused by Carbonation of Reinforced Concrete ». *Materials and Structures* 23 (3): 230-34. https://doi.org/10.1007/BF02473023.

Perlot, Céline. 2005. « Influence de la décalcification de matériaux cimentaires sur les propriétés de transfert : application au stockage profond de déchets radioactifs ». These de doctorat, Toulouse 3. https://www.theses.fr/2005TOU30211.

Pigeon, M. 2014. *Durability of Concrete in Cold Climates*. CRC Press.

Qiao, Chunyu, Prannoy Suraneni, Marisol Tsui Chang, et Jason Weiss. 2018. « Damage in Cement Pastes Exposed to MgCl2 Solutions ». *Materials and Structures* 51 (3): 74. https://doi.org/10.1617/s11527-018-1191-2.

Renhe, Yang, Liu Baoyuan, et Wu Zhongwei. 1990. « Study on the Pore Structure of Hardened Cement Paste by SAXS ». *Cement and Concrete Research* 20 (3): 385-93. https://doi.org/10.1016/0008-8846(90)90028-V.

Richardson, I. G. 1999. « The Nature of C-S-H in Hardened Cements ». *Cement and Concrete Research* 29 (8): 1131-47. https://doi.org/10.1016/S0008-8846(99)00168-4.

References

———. 2000. « The Nature of the Hydration Products in Hardened Cement Pastes ». *Cement and Concrete Composites* 22 (2): 97-113. https://doi.org/10.1016/S0958-9465(99)00036-0.

Richardson, I. G. 2004. « Tobermorite/Jennite- and Tobermorite/Calcium Hydroxide-Based Models for the Structure of C-S-H: Applicability to Hardened Pastes of Tricalcium Silicate, β-Dicalcium Silicate, Portland Cement, and Blends of Portland Cement with Blast-Furnace Slag, Metakaolin, or Silica Fume ». *Cement and Concrete Research*, H. F. W. Taylor Commemorative Issue, 34 (9): 1733-77. https://doi.org/10.1016/j.cemconres.2004.05.034.

———. 2008. « The Calcium Silicate Hydrates ». *Cement and Concrete Research*, Special Issue — The 12th International Congress on the Chemistry of Cement. Montreal, Canada, July 8-13 2007, 38 (2): 137-58. https://doi.org/10.1016/j.cemconres.2007.11.005.

———. 2014. « Model Structures for C-(A)-S-H(I) ». *Acta Crystallographica Section B: Structural Science, Crystal Engineering and Materials* 70 (6): 903-23. https://doi.org/10.1107/S2052520614021982.

Richardson, I. G., A. R. Brough, G. W. Groves, et C. M. Dobson. 1994. « The Characterization of Hardened Alkali-Activated Blast-Furnace Slag Pastes and the Nature of the Calcium Silicate Hydrate (C-S-H) Phase ». *Cement and Concrete Research* 24 (5): 813-29. https://doi.org/10.1016/0008-8846(94)90002-7.

Richardson, I. G., et G. W. Groves. 1992. « Microstructure and Microanalysis of Hardened Cement Pastes Involving Ground Granulated Blast-Furnace Slag ». *Journal of Materials Science* 27 (22): 6204-12. https://doi.org/10.1007/BF01133772.

Richardson, I.G. 2013. « Clarification of Possible Ordered Distributions of Trivalent Cations in Layered Double Hydroxides and an Explanation for the Observed Variation in the Lower Solid-Solution Limit ». *Acta Crystallographica Section B: Structural Science, Crystal Engineering and Materials* 69 (6): 629-33. https://doi.org/10.1107/S2052519213027905.

Roosz, Cédric. 2016. « Propriétés thermodynamiques des phases cimentaires hydratées : C-S-H, C-A-S-H et M-S-H ». *http://www.theses.fr*. Thesis, Poitiers. http://www.theses.fr/2016POIT2264.

Roosz, Cédric, Marie Giroudon, Laurie Lacarrière, Matthieu Peyre-Lavigne, et Alexandra Bertron. 2022. « Contribution of Thermodynamic Modeling to the Understanding of Interactions Between Hydrated Cement Pastes and Organic Acids ». In *Proceedings of the 3rd RILEM Spring Convention and Conference (RSCC 2020)*, édité par José Sena-Cruz, Luis Correia, et Miguel Azenha, 279-89. RILEM Bookseries. Cham: Springer International Publishing. https://doi.org/10.1007/978-3-030-76465-4_25.

Roosz, Cédric, Sylvain Grangeon, Philippe Blanc, Valérie Montouillout, Barbara Lothenbach, Pierre Henocq, Eric Giffaut, Philippe Vieillard, et Stéphane Gaboreau. 2015. « Crystal Structure of Magnesium Silicate Hydrates (M-S-H): The Relation with 2:1 Mg–Si Phyllosilicates ». *Cement and Concrete Research* 73 (juillet): 228-37. https://doi.org/10.1016/j.cemconres.2015.03.014.

Roosz, Cédric, Philippe Vieillard, Philippe Blanc, Stéphane Gaboreau, Hélène Gailhanou, Daniel Braithwaite, Valérie Montouillout, Renaud Denoyel, Pierre Henocq, et Benoit Madé. 2018. « Thermodynamic Properties of C-S-H, C-A-S-H and M-S-H Phases: Results from Direct Measurements and Predictive Modelling ». *Applied Geochemistry* 92 (mai): 140-56. https://doi.org/10.1016/j.apgeochem.2018.03.004.

Rosenqvist, Martin, Alexandra Bertron, Katja Fridh, et Manouchehr Hassanzadeh. 2017. « Concrete Alteration Due to 55years of Exposure to River Water: Chemical and Mineralogical Characterisation ». *Cement and Concrete Research* 92 (février): 110-20. https://doi.org/10.1016/j.cemconres.2016.11.012.

Sakai, Etsuo, Shigeyoshi Miyahara, Shigenari Ohsawa, Seung-Heun Lee, et Masaki Daimon. 2005. « Hydration of Fly Ash Cement ». *Cement and Concrete Research* 35 (6): 1135-40. https://doi.org/10.1016/j.cemconres.2004.09.008.

Sammaljärvi, Juuso, Lalli Jokelainen, Jussi Ikonen, et Marja Siitari-Kauppi. 2012. « Free Radical Polymerisation of MMA with Thermal Initiator in Brick and Grimsel Granodiorite ». *Engineering Geology* 135-136 (mai): 52-59. https://doi.org/10.1016/j.enggeo.2012.03.005.

Sammaljärvi, Juuso, Mallikarjuna Shroff Rama, Jussi Ikonen, Eveliina Muuri, Karl-Heinz Hellmuth, et Marja Siitari-Kauppi. 2016. « Free Radical Polymerisation of Methacrylates with Thermal Initiator in Clay Rock ». *Engineering Geology* 210 (août): 70-83. https://doi.org/10.1016/j.enggeo.2016.06.003.

Sammartino, S., M. Siitari-Kauppi, A. Meunier, P. Sardini, A. Bouchet, et E. Tevissen. 2002. « An Imaging Method for the Porosity of Sedimentary Rocks: Adjustment of the PMMA Method—Example of a Characterization of a Calcareous Shale ». *Journal of Sedimentary Research* 72 (6): 937-43. https://doi.org/10.1306/053002720937.

Sánchez de Rojas, M. I., M. P. Luxán, M. Frías, et N. García. 1993. « The Influence of Different Additions on Portland Cement Hydration Heat ». *Cement and Concrete Research* 23 (1): 46-54. https://doi.org/10.1016/0008-8846(93)90134-U.

References

Sánchez de Rojas, María Isabel, Julián Rivera Lozano, et Moisés Frías. 1999. « Influence of the Microsilica State on Pozzolanic Reaction Rate », juin. https://doi.org/10.1016/S0008-8846(99)00085-X.

Sánchez, Laura, Jaime Cuevas, Susana Ramírez, David Riuiz De León, Raúl Fernández, Raquel Vigil Dela Villa, et Santiago Leguey. 2006. « Reaction Kinetics of FEBEX Bentonite in Hyperalkaline Conditions Resembling the Cement–Bentonite Interface ». *Applied Clay Science* 33 (2): 125-41. https://doi.org/10.1016/j.clay.2006.04.008.

Santhanam, Manu, Menashi D Cohen, et Jan Olek. 2001. « Sulfate Attack Research — Whither Now? » *Cement and Concrete Research* 31 (6): 845-51. https://doi.org/10.1016/S0008-8846(01)00510-5.

———. 2002a. « Mechanism of Sulfate Attack: A Fresh Look: Part 1: Summary of Experimental Results ». *Cement and Concrete Research* 32 (6): 915-21. https://doi.org/10.1016/S0008-8846(02)00724-X.

———. 2002b. « Mechanism of Sulfate Attack: A Fresh Look: Part 1: Summary of Experimental Results ». *Cement and Concrete Research* 32 (6): 915-21. https://doi.org/10.1016/S0008-8846(02)00724-X.

Santhanam, Manu, Menashi D. Cohen, et Jan Olek. 2003a. « Effects of Gypsum Formation on the Performance of Cement Mortars during External Sulfate Attack ». *Cement and Concrete Research* 33 (3): 325-32. https://doi.org/10.1016/S0008-8846(02)00955-9.

———. 2003b. « Mechanism of Sulfate Attack: A Fresh Look: Part 2. Proposed Mechanisms ». *Cement and Concrete Research* 33 (3): 341-46. https://doi.org/10.1016/S0008-8846(02)00958-4.

Sardini, Paul, Marja Siitari-Kauppi, Daniel Beaufort, et Karl-Heinz Hellmuth. 2006. « On the Connected Porosity of Mineral Aggregates in Crystalline Rocks ». *American Mineralogist* 91 (7): 1069-80. https://doi.org/10.2138/am.2006.1939.

Šauman, Zdeněk. 1971. « Carbonization of Porous Concrete and Its Main Binding Components ». *Cement and Concrete Research* 1 (6): 645-62. https://doi.org/10.1016/0008-8846(71)90019-6.

Savage, David, Colin Walker, Randy Arthur, Chris Rochelle, Chie Oda, et Hiro Takase. 2007. « Alteration of Bentonite by Hyperalkaline Fluids: A Review of the Role of Secondary Minerals ». *Physics and Chemistry of the Earth, Parts A/B/C*, Clay in natural and engineered barriers for radioactive waste confinement - Part 1, 32 (1): 287-97. https://doi.org/10.1016/j.pce.2005.08.048.

Shah, Vineet, et Allan Scott. 2021. « Hydration and Microstructural Characteristics of MgO in the Presence of Metakaolin and Silica Fume ». *Cement and Concrete Composites* 121 (août): 104068. https://doi.org/10.1016/j.cemconcomp.2021.104068.

Shehata, Medhat H., Michael D. A. Thomas, et Roland F. Bleszynski. 1999. « The Effects of Fly Ash Composition on the Chemistry of Pore Solution in Hydrated Cement Pastes ». *Cement and Concrete Research* 29 (12): 1915-20. https://doi.org/10.1016/S0008-8846(99)00190-8.

Shi, Caijun. 1996. « Strength, Pore Structure and Permeability of Alkali-Activated Slag Mortars ». *Cement and Concrete Research* 26 (12): 1789-99. https://doi.org/10.1016/S0008-8846(96)00174-3.

Siitari-Kauppi, Marja. 2002. « La caractérisation des milieux à faible porosité avec la méthode 14C-polyméthylmétacrylate (14C-PMMA) : application aux barrières géologiques de stockage des déchets nucléaires ». These de doctorat, Poitiers. https://www.theses.fr/2002POIT2254.

Silva, W. R. L. da, J. Němeček, et P. Štemberk. 2013. « Application of Multiscale Elastic Homogenization Based on Nanoindentation for High Performance Concrete ». *Advances in Engineering Software*, Special Issue dedicated to Professor Zden ek Bittnar on the occasion of his Seventieth Birthday: Part I, 62-63 (août): 109-18. https://doi.org/10.1016/j.advengsoft.2013.04.007.

Sing, K. S. W. 1985. « Reporting physisorption data for gas/solid systems with special reference to the determination of surface area and porosity (Recommendations 1984) ». *Pure and Applied Chemistry* 57 (4): 603-19. https://doi.org/10.1351/pac198557040603.

Snel, Ruud. 1984a. « Control of the Porous Structure of Amorphous Silica-Alumina 2. The Effects of Ph and Reactant Concentration ». *Applied Catalysis* 12 (2): 189-200. https://doi.org/10.1016/S0166-9834(00)80290-0.

———. 1984b. « Control of the Porous Structure of Amorphous Silica-Alumina: 3. The Influence of Pore-Regulating Reagents ». *Applied Catalysis* 12 (4): 347-57. https://doi.org/10.1016/S0166-9834(00)81672-3.

Sonat, C., et C. Unluer. 2019. « Development of Magnesium-Silicate-Hydrate (M-S-H) Cement with Rice Husk Ash ». *Journal of Cleaner Production* 211 (février): 787-803. https://doi.org/10.1016/j.jclepro.2018.11.246.

Souyris, Pierre. 2012. « Prédiction des propriétés poro-élastiques et de sorption d'eau en fonction du développement de la microstructure des matériaux cimentaires ». These de doctorat, Toulouse 3. https://www.theses.fr/2012TOU30327.

Stora, Éric. 2007. « Modélisation multi-échelle et simulations du comportement chimie-mécanique des matériaux cimentaires dégradés ». *http://www.theses.fr*. Thesis, Université de Marne-la-Vallée. http://www.theses.fr/2007MARN0369.

References

Stora, Eric, Benoît Bary, et Qi-Chang He. 2008. « On Estimating the Effective Diffusive Properties of Hardened Cement Pastes ». *Transport in Porous Media* 73 (3): 279-95. https://doi.org/10.1007/s11242-007-9170-z.

Sumra, Yousuf, Shafigh Payam, et Ibrahim Zainah. 2020. « The PH of Cement-Based Materials: A Review ». *Journal of Wuhan University of Technology-Mater. Sci. Ed.* 35 (5): 908-24. https://doi.org/10.1007/s11595-020-2337-y.

Sutter, Lawrence, Karl Peterson, Sayward Touton, Tom Van Dam, et Dan Johnston. 2006. « Petrographic Evidence of Calcium Oxychloride Formation in Mortars Exposed to Magnesium Chloride Solution ». *Cement and Concrete Research*, 10th EUROSEMINAR on microscopy applied to building materials, University of Paisley, June 21-25, 2005, 36 (8): 1533-41. https://doi.org/10.1016/j.cemconres.2006.05.022.

Szczerba, Jacek, Ryszard Prorok, Edyta Śnieżek, Dominika Madej, et Konrad Maślona. 2013. « Influence of Time and Temperature on Ageing and Phases Synthesis in the MgO–SiO2–H2O System ». *Thermochimica Acta*, Calorimetry and Thermal Effects in Catalysis, 567 (septembre): 57-64. https://doi.org/10.1016/j.tca.2013.01.018.

Taylor, H. F. W. 1964. *The Chemistry of cements*. Volume I. London: Academic press inc.

———. 1986. « Proposed Structure for Calcium Silicate Hydrate Gel » 69 (6): 464-67.

———. 1997. *Cement Chemistry*. 2nd edition. Thomas Telford Publishing. https://fazaia.edu.pk/uploads/library/Cement-Chemistry-2nd-Edition_1539670060.pdf.

Taylor, H. F. W., K. Mohan, et G. K. Moir. 1985. « Analytical Study of Pure and Extended Portland Cement Pastes: II, Fly Ash- and Slag-Cement Pastes ». *Journal of the American Ceramic Society* 68 (12): 685-90. https://doi.org/10.1111/j.1151-2916.1985.tb10125.x.

Tennis, Paul D, et Hamlin M Jennings. 2000. « A Model for Two Types of Calcium Silicate Hydrate in the Microstructure of Portland Cement Pastes ». *Cement and Concrete Research* 30 (6): 855-63. https://doi.org/10.1016/S0008-8846(00)00257-X.

Thomas, J. J, H. M Jennings, et A. J Allen. 1998. « The Surface Area of Cement Paste as Measured by Neutron Scattering: Evidence for Two C-S-H Morphologies ». *Cement and Concrete Research* 28 (6): 897-905. https://doi.org/10.1016/S0008-8846(98)00049-0.

Thomas, J. J, et Hamlin M. Jennings. 2006. « A Colloidal Interpretation of Chemical Aging of the C-S-H Gel and Its Effects on the Properties of Cement Paste ». *Cement and Concrete Research* 36 (1): 30-38. https://doi.org/10.1016/j.cemconres.2004.10.022.

Thomas, M. D. A., R. D. Hooton, A. Scott, et H. Zibara. 2012. « The Effect of Supplementary Cementitious Materials on Chloride Binding in Hardened Cement Paste ». *Cement and Concrete Research* 42 (1): 1-7. https://doi.org/10.1016/j.cemconres.2011.01.001.

Tonelli, M., F. Martini, L. Calucci, E. Fratini, M. Geppi, F. Ridi, S. Borsacchi, et P. Baglioni. 2016. « Structural Characterization of Magnesium Silicate Hydrate: Towards the Design of Eco-Sustainable Cements ». *Dalton Transactions* 45 (8): 3294-3304. https://doi.org/10.1039/C5DT03545G.

Tonelli, Monica, Francesca Martini, Lucia Calucci, Marco Geppi, Silvia Borsacchi, et Francesca Ridi. 2017. « Traditional Portland Cement and MgO-Based Cement: A Promising Combination? » *Physics and Chemistry of the Earth, Parts A/B/C*, Mechanisms and Modelling of Waste-Cement and Cement-Host Rock Interactions, 99 (juin): 158-67. https://doi.org/10.1016/j.pce.2017.01.011.

Tonelli, Monica, Francesca Martini, Alessio Milanesi, Lucia Calucci, Marco Geppi, Silvia Borsacchi, et Francesca Ridi. 2019. « Effect of Phosphate Additives on the Hydration Process of Magnesium Silicate Cements ». *Journal of Thermal Analysis and Calorimetry* 138 (5): 3311-21. https://doi.org/10.1007/s10973-019-08847-9.

Tracz, T. 2016. « Open Porosity of Cement Pastes and Their Gas Permeability ». *Bulletin of the Polish Academy of Sciences. Technical Sciences* Vol. 64 (nr 4). https://doi.org/10.1515/bpasts-2016-0086.

Trtik, Pavel, Beat Münch, et Pietro Lura. 2009. « A Critical Examination of Statistical Nanoindentation on Model Materials and Hardened Cement Pastes Based on Virtual Experiments ». *Cement and Concrete Composites* 31 (10): 705-14. https://doi.org/10.1016/j.cemconcomp.2009.07.001.

Ulm, Franz-Josef, Matthieu Vandamme, Chris Bobko, et Jose Alberto Ortega. 2007. « Statistical Indentation Techniques for Hydrated Nanocomposites: Concrete, Bone, and Shale » 90 (9): 2677-92.

Ulm, Franz-Josef, Matthieu Vandamme, Hamlin M. Jennings, James Vanzo, Michelle Bentivegna, Konrad J. Krakowiak, Georgios Constantinides, Christopher P. Bobko, et Krystyn J. Van Vliet. 2010. « Does Microstructure Matter for Statistical Nanoindentation Techniques? » *Cement and Concrete Composites* 32 (1): 92-99. https://doi.org/10.1016/j.cemconcomp.2009.08.007.

Van der Lee, Jan. 1998. « Thermodynamic and mathematical concepts of CHESS ». LHM/RD/98/39. Fontainebleau, France: Ecole des Mines de Paris.

References

Van der Lee, Jan, Laurent De Windt, Vincent Lagneau, et Patrick Goblet. 2003. « Module-Oriented Modeling of Reactive Transport with HYTEC ». *Computers & Geosciences*, Reactive Transport Modeling in the Geosciences, 29 (3): 265-75. https://doi.org/10.1016/S0098-3004(03)00004-9.

Vandamme, Matthieu. 2008. « The Nanogranular Origin of Concrete Creep : A Nanoindentation Investigation of Microstructure and Fundamental Properties of Calcium-Silicate-Hydrates ». Thesis, Massachusetts Institute of Technology. https://dspace.mit.edu/handle/1721.1/43906.

Vandamme, Matthieu, et F. -J. Ulm. 2009. « Nanogranular origin of concrete creep », Proceedings of the National Academy of Sciences, 106 (26): 10552-57.

———. 2013. « Nanoindentation Investigation of Creep Properties of Calcium Silicate Hydrates ». *Cement and Concrete Research* 52 (octobre): 38-52. https://doi.org/10.1016/j.cemconres.2013.05.006.

Vinutha, H. P., B. Poornima, et B. M. Sagar. 2018. « Detection of Outliers Using Interquartile Range Technique from Intrusion Dataset ». In *Information and Decision Sciences*, édité par Suresh Chandra Satapathy, Joao Manuel R.S. Tavares, Vikrant Bhateja, et J. R. Mohanty, 511-18. Advances in Intelligent Systems and Computing. Singapore: Springer. https://doi.org/10.1007/978-981-10-7563-6_53.

Vollpracht, Anya, Barbara Lothenbach, Ruben Snellings, et Johannes Haufe. 2016. « The Pore Solution of Blended Cements: A Review ». *Materials and Structures* 49 (8): 3341-67. https://doi.org/10.1617/s11527-015-0724-1.

Voutilainen, Mikko, Arttu Miettinen, Paul Sardini, Joni Parkkonen, Juuso Sammaljärvi, Björn Gylling, Jan-Olof Selroos, Maarit Yli-Kaila, Lasse Koskinen, et Marja Siitari-Kauppi. 2019. « Characterization of Spatial Porosity and Mineral Distribution of Crystalline Rock Using X-Ray Micro Computed Tomography, C-14-PMMA Autoradiography and Scanning Electron Microscopy ». *Applied Geochemistry* 101 (février): 50-61. https://doi.org/10.1016/j.apgeochem.2018.12.024.

Wan, Keshu, Yan Li, et Wei Sun. 2013. « Experimental and Modelling Research of the Accelerated Calcium Leaching of Cement Paste in Ammonium Nitrate Solution ». *Construction and Building Materials*, Special Section on Recycling Wastes for Use as Construction Materials, 40 (mars): 832-46. https://doi.org/10.1016/j.conbuildmat.2012.11.066.

Wan, Keshu, Qiong Xu, Lin Li, et Wei Sun. 2013. « 3D Porosity Distribution of Partly Calcium Leached Cement Paste ». *Construction and Building Materials* 48 (novembre): 11-15. https://doi.org/10.1016/j.conbuildmat.2013.06.073.

Wang, L., H. Q. Yang, S. H. Zhou, E. Chen, et S. W. Tang. 2018. « Mechanical Properties, Long-Term Hydration Heat, Shinkage Behavior and Crack Resistance of Dam Concrete Designed with Low Heat Portland (LHP) Cement and Fly Ash ». *Construction and Building Materials* 187 (octobre): 1073-91. https://doi.org/10.1016/j.conbuildmat.2018.08.056.

Wang, Shao-Dong, et Karen L. Scrivener. 1995. « Hydration Products of Alkali Activated Slag Cement ». *Cement and Concrete Research* 25 (3): 561-71. https://doi.org/10.1016/0008-8846(95)00045-E.

Wiyantoko, Bayu, Puji Kurniawati, Tri Esti Purbaningtias, et Is Fatimah. 2015. « Synthesis and Characterization of Hydrotalcite at Different Mg/Al Molar Ratios ». *Procedia Chemistry*, 3rd International Seminar on Chemistry 2014, 17 (janvier): 21-26. https://doi.org/10.1016/j.proche.2015.12.115.

Wolery, T. J. 1992. « EQ3NR, a Computer Program for Geochemical Aqueous Speciation-Solubility Calculations: Theoretical Manual, User`s Guide, and Related Documentation (Version 7.0); Part 3 ». UCRL-MA-110662-Pt.3. Lawrence Livermore National Lab. (LLNL), Livermore, CA (United States). https://doi.org/10.2172/138643.

Xi, Y., D. D. Siemer, et B. E. Scheetz. 1997. « Strength Development, Hydration Reaction and Pore Structure of Autoclaved Slag Cement with Added Silica Fume ». *Cement and Concrete Research* 27 (1): 75-82. https://doi.org/10.1016/S0008-8846(96)00196-2.

Xie, Ning, Yudong Dang, et Xianming Shi. 2019. « New Insights into How MgCl2 Deteriorates Portland Cement Concrete ». *Cement and Concrete Research* 120 (juin): 244-55. https://doi.org/10.1016/j.cemconres.2019.03.026.

Xu, Yue. 2004. « Approche multi-échelle pour l'étude du comportement des systèmes polyphasiques : application aux milieux poreux non saturés ». These de doctorat, Marne-la-vallée, ENPC. http://www.theses.fr/2004ENPC0002.

Yajun, Ji, et Jong Herman Cahyadi. 2003. « Effects of Densified Silica Fume on Microstructure and Compressive Strength of Blended Cement Pastes ». *Cement and Concrete Research* 33 (10): 1543-48. https://doi.org/10.1016/S0008-8846(03)00100-5.

Yang, D. Y., et R. Guo. 2011. « Experimental Study on Modulus and Hardness of Ettringite ». *Experimental Techniques* 38 (1): 6-12. https://doi.org/10.1111/j.1747-1567.2011.00744.x.

Yang, Jun, Dongshuai Hou, Qingjun Ding, Gaozhan Zhang, Yang Zhang, et Hao Hu. 2020. « Insight on the Nanoscale Chemical Degradation Mechanism of MgCl2 Attack in Cement Paste ». *Construction and Building Materials* 238 (mars): 117777. https://doi.org/10.1016/j.conbuildmat.2019.117777.

References

Zemnukhova, Ludmila A., Alexander E. Panasenko, Andrey P. Artem'yanov, et Elena A. Tsoy. 2015. « Dependence of Porosity of Amorphous Silicon Dioxide Prepared from Rice Straw on Plant Variety ». *BioResources* 10 (2): 3713-23.

Zhang, Tingting, C. R. Cheeseman, et L. J. Vandeperre. 2011. « Development of Low PH Cement Systems Forming Magnesium Silicate Hydrate (M-S-H) ». *Cement and Concrete Research* 41 (4): 439-42. https://doi.org/10.1016/j.cemconres.2011.01.016.

Zhang, Tingting, Luc J. Vandeperre, et Christopher R. Cheeseman. 2014. « Formation of Magnesium Silicate Hydrate (M-S-H) Cement Pastes Using Sodium Hexametaphosphate ». *Cement and Concrete Research* 65 (novembre): 8-14. https://doi.org/10.1016/j.cemconres.2014.07.001.

Zhang, Tingting, Jing Zou, Baomin Wang, Zhenlin Wu, Yuan Jia, et Christopher R. Cheeseman. 2018. « Characterization of Magnesium Silicate Hydrate (MSH) Gel Formed by Reacting MgO and Silica Fume ». *Materials* 11 (6): 909. https://doi.org/10.3390/ma11060909.

Zhou, Yang, Dongshuai Hou, Jinyang Jiang, et Penggang Wang. 2016. « Chloride Ions Transport and Adsorption in the Nano-Pores of Silicate Calcium Hydrate: Experimental and Molecular Dynamics Studies ». *Construction and Building Materials* 126 (novembre): 991-1001. https://doi.org/10.1016/j.conbuildmat.2016.09.110.

Zhu, Wenzhong, John J. Hughes, Nenad Bicanic, et Chris J. Pearce. 2007. « Nanoindentation Mapping of Mechanical Properties of Cement Paste and Natural Rocks ». *Materials Characterization*, 10th Euroseminar on Microscopy Applied to Building Materials (EMABM), 58 (11): 1189-98. https://doi.org/10.1016/j.matchar.2007.05.018.

Zhuravlev, L. T. 2000. « The Surface Chemistry of Amorphous Silica. Zhuravlev Model ». *Colloids and Surfaces A: Physicochemical and Engineering Aspects* 173 (1): 1-38. https://doi.org/10.1016/S0927-7757(00)00556-2.

APPENDICES

Appendix A. M-S-H pastes

Table A-1 : Summary table of the results obtained on the M-S-H performed in the laboratory

	Reagents	M/S ratios	Protocol	w/s	Results	Source
Suspensions	Silica + aqueous solution of Mg^{2+}	-	impregnation of silica with an aqueous solution of Mg^{2+}	-	- Identification of a new silicate phase: M-S-H	(d'Espinose de la Caillerie, Kermarec, et Clause 1995)
	Sodium silicate + magnesium	0.66 – 0.96	precipitation based on a sodium metasilicate solution	-	- Identification via XRD - Phyllosilicate gel structure - C-S-H et M-S-H immiscible - substitution of Ca by Mg in C-S-H unlikely	(Brew et Glasser 2005b)
	MgO+SF	0.6 et 1.2	Precipitation under N_2 flow, addition of distilled water, stirring for 1 year then flitration	50	- Identification via XRD - lamellar and turbostatic model based on talc, of the nanocrystalline phyllosilicate type	(Roosz et al. 2015)
	MgO+SF+CaO	(Mg + Ca)/Si=0.8		45	- Sheet structure, contrast with C-S-H structure - a lot of bound water in the M-S-H - Identification via TGA	(Lothenbach et al. 2015)
	MgO+SF	0.4; 0.6; 0.8; 1.0; 1.3 et 1.7		45	- Identification via XRD and TGA - link between M/S and the structure of M-S-H and the amount of bound water, proposes sheet structure with gaps or broken chains - calculation of solubility constants	(Nied et al. 2016)

Suspensions	MgO+SF	1	MgO+FS+distilled water mixture, constant stirring	10	- Shell structure: development on the surface of the particles - Hydration kinetics	(Zhang et al. 2018)
	MgO+SF+CaO	0.6 et 1.2	Same as Roosz 2015		- Determination of the thermodynamic properties of the three species M-S-H, C-S-H and C-A-S-H - Predominance diagram, predictive model	(Roosz et al. 2018)
	C-S-H and solutions of $MgCl_2$ and MgO	-	Contact between C-S-H and two solutions based on MgO or $MgCl_2$	22.5 initially then 54	- C-S-H stables for 9,6<pH<11,5, - M-S-H stables for 7,5<pH<12	(Bernard et al. 2017a)
	MgO+SF	0.7 à 1.6	Precipitation under N_2 flow and placement in an automatic shaker, 3 curing temperatures were considered: 20°C, 50°C and 70°C	45	- Hydration kinetics - Solubility constants	(Bernard et al. 2017b)
	MgO+SF+CaO				- Incorporation of Ca into M-S-H is possible but not vice versa (no C-(M)-S-H phase), it would be M-S-H phase containing small amounts of adsorbed and/or incorporated calcium	(Bernard et al. 2018)
	MgO+SF		Precipitation under N_2 flow and placement in an automatic shaker, contacting C-S-H and M-S-H	45	- C-S-H destabilised - no trace of Mg incorporated in C S-H - M-S-H are derived from the dissolution of C-S-H	(Bernard, Dauzères, et Lothenbach 2018a)

	MgO+SF		Precipitation under N_2 flow and placement in an automatic shaker, hydration time up to 3.3 years	45	- Very slow formation - Silicate sheet structure with small ordered regions varying with M/S - 1 to 2.5 water molecules in M-S-H - M-S-H similar to swelling clays - Specific surface area (SSA_{BET}) decreases as M/S increases	(Bernard et al. 2019)

	Reagents	**M/S ratios**	**Protocol**	**w/b**	**Results**	**Source**
Pastes	MgO+Microsilica	1	Mixing of reagents	0.5	- X-ray and TGA identification - The initial byproduct of the interaction between MgO and water is brucite. Brucite likely transitions into M-S-H phase concurrently.	(Szczerba et al. 2013)
	MgO+NaHMP+SF	1	Mixing of reagents, NaHMP allows to fluidize	0.4-0.8	- MgO requires a lot of water - X-ray and TGA identification - When w/b decreases, the mechanical strength increases - With w/b=0.4, R=70 MPa at 28 d	(Zhang, Vandeperre, et Cheeseman 2014)
	MgO+SF	1	Mixing of reagents	2	- Observation of homogeneous morphology at microscopic and globular scale at higher magnification (SEM) - hydration kinetics: (passage through brucite precipitation), FTIR, NMR, XRD, TGA	(Tonelli et al. 2016)

	Portland cement + MgO + SF	1	Mixing of reagents	2	- Hydration kinetics (phase splitting), FTIR, NMR, XRD, TGA	(Tonelli et al. 2017)
	Rice husk ash (RHA) + MgO + NaHMP	1 (mass)	Mixing of reagents, RHA=source of silica	0.55	- Measurement of mechanical strength - influence of the type of RHA (rice husk ash) on the mechanical properties: crystalline RHA bad, amorphous RHA good	(Sonat et Unluer 2019)

Table A-2: Protocol used on M-S-H samples in X-ray diffraction.

Sample Name	Location of Test	Protocol
MS_0-78_SF_T20_19d	Sorbonne Université	PANalytical X'Pert Pro (PANalytical Empyrean instrument) operating at 40 kV and 40 mA with a Cu anti-cathode (λ~1.54 Å)
MS_0-78_SF_T50_19d	Sorbonne Université	
MS_0-78_CS_T20_16d	Sorbonne Université	
MS_0-78_CS_T50_16d	Sorbonne Université	
MS_1_SF_T20_91d	Sorbonne Université	2Θ = 5°–70° with a step size of 0.0131, for a total duration of 4 h
MS_1-3_SF_T20_91d	Sorbonne Université	
Colloidal silica	LMDC	
Silica fume	IRSN	
MS_1_SF_T20_19d	IRSN	
MS_1-3_SF_T20_19d	IRSN	PANalytical Aeris operating at 600 W, 40 kV and 15 mA, with a Cu anti-cathode (λ~1.54 Å), step size of 0.0109, for a total duration of 20 min
MS_1_SF_T50_19d	IRSN	
MS_1-3_SF_T50_19d	IRSN	
MS_0-78_CS_T50_128d	IRSN	
MS_1_CS_T50_156d	IRSN	
MS_1-3_CS_T50_122d	IRSN	
122d	IRSN	

Appendix B. Multiphysics characterization of the low-pH model cement pastes immersed in 5 mM $MgCl_2$ solutions

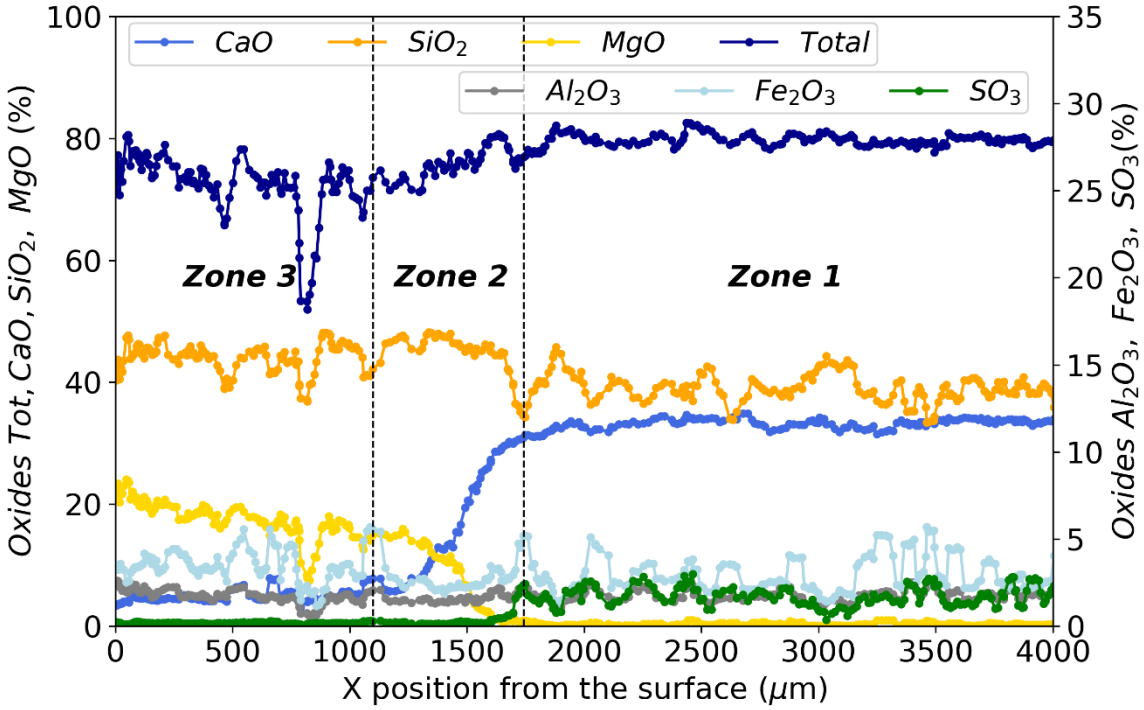

Figure B-1: Chemical composition of oxides of a low-pH model cement paste, immersed in solution with [$MgCl_2$]=5 mmol/L for 6 months according to the surface of the specimen (analysis by electron microprobe, not corrected).

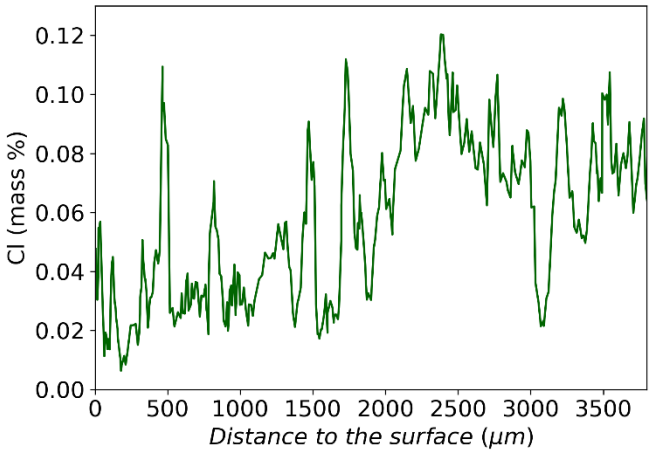

Figure B-2: Cl mass % of a low-pH model cement paste, immersed in solution with [$MgCl_2$] = 5 mmol/L for 6 months according to the distance to the surface of the specimen (analysis by electron microprobe, corrected)

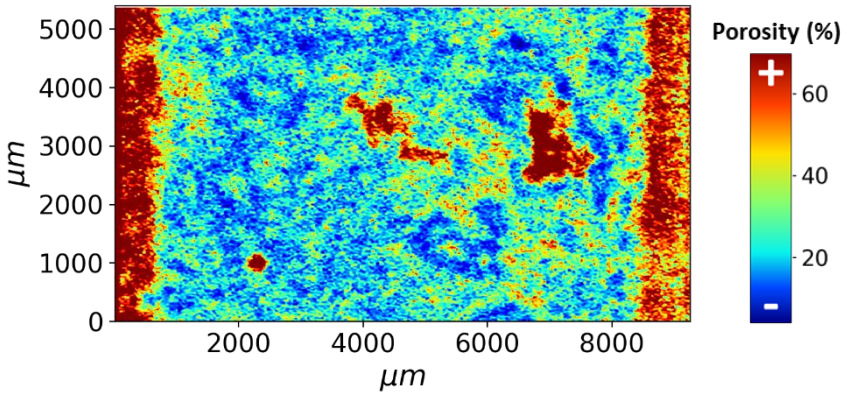

(a)

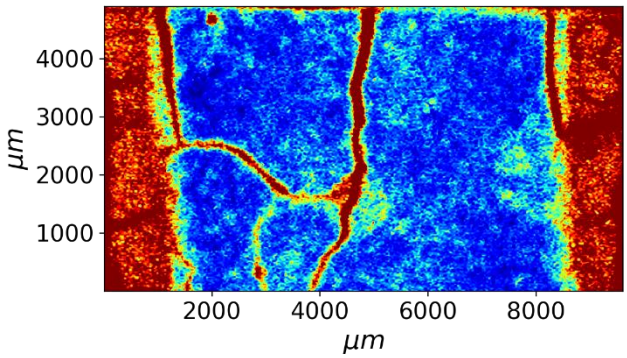

(b) _

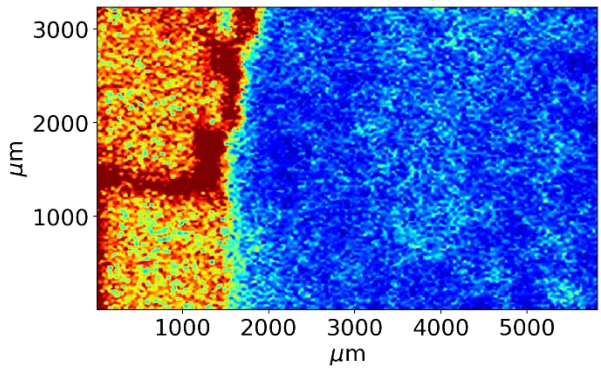

(c)

Figure B-3: Porosity maps after autoradiography characterization of low-pH model cement samples degraded during 2 months (a), 4 months (b) and 6 months (c) in 5 mM [$MgCl_2$] solution

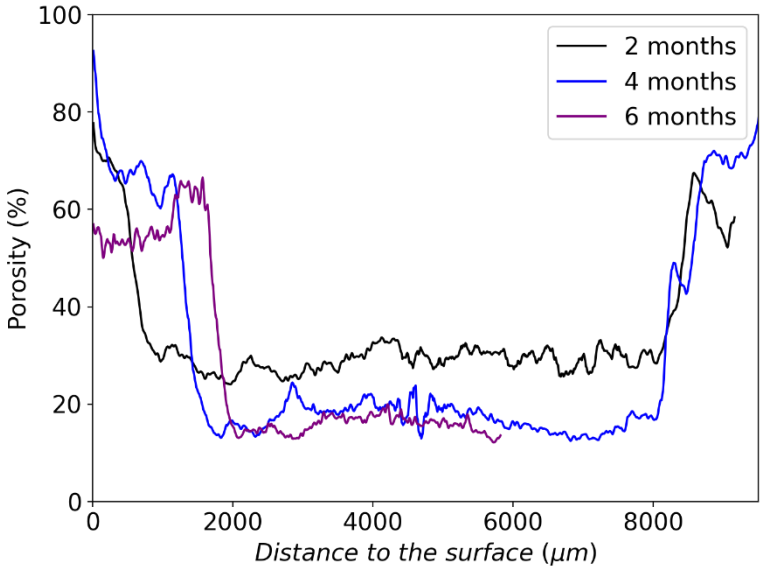

Figure B-4: Porosity profiles after autoradiography characterization of low-pH model cement samples degraded during 2 months, 4 months and 6 months in 5 mM [$MgCl_2$] solution

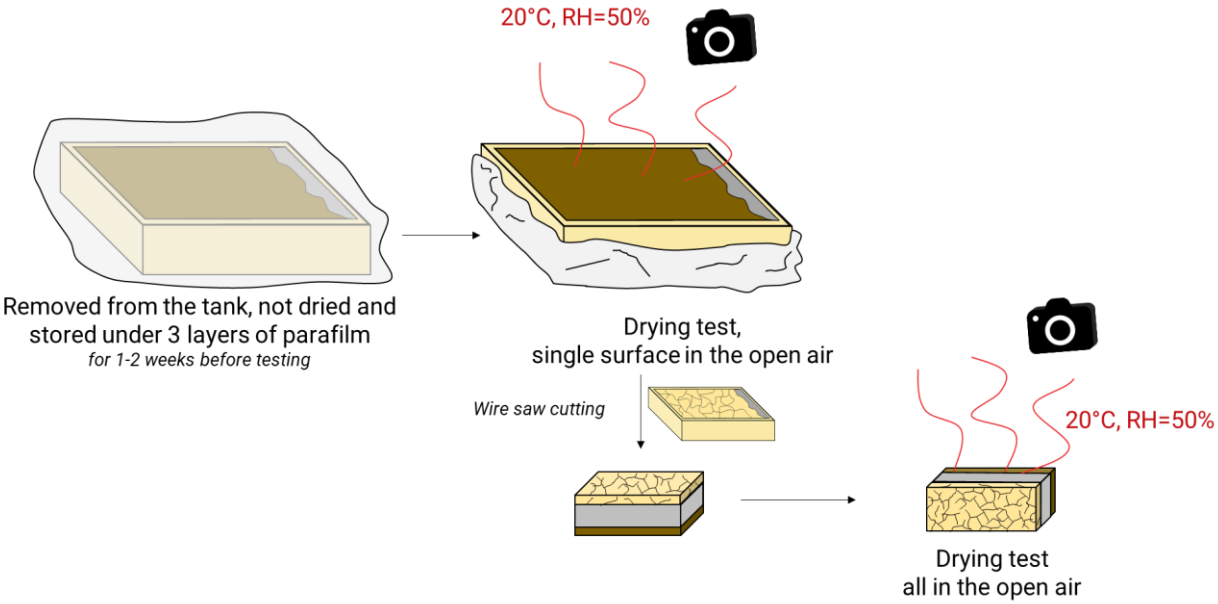

Figure B-5: Illustration of the follow-up (visual) cracking test

Appendix C. Multiphysics characterization of the 50 mM low-pH model cement degraded samples

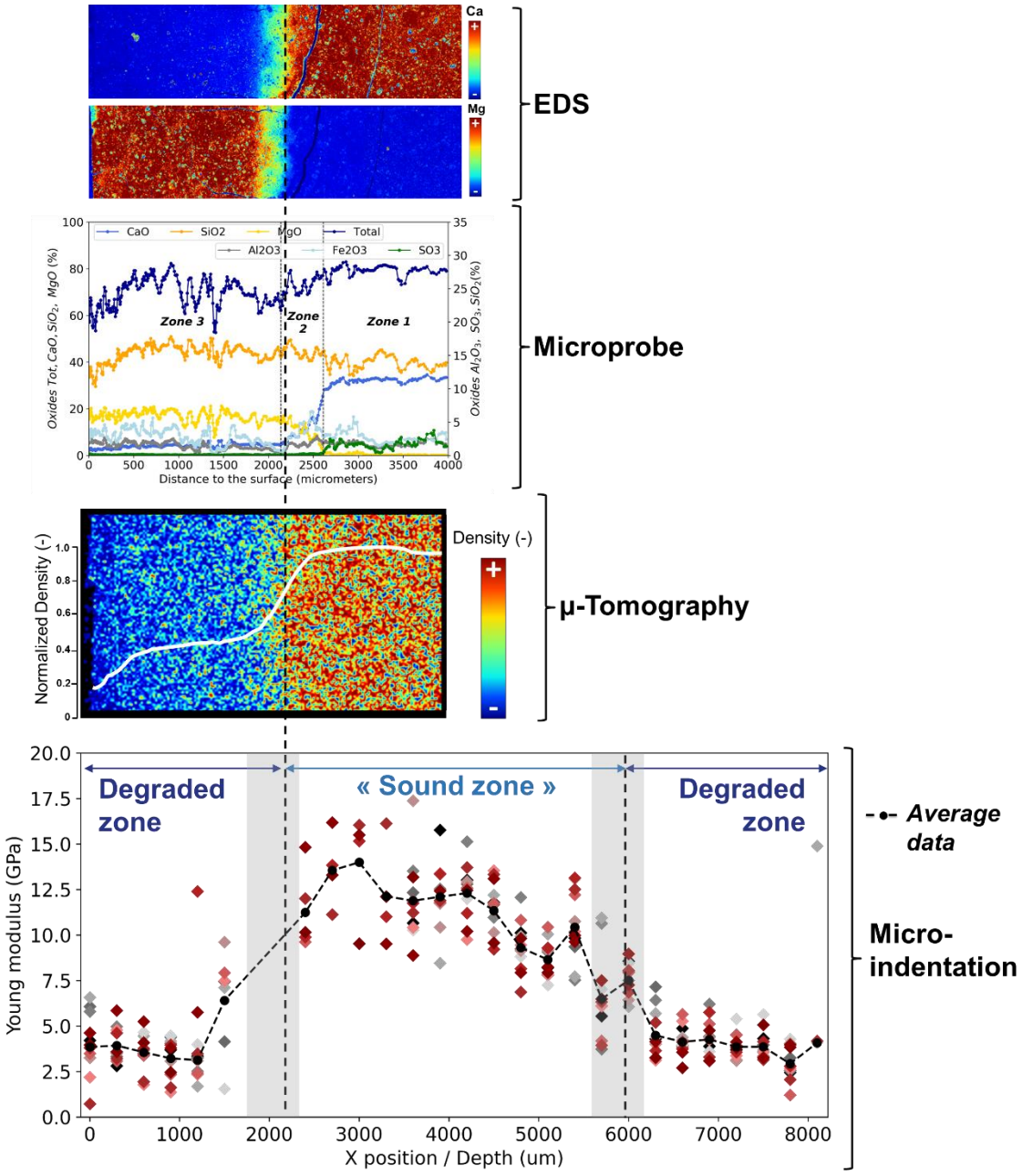

Figure C-1: Multi-physics characterization of model cement paste immerged during 6 months in a solution with [$MgCl_2$] = 50 mmol/L

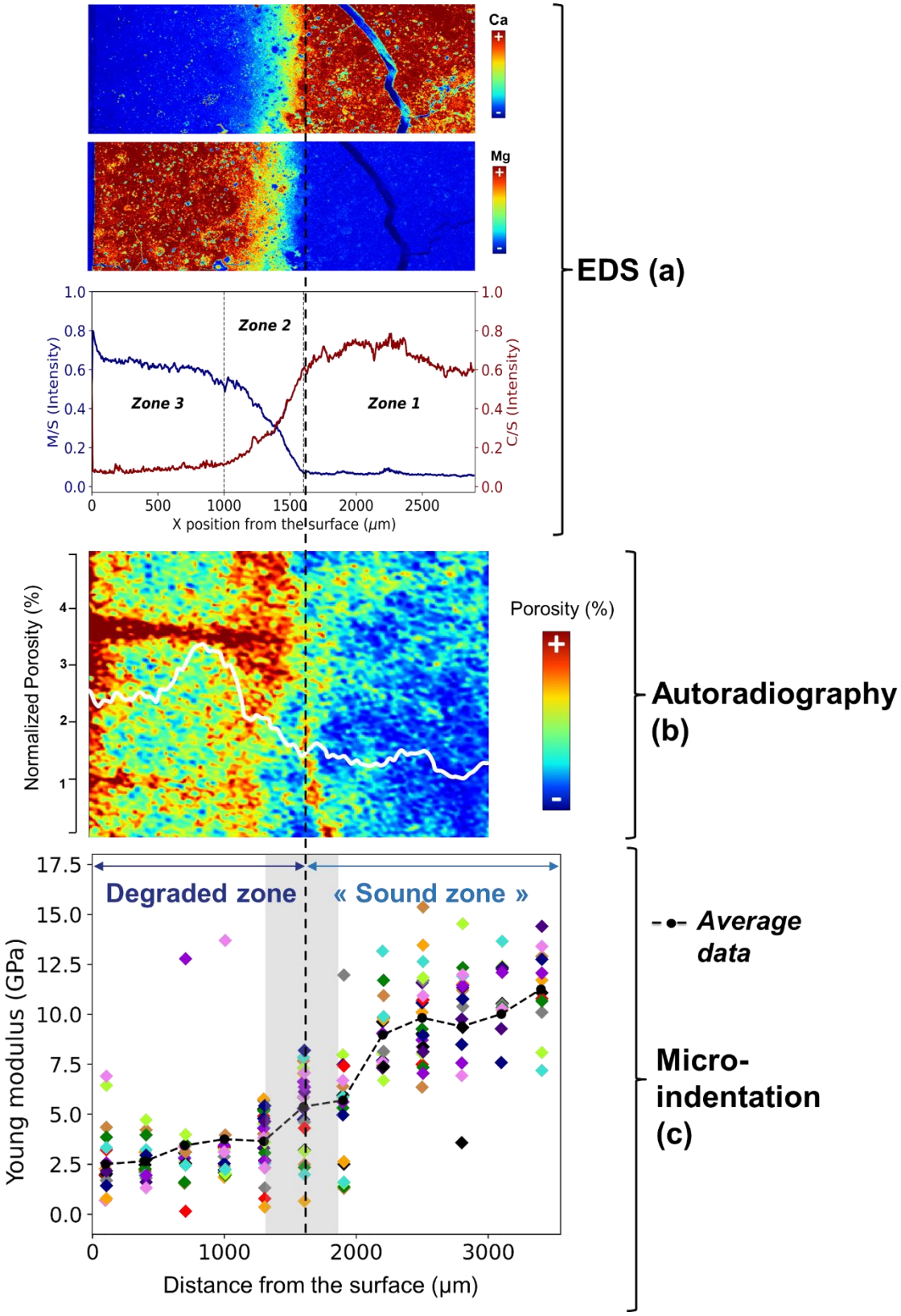

Figure C-2: Multi-physics characterization of model cement paste immerged during 4 months in a solution with [$MgCl_2$] = 50 mmol/L

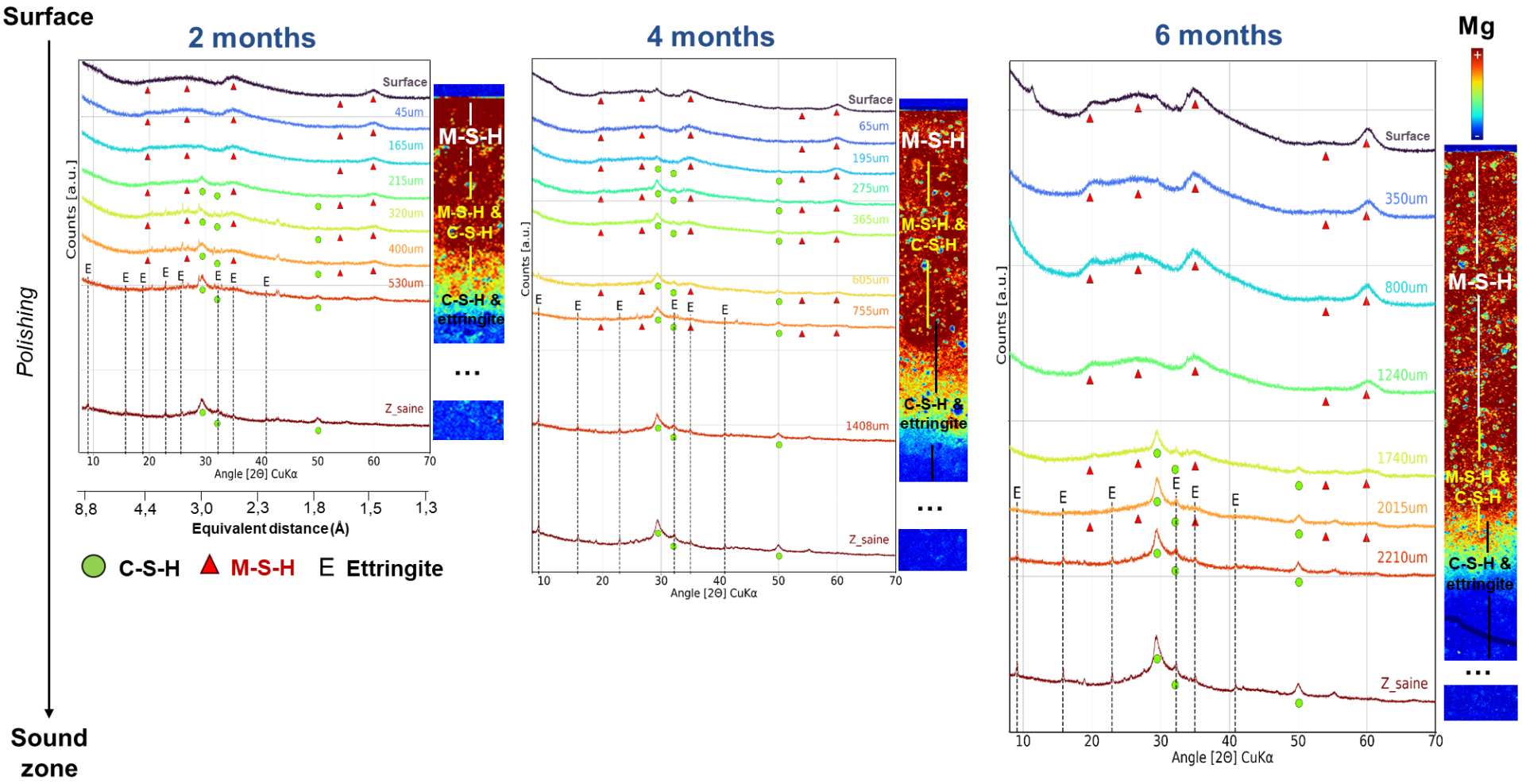

Figure C-3: X-Ray diffractograms along the degradation of a CEMI paste with colloidal silica placed in a solution with [$MgCl_2$] = 50 mmol/L for 2, 4 and 6 months associated to Mg EDS maps.

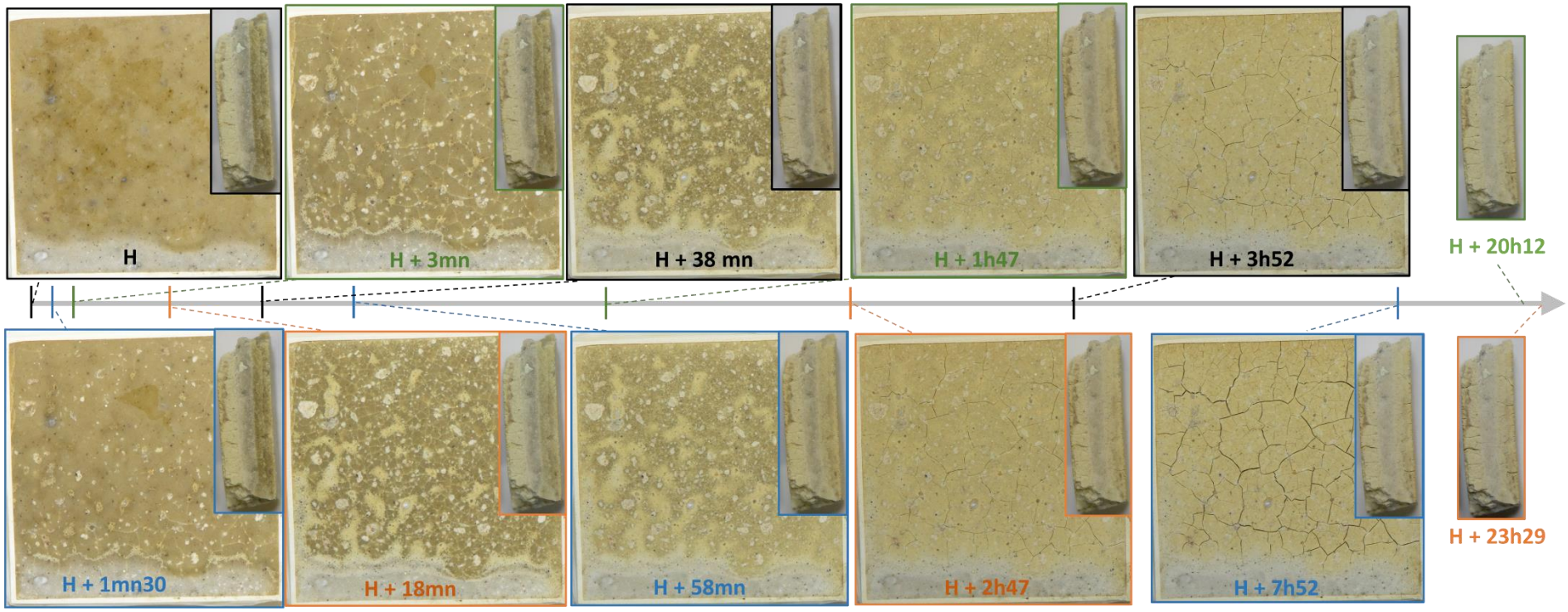

Figure C-4: Pictures from follow-up (visual) cracking test during exposure to a controlled atmosphere (20°C, RH=50%) of low-pH model cement paste immersed in 50 mM $MgCl_2$ during 9 months

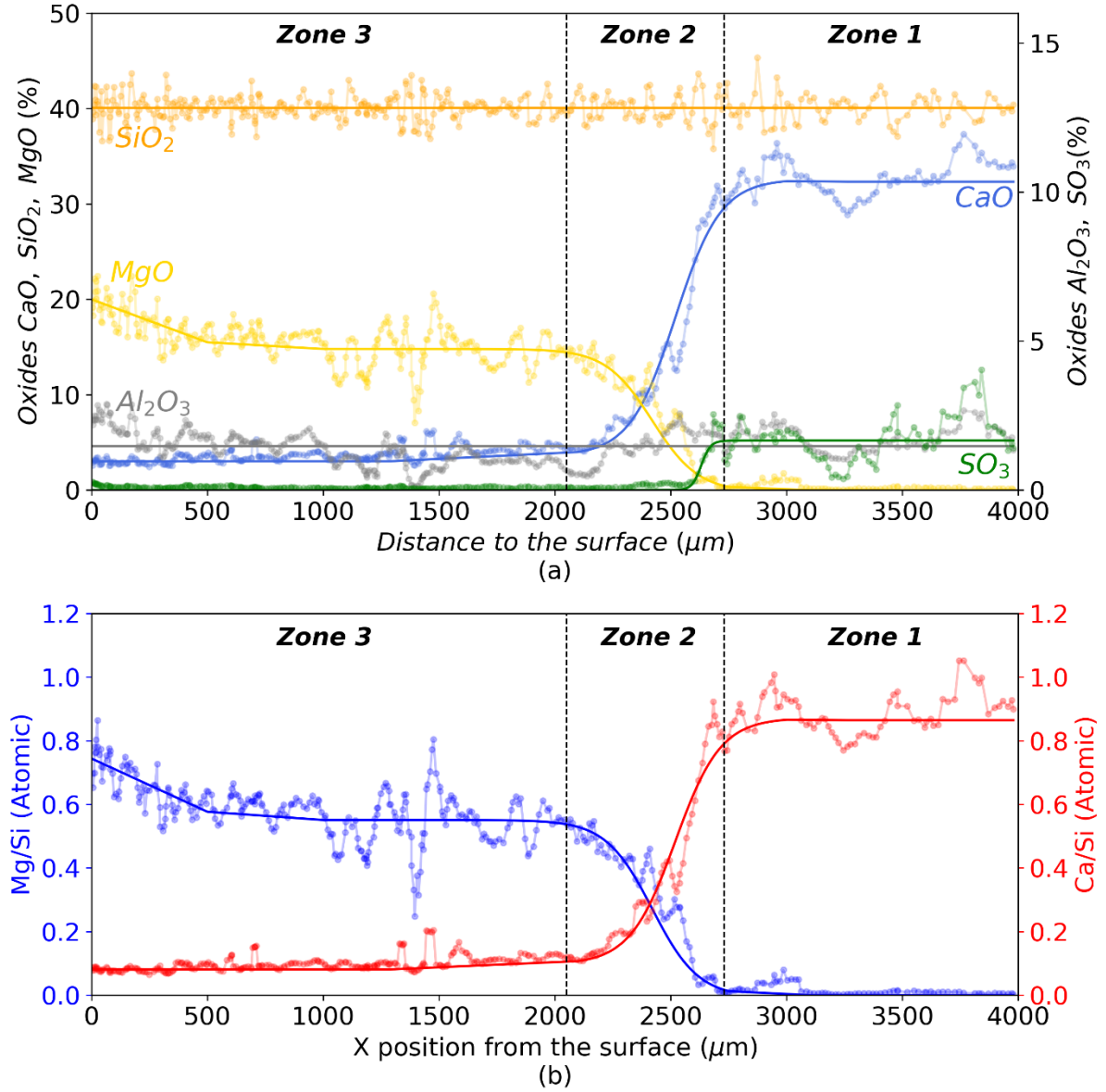

Figure C-5: (a) Chemical composition of oxides of a low-pH model cement paste, immersed in solution with [$MgCl_2$] = 50 mmol/L for 6 months according to the distance to the surface of the specimen (analysis by electron microprobe, corrected), (b) M/S and C/S atomic ratios calculated from (a). The lines represent an approximation of the signal for future calculations.

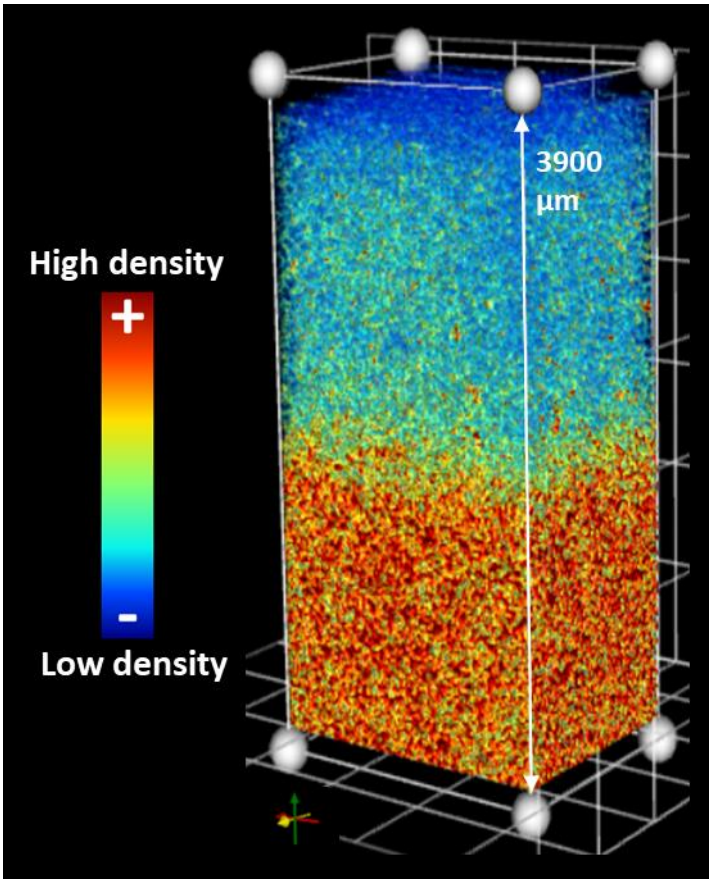

Figure C-6: 3D visualisation of the density after micro-tomography measurements for a low-pH model cement paste, immersed in solution with [$MgCl_2$] = 50 mmol/L for 6 months

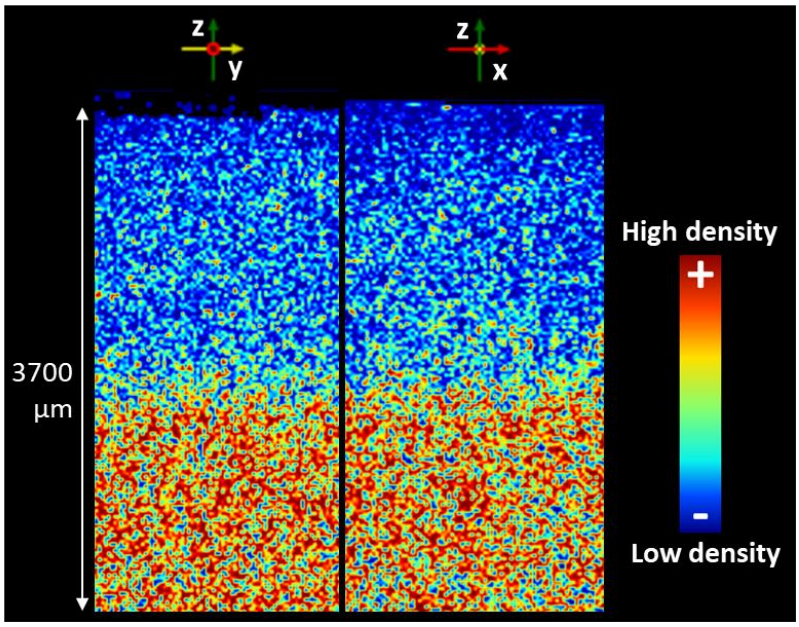

Figure C-7: 2D visualisation of the density after micro-tomography measurements for low-pH model cement paste, immersed in solution with [$MgCl_2$] = 50 mmol/L for 6 months

Table C-1: Average Specific Surface B.E.T (m^2/g) determined by N_2 Physisorption of the sound model cement paste, a degraded sample and a M-S-H paste.

Type of sample	Sound model cement paste	Degraded model cement paste		M-S-H paste, M/S=0.78
Zone	-	Sound Zone (Z1)	Surface (Z2-Z3)	-
Average Specific Surface B.E.T (m^2/g)	36.2	41.7	532.1	562.9

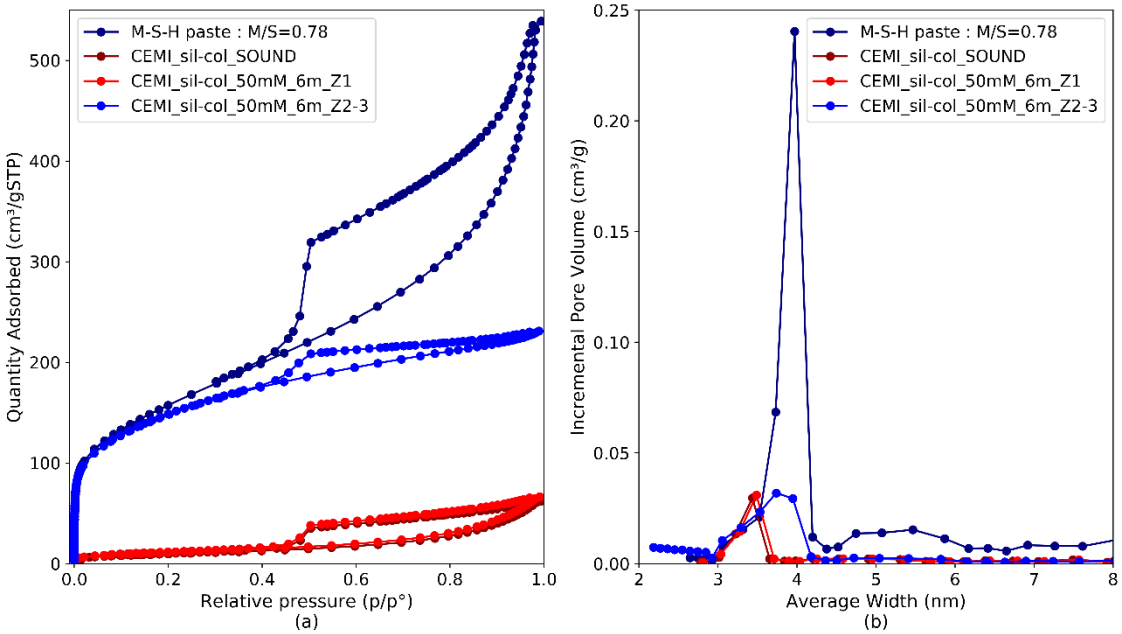

Figure C-8: (a) N_2 adsorption-desorption isotherms of the sound zone and degraded zone, compared to a pure M-S-H paste (M/S=0.78) (Dewitte et al. 2022) and (b) Associated pore size distributions (BJH). Z1 = Zone 1 (sound zone) of the degraded paste, Z2-3 = Assembly of zones 2 and 3 (enriched in Mg) of the degraded paste (50 mM)

Appendix D. Multiphysics characterization of the 0 mM low-pH model cement degraded samples

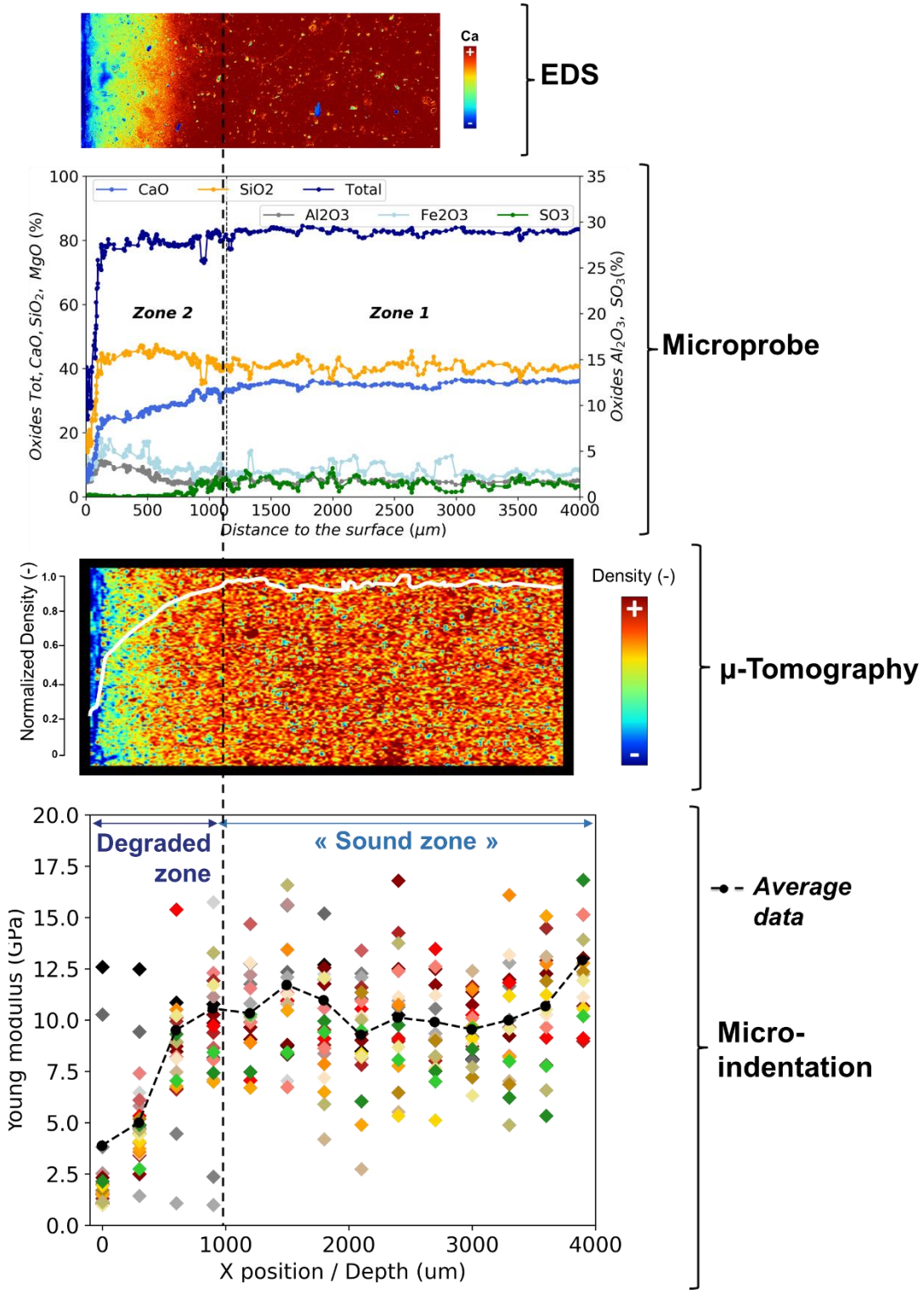

Figure D-1: Multi-physics characterization of low-pH model cement paste immerged during 4 months in pure water

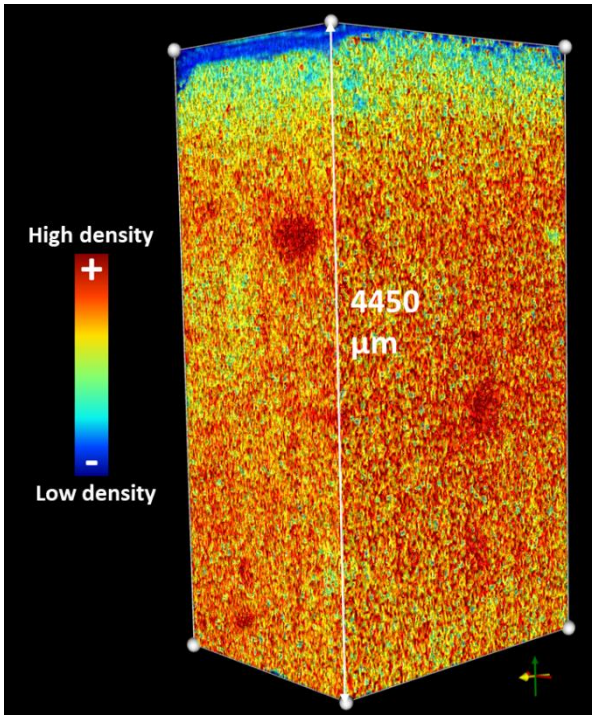

Figure D-2: 3D visualisation of the density after micro-tomography measurements for low-pH model cement paste, immersed in pure water for 4 months

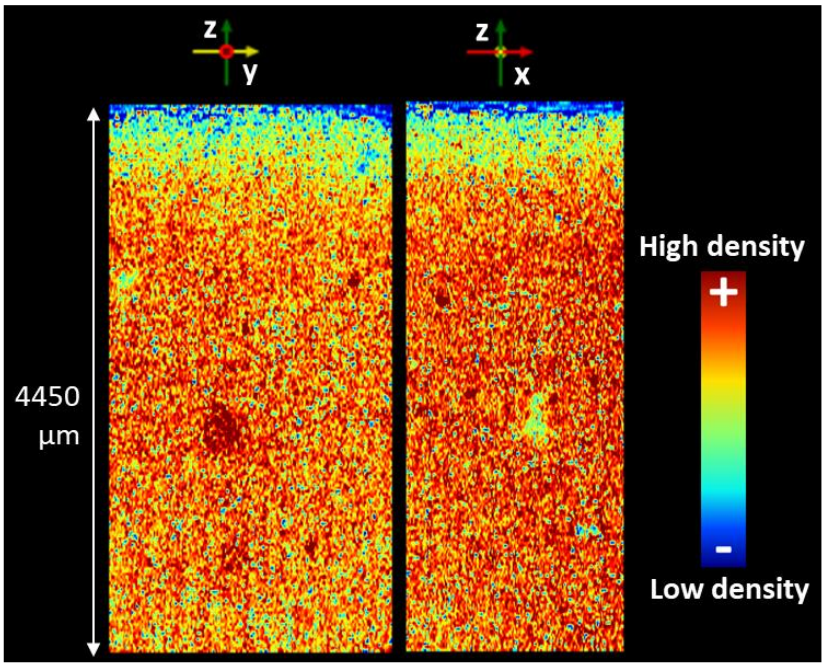

Figure D-3: 2D visualisation of the density after micro-tomography measurements for low-pH model cement paste, immersed in pure water for 4 months

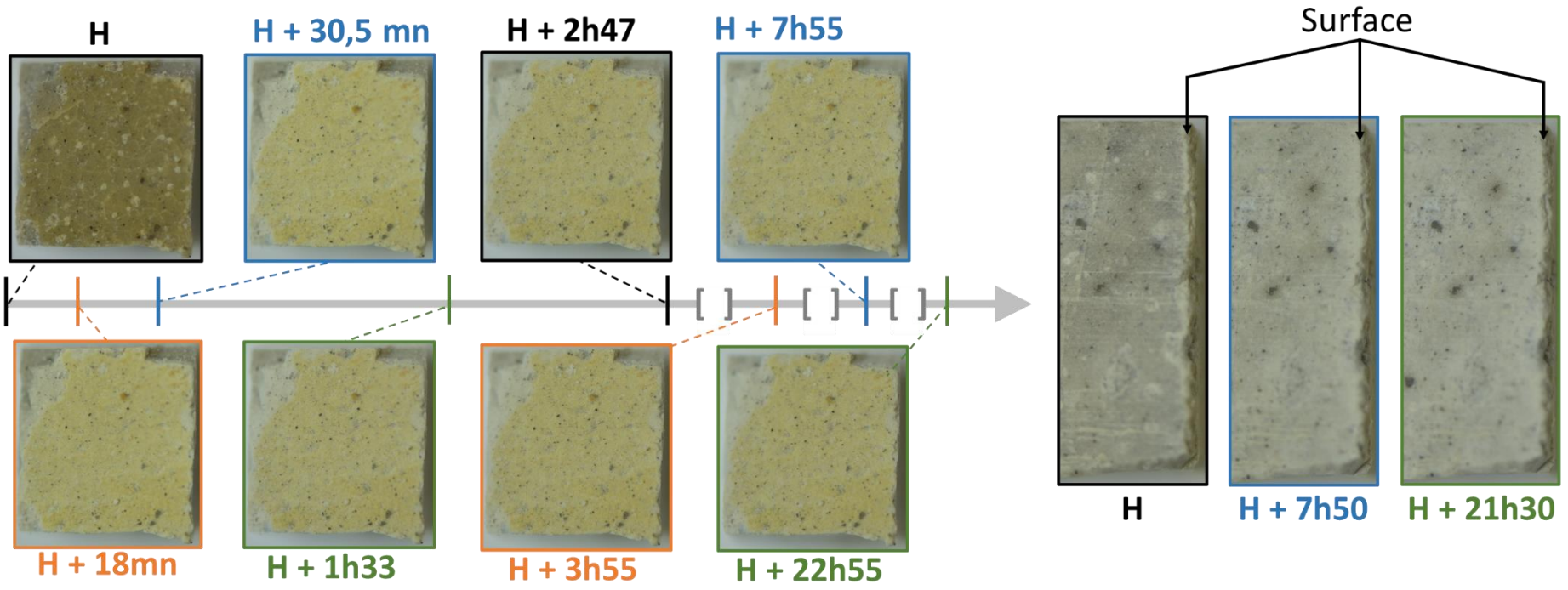

Figure D-4: Follow-up (visual) cracking test during exposure to a controlled atmosphere (20°C, RH=50%) on the low-pH model cement paste immersed in pure water during 4 months

Appendix E. Multiphysics characterization of the industrial low-pH cement paste immersed in 50 mM $MgCl_2$ during 4 months

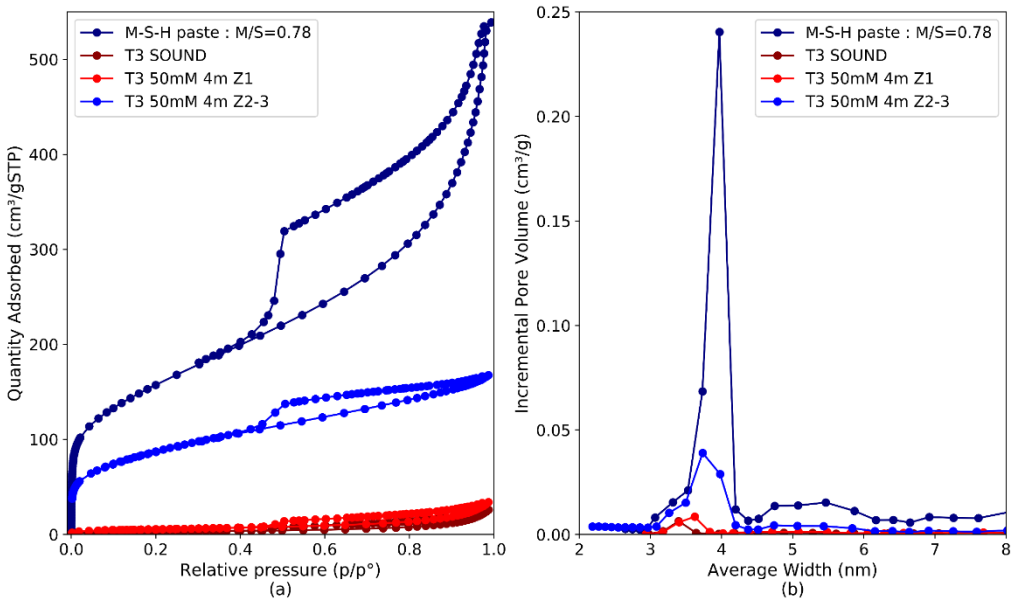

Figure E-1: (a) N_2 adsorption-desorption isotherms of the sound zone (Z1) and degraded zone (Z2-3), compared to the sound material and a pure M-S-H paste (M/S=0.78) and (b) Associated pore size distributions (BJH). Z1 = Zone 1 (sound zone) of the degraded paste, Z2-3 = Assembly of zones 2 and 3 (enriched in Mg) of the degraded paste

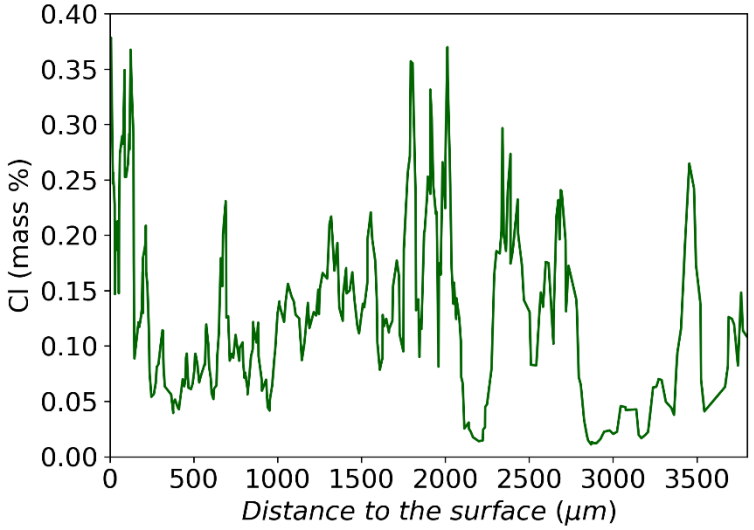

Figure E-2: Cl mass % of a low-pH industrial cement paste, immersed in solution with [$MgCl_2$]=50 mmol/L for 4 months according to the distance to the surface of the specimen (analysis by electron microprobe, corrected)

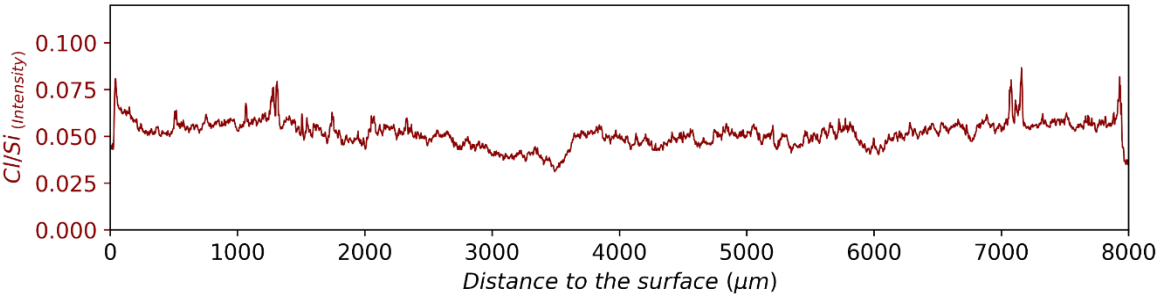

Figure E-3: Cl/Si intensity ratio % of a low-pH industrial cement paste, immersed in solution with [$MgCl_2$]=50 mmol/L for 4 months according to the distance to the surface of the specimen

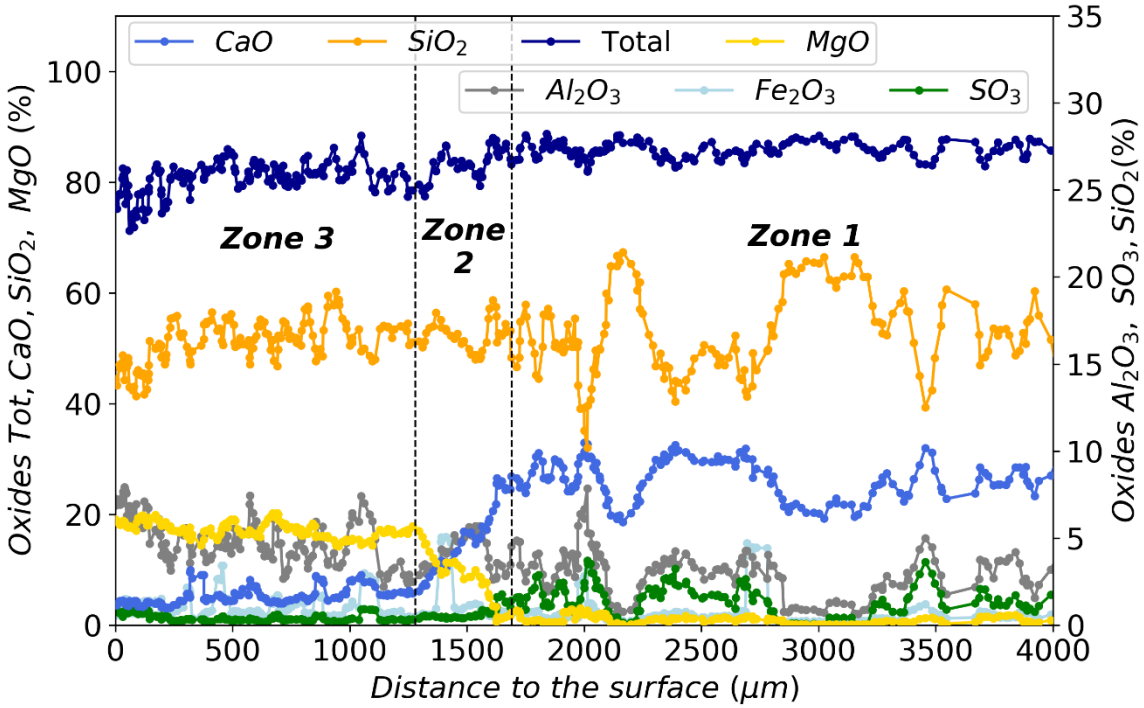

Figure E-4: Chemical composition of oxides of a low-pH industrial cement paste, immersed in solution with [$MgCl_2$] = 50 mmol/L during 4 months according to the distance to the surface of the specimen

Appendix F. Discussion about autoradiography reliability on the degraded cement pastes

1.1. Protocol

Autoradiography is a method to analyse the porosity of a sample. It is based on the measurement of the activity of a radioactive tracer in the sample (Sardini et al. 2006; Hellmuth, Siitari-Kauppi, et Lindberg 1993; Hellmuth, Lukkarinen, et Siitari-kauppi 1994; Sammaljärvi et al. 2016; Lalan et al. 2019). For the measurement to be successful, the tracer must completely penetrate the porous network of the sample. Usually used on rock materials (Hellmuth, Siitari-Kauppi, et Lindberg 1993; Hellmuth, Lukkarinen, et Siitari-kauppi 1994; Hellmuth et al. 1999; Voutilainen et al. 2019; Sardini et al. 2006), this technique is more and more used on cementitious materials (Neji et al. 2022) and on the interface between the two materials (Lalan et al. 2019; Gaboreau et al. 2011). According to the work of Lalan (Lalan et al. 2019), the results of autoradiography give similar results to those of water porosity. This technique was therefore chosen to complement the multi-physics characterization method. Given the shrinkage properties observed on the degraded pastes and the fragility of the samples, the usual methods of drying the samples (by freeze drying) were impossible without causing the separation of the degraded zone from the sound zone. In the case of a separation of the two zones, the analysis of the gradient of properties is impossible. The autoradiography protocol is divided into four steps:

1) Samples were put under vacuum in a freeze dryer (M-S-H pastes) or at room temperature (cement pastes) during five days.
2) Samples were impregnated with C-14 methylmethacrylate under vacuum during 30 days (cement pastes) to 69 days (M-S-H pastes). For the cement pastes, some Lumogen Red F305 fluorophore was added to the impregnation mixture for possible STED analysis.
3) Samples were polymerized by irradiation (≈ 4 days).
4) Samples were sawed, polished and autoradiographed.

Autoradiography on M-S-H pastes gave satisfactory results (Chapter 3). The porosity of the M-S-H pastes determined by autoradiography was between the values obtained by helium pycnometry and water saturation. The following sections propose a discussion about the results on the degraded cement paste.

1.2. Discussion

To calculate the porosity of a material by autoradiography, it is necessary to know its true density. As a reminder, the equation is the following:

$$\varepsilon = \frac{\frac{\rho_r}{\rho_0}}{1 + \left(\frac{\rho_r}{\rho_0} - 1\right) * \frac{A}{A_0}} * \frac{A}{A_0} \qquad \text{(F-1)}$$

with ε the porosity of the sample, ρ_r in g/cm^3 the true density of the material, ρ_0 in g/cm^3 the density of the resin, A the activity of the sample (Bq/ml) and A_0 the activity of the tracer (Bq/ml).

Micro-tomography only gives access to the bulk density. The true density is measured with a helium pycnometer, but it is necessary to have a sufficient quantity of sample. In the case of degraded cementitious pastes, priority was given to measurements by N_2 Physisorption and MIP. The remaining amount of degraded zone did not allow for true density measurements. As part of

the simulation of the mechanical properties along the sample from the microprobe data and the microstructural properties of the sound zone (see 4.5), the true density, bulk density and open porosity were simulated along the sample (Figure F-1, Figure F-2 and Figure F-3).

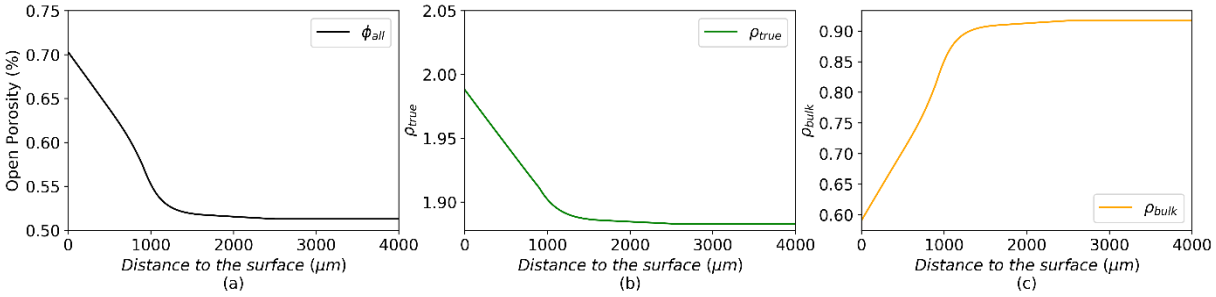

Figure F-1: Open porosity (%) (a), true density (b) and bulk density (c) calculated from the simulation of the low-pH model cement sample degraded during 4 months in pure water (0 mM)

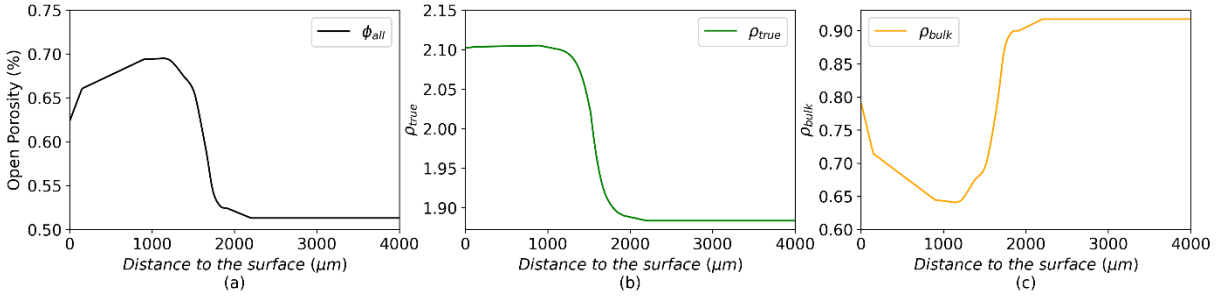

Figure F-2: Open porosity (%) (a), true density (b) and bulk density (c) calculated from the simulation of the low-pH model cement sample degraded during 6 months in pure water (5 mM)

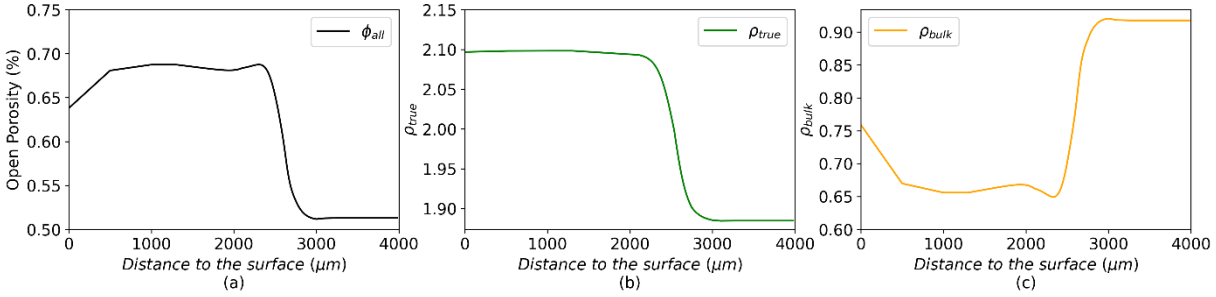

Figure F-3: Open porosity (%) (a), true density (b) and bulk density (c) calculated from the simulation of the low-pH model cement sample degraded during 6 months in pure water (50 mM)

The open porosity profile calculated from the simulation shows a porosity of about 51.5% in the sound zone and 68% in the degraded zone for the 5 mM and 50 mM degraded samples (Figure F-2a and Figure F-3a). As one of the inputs to the model is the porosity of the sound zone, it is logical to find the value of the measured water porosity. The shape of the curve is consistent with the micro-tomography results (4.4.3, Figure 4-23). As the density is inversely proportional to the porosity, the variation is similar. For the pure leached sample, the open porosity (Figure F-1a) increases until the surface, as the density decrease in micro-tomography (Figure 5-7).

The simulated true density shows two steps for 5 mM and 50 mM. In the sound zone, the simulated value is very close to that measured on the sound material in helium pycnometry (1.9, see 4.2.2).

In the degraded zone, it rises to about 2.10, in agreement with what is measured on M-S-H pastes (2.25, see Chapter 3). The variation is therefore consistent.

The simulated bulk density (Figure F-1c, Figure F-2c and Figure F-3c) is comparable to the density from micro-tomography. The shape of the curve is the same. The simulated bulk density in the sound zone is close to that measured by hydrostatic measurement (1.1 versus 0.9 with simulation).

As the simulation gives consistent results, the true density considered in the autoradiography calculations is 1.919 (ρ_s) in the sound zone (true measurement) and 1.11*ρ_s or 1.06*ρ_s (i.e. 2.13 or 2.03) for Mg attacked samples and leached sample respectively. 1.11 and 1.06 correspond to the ratio between the true density of the sound zone and the degraded zone from the simulation for Mg attacked samples and leached sample respectively. In the transition zone (Z2 EDS), the density is considered to vary linearly between these two extremes. This zone was determined on the initial intensity graphs by the area where the average intensity per column of pixels varies linearly between the two levels of the sound and degraded zones.

The porosity maps and profiles obtained by averaging each pixel column for the low-pH model cement pastes degraded in 50 mM $MgCl_2$ solutions or in pure water (0 mM) are respectively presented in Figure F-4, Figure F-5, Figure F-6 and Figure F-7. The same figures are available for the 5 mM samples in Appendix B.

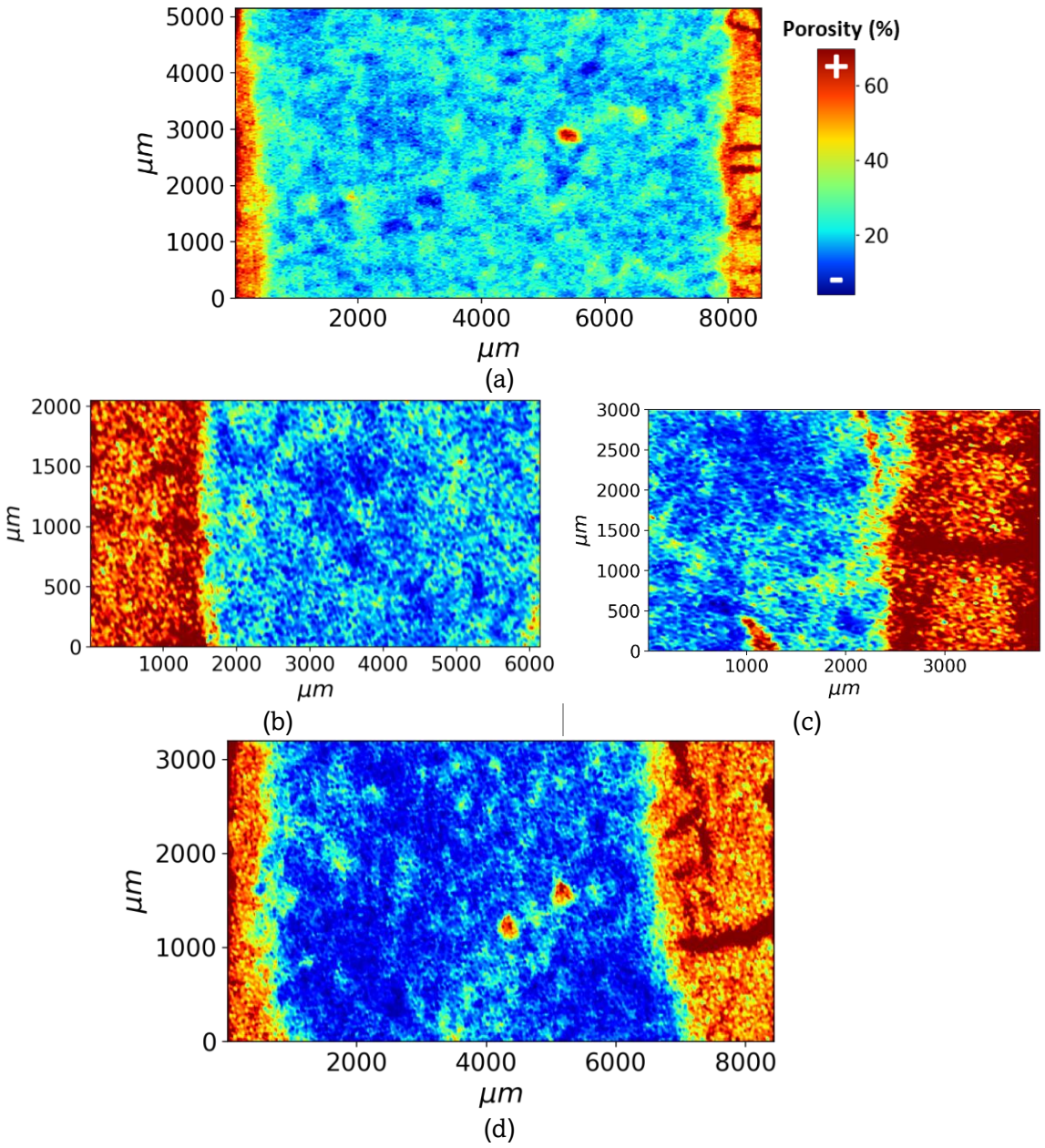

Figure F-4: Porosity maps after autoradiography characterization of low-pH model cement samples degraded during 2 months (a), 4 months (b) and 6 months (c) in 50 mM [$MgCl_2$] solution

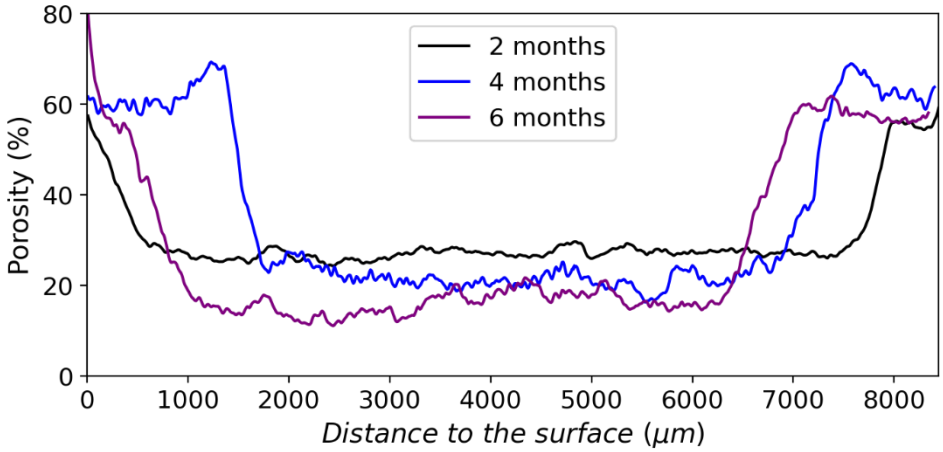

Figure F-5: Porosity profiles after autoradiography characterization of low-pH model cement samples degraded during 2 months, 4 months and 6 months in 50 mM [$MgCl_2$] solution

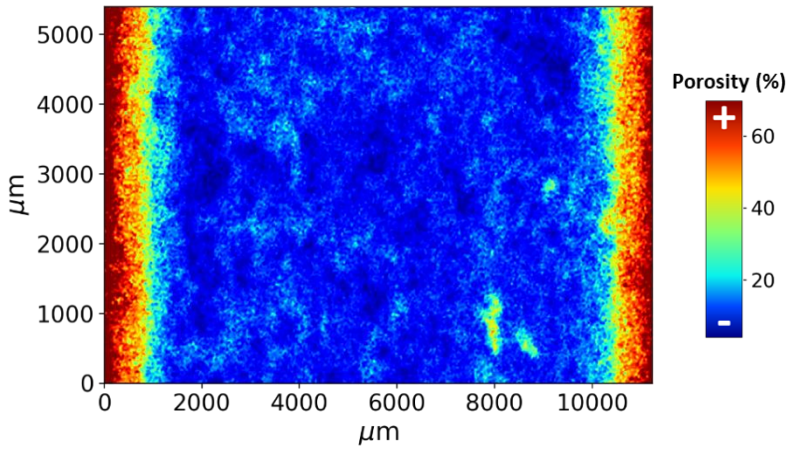

Figure F-6: Porosity map after autoradiography characterization of low-pH model cement samples degraded during 4 months in pure water

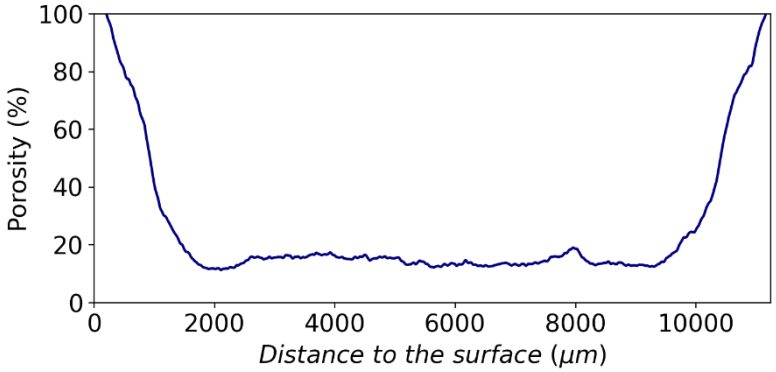

Figure F-7: Porosity profiles after autoradiography characterization of low-pH model cement samples degraded during 4 months in pure water

Overall, the porosity determined by autoradiography in the sound zone (Table F-1) remained below the values obtained by the other techniques on the sound sample (see 4.2, Table 4-4). The

values measured in the sound zone varies depending on the sample. It appears that the porosity measured in the sound zone decreases with increasing degradation time.

Table F-1 : Porosity in the sound zone in the degraded low-pH model cement pastes

	0 mM	5 mM			50 mM		
Degradation time (months)	4	2	4	6	2	4	6
Porosity (%)	14.7	28.7	17	15.3	26.4	22	15.4

The source of such a difference with the 51.5% value obtained by water porosity seems to be the partial penetration of the tracer. Indeed, there are several differences between the protocol used for the M-S-H pastes and the cementitious pastes: the vacuum machine for drying (freeze dryer or dessicator), the duration of the impregnation (30 days against 69 days) and the presence or absence of Lumogen Red F305 fluorophore in the mixture. The machine used to dry the samples may be important as the vacuum and temperature are not identical. The duration of impregnation is very important. If it is too short, the tracer does not penetrate everywhere. If it is too long, the porosity can be underestimated due to a larger amount of the autoradiograph shifts to the saturation range (Hellmuth, Lukkarinen, et Siitari-kauppi 1994; Lalan et al. 2019; Siitari-Kauppi 2002; Sammartino et al. 2002). The association of Lumogen Red F305 with the tracer is recent. The study by Hellmuth et al. (Hellmuth et al. 2021) focuses on the use of the Lumogen for STED. It is not noted that the addition of Lumogen to the mixture does not alter the autoradiography results. Furthermore, no sound rock samples are used as control samples, i.e. without fluorophore. Only a damaged, and therefore inhomogeneous, sample has no fluorophore in the impregnation solution. All these differences could explain the results obtained on degraded cementitious pastes. In conclusion, the lack of drying, the incorporation of another substance in the penetration solution and the short impregnation time (1 month) may imply a partial penetration of the tracer into the samples.

The degraded area shows a high shrinkage phenomenon and a low bulk density. Drying could be effective in this zone but in the sound zone it does not seem to be sufficient. It seems possible that the tracer penetrates correctly in the degraded zone since it shows a porosity similar to the one obtained from the simulations. In the sound zone, however, the results do not seem to be consistent.

To see if the underestimation of the porosity in the sound zone was due to the density value used in the calculations, a statistical study was performed. Figure F-8 shows the results. The change in density modifies the porosity but not enough to explain the difference with other porosity measurement techniques.

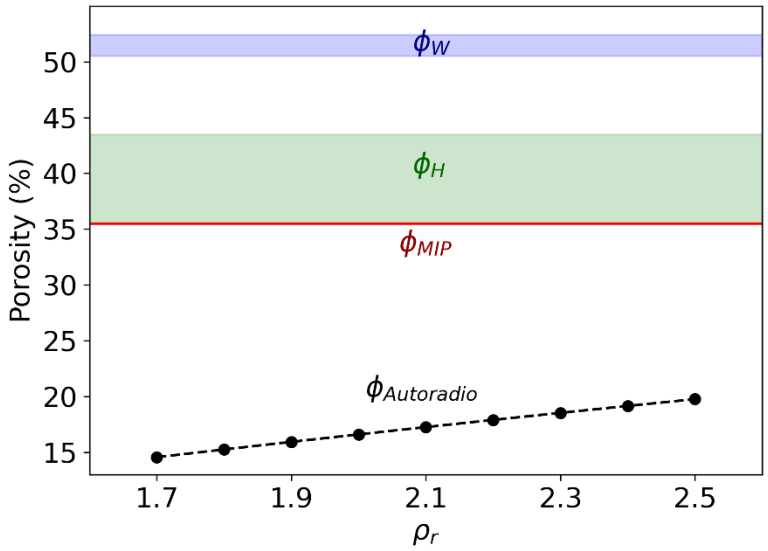

Figure F-8: Statistical study of the impact of density value considered for autoradiography calculations on the porosity in the sound zone of the low-pH model cement paste degraded during 6 months in 50 mM of $MgCl_2$

Thus, data from the sound zone will not be used. For future studies where the samples are as fragile as the ones in this thesis, it will be necessary to design a protocol to better dry or impregnate the samples. Drying by solvent exchange, making a suitable sample holder during drying or a longer impregnation could be tested. It would also be interesting to carry out a study to check that the Lumogen does not limit the penetration of the solvent.

1.3. Results in the degraded zone

As in EDS, cracks appear on the autoradiographs (red zones on Figure F-4). To evaluate the impact of the cracking on the microstructural profile along the degradation depth, the 2D results of the sample degraded in 5 mM during 6 months were separated in two zones: a zone without a crack (ZA, Figure F-9a) and a zone with a vertical crack (ZB, Figure F-9b). Porosity profiles along the degradation were obtained by averaging each pixel column and are given on Figure F-10. The influence of the crack appears very clearly on the profiles. At the limit of the sound zone and the degraded zone, the cracked zone (ZB) shows a porosity peak contrary to ZA. Beyond the effect of the crack, the porosity of the degraded area in zones A and B is similar.

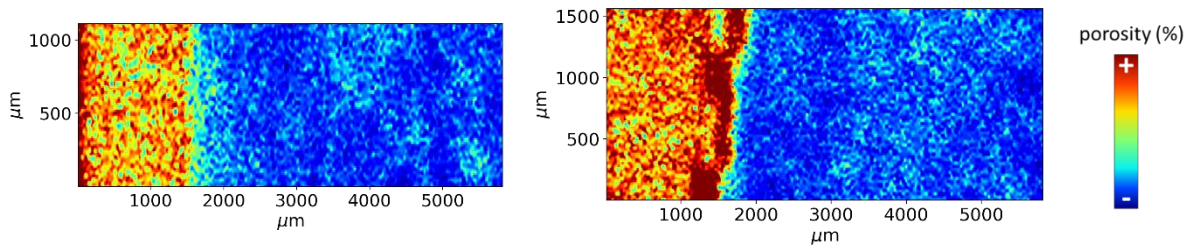

(a) (b)

Figure F-9 : Porosity maps after autoradiography characterization of model cement samples degraded during 6 months of zone A (a) and zone B (b)

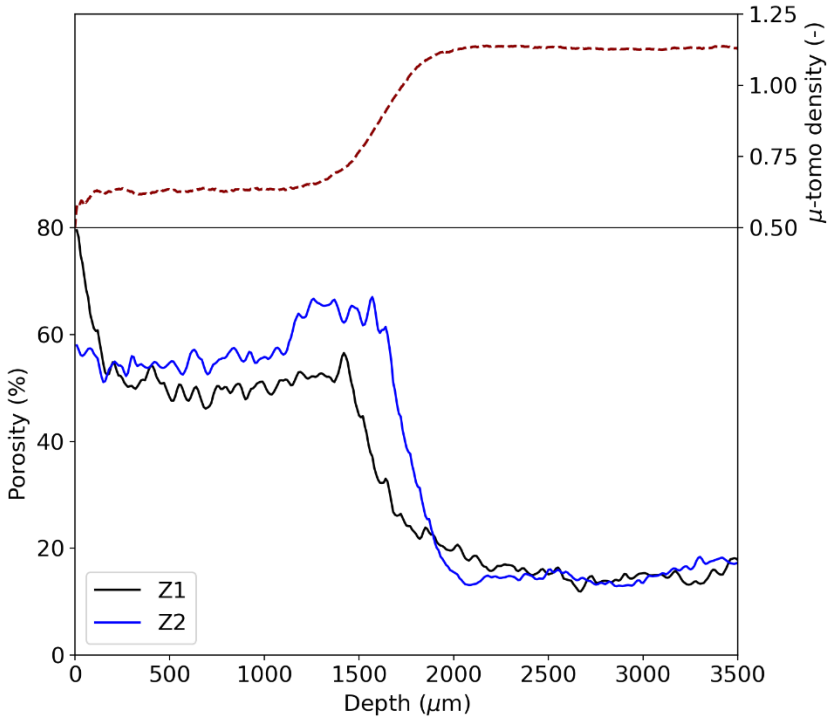

Figure F-10 : Porosity profiles after autoradiography characterization and micro-tomography density for samples degraded 6 months

For the pastes subjected to magnesium attack, the porosity of the degraded zone is about 62% (mean value of all tested pastes), slightly below the 70% predicted by the simulation, but it remains higher than that measured in the sound zone (51.5%). Beyond the value of the porosity in the sound zone, the porosity profile is well reversed compared to the apparent density profile observed in micro-tomography (Figure F-10 top). The normalized density obtained in micro-tomography has been multiplied by the measured apparent density of the sound zone by hydrostatic weighing. In conclusion, the magnesium attack seems to imply an increase of the porosity in the degraded zone despite the formation of M-S-H. This confirms previous results.

Appendix G. Chemical simulation

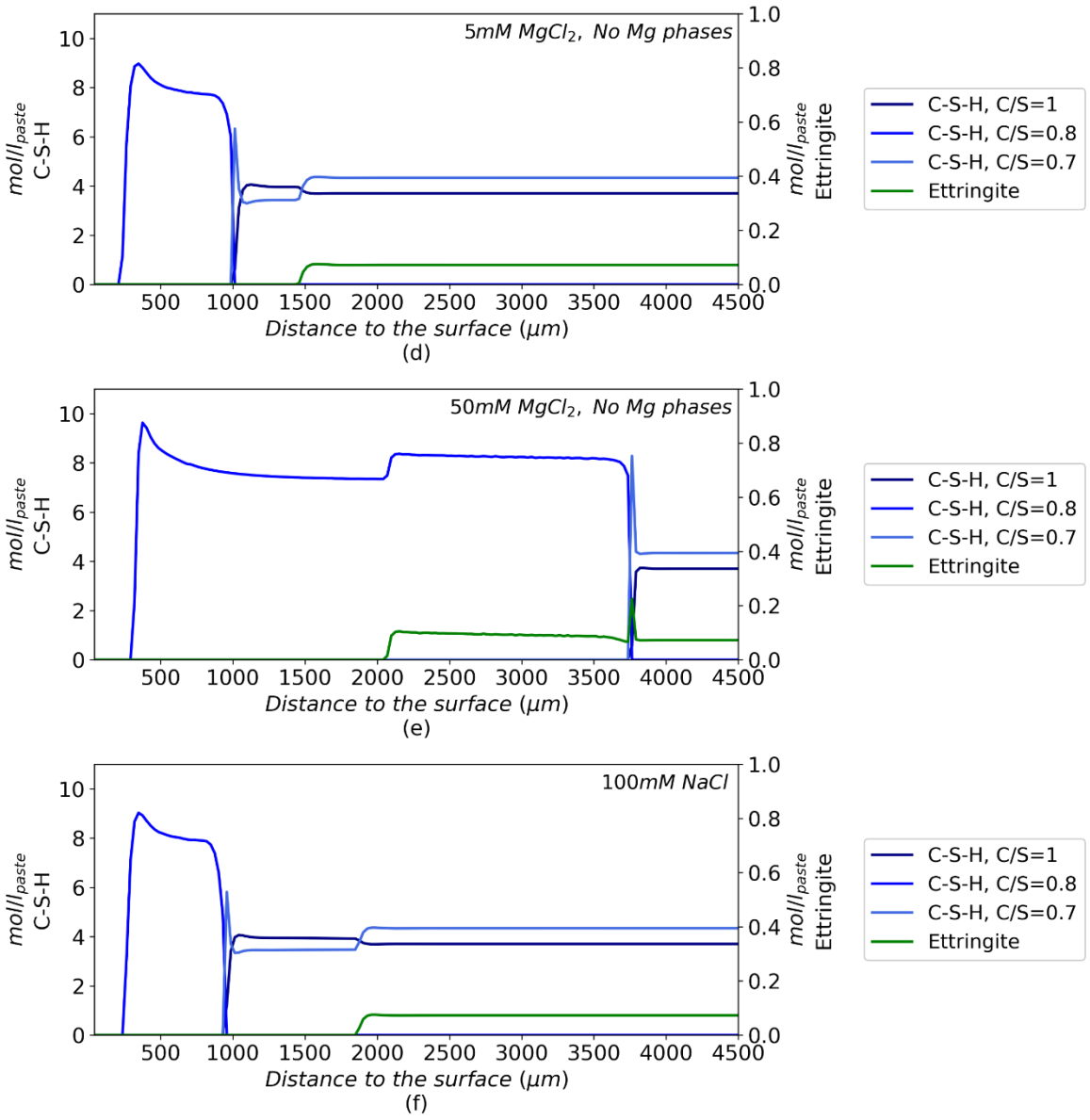

Figure G-1: Hytec simulation of a 1D degradation of model low-pH cement paste in (a) 5 mM and (b) 50 mM of $MgCl_2$, without allowing the precipitation of Mg phases

Appendix H. Product data sheet of CEMI 52.5 N

LAFARGE CIMENTS
Usine de VAL D'AZERGUES

CEM I 52,5 N CE PM-ES-CP2 NF

NF EN 197-1 NF P 15-317 NF P 15-318 NF P 15-319

NF EN 196-10

Fiche produit technique

CE NF

N°de certificat CE : 0333-CPD-4102

• Constituants et composition du ciment

Principaux (%)		Secondaires (%)		Sulfate de calcium (%)		Additifs sur sec (%)		
Clinker	99	Filler (F)	1	Gypse	4	Agent de mouture	ADM 72	0,01
C3S	64,4					Agent réducteur de CR VI	Sulfate de Fer	0,5
C3A	1,4					Agent de mouture	AMA5	0,5
C4AF	15,3							

• Caractéristiques physiques et mécaniques

	Valeur usine	Limites applicables à chacun des résultats (Réf : NF EN 197-1)		Limites applicables à chacun des résultats (Réf : annexe 1 du règlement de certification NF002)	
	moyenne	minimum	maximum	minimum	maximum
Résistance à la compression 1 jour (MPa)	21,3				
Résistance à la compression 2 jours (MPa)	34,1	18,0		18	
Résistance à la compression 7 jours (MPa)	48,5				
Résistance à la compression 28 jours (MPa)	63	50,0		50	
Retrait à 28 jours (µm/m)	548				
Début de prise (min)	182	40		60	
Stabilité (mm)	1,2		10		5
Masse volumique (g/cm3)	3,19				
Surface spécifique Blaine (cm²/g)	3583				
Q12h (J/g)	214				
Q41h (J/g)	305				
L*	57				

• Caractéristiques chimiques (%)

MAXI : Valeurs limites applicables à chacun des résultats (Réf : NF EN 197-1, NF P 15-318, NF P 15-317, NF P 15-319)

	Valeur usine moyenne	MAXI		Valeur usine moyenne	MAXI		Valeur usine moyenne	MAXI
SiO2	20,6		S– <	0,01	0,20	Insolubles	0,41	0,75
Al2O3	3,60		Cl-	0,06	0,10	CO2	0,90	
Fe2O3	5,00		Perte au feu	1,10	3,00	CaO libre	1,60	
CaO	64,3		TiO2	ND			Valeur usine moyenne	Coef var (%)
MgO	0,70	3,00	MnO	ND				
K2O	0,70		P2O5	0,40				
Na2O	0,20		Non dosé	0,63		Na2OEq	0,6	
SO3	2,70	3,00						
Total : 100								

Ces valeurs, extraites de notre autocontrôle, permettent de vérifier la conformité de notre produit aux spécifications normatives et donnent une indication pour les caractéristiques complémentaires. Elles ne constituent pas un engagement sur les résultats à venir.

■ : Caractéristique modifiée / fiche précédente ND : non dosé *Révision du 06/02/2012*